Nano Active Stabilization of samples for tomography experiments: A mechatronic design approach

PhD Thesis

by

Dehaeze Thomas

A thesis submitted in partial fulfillment of the requirements for the degree of Doctor of Philosophy (PhD) in Engineering Science

at

Liège Université

Members of the Examination Committee

Prof. Loïc Salles (President of the Committee)
University of Liège (Liège, Belgium)

Prof. Christophe Collette (Supervisor)
University of Liège (Liège, Belgium)

Prof. Olivier Bruls
University of Liège (Liège, Belgium)

Dr. Jonathan Kelly
Diamond Light Source (Oxfordshire, United Kingdom)

Prof. Gérard Scorletti
École Centrale de Lyon, Laboratoire Ampère (Écully, France)

Dr. Olivier Mathon
European Synchrotron Radiation Facility (Grenoble, France)

Abstract

The 4^{th} generation synchrotron light sources have yielded X-ray beams with a 100-fold increase in brightness and sub-micron focusing capabilities, offering unprecedented scientific opportunities while requiring end-stations with enhanced sample positioning accuracy. At the European Synchrotron (ESRF), the ID31 beamline features an end-station for positioning samples along complex trajectories. However, its micrometer-range accuracy, limited by thermal drifts and mechanical vibrations, prevents maintaining the point of interest on the focused beam during experiments.

To address this limitation, this thesis aims to develop a system for actively stabilizing the sample's position down to the nanometer range while the end-station moves the sample through the beam. The developed system integrates an external metrology for sample position measurement, an active stabilization stage mounted between the end-station and the sample, and a dedicated control architecture. The design of this system presented key challenges, first of which involved the design process. To effectively predict how this complex mechatronic system would perform, a series of dynamical models with increasing accuracy were employed. These models allowed simulation of the system's behavior at different design stages, identifying potential weaknesses early on before physical construction, ultimately leading to a design that fully satisfies the requirements. The second challenge stems from control requirements, specifically the need to stabilize samples with masses from 1 to 50 kg, which required the development of specialized robust control architectures. Finally, the developed Nano Active Stabilization System underwent thorough experimental validation on the ID31 beamline, validating both its performance and the underlying concept.

Résumé

L'avènement des sources de lumière synchrotron de $4^{ème}$ génération a produit des faisceaux de rayons X avec une luminosité multipliée par 100 et des capacités de focalisation sub-microniques, offrant des opportunités scientifiques sans précédent tout en nécessitant des stations expérimentales avec une précision de positionnement d'échantillons améliorée. À l'Installation Européenne de Rayonnement Synchrotron (ESRF), la ligne de lumière ID31 dispose d'une station expérimentale conçue pour positionner des échantillons le long de trajectoires complexes. Cependant, sa précision de l'ordre du micromètre, limitée par des effets tels que les dérives thermiques et les vibrations mécaniques, empêche de maintenir le point d'intérêt sur le faisceau focalisé durant les expériences.

Pour remédier à cette limitation, cette thèse vise à développer un système permettant de stabiliser activement la position de l'échantillon pendant que la station expérimentale déplace l'échantillon à travers le faisceau. Le système développé intègre une métrologie externe pour la mesure de la position de l'échantillon, une platine de stabilisation active montée entre la station expérimentale et l'échantillon, et une architecture de contrôle dédiée. La conception de ce système présente des défis majeurs, dont le premier concerne le processus de conception lui-même. Pour prédire efficacement les performances, une série de modèles dynamiques ont été utilisés. Ces modèles ont permis de simuler le comportement du système aux différentes étapes de conception, identifiant ainsi les limitations potentielles, pour aboutir à une conception répondant aux spécifications. Le deuxième défi provient des exigences de contrôle, notamment la nécessité de stabiliser des échantillons dont la masse peut varier de 1 à 50 kg, ce qui a nécessité le développement d'architectures de contrôle robustes. Enfin, le Système de Stabilisation Active développé a fait l'objet d'une validation expérimentale sur la ligne de lumière ID31, validant à la fois ses performances et le concept sous-jacent.

Acknowledgments

First and foremost, I would like to express my deepest gratitude to my advisor, Professor Christophe Collette, for his constant support throughout this journey. His ability to challenge my thinking and dedication to mentoring my growth as a researcher has been invaluable. His door was always open, and he generously shared his time and expertise, providing feedback and guidance at every stage of the research process. Our discussions during the regular journeys between Liege and Brussels laboratories transformed routine travel into moments of scientific inspiration. His passion and dedication for research were truly inspiring, and I could not have wished for a better advisor.

I am honored that Professor Loïc Salles accepted the role of president of the jury for this thesis. My sincere appreciation goes to my thesis committee members, Professor Olivier Bruls and Professor Jean-Claude Golinval, for following my work and providing insightful advice through the years.

I extend my gratitude to the jury members: Dr. Jonathan Kelly, Professor Gérard Scorletti, Dr. Olivier Mathon and Professor Olivier Bruls for their willingness to participate in the examination committee of this doctoral thesis. Their time, expertise, and careful consideration of my work are greatly appreciated.

My time at the Precision Mechatronics Laboratory during the first two years of this project was enriched by interesting discussions and collaborations with Ahmad, Mohit, Jennifer, Vicente, Guoying, and Haidar. I am particularly grateful for the opportunity to have worked alongside such talented and dedicated individuals. Thank you, my friends, for making my stay in Belgium such a wonderful souvenir.

The subsequent five years at the ESRF were made possible by several key individuals: Veijo Honkimaki (ID31's Scientist), Michael Krisch (Head of the Instrumentation Division), Philippe Marion (Head of the Mechanical Engineering Group), Yves Dabin (Head of the Analysis and Modelling group), and Muriel Magnin-Mattenet (Mechanical Engineer in charge of ID31). I especially want to acknowledge their efforts in providing me with the resources, facilities, and technical expertise necessary to conduct my research at the ESRF.

The technical aspects of this work benefited greatly from various collaborations. I am grateful for the fruitful collaboration on mechanical design with Julien Bonnefoy and Damien Coulon. Special thanks to Philipp Brumund for his invaluable Finite Element Analysis expertise and constant encouragement to complete my PhD thesis. I am especially thankful to Marc Lesourd for introducing me to the world of vibration measurements and modal analysis, and Noel Levet for our interesting discussions about dimensional metrology and his tremendous support with the alignment of the developed instrument. The remarkable technical support from Pierrick Got and Kader Amraoui in electronics allowed smooth implementation of the developed system on the ID31 beamline. I also thank Hans Peter and Ludovic for granting me access to the outstanding mechatronics laboratory at the ESRF.

I am grateful to the master thesis students I had the chance to supervise: Adrien Jublan for his work on multi-body modelling, Youness Benyaklhef for his contribution to the metrology system and Caio Belle for his research on multi-variable control.

Finally, my profound thanks go to my family and close friends. To my father, who inspired me to pursue research, and my mother, whose unwavering support has been precious beyond words. And to Juliette, for being incredibly supportive through the inevitable tough times that are part of the PhD journey.

Reproducible Research

The foundation of this PhD thesis is built upon the principles of reproducible research. Reproducible research is the practice of ensuring that the results of a study can be independently verified by others using the original data, code, and documentation.

This approach was adopted to increase transparency and trust in the presented research findings. Furthermore, it is anticipated that the methods and data shared will facilitate knowledge transfer and reuse within the scientific community, thereby reducing research redundancy and increasing overall efficiency. It is hoped that some aspects of this work may be reused by the synchrotron community.

The fundamental objective has been to ensure that anyone should be capable of reproducing precisely the same results and figures as presented in this manuscript. To achieve this goal of reproducibility, comprehensive sharing of all elements has been implemented. This includes the mathematical models developed, raw experimental data collected, and scripts used to generate the figures.

For those wishing to engage with the reproducible aspects of this work, all data and code are freely accessible [33]. The organization of the code mirrors that of the manuscript, with corresponding chapters and sections. All materials have been made available under the MIT License, permitting free reuse.

This approach represents a modest contribution towards a more open, reliable, and collaborative scientific ecosystem.

The research presented in this manuscript has been possible thanks to the Fonds de la recherche scientifique (FRS-FNRS) through a FRIA grant given to Thomas Dehaeze.

Contents

I Introduction

1.1 Context of this thesis

Synchrotron radiation facilities are particle accelerators where electrons are accelerated to near the speed of light. As these electrons interact with magnetic fields, typically generated by insertion devices or bending magnets, they produce exceptionally bright light known as synchrotron light. This intense electromagnetic radiation, centered mainly in the X-ray spectrum domain, is subsequently used for the detailed study of matter. Approximately 70 synchrotron light sources are operational worldwide, some of which are indicated in Figure 1.1. This global distribution of such facilities underscores the significant utility of synchrotron light for the scientific community.

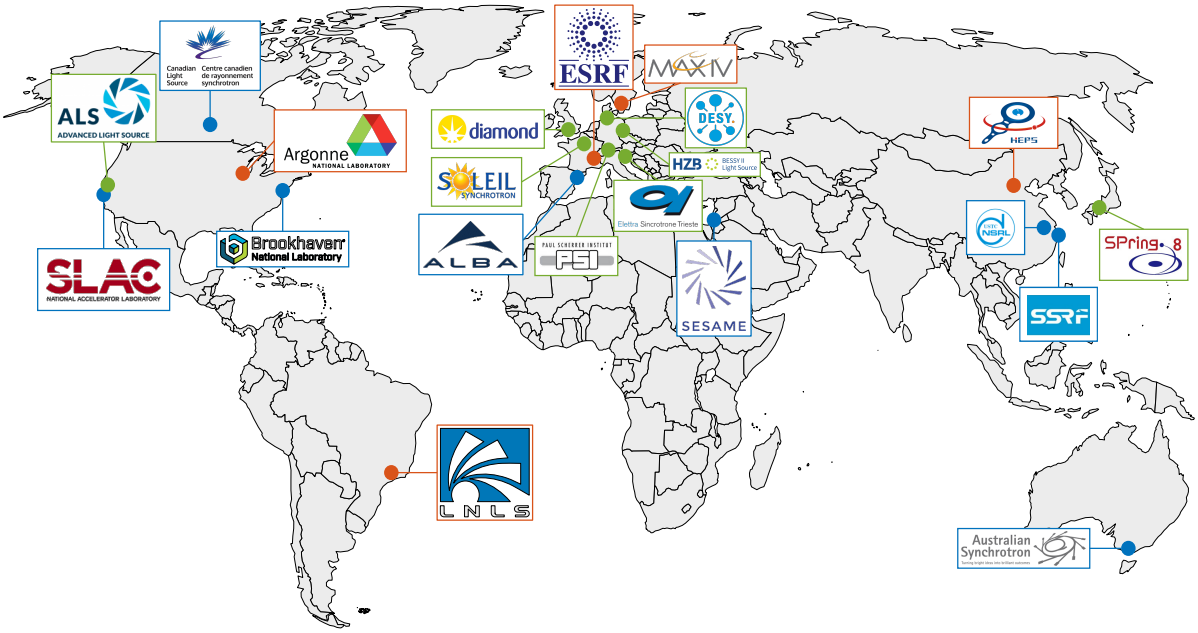

Figure 1.1: Major synchrotron radiation facilities in the world. 3rd generation Synchrotrons are shown in blue. Planned upgrades to 4th generation are shown in green, and 4th generation Synchrotrons in operation are shown in red.

These facilities fundamentally comprise two main parts: the accelerator and storage ring, where electron acceleration and light generation occur, and the beamlines, where the intense X-ray beams are conditioned and directed for experimental use.

The European Synchrotron Radiation Facility (ESRF), shown in Figure 1.2b, is a joint research institution supported by 19 partner nations. The ESRF started user operations in 1994 as the world's first third-generation synchrotron. Its accelerator complex, schematically depicted in Figure 1.2a, includes a linear accelerator where electrons are initially generated and accelerated, a booster synchrotron to further accelerate the electrons, and an 844-meter circumference storage ring where electrons are maintained in a stable orbit.

Synchrotron light is emitted in more than 40 beamlines surrounding the storage ring, each having specialized experimental stations. These beamlines host diverse instrumentation that enables a wide spectrum of scientific investigations, including structural biology, materials science, and study of matter under extreme conditions.

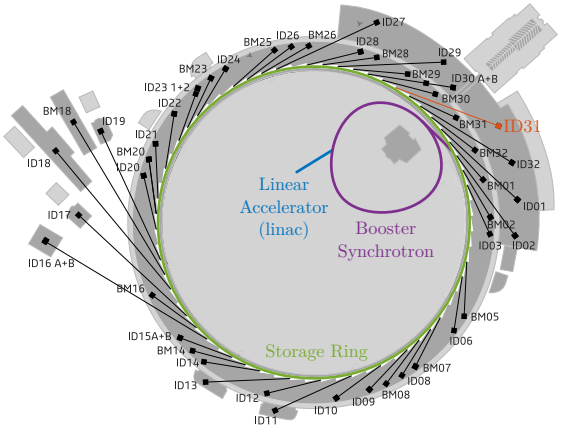

(a) Schematic of the ESRF. The linear accelerator is shown in blue, the booster synchrotron in purple and the storage ring in green. There are over 40 beamlines. The ID31 beamline is highlighted in red

(b) European Synchrotron Radiation Facility

Figure 1.2: Schematic (a) and picture (b) of the European Synchrotron Radiation Facility, situated in Grenoble, France.

In August 2020, following an extensive 20-month upgrade period, the ESRF inaugurated its Extremely Brilliant Source (EBS), establishing it as the world's premier fourth-generation synchrotron [120]. This upgrade implemented a novel storage ring concept that substantially increases the brilliance and coherence of the X-ray beams.

Brilliance, a measure of the photon flux, is a key figure of merit for synchrotron facilities. It experienced an approximate 30-fold increase with the implementation of EBS, as shown in the historical evolution depicted in Figure 1.3. While this enhanced beam quality presents unprecedented scientific opportunities, it concurrently introduces considerable engineering challenges, particularly regarding experimental instrumentation and sample positioning systems.

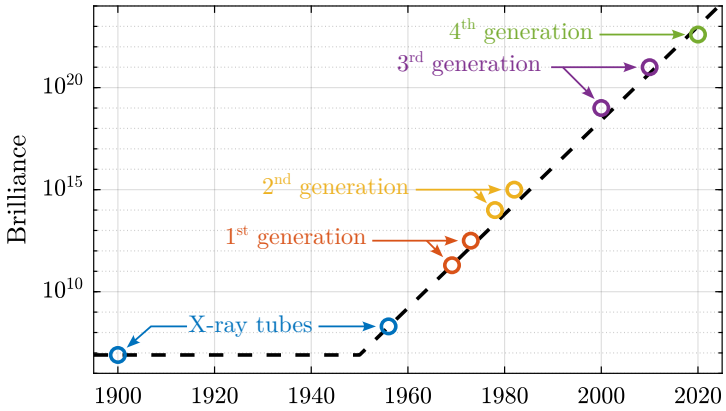

Figure 1.3: Evolution of the peak brilliance (expressed in photons/s/mm^2/mrad^2/0.1%BW) of synchrotron radiation facilities. Note the vertical logarithmic scale.

The ID31 ESRF Beamline

Each beamline begins with a "white" beam generated by the insertion device. This beam carries substantial power, typically exceeding kilowatts, and is generally unsuitable for direct application to samples.

The goal of the beamline is therefore to filter and shape the X-rays to the desired specifications using a series of optical elements such as absorbers, mirrors, slits, and monochromators. These components are housed in multiple Optical Hutches, as depicted in Figure 1.4.

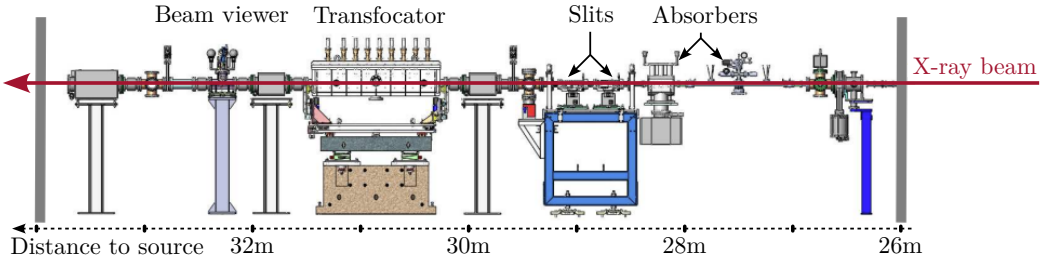

(a) OH1

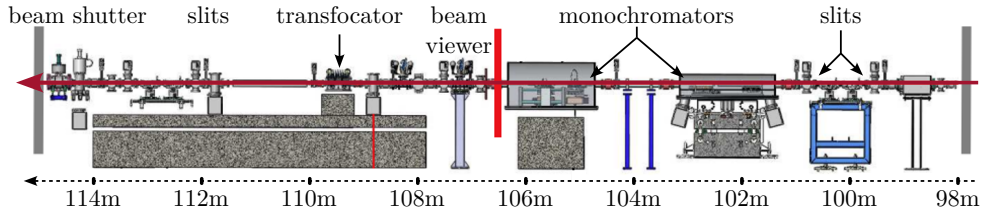

(b) OH2

Figure 1.4: Schematic of the two ID31 optical hutches: OH1 (a) and OH2 (b). Distance from the source (i.e. from the insertion device) is indicated in meters.

Following the optical hutches, the conditioned beam enters the Experimental Hutch (Figure 1.5a), where, for experiments pertinent to this work, focusing optics are used. The sample is mounted on a positioning stage, referred to as the "end-station", which enables precise alignment relative to the X-ray beam. Detectors are used to capture the X-rays beam after interaction with the sample.

Throughout this thesis, the standard ESRF coordinate system is adopted, wherein the X-axis aligns with the beam direction, Y is transverse horizontal, and Z is vertical upwards against gravity.

The specific end-station employed on the ID31 beamline is referred to as the "micro-station". As depicted in Figure 1.5b, it comprises a stack of positioning stages: a translation stage (in blue), a tilt stage (in red), a spindle for continuous rotation (in yellow), and a positioning hexapod (in purple). The sample itself (cyan), potentially housed within complex sample environments (e.g., for high pressure or extreme temperatures), is mounted on top of this assembly. Each stage serves distinct positioning functions; for example, the positioning hexapod enables fine static adjustments, while the T_y translation and R_z rotation stages are used for specific scanning applications.

The "stacked-stages" configuration of the micro-station provides high mobility, enabling diverse scientific experiments and imaging techniques. Two illustrative examples are provided.

Tomography experiments, schematically represented in Figure 1.6a, involve placing a sample in the X-ray beam path while controlling its vertical rotation angle using a dedicated stage. Detector images are captured at numerous rota-

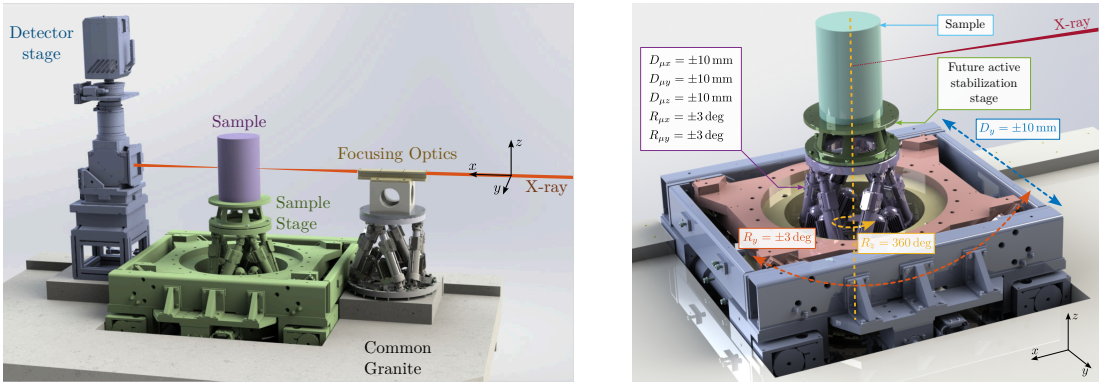

(a) Experimental Hutch **(b)** Micro-Station

Figure 1.5: 3D view of the ID31 Experimental Hutch (a). There are typically four main elements: the focusing optics in yellow, the sample stage in green, the sample itself in purple and the detector in blue. All these elements are fixed to the same granite. 3D view of the micro-station with associated degrees of freedom (b).

tion angles, allowing the reconstruction of three-dimensional sample structure (Figure 1.6b) [128]. This reconstruction depends critically on maintaining the sample's Point of Interest (PoI) within the beam during the rotation process.

Mapping or scanning experiments, depicted in Figure 1.7a, typically use focusing optics to have a small beam size at the sample's location. The sample is then translated perpendicular to the beam (along Y and Z axes), while data are collected at each position. An example [125] of a resulting two-dimensional map, acquired with 20 nm step increments, is shown in Figure 1.7b. The fidelity and resolution of such images are intrinsically linked to the focused beam size and the positioning precision of the sample relative to the focused beam. Positional instabilities, such as vibrations and thermal drifts, inevitably lead to blurring and distortion in the obtained image. Other advanced imaging modalities practiced on ID31 include reflectivity, diffraction tomography, and small/wide-angle X-ray scattering (SAXS/WAXS).

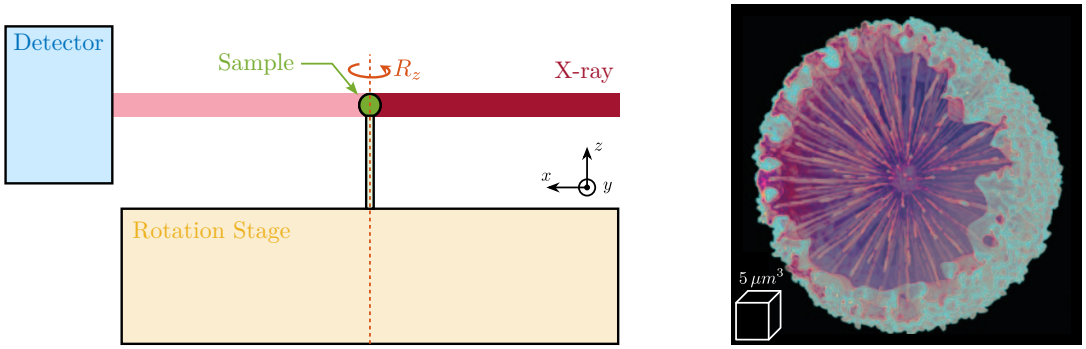

(a) Typical experimental setup for tomography experiment **(b)** Obtained image [128]

Figure 1.6: Example of a tomography experiment. The sample is rotated and images are taken at several angles (a). Example of one 3D image obtained using tomography (b).

Need of Accurate Positioning End-Stations with High Dynamics

Continuous progress in both synchrotron source technology and X-ray optics have led to the availability of smaller, more intense, and more stable X-ray beams. The ESRF-EBS upgrade, for instance, resulted in a significantly reduction of the

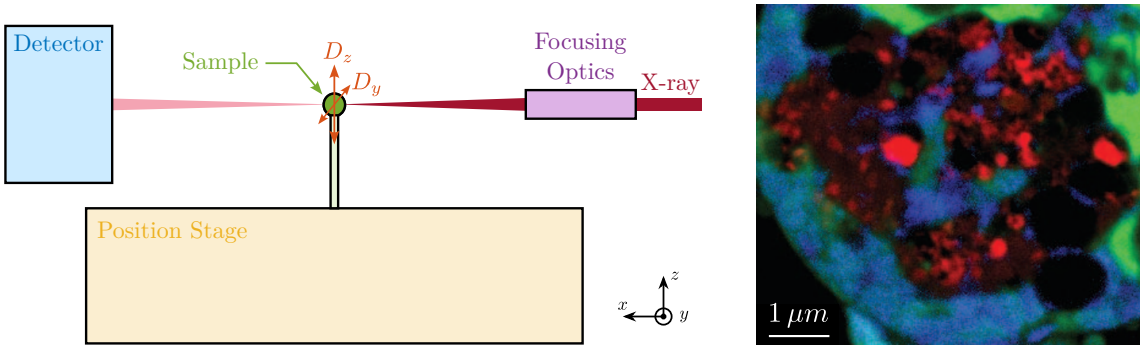

(a) Typical experimental setup for a scanning experiment **(b)** Obtained image [125]

Figure 1.7: Example of a scanning experiment. The sample is scanned in the YZ plane (a). Example of one 2D image obtained after scanning with a step size of 20 nm (b).

horizontal source size, coupled with a decrease of the beam horizontal divergence, leading to an increased brilliance, as illustrated in Figure 1.8.

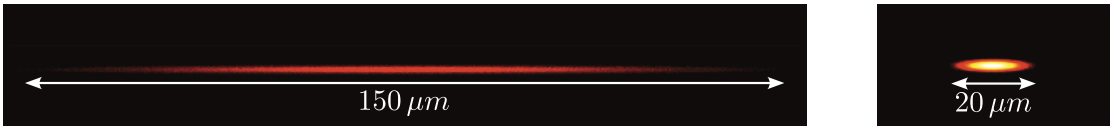

(a) 3^{rd} generation **(b)** 4^{th} generation

Figure 1.8: View of the ESRF X-ray beam before the EBS upgrade (a) and after the EBS upgrade (b). The brilliance is increased, whereas the horizontal size and emittance are reduced.

Concurrently, substantial progress has been made in micro- and nano-focusing optics since the early days of ESRF, where typical spot sizes were on the order of 10 µm [122]. Various technologies, including Fresnel Zone Plates (FZP), Kirkpatrick-Baez (KB) mirrors, Multilayer Laue Lenses (MLL), and Compound Refractive Lenses (CRL), have been developed and refined, each presenting unique advantages and limitations [10]. The historical reduction in achievable spot sizes is represented in Figure 1.9. Presently, focused beam dimensions in the range of 10 to 20 nm (Full Width at Half Maximum, FWHM) may be achieved on specialized nano-focusing beamlines.

The increased brilliance introduces challenges related to radiation damage, particularly at high-energy beamlines like ID31. Consequently, long exposure of a single sample area to the focused beam must be avoided. Traditionally, experiments were conducted in a "step-scan" mode, illustrated in Figure 1.10a. In this mode, the sample is moved to the desired position, the detector acquisition is initiated, and a beam shutter is opened for a brief, controlled duration to limit radiation damage before closing; this cycle is repeated for each measurement point. While effective for mitigating radiation damage, this sequential process can be time-consuming, especially for high-resolution maps requiring numerous points.

An alternative, more efficient approach is the "fly-scan" or "continuous-scan" methodology [159], depicted in Figure 1.10b. Here, the sample is moved continuously while the detector is triggered to acquire data "on the fly" at predefined positions or time intervals. This technique significantly accelerates data acquisition, enabling better use of valuable beamtime while potentially enabling finer spatial resolution [71].

Recent developments in detector technology have yielded sensors with improved spatial resolution, lower noise characteristics, better efficiency, and substantially higher frame rates [58]. Historically, detector integration times for scanning

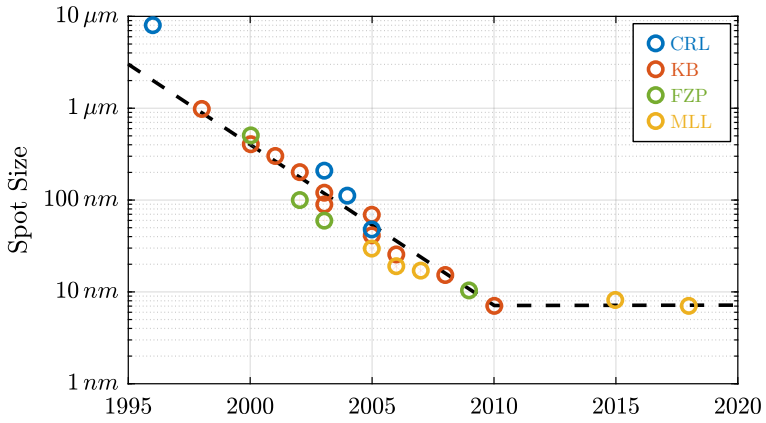

Figure 1.9: Evolution of the measured spot size for different hard X-ray focusing elements. Adapted from [9].

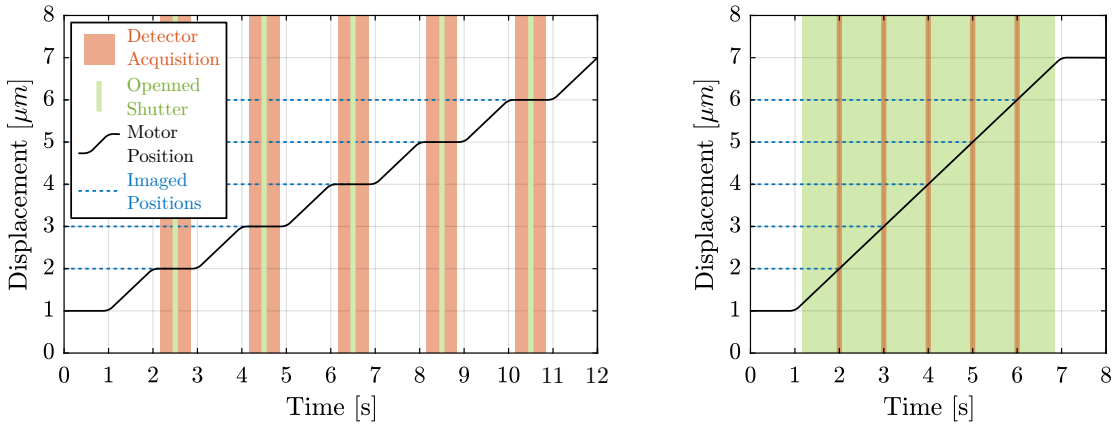

(a) Step by step scan

(b) Fly scan

Figure 1.10: Two acquisition modes. In step-by-step mode (a), the motor moves to the desired imaged position, the detector acquisition is started, the shutter is opened briefly to have the wanted exposure, the detector acquisition is stopped, and the motor can move to a new position. In *fly-scan* mode (b), the shutter is opened while the sample is in motion, and the detector acquires data only at the desired positions while in motion ("on the fly").

and tomography experiments were in the range of 0.1 to 1 second. This extended integration effectively filtered high-frequency vibrations in beam or sample position, resulting in apparently stable but larger beam.

With higher X-ray flux and reduced detector noise, integration times can now be shortened down to approximately 1 millisecond, with frame rates exceeding 100 Hz. This reduction in integration time has two major implications for positioning requirements. Firstly, for a given spatial sampling ("pixel size"), faster integration necessitates proportionally higher scanning velocities. Secondly, the shorter integration times make the measurements more sensitive to high-frequency vibrations. Therefore, not only the sample position must be stable against long-term drifts, but it must also be actively controlled to minimize vibrations, especially during dynamic fly-scan acquisitions.

Existing Nano Positioning End-Stations

To contextualize the system developed within this thesis, a brief overview of existing strategies and technologies for high-accuracy, high-dynamics end-stations is provided. The aim is to identify the specific characteristics that distinguish the proposed system from current state-of-the-art implementations.

Positioning systems can be broadly categorized based on their kinematic architecture, typically serial or parallel, as exemplified by the 3-Degree-of-Freedom (DoF) platforms in Figure 1.11. Serial kinematics (Figure 1.11a) is composed of stacked stages where each DoF is controlled by a dedicated actuator. This configuration offers great mobility, but positioning errors (e.g., guiding inaccuracies, thermal expansion) accumulate through the stack, compromising overall accuracy. Similarly, the overall dynamic performance (stiffness, resonant frequencies) is limited by the softest component in the stack, often resulting in poor dynamic behavior when many stages are combined.

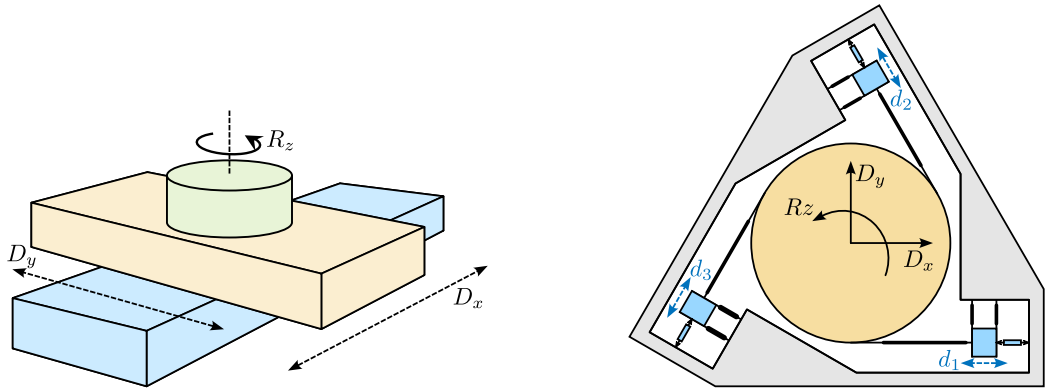

(a) Serial Kinematics **(b)** Parallel Kinematics

Figure 1.11: Two positioning platforms with $D_x/D_y/R_z$ degrees of freedom. One is using serial kinematics (a), while the other uses parallel kinematics (b).

Conversely, parallel kinematic architectures (Figure 1.11b) involve the coordinated motion of multiple actuators to achieve the desired end-effector motion. While theoretically offering the same controlled degrees of freedom as stacked stages, parallel systems generally provide limited stroke but significantly enhanced stiffness and superior dynamic performance.

Most end stations, particularly those requiring extensive mobility, employ stacked stages. Their positioning performance consequently depends entirely on the accuracy of individual components. Strategies include employing a limited number of high-performance stages, such as air-bearing spindles [123], and maintaining extremely stable thermal environments within the experimental hutch, often requiring extended stabilization times [85]. Examples of such end-stations, including those at beamlines ID16B [94] and ID11 [157], are shown in Figure 1.12. However, when a large number of degrees of freedom are required, the cumulative errors and limited dynamic stiffness of stacked configurations can make experiments with nano-focused beams extremely challenging or infeasible.

The concept of using an external metrology to measure and potentially correct for positioning errors is increasingly used for nano-positioning end-stations. Ideally, the relative position between the sample's Point of Interest (PoI) and the X-ray beam focus would be measured directly. In practice, direct measurement is often impossible; instead, the sample position is typically measured relative to a reference frame associated with the focusing optics, providing an indirect measurement.

This measured position can be used in several ways: for post-processing correction of acquired data; for calibration routines to compensate for repeatable errors; or, most relevantly here, for real-time feedback control. Various sensor tech-

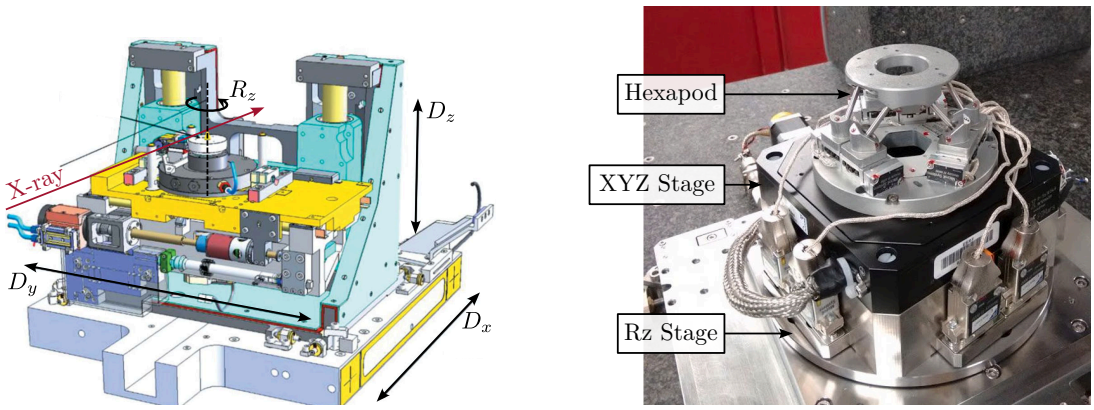

(a) ID16b end-station [94]

(b) ID11 end-station [157]

Figure 1.12: Example of two nano end-stations lacking online metrology for measuring the sample's position.

nologies have been employed, with capacitive sensors [129, 130, 152] and, increasingly, fiber-based interferometers [43, 54, 65, 66, 79, 105, 106, 130, 138, 159] being prominent choices.

Two examples illustrating the integration of online metrology are presented in Figure 1.13. The system at NSLS X8C (Figure 1.13a) used capacitive sensors for rotation stage calibration and image alignment during tomography post-processing [154]. The PtiNAMi microscope at DESY P06 (Figure 1.13b) employs interferometers directed at a spherical target below the sample for position monitoring during tomography, with plans for future feedback loop implementation [130].

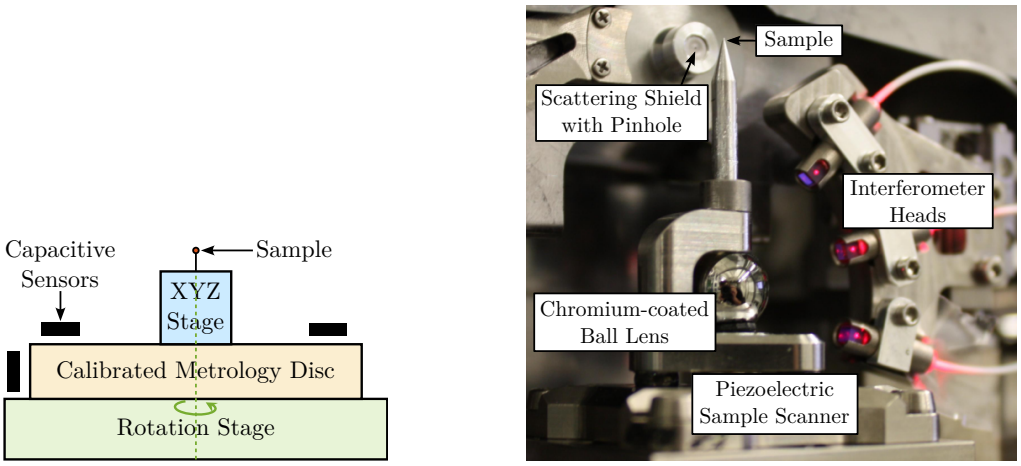

(a) NSLS X8C - TXM [154]

(b) DESY P06 - PtiNAMi microscope [129]

Figure 1.13: Two examples of end-station with integrated online metrology.

For applications requiring active compensation of measured errors, particularly with nano-beams, feedback control loops are implemented. Actuation is typically achieved using piezoelectric actuators [65, 66, 105, 106, 152], 3-phase linear motors [43, 138], or Voice Coil (VC) actuators [54, 79]. While often omitted, feedback bandwidth for such stages are relatively low (around 1 Hz), primarily targeting the compensation of slow thermal drifts. More recently, higher bandwidths (up to 100 Hz) have been demonstrated, particularly with the use of voice coil actuators [54, 79].

Figure 1.14 showcases two end-stations incorporating online metrology and active feedback control. The ID16A system at ESRF (Figure 1.14a) uses capacitive sensors and a piezoelectric Stewart platform to compensate for rotation stage

errors and to perform accurate scans [152]. Another example, shown in Figure 1.14b, employs interferometers and piezoelectric stages to compensate for thermal drifts [106, 107]. A more comprehensive review of actively controlled end-stations is provided in Section 2.5.1.

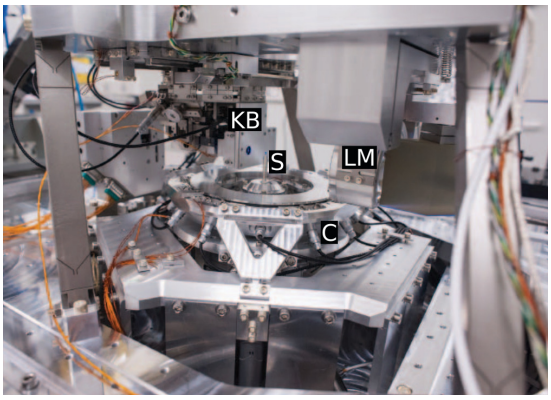

(a) ESRF ID16a - HPZ. KB is the focusing optics, S the sample, C the capacitive sensors and LM is the light microscope [152]

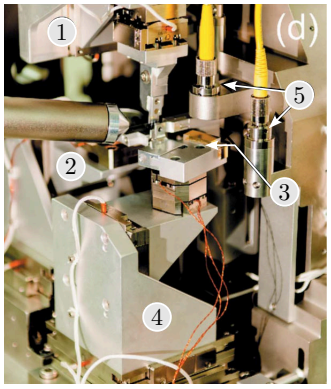

(b) NSLS-II HXN - Microscope. 1 and 2 are focusing optics, 3 is the sample location, 4 the sample stage and 5 the interferometers [107]

Figure 1.14: Example of two end-stations with real-time position feedback based on an online metrology.

For tomography experiments, correcting spindle guiding errors is critical. Correction stages are typically placed either below the spindle [43, 65, 66, 105, 138, 152, 159] or above it [54, 129, 130, 154]. In most reported cases, only translation errors are actively corrected. Payload capacities for these high-precision systems are usually limited, typically handling calibrated samples on the micron scale, although capacities up to 500g have been reported [79, 105]. The system developed in this thesis aims for payload capabilities approximately 100 times heavier (up to 50 kg) than previous stations with similar positioning requirements.

End-stations integrating online metrology for active nano-positioning often exhibit limited operational ranges, typically constrained to a few degrees of freedom with strokes around 100 µm. Recently, Voice Coil (VC) actuators were used to increase the stroke up to 3 mm [54, 79] An alternative strategy involves a "long stroke-short stroke" architecture, illustrated conceptually in Figure 1.15a. In this configuration, a high-accuracy, high-bandwidth short-stroke stage is mounted on top of a less precise long-stroke stage. The short-stroke stage actively compensates for errors based on metrology feedback, while the long-stroke stage performs the larger movements. This approach allows the combination of extended travel with high precision and good dynamical response, but is often implemented for only one or a few degrees of freedom, as seen in Figures 1.15a and 1.15b.

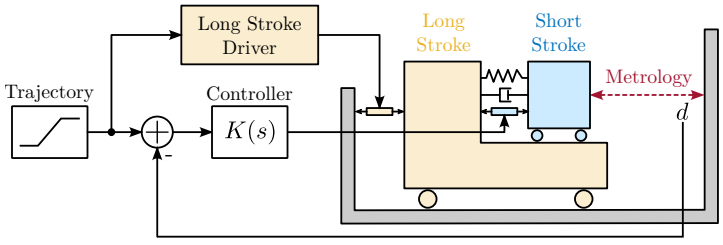

(a) Typical Long Stroke-Short Stroke control architecture

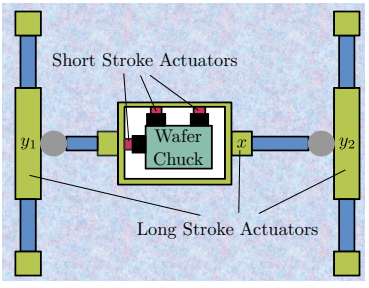

(b) Schematic of the "H-bridge" [127]

Figure 1.15: Schematic of a typical Long stroke-Short stroke control architecture (a). A 3-DoF long stroke-short stroke is shown in (b) where y_1, y_2 and x are 3-phase linear motors and short stroke actuators are voice coils.

1.2 Challenge definition

The advent of fourth-generation light sources, coupled with advancements in focusing optics and detector technology, imposes stringent new requirements on sample positioning systems.

With ID31's anticipated minimum beam dimensions of approximately 200 nm × 100 nm, the primary experimental objective is maintaining the sample's PoI within this beam. This necessitates peak-to-peak positioning errors below 200 nm in D_y and 200 nm in D_z, corresponding to Root Mean Square (RMS) errors of 30 nm and 15 nm, respectively. Additionally, the R_y tilt angle error must remain below 0.1 mdeg (250 nrad RMS). Given the high frame rates of modern detectors, these specified positioning errors must be maintained even when considering high-frequency vibrations (typically up to 1 kHz).

These demanding stability requirements must be achieved within the specific context of the ID31 beamline, which necessitates the integration with the existing micro-station, accommodating a wide range of experimental configurations requiring high mobility, and handling substantial payloads up to 50 kg.

The existing micro-station, despite being composed of high-performance stages, has a positioning accuracy limited to approximately 10 μm and 10 µrad (peak to peak) due to inherent factors such as backlash, thermal expansion, imperfect guiding, and vibrations.

The primary objective of this project is therefore defined as enhancing the positioning accuracy and stability of the ID31 micro-station by roughly two orders of magnitude, to fully leverage the capabilities offered by the ESRF-EBS source and modern detectors, without compromising its existing mobility and payload capacity.

The Nano Active Stabilization System Concept To address these challenges, the concept of a Nano Active Stabilization System (NASS) is proposed. As schematically illustrated in Figure 1.16, the NASS comprises three principal components integrated with the existing micro-station (yellow): a 5-DoF online metrology system (red), an active stabilization platform (blue), and the associated control system and instrumentation (purple). This system essentially functions as a high-performance, multi-axis vibration isolation and error correction platform situated between the micro-station and the sample. It actively compensates for positioning errors measured by the external metrology system.

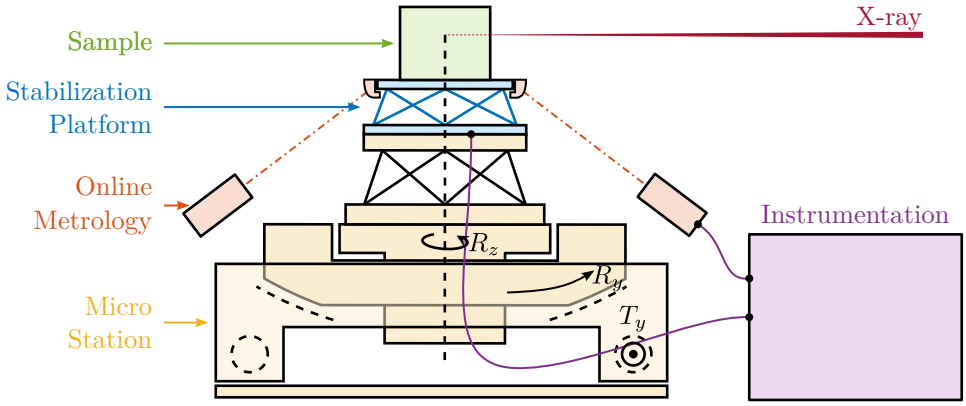

Figure 1.16: The Nano Active Stabilization System concept.

Online Metrology system The performance of the NASS is fundamentally reliant on the accuracy and bandwidth of its online metrology system, as the active control is based directly on these measurements. This metrology system must fulfill several criteria: measure the sample position in 5-DoF (excluding rotation about the vertical Z-axis);

possess a measurement range compatible with the micro-station's extensive mobility and continuous spindle rotation; achieve an accuracy compatible with the sub-100 nm positioning target; and offer high bandwidth for real-time control.

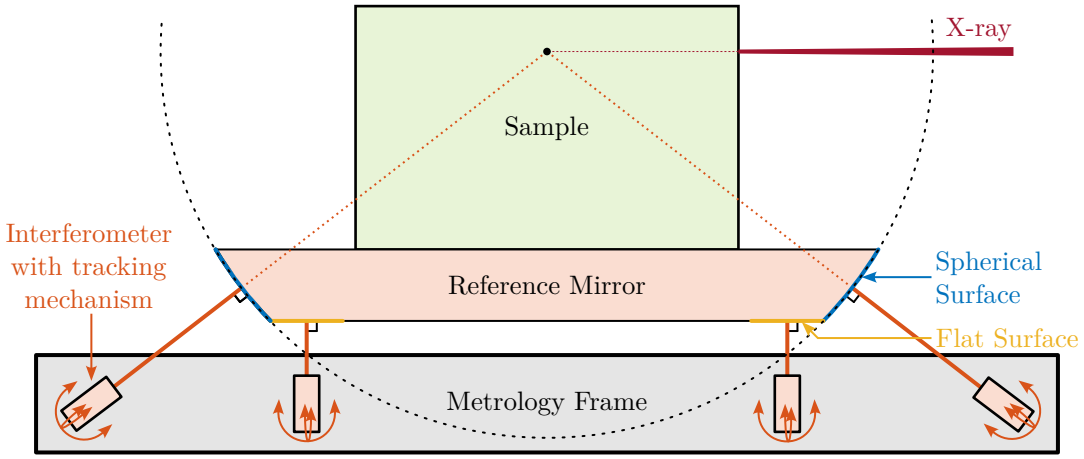

Figure 1.17: 2D representation of the NASS metrology system.

A proposed concept (illustrated in Figure 1.17) features a spherical reflector with a flat bottom attached below the sample, with its center aligned to the X-ray focus. Fiber interferometers target both surfaces. A tracking system maintains perpendicularity between the interferometer beams and the mirror, such that Abbe errors are eliminated. Interferometers pointing at the spherical surface provides translation measurement, while the ones pointing at the flat bottom surface yield tilt angles. The development of this complex metrology system constitutes a significant mechatronic project in itself and is currently ongoing; it is not further detailed within this thesis. For the work presented herein, the metrology system is assumed to provide accurate, high-bandwidth 5-DoF position measurements.

Active Stabilization Platform Design The active stabilization platform, positioned between the micro-station top plate and the sample, must satisfy several demanding requirements. It needs to provide active motion compensation in 5-DoF (D_x, D_y, D_z, R_x and R_y). It must possess excellent dynamic properties to enable high-bandwidth control capable of suppressing vibrations and tracking desired trajectories with nanometer-level precision. Consequently, it must be free from backlash and play, and its active components (e.g., actuators) should introduce minimal vibrations. Critically, it must accommodate payloads up to 50 kg.

A suitable candidate architecture for this platform is the Stewart platform (also known as "hexapod"), a parallel kinematic mechanism capable of 6-DoF motion. Stewart platforms are widely employed in positioning and vibration isolation applications due to their inherent stiffness and potential for high precision. Various designs exist, differing in geometry, actuation technology, sensing methods, and control strategies, as exemplified in Figure 1.18. A central challenge addressed in this thesis is the optimal mechatronic design of such an active platform tailored to the specific requirements of the NASS. A more detailed review of Stewart platform and its main components will be given in Section 3.1.1.

Robust Control The control system must compute the position measurements from the online metrology system and computes the reference positions derived from each micro-station desired movement. It then commands the active platform in real-time to stabilize the sample and compensate for all error sources, including stage imperfections, thermal drifts, and vibrations. Ensuring the stability and robustness of these feedback loops is crucial, especially within the demanding operational context of a synchrotron beamline, which requires reliable 24/7 operation with minimal intervention.

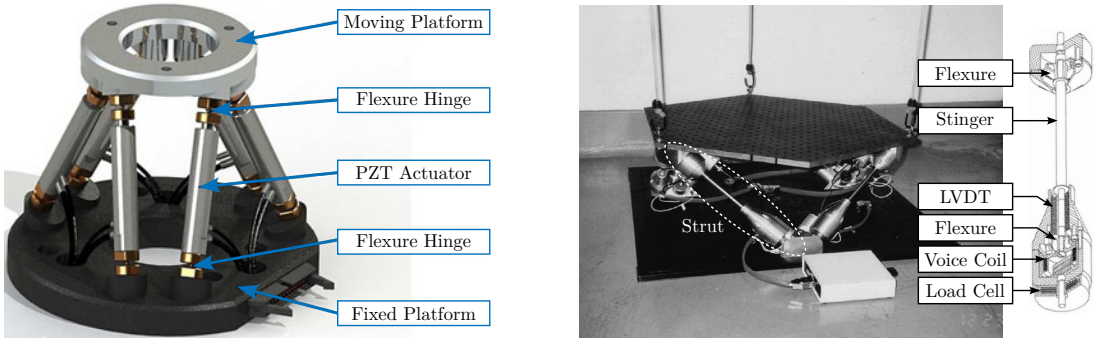

(a) Piezo based, for positioning purposes [41]

(b) Voice coil based, for vibration isolation [59]

Figure 1.18: Two examples of very different Stewart platforms geometries and strut configurations.

Several factors complicate the design of robust feedback control for the NASS. First, the system must operate under across diverse experimental conditions, including different scan types (tomography, linear scans) and payloads' inertia. The continuous rotation of the spindle introduces gyroscopic effects that can affect the system dynamics. As actuators of the active platforms rotate relative to stationary sensors, the control kinematics to map the errors in the frame of the active platform is complex. But perhaps the most significant challenge is the wide variation in payload mass (1 kg up to 50 kg) that the system must accommodate. Designing for robustness against large payload variations typically necessitates larger stability margins, which can compromise achievable performance. Consequently, high-performance positioning stages often work with well-characterized payload, as seen in systems like wafer-scanners or atomic force microscopes.

Furthermore, unlike many systems where the active stage and sample are significantly lighter than the underlying coarse stages, the NASS payload mass can be substantially greater than the mass of the micro-station's top stage. This leads to strong dynamic coupling between the active platform and the micro-station structure, resulting in a more complex Multi Inputs Multi Outputs (MIMO) system with significant cross-talk between axes.

These variations in operating conditions and payload translate into significant uncertainty or changes in the plant dynamics that the controller must handle. Therefore, the feedback controller must be designed to be robust against this plant uncertainty while still delivering the required nanometer-level performance.

Predictive Design The overall performance achieved by the NASS is determined by numerous factors, such as external disturbances, the noise characteristics of the instrumentation, the dynamics resulting from the chosen mechanical architecture, and the achievable bandwidth dictated by the control architecture. Ensuring the final system meets its stringent specifications requires the implementation of a predictive design methodology, also known as a mechatronic design approach. The goal is to rigorously evaluate different concepts, predict performance limitations, and guide the design process. Key challenges within this approach include developing appropriate design methodologies, creating accurate models capable of comparing different concepts quantitatively, and converging on a final design that achieves the target performance levels.

1.3 Original Contributions

This thesis presents several original contributions aimed at addressing the challenges inherent in the design, control, and implementation of the Nano Active Stabilization System, primarily within the fields of Control Theory, Mechatronic Design, and Experimental Validation.

6-DoF vibration control of a rotating platform Traditional long-stroke/short-stroke architectures typically operate in one or two degrees of freedom. This work extends the concept to six degrees of freedom, with the active platform designed not only to correct rotational errors but to simultaneously compensate for errors originating from all underlying micro-station stages. The application of a continuously rotating Stewart platform for active vibration control and error compensation in this manner is believed to be novel in the reviewed literature.

Mechatronic design approach A rigorous mechatronic design methodology was applied consistently throughout the NASS development life-cycle [34, 38]. Although the mechatronic approach itself is not new, its comprehensive application here, from initial concept evaluation using simplified models to detailed design optimization and experimental validation informed by increasingly sophisticated models, potentially offers useful insights to the existing literature. This thesis documents this process chronologically, illustrating how models of varying complexity can be effectively used at different project phases and how design decisions were systematically based on quantitative model predictions and analyses. While the resulting system is highly specific, the documented effectiveness of this design approach may contribute to the broader adoption of mechatronic methodologies in the design of future synchrotron instrumentation.

Experimental validation of multi-body simulations with reduced order flexible bodies obtained by FEA A key tool employed extensively in this work was a combined multi-body simulation and Finite Element Analysis (FEA) technique, specifically using Component Mode Synthesis to represent flexible bodies within the multi-body framework [17]. This hybrid approach, while established, was experimentally validated in this work for components critical to the NASS, namely amplified piezoelectric actuators and flexible joints. It proved invaluable for designing and optimizing components intended for integration into a larger, complex dynamic system. This methodology, detailed in Section 3.2, is presented as a potentially useful tool for future mechatronic instrument development.

Control Robustness by design The requirement for robust operation across diverse conditions—including payloads up to 50 kg, complex underlying dynamics from the micro-station, and varied operational modes like different rotation speeds—presented a critical design challenge. This challenge was met by embedding robustness directly into the active platform's design, rather than depending solely on complex post-design control synthesis techniques such as $\mathcal{H}_\infty$-synthesis and μ-synthesis. Key elements of this strategy included the model-based evaluation of active stage designs to identify architectures inherently easier to control, the incorporation of collocated actuator/sensor pairs to leverage passivity-based guaranteed stability, and the comparison of architecture to combine several sensors such as sensor fusion and High Authority Control / Low Authority Control (HAC-LAC). Furthermore, decoupling strategies for parallel manipulators were compared (Section 3.3.2), addressing a topic identified as having limited treatment in the literature. Consequently, the specified performance targets were met using controllers which, facilitated by this design approach, proved to be robust, readily tunable, and easily maintained.

Active Damping of rotating mechanical systems using Integral Force Feedback During conceptual design, it was found that the guaranteed stability property of the established active damping technique known as Integral Force Feedback (IFF) is compromised when applied to rotating platforms like the NASS. To address this instability issue, two modifications to the classical IFF control scheme were proposed and analyzed. The first involves a minor

adjustment to the control law itself, while the second incorporates physical springs in parallel with the force sensors. Stability conditions and optimal parameter tuning guidelines were derived for both modified schemes. This is further discussed in Section 2.2 and was the subject of a publication [35].

Design of complementary filters using $\mathcal{H}_\infty$ Synthesis For implementing sensor fusion, where signals from multiple sensors are combined, complementary filters are often employed. A novel method for designing these filters using $\mathcal{H}_\infty$ synthesis techniques was developed [39]. This method allows explicit shaping of the filter norms, providing guarantees on the performance of the sensor fusion process. This synthesis technique, discussed further in Section 3.3.1, has subsequently found application in optimizing sensor fusion for gravitational wave detectors [149]. The integration of such filters into feedback control architectures can also lead to advantageous control structures, as proposed in [150] and further studied in Section 3.3.3.

Experimental validation of the Nano Active Stabilization System The conclusion of this work involved the experimental implementation and validation of the complete NASS on the ID31 beamline. Experimental results, presented in Section 4.5, demonstrate that the system successfully improves the effective positioning accuracy of the micro-station from its native $\approx 10\,\mu m$ level down to the target $\approx 100\,nm$ range during representative scientific experiments. Crucially, robustness to variations in sample mass and diverse experimental conditions was verified. The NASS thus provides a versatile end-station solution, uniquely combining high payload capacity with nanometer-level accuracy, enabling optimal use of the advanced capabilities of the ESRF-EBS beam and associated detectors. To the author's knowledge, this represents the first demonstration of such a 5-DoF active stabilization platform being used to enhance the accuracy of a complex positioning system to this level.

1.4 Outline

This is divided into three chapters, each corresponding to a distinct phase of this methodology: Conceptual Design, Detailed Design, and Experimental Validation. While the chapters follow this logical progression, care has been taken to structure each chapter such that its constitutive sections may also be consulted independently based on the reader's specific interests.

Conceptual design development The conceptual design phase, detailed in Chapter 2, followed a methodical progression from simplified uniaxial models to more complex multi-body representations. Initial uniaxial analysis (Section 2.1) provided fundamental insights, particularly regarding the influence of active platform stiffness on performance. The introduction of rotation in a 3-DoF model (Section 2.2) allowed investigation of gyroscopic effects, revealing challenges for softer platform designs. Experimental modal analysis of the existing micro-station (Section 2.3) confirmed its complex dynamics but supported a rigid-body assumption for the different stages, justifying the development of a detailed multi-body model. This model, tuned against experimental data and incorporating measured disturbances, was validated through simulation (Section 2.4). The Stewart platform architecture was selected for the active stage, and its kinematics, dynamics, and control were analyzed (Section 2.5). The chapter culminates in Section 2.6 with closed-loop simulations of the integrated NASS concept under realistic conditions, validating its feasibility and providing confidence for proceeding to the detailed design phase. Dynamic error budgeting [102, 108] was employed throughout this phase to identify performance limitations and guide concept selection.

Detailed design Chapter 3 focuses on translating the validated NASS concept into an optimized, implementable design. Building upon the conceptual model which used idealized components, this phase addresses the detailed specification and optimization of each subsystem. It starts with the determination of the optimal active platform geometry (Section 3.1), analyzing the influence of geometric parameters on mobility, stiffness, and dynamics, leading to specific requirements for actuator stroke and joint mobility. A hybrid multi-body/FEA modeling methodology is introduced and experimentally validated (Section 3.2), then applied to optimize the actuators (Section 3.2.2) and flexible joints (Section 3.2.3) while maintaining system-level simulation capability. Control strategy refinement (Section 3.3) involves optimal integration of multiple sensors in the control architecture, evaluating decoupling strategies, and discussing controller optimization for decoupled systems. Instrumentation selection (Section 3.4) is guided by dynamic error budgeting to establish noise specifications, followed by experimental characterization. The chapter concludes (Section 3.5) by presenting the final, optimized active platform design, ready for procurement and assembly.

Experimental validation Chapter 4 details the experimental validation process, proceeding systematically from component-level characterization to full system evaluation on the beamline. Actuators of the active platform were characterized, models validated, and active damping tested (Section 4.1). Flexible joints were tested on a dedicated bench to verify stiffness and stroke specifications (Section 4.2). Assembled struts (actuators + joints) were then characterized to ensure consistency and validate multi-body models (Section 4.3). The complete active platform assembly was tested on an isolated table, allowing accurate dynamic identification and model validation under various payload conditions (Section 4.4). Finally, the integrated NASS was validated on the ID31 beamline using a purpose-built short-stroke metrology system (Section 4.5). The implemented control architecture was tested under realistic experimental scenarios, including tomography with heavy payloads, confirming the system's performance and robustness.

2 Conceptual Design Development

Contents

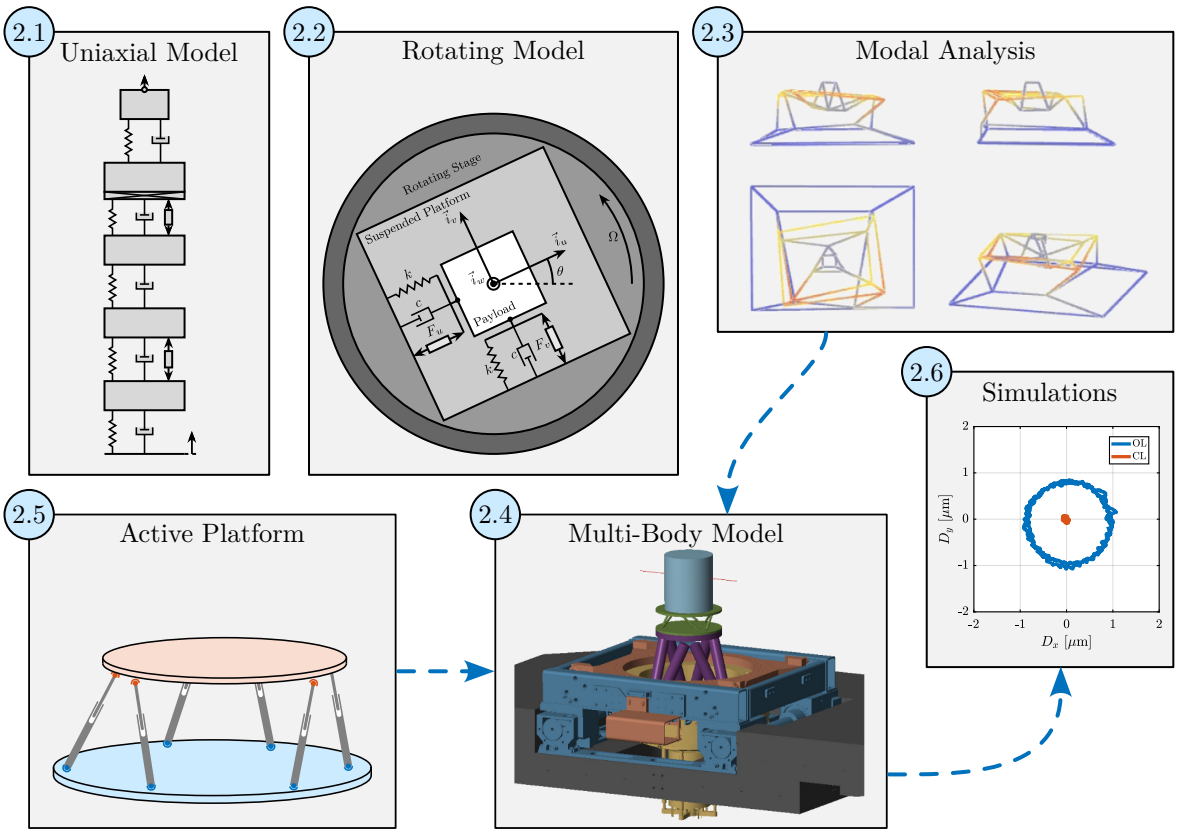

Figure 2.1: Overview of the conceptual design development. The approach evolves from simplified analytical models to a multi-body model tuned from experimental modal analysis. Closed-loop simulations of tomography experiments are used to validate the concept.

Abstract

The conceptual design of the Nano Active Stabilization System (NASS) follows a methodical progression from simple to more accurate modeling approaches, as illustrated in Figure 2.1.

The design process begins with a uniaxial model, presented in Section 2.1, which provides initial insights into fundamental challenges associated with this complex system. This simplified representation focuses exclusively on the vertical direction—having the most stringent requirements—though similar conclusions were drawn from analyses of other axes. Despite its simplicity, this uniaxial model proves valuable for testing initial control strategies and, more importantly, for evaluating how the active platform stiffness affects overall system performance.

Building upon these findings, Section 2.2 introduces the rotational aspect through a three-degree-of-freedom model. This new model allows to study the gyroscopic effects induced by the spindle's continuous rotation—a distinctive characteristic of the NASS. The investigation reveals that these gyroscopic effects have more impact on softer active platforms, creating significant challenges for stability and control.

As the investigation progressed, the need for a more accurate representation of the micro-station dynamics became increasingly evident. To construct such a model, a comprehensive modal analysis was conducted, as detailed in Section 2.3. This experimental modal analysis confirmed the complex nature of the micro-station dynamics while validating that each

stage behaves predominantly as a rigid body within the frequency range of interest—thus supporting the subsequent development of a multi-body model.

Section 2.4 presents the development of this multi-body model for the micro-station. Parameters were meticulously tuned to match measured compliance characteristics, and disturbance sources were carefully modelled based on experimental data. This refined model was then validated through simulations of scientific experiments, demonstrating its accuracy in representing the micro-station behavior under typical operating conditions.

For the active stabilization stage, the Stewart platform architecture was selected after careful evaluation of various options. Section 2.5 examines the kinematic and dynamic properties of this parallel manipulator, exploring its control challenges and developing appropriate control strategies for implementation within the NASS. The multi-body modeling approach facilitated the seamless integration of the active platform with the micro-station model.

Finally, Section 2.6 validates the NASS concept through Closed Loop (CL) simulations of tomography experiments. These simulations incorporate realistic disturbance sources, confirming the viability of the proposed design approach and control strategies.

This progressive approach, beginning with easily comprehensible simplified models, proved instrumental in developing a thorough understanding of the physical phenomena at play. By methodically increasing model complexity only as needed, the design process converged efficiently toward a concept capable of delivering the required performance levels. The confidence gained through this systematic investigation provides a solid foundation for transitioning to the detailed design phase, which will be addressed in the following chapter.

2.1 Uni-axial Model

In this report, a uniaxial model of the Nano Active Stabilization System (NASS) is developed and used to obtain a first idea of the challenges involved in this complex system. Note that in this study, only the vertical direction is considered (which is the most stiff), but other directions were considered as well, leading to similar conclusions.

To have a relevant model, the micro-station dynamics is first identified and its model is tuned to match the measurements (Section 2.1.1). Then, a model of the active platform is added on top of the micro-station. With the added sample and sensors, this gives a uniaxial dynamical model of the NASS that will be used for further analysis (Section 2.1.2).

The disturbances affecting position stability are identified experimentally (Section 2.1.3) and included in the model for dynamical error budgeting (Section 2.1.4). In all the following analysis, three active platform stiffnesses are considered to better understand the trade-offs and to find the most adequate active platform design. Three sample masses are also considered to verify the robustness of the applied control strategies with respect to a change of sample.

To improve the position stability of the sample, an High Authority Control / Low Authority Control (HAC-LAC) strategy is applied. It consists of first actively damping the plant (the LAC part), and then applying a position control on the damped plant (the HAC part).

Three active damping techniques are studied (Section 2.1.5) which are used to both reduce the effect of disturbances and make the system easier to control afterwards. Once the system is well damped, a feedback position controller is applied and the obtained performance is analyzed (Section 2.1.6).

Two key effects that may limit that positioning performances are then considered: the limited micro-station compliance (Section 2.1.7) and the presence of dynamics between the active platform and the sample's Point of Interest (Section 2.1.8).

2.1.1 Micro Station Model

In this section, a uniaxial model of the micro-station is tuned to match measurements made on the micro-station.

Measured Dynamics The measurement setup is schematically shown in Figure 2.2a where two vertical hammer hits are performed, one on the Granite (force F_g) and the other on the positioning hexapod's top platform (force F_h). The vertical inertial motion of the granite x_g and the top platform of the positioning hexapod x_h are measured using geophones[1]. Three Frequency Response Functions (FRFs) were computed: one from F_h to x_h (i.e., the compliance of the micro-station), one from F_g to x_h (or from F_h to x_g) and one from F_g to x_g.

Due to the poor coherence[2] at low frequencies, these Frequency Response Functions will only be shown between 20 and 200 Hz (solid lines in Figure 2.3).

Uniaxial Model The uniaxial model of the micro-station is shown in Figure 2.2b. It consists of a mass spring damper system with three degrees of freedom. A mass-spring-damper system represents the granite (with mass m_g, stiffness k_g and damping c_g). Another mass-spring-damper system represents the different micro-station stages (the T_y

[1] Mark Product L4-C geophones are used with a sensitivity of 171 $\frac{V}{m/s}$ and a natural frequency of $\approx$ 1 Hz.

[2] Coherence is a statistical measure (ranging from 0 to 1) used in system identification to assess how well the output of a linear system can be predicted from its input. Values near 1 indicate strong linear correlation, while noise or non-linearities reduce coherence and indicate poor data quality.

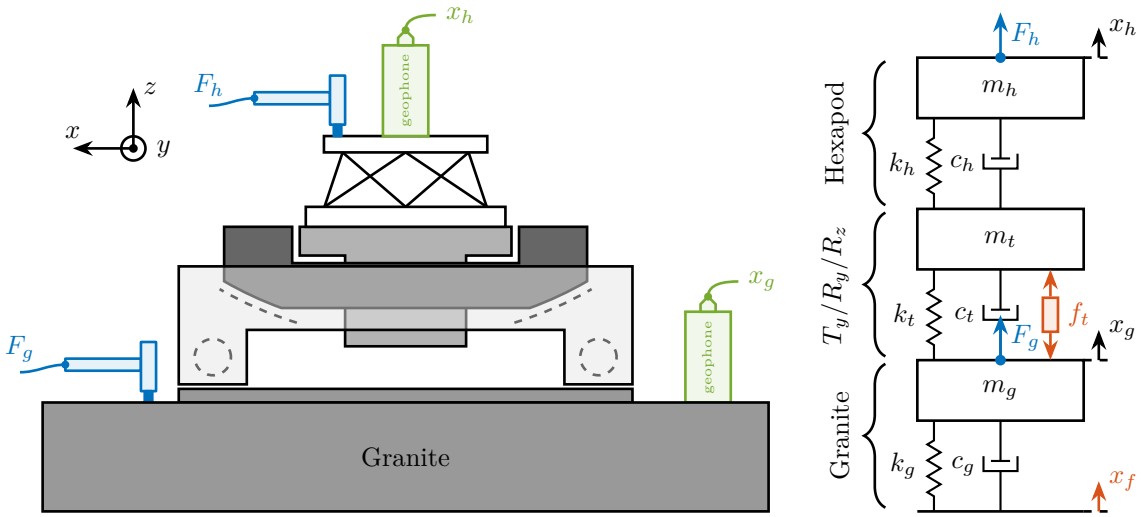

(a) Measurement setup - Schematic

(b) Uniaxial model of the micro-station

Figure 2.2: Schematic of the Micro-Station measurement setup and uniaxial model.

stage, the R_y stage and the R_z stage) with mass m_t, damping c_t and stiffness k_t. Finally, a third mass-spring-damper system represents the positioning hexapod with mass m_h, damping c_h and stiffness k_h.

The masses of the different stages are computed from the 3D model, while the stiffness values are taken from the manufacturers' datasheets for the various guiding elements used. The damping coefficients were tuned to match the damping identified from the measurements. The parameters obtained are summarized in Table 2.1.

Table 2.1: Physical parameters used for the micro-station uniaxial model.

Stage	Mass	Stiffness	Damping
Hexapod	$m_h = 15\,\text{kg}$	$k_h = 61\,\text{N}/\mu\text{m}$	$c_h = 3\,\frac{\text{kN}}{\text{m/s}}$
T_y, R_y, R_z	$m_t = 1200\,\text{kg}$	$k_t = 520\,\text{N}/\mu\text{m}$	$c_t = 80\,\frac{\text{kN}}{\text{m/s}}$
Granite	$m_g = 2500\,\text{kg}$	$k_g = 950\,\text{N}/\mu\text{m}$	$c_g = 250\,\frac{\text{kN}}{\text{m/s}}$

Two disturbances are considered which are shown in red: the floor motion x_f and the stage vibrations represented by f_t. The hammer impacts F_h, F_g are shown in blue, whereas the measured inertial motions x_h, x_g are shown in black.

Comparison of Model and Measurements The transfer functions from the forces injected by the hammers to the measured inertial motion of the positioning hexapod and granite are extracted from the uniaxial model and compared to the measurements in Figure 2.3.

Because the uniaxial model has three degrees of freedom, only three modes with frequencies at 70 Hz, 140 Hz and 320 Hz are modelled. Many more modes can be observed in the measurements (see Figure 2.3). However, the goal is not to have a perfect match with the measurement (this would require a much more complex model), but to have a first approximation. More accurate models will be used later on.

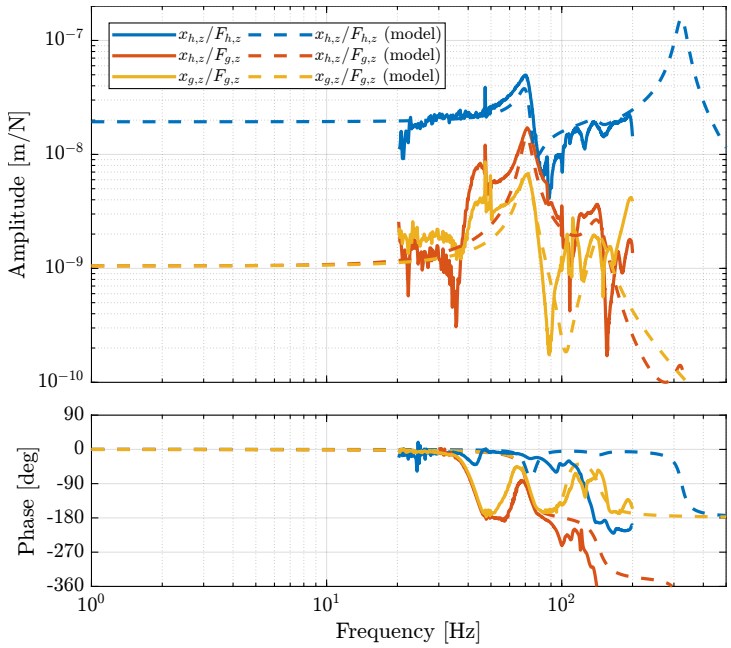

Figure 2.3: Comparison of the measured Frequency Response Functions (FRF) and the uniaxial model dynamics.

2.1.2 Active Platform Model

A model of the active platform and sample is now added on top of the uniaxial model of the micro-station (Figure 2.4a). Disturbances (shown in red) are f_s the direct forces applied to the sample (for example cable forces), f_t representing the vibrations induced when scanning the different stages and x_f the floor motion. The control signal is the force applied by the active platform f and the measurement is the relative motion between the sample and the granite d. The sample is here considered as a rigid body and rigidly fixed to the active platform. The effect of resonances between the sample's PoI and the active platform actuator will be considered in Section 2.1.8.

Active Platform Parameters The active platform is represented by a mass spring damper system (shown in blue in Figure 2.4a). Its mass m_n is set to 15 kg while its stiffness k_n can vary depending on the chosen architecture/technology. The sample is represented by a mass m_s that can vary from 1 kg up to 50 kg.

As a first example, the active platform stiffness of is set at $k_n = 10\,\text{N}/\mu\text{m}$ and the sample mass is chosen at $m_s = 10\,\text{kg}$.

Obtained Dynamic Response The sensitivity to disturbances (i.e., the transfer functions from x_f, f_t, f_s to d) can be extracted from the uniaxial model of Figure 2.4a and are shown in Figure 2.5. The *plant* (i.e., the transfer function from actuator force f to displacement d) is shown in Figure 2.4b.

For further analysis, 9 "configurations" of the uniaxial NASS model of Figure 2.4a will be considered: three active platform stiffnesses ($k_n = 0.01\,\text{N}/\mu\text{m}$, $k_n = 1\,\text{N}/\mu\text{m}$ and $k_n = 100\,\text{N}/\mu\text{m}$) combined with three sample's masses ($m_s = 1\,\text{kg}$, $m_s = 25\,\text{kg}$ and $m_s = 50\,\text{kg}$).

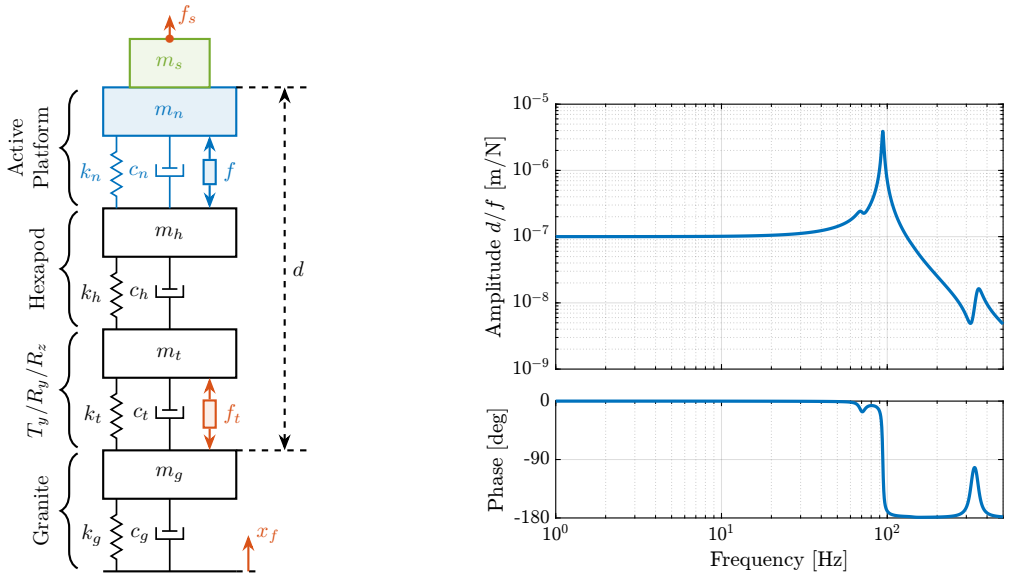

(a) Uniaxial mass-spring-damper model of the NASS

(b) Plant Dynamics

Figure 2.4: Uniaxial model of the NASS (a) with the micro-station shown in black, the active platform in blue, the sample in green and disturbances in red. Transfer function from f to d (b).

2.1.3 Identification of Disturbances

To quantify disturbances (red signals in Figure 2.4a), three geophones[1] are used. One is located on the floor, another one on the granite, and the last one on the positioning hexapod's top platform (see Figure 2.6a). The geophone located on the floor was used to measure the floor motion x_f while the other two geophones were used to measure vibrations introduced by scanning of the T_y stage and R_z stage (see Figure 2.6b).

Ground Motion To acquire the geophone signals, the measurement setup shown in Figure 2.7 is used. The voltage generated by the geophone is amplified using a low noise voltage amplifier[2] with a gain of 60 dB before going to the Analog to Digital Converter (ADC). This is done to improve the signal-to-noise ratio.

To reconstruct the displacement x_f from the measured voltage $\hat{V}_{x_f}$, the transfer function of the measurement chain from x_f to $\hat{V}_{x_f}$ needs to be estimated. First, the transfer function G_{geo} from the floor motion x_f to the generated geophone voltage V_{x_f} is shown in (2.1), with $T_g = 88\,\frac{V}{\text{m/s}}$ the sensitivity of the geophone, $f_0 = \frac{\omega_0}{2\pi} = 2\,\text{Hz}$ its resonance frequency and $\xi = 0.7$ its damping ratio. This model of the geophone was taken from [27]. The gain of the voltage amplifier is $V'_{x_f}/V_{x_f} = g_0 = 1000$.

$$G_{geo}(s) = \frac{V_{x_f}}{x_f}(s) = T_g \cdot s \cdot \frac{s^2}{s^2 + 2\xi\omega_0 s + \omega_0^2} \quad [\text{V/m}] \tag{2.1}$$

The Amplitude Spectrum Density (ASD) of the floor motion Γ_{x_f} can be computed from the Amplitude Spectrum Density of measured voltage $\Gamma_{\hat{V}_{x_f}}$ using (2.2). The estimated ASD Γ_{x_f} of the floor motion x_f is shown in Figure 2.8a.

[1] Mark Product L-22D geophones are used with a sensitivity of 88 $\frac{V}{\text{m/s}}$ and a natural frequency of $\approx$ 2 Hz.
[2] DLPVA-100-B from Femto with a voltage input noise is 2.4 nV/$\sqrt{\text{Hz}}$.

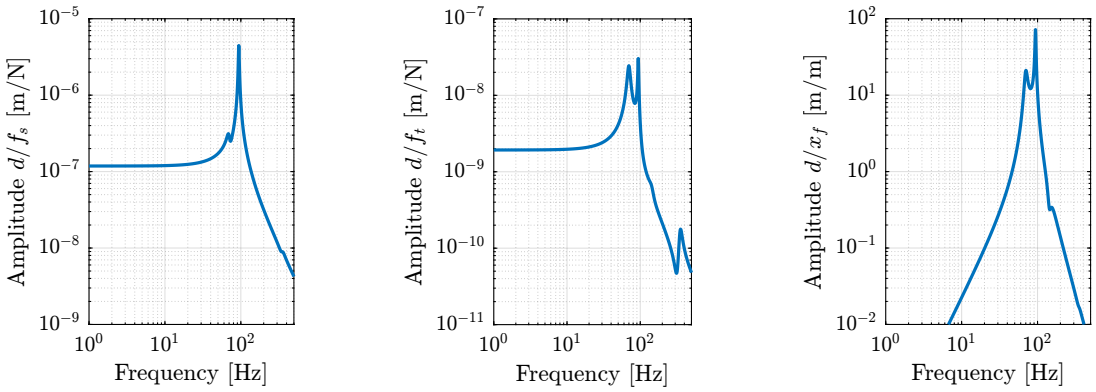

(a) Direct forces **(b)** μ-station disturbances **(c)** Floor motion

Figure 2.5: Sensitivity of the relative motion d to the following disturbances: f_s the direct forces applied on the sample (a), f_t disturbances from the micro-station stages (b) and x_f the floor motion (c).

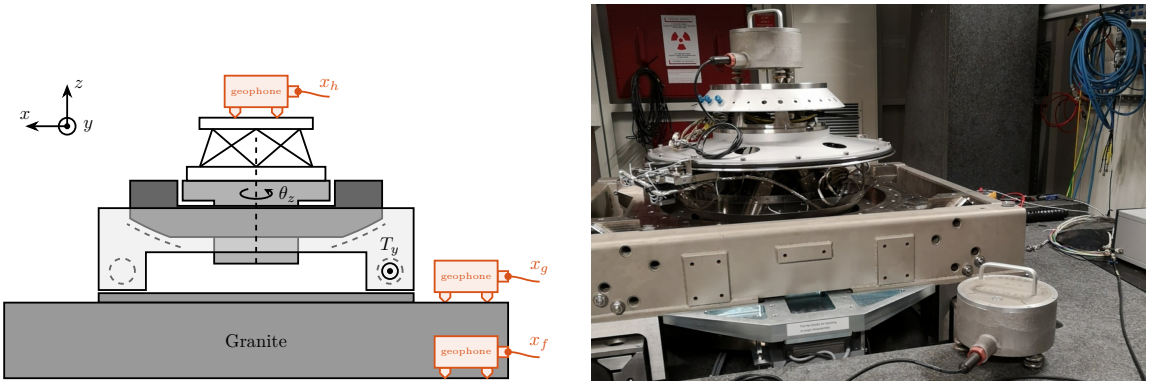

(a) Disturbance measurement setup - Schematic **(b)** Geophones used to measure vibrations induced by T_y and R_z scans

Figure 2.6: Identification of the disturbances coming from the micro-station. The measurement schematic is shown in (a). A picture of the setup is shown in (b).

$$\Gamma_{x_f}(\omega) = \frac{\Gamma_{\hat{V}_{x_f}}(\omega)}{|G_{geo}(j\omega)| \cdot g_0} \quad \left[m/\sqrt{\text{Hz}}\right] \tag{2.2}$$

Stage Vibration To estimate the vibrations induced by scanning the micro-station stages, two geophones are used, as shown in Figure 2.6b. The vertical relative velocity between the top platform of the positioning hexapod and the granite is estimated in two cases: without moving the micro-station stages, and then during a Spindle rotation at 6 Rotations Per Minute (RPM). The vibrations induced by the T_y stage are not considered here because they have less amplitude than the vibrations induced by the R_z stage and because the T_y stage can be scanned at lower velocities if the induced vibrations are found to be an issue.

The amplitude spectral density of the relative motion with and without the Spindle rotation are compared in Figure 2.9. It is shown that the spindle rotation increases the vibrations above 20 Hz. The sharp peak observed at 24 Hz is believed to be induced by electromagnetic interference between the currents in the spindle motor phases and the geophone cable because this peak is not observed when rotating the spindle “by hand”.

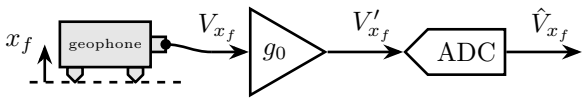

Figure 2.7: Measurement setup for one geophone. The inertial displacement x_f is converted to a voltage V_{x_f} by the geophone. This voltage is amplified by a factor $g_0 = 60$ dB using a low-noise voltage amplifier. It is then converted to a digital value $\hat{V}_{x_f}$ using a 16bit ADC.

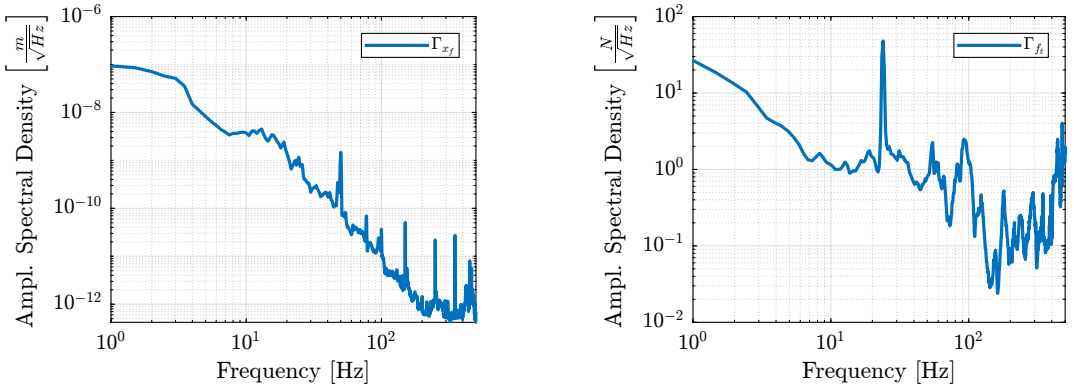

(a) Estimated ASD of x_f

(b) Estimated ASD of f_t

Figure 2.8: Estimated amplitude spectral density of the floor motion x_f (a) and of the stage disturbances f_t (b). Data are shown between 1 and 500 Hz, a frequency range for which the measurement quality is good.

To compute the equivalent disturbance force f_t (Figure 2.2b) that induces such motion, the transfer function $G_{f_t}(s)$ from f_t to the relative motion between the positioning hexapod's top platform and the granite $(x_h - x_g)$ is extracted from the model. The amplitude spectral density Γ_{f_t} of the disturbance force is them computed from (2.3) and is shown in Figure 2.8b.

$$\Gamma_{f_t}(\omega) = \frac{\Gamma_{R_z}(\omega)}{|G_{f_t}(j\omega)|} \tag{2.3}$$

2.1.4 Open-Loop Dynamic Error Budgeting

Now that a model of the NASS has been obtained (see section 2.1.2) and that the disturbances have been estimated (see section 2.1.3), it is possible to perform an *open-loop dynamic error budgeting*.

To perform such error budget, the disturbances need to be modelled by their spectral densities (done in section 2.1.3). Then, the transfer functions from disturbances to the performance metric (here the distance d) are computed. Finally, these two types of information are combined to estimate the corresponding spectral density of the performance metric. This is very useful to identify what is limiting the performance of the system, and to compare the achievable performance with different system parameters.

Sensitivity to Disturbances From the uniaxial model of the NASS (Figure 2.4a), the transfer function from the disturbances (f_s, x_f and f_t) to the displacement d are computed.

This is done for two extreme sample masses $m_s = 1$ kg and $m_s = 50$ kg and three active platform stiffnesses:

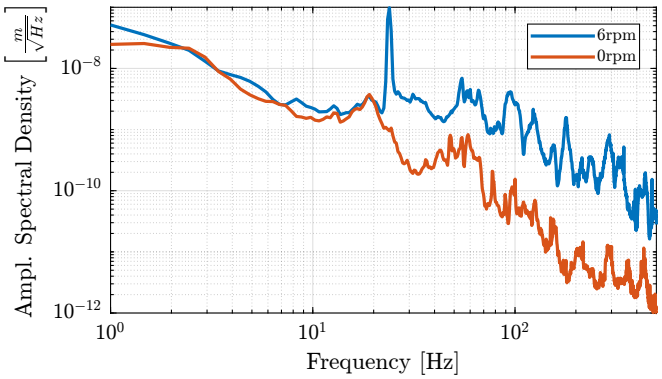

Figure 2.9: Amplitude Spectral Density Γ_{R_z} of the relative motion measured between the granite and the positioning hexapod's top platform during continuous Spindle rotation.

- $k_n = 0.01\,\text{N}/\mu\text{m}$ that represents a voice coil actuator with soft flexible guiding
- $k_n = 1\,\text{N}/\mu\text{m}$ that represents a voice coil actuator with a stiff flexible guiding or a mechanically amplified piezoelectric actuator
- $k_n = 100\,\text{N}/\mu\text{m}$ that represents a stiff piezoelectric stack actuator

The obtained sensitivity to disturbances for the three active platform stiffnesses are shown in Figure 2.10 for the sample mass $m_s = 1\,\text{kg}$ (the same conclusions can be drawn with $m_s = 50\,\text{kg}$):

- The soft active platform is more sensitive to forces applied on the sample (cable forces for instance), which is expected due to its lower stiffness (Figure 2.10a)
- Between the suspension mode[1] of the active platform (here at 5 Hz) and the first mode of the micro-station (here at 70 Hz), the disturbances induced by the stage vibrations are filtered out (Figure 2.10b)
- Above the suspension mode of the active platform, the sample's inertial motion is unaffected by the floor motion; therefore, the sensitivity to floor motion is close to 1 (Figure 2.10c)

Open-Loop Dynamic Error Budgeting Now, the amplitude spectral densities of the disturbances are considered to estimate the residual motion d for each active platform and sample configuration. The Cumulative Amplitude Spectrum (CAS) of the relative motion d due to both floor motion x_f and stage vibrations f_t are shown in Figure 2.11a for the three active platform stiffnesses. It is shown that the effect of floor motion is much less than that of stage vibrations, except for the soft active platform below 5 Hz.

The total cumulative amplitude spectrum of d for the three active platform stiffnesses and for the two samples masses are shown in Figure 2.11b. The conclusion is that the sample mass has little effect on the cumulative amplitude spectrum of the relative motion d.

Conclusion The open-loop residual vibrations of d can be estimated from the low-frequency value of the cumulative amplitude spectrum in Figure 2.11b. This residual vibration of d is found to be in the order of 100 nm RMS for the stiff active platform ($k_n = 100\,\text{N}/\mu\text{m}$), 200 nm RMS for the relatively stiff active platform ($k_n = 1\,\text{N}/\mu\text{m}$) and

[1] In this work, the "suspension mode" of a platform refers to a low-frequency vibration mode in which the supported payload behaves as a rigid body, while the platform acts as a compliant support.

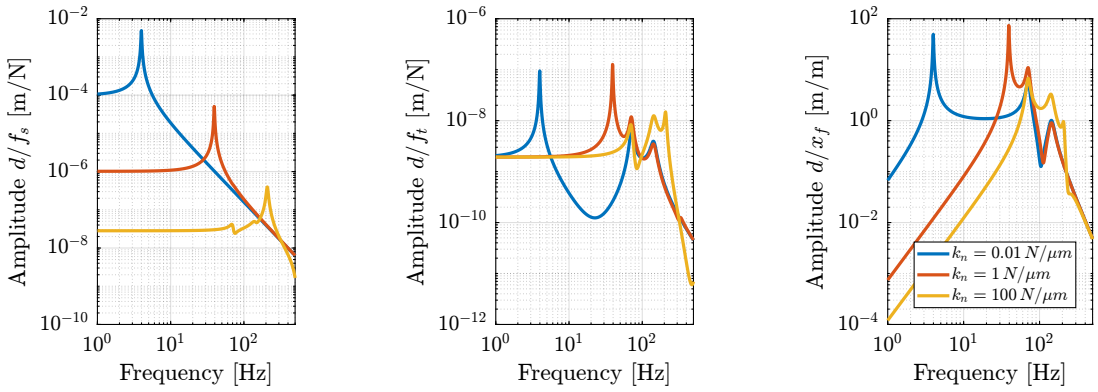

(a) Direct forces **(b)** μ-station disturbances **(c)** Floor motion

Figure 2.10: Sensitivity of d to disturbances for three different active platform stiffnesses. f_s the direct forces applied on the sample (a), f_t disturbances from the micro-station stages (b) and x_f the floor motion (c).

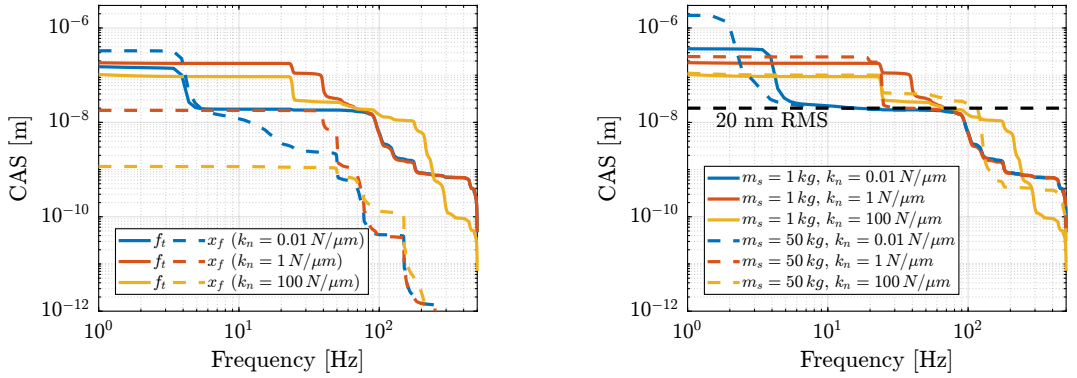

(a) Effect of floor motion x_f and stage disturbances f_t **(b)** Effect of active platform stiffness k_n and payload mass m_s

Figure 2.11: Cumulative Amplitude Spectrum of the relative motion d. The effect of x_f and f_t are shown in (a). The effect of sample mass for the three active platform stiffnesses is shown in (b). The control objective of having a residual error of 20 nm RMS is shown by the horizontal black dashed line.

1 µm RMS for the soft active platform ($k_n = 0.01$ N/µm). From this analysis, it may be concluded that the stiffer the active platform the better.

However, what is more important is the *closed-loop* residual vibration of d (i.e., while the feedback controller is used). The goal is to obtain a closed-loop residual vibration $\epsilon_d \approx 20$ nm RMS (represented by an horizontal dashed black line in Figure 2.11b). The bandwidth of the feedback controller leading to a closed-loop residual vibration of 20 nm RMS can be estimated as the frequency at which the cumulative amplitude spectrum crosses the black dashed line in Figure 2.11b.

This is why, in this document, cumulative amplitude spectra are computed by integrating from high to low frequency. Another important point is that cumulative \ spectra are plotted instead of cumulative \ spectra, despite the warnings discussed in [127, Chapt. 8.1.5]. This choice comes at the cost of losing the straightforward interpretation of the relative importance of different frequencies, but it makes the plots easier to read and simplifies the estimation of the bandwidth required to achieve a desired residual RMS value.

A closed loop bandwidth of ≈ 10 Hz is found for the soft active platform ($k_n = 0.01\,\mathrm{N/\mu m}$), ≈ 50 Hz for the relatively stiff active platform ($k_n = 1\,\mathrm{N/\mu m}$), and ≈ 100 Hz for the stiff active platform ($k_n = 100\,\mathrm{N/\mu m}$). Therefore, while the *open-loop* vibration is the lowest for the stiff active platform, it requires the largest feedback bandwidth to meet the specifications.

The advantage of the soft active platform can be explained by its natural isolation from the micro-station vibration above its suspension mode, as shown in Figure 2.10b.

2.1.5 Active Damping

In this section, three active damping techniques are applied to the active platform (see Figure 2.12): Integral Force Feedback (IFF) [115], Relative Damping Control (RDC) [113, Chapt. 7.2] and Direct Velocity Feedback (DVF) [77, 116, 131].

These damping strategies are first described and are then compared in terms of achievable damping of the active platform mode, reduction of the effect of disturbances (i.e., x_f, f_t and f_s) on the displacement d.

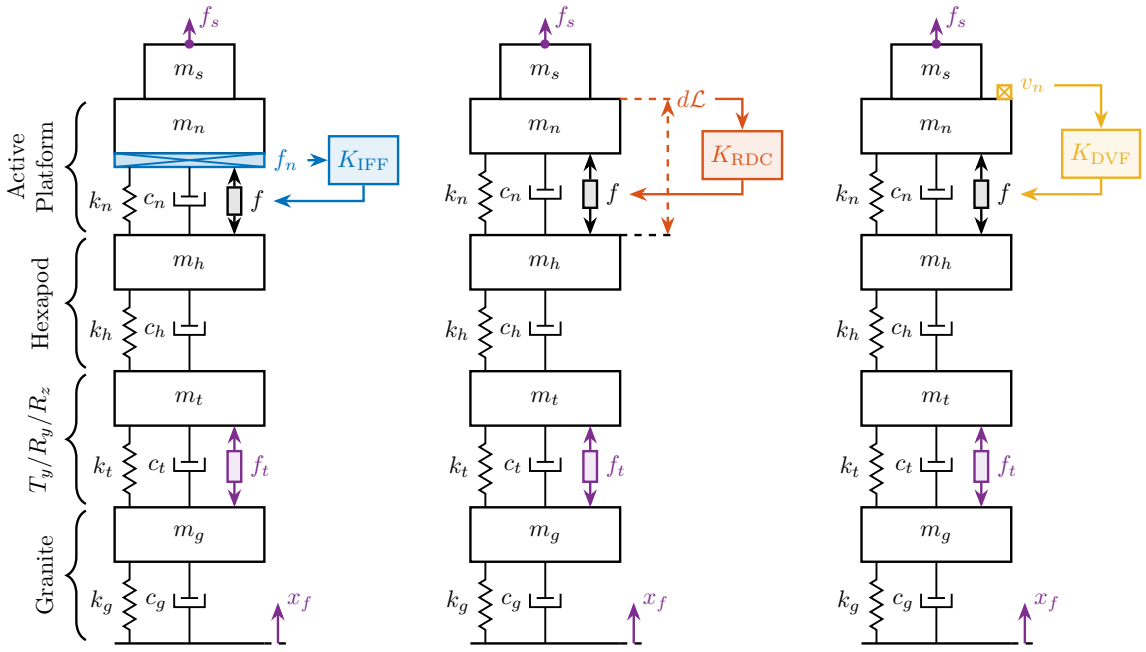

(a) IFF **(b)** RDC **(c)** DVF

Figure 2.12: Three active damping strategies. Integral Force Feedback (a) using a force sensor, Relative Damping Control (b) using a relative displacement sensor, and Direct Velocity Feedback (c) using a geophone.

Integral Force Feedback (IFF) The Integral Force Feedback strategy consists of using a force sensor in series with the actuator (see Figure 2.13a) and applying an "integral" feedback controller (2.4).

$$\boxed{K_{\text{IFF}}(s) = \frac{g}{s}} \tag{2.4}$$

The mechanical equivalent of this IFF strategy is a dashpot in series with the actuator stiffness with a damping coefficient equal to the stiffness of the actuator divided by the controller gain k/g (see Figure 2.13b).

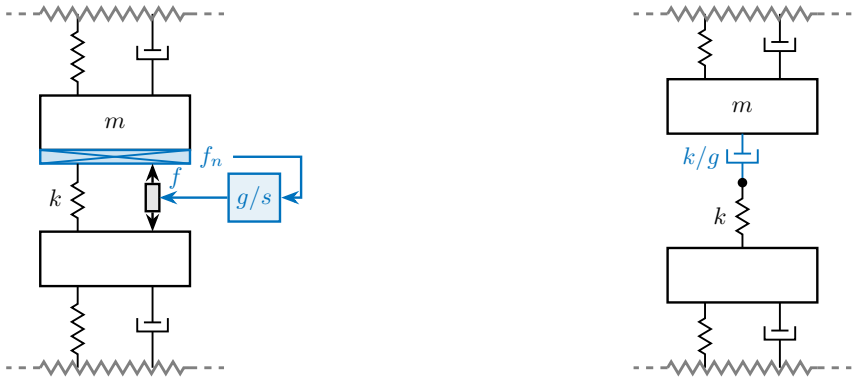

(a) Integral Force Feedback

(b) Equivalent mechanical representation

Figure 2.13: Integral Force Feedback (a) is equivalent to a damper in series with the actuator stiffness (b).

Relative Damping Control (RDC) For the Relative Damping Control strategy, a relative motion sensor that measures the motion of the actuator is used (see Figure 2.14a) and a "derivative" feedback controller is used (2.5).

$$\boxed{K_{\text{RDC}}(s) = -g \cdot s} \tag{2.5}$$

The mechanical equivalent of RDC is a dashpot in parallel with the actuator with a damping coefficient equal to the controller gain g (see Figure 2.14b).

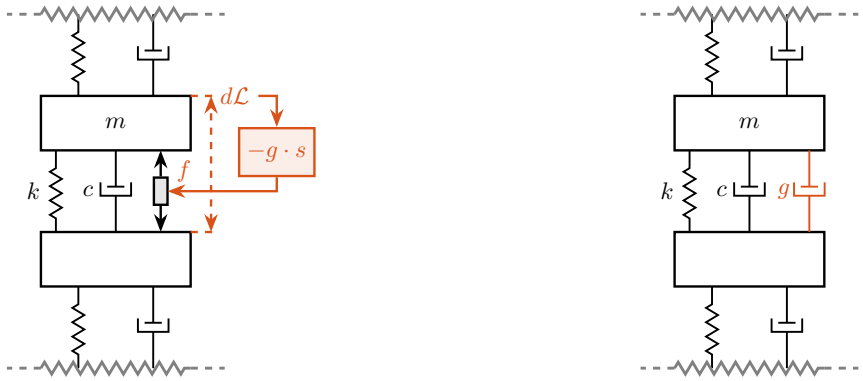

(a) Relative motion control

(b) Equivalent mechanical representation

Figure 2.14: Relative Damping Control (a) is equivalent to a damper in parallel with the actuator (b).

Direct Velocity Feedback (DVF) Finally, the direct velocity feedback strategy consists of using an inertial sensor (usually a geophone) that measures the "absolute" velocity of the body fixed on top of the actuator (see Figure 2.15a). This velocity is fed back to the actuator with a "proportional" controller (2.6).

$$\boxed{K_{\text{DVF}}(s) = -g} \tag{2.6}$$

This is equivalent to a dashpot (with a damping coefficient equal to the controller gain g) between the body (on which the inertial sensor is fixed) and an inertial reference frame (see Figure 2.15b). This is usually referred to as "*sky hook damper*".

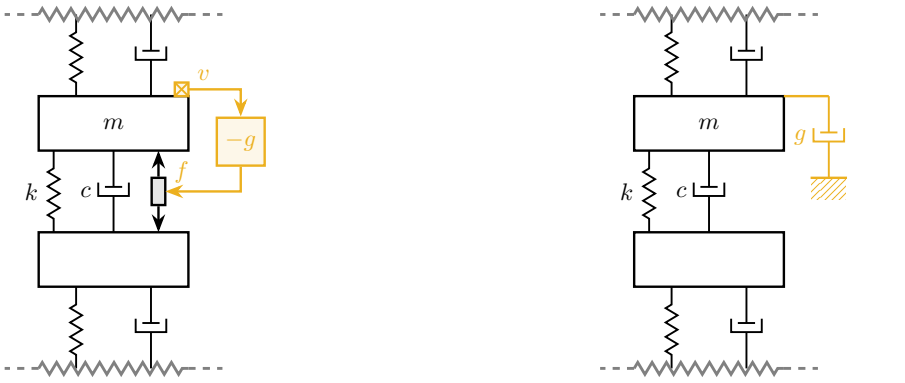

(a) Direct velocity feedback

(b) Equivalent mechanical representation

Figure 2.15: Direct velocity Feedback (a) is equivalent to a "sky hook damper" (b).

Plant Dynamics for Active Damping The plant dynamics for all three active damping techniques are shown in Figure 2.16. All have *alternating poles and zeros* meaning that the phase does not vary by more than 180 deg which makes the design of a *robust* damping controller very easy.

This alternating poles and zeros property is guaranteed for the IFF and RDC cases because the sensors are collocated with the actuator [113, Chapt. 7]. For the DVF controller, this property is not guaranteed, and may be lost if some flexibility between the active platform and the sample is considered [113, Chapt. 8.4].

When the active platform's suspension modes are at frequencies lower than the resonances of the micro-station (blue and red curves in Figure 2.16), the resonances of the micro-stations have little impact on the IFF and DVF transfer functions. For the stiff active platform (yellow curves), the micro-station dynamics can be seen on the transfer functions in Figure 2.16. Therefore, it is expected that the micro-station dynamics might impact the achievable damping if a stiff active platform is used.

Achievable Damping and Damped Plants To compare the added damping using the three considered active damping strategies, the root locus plot is used. Indeed, the damping ratio ξ of a pole in the complex plane can be estimated from the angle ϕ it makes with the imaginary axis (2.7). Increasing the angle with the imaginary axis therefore means that more damping is added to the considered resonance. This is illustrated in Figure 2.18 by the dashed black line indicating the maximum achievable damping.

$$\xi = \sin(\phi) \tag{2.7}$$

The root locus for the three active platform stiffnesses and the three active damping techniques are shown in Figure 2.17. All three active damping approaches can lead to *critical damping* of the active platform suspension mode (angle ϕ can be increased up to 90 degrees). There is even some damping authority on micro-station modes in the following cases:

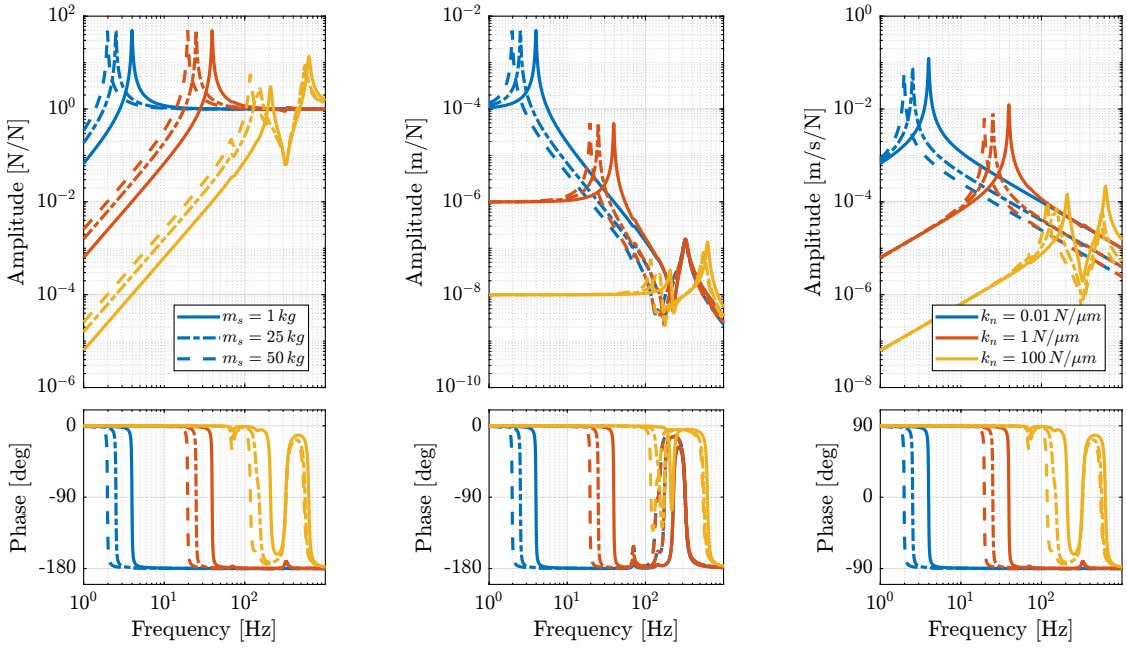

(a) IFF **(b)** RDC **(c)** DVF

Figure 2.16: Plant dynamics for the three active damping techniques: IFF (a), RDC (b) and DVF (c)). Three active platform stiffnesses ($k_n = 0.01$ N/µm in blue, $k_n = 1$ N/µm in red and $k_n = 100$ N/µm in yellow) and three sample's masses ($m_s = 1$ kg: solid curves, $m_s = 25$ kg: dot-dashed curves, and $m_s = 50$ kg: dashed curves) are considered in each case.

IFF with a stiff active platform (Figure 2.17c) This can be understood from the mechanical equivalent of IFF shown in Figure 2.13b considering an high stiffness k. The micro-station top platform is connected to an inertial mass (the active platform) through a damper, which dampens the micro-station suspension mode.

DVF with a stiff active platform (Figure 2.17c) In that case, the "sky hook damper" (see mechanical equivalent of DVF in Figure 2.15b) is connected to the micro-station top platform through the stiff active platform.

RDC with a soft active platform (Figure 2.18) At the frequency of the micro-station mode, the active platform top mass behaves as an inertial reference because the suspension mode of the soft active platform is at much lower frequency. The micro-station and the active platform masses are connected through a large damper induced by RDC (see mechanical equivalent in Figure 2.14b) which allows some damping of the micro-station.

The transfer functions from the plant input f to the relative displacement d while active damping is implemented are shown in Figure 2.19. All three active damping techniques yielded similar damped plants.

Sensitivity to Disturbances and Error Budget Reasonable gains are chosen for the three active damping strategies such that the active platform suspension mode is well damped. The sensitivity to disturbances (direct forces f_s, stage vibrations f_t and floor motion x_f) for all three active damping techniques are compared in Figure 2.20. The comparison is done with the active platform having a stiffness $k_n = 1$ N/µm.

Several conclusions can be drawn by comparing the obtained sensitivity transfer functions:

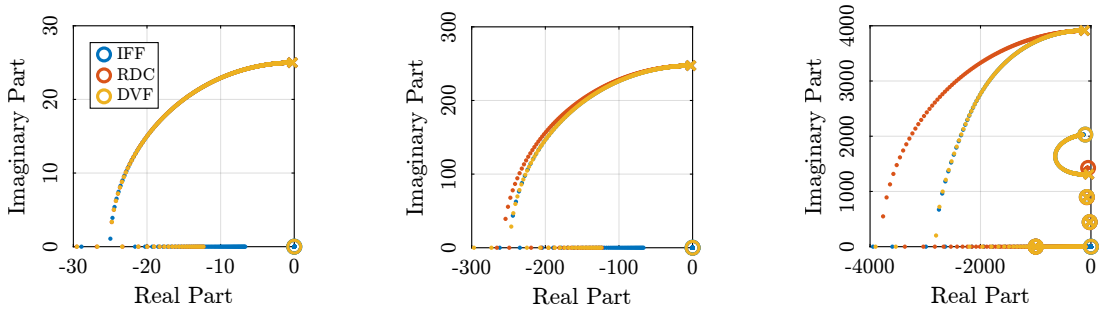

(a) $k_n = 0.01\,\mathrm{N/\mu m}$ **(b)** $k_n = 1\,\mathrm{N/\mu m}$ **(c)** $k_n = 100\,\mathrm{N/\mu m}$

Figure 2.17: Root loci for the three active damping techniques (IFF in blue, RDC in red and DVF in yellow). This is shown for the three active platform stiffnesses. The root loci are zoomed on the suspension mode of the active platform.

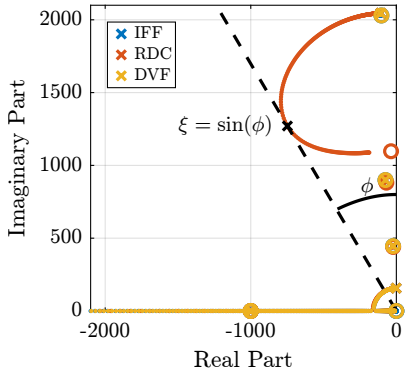

Figure 2.18: Root locus for the three damping techniques applied with the soft active platform. It is shown that the RDC active damping technique has some authority on one mode of the micro-station. This mode corresponds to the suspension mode of the positioning hexapod.

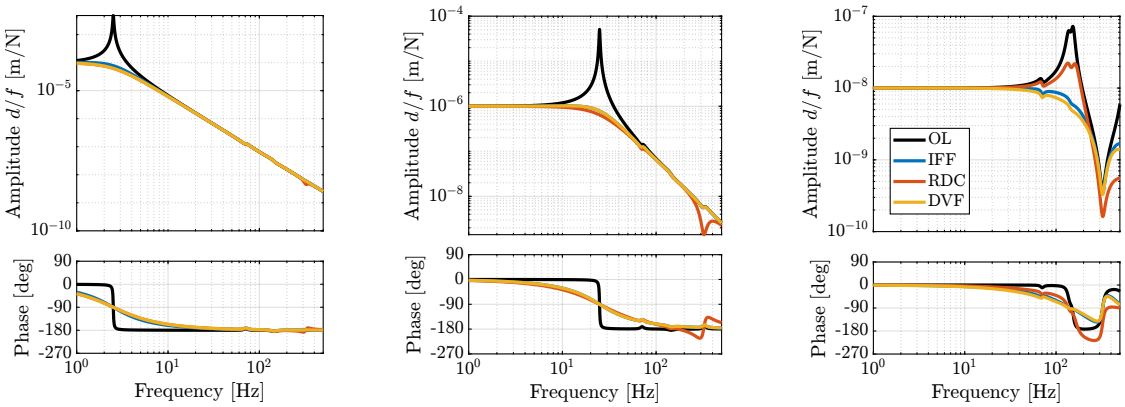

(a) $k_n = 0.01\,\mathrm{N/\mu m}$ **(b)** $k_n = 1\,\mathrm{N/\mu m}$ **(c)** $k_n = 100\,\mathrm{N/\mu m}$

Figure 2.19: Obtained damped transfer functions from f to d for the three damping techniques.

- IFF degrades the sensitivity to direct forces on the sample (i.e., the compliance) below the resonance of the active platform (Figure 2.20a). This is a well-known effect of using IFF for vibration isolation [28].
- RDC degrades the sensitivity to stage vibrations around the active platform's resonance as compared to the other two methods (Figure 2.20b). This is because the equivalent damper in parallel with the actuator (see Figure 2.14b) increases the transmission of the micro-station vibration to the sample which is not the same for the other two active damping strategies.
- both IFF and DVF degrade the sensitivity to floor motion below the resonance of the active platform (Figure 2.20c).

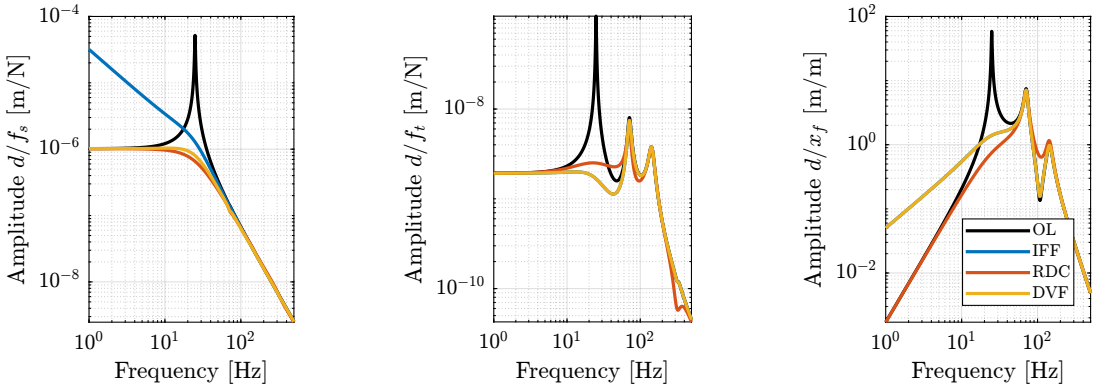

(a) Direct forces **(b)** μ-station disturbances **(c)** Floor motion

Figure 2.20: Change of sensitivity to disturbances for all three active damping strategies. Considered disturbances are f_s the direct forces applied on the sample (a), f_t disturbances from the micro-station stages (b) and x_f the floor motion (c). Sensitivity for IFF (displayed in blue) is superimposed with the sensitivity for DVF (yellow).

From the amplitude spectral density of the disturbances (computed in Section 2.1.3) and the sensitivity to disturbances estimated using the three active damping strategies, a noise budget can be calculated. The cumulative amplitude spectrum of the distance d with all three active damping techniques is shown in Figure 2.21 and compared with the open-loop case. All three active damping methods give similar results.

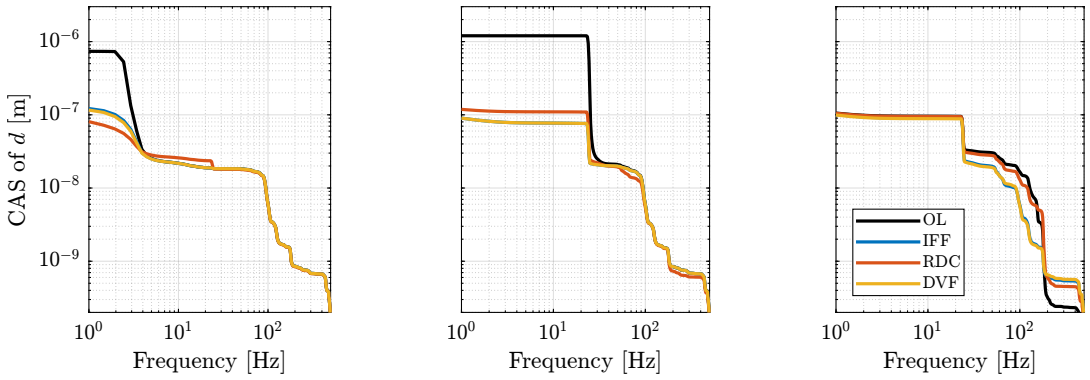

(a) $k_n = 0.01\,\mathrm{N/\mu m}$ **(b)** $k_n = 1\,\mathrm{N/\mu m}$ **(c)** $k_n = 100\,\mathrm{N/\mu m}$

Figure 2.21: Comparison of the Cumulative Amplitude Spectrum of the distance d for all three active damping techniques.

Conclusion Three active damping strategies have been studied for the Nano Active Stabilization System (NASS). Equivalent mechanical representations were derived which are helpful for understanding the specific effects of each

strategy. The plant dynamics were then compared and were found to all have alternating poles and zeros, which helps in the design of the active damping controller. However, this property is not guaranteed for DVF. The achievable damping of the active platform suspension mode can be made as large as possible for all three active damping techniques. Even some damping can be applied to some micro-station modes in specific cases. The obtained damped plants were found to be similar. The damping strategies were then compared in terms of disturbance reduction.

The comparison between the three active damping strategies is summarized in Table 2.2. It is difficult to conclude on the best active damping strategy for the Nano Active Stabilization System (NASS) yet. The one used will be determined by the use of more accurate models and will depend on which is easiest to implement in practice

Table 2.2: Comparison of active damping strategies for the NASS.

	IFF	**RDC**	**DVF**
Sensor	Force sensor	Relative motion sensor	Inertial sensor
Damping	Up to critical	Up to critical	Up to Critical
Robustness	Requires collocation	Requires collocation	Impacted by geophone resonances
f_s **Disturbance**	↗ at low frequency	↘ near resonance	↘ near resonance
f_t **Disturbance**	↘ near resonance	↗ near resonance	↘ near resonance
x_f **Disturbance**	↗ at low frequency	↘ near resonance	↗ at low frequency

2.1.6 Position Feedback Controller

The High Authority Control / Low Authority Control (HAC-LAC) architecture is shown in Figure 2.22a. This corresponds to a *two step* control strategy:

- First, an active damping controller $\boldsymbol{K}_{\text{LAC}}$ is implemented (see Section 2.1.5). It allows the vibration level to be reduced, and it also makes the damped plant (transfer function from u' to y) easier to control than the undamped plant (transfer function from u to y). This is called *low authority* control as it only slightly affects the system poles [113, Chapt. 14.6].

- Then, a position controller $\boldsymbol{K}_{\text{HAC}}$ is implemented and is used to control the position d. This is called *high authority* control as it usually relocates the system's poles.

In this section, Integral Force Feedback is used as the Low Authority Controller (the other two damping strategies would lead to the same conclusions here). This control architecture applied to the uniaxial model is shown in Figure 2.22b.

Damped Plant Dynamics The damped plants obtained for the three active platform stiffnesses are shown in Figure 2.23. For $k_n = 0.01\,\text{N}/\mu\text{m}$ and $k_n = 1\,\text{N}/\mu\text{m}$, the dynamics are quite simple and can be well approximated by a second-order plant (Figures 2.23a and 2.23b). However, this is not the case for the stiff active platform ($k_n = 100\,\text{N}/\mu\text{m}$) where two modes can be seen (Figure 2.23c). This is due to the interaction between the micro-station (modelled modes at 70 Hz, 140 Hz and 320 Hz) and the active platform. This effect will be further explained in Section 2.1.7.

Position Feedback Controller The objective is to design high-authority feedback controllers for the three active platforms. This controller must be robust to the change of sample's mass (from 1 kg up to 50 kg).

The required feedback bandwidths were estimated in Section 2.1.4:

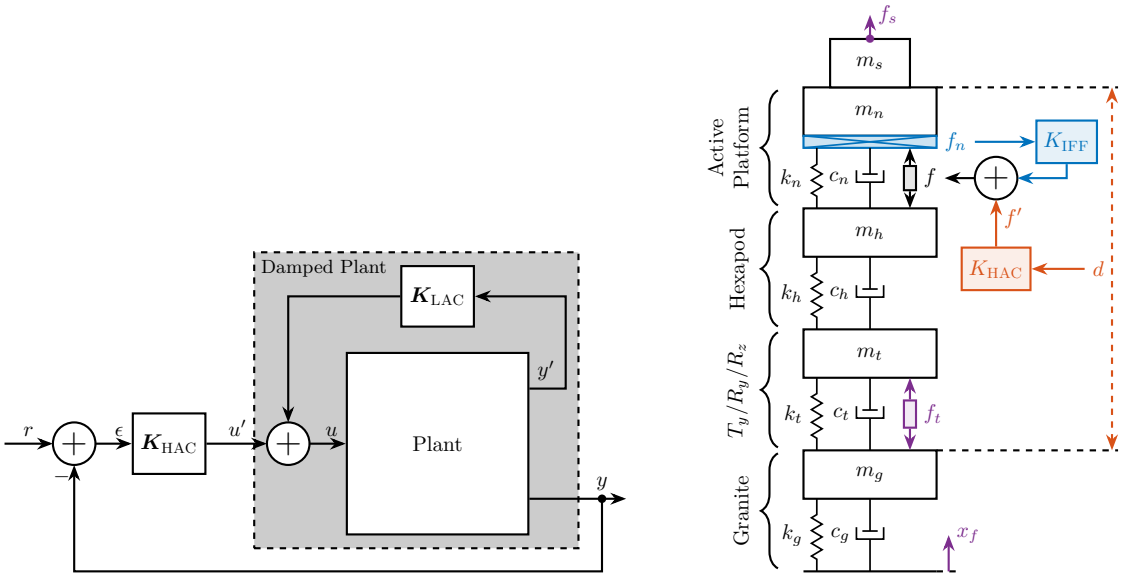

(a) Typical HAC-LAC Architecture

(b) Uniaxial model with HAC-IFF strategy

Figure 2.22: High Authority Control / Low Authority Control (HAC-LAC).

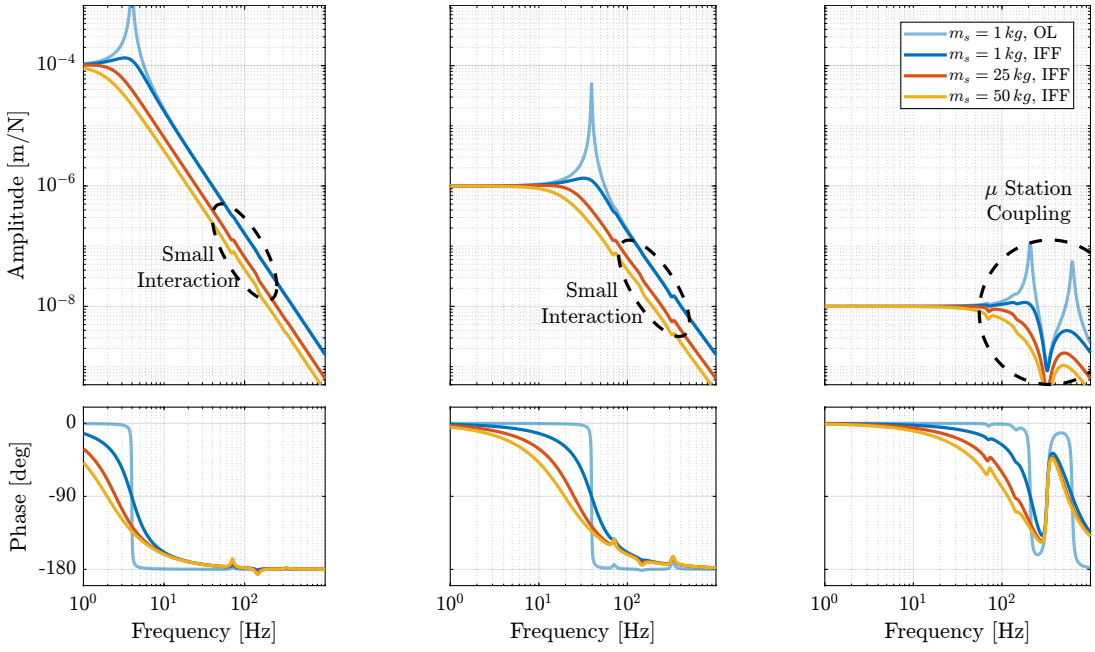

(a) $k_n = 0.01\,\mathrm{N/\mu m}$

(b) $k_n = 1\,\mathrm{N/\mu m}$

(c) $k_n = 100\,\mathrm{N/\mu m}$

Figure 2.23: Obtained damped plant using Integral Force Feedback for three sample masses.

- $f_b \approx 10\,\text{Hz}$ for the soft active platform ($k_n = 0.01\,\text{N}/\mu\text{m}$). Near this frequency, the plants (shown in Figure 2.23a) are equivalent to a mass line (i.e., slope of -40 dB/dec and a phase of -180 degrees). The gain of this mass line can vary up to a factor ≈ 5 (suspended mass from 16 kg up to 65 kg). This means that the designed controller will need to have *large gain margins* to be robust to the change of sample's mass.

- ≈ 50 Hz for the relatively stiff active platform ($k_n = 1\,\text{N}/\mu\text{m}$). Similar to the soft active platform, the plants near the crossover frequency are equivalent to a mass line (Figure 2.23b). It will probably be easier to have a little bit more bandwidth in this configuration to be further away from the active platform suspension mode.

- ≈ 100 Hz for the stiff active platform ($k_n = 100\,\text{N}/\mu\text{m}$). Contrary to the two first active platform stiffnesses, here the plants have more complex dynamics near the desired crossover frequency (see Figure 2.23c). The micro-station is not stiff enough to have a clear stiffness line at this frequency. Therefore, there is both a change of phase and gain depending on the sample mass. This makes the robust design of the controller more complicated.

Position feedback controllers are designed for each active platform such that it is stable for all considered sample masses with similar stability margins (see Nyquist plots in Figure 2.24). An arbitrary minimum modulus margin of 0.25 was chosen when designing the controllers. These High Authority Controls (HACs) are generally composed of a lag at low frequency for disturbance rejection, a lead to increase the phase margin near the crossover frequency, and a Low Pass Filter (LPF) to increase the robustness to high-frequency dynamics. The controllers used for the three active platform are shown in Equation (2.8), and the parameters used are summarized in Table 2.3.

$$K_{\text{soft}}(s) = g \cdot \underbrace{\frac{s+\omega_0}{s+\omega_i}}_{\text{lag}} \cdot \underbrace{\frac{1+\frac{s}{\omega_c/\sqrt{a}}}{1+\frac{s}{\omega_c\sqrt{a}}}}_{\text{lead}} \cdot \underbrace{\frac{1}{1+\frac{s}{\omega_l}}}_{\text{LPF}} \tag{2.8a}$$

$$K_{\text{mid}}(s) = g \cdot \underbrace{\left(\frac{s+\omega_0}{s+\omega_i}\right)^2}_{\text{2 lags}} \cdot \underbrace{\frac{1+\frac{s}{\omega_c/\sqrt{a}}}{1+\frac{s}{\omega_c\sqrt{a}}}}_{\text{lead}} \cdot \underbrace{\frac{1}{1+\frac{s}{\omega_l}}}_{\text{LPF}} \tag{2.8b}$$

$$K_{\text{stiff}}(s) = g \cdot \underbrace{\left(\frac{1}{s+\omega_i}\right)^2}_{\text{2 lags}} \cdot \underbrace{\left(\frac{1+\frac{s}{\omega_c/\sqrt{a}}}{1+\frac{s}{\omega_c\sqrt{a}}}\right)^2}_{\text{2 leads}} \cdot \underbrace{\frac{1}{1+\frac{s}{\omega_l}}}_{\text{LPF}} \tag{2.8c}$$

Table 2.3: Parameters used for the position feedback controllers.

	Soft	Moderately stiff	Stiff
Gain	$g = 4 \cdot 10^5$	$g = 3 \cdot 10^6$	$g = 6 \cdot 10^{12}$
Lead	$a = 5$, $\omega_c = 20$ Hz	$a = 4$, $\omega_c = 70$ Hz	$a = 5$, $\omega_c = 100$ Hz
Lag	$\omega_0 = 5$ Hz, $\omega_i = 0.01$ Hz	$\omega_0 = 20$ Hz, $\omega_i = 0.01$ Hz	$\omega_i = 0.01$ Hz
LPF	$\omega_l = 200$ Hz	$\omega_l = 300$ Hz	$\omega_l = 500$ Hz

The loop gains corresponding to the designed High Authority Controls for the three active platform are shown in Figure 2.25. We can see that for the soft and moderately stiff active platform (Figures 2.24a and 2.24b), the crossover frequency varies significantly with the sample mass. This is because the crossover frequency corresponds to the mass line of the plant (whose gain is inversely proportional to the mass). For the stiff active platform (Figure 2.24c), it was difficult to achieve the desired closed-loop bandwidth of ≈ 100 Hz. A crossover frequency of ≈ 65 Hz was achieved instead.

Note that these controllers were not designed using any optimization methods. The goal is to have a first estimation of the attainable performance.

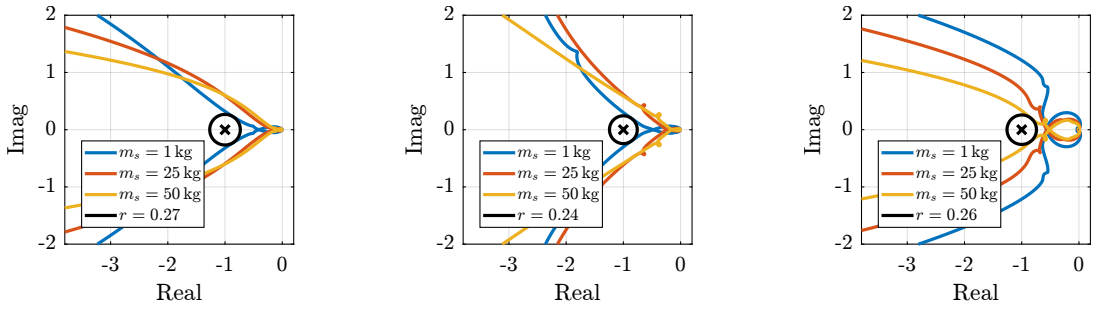

(a) $k_n = 0.01\,\mathrm{N/\mu m}$ **(b)** $k_n = 1\,\mathrm{N/\mu m}$ **(c)** $k_n = 100\,\mathrm{N/\mu m}$

Figure 2.24: Nyquist Plot for the High Authority Controllers. The modulus margin is illustrated by the black circles.

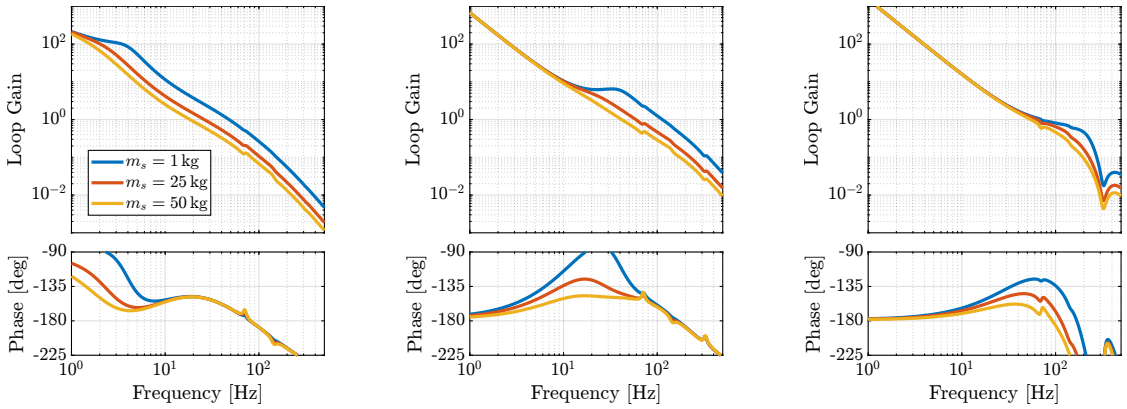

(a) $k_n = 0.01\,\mathrm{N/\mu m}$ **(b)** $k_n = 1\,\mathrm{N/\mu m}$ **(c)** $k_n = 100\,\mathrm{N/\mu m}$

Figure 2.25: Loop gains for the High Authority Controllers.

Closed-Loop Error Budgeting The developed High Authority Controls are then implemented and the closed-loop sensitivities to disturbances are computed. These are compared with the open-loop and damped plants cases in Figure 2.26 for just one configuration (moderately stiff active platform with 25 kg sample's mass). As expected, the sensitivity to disturbances decreased in the controller bandwidth and slightly increased outside this bandwidth.

The cumulative amplitude spectrum of the motion d is computed for all active platform configurations, all sample masses and in the Open Loop (OL), damped (IFF) and position controlled (HAC-IFF) cases. The results are shown in Figure 2.27. Obtained root mean square values of the distance d are better for the soft active platform ($\approx$ 25 nm to $\approx$ 35 nm depending on the sample's mass) than for the stiffer active platform (from $\approx$ 30 nm to $\approx$ 70 nm).

Conclusion On the basis of the open-loop error budgeting made in Section 2.1.4, the closed-loop bandwidth required to obtain a vibration level of $\approx$ 20 nm RMS was estimated. To achieve such bandwidth, the HAC-LAC strategy was followed, which consists of first using an active damping controller (studied in Section 2.1.5) and then adding a high authority position feedback controller.

In this section, feedback controllers were designed in such a way that the required closed-loop bandwidth was reached while being robust to changes in the payload mass. The attainable vibration control performances were estimated for the three active platform stiffnesses and were found to be close to the required values. However, the stiff active platform ($k_n = 100\,\mathrm{N/\mu m}$) requires the largest feedback bandwidth, which is difficult to achieve while being robust to the

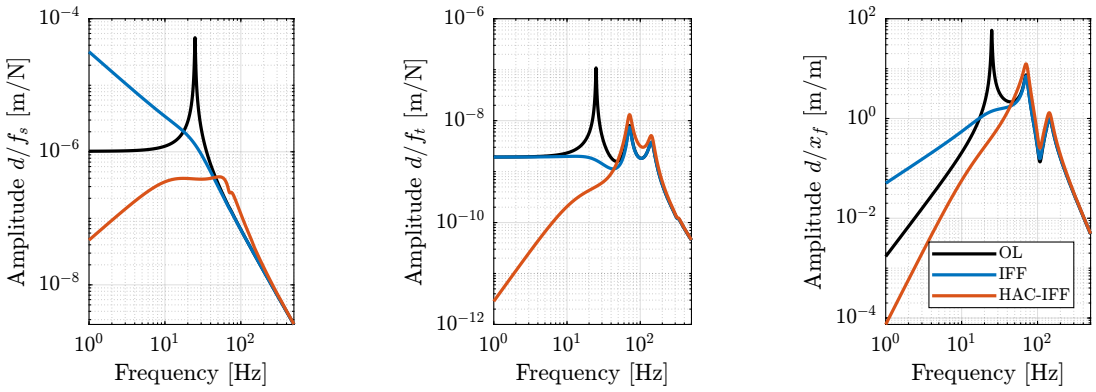

(a) Direct forces **(b)** μ-station disturbances **(c)** Floor motion

Figure 2.26: Change of sensitivity to disturbances with LAC and with HAC-LAC. An active platform with $k_n = 1\,\text{N}/\mu\text{m}$ and a sample mass of 25 kg are used. Disturbances are: f_s the direct forces applied on the sample (a), f_t the disturbances from the micro-station stages (b) and x_f the floor motion (c).

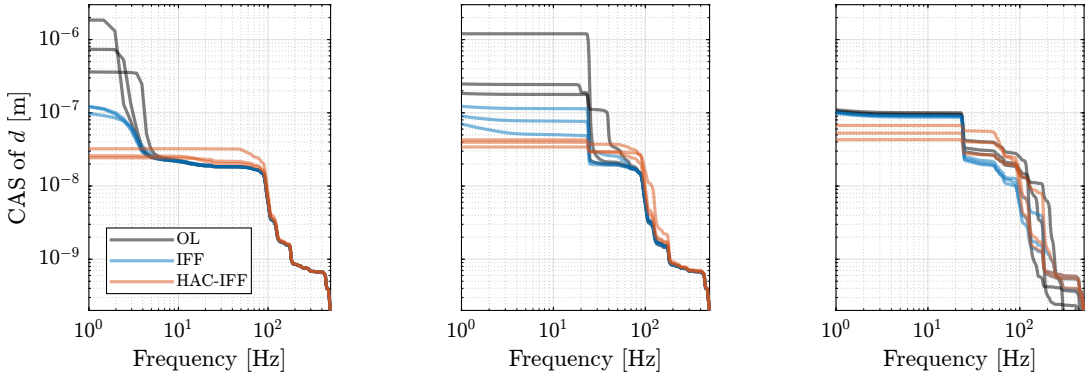

(a) $k_n = 0.01\,\text{N}/\mu\text{m}$ **(b)** $k_n = 1\,\text{N}/\mu\text{m}$ **(c)** $k_n = 100\,\text{N}/\mu\text{m}$

Figure 2.27: Cumulative Amplitude Spectra for all three active platform stiffnesses in OL, with IFF and with HAC-LAC. The three lines of each color are corresponding to the considered three sample masses.

change of payload mass. A slight advantage can be given to the soft active platform as it requires less feedback bandwidth while providing better stability results.

2.1.7 Effect of Limited Support Compliance

In this section, the impact of the compliance of the support (i.e., the micro-station) on the dynamics of the plant to control is studied. This is a critical point because the dynamics of the micro-station is complex, depends on the considered direction (see measurements in Figure 2.3) and may vary with position and time. It would be much better to have a plant dynamics that is not impacted by the micro-station.

Therefore, the objective of this section is to obtain some guidance for the design of an active platform that will not be impacted by the complex micro-station dynamics. To study this, two models are used (Figure 2.28). The first one consists of the active platform directly fixed on top of the granite, thus neglecting any support compliance (Figure 2.28a).

The second one consists of the active platform fixed on top of the micro-station having some limited compliance (Figure 2.28b)

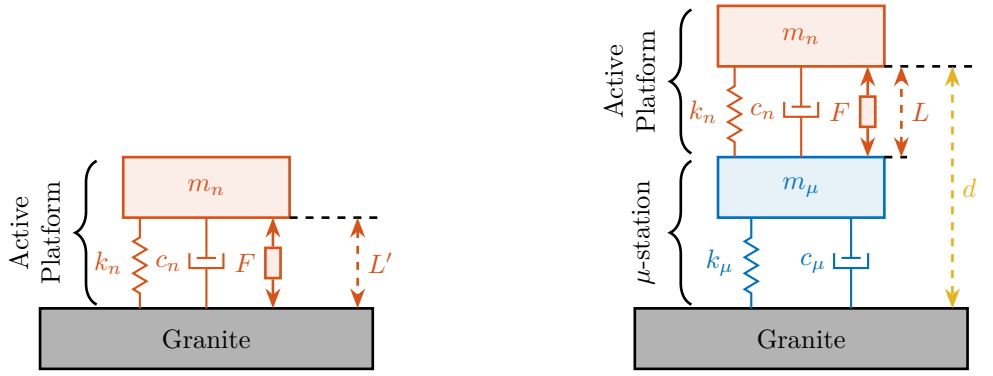

(a) Active platform fixed directly on the Granite

(b) Active platform fixed on top of the Micro-Station

Figure 2.28: Models used to study the effect of limited support compliance.

Neglected support compliance The limited compliance of the micro-station is first neglected and the uniaxial model shown in Figure 2.28a is used. The active platform mass (including the payload) is set at 20 kg and three active platform stiffnesses are considered, such that their resonance frequencies are at $\omega_n = 10$ Hz, $\omega_n = 70$ Hz and $\omega_n = 400$ Hz. Obtained transfer functions from F to L' (shown in Figure 2.29) are simple second-order low-pass filters. When neglecting the support compliance, a large feedback bandwidth can be achieved for all three active platforms.

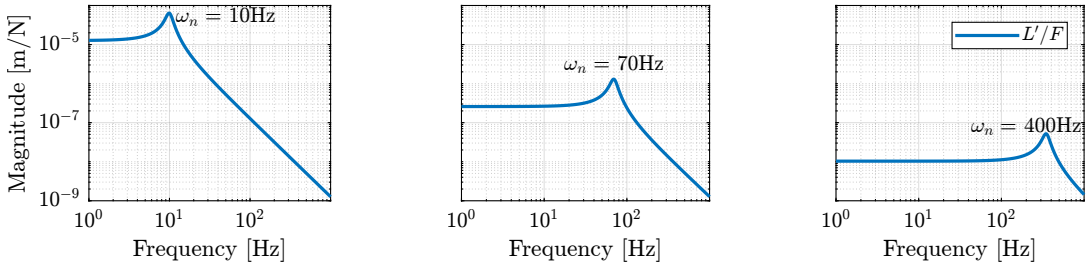

(a) $\omega_n \ll \omega_\mu$

(b) $\omega_n = \omega_\mu$

(c) $\omega_n \gg \omega_\mu$

Figure 2.29: Obtained transfer functions from F to L' when neglecting support compliance.

Effect of support compliance on L/f Some support compliance is now added and the model shown in Figure 2.28b is used. The parameters of the support (i.e., m_μ, c_μ and k_μ) are chosen to match the vertical mode at 70 Hz seen on the micro-station (Figure 2.3). The transfer functions from F to L (i.e., control of the relative motion of the active platform) and from L to d (i.e., control of the position between the active platform and the fixed granite) can then be computed.

When the relative displacement of the active platform L is controlled (dynamics shown in Figure 2.30), having a stiff active platform (i.e., with a suspension mode at higher frequency than the mode of the support) makes the dynamics less affected by the limited support compliance (Figure 2.30c). This is why it is very common to have stiff piezoelectric stages fixed at the very top of positioning stages. In such a case, the control of the piezoelectric stage using its integrated metrology (typically capacitive sensors) is quite simple as the plant is not much affected by the dynamics of the support on which it is fixed.

If a soft active platform is used, the support dynamics appears in the dynamics between F and L (see Figure 2.30a) which will impact the control robustness and performance.

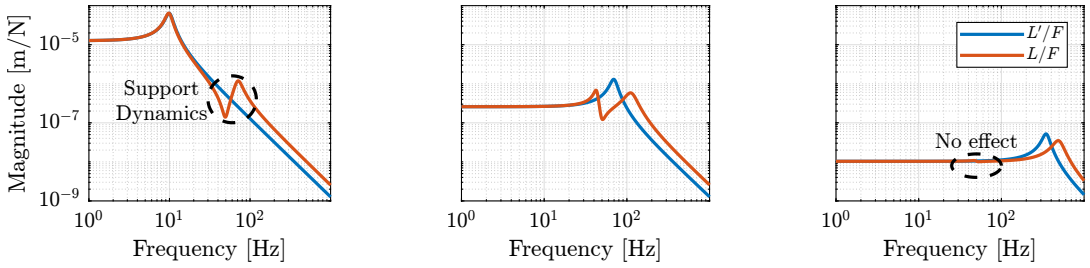

(a) $\omega_n \ll \omega_\mu$ **(b)** $\omega_n = \omega_\mu$ **(c)** $\omega_n \gg \omega_\mu$

Figure 2.30: Effect of the support compliance on the transfer functions from F to L.

Effect of support compliance on d/F When the motion to be controlled is the relative displacement d between the granite and the active platform's top platform (which is the case for the NASS), the effect of the support compliance on the plant dynamics is opposite to that previously observed. Indeed, using a "soft" active platform (i.e., with a suspension mode at lower frequency than the mode of the support) makes the dynamics less affected by the support dynamics (Figure 2.31a). Conversely, if a "stiff" active platform is used, the support dynamics appears in the plant dynamics (Figure 2.31c).

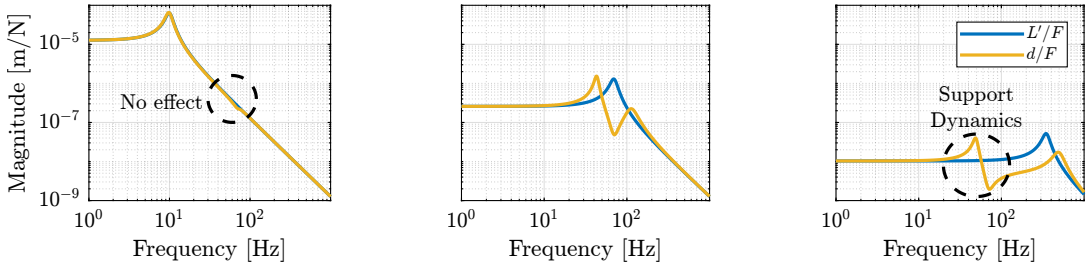

(a) $\omega_n \ll \omega_\mu$ **(b)** $\omega_n = \omega_\mu$ **(c)** $\omega_n \gg \omega_\mu$

Figure 2.31: Effect of the support compliance on the transfer functions from F to d.

Conclusion To study the impact of support compliance on plant dynamics, simple models shown in Figure 2.28 were used. Depending on the quantity to be controlled (L or d in Figure 2.28b) and on the relative location of ω_ν (suspension mode of the active platform) with respect to ω_μ (modes of the support), the interaction between the support and the active platform dynamics can drastically change (observations made are summarized in Table 2.4).

For the Nano Active Stabilization System (NASS), having the suspension mode of the active platform at lower frequencies than the suspension modes of the micro-station would make the plant less dependent on the micro-station dynamics, and therefore easier to control. Note that the observations made in this section are also affected by the ratio between the support mass m_μ and the active platform mass m_n (the effect is more pronounced when the ratio m_n/m_μ increases).

Table 2.4: Impact of the support dynamics on the plant dynamics.

	$\omega_\nu \ll \omega_\mu$	$\omega_\nu \approx \omega_\mu$	$\omega_\nu \gg \omega_\mu$
d/F	small	large	large
L/F	large	large	small

2.1.8 Effect of Payload Dynamics

Up to this section, the sample was modelled as a mass rigidly fixed to the active platform (as shown in Figure 2.32a). However, such a sample may present internal dynamics, and its mounting on the active platform may have limited stiffness. To study the effect of the sample dynamics, the models shown in Figure 2.32b are used.

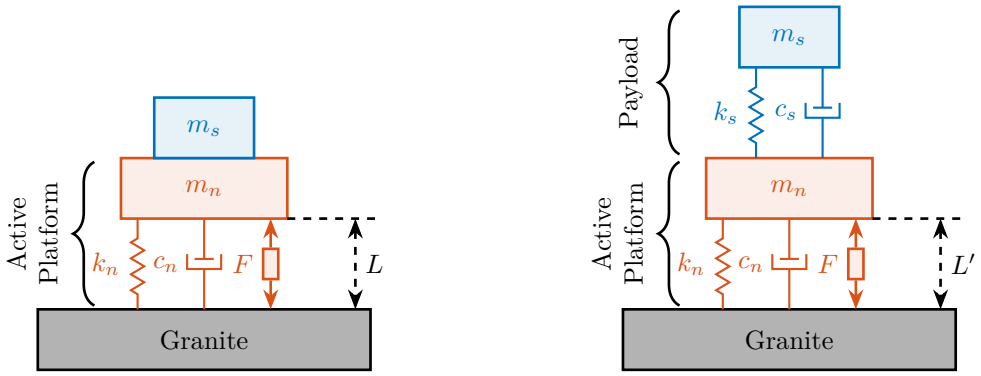

(a) Rigid payload

(b) Flexible payload

Figure 2.32: Models used to study the effect of payload dynamics. Active platform mass is $m_n = 15\,\text{kg}$.

Impact on Plant Dynamics To study the impact of the flexibility between the active platform and the payload, a first (reference) model with a rigid payload, as shown in Figure 2.32a is used. Then "flexible" payload whose model is shown in Figure 2.32b are considered. The resonances of the payload are set at $\omega_s = 20\,\text{Hz}$ and at $\omega_s = 200\,\text{Hz}$ while its mass is either $m_s = 1\,\text{kg}$ or $m_s = 50\,\text{kg}$.

The transfer functions from the active platform force F to the motion of the active platform top platform L and L' are computed and are compared for a soft active platform ($k_n = 0.01\,\text{N}/\mu\text{m}$) in Figure 2.33. It can be seen that the mode of the sample adds an anti-resonance followed by a resonance (zero/pole pattern). The frequency of the anti-resonance corresponds to the "free" resonance of the sample $\omega_s = \sqrt{k_s/m_s}$. The flexibility of the sample also changes the high-frequency gain (the mass line is shifted from $\frac{1}{(m_n+m_s)s^2}$ to $\frac{1}{m_n s^2}$).

The same transfer functions are now compared when using a stiff active platform ($k_n = 100\,\text{N}/\mu\text{m}$) in Figure 2.34. In this case, the sample's resonance ω_s is smaller than the active platform resonance ω_n. This changes the zero/pole pattern to a pole/zero pattern (the frequency of the zero still being equal to ω_s). Even though the added sample's flexibility still shifts the high-frequency mass line as for the soft active platform, the dynamics below the active platform resonance is much less impacted, even when the sample mass is high and when the sample resonance is at low frequency (see yellow curve in Figure 2.34b).

Impact on Close Loop Performances Having a flexibility between the measured position (i.e., the top platform of the active platform) and the Point of Interest (i.e., the sample point to be position on the x-ray) may also impact the closed-loop performance (i.e., the remaining sample's vibration).

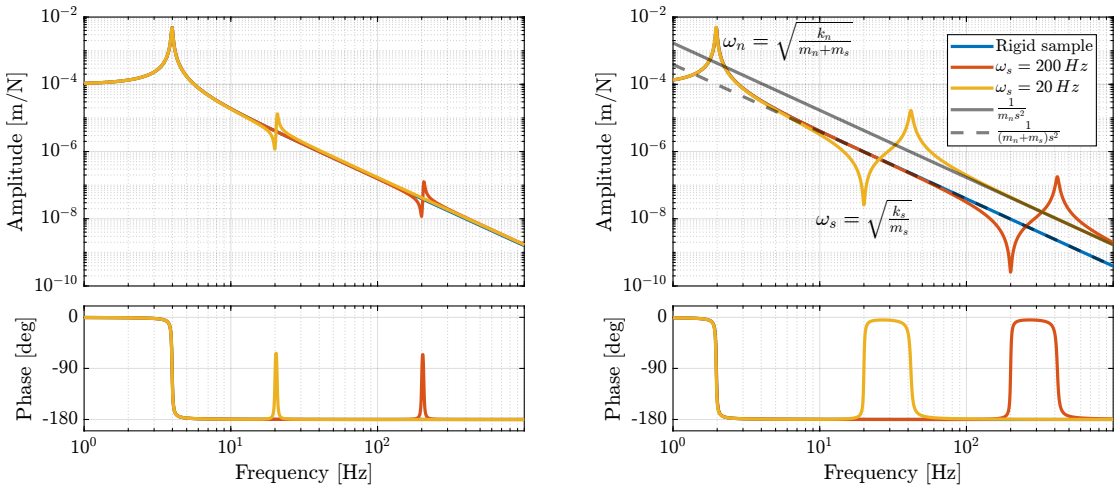

(a) $k_n = 0.01\,\mathrm{N/\mu m}$, $m_s = 1\,\mathrm{kg}$ **(b)** $k_n = 0.01\,\mathrm{N/\mu m}$, $m_s = 50\,\mathrm{kg}$

Figure 2.33: Effect of the payload dynamics on the soft active platform dynamics L'/F with light sample (a), and heavy sample (b).

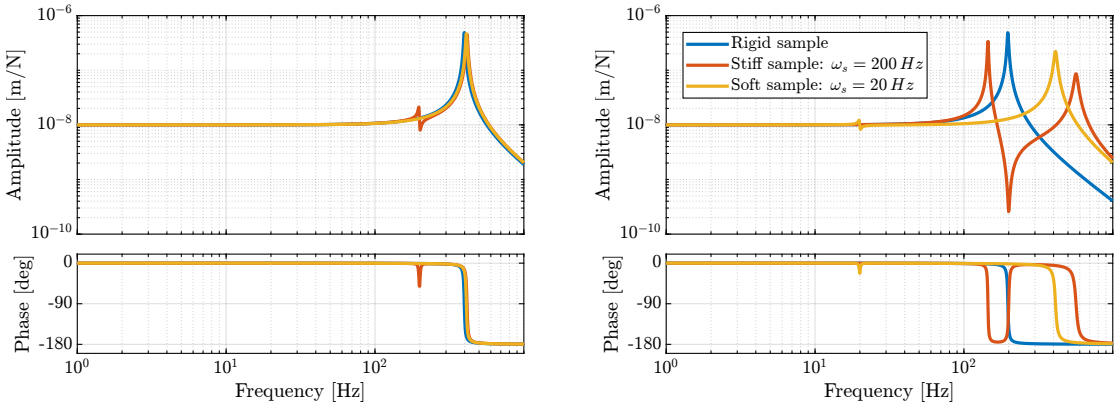

(a) $k_n = 100\,\mathrm{N/\mu m}$, $m_s = 1\,\mathrm{kg}$ **(b)** $k_n = 100\,\mathrm{N/\mu m}$, $m_s = 50\,\mathrm{kg}$

Figure 2.34: Effect of the payload dynamics on the stiff active platform with light sample (a), and heavy sample (b).

To estimate whether the sample flexibility is critical for the closed-loop position stability of the sample, the model shown in Figure 2.35 is used. This is the same model that was used in Section 2.1.6 but with an added flexibility between the active platform and the sample (considered sample modes are at $\omega_s = 20$ Hz and $\omega_n = 200$ Hz). In this case, the measured (i.e., controlled) distance d is no longer equal to the real performance index (the distance y).

The system dynamics is computed and IFF is applied using the same gains as those used in Section 2.1.5. Due to the collocation of the active platform and the force sensor used for IFF, the damped plants remain stable, and damping values similar to those obtained with a rigid sample are observed. The High Authority Control used in Section 2.1.6 is then implemented on the damped plants. The obtained closed-loop systems are stable, indicating good robustness.

Finally, closed-loop error budgeting is computed for the obtained closed-loop system, and the cumulative amplitude spectrum of d and y are shown in Figure 2.36b. The cumulative amplitude spectrum of the measured distance d (Figure 2.36a) shows that the added flexibility at the sample location has very little effect on the control performance. However, the cumulative amplitude spectrum of the distance y (Figure 2.36b) shows that the stability of y is degraded when the sample flexibility is considered and is degraded as ω_s is lowered.

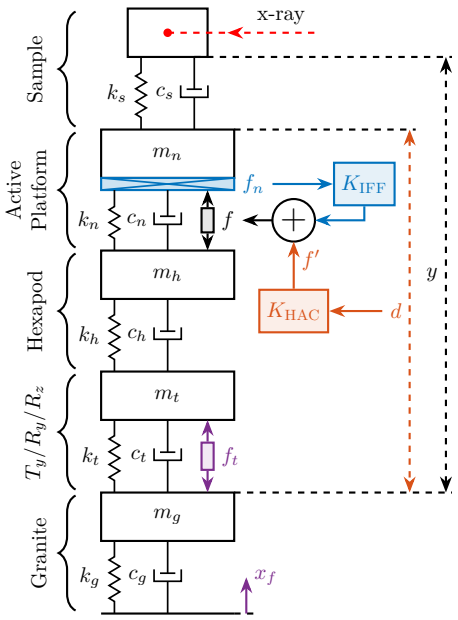

Figure 2.35: Uniaxial model considering some flexibility between the active platform top platform and the sample. In this case, the measured and controlled distance d is different from the distance y which is the real performance index.

What happens is that above ω_s, even though the motion d can be controlled perfectly, the sample's mass is "isolated" from the motion of the active platform and the control on y is not effective.

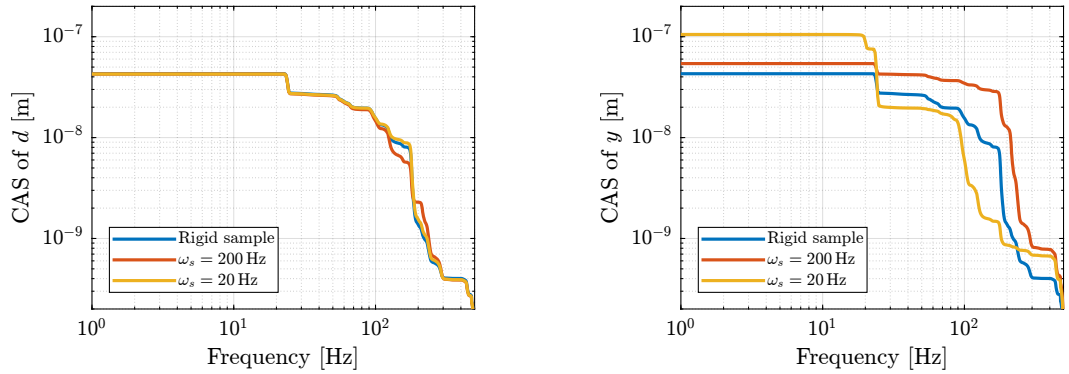

(a) Cumulative Amplitude Spectrum of d

(b) Cumulative Amplitude Spectrum of y

Figure 2.36: Cumulative Amplitude Spectrum of the distances d and y. The effect of the sample's flexibility does not affect much d but is detrimental to the stability of y. A sample mass $m_s = 1$ kg and an active platform stiffness of 100 N/µm are used for the simulations.

Conclusion Payload dynamics is usually a major concern when designing a positioning system. In this section, the impact of the sample dynamics on the plant was found to vary with the sample mass and the relative resonance frequency of the sample ω_s and of the active platform ω_n. The larger the sample mass, the larger the effect (i.e., change of high-frequency gain, appearance of additional resonances and anti-resonances). A zero/pole pattern is observed if $\omega_s > \omega_n$ and a pole/zero pattern if $\omega_s < \omega_n$. Such additional dynamics can induce stability issues depending on their position relative to the desired feedback bandwidth, as explained in [121, Chapt. 4.2]. The general conclusion is that the stiffer the active platform, the less it is impacted by the payload's dynamics, which would make the feedback controller more

robust to a change of payload. This is why high-bandwidth soft positioning stages are usually restricted to constant and calibrated payloads (CD-player, lithography machines, isolation system for gravitational wave detectors, ...), whereas stiff positioning systems are usually used when the control must be robust to a change of payload's mass (stiff piezo nano-positioning stages for instance).

Having some flexibility between the measurement point and the PoI also degrades the position stability. Therefore, it is important to take special care when designing sampling environments, especially if a soft active platform is used.

Conclusion

In this study, a uniaxial model of the nano-active-stabilization-system was tuned from both dynamical measurements (Section 2.1.1) and from disturbances measurements (Section 2.1.3).

Three active damping techniques can be used to critically damp the active platform resonances (Section 2.1.5). However, this model does not allow the determination of which one is most suited to this application (a comparison of the three active damping techniques is done in Table 2.2).

Position feedback controllers have been developed for three considered active platform stiffnesses (Section 2.1.6). These controllers were shown to be robust to the change of sample's masses, and to provide good rejection of disturbances. Having a soft active platform makes the plant dynamics easier to control (because its dynamics is decoupled from the micro-station dynamics, see Section 2.1.7) and requires less position feedback bandwidth to fulfill the requirements. The moderately stiff active platform ($k_n = 1\,\mathrm{N}/\mu\mathrm{m}$) requires a higher feedback bandwidth, but still gives acceptable results. However, the stiff active platform is the most complex to control and gives the worst positioning performance.

2.2 Effect of Rotation

An important aspect of the Nano Active Stabilization System (NASS) is that the active platform continuously rotates around a vertical axis, whereas the external metrology is not. Such rotation induces gyroscopic effects that may impact the system dynamics and obtained performance. To study these effects, a model of a rotating suspended platform is first presented (Section 2.2.1) This model is simple enough to be able to derive its dynamics analytically and to understand its behavior, while still allowing the capture of important physical effects at play.

Integral Force Feedback (IFF) is then applied to the rotating platform, and it is shown that the unconditional stability of IFF is lost due to the gyroscopic effects induced by the rotation (Section 2.2.2). Two modifications of the Integral Force Feedback are then proposed. The first modification involves adding a High Pass Filter (HPF) to the IFF controller (Section 2.2.3). It is shown that the IFF controller is stable for some gain values, and that damping can be added to the suspension modes. The optimal High Pass Filter cut-off frequency is computed. The second modification consists of adding a stiffness in parallel to the force sensors (Section 2.2.4). Under certain conditions, the unconditional stability of the IFF controller is regained. The optimal parallel stiffness is then computed. This study of adapting IFF for the damping of rotating platforms has been the subject of two published papers [35, 36].

It is then shown that Relative Damping Control (RDC) is less affected by gyroscopic effects (Section 2.2.5). Once the optimal control parameters for the three tested active damping techniques are obtained, they are compared in terms of achievable damping, damped plant and closed-loop compliance and transmissibility (Section 2.2.6).

The previous analysis was applied to three considered active platform stiffnesses ($k_n = 0.01\,\mathrm{N/\mu m}$, $k_n = 1\,\mathrm{N/\mu m}$ and $k_n = 100\,\mathrm{N/\mu m}$) and the optimal active damping controller was obtained in each case (Section 2.2.7). Up until this section, the study was performed on a very simplistic model that only captures the rotation aspect, and the model parameters were not tuned to correspond to the NASS. In the last section (Section 2.2.8), a model of the micro-station is added below the active platform with a rotating spindle and parameters tuned to match the NASS dynamics. The goal is to determine whether the rotation imposes performance limitation on the NASS.

2.2.1 System Description and Analysis

The system used to study gyroscopic effects consists of a 2-DoF translation stage on top of a rotating stage (Figure 2.37). The rotating stage is supposed to be ideal, meaning it induces a perfect rotation $\theta(t) = \Omega t$ where Ω is the rotational speed in rad s^{-1}. The suspended platform consists of two orthogonal actuators, each represented by three elements in parallel: a spring with a stiffness k in $\mathrm{N\,m}^{-1}$, a dashpot with a damping coefficient c in $\mathrm{N/(m/s)}$ and an ideal force source F_u, F_v. A payload with a mass m in kg, is mounted on the (rotating) suspended platform. Two reference frames are used: an *inertial* frame $(\vec{i}_x, \vec{i}_y, \vec{i}_z)$ and a *uniform rotating* frame $(\vec{i}_u, \vec{i}_v, \vec{i}_w)$ rigidly fixed on top of the rotating stage with $\vec{i}_w$ aligned with the rotation axis. The position of the payload is represented by $(d_u, d_v, 0)$ expressed in the rotating frame. After the dynamics of this system is studied, the objective will be to dampen the two suspension modes of the payload while the rotating stage performs a constant rotation.

Equations of Motion and Transfer Functions To obtain the equations of motion for the system represented in Figure 2.37, the Lagrangian equation (2.9) is used. $L = T - V$ is the Lagrangian, T the kinetic energy, V the potential energy, D the dissipation function, and Q_i the generalized force associated with the generalized variable $\begin{bmatrix} q_1 & q_2 \end{bmatrix} = \begin{bmatrix} d_u & d_v \end{bmatrix}$. These terms are derived in (2.10). Note that the equation of motion corresponding to constant rotation around $\vec{i}_w$ is disregarded because this motion is imposed by the rotation stage.

$$\frac{d}{dt}\left(\frac{\partial L}{\partial \dot{q}_i}\right) + \frac{\partial D}{\partial \dot{q}_i} - \frac{\partial L}{\partial q_i} = Q_i \tag{2.9}$$

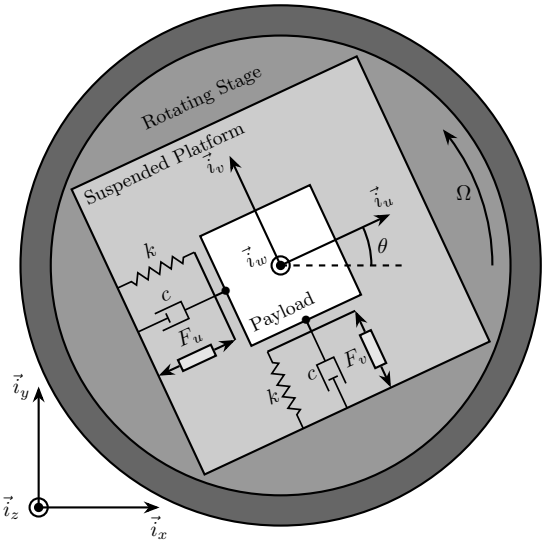

Figure 2.37: Schematic of the studied 2-DoF translation stage on top of a rotation stage.

$$\begin{aligned} T &= \frac{1}{2}m\Big((\dot{d}_u - \Omega d_v)^2 + (\dot{d}_v + \Omega d_u)^2\Big), \quad Q_u = F_u, \quad Q_v = F_v, \\ V &= \frac{1}{2}k\big({d_u}^2 + {d_v}^2\big), \quad D = \frac{1}{2}c\big({\dot{d}_u}^2 + {\dot{d}_v}^2\big) \end{aligned} \tag{2.10}$$

Substituting equations (2.10) into equation (2.9) for both generalized coordinates gives two coupled differential equations (2.11a) and (2.11b).

$$m\ddot{d}_u + c\dot{d}_u + (k - m\Omega^2)d_u = F_u + 2m\Omega\dot{d}_v \tag{2.11a}$$

$$m\ddot{d}_v + c\dot{d}_v + (k \underbrace{- m\Omega^2}_{\text{Centrif.}})d_v = F_v \underbrace{- 2m\Omega\dot{d}_u}_{\text{Coriolis}} \tag{2.11b}$$

The uniform rotation of the system induces two *gyroscopic effects* as shown in equation (2.11):

- *Centrifugal forces*: that can be seen as an added *negative stiffness* $-m\Omega^2$ along $\vec{i}_u$ and $\vec{i}_v$
- *Coriolis forces*: that adds *coupling* between the two orthogonal directions.

One can verify that without rotation ($\Omega = 0$), the system becomes equivalent to two *uncoupled* one DoF mass-spring-damper systems.

To study the dynamics of the system, the two differential equations of motions (2.11) are converted into the Laplace domain and the 2×2 transfer function matrix $\boldsymbol{G}_d$ from $\begin{bmatrix} F_u & F_v \end{bmatrix}$ to $\begin{bmatrix} d_u & d_v \end{bmatrix}$ in equation (2.12) is obtained. The four transfer functions in $\boldsymbol{G}_d$ are shown in equation (2.13).

$$\begin{bmatrix} d_u \\ d_v \end{bmatrix} = \boldsymbol{G}_d \begin{bmatrix} F_u \\ F_v \end{bmatrix} \tag{2.12}$$

$$\boldsymbol{G}_d(1,1) = \boldsymbol{G}_d(2,2) = \frac{ms^2 + cs + k - m\Omega^2}{\left(ms^2 + cs + k - m\Omega^2\right)^2 + \left(2m\Omega s\right)^2} \tag{2.13a}$$

$$\boldsymbol{G}_d(1,2) = -\boldsymbol{G}_d(2,1) = \frac{2m\Omega s}{\left(ms^2 + cs + k - m\Omega^2\right)^2 + \left(2m\Omega s\right)^2} \tag{2.13b}$$

To simplify the analysis, the undamped natural frequency ω_0 and the damping ratio ξ defined in (2.14) are used instead. The elements of the transfer function matrix $\boldsymbol{G}_d$ are described by equation (2.15).

$$\omega_0 = \sqrt{\frac{k}{m}} \text{ in rad s}^{-1}, \quad \xi = \frac{c}{2\sqrt{km}} \tag{2.14}$$

$$\boldsymbol{G}_d(1,1) = \frac{\frac{1}{k}\left(\frac{s^2}{{\omega_0}^2} + 2\xi\frac{s}{\omega_0} + 1 - \frac{\Omega^2}{{\omega_0}^2}\right)}{\left(\frac{s^2}{{\omega_0}^2} + 2\xi\frac{s}{\omega_0} + 1 - \frac{\Omega^2}{{\omega_0}^2}\right)^2 + \left(2\frac{\Omega}{\omega_0}\frac{s}{\omega_0}\right)^2} \tag{2.15a}$$

$$\boldsymbol{G}_d(1,2) = \frac{\frac{1}{k}\left(2\frac{\Omega}{\omega_0}\frac{s}{\omega_0}\right)}{\left(\frac{s^2}{{\omega_0}^2} + 2\xi\frac{s}{\omega_0} + 1 - \frac{\Omega^2}{{\omega_0}^2}\right)^2 + \left(2\frac{\Omega}{\omega_0}\frac{s}{\omega_0}\right)^2} \tag{2.15b}$$

System Poles: Campbell Diagram The poles of $\boldsymbol{G}_d$ are the complex solutions p of equation (2.16) (i.e. the roots of its denominator).

$$\left(\frac{p^2}{{\omega_0}^2} + 2\xi\frac{p}{\omega_0} + 1 - \frac{\Omega^2}{{\omega_0}^2}\right)^2 + \left(2\frac{\Omega}{\omega_0}\frac{p}{\omega_0}\right)^2 = 0 \tag{2.16}$$

Supposing small damping ($\xi \ll 1$), two pairs of complex conjugate poles $[p_+, p_-]$ are obtained as shown in equation (2.17).

$$p_+ = -\xi\omega_0\left(1 + \frac{\Omega}{\omega_0}\right) \pm j\omega_0\left(1 + \frac{\Omega}{\omega_0}\right) \tag{2.17a}$$

$$p_- = -\xi\omega_0\left(1 - \frac{\Omega}{\omega_0}\right) \pm j\omega_0\left(1 - \frac{\Omega}{\omega_0}\right) \tag{2.17b}$$

The real and complex parts of these two pairs of complex conjugate poles are represented in Figure 2.38 as a function of the rotational speed Ω. As the rotational speed increases, p_+ goes to higher frequencies and p_- goes to lower frequencies (Figure 2.38b). The system becomes unstable for $\Omega > \omega_0$ as the real part of p_- is positive (Figure 2.38a). Physically, the negative stiffness term $-m\Omega^2$ induced by centrifugal forces exceeds the spring stiffness k.

System Dynamics: Effect of rotation The system dynamics from actuator forces $[F_u, F_v]$ to the relative motion $[d_u, d_v]$ is identified for several rotating velocities. Looking at the transfer function matrix $\boldsymbol{G}_d$ in equation (2.15), one can see that the two diagonal (direct) terms are equal and that the two off-diagonal (coupling) terms are opposite.

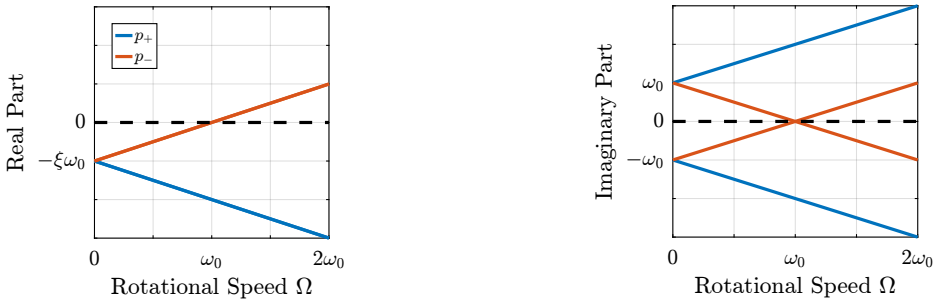

(a) Real part

(b) Imaginary part

Figure 2.38: Campbell diagram: Real (a) and Imaginary (b) parts of the poles as a function of the rotating velocity Ω.

The bode plots of these two terms are shown in Figure 2.39 for several rotational speeds Ω. These plots confirm the expected behavior: the frequencies of the two pairs of complex conjugate poles are further separated as Ω increases. For $\Omega > \omega_0$, the low-frequency pair of complex conjugate poles p_- becomes unstable (shown be the 180 degrees phase lead instead of phase lag).

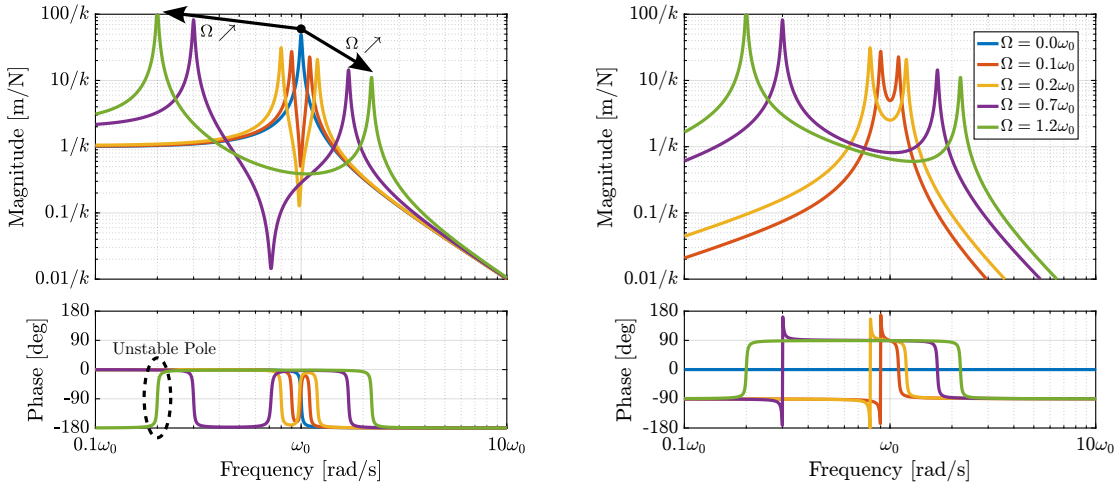

(a) Direct terms: $d_u/F_u, d_v/F_v$

(b) Coupling terms: $d_u/F_v, d_v/F_u$

Figure 2.39: Bode plot of the direct (a) and coupling (b) terms for several rotating velocities.

2.2.2 Integral Force Feedback

The goal is now to damp the two suspension modes of the payload using an active damping strategy while the rotating stage performs a constant rotation. As was explained with the uniaxial model, such an active damping strategy is key to both reducing the magnification of the response in the vicinity of the resonances [26] and for making the plant easier to control for the high authority controller.

Many active damping techniques have been developed over the years, such as Positive Position Feedback (PPF) [46, 89], Integral Force Feedback (IFF) [115] and Direct Velocity Feedback (DVF) [77, 116, 131]. In [115], the IFF control scheme has been proposed, where a force sensor, a force actuator, and an integral controller are used to increase the damping of a mechanical system. When the force sensor is collocated with the actuator, the open-loop transfer function

has alternating poles and zeros, which guarantees the stability of the closed-loop system [116]. It was later shown that this property holds for multiple collated actuator/sensor pairs [114].

The main advantages of IFF over other active damping techniques are the guaranteed stability even in the presence of flexible dynamics, good performance, and robustness properties [116].

Several improvements to the classical IFF have been proposed, such as adding a feed-through term to increase the achievable damping [143] or adding a HPF to recover the loss of compliance at low-frequency [23]. Recently, an $\mathcal{H}_\infty$ optimization criterion has been used to derive optimal gains for the IFF controller [165].

However, none of these studies have been applied to rotating systems. In this section, the IFF strategy is applied on the rotating suspended platform, and it is shown that gyroscopic effects alter the system dynamics and that IFF cannot be applied as is.

System and Equations of motion To apply Integral Force Feedback, two force sensors are added in series with the actuators (Figure 2.40a). Two identical controllers K_F described by (2.18) are then used to feedback each of the sensed force to its associated actuator.

$$K_F(s) = g \cdot \frac{1}{s} \tag{2.18}$$

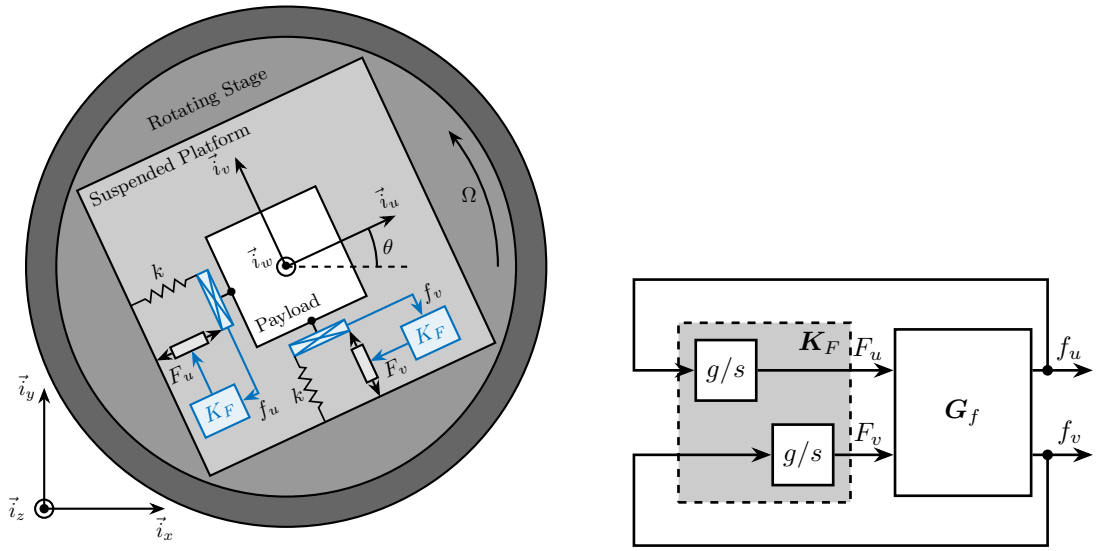

(a) System with added Force Sensor in series with the actuators

(b) Control diagram

Figure 2.40: Integral Force Feedback applied to the suspended rotating platform. The damper c in (a) is omitted for readability.

The forces $\begin{bmatrix} f_u & f_v \end{bmatrix}$ measured by the two force sensors represented in Figure 2.40a are described by equation (2.19).

$$\begin{bmatrix} f_u \\ f_v \end{bmatrix} = \begin{bmatrix} F_u \\ F_v \end{bmatrix} - (cs + k) \begin{bmatrix} d_u \\ d_v \end{bmatrix} \tag{2.19}$$

The transfer function matrix $\boldsymbol{G}_f$ from actuator forces to measured forces in equation (2.20) can be obtained by inserting equation (2.15) into equation (2.19). Its elements are shown in equation (2.21).

$$\begin{bmatrix} f_u \\ f_v \end{bmatrix} = \boldsymbol{G}_f \begin{bmatrix} F_u \\ F_v \end{bmatrix} \tag{2.20}$$

$$\boldsymbol{G}_f(1,1) = \boldsymbol{G}_f(2,2) = \frac{\left(\frac{s^2}{{\omega_0}^2} - \frac{\Omega^2}{{\omega_0}^2}\right)\left(\frac{s^2}{{\omega_0}^2} + 2\xi\frac{s}{\omega_0} + 1 - \frac{\Omega^2}{{\omega_0}^2}\right) + \left(2\frac{\Omega}{\omega_0}\frac{s}{\omega_0}\right)^2}{\left(\frac{s^2}{{\omega_0}^2} + 2\xi\frac{s}{\omega_0} + 1 - \frac{\Omega^2}{{\omega_0}^2}\right)^2 + \left(2\frac{\Omega}{\omega_0}\frac{s}{\omega_0}\right)^2} \tag{2.21a}$$

$$\boldsymbol{G}_f(1,2) = -\boldsymbol{G}_f(2,1) = \frac{-\left(2\xi\frac{s}{\omega_0} + 1\right)\left(2\frac{\Omega}{\omega_0}\frac{s}{\omega_0}\right)}{\left(\frac{s^2}{{\omega_0}^2} + 2\xi\frac{s}{\omega_0} + 1 - \frac{\Omega^2}{{\omega_0}^2}\right)^2 + \left(2\frac{\Omega}{\omega_0}\frac{s}{\omega_0}\right)^2} \tag{2.21b}$$

The zeros of the diagonal terms of $\boldsymbol{G}_f$ in equation (2.21a) are computed, and neglecting the damping for simplicity, two complex conjugated zeros z_c (2.22a), and two real zeros z_r (2.22b) are obtained.

$$z_c = \pm j\omega_0\sqrt{\frac{1}{2}\sqrt{8\frac{\Omega^2}{{\omega_0}^2} + 1} + \frac{\Omega^2}{{\omega_0}^2} + \frac{1}{2}} \tag{2.22a}$$

$$z_r = \pm\omega_0\sqrt{\frac{1}{2}\sqrt{8\frac{\Omega^2}{{\omega_0}^2} + 1} - \frac{\Omega^2}{{\omega_0}^2} - \frac{1}{2}} \tag{2.22b}$$

It is interesting to see that the frequency of the pair of complex conjugate zeros z_c in equation (2.22a) always lies between the frequency of the two pairs of complex conjugate poles p_- and p_+ in equation (2.17). This is what usually gives the unconditional stability of IFF when collocated force sensors are used.

However, for non-null rotational speeds, the two real zeros z_r in equation (2.22b) are inducing a *non-minimum phase behavior*. This can be seen in the Bode plot of the diagonal terms (Figure 2.41) where the low-frequency gain is no longer zero while the phase stays at 180°.

The low-frequency gain of $\boldsymbol{G}_f$ increases with the rotational speed Ω as shown in equation (2.23). This can be explained as follows: a constant actuator force F_u induces a small displacement of the mass $d_u = \frac{F_u}{k - m\Omega^2}$ (Hooke's law considering the negative stiffness induced by the rotation). This small displacement then increases the centrifugal force $m\Omega^2 d_u = \frac{\Omega^2}{{\omega_0}^2 - \Omega^2} F_u$ which is then measured by the force sensors.

$$\lim_{\omega\to 0} |\boldsymbol{G}_f(j\omega)| = \begin{bmatrix} \frac{\Omega^2}{{\omega_0}^2 - \Omega^2} & 0 \\ 0 & \frac{\Omega^2}{{\omega_0}^2 - \Omega^2} \end{bmatrix} \tag{2.23}$$

Effect of Rotation Speed on IFF Plant Dynamics The transfer functions from actuator forces $[F_u,\ F_v]$ to the measured force sensors $[f_u,\ f_v]$ are identified for several rotating velocities and are shown in Figure 2.41. As expected from the derived equations of motion:

- when $\Omega < \omega_0$: the low-frequency gain is no longer zero and two (non-minimum phase) real zeros appear at low-frequencies. The low-frequency gain increases with Ω. A pair of (minimum phase) complex conjugate zeros appears between the two complex conjugate poles, which are split further apart as Ω increases.

- when $\omega_0 < \Omega$: the low-frequency pole becomes unstable.

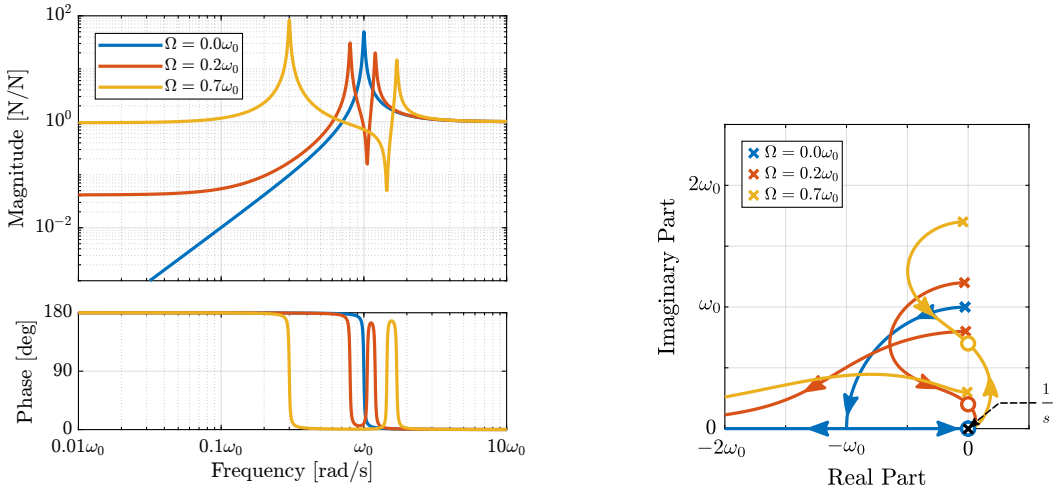

(a) Direct terms: $d_u/F_u, d_v/F_v$

(b) Root locus

Figure 2.41: Effect of the rotation velocity on the bode plot of the direct terms (a) and on the IFF root locus (b).

Decentralized Integral Force Feedback The control diagram for decentralized IFF is shown in Figure 2.40b. The decentralized IFF controller $\boldsymbol{K}_F$ corresponds to a diagonal controller with integrators (2.24).

$$\begin{aligned} \boldsymbol{K}_F(s) &= \begin{bmatrix} K_F(s) & 0 \\ 0 & K_F(s) \end{bmatrix} \\ K_F(s) &= g \cdot \frac{1}{s} \end{aligned} \tag{2.24}$$

To determine how the IFF controller affects the poles of the closed-loop system, a Root locus plot (Figure 2.41b) is constructed as follows: the poles of the closed-loop system are drawn in the complex plane as the controller gain g varies from 0 to ∞ for the two controllers K_F simultaneously. As explained in [114, 134], the closed-loop poles start at the open-loop poles (shown by crosses) for $g = 0$ and coincide with the transmission zeros (shown by circles) as $g \to \infty$.

Whereas collocated IFF is usually associated with unconditional stability [115], this property is lost due to gyroscopic effects as soon as the rotation velocity becomes non-null. This can be seen in the Root locus plot (Figure 2.41b) where poles corresponding to the controller are bound to the right half plane implying closed-loop system instability. Physically, this can be explained as follows: at low frequencies, the loop gain is huge due to the pure integrator in K_F and the finite gain of the plant (Figure 2.41). The control system is thus canceling the spring forces, which makes the suspended platform not capable to hold the payload against centrifugal forces, hence the instability.

2.2.3 Integral Force Feedback with a High-Pass Filter

As explained in the previous section, the instability of the IFF controller applied to the rotating system is due to the high gain of the integrator at low-frequency. To limit the low-frequency controller gain, a High Pass Filter (HPF) can be added to the controller, as shown in equation (2.25). This is equivalent to slightly shifting the controller pole to the left along the real axis. This modification of the IFF controller is typically performed to avoid saturation associated with the pure integrator [93, 115]. This is however not the reason why this High Pass Filter is added here.

$$K_F(s) = g \cdot \frac{1}{s} \cdot \underbrace{\frac{s/\omega_i}{1 + s/\omega_i}}_{\text{HPF}} = g \cdot \frac{1}{s + \omega_i} \tag{2.25}$$

Modified Integral Force Feedback Controller The Integral Force Feedback Controller is modified such that instead of using pure integrators, pseudo integrators (i.e. low pass filters) are used (2.25) where ω_i characterize the frequency down to which the signal is integrated. The loop gains ($K_F(s)$ times the direct dynamics f_u/F_u) with and without the added HPF are shown in Figure 2.42a. The effect of the added HPF limits the low-frequency gain to finite values as expected.

The Root locus plots for the decentralized IFF with and without the HPF are displayed in Figure 2.42b. With the added HPF, the poles of the closed-loop system are shown to be stable up to some value of the gain g_{max} given by equation (2.26). It is interesting to note that g_{max} also corresponds to the controller gain at which the low-frequency loop gain reaches one (for instance the gain g can be increased by a factor 5 in Figure 2.42a before the system becomes unstable).

$$g_{\text{max}} = \omega_i \left(\frac{{\omega_0}^2}{\Omega^2} - 1 \right) \tag{2.26}$$

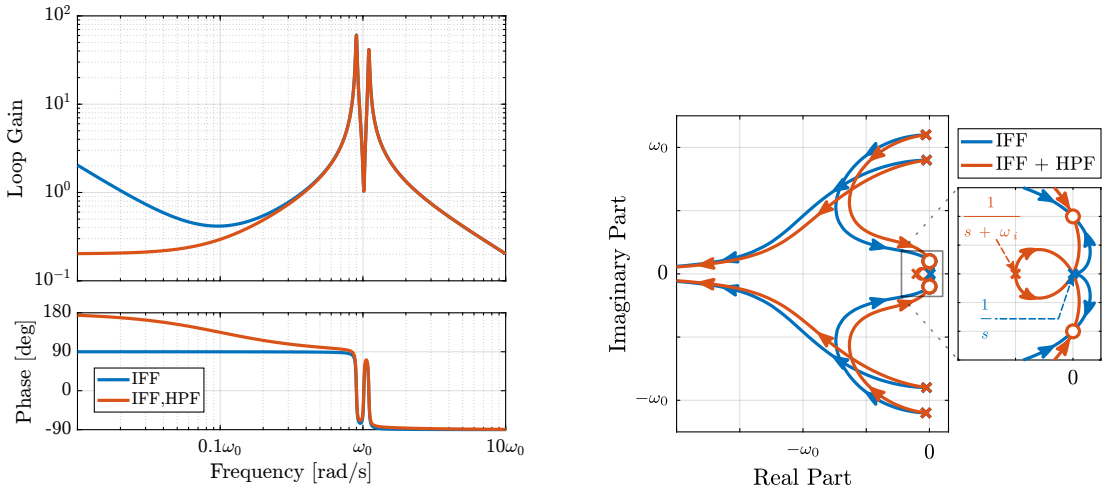

(a) Loop gain **(b)** Root locus

Figure 2.42: Comparison of the IFF with pure integrator and modified IFF with added high-pass filter ($\Omega = 0.1\omega_0$). The loop gain is shown in (a) with $\omega_i = 0.1\omega_0$ and $g = 2$. The root locus is shown in (b).

Optimal IFF with HPF parameters ω_i and g Two parameters can be tuned for the modified controller in equation (2.25): the gain g and the pole's location ω_i. The optimal values of ω_i and g are considered here as the values for which the damping of all the closed-loop poles is simultaneously maximized.

To visualize how ω_i does affect the attainable damping, the Root locus plots for several ω_i are displayed in Figure 2.43a. It is shown that even though small ω_i seem to allow more damping to be added to the suspension modes (see Root locus in Figure 2.43a), the control gain g may be limited to small values due to equation (2.26). To study this trade-off, the attainable closed-loop damping ratio ξ_{cl} is computed as a function of ω_i/ω_0. The gain g_{opt} at which this maximum damping is obtained is also displayed and compared with the gain g_{max} at which the system becomes unstable (Figure 2.43b).

For small values of ω_i, the added damping is limited by the maximum allowed control gain $g_{\max}$ (red curve and dashed red curve superimposed in Figure 2.43b) at which point the pole corresponding to the controller becomes unstable. For larger values of ω_i, the attainable damping ratio decreases as a function of ω_i as was predicted from the root locus plot of Figure 2.42b.

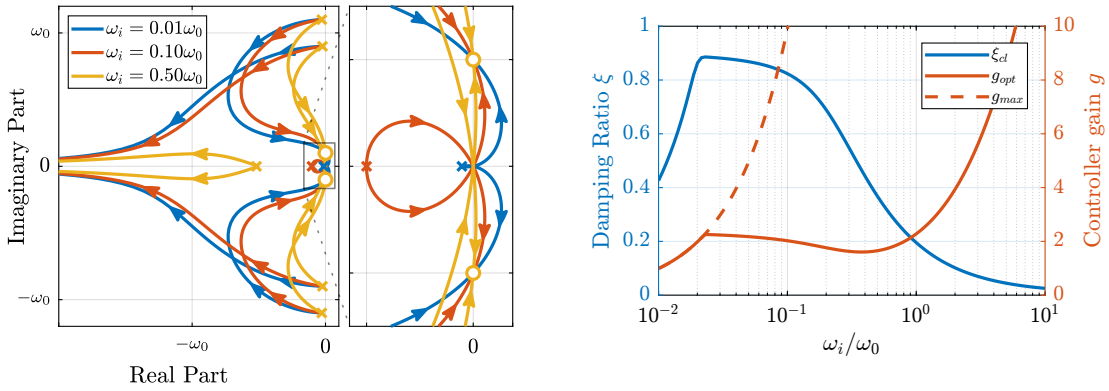

(a) Root locus

(b) Attainable damping ratio as a function of ω_i/ω_0. Maximum and optical control gains are also shown

Figure 2.43: Root loci for several high-pass filter cut-off frequency (a). The achievable damping ratio decreases as ω_i increases (b).

Obtained Damped Plant To study how the parameter ω_i affects the damped plant, the obtained damped plants for several ω_i are compared in Figure 2.44a. It can be seen that the low-frequency coupling increases as ω_i increases. Therefore, there is a trade-off between achievable damping and added coupling when tuning ω_i. The same trade-off can be seen between achievable damping and loss of compliance at low-frequency (see Figure 2.44b).

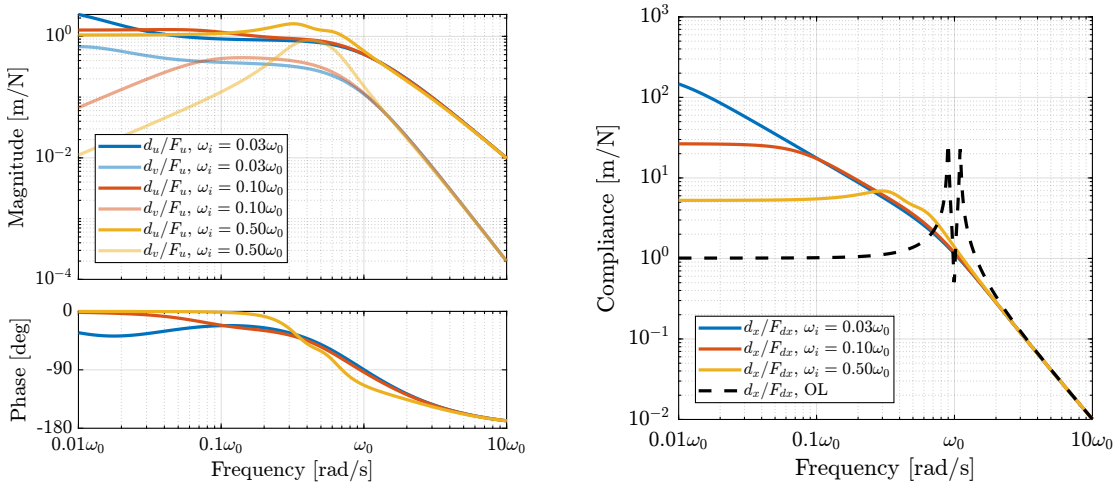

(a) Obtained plants

(b) Effect of ω_i on the compliance

Figure 2.44: Effect of ω_i on the damped plant coupling (a) and on the compliance (b).

2.2.4 IFF with a Stiffness in Parallel with the Force Sensor

In this section it is proposed to add springs in parallel with the force sensors to counteract the negative stiffness induced by the gyroscopic effects. Such springs are schematically shown in Figure 2.45 where k_a is the stiffness of the actuator and k_p the added stiffness in parallel with the actuator and force sensor.

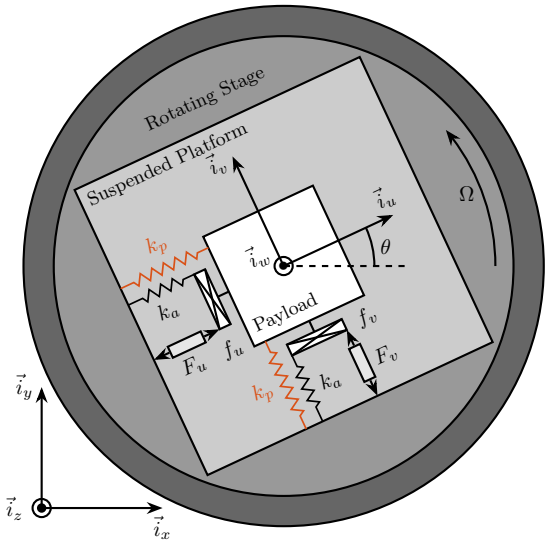

Figure 2.45: Studied system with additional springs in parallel with the actuators and force sensors (shown in red).

Equations The forces measured by the two force sensors represented in Figure 2.45 are described by (2.27).

$$\begin{bmatrix} f_u \\ f_v \end{bmatrix} = \begin{bmatrix} F_u \\ F_v \end{bmatrix} - (cs + k_a) \begin{bmatrix} d_u \\ d_v \end{bmatrix} \tag{2.27}$$

To keep the overall stiffness $k = k_a + k_p$ constant, thus not modifying the open-loop poles as k_p is changed, a scalar parameter α ($0 \leq \alpha < 1$) is defined to describe the fraction of the total stiffness in parallel with the actuator and force sensor as in (2.28).

$$k_p = \alpha k, \quad k_a = (1 - \alpha)k \tag{2.28}$$

After the equations of motion are derived and transformed in the Laplace domain, the transfer function matrix $\boldsymbol{G}_k$ in Eq. (2.29) is computed. Its elements are shown in Eqs. (2.30a) and (2.30b).

$$\begin{bmatrix} f_u \\ f_v \end{bmatrix} = \boldsymbol{G}_k \begin{bmatrix} F_u \\ F_v \end{bmatrix} \tag{2.29}$$

$$\boldsymbol{G}_k(1,1) = \boldsymbol{G}_k(2,2) = \frac{\left(\frac{s^2}{{\omega_0}^2} - \frac{\Omega^2}{{\omega_0}^2} + \alpha\right)\left(\frac{s^2}{{\omega_0}^2} + 2\xi\frac{s}{\omega_0} + 1 - \frac{\Omega^2}{{\omega_0}^2}\right) + \left(2\frac{\Omega}{\omega_0}\frac{s}{\omega_0}\right)^2}{\left(\frac{s^2}{{\omega_0}^2} + 2\xi\frac{s}{\omega_0} + 1 - \frac{\Omega^2}{{\omega_0}^2}\right)^2 + \left(2\frac{\Omega}{\omega_0}\frac{s}{\omega_0}\right)^2} \tag{2.30a}$$

$$\boldsymbol{G}_k(1,2) = -\boldsymbol{G}_k(2,1) = \frac{-\left(2\xi\frac{s}{\omega_0} + 1 - \alpha\right)\left(2\frac{\Omega}{\omega_0}\frac{s}{\omega_0}\right)}{\left(\frac{s^2}{{\omega_0}^2} + 2\xi\frac{s}{\omega_0} + 1 - \frac{\Omega^2}{{\omega_0}^2}\right)^2 + \left(2\frac{\Omega}{\omega_0}\frac{s}{\omega_0}\right)^2} \tag{2.30b}$$

Comparing $\boldsymbol{G}_k$ in (2.30) with $\boldsymbol{G}_f$ in (2.21) shows that while the poles of the system remain the same, the zeros of the diagonal terms change. The two real zeros z_r in (2.22b) that were inducing a non-minimum phase behavior are transformed into two complex conjugate zeros if the condition in (2.31) holds. Thus, if the added *parallel stiffness* k_p is higher than the *negative stiffness* induced by centrifugal forces $m\Omega^2$, the dynamics from the actuator to its collocated force sensor will show *minimum phase behavior*.

$$\boxed{\alpha > \frac{\Omega^2}{{\omega_0}^2} \quad \Leftrightarrow \quad k_p > m\Omega^2} \tag{2.31}$$

Effect of Parallel Stiffness on the IFF plant The IFF plant (transfer function from $[F_u, F_v]$ to $[f_u, f_v]$) is identified without parallel stiffness $k_p = 0$, with a small parallel stiffness $k_p < m\Omega^2$ and with a large parallel stiffness $k_p > m\Omega^2$. Bode plots of the obtained dynamics are shown in Figure 2.46a. The two real zeros for $k_p < m\Omega^2$ are transformed into two complex conjugate zeros for $k_p > m\Omega^2$. In that case, the system shows alternating complex conjugate poles and zeros as what is the case in the non-rotating case.

Figure 2.46b shows the Root locus plots for $k_p = 0$, $k_p < m\Omega^2$ and $k_p > m\Omega^2$ when K_F is a pure integrator, as shown in Eq. (2.24). It is shown that if the added stiffness is higher than the maximum negative stiffness, the poles of the closed-loop system are bounded on the (stable) left half-plane, and hence the unconditional stability of IFF is recovered.

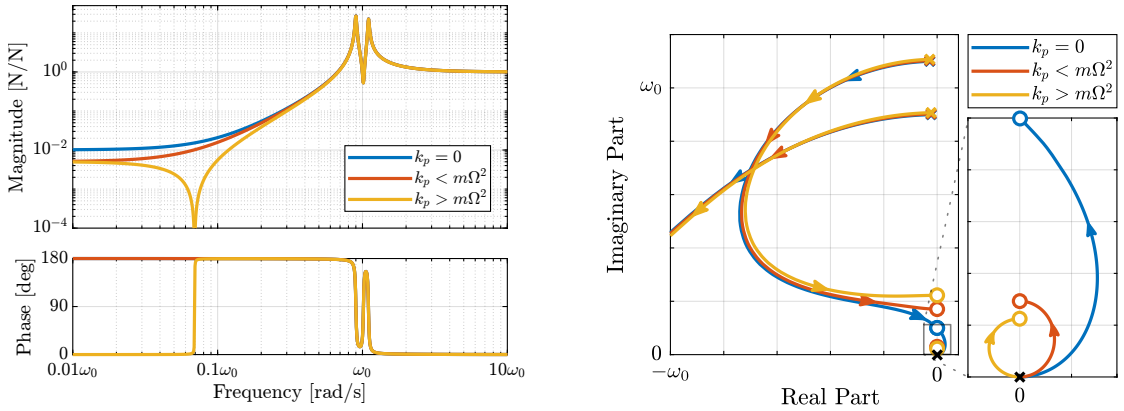

(a) Bode plots of f_u/F_u without parallel spring (blue), with parallel spring $k_p < m\Omega^2$ (red) and $k_p > m\Omega^2$, $\Omega = 0.1\omega_0$ (yellow)

(b) Root locus for IFF without parallel spring, with soft parallel spring and with stiff parallel spring

Figure 2.46: Effect of parallel stiffness on the IFF plant (a) and on the control stability (b).

Effect of k_p on the Attainable Damping Even though the parallel stiffness k_p has no impact on the open-loop poles (as the overall stiffness k is kept constant), it has a large impact on the transmission zeros. Moreover, as the attainable damping is generally proportional to the distance between poles and zeros [113], the parallel stiffness k_p is expected to have some impact on the attainable damping. To study this effect, Root locus plots for several parallel stiffnesses $k_p > m\Omega^2$ are shown in Figure 2.47a. The frequencies of the transmission zeros of the system increase with an increase in the parallel stiffness k_p (thus getting closer to the poles), and the associated attainable damping is reduced. Therefore, even though the parallel stiffness k_p should be larger than $m\Omega^2$ for stability reasons, it should not be taken too large as this would limit the attainable damping. This is confirmed by the Figure 2.47b where the attainable closed-loop damping ratio ξ_{cl} and the associated optimal control gain g_{opt} are computed as a function of the parallel stiffness.

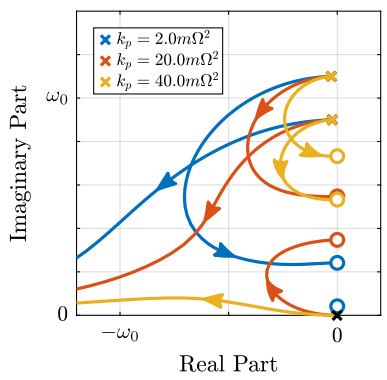

(a) Root locus: Effect of parallel stiffness, $\Omega = 0.1\omega_0$

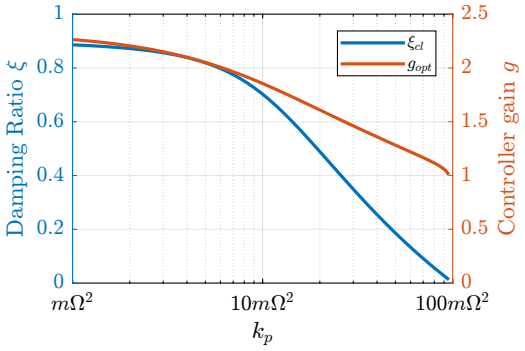

(b) Attainable damping ratio ξ_{cl} as a function of the parallel stiffness k_p. The corresponding control gain g_{opt} is also shown

Figure 2.47: Effect of the parallel stiffness on the achievable damping with IFF.

Damped Plant The parallel stiffness are chosen to be $k_p = 2m\Omega^2$ and the damped plant is computed. The damped and undamped transfer functions from F_u to d_u are compared in Figure 2.48b. Even though the two resonances are well damped, the IFF changes the low-frequency behavior of the plant, which is usually not desired. This is because "pure" integrators are used which are inducing large low-frequency loop gains.

To lower the low-frequency gain, a HPF is added to the IFF controller (which is equivalent as shifting the controller pole to the left in the complex plane):

$$K_{\text{IFF}}(s) = g\frac{1}{\omega_i + s}\begin{bmatrix}1 & 0\\ 0 & 1\end{bmatrix} \tag{2.32}$$

To determine how the HPF impacts the attainable damping, the controller gain g is kept constant while ω_i is changed, and the minimum damping ratio of the damped plant is computed. The obtained damping ratio as a function of ω_i/ω_0 (where ω_0 is the resonance of the system without rotation) is shown in Figure 2.48a. It is shown that the attainable damping ratio reduces as ω_i is increased (same conclusion than in Section 2.2.3). Let's choose $\omega_i = 0.1 \cdot \omega_0$ and compare the obtained damped plant again with the undamped and with the "pure" IFF in Figure 2.48b. The added HPF gives almost the same damping properties to the suspension while exhibiting good low-frequency behavior.

2.2.5 Relative Damping Control

To apply a Relative Damping Control (RDC) strategy, relative motion sensors are added in parallel with the actuators as shown in Figure 2.49. Two controllers K_d are used to feed back the relative motion to the actuator. These controllers have in principle pure derivative action ($K_d = s$), but to be implemented in practice they are usually replaced by a high-pass filter (2.33).

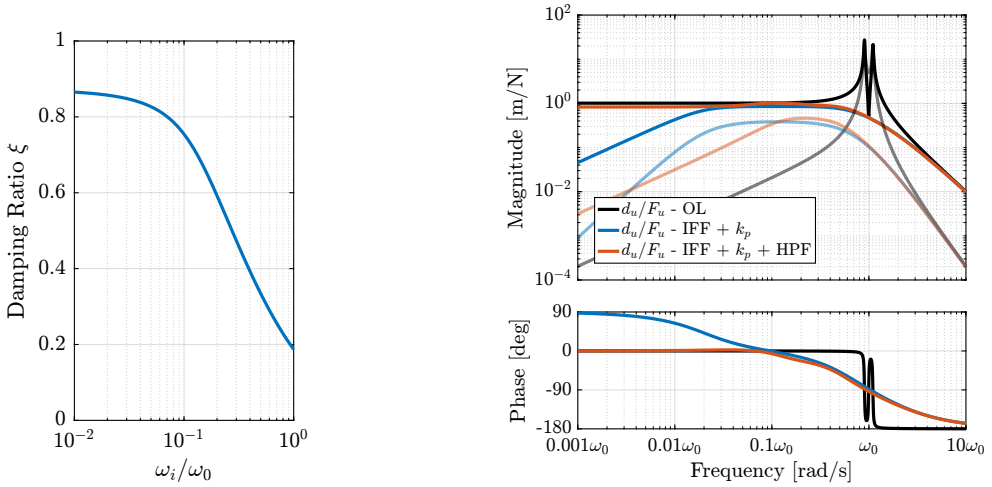

(a) Reduced damping ratio with increased cut-off frequency ω_i

(b) Effect of the added HPF on the damped plant

Figure 2.48: Effect of high-pass filter cut-off frequency on the obtained damping (a) and on the damped plant (b).

$$K_d(s) = g \cdot \frac{s}{s + \omega_d} \tag{2.33}$$

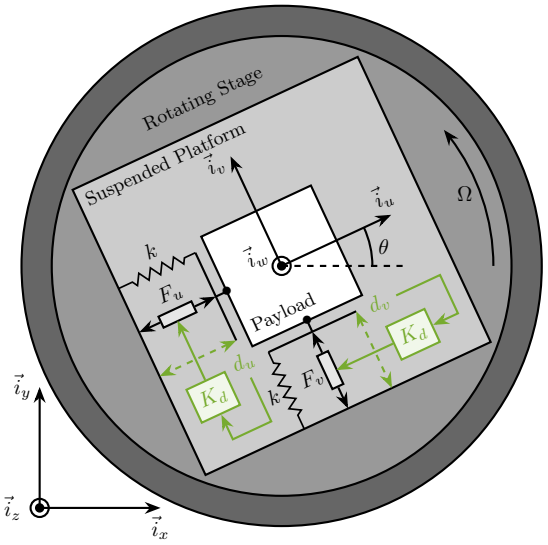

Figure 2.49: System with relative motion sensors and decentralized Relative Damping Control (RDC) applied.

Equations of Motion Let's note $\boldsymbol{G}_d$ the transfer function between actuator forces and measured relative motion in parallel with the actuators (2.34). The elements of $\boldsymbol{G}_d$ were derived in Section 2.2.1 are shown in (2.35).

$$\begin{bmatrix} d_u \\ d_v \end{bmatrix} = \boldsymbol{G}_d \begin{bmatrix} F_u \\ F_v \end{bmatrix} \tag{2.34}$$

$$\boldsymbol{G}_d(1,1) = \boldsymbol{G}_d(2,2) = \frac{\frac{1}{k}\left(\frac{s^2}{{\omega_0}^2} + 2\xi\frac{s}{\omega_0} + 1 - \frac{\Omega^2}{{\omega_0}^2}\right)}{\left(\frac{s^2}{{\omega_0}^2} + 2\xi\frac{s}{\omega_0} + 1 - \frac{\Omega^2}{{\omega_0}^2}\right)^2 + \left(2\frac{\Omega}{\omega_0}\frac{s}{\omega_0}\right)^2} \tag{2.35a}$$

$$\boldsymbol{G}_d(1,2) = -\boldsymbol{G}_d(2,1) = \frac{\frac{1}{k}\left(2\frac{\Omega}{\omega_0}\frac{s}{\omega_0}\right)}{\left(\frac{s^2}{{\omega_0}^2} + 2\xi\frac{s}{\omega_0} + 1 - \frac{\Omega^2}{{\omega_0}^2}\right)^2 + \left(2\frac{\Omega}{\omega_0}\frac{s}{\omega_0}\right)^2} \tag{2.35b}$$

Neglecting the damping for simplicity ($\xi \ll 1$), the direct terms have two complex conjugate zeros between the two pairs of complex conjugate poles (2.36). Therefore, for $\Omega < \sqrt{k/m}$ (i.e. stable system), the transfer functions for Relative Damping Control have alternating complex conjugate poles and zeros.

$$z = \pm j\sqrt{\omega_0^2 - \omega^2}, \quad p_1 = \pm j(\omega_0 - \omega), \quad p_2 = \pm j(\omega_0 + \omega) \tag{2.36}$$

Decentralized Relative Damping Control The transfer functions from $[F_u,\ F_v]$ to $[d_u,\ d_v]$ were identified for several rotating velocities in Section 2.2.1 and are shown in Figure 2.39 (page 55).

To see if large damping can be added with Relative Damping Control, the root locus is computed (Figure 2.50a). The closed-loop system is unconditionally stable as expected and the poles can be damped as much as desired.

Let us select a reasonable "Relative Damping Control" gain, and compute the closed-loop damped system. The open-loop and damped plants are compared in Figure 2.50b. The rotating aspect does not add any complexity to the use of Relative Damping Control. It does not increase the low-frequency coupling as compared to the Integral Force Feedback.

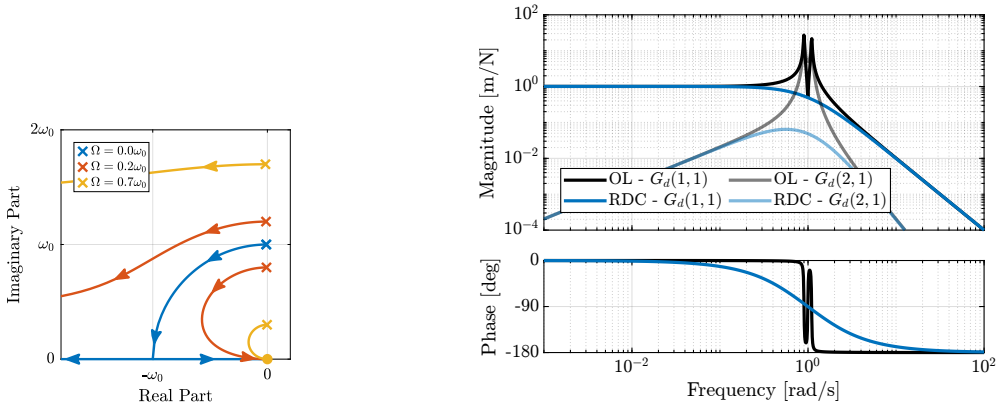

(a) Root locus for Relative Damping Control

(b) Damped plant using Relative Damping Control

Figure 2.50: Relative Damping Control. Root locus (a) and obtained damped plant (b).

2.2.6 Comparison of Active Damping Techniques

These two proposed IFF modifications and relative damping control are compared in terms of added damping and closed-loop behavior. For the following comparisons, the cut-off frequency for the added HPF is set to $\omega_i = 0.1\omega_0$ and

the stiffness of the parallel springs is set to $k_p = 5m\Omega^2$ (corresponding to $\alpha = 0.05$). These values are chosen one the basis of previous discussions about optimal parameters.

Root Locus Figure 2.51a shows the root locus plots for the two proposed IFF modifications and the relative damping control. While the two pairs of complex conjugate open-loop poles are identical for both IFF modifications, the transmission zeros are not. This means that the closed-loop behavior of both systems will differ when large control gains are used.

The closed-loop poles corresponding to the system with added springs (in red) are bounded to the left half plane implying unconditional stability. This is not the case for the system in which the controller is augmented with an HPF (in blue). It is interesting to note that the maximum added damping is very similar for both modified IFF techniques.

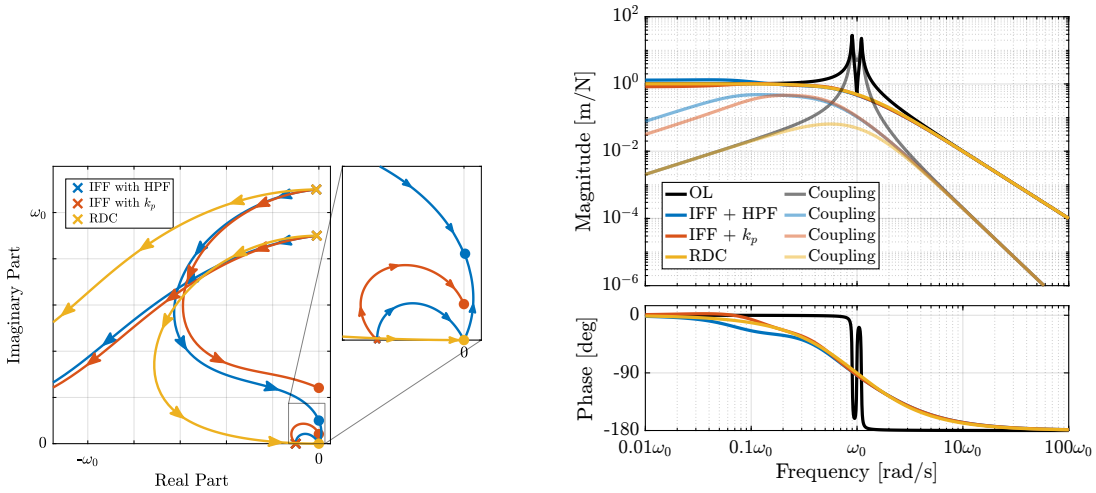

(a) Root locus

(b) Damped plants

Figure 2.51: Comparison of active damping techniques for rotating platform.

Obtained Damped Plant The actively damped plants are computed for the three techniques and compared in Figure 2.51b. It is shown that while the diagonal (direct) terms of the damped plants are similar for the three active damping techniques, the off-diagonal (coupling) terms are not. The IFF strategy is adding some coupling at low-frequency, which may negatively impact the positioning performance.

Transmissibility And Compliance The proposed active damping techniques are now compared in terms of closed-loop transmissibility and compliance. The transmissibility is defined as the transfer function from the displacement of the rotating stage along $\vec{i}_x$ to the displacement of the payload along the same direction. It is used to characterize the amount of vibration is transmitted through the suspended platform to the payload. The compliance describes the displacement response of the payload to the external forces applied to it. This is a useful metric when disturbances are directly applied to the payload. Here, it is defined as the transfer function from external forces applied on the payload along $\vec{i}_x$ to the displacement of the payload along the same direction.

Very similar results were obtained for the two proposed IFF modifications in terms of transmissibility and compliance (Figure 2.52). Using IFF degrades the compliance at low frequencies, whereas using relative damping control degrades the transmissibility at high-frequencies. This is very well known characteristics of these common active damping techniques that hold when applied to rotating platforms.

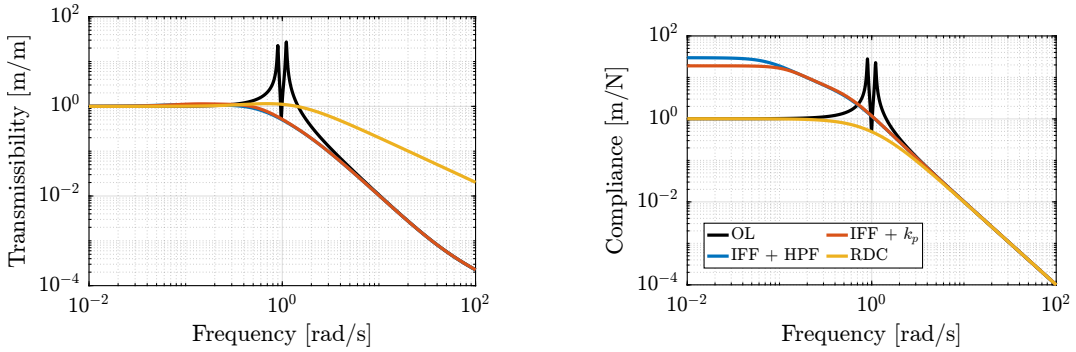

(a) Transmissibility

(b) Compliance

Figure 2.52: Comparison of the obtained transmissibility (a) and compliance (b) for the three tested active damping techniques.

2.2.7 Rotating Active Platform

The previous analysis is now applied to a model representing a rotating active platform. Three active platform stiffnesses are tested as for the uniaxial model: $k_n = 0.01\,\text{N}\,\mu\text{m}^{-1}$, $k_n = 1\,\text{N}\,\mu\text{m}^{-1}$ and $k_n = 100\,\text{N}\,\mu\text{m}^{-1}$. Only the maximum rotating velocity is here considered ($\Omega = 60$ rpm) with the light sample ($m_s = 1$ kg) because this is the worst identified case scenario in terms of gyroscopic effects.

Nano-Active-Stabilization-System - Plant Dynamics For the NASS, the maximum rotating velocity is $\Omega = 2\pi\,\text{rad}\,\text{s}^{-1}$ for a suspended mass on top of the active platform's actuators equal to $m_n + m_s = 16$ kg. The parallel stiffness corresponding to the centrifugal forces is $m\Omega^2 \approx 0.6\,\text{N}\,\text{mm}^{-1}$.

The transfer functions from the active platform actuator force F_u to the displacement of the active platform in the same direction d_u as well as in the orthogonal direction d_v (coupling) are shown in Figure 2.53 for all three considered active platform stiffnesses. The soft active platform is the most affected by rotation. This can be seen by the large shift of the resonance frequencies, and by the induced coupling, which is larger than that for the stiffer active platforms. The coupling (or interaction) in a MIMO 2×2 system can be visually estimated as the ratio between the diagonal term and the off-diagonal terms (see corresponding Appendix).

Optimal IFF with a High-Pass Filter Integral Force Feedback with an added High Pass Filter is applied to the three active platforms. First, the parameters (ω_i and g) of the IFF controller that yield the best simultaneous damping are determined from Figure 2.54. The IFF parameters are chosen as follows:

- for $k_n = 0.01\,\text{N}\,\mu\text{m}^{-1}$ (Figure 2.54): ω_i is chosen such that maximum damping is achieved while the gain is less than half of the maximum gain at which the system is unstable. This is done to have some control robustness.
- for $k_n = 1\,\text{N}\,\mu\text{m}^{-1}$ and $k_n = 100\,\text{N}\,\mu\text{m}^{-1}$ (Figure 2.54b and 2.54c): the largest ω_i is chosen such that the obtained damping is 95 % of the maximum achievable damping. Large ω_i is chosen here to limit the loss of compliance and the increase of coupling at low-frequency as shown in Section 2.2.3.

The obtained IFF parameters and the achievable damping are visually shown by large dots in Figure 2.54 and are summarized in Table 2.5.

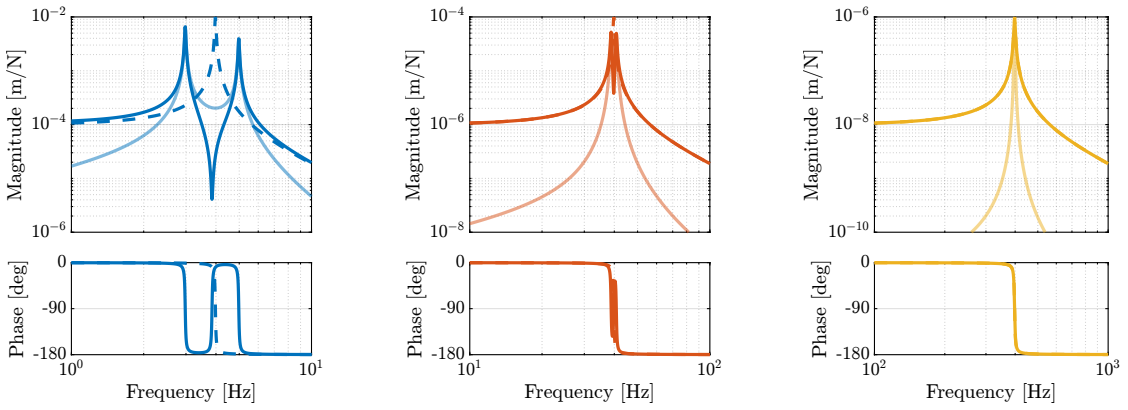

(a) $k_n = 0.01\,\mathrm{N/\mu m}$ **(b)** $k_n = 1\,\mathrm{N/\mu m}$ **(c)** $k_n = 100\,\mathrm{N/\mu m}$

Figure 2.53: Effect of rotation on the active platform dynamics. Dashed lines represent plants without rotation, solid lines represent plants at maximum rotating velocity ($\Omega = 60$ rpm), and shaded lines are coupling terms at maximum rotating velocity.

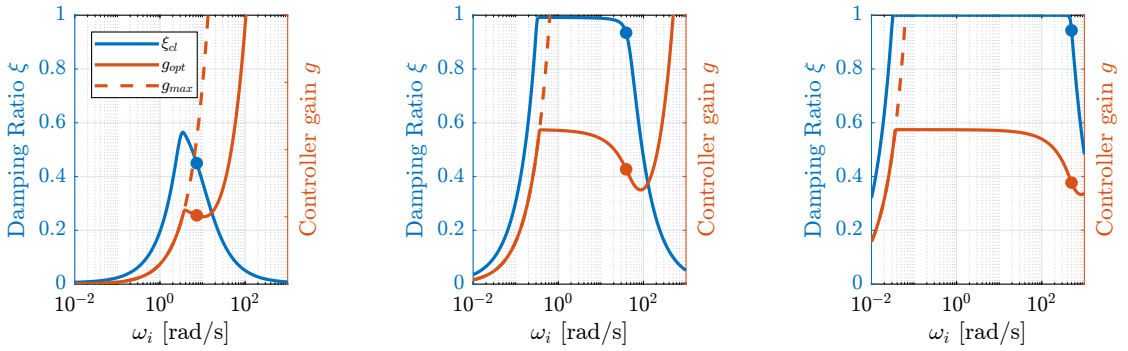

(a) $k_n = 0.01\,\mathrm{N/\mu m}$ **(b)** $k_n = 1\,\mathrm{N/\mu m}$ **(c)** $k_n = 100\,\mathrm{N/\mu m}$

Figure 2.54: For each value of ω_i, the maximum damping ratio ξ is computed (blue), and the corresponding controller gain is shown (in red). The chosen controller parameters used for further analysis are indicated by the large dots.

Optimal IFF with Parallel Stiffness For each considered active platform stiffness, the parallel stiffness k_p is varied from $k_{p,\min} = m\Omega^2$ (the minimum stiffness that yields unconditional stability) to $k_{p,\max} = k_n$ (the total active platform stiffness). To keep the overall stiffness constant, the actuator stiffness k_a is decreased when k_p is increased ($k_a = k_n - k_p$, with k_n the total active platform stiffness). A high-pass filter is also added to limit the low-frequency gain with a cut-off frequency ω_i equal to one tenth of the system resonance ($\omega_i = \omega_0/10$).

The achievable maximum simultaneous damping of all the modes is computed as a function of the parallel stiffnesses (Figure 2.55). It is shown that the soft active platform cannot yield good damping because the parallel stiffness cannot be sufficiently large compared to the negative stiffness induced by the rotation. For the two stiff options, the achievable damping decreases when the parallel stiffness is too high, as explained in Section 2.2.4. Such behavior can be explained by the fact that the achievable damping can be approximated by the distance between the open-loop pole and the open-loop zero [113, chapt 7.2]. This distance is larger for stiff active platform because the open-loop pole will be at higher frequencies while the open-loop zero, whereas depends on the value of the parallel stiffness, can only be made large for stiff active platforms.

Table 2.5: Obtained optimal parameters (ω_i and g) for the modified IFF controller including a high-pass filter. The corresponding achievable simultaneous damping ξ_{opt} of the two modes is also shown.

k_n	ω_i	g	ξ_{opt}
0.01 N/µm	7.3	51	0.45
1 N/µm	39	427	0.93
100 N/µm	500	3775	0.94

Let's choose $k_p = 1\,\text{N/mm}$, $k_p = 0.01\,\text{N/µm}$ and $k_p = 1\,\text{N/µm}$ for the three considered active platforms. The corresponding optimal controller gains and achievable damping are summarized in Table 2.6.

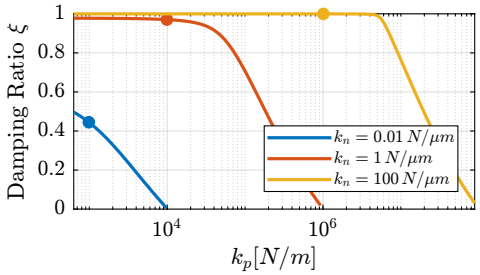

Figure 2.55: Maximum damping ξ as a function of the parallel stiffness k_p.

k_n	k_p	g	ξ_{opt}
0.01 N/µm	1 N/mm	48	0.44
1 N/µm	0.01 N/µm	465	0.97
100 N/µm	1 N/µm	4624	0.99

Table 2.6: Obtained optimal parameters for the IFF controller when using parallel stiffnesses

Optimal Relative Motion Control For each considered active platform stiffness, relative damping control is applied and the achievable damping ratio as a function of the controller gain is computed (Figure 2.56). The gain is chosen such that 99% of modal damping is obtained (obtained gains are summarized in Table 2.7).

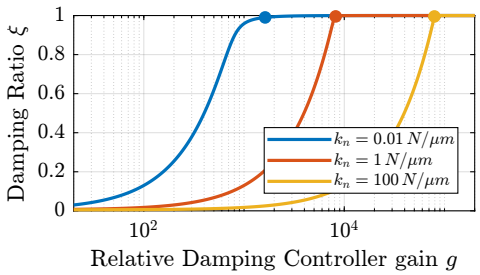

Figure 2.56: Maximum damping ξ as a function of the RDC gain g.

k_n	g	ξ_{opt}
0.01 N/µm	1600	0.99
1 N/µm	8200	0.99
100 N/µm	80000	0.99

Table 2.7: Obtained optimal parameters for the acr-long:rdc

Comparison of the Obtained Damped Plants Now that the optimal parameters for the three considered active damping techniques have been determined, the obtained damped plants are computed and compared in Figure 2.57.

Similar to what was concluded in the previous analysis:

- IFF adds more coupling below the resonance frequency as compared to the open-loop and RDC cases
- All three methods yield good damping, except for IFF applied on the soft active platform
- Coupling is smaller for stiff active platforms

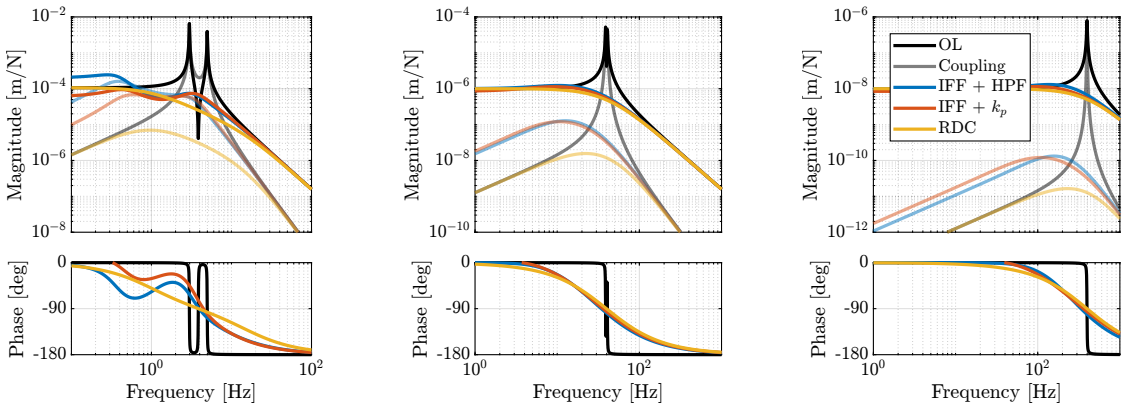

(a) $k_n = 0.01\,\mathrm{N/\mu m}$ **(b)** $k_n = 1\,\mathrm{N/\mu m}$ **(c)** $k_n = 100\,\mathrm{N/\mu m}$

Figure 2.57: Comparison of the damped plants for the three proposed active damping techniques (IFF with HPF in blue, IFF with k_p in red and RDC in yellow). The direct terms are shown by solid lines, and the coupling terms are shown by the shaded lines. Three active platform stiffnesses are considered. Rotating velocity is $\Omega = 60$ rpm and the suspended mass is $m_n + m_s = 16\,\mathrm{kg}$.

2.2.8 Nano Active Stabilization System with Rotation

Until now, the model used to study gyroscopic effects consisted of an infinitely stiff rotating stage with a X-Y suspended stage on top. While quite simplistic, this allowed us to study the effects of rotation and the associated limitations when active damping is to be applied. In this section, the limited compliance of the micro-station is considered as well as the rotation of the spindle.

Nano Active Stabilization System Model To have a more realistic dynamics model of the NASS, the 2-DoF active platform (modelled as shown in Figure 2.37) is now located on top of a model of the micro-station including (see Figure 2.58 for a 3D view):

- the floor whose motion is imposed
- a 2-DoF granite ($k_{g,x} = k_{g,y} = 950\,\mathrm{N\,\mu m^{-1}}$, $m_g = 2500\,\mathrm{kg}$)
- a 2-DoF T_y stage ($k_{t,x} = k_{t,y} = 520\,\mathrm{N\,\mu m^{-1}}$, $m_t = 600\,\mathrm{kg}$)
- a spindle (vertical rotation) stage whose rotation is imposed ($m_s = 600\,\mathrm{kg}$)
- a 2-DoF positioning hexapod ($k_{h,x} = k_{h,y} = 61\,\mathrm{N\,\mu m^{-1}}$, $m_h = 15\,\mathrm{kg}$)

A payload is rigidly fixed to the active platform and the x, y motion of the payload is measured with respect to the granite.

System Dynamics The dynamics of the undamped and damped plants are identified using the optimal parameters found in Section 2.2.7. The obtained dynamics are compared in Figure 2.59 in which the direct terms are shown by the solid curves and the coupling terms are shown by the shaded ones. It can be observed that:

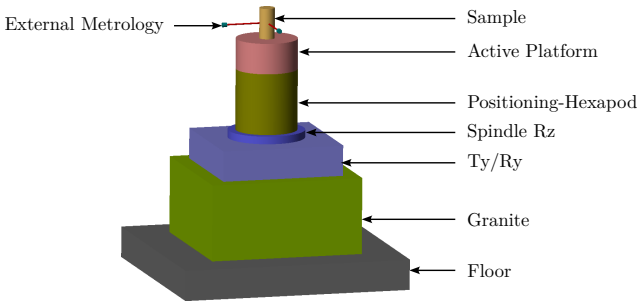

Figure 2.58: 3D view of the Nano-Active-Stabilization-System model.

- The coupling (quantified by the ratio between the off-diagonal and direct terms) is higher for the soft active platform
- Damping added using the three proposed techniques is quite high, and the obtained plant is rather easy to control
- There is some coupling between active platform and micro-station dynamics for the stiff active platform (mode at 200 Hz)
- The two proposed IFF modifications yield similar results

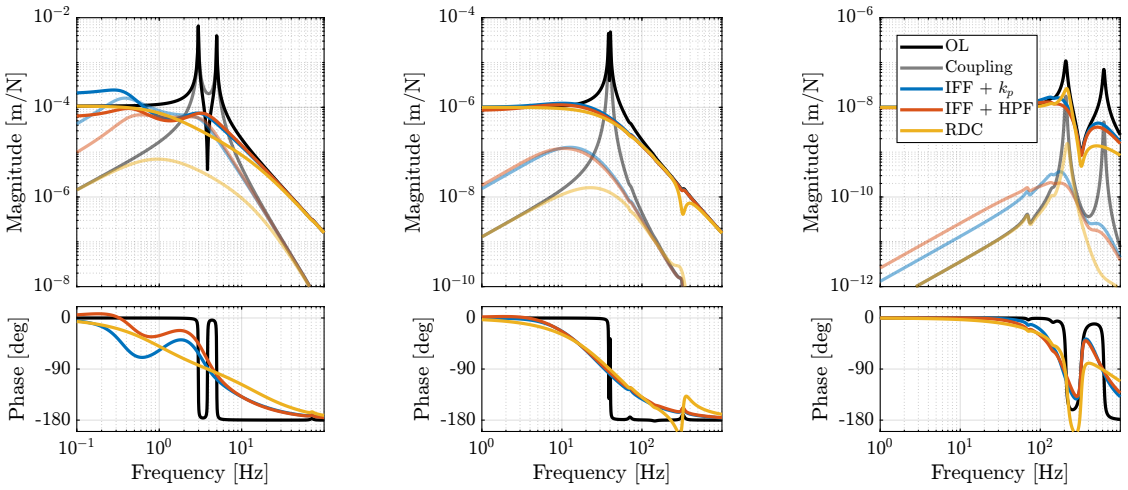

(a) $k_n = 0.01\,\mathrm{N/\mu m}$ **(b)** $k_n = 1\,\mathrm{N/\mu m}$ **(c)** $k_n = 100\,\mathrm{N/\mu m}$

Figure 2.59: Bode plot of the transfer function from active platform actuator to measured motion by the external metrology.

Effect of Disturbances The effect of three disturbances are considered (as for the uniaxial model), floor motion $[x_{f,x},\ x_{f,y}]$ (Figure 2.60), micro-Station vibrations $[f_{t,x},\ f_{t,y}]$ (Figure 2.61) and direct forces applied on the sample $[f_{s,x},\ f_{s,y}]$ (Figure 2.62). Note that only the transfer functions from the disturbances in the x direction to the relative position d_x between the sample and the granite in the x direction are displayed because the transfer functions in the y direction are the same due to the system symmetry.

Conclusions are similar than those of the uniaxial (non-rotating) model:

- Regarding the effect of floor motion and forces applied on the payload:

- The stiffer, the better. This can be seen in Figures 2.60 and 2.62 where the magnitudes for the stiff active platform are lower than those for the soft one
- IFF degrades the performance at low-frequency compared to RDC

- Regarding the effect of micro-station vibrations:
  - Having a soft active platform allows filtering of these vibrations between the suspension modes of the active platform and some flexible modes of the micro-station. Using relative damping control reduces this filtering (Figure 2.61a).

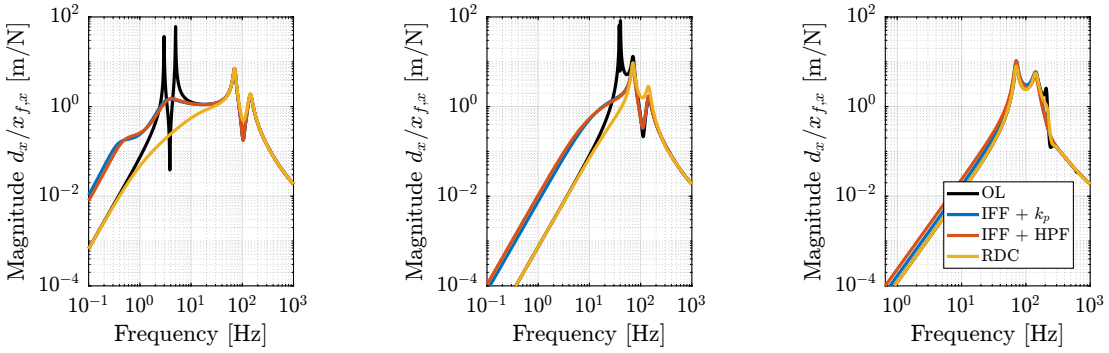

(a) $k_n = 0.01\,\mathrm{N/\mu m}$ **(b)** $k_n = 1\,\mathrm{N/\mu m}$ **(c)** $k_n = 100\,\mathrm{N/\mu m}$

Figure 2.60: Effect of floor motion $x_{f,x}$ on the position error d_x - Comparison of active damping techniques for the three active platform stiffnesses. IFF is shown to increase the sensitivity to floor motion at low-frequency.

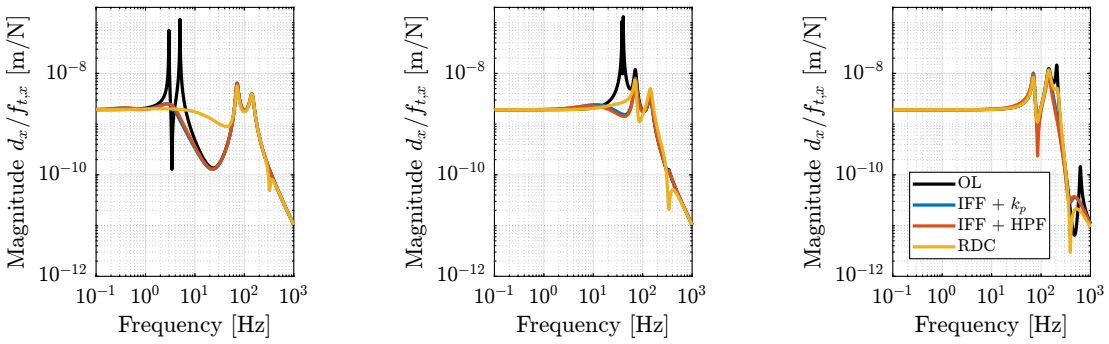

(a) $k_n = 0.01\,\mathrm{N/\mu m}$ **(b)** $k_n = 1\,\mathrm{N/\mu m}$ **(c)** $k_n = 100\,\mathrm{N/\mu m}$

Figure 2.61: Effect of micro-station vibrations $f_{t,x}$ on the position error d_x - Comparison of active damping techniques for the three active platform stiffnesses. Relative Damping Control increases the sensitivity to micro-station vibrations between the soft active platform suspension modes and the micro-station modes (a).

Conclusion

In this study, the gyroscopic effects induced by the spindle's rotation have been studied using a simplified model. Decentralized Integral Force Feedback with pure integrators was shown to be unstable when applied to rotating platforms. Two modifications of the classical IFF control have been proposed to overcome this issue.

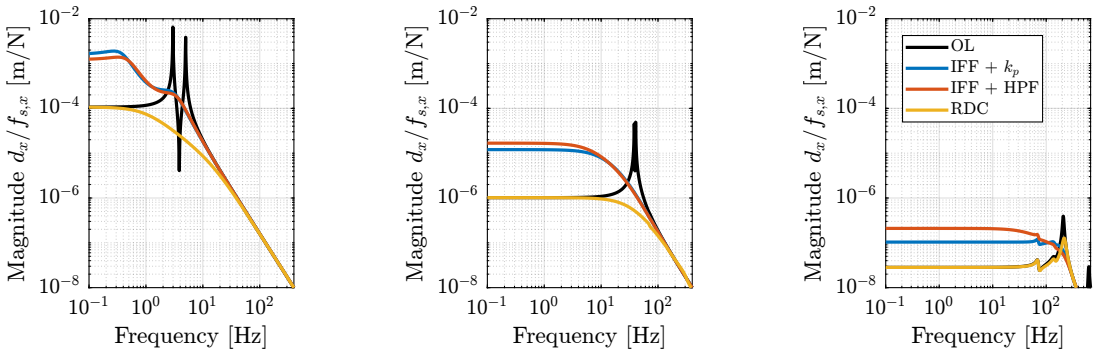

(a) $k_n = 0.01\,\mathrm{N/\mu m}$ **(b)** $k_n = 1\,\mathrm{N/\mu m}$ **(c)** $k_n = 100\,\mathrm{N/\mu m}$

Figure 2.62: Effect of sample forces $f_{s,x}$ on the position error d_x - Comparison of active damping techniques for the three active platform stiffnesses. Integral Force Feedback degrades this compliance at low-frequency.

The first modification concerns the controller and consists of adding a high-pass filter to the pure integrators. This is equivalent to moving the controller pole to the left along the real axis. This allows the closed-loop system to be stable up to some value of the controller gain.

The second proposed modification concerns the mechanical system. Additional springs are added in parallel with the actuators and force sensors. It was shown that if the stiffness k_p of the additional springs is larger than the negative stiffness $m\Omega^2$ induced by centrifugal forces, the classical decentralized IFF regains its unconditional stability property.

These two modifications were compared with Relative Damping Control. While having very different implementations, both proposed modifications were found to be very similar with respect to the attainable damping and the obtained closed-loop system behavior.

This study has been applied to a rotating platform that corresponds to the active platform parameters. As for the uniaxial model, three active platform stiffnesses values were considered. The dynamics of the soft active platform ($k_n = 0.01\,\mathrm{N/\mu m}$) was shown to be more depend more on the rotation velocity (higher coupling and change of dynamics due to gyroscopic effects). In addition, the attainable damping ratio of the soft active platform when using IFF is limited by gyroscopic effects.

To better match the Nano Active Stabilization System dynamics, the limited compliance of the micro-station has been considered. The results are similar to those of the uniaxial model, except for additional complexity introduced by the spindle's rotation in the case of the soft active platform. For the moderately stiff active platform ($k_n = 1\,\mathrm{N/\mu m}$), the gyroscopic effects only slightly affect the system dynamics, and therefore could represent a good alternative to the soft active platform that showed better results with the uniaxial model.

2.3 Micro Station - Modal Analysis

To further improve the accuracy of the performance predictions, a model that better represents the micro-station dynamics is required. A multi-body model consisting of several rigid bodies connected by kinematic constraints (i.e. joints), springs and damper elements is a good candidate to model the micro-station.

Although the inertia of each solid body can easily be estimated from its geometry and material density, it is more difficult to properly estimate the stiffness and damping properties of the guiding elements connecting each solid body. Experimental modal analysis will be used to tune the model, and to verify that a multi-body model can accurately represent the dynamics of the micro-station.

The tuning approach for the multi-body model based on measurements is illustrated in Figure 2.63. First, a *response model* is obtained, which corresponds to a set of Frequency Response Functions (FRFs) computed from experimental measurements. From this response model, the modal model can be computed, which consists of two matrices: one containing the natural frequencies and damping factors of the considered modes, and another describing the mode shapes. This modal model can then be used to tune the spatial model (i.e. the multi-body model), that is, to tune the mass of the considered solid bodies and the springs and dampers connecting the solid bodies.

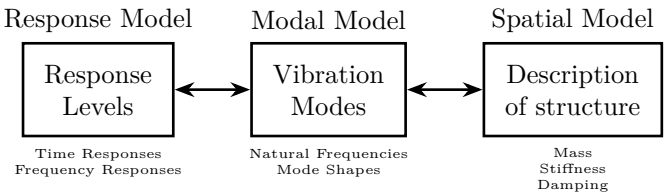

Figure 2.63: Three models of the same structure. The goal is to tune a spatial model (i.e. mass, stiffness and damping properties) from a response model. The modal model can be used as an intermediate step.

The measurement setup used to obtain the response model is described in Section 2.3.1. This includes the instrumentation used (i.e. instrumented hammer, accelerometers and acquisition system), test planning, and a first analysis of the obtained signals.

In Section 2.3.2, the obtained FRFs between the forces applied by the instrumented hammer and the accelerometers fixed to the structure are computed. These measurements are projected at the Center of Mass (CoM) of each considered solid body to facilitate the further use of the results. The solid body assumption is then verified, validating the use of the multi-body model.

Finally, the modal analysis is performed in Section 2.3.3. This shows how complex the micro-station dynamics is, and the necessity of having a model representing its complex dynamics.

2.3.1 Measurement Setup

In order to perform an experimental modal analysis, a suitable measurement setup is essential. This includes using appropriate instrumentation (presented in Section 2.3.1.1) and properly preparing the structure to be measured (Section 2.3.1.2). Then, the locations of the measured motions (Section 2.3.1.3) and the locations of the hammer impacts (Section 2.3.1.4) have to be chosen carefully. The obtained force and acceleration signals are described in Section 2.3.1.5, and the quality of the measured data is assessed.

2.3.1.1 Instrumentation

Three types of equipment are essential for a good modal analysis. First, *accelerometers* are used to measure the response of the structure. Here, 3-axis accelerometers[1] shown in figure 2.64a are used. These accelerometers were glued to the micro-station using a thin layer of wax for best results [44, chapt. 3.5.7].

(a) 3-axis accelerometer **(b)** Instrumented hammer **(c)** OROS acquisition system

Figure 2.64: Instrumentation used for the modal analysis.

Then, an *instrumented hammer*[2] (figure 2.64b) is used to apply forces to the structure in a controlled manner. Tests were conducted to determine the most suitable hammer tip (ranging from a metallic one to a soft plastic one). The softer tip was found to give best results as it injects more energy in the low-frequency range where the coherence was low, such that the overall coherence was improved.

Finally, an *acquisition system*[3] (figure 2.64c) is used to acquire the injected force and response accelerations in a synchronized manner and with sufficiently low noise.

2.3.1.2 Structure Preparation and Test Planning

To obtain meaningful results, the modal analysis of the micro-station is performed *in-situ*. To do so, all the micro-station stage controllers are turned on. This is especially important for stages for which the stiffness is provided by local feedback control, such as the air bearing spindle, and the translation stage. If these local feedback controls were turned off, this would have resulted in very low-frequency modes that were difficult to measure in practice, and it would also have led to decoupled dynamics, which would not be the case in practice.

The top part representing the active stabilization stage was disassembled as the active stabilization stage will be added in the multi-body model afterwards.

To perform the modal analysis from the measured responses, the $n \times n$ FRF matrix $\boldsymbol{H}$ needs to be measured, where n is the considered number of degrees of freedom. The H_{jk} element of this Frequency Response Function (FRF) matrix corresponds to the FRF from a force F_k applied at Degrees of Freedom (DoF) k to the displacement of the structure

[1] PCB 356B18. Sensitivity is 1 V/g, measurement range is ± 5 g and bandwidth is 0.5 to 5 kHz.
[2] Kistler 9722A2000. Sensitivity of 2.3 mV/N and measurement range of 2 kN.
[3] OROS OR36. 24bits signal-delta ADC.

X_j at DoF j. Measuring this FRF matrix is time consuming as it requires making $n \times n$ measurements. However, due to the principle of reciprocity ($H_{jk} = H_{kj}$) and using the *point measurement* (H_{jj}), it is possible to reconstruct the full matrix by measuring only one column or one line of the matrix $\boldsymbol{H}$ [44, chapt. 5.2]. Therefore, a minimum set of n FRFs is required. This can be done either by measuring the response X_j at a fixed DoF j while applying forces F_i at all n considered DoF, or by applying a force F_k at a fixed DoF k and measuring the response X_i for all n DoF.

It is however not advised to measure only one row or one column, as one or more modes may be missed by an unfortunate choice of force or acceleration measurement location (for instance if the force is applied at a vibration node of a particular mode). In this modal analysis, it is chosen to measure the response of the structure at all considered DoF, and to excite the structure at one location in three directions in order to have some redundancy, and to ensure that all modes are properly identified.

2.3.1.3 Location of the Accelerometers

The location of the accelerometers fixed to the micro-station is essential because it defines where the dynamics is measured. A total of 23 accelerometers were fixed to the six key stages of the micro station: the lower and upper granites, the translation stage, the tilt stage, the spindle and the positioning hexapod. The positions of the accelerometers are visually shown on a 3D model in Figure 2.65 and their precise locations with respect to a frame located at the PoI are summarized in Table 2.8. Pictures of the accelerometers fixed to the translation stage and to the positioning hexapod are shown in Figure 2.66.

As all key stages of the micro-station are expected to behave as solid bodies, only 6 DoF can be considered for each solid body. However, it was chosen to use four 3-axis accelerometers (i.e. 12 measured DoF) for each considered solid body to have some redundancy and to be able to verify the solid body assumption (see Section 2.3.2.2).

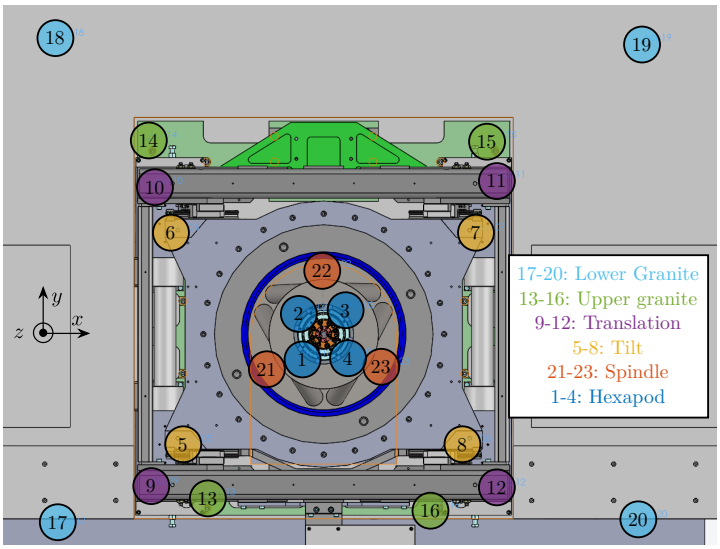

Figure 2.65: Position of the accelerometers.

	x	y	z
(17) Low. Granite	-730	-526	-951
(18) Low. Granite	-735	814	-951
(19) Low. Granite	875	799	-951
(20) Low. Granite	865	-506	-951
(13) Up. Granite	-320	-446	-786
(14) Up. Granite	-480	534	-786
(15) Up. Granite	450	534	-786
(16) Up. Granite	295	-481	-786
(9) Translation	-475	-414	-427
(10) Translation	-465	407	-427
(11) Translation	475	424	-427
(12) Translation	475	-419	-427
(5) Tilt	-385	-300	-417
(6) Tilt	-420	280	-417
(7) Tilt	420	280	-417
(8) Tilt	380	-300	-417
(21) Spindle	-155	-90	-594
(22) Spindle	0	180	-594
(23) Spindle	155	-90	-594
(1) Hexapod	-64	-64	-270
(2) Hexapod	-64	64	-270
(3) Hexapod	64	64	-270
(4) Hexapod	64	-64	-270

Table 2.8: Positions in mm

2.3.1.4 Hammer Impacts

The selected location of the hammer impact corresponds to the location of accelerometer number 11 fixed to the translation stage. It was chosen to match the location of one accelerometer, because a *point measurement* (i.e. a measurement of H_{kk}) is necessary to be able to reconstruct the full FRF matrix [44].

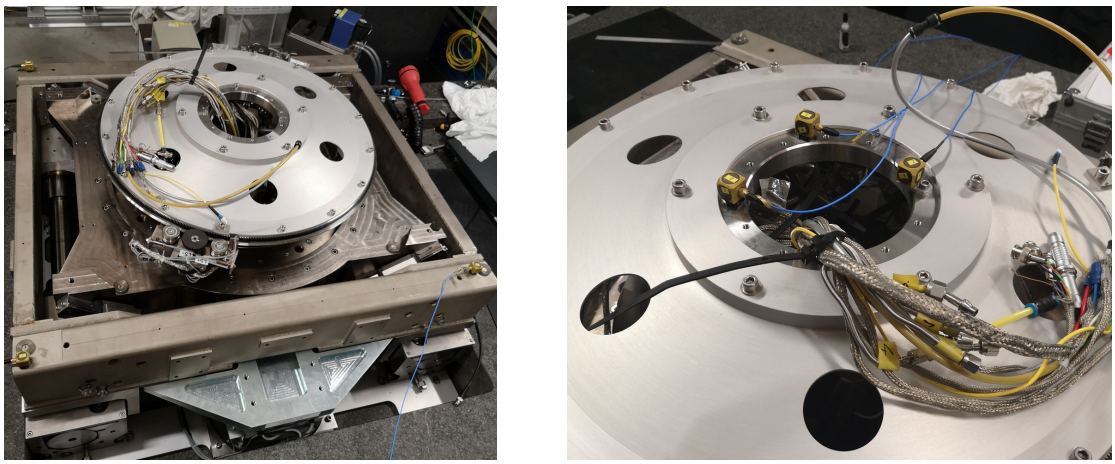

(a) T_y stage **(b)** Positioning Hexapod

Figure 2.66: Accelerometers fixed on the micro-station stages.

The impacts were performed in three directions, as shown in figures 2.67a, 2.67b and 2.67c.

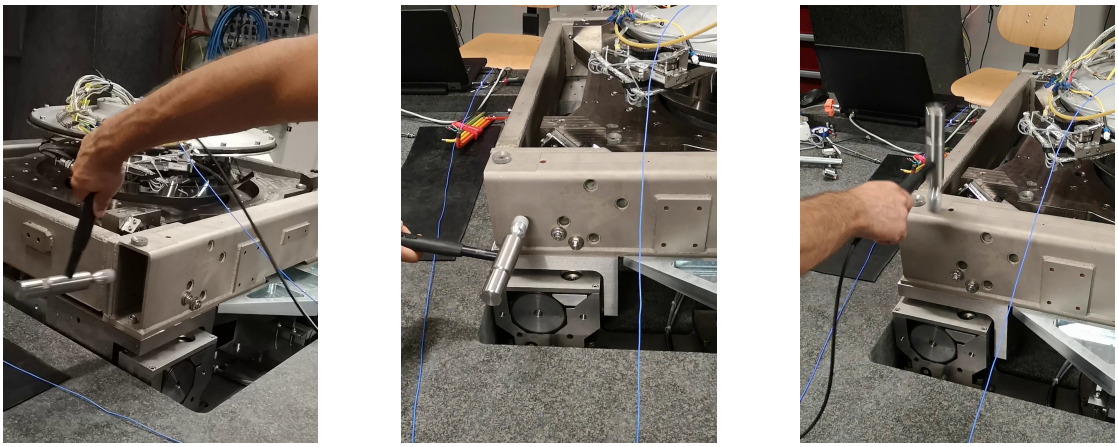

(a) X impact **(b)** Y impact **(c)** Z impact

Figure 2.67: The three hammer impacts used for the modal analysis.

2.3.1.5 Force and Response signals

The force sensor of the instrumented hammer and the accelerometer signals are shown in the time domain in Figure 2.68a. Sharp "impacts" can be observed for the force sensor, indicating wide frequency band excitation. For the accelerometer, a much more complex signal can be observed, indicating complex dynamics.

The "normalized" Amplitude Spectrum Density (ASD) of the two signals were computed and shown in Figure 2.68b. Conclusions based on the time domain signals can be clearly observed in the frequency domain (wide frequency content for the force signal and complex dynamics for the accelerometer). These data are corresponding to a hammer impact in the vertical direction and to the measured acceleration in the x direction by accelerometer 1 (fixed to the positioning hexapod). Similar results were obtained for all measured FRFs.

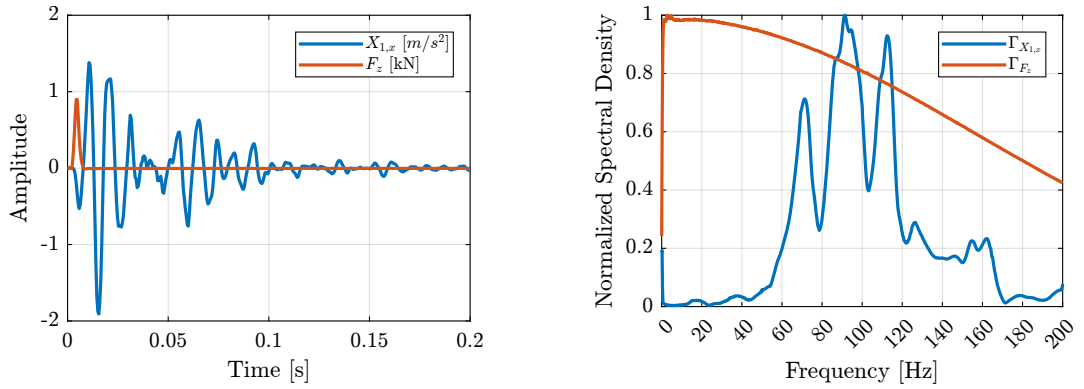

(a) Time domain signals

(b) Amplitude Spectral Density (normalized)

Figure 2.68: Raw measurement of the accelerometer 1 in the x direction (blue) and of the force sensor at the Hammer tip (red) for an impact in the z direction (a). Computed Amplitude Spectral Densities of the two signals (normalized) (b).

The FRF from the applied force to the measured acceleration is then computed and shown Figure 2.69a. The quality of the obtained data can be estimated using the *coherence* function (Figure 2.69b). Good coherence is obtained from 20 Hz to 200 Hz which corresponds to the frequency range of interest.

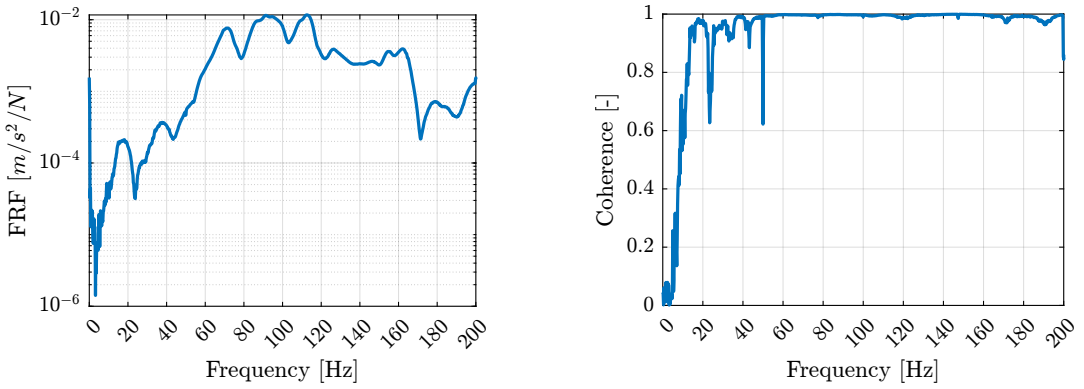

(a) Frequency Response Function

(b) Coherence

Figure 2.69: Computed FRF from the applied force F_z to the measured response $X_{1,x}$ (a) as well as computed coherence (b).

2.3.2 Frequency Analysis

After all measurements are conducted, a $n \times p \times q$ Frequency Response Functions matrix can be computed with:

- $n = 69$: number of output measured acceleration (23 3-axis accelerometers)
- $p = 3$: number of input force excitation
- $q = 801$: number of frequency points ω_i

For each frequency point ω_i, a 2D complex matrix is obtained that links the 3 force inputs to the 69 output accelerations (2.37).

$$\boldsymbol{H}(\omega_i) = \begin{bmatrix} \frac{D_{1_x}}{F_x}(\omega_i) & \frac{D_{1_x}}{F_y}(\omega_i) & \frac{D_{1_x}}{F_z}(\omega_i) \\ \frac{D_{1_y}}{F_x}(\omega_i) & \frac{D_{1_y}}{F_y}(\omega_i) & \frac{D_{1_y}}{F_z}(\omega_i) \\ \frac{D_{1_z}}{F_x}(\omega_i) & \frac{D_{1_z}}{F_y}(\omega_i) & \frac{D_{1_z}}{F_z}(\omega_i) \\ \frac{D_{2_x}}{F_x}(\omega_i) & \frac{D_{2_x}}{F_y}(\omega_i) & \frac{D_{2_x}}{F_z}(\omega_i) \\ \vdots & \vdots & \vdots \\ \frac{D_{23_z}}{F_x}(\omega_i) & \frac{D_{23_z}}{F_y}(\omega_i) & \frac{D_{23_z}}{F_z}(\omega_i) \end{bmatrix} \tag{2.37}$$

However, for the multi-body model, only 6 solid bodies are considered, namely: the bottom granite, the top granite, the translation stage, the tilt stage, the spindle and the positioning hexapod. Therefore, only $6 \times 6 = 36$ degrees of freedom are of interest. Therefore, the objective of this section is to process the Frequency Response Matrix to reduce the number of measured DoF from 69 to 36.

The coordinate transformation from accelerometers DoF to the solid body 6-DoF (three translations and three rotations) is performed in Section 2.3.2.1. The $69 \times 3 \times 801$ frequency response matrix is then reduced to a $36 \times 3 \times 801$ frequency response matrix where the motion of each solid body is expressed with respect to its Center of Mass.

To validate this reduction of DoF and the solid body assumption, the frequency response function at the accelerometer location are "reconstructed" from the reduced frequency response matrix and are compared with the initial measurements in Section 2.3.2.2.

2.3.2.1 From Accelerometer DoF to Solid Body DoF

Let us consider the schematic shown in Figure 2.70 where the motion of a solid body is measured at 4 distinct locations (in x, y and z directions). The goal here is to link these $4 \times 3 = 12$ measurements to the 6 DoF of the solid body expressed in the frame $\{O\}$.

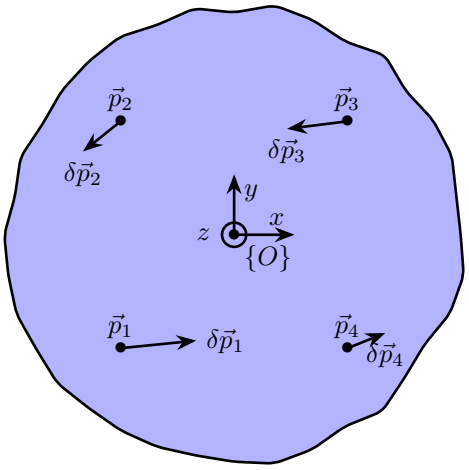

Figure 2.70: Schematic of the measured motion of a solid body at 4 distinct locations.

The motion of the rigid body of figure 2.70 can be described by its displacement $\vec{\delta p} = [\delta p_x,\ \delta p_y,\ \delta p_z]$ and (small) rotations $[\delta\Omega_x,\ \delta\Omega_y,\ \delta\Omega_z]$ with respect to the reference frame $\{O\}$.

The motion $\vec{\delta p}_i$ of a point p_i can be computed from $\vec{\delta p}$ and $\boldsymbol{\delta\Omega}$ using equation (2.38), with $\boldsymbol{\delta\Omega}$ defined in equation (2.39) [44, chapt. 4.3.2].

$$\vec{\delta p}_i = \vec{\delta p} + \boldsymbol{\delta\Omega} \cdot \vec{p}_i \tag{2.38}$$

$$\boldsymbol{\delta\Omega} = \begin{bmatrix} 0 & -\delta\Omega_z & \delta\Omega_y \\ \delta\Omega_z & 0 & -\delta\Omega_x \\ -\delta\Omega_y & \delta\Omega_x & 0 \end{bmatrix} \tag{2.39}$$

Writing this in matrix form for the four points gives (2.40).

$$\left[\begin{array}{c} \delta p_{1x} \\ \delta p_{1y} \\ \delta p_{1z} \\ \hline \vdots \\ \hline \delta p_{4x} \\ \delta p_{4y} \\ \delta p_{4z} \end{array}\right] = \left[\begin{array}{ccc|ccc} 1 & 0 & 0 & 0 & p_{1z} & -p_{1y} \\ 0 & 1 & 0 & -p_{1z} & 0 & p_{1x} \\ 0 & 0 & 1 & p_{1y} & -p_{1x} & 0 \\ \hline & \vdots & & & \vdots & \\ \hline 1 & 0 & 0 & 0 & p_{4z} & -p_{4y} \\ 0 & 1 & 0 & -p_{4z} & 0 & p_{4x} \\ 0 & 0 & 1 & p_{4y} & -p_{4x} & 0 \end{array}\right] \left[\begin{array}{c} \delta p_x \\ \delta p_y \\ \delta p_z \\ \hline \delta\Omega_x \\ \delta\Omega_y \\ \delta\Omega_z \end{array}\right] \tag{2.40}$$

Provided that the four sensors are properly located, the system of equation (2.40) can be solved by matrix inversion[1]. The motion of the solid body expressed in a chosen frame $\{O\}$ can be determined by inverting equation (2.40). Note that this matrix inversion is equivalent to resolving a mean square problem. Therefore, having more accelerometers permits better approximation of the motion of a solid body.

From the 3D model, the position of the Center of Mass of each solid body is computed (see Table 2.9). The position of each accelerometer with respect to the Center of Mass of the corresponding solid body can easily be determined.

Table 2.9: Center of mass of considered solid bodies with respect to the Point of Interest.

	X	Y	Z
Bottom Granite	45 mm	144 mm	−1251 mm
Top granite	52 mm	258 mm	−778 mm
Translation stage	0	14 mm	−600 mm
Tilt Stage	0	−5 mm	−628 mm
Spindle	0	0	−580 mm
Positioning Hexapod	−4 mm	6 mm	−319 mm

Using (2.40), the frequency response matrix $\boldsymbol{H}_{\text{CoM}}$ (2.41) expressing the response at the Center of Mass of each solid body D_i (i from 1 to 6 for the 6 considered solid bodies) can be computed from the initial FRF matrix $\boldsymbol{H}$.

[1] As this matrix is in general non-square, the Moore–Penrose inverse can be used instead.

$$\boldsymbol{H}_{\text{CoM}}(\omega_i) = \begin{bmatrix} \frac{D_{1,T_x}}{F_x}(\omega_i) & \frac{D_{1,T_x}}{F_y}(\omega_i) & \frac{D_{1,T_x}}{F_z}(\omega_i) \\ \frac{D_{1,T_y}}{F_x}(\omega_i) & \frac{D_{1,T_y}}{F_y}(\omega_i) & \frac{D_{1,T_y}}{F_z}(\omega_i) \\ \frac{D_{1,T_z}}{F_x}(\omega_i) & \frac{D_{1,T_z}}{F_y}(\omega_i) & \frac{D_{1,T_z}}{F_z}(\omega_i) \\ \frac{D_{1,R_x}}{F_x}(\omega_i) & \frac{D_{1,R_x}}{F_y}(\omega_i) & \frac{D_{1,R_x}}{F_z}(\omega_i) \\ \frac{D_{1,R_y}}{F_x}(\omega_i) & \frac{D_{1,R_y}}{F_y}(\omega_i) & \frac{D_{1,R_y}}{F_z}(\omega_i) \\ \frac{D_{1,R_z}}{F_x}(\omega_i) & \frac{D_{1,R_z}}{F_y}(\omega_i) & \frac{D_{1,R_z}}{F_z}(\omega_i) \\ \frac{D_{2,T_x}}{F_x}(\omega_i) & \frac{D_{2,T_x}}{F_y}(\omega_i) & \frac{D_{2,T_x}}{F_z}(\omega_i) \\ \vdots & \vdots & \vdots \\ \frac{D_{6,R_z}}{F_x}(\omega_i) & \frac{D_{6,R_z}}{F_y}(\omega_i) & \frac{D_{6,R_z}}{F_z}(\omega_i) \end{bmatrix} \tag{2.41}$$

2.3.2.2 Verification of the Solid Body Assumption

From the response of one solid body expressed by its 6-DoF (i.e. from $\boldsymbol{H}_{\text{CoM}}$), and using equation (2.40), it is possible to compute the response of the same solid body at any considered location. In particular, the responses at the locations of the four accelerometers can be computed and compared with the original measurements $\boldsymbol{H}$. This is what is done here to check whether the solid body assumption is correct in the frequency band of interest.

The comparison is made for the 4 accelerometers fixed on the positioning hexapod (Figure 2.71). The original FRFs and those computed from the CoM responses match well in the frequency range of interest. Similar results were obtained for the other solid bodies, indicating that the solid body assumption is valid and that a multi-body model can be used to represent the dynamics of the micro-station. This also validates the reduction in the number of degrees of freedom from 69 (23 accelerometers with each 3 DoF) to 36 (6 solid bodies with 6 DoF).

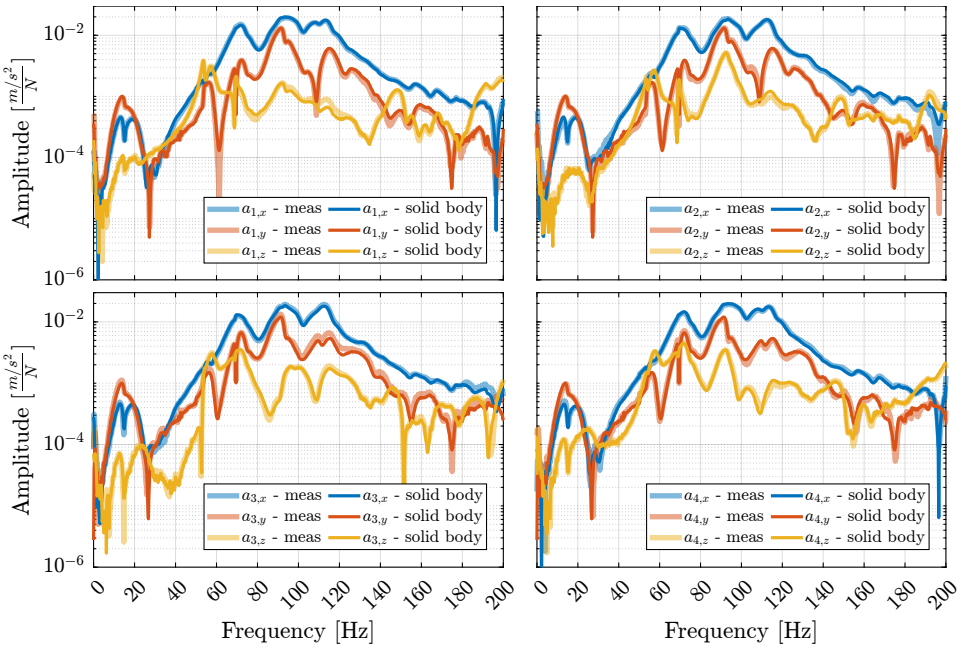

Figure 2.71: Comparison of the original accelerometer responses with responses reconstructed from the solid body response. Accelerometers 1 to 4, corresponding to the positioning hexapod, are shown. Input is a hammer force applied on the positioning hexapod in the x direction.

2.3.3 Modal Analysis

The goal here is to extract the modal parameters describing the modes of the micro station being studied, namely, the natural frequencies and the modal damping (i.e. the eigenvalues) as well as the mode shapes (.i.e. the eigenvectors). This is performed from the FRF matrix previously extracted from the measurements.

In order to perform the modal parameter extraction, the order of the modal model has to be estimated (i.e. the number of modes in the frequency band of interest). This is achieved using the Modal Indication Function (MIF) in section 2.3.3.1.

In section 2.3.3.2, the modal parameter extraction is performed. The graphical display of the mode shapes can be computed from the modal model, which is quite useful for physical interpretation of the modes.

To validate the quality of the modal model, the full FRF matrix is computed from the modal model and compared to the initial measured FRF (section 2.3.3.3).

2.3.3.1 Determination of the Number of Modes

The MIF is applied to the $n \times p$ FRF matrix where n is a relatively large number of measurement degrees of freedom (here $n = 69$) and p is the number of excitation degrees of freedom (here $p = 3$).

The Complex Modal Indication Function (CMIF) is defined in equation (2.42) where the diagonal matrix Σ is obtained from a Singular Value Decomposition (SVD) of the FRF matrix as shown in equation (2.43).

$$[CMIF(\omega)]_{p\times p} = [\Sigma(\omega)]^{\intercal}_{p\times n}[\Sigma(\omega)]_{n\times p} \tag{2.42}$$

$$[H(\omega)]_{n\times p} = [U(\omega)]_{n\times n}[\Sigma(\omega)]_{n\times p}[V(\omega)]^{H}_{p\times p} \tag{2.43}$$

The MIF therefore yields to p values that are also frequency dependent. A peak in the MIF plot indicates the presence of a mode. Repeated modes can also be detected when multiple singular values have peaks at the same frequency. The obtained MIF is shown on Figure 2.72. A total of 16 modes were found between 0 and 200 Hz. The obtained natural frequencies and associated modal damping are summarized in Table 2.10.

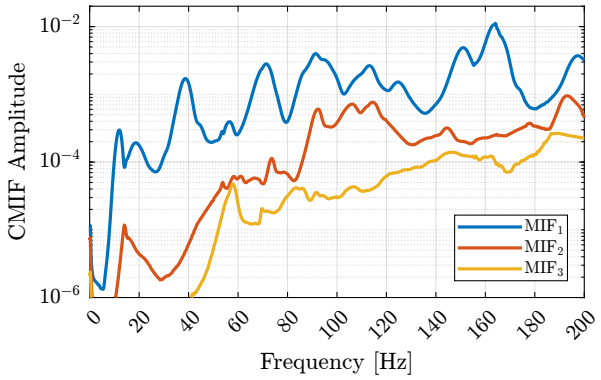

Figure 2.72: Modal Indication Function.

Mode	Frequency	Damping
1	11.9 Hz	12.2 %
2	18.6 Hz	11.7 %
3	37.8 Hz	6.2 %
4	39.1 Hz	2.8 %
5	56.3 Hz	2.8 %
6	69.8 Hz	4.3 %
7	72.5 Hz	1.3 %
8	84.8 Hz	3.7 %
9	91.3 Hz	2.9 %
10	105.5 Hz	3.2 %
11	106.6 Hz	1.6 %
12	112.7 Hz	3.1 %
13	124.2 Hz	2.8 %
14	145.3 Hz	1.3 %
15	150.5 Hz	2.4 %
16	165.4 Hz	1.4 %

Table 2.10: Identified modes

2.3.3.2 Modal Parameter Extraction

Generally, modal identification involves curve-fitting a theoretical model to the measured FRF data. However, there are multiple levels of complexity, from fitting of a single resonance, to fitting a complete curve encompassing several resonances and working on a set of many FRF plots all obtained from the same structure.

Here, the last method is used because it provides a unique and consistent model. It takes into account the fact that the properties of all individual curves are related by being from the same structure: all FRF plots on a given structure should indicate the same values for the natural frequencies and damping factor of each mode.

From the obtained modal parameters, the mode shapes are computed and can be displayed in the form of animations (three mode shapes are shown in Figure 2.73).

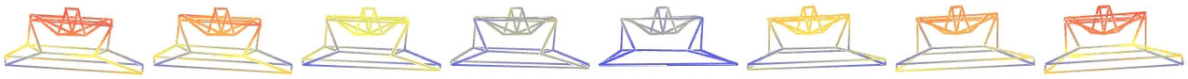

(a) 1^{st} mode at 11.9 Hz: tilt suspension mode of the granite

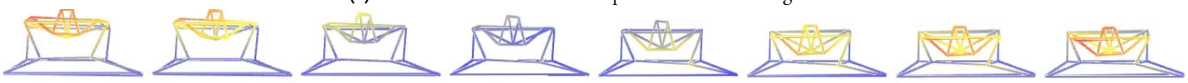

(b) 6^{th} mode at 69.8 Hz: vertical resonance of the spindle

(c) 13^{th} mode at 124.2 Hz: lateral hexapod resonance

Figure 2.73: Three obtained mode shape animations.

These animations are useful for visually obtaining a better understanding of the system's dynamic behavior. For instance, the mode shape of the first mode at 11 Hz (figure 2.73a) indicates an issue with the lower granite. It turns out that four *Airloc Levelers* are used to level the lower granite (figure 2.74). These are difficult to adjust and can lead to a situation

in which the granite is only supported by two of them; therefore, it has a low frequency "tilt mode". The levelers were then better adjusted.

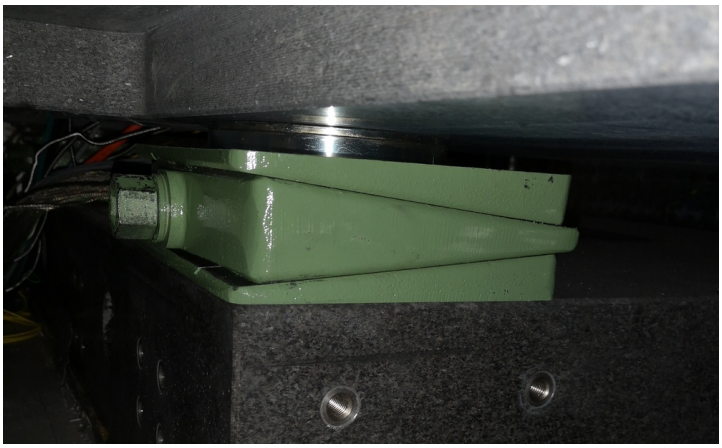

Figure 2.74: AirLoc used for the granite (2120-KSKC).

The modal parameter extraction is made using a proprietary software[1]. For each mode r (from 1 to the number of considered modes $m = 16$), it outputs the frequency ω_r, the damping ratio ξ_r, the eigenvectors $\{\phi_r\}$ (vector of complex numbers with a size equal to the number of measured DoF $n = 69$, see equation (2.44)) and a scaling factor a_r.

$$\{\phi_i\} = \begin{Bmatrix} \phi_{i,1_x} & \phi_{i,1_y} & \phi_{i,1_z} & \phi_{i,2_x} & \dots & \phi_{i,23_z} \end{Bmatrix}^\mathsf{T} \tag{2.44}$$

The eigenvalues s_r and s_r^* can then be computed from equation (2.45).

$$s_r = \omega_r(-\xi_r + i\sqrt{1-\xi_r^2}), \quad s_r^* = \omega_r(-\xi_r - i\sqrt{1-\xi_r^2}) \tag{2.45}$$

2.3.3.3 Verification of the Modal Model Validity

To check the validity of the modal model, the complete $n \times n$ FRF matrix $\boldsymbol{H}_{\text{syn}}$ is first synthesized from the modal parameters. Then, the elements of this FRF matrix $\boldsymbol{H}_{\text{syn}}$ that were already measured can be compared to the measured FRF matrix $\boldsymbol{H}$.

In order to synthesize the full FRF matrix, the eigenvectors ϕ_r are first organized in matrix from as shown in equation (2.46).

$$\boldsymbol{\Phi} = \begin{bmatrix} \phi_1 & \dots & \phi_N & \phi_1^* & \dots & \phi_N^* \end{bmatrix}_{n \times 2m} \tag{2.46}$$

The full FRF matrix $\boldsymbol{H}_{\text{syn}}$ can be obtained using (2.47).

$$\left[\boldsymbol{H}_{\text{syn}}(\omega)\right]_{n\times n} = [\boldsymbol{\Phi}]_{n\times 2m}[\boldsymbol{H}_{\text{mod}}(\omega)]_{2m\times 2m}[\boldsymbol{\Phi}]^\mathsf{T}_{2m\times n} \tag{2.47}$$

[1] NVGate software from OROS company.

With $\boldsymbol{H}_{\text{mod}}(\omega)$ a diagonal matrix representing the response of the different modes (2.48).

$$\boldsymbol{H}_{\text{mod}}(\omega) = \text{diag}\left(\frac{1}{a_1(j\omega - s_1)}, \ldots, \frac{1}{a_m(j\omega - s_m)}, \frac{1}{a_1^*(j\omega - s_1^*)}, \ldots, \frac{1}{a_m^*(j\omega - s_m^*)} \right)_{2m \times 2m} \tag{2.48}$$

A comparison between original measured FRFs and synthesized ones from the modal model is presented in Figure 2.75. Whether the obtained match is good or bad is quite arbitrary. However, the modal model seems to be able to represent the coupling between different nodes and different directions, which is quite important from a control perspective. This can be seen in Figure 2.75c that shows the FRF from the force applied on node 11 (i.e. on the translation stage) in the y direction to the measured acceleration at node 2 (i.e. at the top of the positioning hexapod) in the x direction.

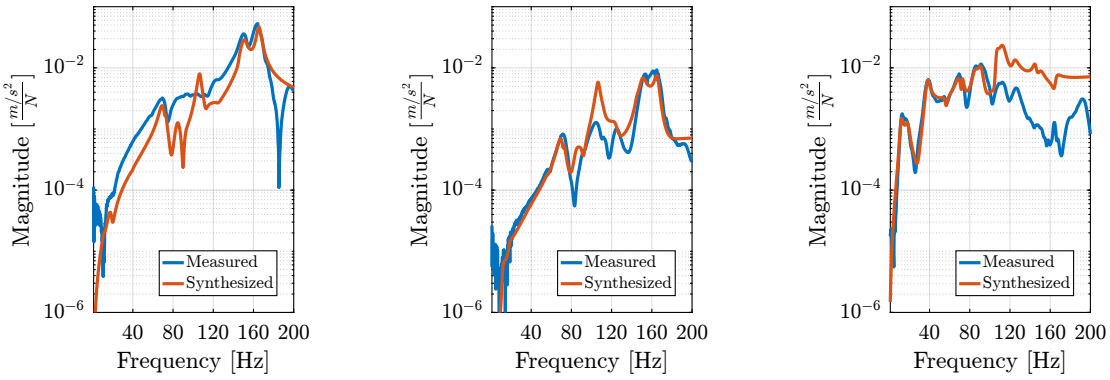

(a) From $F_{11,z}$ to $a_{11,z}$ **(b)** From $F_{11,z}$ to $a_{15,z}$ **(c)** From $F_{11,y}$ to $a_{2,x}$

Figure 2.75: Comparison of the measured FRF with the FRF synthesized from the modal model.

Conclusion

In this study, a modal analysis of the micro-station was performed. Thanks to an adequate choice of instrumentation and proper set of measurements, high quality FRFs can be obtained. The obtained FRFs indicate that the dynamics of the micro-station is complex, which is expected from a heavy stack stage architecture. It shows a lot of coupling between stages and different directions, and many modes.

By measuring 12 degrees of freedom on each "stage", it could be verified that in the frequency range of interest, each stage behaved as a rigid body. This confirms that a multi-body model can be used to properly model the micro-station.

Although a lot of effort was put into this experimental modal analysis of the micro-station, it was difficult to obtain an accurate modal model. However, the measurements are useful for tuning the parameters of the micro-station multi-body model.

2.4 Micro Station - Multi Body Model

From the start of this work, it became increasingly clear that an accurate micro-station model was necessary.

First, during the uniaxial study, it became clear that the micro-station dynamics affects the active platform dynamics. Then, using the 3-DoF rotating model, it was discovered that the rotation of the active platform induces gyroscopic effects that affect the system dynamics and should therefore be modelled. Finally, a modal analysis of the micro-station showed how complex the dynamics of the station is. The modal analysis also confirms that each stage behaves as a rigid body in the frequency range of interest. Therefore, a multi-body model is a good candidate to accurately represent the micro-station dynamics.

In this report, the development of such a multi-body model is presented.

First, each stage of the micro-station is described. The kinematics of the micro-station (i.e. how the motion of the stages are combined) is presented in Section 2.4.1.

Then, the multi-body model is presented and tuned to match the measured dynamics of the micro-station (Section 2.4.2).

Disturbances affecting the positioning accuracy also need to be modelled properly. To do so, the effects of these disturbances were first measured experimentally and then injected into the multi-body model (Section 2.4.3).

To validate the accuracy of the micro-station model, "real world" experiments are simulated and compared with measurements in Section 2.4.4.

The multi-body software used in this work is Simscape [72]. This environment was chosen because it is fully integrated within Matlab/Simulink, which provides a comprehensive suite of tools for control analysis and synthesis. Moreover, the Speedgoat real-time target machine used in the experimental phase is programmed directly from Simulink, ensuring seamless transition from simulation to real-time implementation.

2.4.1 Micro-Station Kinematics

The micro-station consists of 4 stacked positioning stages (Figure 2.76). From bottom to top, the stacked stages are the translation stage D_y, the tilt stage R_y, the rotation stage (Spindle) R_z and the positioning hexapod. Such a stacked architecture allows high mobility, but the overall stiffness is reduced, and the dynamics is very complex.

There are different ways of modeling the stage dynamics in a multi-body model. The one chosen in this work consists of modeling each stage by two solid bodies connected by one 6-DoF joint. The stiffness and damping properties of the joints can be tuned separately for each degree of freedom.

The "controlled" degree of freedom of each stage (for instance the D_y direction for the translation stage) is modelled as infinitely rigid (i.e. its motion is imposed by a "setpoint") while the other degrees of freedom have limited stiffness to model the different micro-station modes.

2.4.1.1 Motion Stages

Translation Stage The translation stage is used to position and scan the sample laterally with respect to the X-ray beam.

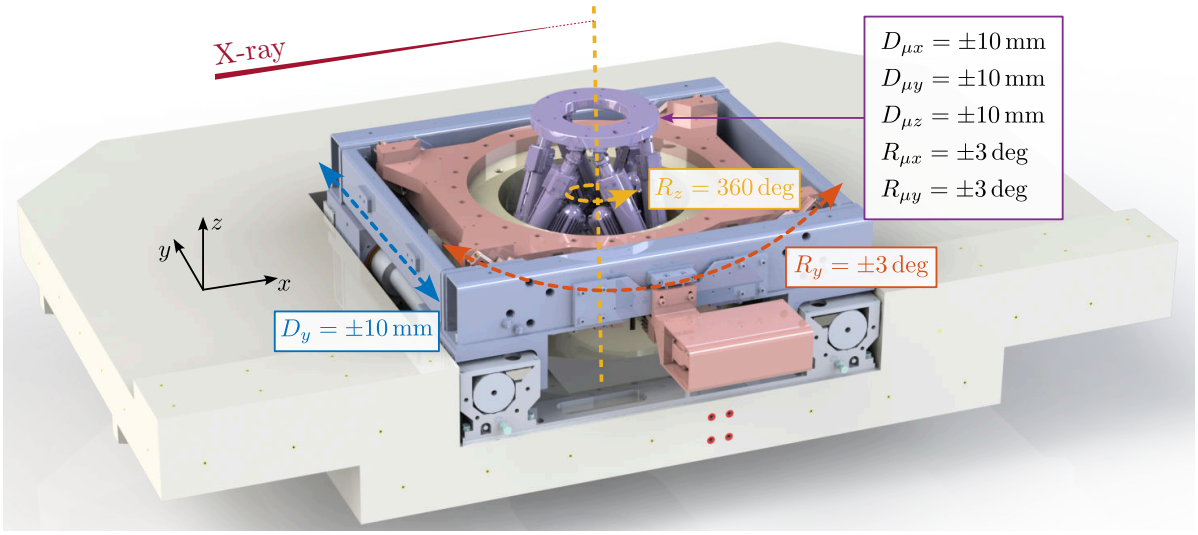

Figure 2.76: 3D view of the micro-station with the translation stage (in blue), tilt stage (in red), rotation stage (in yellow) and positioning hexapod (in purple).

A linear motor was first used to enable fast and accurate scans. It was later replaced with a stepper motor and lead-screw, as the feedback control used for the linear motor was unreliable[1]. An optical linear encoder is used to measure the stage motion and for controlling the position.

Four cylindrical bearings[2] are used to guide the motion (i.e. minimize the parasitic motions) and have high stiffness.

Tilt Stage The tilt stage is guided by four linear motion guides[3] which are placed such that the center of rotation coincide with the X-ray beam. Each linear guide is very stiff in radial directions such that the only degree of freedom with low stiffness is in R_y.

This stage is mainly used in *reflectivity* experiments where the sample R_y angle is scanned. This stage can also be used to tilt the rotation axis of the Spindle.

To precisely control the R_y angle, a stepper motor and two optical encoders are used in a Proportional Integral Derivative (PID) feedback loop.

[1] It was probably caused by rust of the linear guides along its stroke.
[2] Ball cage (N501) and guide bush (N550) from Mahr are used.
[3] HCR 35 A C1, from THK.

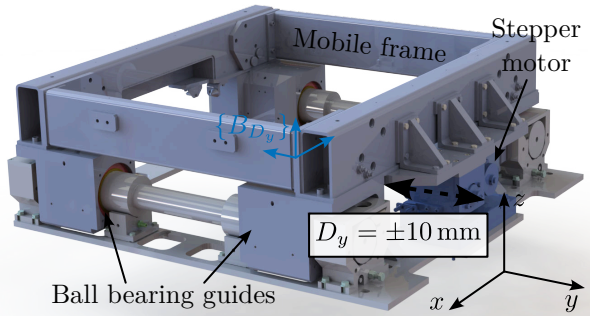

Figure 2.77: Translation Stage.

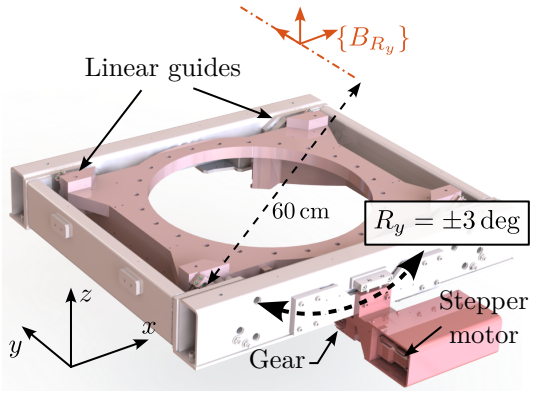

Figure 2.78: Tilt Stage.

Spindle Then, a rotation stage is used for tomography experiments. It is composed of an air bearing spindle[1], whose angular position is controlled with a 3 phase synchronous motor based on the reading of 4 optical encoders.

Additional rotary unions and slip-rings are used to be able to pass electrical signals, fluids and gazes through the rotation stage.

Positioning Hexapod Finally, a Stewart platform[2] is used to position the sample. It includes a DC motor and an optical linear encoders in each of the six struts.

This stage is used to position the Point of Interest (PoI) of the sample on the spindle rotation axis. It can also be used to precisely position the PoI vertically with respect to the x-ray.

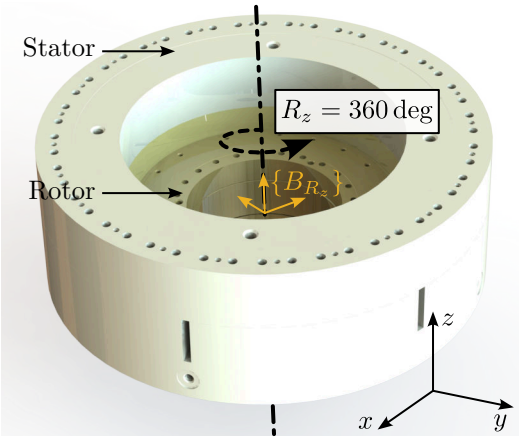

Figure 2.79: Rotation Stage (Spindle).

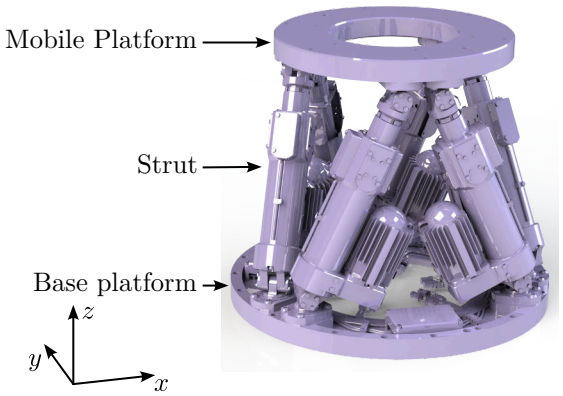

Figure 2.80: Positioning Hexapod.

2.4.1.2 Mathematical description of a rigid body motion

In this section, mathematical tools[3] that are used to describe the motion of positioning stages are introduced.

[1] Made by LAB Motion Systems.
[2] Modified Zonda Hexapod by Symetrie.
[3] The tools presented here are largely taken from [141].

First, the tools to describe the pose of a solid body (i.e. it's position and orientation) are introduced. The motion induced by a positioning stage is described by transformation matrices. Finally, the motions of all stacked stages are combined, and the sample's motion is computed from each stage motion.

Spatial Representation of Motion The *pose* of a solid body relative to a specific frame can be described by six independent parameters. Three parameters are typically used to describe its position, and three other parameters describe its orientation.

The *position* of a point P with respect to a frame $\{A\}$ can be described by a 3×1 position vector (2.49). The name of the frame is usually added as a leading superscript: ${}^{A}P$ which reads as vector P in frame $\{A\}$.

$$ {}^{A}P = \begin{bmatrix} P_x \\ P_y \\ P_z \end{bmatrix} \tag{2.49} $$

A pure translation of a solid body (i.e., of a frame $\{B\}$ attached to the solid body) can be described by the position ${}^{A}P_{O_B}$ as shown in Figure 2.81a.

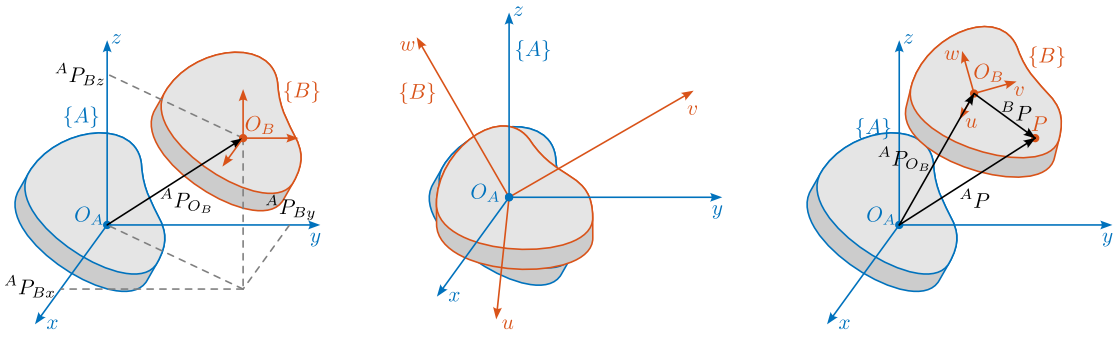

(a) Pure translation **(b)** Pure rotation **(c)** General transformation

Figure 2.81: Rigid body motion representation. (a) pure translation. (b) pure rotation. (c) combined rotation and translation.

The *orientation* of a rigid body is the same at all its points (by definition). Hence, the orientation of a rigid body can be viewed as that of a moving frame attached to the rigid body. It can be represented in several different ways: the rotation matrix, the screw axis representation, and the Euler angles are common descriptions.

The rotation matrix ${}^{A}\boldsymbol{R}_{B}$ is a 3×3 matrix containing the Cartesian unit vectors $[{}^{A}\hat{\boldsymbol{x}}_B,\ {}^{A}\hat{\boldsymbol{y}}_B,\ {}^{A}\hat{\boldsymbol{z}}_B]$ of frame $\{\boldsymbol{B}\}$ represented in frame $\{\boldsymbol{A}\}$ (2.50).

$$ {}^{A}\boldsymbol{R}_{B} = \left[{}^{A}\hat{\boldsymbol{x}}_B | {}^{A}\hat{\boldsymbol{y}}_B | {}^{A}\hat{\boldsymbol{z}}_B \right] \tag{2.50} $$

Consider a pure rotation of a rigid body ($\{\boldsymbol{A}\}$ and $\{\boldsymbol{B}\}$ are coincident at their origins, as shown in Figure 2.81b). The rotation matrix can be used to express the coordinates of a point P in a fixed frame $\{A\}$ (i.e. ${}^{A}P$) from its coordinate in the moving frame $\{B\}$ using Equation (2.51).

$$ {}^{A}P = {}^{A}\boldsymbol{R}_{B}\, {}^{B}P \tag{2.51} $$

For rotations around x, y or z axis, the formulas of the corresponding rotation matrices are given in Equation (2.52).

$$\boldsymbol{R}_x(\theta_x) = \begin{bmatrix} 1 & 0 & 0 \\ 0 & \cos(\theta_x) & -\sin(\theta_x) \\ 0 & \sin(\theta_x) & \cos(\theta_x) \end{bmatrix} \tag{2.52a}$$

$$\boldsymbol{R}_y(\theta_y) = \begin{bmatrix} \cos(\theta_y) & 0 & \sin(\theta_y) \\ 0 & 1 & 0 \\ -\sin(\theta_y) & 0 & \cos(\theta_y) \end{bmatrix} \tag{2.52b}$$

$$\boldsymbol{R}_z(\theta_z) = \begin{bmatrix} \cos(\theta_z) & -\sin(\theta_z) & 0 \\ \sin(\theta_z) & \cos(\theta_z) & 0 \\ 0 & 0 & 1 \end{bmatrix} \tag{2.52c}$$

Sometimes, it is useful to express a rotation as a combination of three rotations described by $\boldsymbol{R}_x$, $\boldsymbol{R}_y$ and $\boldsymbol{R}_z$. The order of rotation is very important[1], therefore, in this study, rotations are expressed as three successive rotations about the coordinate axes of the moving frame (2.53).

$${}^{A}\boldsymbol{R}_B(\alpha, \beta, \gamma) = \boldsymbol{R}_u(\alpha)\boldsymbol{R}_v(\beta)\boldsymbol{R}_c(\gamma) \tag{2.53}$$

Such rotation can be parameterized by three Euler angles $(\alpha,\ \beta,\ \gamma)$, which can be computed from a given rotation matrix using equations (2.54).

$$\alpha = \text{atan2}(-R_{23}/\cos(\beta),\ R_{33}/\cos(\beta)) \tag{2.54a}$$

$$\beta = \text{atan2}(R_{13},\ \sqrt{R_{11}^2 + R_{12}^2}) \tag{2.54b}$$

$$\gamma = \text{atan2}(-R_{12}/\cos(\beta),\ R_{11}/\cos(\beta)) \tag{2.54c}$$

Motion of a Rigid Body Since the relative positions of a rigid body with respect to a moving frame $\{B\}$ attached to it are fixed for all time, it is sufficient to know the position of the origin of the frame O_B and the orientation of the frame $\{B\}$ with respect to the fixed frame $\{A\}$, to represent the position of any point P in the space.

Therefore, the pose of a rigid body can be fully determined by:

1. The position vector of point O_B with respect to frame $\{A\}$ which is denoted ${}^{A}P_{O_B}$
2. The orientation of the rigid body, or the moving frame $\{B\}$ attached to it with respect to the fixed frame $\{A\}$, that is represented by ${}^{A}\boldsymbol{R}_B$.

The position of any point P of the rigid body with respect to the fixed frame $\{\boldsymbol{A}\}$, which is denoted ${}^{A}\boldsymbol{P}$ may be determined thanks to the *Chasles' theorem*, which states that if the pose of a rigid body $\{{}^{A}\boldsymbol{R}_B, {}^{A}P_{O_B}\}$ is given, then the position of any point P of this rigid body with respect to $\{\boldsymbol{A}\}$ is given by Equation (2.55).

$${}^{A}P = {}^{A}\boldsymbol{R}_B\,{}^{B}P + {}^{A}P_{O_B} \tag{2.55}$$

[1] Rotations are non commutative in 3D.

While equation (2.55) can describe the motion of a rigid body, it can be written in a more convenient way using 4×4 homogeneous transformation matrices and 4×1 homogeneous coordinates. The homogeneous transformation matrix is composed of the rotation matrix ${}^{A}\boldsymbol{R}_{B}$ representing the orientation and the position vector ${}^{A}P_{O_B}$ representing the translation. It is partitioned as shown in Equation (2.56).

$$ {}^{A}\boldsymbol{T}_{B} = \left[\begin{array}{ccc|c} & {}^{A}\boldsymbol{R}_{B} & & {}^{A}P_{O_B} \\ \hline 0 & 0 & 0 & 1 \end{array}\right] \tag{2.56} $$

Then, ${}^{A}P$ can be computed from ${}^{B}P$ and the homogeneous transformation matrix using (2.57).

$$ \left[\begin{array}{c} {}^{A}P \\ \hline 1 \end{array}\right] = \left[\begin{array}{ccc|c} & {}^{A}\boldsymbol{R}_{B} & & {}^{A}P_{O_B} \\ \hline 0 & 0 & 0 & 1 \end{array}\right] \left[\begin{array}{c} {}^{B}P \\ \hline 1 \end{array}\right] \quad \Rightarrow \quad {}^{A}P = {}^{A}\boldsymbol{R}_{B}\,{}^{B}P + {}^{A}P_{O_B} \tag{2.57} $$

One key advantage of homogeneous transformation is that it can easily be generalized for consecutive transformations. Let us consider the motion of a rigid body described at three locations (Figure 2.82). Frame $\{A\}$ represents the initial location, frame $\{B\}$ is an intermediate location, and frame $\{C\}$ represents the rigid body at its final location.

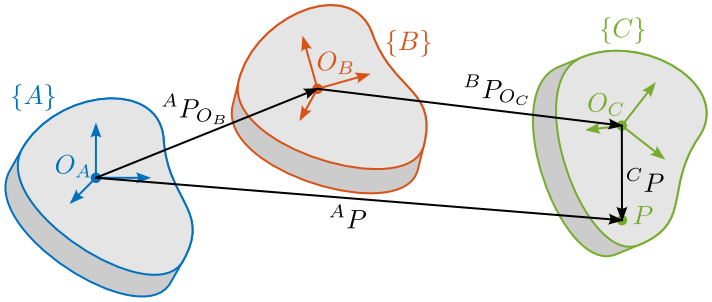

Figure 2.82: Motion of a rigid body represented at three locations by frame $\{A\}$, $\{B\}$ and $\{C\}$.

Furthermore, suppose the position vector of a point P of the rigid body is given in the final location, that is ${}^{C}P$ is given, and the position of this point is to be found in the fixed frame $\{A\}$, that is ${}^{A}P$. Since the locations of the rigid body are known relative to each other, ${}^{C}P$ can be transformed to ${}^{B}P$ using ${}^{B}\boldsymbol{T}_{C}$ using ${}^{B}P = {}^{B}\boldsymbol{T}_{C}\,{}^{C}P$. Similarly, ${}^{B}P$ can be transformed into ${}^{A}P$ using ${}^{A}P = {}^{A}\boldsymbol{T}_{B}\,{}^{B}P$.

Combining the two relations, Equation (2.58) is obtained. This shows that combining multiple transformations is equivalent as to compute 4×4 matrix multiplications.

$$ {}^{A}P = \underbrace{{}^{A}\boldsymbol{T}_{B}\,{}^{B}\boldsymbol{T}_{C}}_{{}^{A}\boldsymbol{T}_{C}}\,{}^{C}P \tag{2.58} $$

Another key advantage of homogeneous transformation is the easy inverse transformation, which can be computed using Equation (2.59).

$$ {}^{B}\boldsymbol{T}_{A} = {}^{A}\boldsymbol{T}_{B}^{-1} = \left[\begin{array}{ccc|c} & {}^{A}\boldsymbol{R}_{B}^{\intercal} & & -{}^{A}\boldsymbol{R}_{B}^{\intercal}\,{}^{A}P_{O_B} \\ \hline 0 & 0 & 0 & 1 \end{array}\right] \tag{2.59} $$

2.4.1.3 Micro-Station Kinematics

Each stage is described by two frames; one is attached to the fixed platform $\{A\}$ while the other is fixed to the mobile platform $\{B\}$. At "rest" position, the two have the same pose and coincide with the PoI ($O_A = O_B$). An example of the tilt stage is shown in Figure 2.83. The mobile frame of the translation stage is equal to the fixed frame of the tilt stage: $\{B_{D_y}\} = \{A_{R_y}\}$. Similarly, the mobile frame of the tilt stage is equal to the fixed frame of the spindle: $\{B_{R_y}\} = \{A_{R_z}\}$.

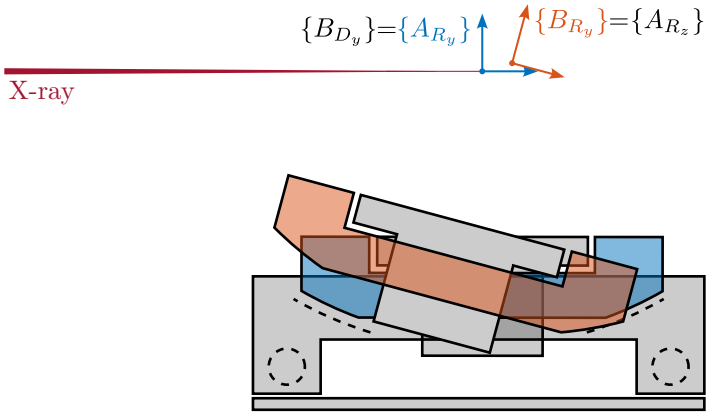

Figure 2.83: Example of the motion induced by the tilt-stage R_y. Initial position is shown in blue while an arbitrary position is shown in red. Parasitic motions are here magnified for clarity.

The motion induced by a positioning stage can be described by a homogeneous transformation matrix from frame $\{A\}$ to frame $\{B\}$ as explain in Section 2.4.1.3. As any motion stage induces parasitic motion in all 6-DoF, the transformation matrix representing its induced motion can be written as in (2.60).

$$ {}^{A}\boldsymbol{T}_{B}(D_x, D_y, D_z, \theta_x, \theta_y, \theta_z) = \left[\begin{array}{ccc|c} & \boldsymbol{R}_x(\theta_x)\boldsymbol{R}_y(\theta_y)\boldsymbol{R}_z(\theta_z) & & \begin{matrix} D_x \\ D_y \\ D_z \end{matrix} \\ \hline 0 & 0 & 0 & 1 \end{array}\right] \tag{2.60} $$

The homogeneous transformation matrix corresponding to the micro-station $\boldsymbol{T}_{\mu\text{-station}}$ is simply equal to the matrix multiplication of the homogeneous transformation matrices of the individual stages as shown in Equation (2.61).

$$ \boldsymbol{T}_{\mu\text{-station}} = \boldsymbol{T}_{D_y} \cdot \boldsymbol{T}_{R_y} \cdot \boldsymbol{T}_{R_z} \cdot \boldsymbol{T}_{\text{hexapod}} \tag{2.61} $$

$\boldsymbol{T}_{\mu\text{-station}}$ represents the pose of the sample (supposed to be rigidly fixed on top of the positioning-hexapod) with respect to the granite.

If the transformation matrices of the individual stages are each representing a perfect motion (i.e. the stages are supposed to have no parasitic motion), $\boldsymbol{T}_{\mu\text{-station}}$ then represents the pose setpoint of the sample with respect to the granite. The transformation matrices for the translation stage, tilt stage, spindle, and positioning hexapod can be written as shown in Equation (2.62). The setpoints are D_y for the translation stage, θ_y for the tilt-stage, θ_z for the spindle, $[D_{\mu x},\ D_{\mu y}, D_{\mu z}]$ for the positioning hexapod translations and $[\theta_{\mu x},\ \theta_{\mu y}, \theta_{\mu z}]$ for the positioning hexapod rotations.

$$\begin{aligned}
\boldsymbol{T}_{D_y} &= \begin{bmatrix} 1 & 0 & 0 & 0 \\ 0 & 1 & 0 & D_y \\ 0 & 0 & 1 & 0 \\ 0 & 0 & 0 & 1 \end{bmatrix} \quad \boldsymbol{T}_{\text{hexapod}} = \left[\begin{array}{ccc|c} & \boldsymbol{R}_x(\theta_{\mu x})\boldsymbol{R}_y(\theta_{\mu y})\boldsymbol{R}_z(\theta_{\mu z}) & & \begin{matrix} D_{\mu x} \\ D_{\mu y} \\ D_{\mu z} \end{matrix} \\ \hline 0 & 0 & 0 & 1 \end{array}\right] \\
\boldsymbol{T}_{R_z} &= \begin{bmatrix} \cos(\theta_z) & -\sin(\theta_z) & 0 & 0 \\ \sin(\theta_z) & \cos(\theta_z) & 0 & 0 \\ 0 & 0 & 1 & 0 \\ 0 & 0 & 0 & 1 \end{bmatrix} \quad \boldsymbol{T}_{R_y} = \begin{bmatrix} \cos(\theta_y) & 0 & \sin(\theta_y) & 0 \\ 0 & 1 & 0 & 0 \\ -\sin(\theta_y) & 0 & \cos(\theta_y) & 0 \\ 0 & 0 & 0 & 1 \end{bmatrix}
\end{aligned} \tag{2.62}$$

2.4.2 Micro-Station Dynamics

In this section, the multi-body model of the micro-station is presented. Such model consists of several rigid bodies connected by springs and dampers. The inertia of the solid bodies and the stiffness properties of the guiding mechanisms were first estimated based on the 3D model and data-sheets (Section 2.4.2.1).

The obtained dynamics is then compared with the modal analysis performed on the micro-station (Section 2.4.2.2).

As the dynamics of the active platform is impacted by the micro-station compliance (see Section 2.1.7), the most important dynamical characteristic that should be well modelled is the overall compliance of the micro-station. To do so, the 6-DoF compliance of the micro-station is measured and then compared with the 6-DoF compliance extracted from the multi-body model (Section 2.4.2.3).

2.4.2.1 Multi-Body Model

By performing a modal analysis of the micro-station, it was verified that in the frequency range of interest, each stage behaved as a rigid body. This confirms that a multi-body model can be used to properly model the micro-station.

A multi-body model consists of several solid bodies connected by joints. Each solid body can be represented by its inertia properties (most of the time computed automatically from the 3D model and material density). Joints are used to impose kinematic constraints between solid bodies and to specify dynamical properties (i.e. spring stiffness and damping coefficient). External forces can be used to model disturbances, and "sensors" can be used to measure the relative pose between two defined frames.

Therefore, the micro-station is modelled by several solid bodies connected by joints. A typical stage (here the tilt-stage) is modelled as shown in Figure 2.84 where two solid bodies (the fixed part and the mobile part) are connected by a 6-DoF joint. One degree of freedom of the 6-DoF joint is "imposed" by a setpoint (i.e. modelled as infinitely stiff), while the other 5 are each modelled by a spring and damper. Additional forces can be used to model disturbances induced by the stage motion. The obtained 3D representation of the multi-body model is shown in Figure 2.85.

The ground is modelled by a solid body connected to the "world frame" through a joint only allowing 3 translations. The granite was then connected to the ground using a 6-DoF joint. The translation stage is connected to the granite by

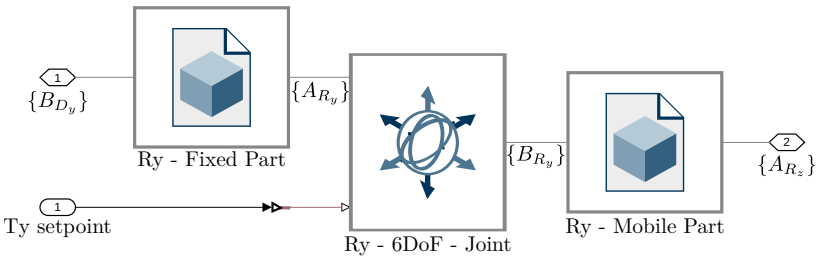

Figure 2.84: Example of a stage (here the tilt-stage) represented in the multi-body model software (Simulink - Simscape). It is composed of two solid bodies connected by a 6-DoF joint. One joint degree of freedom (here the tilt angle) can be "controlled", the other degrees of freedom are represented by springs and dampers. Additional disturbing forces for all degrees of freedom can be included.

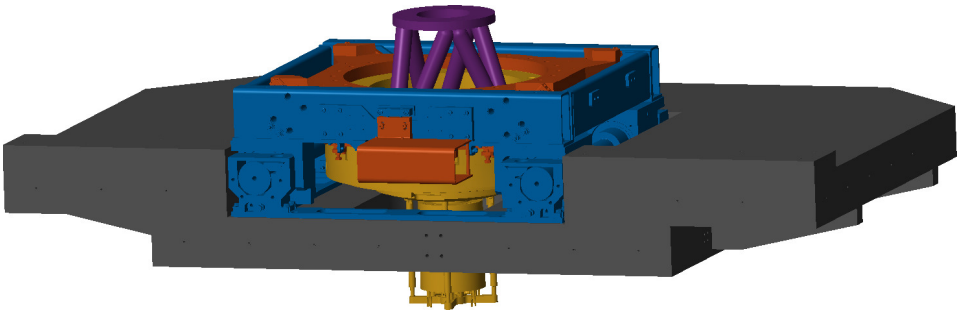

Figure 2.85: 3D view of the micro-station multi-body model.

a 6-DoF joint, but the D_y motion is imposed. Similarly, the tilt-stage and the spindle are connected to the stage below using a 6-DoF joint, with 1 imposed degree of freedom each time. Finally, the positioning hexapod has 6-DoF.

The total number of "free" degrees of freedom is 27, so the model has 54 states. The springs and dampers values were first estimated from the joint/stage specifications and were later fined-tuned based on the measurements. The spring values are summarized in Table 2.11.

Table 2.11: Summary of the stage stiffnesses. The constrained degrees of freedom are indicated by "-". The frames in which the 6-DoF joints are defined are indicated in figures found in Section 2.4.1.1.

Stage	D_x	D_y	D_z	R_x	R_y	R_z
Granite	5 kN/µm	5 kN/µm	5 kN/µm	25 Nm/µrad	25 Nm/µrad	10 Nm/µrad
Translation	200 N/µm	-	200 N/µm	60 Nm/µrad	90 Nm/µrad	60 Nm/µrad
Tilt	380 N/µm	400 N/µm	380 N/µm	120 Nm/µrad	-	120 Nm/µrad
Spindle	700 N/µm	700 N/µm	2 kN/µm	10 Nm/µrad	10 Nm/µrad	-
Hexapod	10 N/µm	10 N/µm	100 N/µm	1.5 Nm/µrad	1.5 Nm/µrad	0.27 Nm/µrad

2.4.2.2 Comparison with the Measured Dynamics

The dynamics of the micro-station was measured by placing accelerometers on each stage and by impacting the translation stage with an instrumented hammer in three directions. The obtained FRFs were then projected at the CoM of each stage.

To gain a first insight into the accuracy of the obtained model, the FRFs from the hammer impacts to the acceleration of each stage were extracted from the multi-body model and compared with the measurements in Figure 2.86.

Even though there is some similarity between the model and the measurements (similar overall shapes and amplitudes), it is clear that the multi-body model does not accurately represent the complex micro-station dynamics. Tuning the numerous model parameters to better match the measurements is a highly non-linear optimization problem that is difficult to solve in practice.

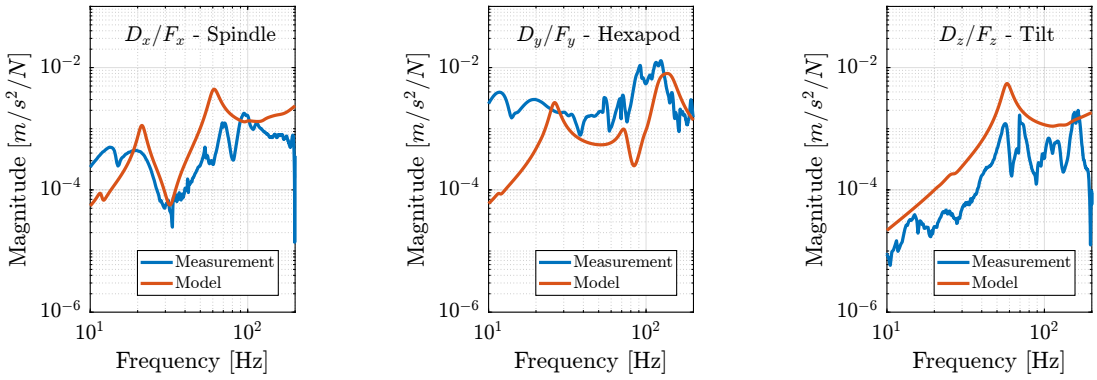

(a) Spindle, x response

(b) Hexapod, y response

(c) Tilt, z response

Figure 2.86: FRFs from a hammer impact to the stage acceleration, both expressed at its CoM. The measured FRFs are compared with the multi-body model. Different directions are computed for different stages.

2.4.2.3 Micro-station Compliance

As discussed in the previous section, the dynamics of the micro-station is complex, and tuning the multi-body model parameters to obtain a perfect match is difficult.

When considering the NASS, the most important dynamical characteristics of the micro-station is its compliance, as it can affect the plant dynamics. Therefore, the adopted strategy is to accurately model the micro-station compliance.

The micro-station compliance was experimentally measured using the setup illustrated in Figure 2.87. Four 3-axis accelerometers were fixed to the positioning hexapod top platform. The positioning hexapod top platform was impacted at 10 different points. For each impact position, 10 impacts were performed to average and improve the data quality.

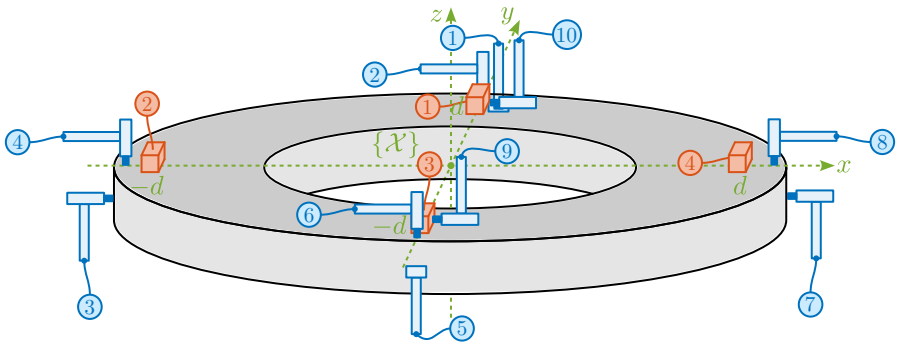

Figure 2.87: Schematic of the measurement setup used to estimate the compliance of the micro-station. Four 3-axis accelerometers (shown in red) are fix on top of the positioning hexapod platform. 10 hammer impacts are performed at different locations (shown in blue).

To convert the 12 acceleration signals $a_{\mathcal{L}} = [a_{1x}\ a_{1y}\ a_{1z}\ a_{2x}\ \dots\ a_{4z}]$ to the acceleration expressed in the $\{\mathcal{X}\}$ frame $a_{\mathcal{X}} = [a_{dx}\ a_{dy}\ a_{dz}\ a_{rx}\ a_{ry}\ a_{rz}]$, a Jacobian matrix $\boldsymbol{J}_a$ is written based on the positions and orientations of the accelerometers (2.63).

$$\boldsymbol{J}_a = \begin{bmatrix} 1 & 0 & 0 & 0 & 0 & -d \\ 0 & 1 & 0 & 0 & 0 & 0 \\ 0 & 0 & 1 & d & 0 & 0 \\ 1 & 0 & 0 & 0 & 0 & 0 \\ 0 & 1 & 0 & 0 & 0 & -d \\ 0 & 0 & 1 & 0 & d & 0 \\ 1 & 0 & 0 & 0 & 0 & d \\ 0 & 1 & 0 & 0 & 0 & 0 \\ 0 & 0 & 1 & -d & 0 & 0 \\ 1 & 0 & 0 & 0 & 0 & 0 \\ 0 & 1 & 0 & 0 & 0 & d \\ 0 & 0 & 1 & 0 & -d & 0 \end{bmatrix} \tag{2.63}$$

Then, the acceleration in the cartesian frame can be computed using (2.64).

$$a_{\mathcal{X}} = \boldsymbol{J}_a^{-1} \cdot a_{\mathcal{L}} \tag{2.64}$$

Similar to what is done for the accelerometers, a Jacobian matrix $\boldsymbol{J}_F$ is computed (2.65) and used to convert the individual hammer forces $F_{\mathcal{L}}$ to force and torques $F_{\mathcal{X}}$ applied at the center of the positioning hexapod top plate (defined by frame $\{\mathcal{X}\}$ in Figure 2.87).

$$\boldsymbol{J}_F = \begin{bmatrix} 0 & -1 & 0 & 0 & 0 & 0 \\ 0 & 0 & -1 & -d & 0 & 0 \\ 1 & 0 & 0 & 0 & 0 & 0 \\ 0 & 0 & -1 & 0 & -d & 0 \\ 0 & 1 & 0 & 0 & 0 & 0 \\ 0 & 0 & -1 & d & 0 & 0 \\ -1 & 0 & 0 & 0 & 0 & 0 \\ 0 & 0 & -1 & 0 & d & 0 \\ -1 & 0 & 0 & 0 & 0 & -d \\ -1 & 0 & 0 & 0 & 0 & d \end{bmatrix} \tag{2.65}$$

The equivalent forces and torques applied at center of $\{\mathcal{X}\}$ are then computed using (2.66).

$$F_{\mathcal{X}} = \boldsymbol{J}_F^{\intercal} \cdot F_{\mathcal{L}} \tag{2.66}$$

Using the two Jacobian matrices, the FRF from the 10 hammer impacts to the 12 accelerometer outputs can be converted to the FRF from 6 forces/torques applied at the origin of frame $\{\mathcal{X}\}$ to the 6 linear/angular accelerations of the top platform expressed with respect to $\{\mathcal{X}\}$. These FRFs were then used for comparison with the multi-body model.

The compliance of the micro-station multi-body model was extracted by computing the transfer function from forces/-torques applied on the hexapod's top platform to the "absolute" motion of the top platform. These results are compared with the measurements in Figure 2.88. Considering the complexity of the micro-station compliance dynamics, the model compliance matches sufficiently well for the current application.

2.4.3 Estimation of Disturbances

The goal of this section is to obtain a realistic representation of disturbances affecting the micro-station. These disturbance sources are then used during time domain simulations to accurately model the micro-station behavior. The focus is on stochastic disturbances because, in principle, it is possible to calibrate the repeatable part of disturbances. Such disturbances include ground motions and vibrations induce by scanning the translation stage and the spindle.

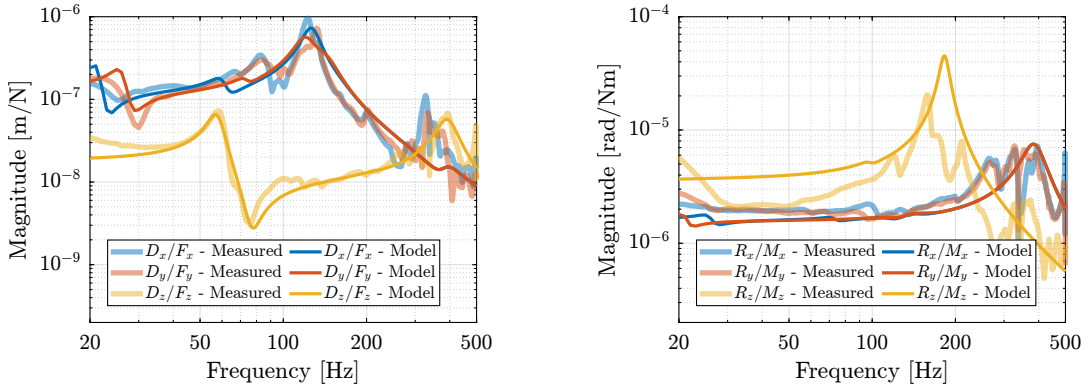

(a) Compliance in translation

(b) Compliance in rotation

Figure 2.88: Compliance of the micro-station expressed in frame $\{\mathcal{X}\}$. The measured FRFs are displayed by translucent lines, while the FRFs extracted from the multi-body models are shown by opaque lines. Both translation terms (a) and rotational terms (b) are displayed.

In the multi-body model, stage vibrations are modelled as internal forces applied in the stage joint. In practice, disturbance forces cannot be directly measured. Instead, the vibrations of the micro-station's top platform induced by the disturbances were measured (Section 2.4.3.1).

To estimate the equivalent disturbance force that induces such vibration, the transfer functions from disturbance sources (i.e. forces applied in the stages' joint) to the displacements of the micro-station's top platform with respect to the granite are extracted from the multi-body model (Section 2.4.3.2). Finally, the obtained disturbance sources are compared in Section 2.4.3.3.

2.4.3.1 Disturbance Measurements

In this section, ground motion is directly measured using geophones. Vibrations induced by scanning the translation stage and the spindle are also measured using dedicated setups.

The tilt stage and the positioning hexapod also have positioning errors; however, they are not modelled here because these two stages are only used for pre-positioning and not for scanning. Therefore, from a control perspective, they are not important.

Ground Motion The ground motion was measured by using a sensitive 3-axis geophone shown in Figure 2.90 placed on the ground. The generated voltages were recorded with a high resolution ADC, and converted to displacement using the Geophone sensitivity transfer function. The obtained ground motion displacement is shown in Figure 2.89.

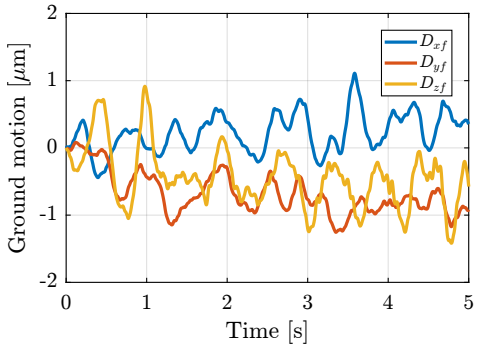

Figure 2.89: Measured ground motion.

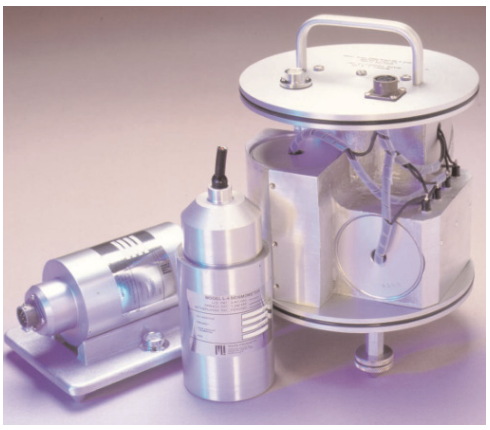

Figure 2.90: (3D) L-4C geophone.

Translation Stage To measure the positioning errors of the translation stage, the setup shown in Figure 2.91 is used. A special optical element (called a "straightness interferometer"[1]) is fixed on top of the micro-station, while a laser source[2] and a straightness reflector are fixed on the ground. A similar setup was used to measure the horizontal deviation (i.e. in the x direction), as well as the pitch and yaw errors of the translation stage.

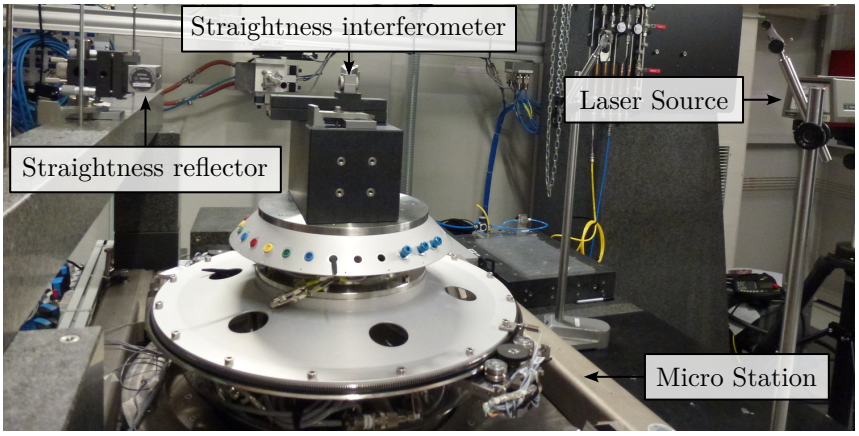

Figure 2.91: Experimental setup to measure the straightness (vertical deviation) of the translation stage.

Six scans were performed between -4.5 mm and 4.5 mm. The results for each individual scan are shown in Figure 2.92a. The measurement axis may not be perfectly aligned with the translation stage axis; this, a linear fit is removed from the measurement. The remaining vertical displacement is shown in Figure 2.92b. A vertical error of ± 300 nm induced by the translation stage is expected. Similar result is obtained for the x lateral direction.

Spindle To measure the positioning errors induced by the Spindle, a "Spindle error analyzer"[3] is used as shown in Figure 2.93. A specific target is fixed on top of the micro-station, which consists of two sphere with 1 inch diameter precisely aligned with the spindle rotation axis. Five capacitive sensors[4] are pointing at the two spheres, as shown in Figure 2.93b. From the 5 measured displacements $[d_1,\ d_2,\ d_3,\ d_4,\ d_5]$, the translations and rotations $[D_x,\ D_y,\ D_z,\ R_x,\ R_y]$ of the target can be estimated.

[1] The special optics (straightness interferometer and reflector) are manufactured by Agilent (10774A).
[2] Laser source is manufactured by Agilent (5519b).
[3] The Spindle Error Analyzer is made by Lion Precision.
[4] C8 capacitive sensors and CPL290 capacitive driver electronics from Lion Precision.

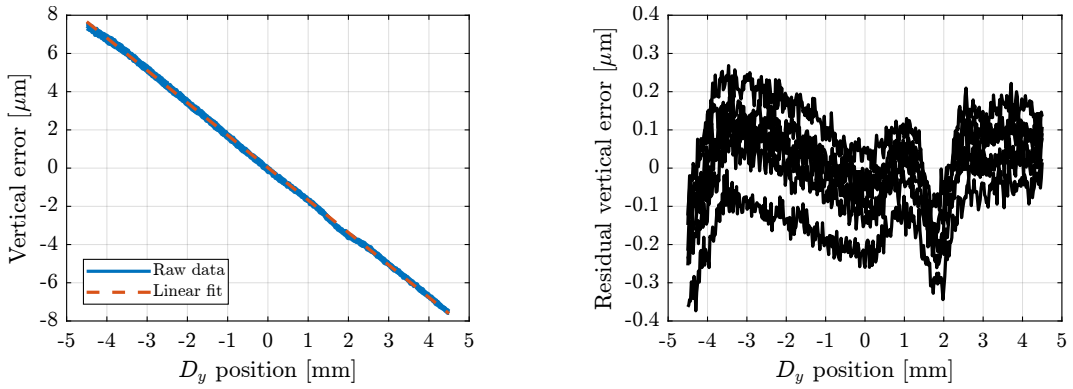

(a) Measured vertical error

(b) Error after removing a linear fit

Figure 2.92: Measurement of the straightness (vertical error) of the translation stage (a). A linear fit is then removed from the data (b).

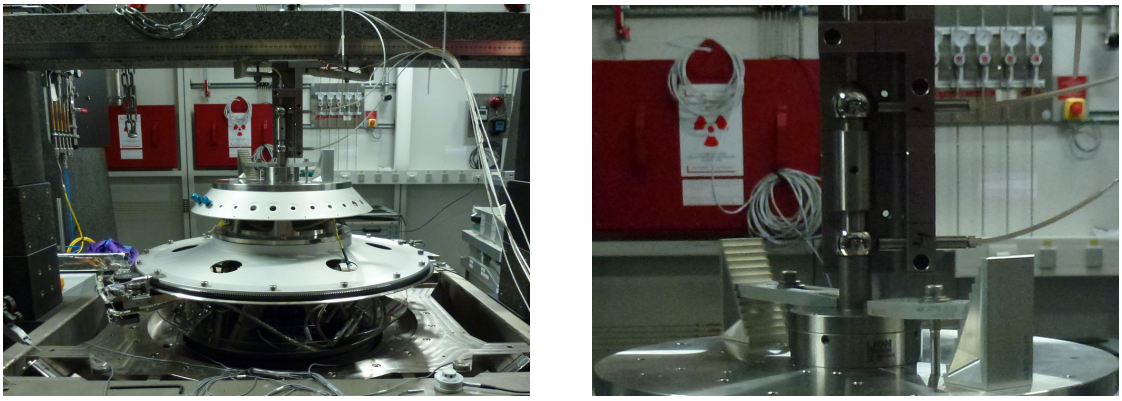

(a) Micro-station and 5-DoF metrology

(b) Zoom on the metrology system

Figure 2.93: Experimental setup used to estimate the errors induced by the Spindle rotation (a). The motion of the two reference spheres is measured using 5 capacitive sensors (b).

A measurement was performed during a constant rotational velocity of the spindle of 60 rpm and during 10 turns. The obtained results are shown in Figure 2.94. A large fraction of the radial (Figure 2.94a) and tilt (Figure 2.94c) errors are linked to the fact that the two spheres are not perfectly aligned with the rotation axis of the Spindle. This is displayed by the dashed circle. After removing the best circular fit from the data, the vibrations induced by the Spindle may be viewed as stochastic disturbances. However, some misalignment between the PoI of the sample and the rotation axis will be considered because the alignment is not perfect in practice. The vertical motion induced by scanning the spindle is in the order of ± 30 nm (Figure 2.94b).

2.4.3.2 Sensitivity to Disturbances

To compute the disturbance source (i.e. forces) that induced the measured vibrations in Section 2.4.3.1, the transfer function from the disturbance sources to the stage vibration (i.e. the "sensitivity to disturbances") needs to be estimated. This is achieved using the multi-body model presented in Section 2.4.2. The obtained transfer functions are shown in Figure 2.95.

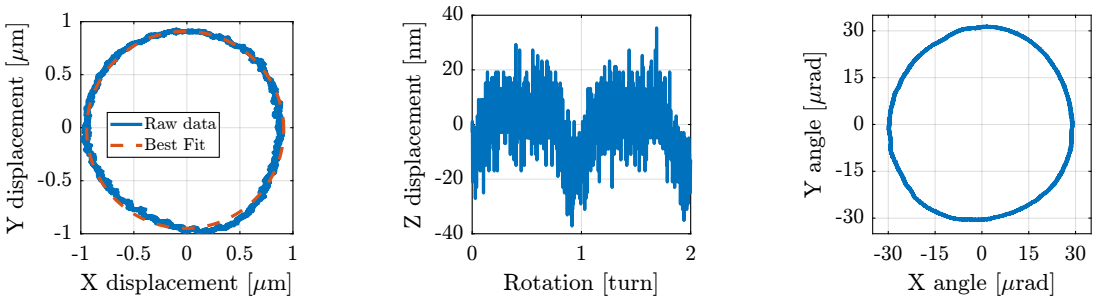

(a) Radial errors **(b)** Axial error **(c)** Tilt errors

Figure 2.94: Measurement of the radial (a), axial (b) and tilt (c) errors during a Spindle rotation at 60 rpm. The circular best fit is shown by the dashed circle. It represents the misalignment of the spheres with the rotation axis.

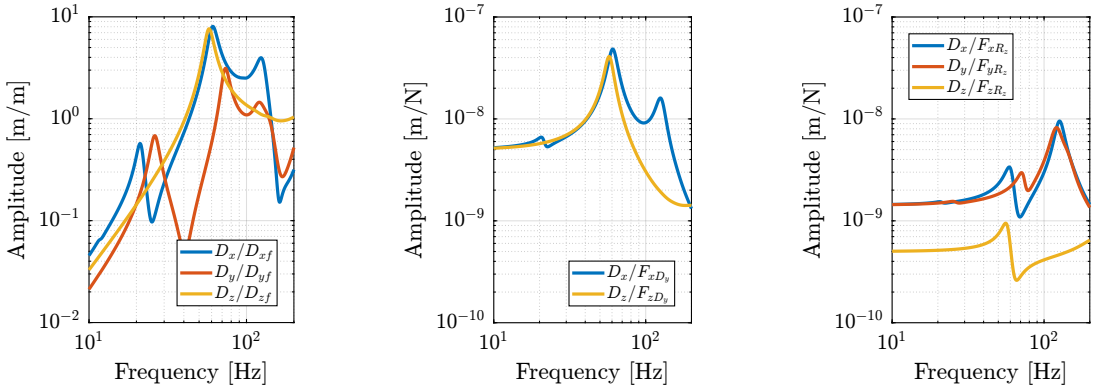

(a) Ground motion **(b)** Translation stage **(c)** Spindle

Figure 2.95: Extracted transfer functions from disturbances to relative motion between the micro-station's top platform and the granite. The considered disturbances are the ground motion (a), the translation stage vibrations (b), and the spindle vibrations (c).

2.4.3.3 Obtained Disturbance Sources

From the measured effect of disturbances in Section 2.4.3.1 and the sensitivity to disturbances extracted from the multi-body model in Section 2.4.3.2, the power spectral density of the disturbance sources (i.e. forces applied in the stage's joint) can be estimated. The obtained power spectral density of the disturbances are shown in Figure 2.96.

The disturbances are characterized by their power spectral densities, as shown in Figure 2.96. However, to perform time domain simulations, disturbances must be represented by a time domain signal. To generate stochastic time-domain signals with a specific power spectral density, the discrete inverse Fourier transform is used, as explained in [112, chap. 12.11]. Examples of the obtained time-domain disturbance signals are shown in Figure 2.97.

2.4.4 Simulation of Scientific Experiments

To fully validate the micro-station multi-body model, two time-domain simulations corresponding to typical use cases were performed.

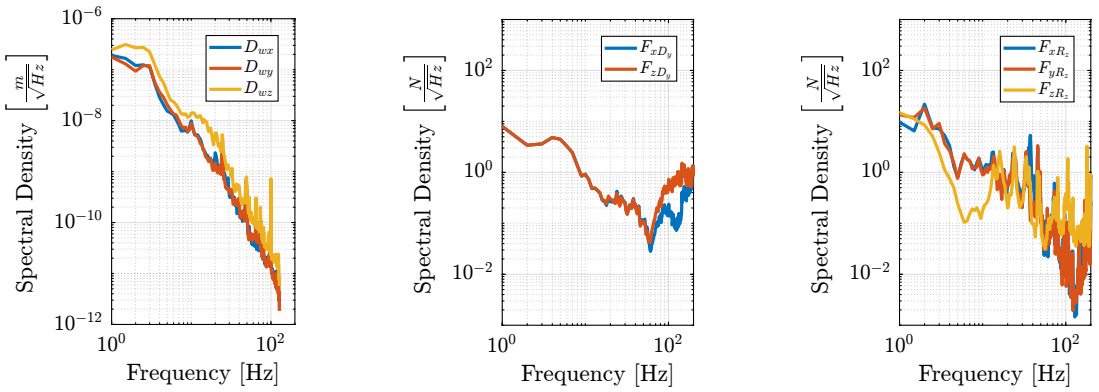

(a) Ground Motion **(b)** Translation Stage **(c)** Spindle

Figure 2.96: Measured ASD of the micro-station disturbance sources. Ground motion (a), translation stage (b) and spindle (c).

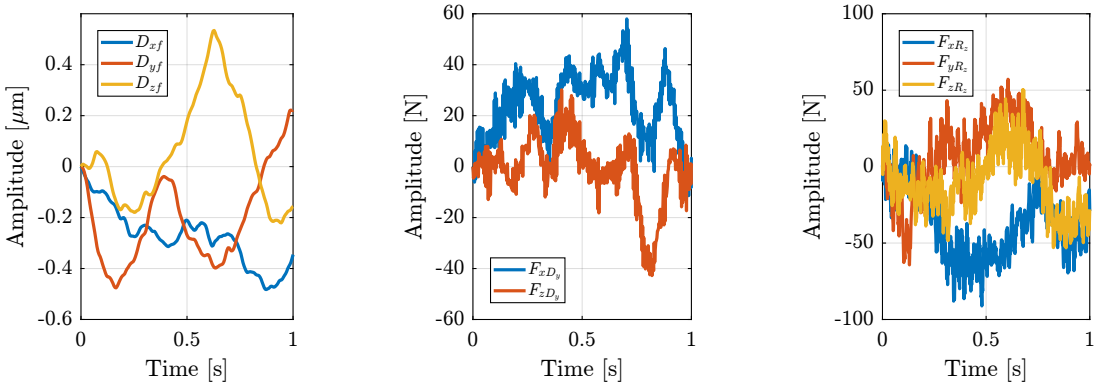

(a) Ground Motion **(b)** Translation Stage **(c)** Spindle

Figure 2.97: Generated time domain disturbance signals. Ground motion (a), translation stage (b) and spindle (c).

First, a tomography experiment (i.e. a constant Spindle rotation) was performed and was compared with experimental measurements (Section 2.4.4.1). Second, a constant velocity scans with the translation stage was performed and also compared with the experimental data (Section 2.4.4.2).

2.4.4.1 Tomography Experiment

To simulate a tomography experiment, the setpoint of the Spindle is configured to perform a constant rotation with a rotational velocity of 60 rpm. Both ground motion and spindle vibration disturbances were simulated based on what was computed in Section 2.4.3. A radial offset of $\approx$ 1 µm between the Point of Interest (PoI) and the spindle's rotation axis is introduced to represent what is experimentally observed. During the 10 second simulation (i.e. 10 spindle turns), the position of the PoI with respect to the granite was recorded. Results are shown in Figure 2.98. A good correlation with the measurements is observed both for radial errors (Figure 2.98a) and axial errors (Figure 2.98b).

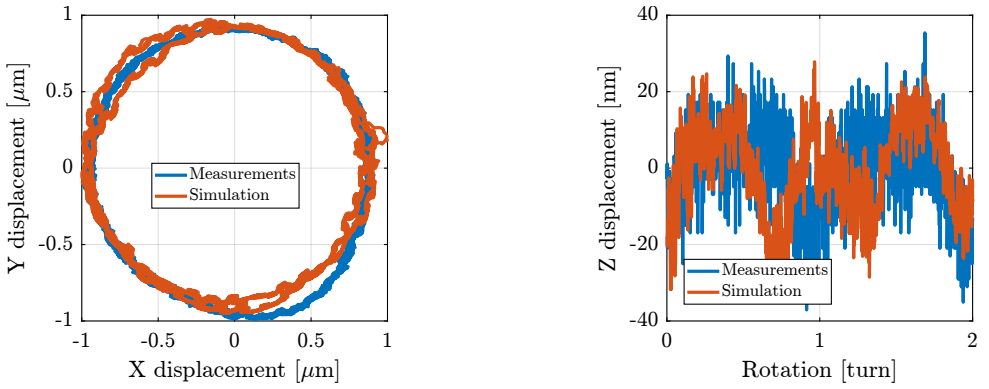

(a) Radial error

(b) Axial error

Figure 2.98: Simulation results for a tomography experiment at constant velocity of 60 rpm. The comparison is made with measurements for both radial (a) and axial errors (b).

2.4.4.2 Scans with the Translation Stage

A second experiment was performed in which the translation stage was scanned at constant velocity. The translation stage setpoint is configured to have a "triangular" shape with stroke of ± 4.5 mm. Both ground motion and translation stage vibrations were included in the simulation. Similar to what was performed for the tomography simulation, the PoI position with respect to the granite was recorded and compared with the experimental measurements in Figure 2.99. A similar error amplitude was observed, thus indicating that the multi-body model with the included disturbances accurately represented the micro-station behavior in typical scientific experiments.

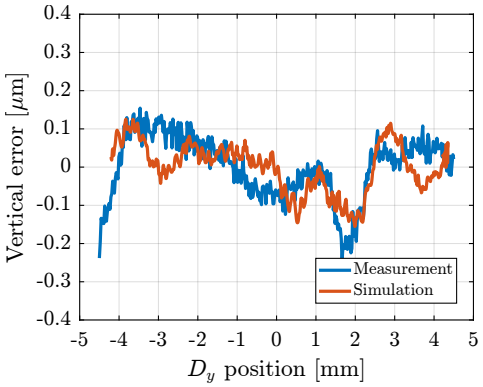

Figure 2.99: Vertical errors during a constant-velocity scan of the translation stage.

Conclusion

In this study, a multi-body model of the micro-station was developed. It was difficult to match the measured dynamics obtained from the modal analysis of the micro-station. However, the most important dynamical characteristic to be modelled is the compliance, as it affects the dynamics of the NASS. After tuning the model parameters, a good match with the measured compliance was obtained (Figure 2.88).

The disturbances affecting the sample position should also be well modelled. After experimentally estimating the disturbances (Section 2.4.3), the multi-body model was finally validated by performing a tomography simulation (Figure 2.98) as well as a simulation in which the translation stage was scanned (Figure 2.99).

2.5 Active Platform - Multi Body Model

Building upon the validated multi-body model of the micro-station presented in previous sections, this section focuses on the development and integration of an active vibration platform model.

A review of existing active vibration platforms is given in Section 2.5.1, leading to the selection of the Stewart platform architecture. This parallel manipulator architecture, described in Section 2.5.2, requires specialized analytical tools for kinematic analysis. However, the complexity of its dynamic behavior poses significant challenges for purely analytical approaches.

Consequently, a multi-body modeling approach was adopted (Section 2.5.3), facilitating seamless integration with the existing micro-station model.

The control of the Stewart platform introduces additional complexity due to its Multi Inputs Multi Outputs (MIMO) nature. Section 2.5.4 explores how the High Authority Control / Low Authority Control (HAC-LAC) strategy, previously validated on the uniaxial model, can be adapted to address the coupled dynamics of the Stewart platform. This adaptation requires fundamental decisions regarding both the control architecture (centralized versus decentralized) and the control frame (Cartesian versus strut space). Through careful analysis of system interactions and plant characteristics in different frames, a control architecture combining decentralized Integral Force Feedback for active damping with a centralized high authority controller for positioning was developed, with both controllers implemented in the frame of the struts.

2.5.1 Review of Active Vibration Platforms

The conceptual phase started with the use of simplified models, such as uniaxial and three-degree-of-freedom rotating systems. These models were chosen for their ease of analysis, and despite their simplicity, the principles derived from them usually apply to more complex systems. However, the development of the Nano Active Stabilization System (NASS) now requires the use of a more accurate model that will be integrated with the multi-body representation of the micro-station. To develop this model, the architecture of the active platform must first be determined.

The selection of an appropriate architecture begins with a review of existing positioning stages that incorporate active platforms similar to NASS (Section 2.5.1.1). This review reveals two distinctive features of the NASS that set it apart from existing systems: the fact that the active platform is continuously rotating and its requirement to accommodate variable payload masses. In existing systems, the sample mass is typically negligible compared to the stage mass, whereas in NASS, the sample mass significantly influences the system's dynamic behavior.

These distinctive requirements drive the selection of the active platform architecture. In Section 2.5.1.2, different active platform configurations, including serial and parallel configurations, are evaluated, ultimately leading to the choice of a Stewart platform architecture.

2.5.1.1 Sample Stages with Active Control

The positioning of samples with respect to X-ray beam, that can be focused to sizes below 100 nanometers, presents significant challenges, because mechanical positioning systems are typically limited to micron-scale accuracy. To overcome this limitation, external metrology systems have been implemented to measure sample positions with nanometer accuracy, enabling real-time feedback control for sample stabilization.

A review of existing sample stages with active vibration control reveals various approaches to implementing such feedback systems. In many cases, sample position control is limited to translational degrees of freedom. At NSLS-II, for

instance, a system capable of 100 µm stroke has been developed for payloads up to 500g, using interferometric measurements for position feedback (Figure 2.100a). Similarly, at the Sirius facility, a tripod configuration based on voice coil actuators has been implemented for XYZ position control, achieving feedback bandwidths of approximately 100 Hz (Figure 2.100b).

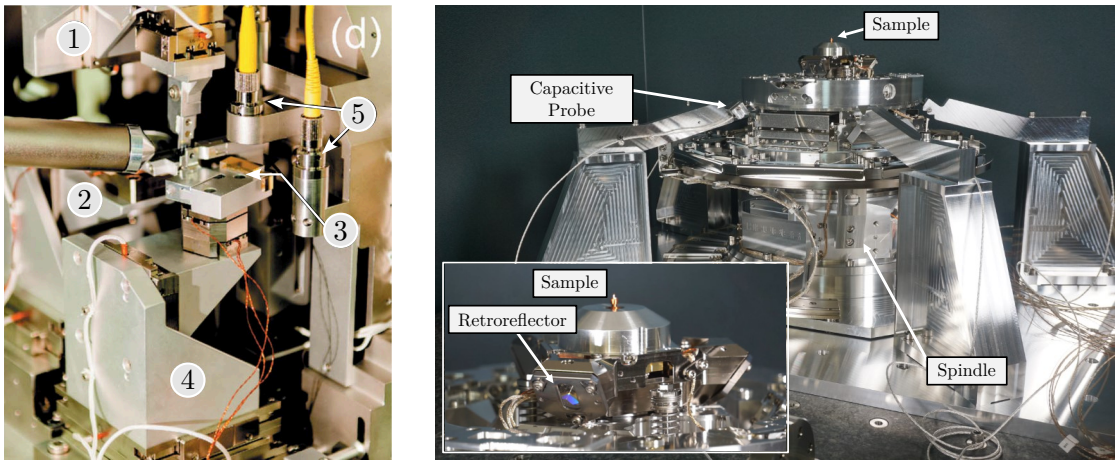

(a) MLL microscope [106]

(b) SAPOTI sample stage [54]

Figure 2.100: Example of sample stage with active XYZ corrections based on external metrology. The MLL microscope at NSLS-II (a). Sample stage on SAPOTI beamline at Sirius facility (b).

The integration of R_z rotational capability, which is necessary for tomography experiments, introduces additional complexity. At ESRF's ID16A beamline, a Stewart platform (whose architecture will be presented in Section 2.5.2) using piezoelectric actuators has been positioned below the spindle (Figure 2.101a). While this configuration enables the correction of spindle motion errors through 5-DoF control based on capacitive sensor measurements, the stroke is limited to 50 µm due to the inherent constraints of piezoelectric actuators. In contrast, at PETRA III, an alternative approach places a XYZ-stacked stage above the spindle, offering 100 µm stroke (Figure 2.101b). However, attempts to implement real-time feedback using YZ external metrology proved challenging, possibly due to the poor dynamical response of the serial stage configuration.

Table 2.12 provides an overview of existing end-stations that incorporate feedback loops based on online metrology for sample positioning. Although direct performance comparisons between these systems are challenging due to their varying experimental requirements, scanning velocities, and specific use cases, several distinctive characteristics of the NASS can be identified.

The first key distinction of the NASS is in the continuous rotation of the active vibration platform. This feature introduces significant complexity through gyroscopic effects and real-time changes in the platform orientation, which substantially impact both the system's kinematics and dynamics. In addition, NASS implements a unique Long-Stroke/Short-Stroke architecture. In conventional systems, active platforms typically correct spindle positioning errors - for example, unwanted translations or tilts that occur during rotation, whereas the intended rotational motion (R_z) is performed by the spindle itself and is not corrected. The NASS, however, faces a more complex task: it must compensate for positioning errors of the translation and tilt stages in real-time during their operation, including corrections along their primary axes of motion. For instance, when the translation stage moves along Y, the active platform must not only correct for unwanted motions in other directions but also correct the position along Y, which necessitate some synchronization between the control of the long stroke stages and the control of the active platform.

The second major distinguishing feature of the NASS is its capability to handle payload masses up to 50 kg, exceeding typical capacities in the literature by two orders of magnitude. This substantial increase in payload mass fundamentally alters the system's dynamic behavior, as the sample mass significantly influences the overall system dynamics, in

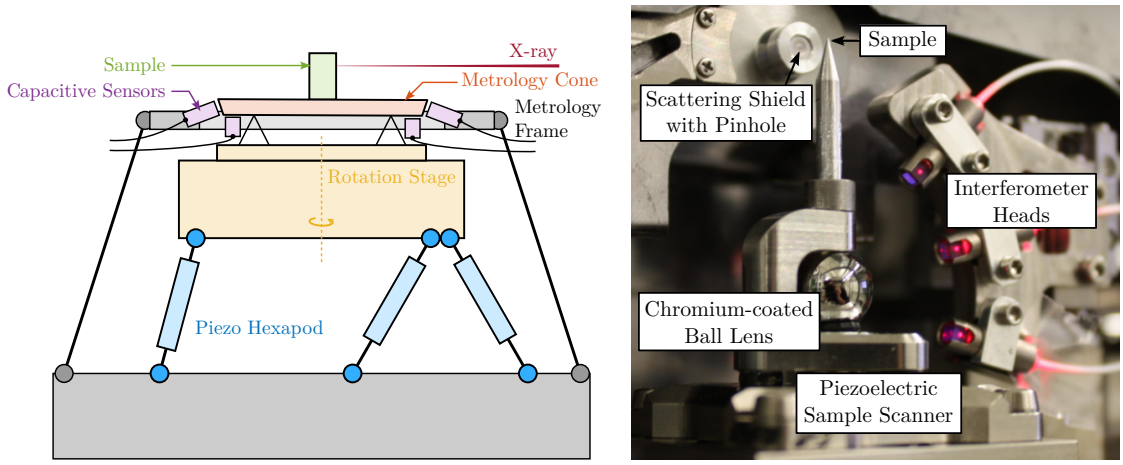

(a) Simplified schematic of ID16a end-station [152]

(b) PtyNAMi microscope [129, 130]

Figure 2.101: Example of two sample stages for tomography experiments. ID16a endstation at the ESRF (a). PtyNAMi microscope at PETRA III (b).

contrast to conventional systems where sample masses are negligible relative to the stage mass. This characteristic introduces significant control challenges, as the feedback system must remain stable and maintain performance across a wide range of payload masses (from a few kilograms to 50 kg), requiring robust control strategies to handle such large plant variations.

The NASS also distinguishes itself through its high mobility and versatility, which are achieved through the use of multiple stacked stages (translation stage, tilt stage, spindle, positioning hexapod) that enable a wide range of experimental configurations. The resulting mechanical structure exhibits complex dynamics with multiple resonance modes in the low frequency range. This dynamic complexity poses significant challenges for the design and control of the active platform.

The primary control requirements focus on $[D_y,\ D_z,\ R_y]$ motions; however, the continuous rotation of the active platform requires the control of $[D_x,\ D_y,\ D_z,\ R_x,\ R_y]$ in the active platform's reference frame.

2.5.1.2 Active Vibration Platform

The choice of the active platform architecture for the NASS requires careful consideration of several critical specifications. The platform must provide control over 5-DoF (D_x, D_y, D_z, R_x, and R_y), with strokes exceeding 100 µm to correct for micro-station positioning errors, while fitting within a cylindrical envelope of 300 mm diameter and 95 mm height. It must accommodate payloads up to 50 kg while maintaining high dynamical performance. For light samples, the typical design strategy of maximizing actuator stiffness works well because resonance frequencies in the kilohertz range can be achieved, enabling control bandwidths up to 100 Hz. However, achieving such resonance frequencies with a 50 kg payload would require unrealistic stiffness values of approximately 2000 N/µm. This limitation necessitates alternative control approaches, and the High High Authority Control / Low Authority Control (HAC-LAC) strategy is proposed to address this challenge. To this purpose, the design includes force sensors for active damping. Compliant mechanisms must also be used to eliminate friction and backlash, which would otherwise compromise the nano-positioning capabilities.

Two primary categories of positioning platform architectures are considered: serial and parallel mechanisms. Serial robots, characterized by open-loop kinematic chains, typically dedicate one actuator per DoF as shown in Figure 2.102a.

Table 2.12: End-Stations with integrated feedback loops based on online metrology. The stages used for feedback are indicated in bold font. Stages not used for scanning purposes are omitted or indicated between parentheses. The specifications for the NASS are indicated in the last row.

Stacked Stages	Specifications	Measured DoF	Bandwidth	Reference
Sample **XYZ stage (piezo)**	light D_{xyz} : 0.05 mm	Interferometers D_{xyz}	3 PID, n/a	APS [106]
Sample Spindle **Hexapod (piezo)**	light R_z : ±90 deg D_{xyz} : 0.05 mm R_{xy} : 500 µrad	Capacitive sensors D_{xyz}, R_{xy}	≈ 10 Hz	ESRF ID16a [152]
Sample **XYZ stage (piezo)** Spindle	light D_{xyz} : 0.1 mm R_z : 180 deg	Interferometers D_{yz}	n/a	PETRA III P06 [129, 130]
Sample Spindle **Tripod (piezo)**	light R_z : ±182 deg D_{xyz} : 0.4 mm	Interferometers D_{yz}, R_x	PID, n/a	PSI OMNY [65, 66]
Sample (XY stage) Spindle **XYZ linear motors**	light R_z : 360 deg D_{xyz} : 0.4 mm	Interferometers D_{xyz}, R_{xy}	n/a	Soleil Nanoprobe [43, 138]
Sample Spindle **XYZ stage (piezo)**	up to 0.5 kg R_z : 360 deg D_{xyz} : 0.1 mm	Interferometers D_{xyz}	n/a	NSLS SRX [105]
Sample **Parallel XYZ VC**	up to 0.35 kg D_{xyz} : 3 mm	Interferometers D_{xyz}	≈ 100 Hz	Diamond, I14 [79]
Sample **Parallel XYZ VC** (Spindle)	light D_{xyz} : 3 mm R_z : ±110 deg	Capacitive sensors and interferometers D_{xyz}	≈ 100 Hz	LNLS CARNAUBA [54]
Sample **Active Platform** (Hexapod) Spindle Tilt-Stage Translation Stage	up to 50 kg R_z : 360 deg R_y : ±3 deg D_y : ±10 mm	D_{xyz}, R_{xy}		ESRF ID31 [34, 38]

While offering large workspaces and high maneuverability, serial mechanisms suffer from several inherent limitations. These include low structural stiffness, cumulative positioning errors along the kinematic chain, high mass-to-payload ratios due to actuator placement, and limited payload capacity [141]. These limitations generally make serial architectures unsuitable for nano-positioning applications, except when handling very light samples, as was used in [106] and shown in Figure 2.100a.

In contrast, parallel mechanisms, which connect the mobile platform to the fixed base through multiple parallel struts, offer several advantages for precision positioning. Their closed-loop kinematic structure provides inherently higher structural stiffness, as the platform is simultaneously supported by multiple struts [141]. Although parallel mechanisms typically exhibit limited workspace compared to serial architectures, this limitation is not critical for NASS given its modest stroke requirements. Numerous parallel kinematic architectures have been developed [40] to address various positioning requirements, with designs varying based on the intended degrees of freedom and specific application constraints. Furthermore, hybrid architectures combining both serial and parallel elements have been proposed [133], as illustrated in Figure 2.102, offering potential compromises between the advantages of both approaches.

After evaluating the different options, the Stewart platform architecture was selected for several reasons. In addition to allow control over all required degrees of freedom, its compact design and predictable dynamic characteristics make it particularly suitable for nano-positioning when combined with flexible joints. Stewart platforms have been imple-

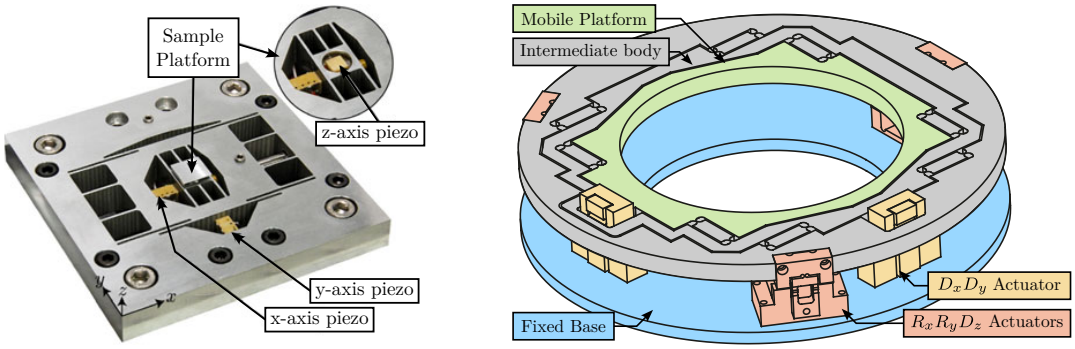

(a) XYZ Serial positioning stage [80]

(b) Hybrid 5-DoF stage [133]

Figure 2.102: Examples of a serial positioning stage (a) and of a hybrid (parallel/serial) positioning platform (b).

mented in a wide variety of configurations, as illustrated in Figure 2.103, which shows two distinct implementations: one implementing piezoelectric actuators for nano-positioning applications, and another based on voice coil actuators for vibration isolation. These examples demonstrate the architecture's versatility in terms of geometry, actuator selection, and scale, all of which can be optimized for specific applications. Furthermore, the successful implementation of Integral Force Feedback (IFF) control on Stewart platforms has been well documented [4, 5, 117], and the extensive body of research on this architecture enables thorough optimization specifically for the NASS.

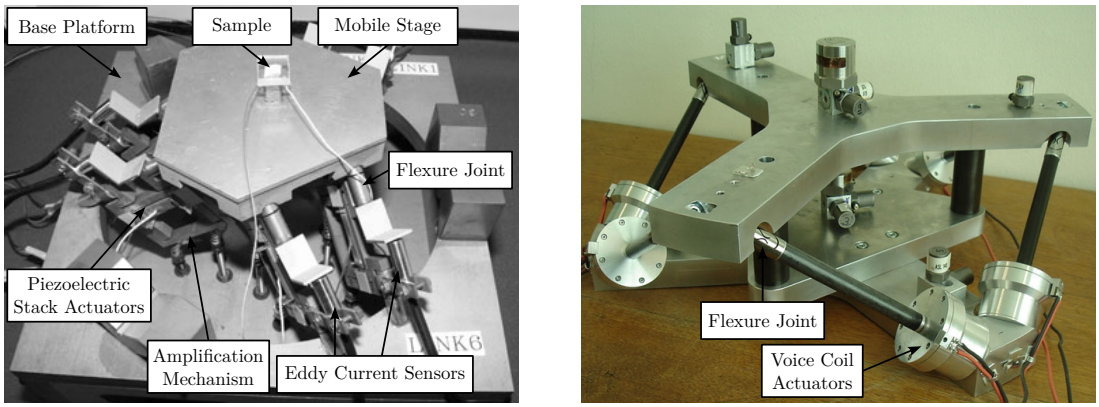

(a) Stewart platform for Nano-positioning [51]

(b) Stewart platform for vibration isolation [113, 117]

Figure 2.103: Two examples of Stewart platforms. (a) Stewart platform based on piezoelectric actuators and used for nano-positioning. (b) Stewart platform based on voice coil actuators and used for vibration isolation.

2.5.2 The Stewart Platform

The Stewart platform, first introduced by Stewart in 1965 [139] for flight simulation applications, represents a significant milestone in parallel manipulator design. This mechanical architecture has evolved far beyond its original purpose, and has been applied across diverse field, from precision positioning systems to robotic surgery. The fundamental design consists of two platforms connected by six adjustable struts in parallel, creating a fully parallel manipulator capable of six degrees of freedom motion.

Unlike serial manipulators, in which errors worsen through the kinematic chain, parallel architectures distribute loads across multiple actuators, leading to enhanced mechanical stiffness and improved positioning accuracy. This parallel

configuration also results in superior dynamic performance because the actuators directly contribute to the platform's motion without intermediate linkages. These characteristics make the Stewart platforms particularly valuable in applications requiring high precision and stiffness.

For the NASS application, the Stewart platform architecture offers three key advantages. First, as a fully parallel manipulator, all the motion errors of the micro-station can be compensated through the coordinated action of the six actuators. Second, its compact design compared to serial manipulators makes it ideal for integration on top micro-station where only 95 mm of height is available. Third, the good dynamical properties should enable high-bandwidth positioning control.

While Stewart platforms excel in precision and stiffness, they typically exhibit a relatively limited workspace compared to serial manipulators. However, this limitation is not significant for the NASS application, as the required motion range corresponds to the positioning errors of the micro-station, which are in the order of 10 µm.

This section provides a comprehensive analysis of the Stewart platform's properties, focusing on aspects crucial for precision positioning applications. The analysis encompasses the platform's kinematic relationships (Section 2.5.2.2), the use of the Jacobian matrix (Section 2.5.2.3), static behavior (Section 2.5.2.4), and dynamic characteristics (Section 2.5.2.5). These theoretical foundations form the basis for subsequent design decisions and control strategies, which will be elaborated in later sections.

2.5.2.1 Mechanical Architecture

The Stewart platform consists of two rigid platforms connected by six parallel struts (Figure 2.104). Each strut is modelled with an active prismatic joint that allows for controlled length variation, with its ends attached to the fixed and mobile platforms through joints. The typical configuration consists of a universal joint at one end and a spherical joint at the other, providing the necessary degrees of freedom[1].

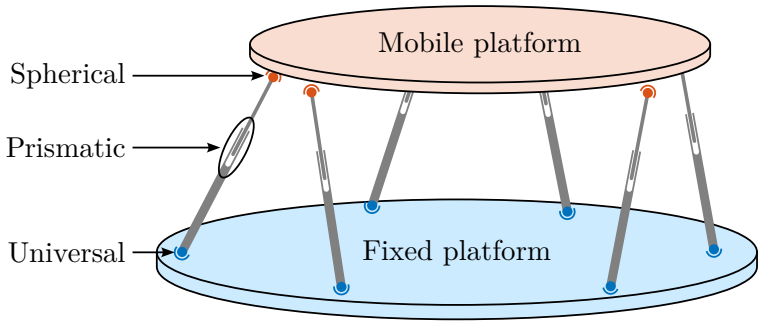

Figure 2.104: Schematic representation of the Stewart platform architecture.

To facilitate the rigorous analysis of the Stewart platform, four reference frames were defined:

- The fixed base frame $\{F\}$, which is located at the center of the base platform's bottom surface, serves as the mounting reference for the support structure.
- The mobile frame $\{M\}$, which is located at the center of the top platform's upper platform, provides a reference for payload mounting.
- The Point of Interest frame $\{A\}$, fixed to the base but positioned at the workspace center.

[1] Different architecture exists, typically referred as "6-SPS" (Spherical, Prismatic, Spherical) or "6-UPS" (Universal, Prismatic, Spherical).

- The moving Point of Interest frame $\{B\}$, attached to the mobile platform coincides with frame $\{A\}$ in the home position.

Frames $\{F\}$ and $\{M\}$ serve primarily to define the joint locations. In contrast, frames $\{A\}$ and $\{B\}$ are used to describe the relative motion of the two platforms through the position vector ${}^{A}\boldsymbol{P}_{B}$ of frame $\{B\}$ expressed in frame $\{A\}$ and the rotation matrix ${}^{A}\boldsymbol{R}_{B}$ expressing the orientation of $\{B\}$ with respect to $\{A\}$. For the active platform, frames $\{A\}$ and $\{B\}$ are chosen to be located at the theoretical focus point of the X-ray light which is 150 mm above the top platform, i.e. above $\{M\}$.

The location of the joints and the orientation and length of the struts are crucial for subsequent kinematic, static, and dynamic analyses of the Stewart platform. The center of rotation for the joint fixed to the base is noted $\boldsymbol{a}_i$, while $\boldsymbol{b}_i$ is used for the top platform joints. The struts' orientations are represented by the unit vectors $\hat{\boldsymbol{s}}_i$ and their lengths are represented by the scalars l_i. This is summarized in Figure 2.105.

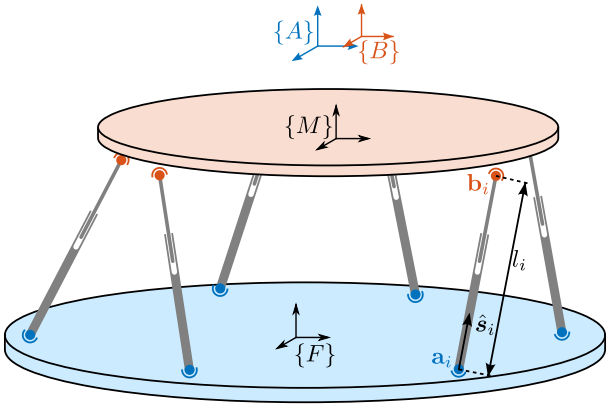

Figure 2.105: Typical defined frames for the Stewart platform and key notations.

2.5.2.2 Kinematic Analysis

Loop Closure The foundation of the kinematic analysis lies in the geometric constraints imposed by each strut, which can be expressed using loop closure equations. For each strut i (illustrated in Figure 2.106), the loop closure equation (2.67) can be written.

$$ {}^{A}\boldsymbol{P}_{B} = {}^{A}\boldsymbol{a}_i + l_i\,{}^{A}\hat{\boldsymbol{s}}_i - \underbrace{{}^{B}\boldsymbol{b}_i}_{{}^{A}\boldsymbol{R}_{B}\,{}^{B}\boldsymbol{b}_i} \qquad \text{for } i = 1 \text{ to } 6 \tag{2.67} $$

This equation links the pose[1] variables ${}^{A}\boldsymbol{P}$ and ${}^{A}\boldsymbol{R}_{B}$, the position vectors describing the known geometry of the base and the moving platform, $\boldsymbol{a}_i$ and $\boldsymbol{b}_i$, and the strut vector $l_i\,{}^{A}\hat{\boldsymbol{s}}_i$:

Inverse Kinematics The inverse kinematic problem involves determining the required strut lengths $\boldsymbol{\mathcal{L}} = [l_1, l_2, \ldots, l_6]^{\intercal}$ for a desired platform pose $\boldsymbol{\mathcal{X}}$ (i.e. position ${}^{A}\boldsymbol{P}$ and orientation ${}^{A}\boldsymbol{R}_{B}$). This problem can be solved analytically using the loop closure equations (2.67). The obtained strut lengths are given by (2.68).

$$ l_i = \sqrt{{}^{A}\boldsymbol{P}^{\intercal}\,{}^{A}\boldsymbol{P} + {}^{B}\boldsymbol{b}_i^{\intercal}\,{}^{B}\boldsymbol{b}_i + {}^{A}\boldsymbol{a}_i^{\intercal}\,{}^{A}\boldsymbol{a}_i - 2\,{}^{A}\boldsymbol{P}^{\intercal}\,{}^{A}\boldsymbol{a}_i + 2\,{}^{A}\boldsymbol{P}^{\intercal}[{}^{A}\boldsymbol{R}_{B}\,{}^{B}\boldsymbol{b}_i] - 2[{}^{A}\boldsymbol{R}_{B}\,{}^{B}\boldsymbol{b}_i]^{\intercal}\,{}^{A}\boldsymbol{a}_i} \tag{2.68} $$

[1] The *pose* represents the position and orientation of an object.

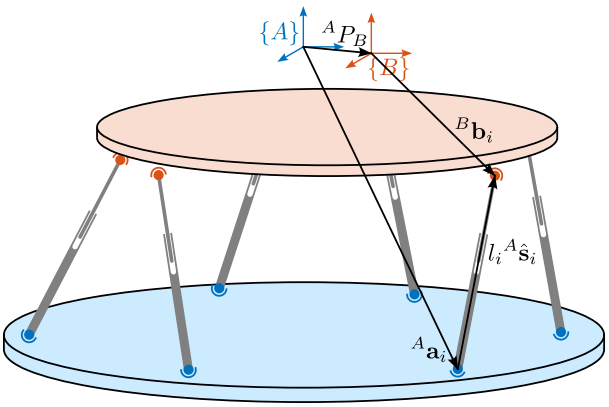

Figure 2.106: Geometrical representation of the loop closure.

If the position and orientation of the platform lie in the feasible workspace, the solution is unique. While configurations outside this workspace yield complex numbers, this only becomes relevant for large displacements that far exceed the active platform's operating range.

Forward Kinematics The forward kinematic problem seeks to determine the platform pose $\boldsymbol{\mathcal{X}}$ given a set of strut lengths $\boldsymbol{\mathcal{L}}$. Unlike inverse kinematics, this presents a significant challenge because it requires solving a system of nonlinear equations. Although various numerical methods exist for solving this problem, they can be computationally intensive and may not guarantee convergence to the correct solution.

For the active platform application, where displacements are typically small, an approximate solution based on linearization around the operating point provides a practical alternative. This approximation, which is developed in subsequent sections through the Jacobian matrix analysis, is particularly useful for real-time control applications.

2.5.2.3 The Jacobian Matrix

The Jacobian matrix plays a central role in analyzing the Stewart platform's behavior, providing a linear mapping between the platform and actuator velocities. While the previously derived kinematic relationships are essential for position analysis, the Jacobian enables velocity analysis and forms the foundation for both static and dynamic studies.

Jacobian Computation As discussed in Section 2.5.2.2, the strut lengths $\boldsymbol{\mathcal{L}}$ and the platform pose $\boldsymbol{\mathcal{X}}$ are related through a system of nonlinear algebraic equations representing the kinematic constraints imposed by the struts.

By taking the time derivative of the position loop close (2.67), equation (2.69) is obtained[1].

$$ {}^{A}\boldsymbol{v}_p + {}^{A}\dot{\boldsymbol{R}}_B\,{}^{B}\boldsymbol{b}_i + {}^{A}\boldsymbol{R}_B \underbrace{{}^{B}\dot{\boldsymbol{b}}_i}_{=0} = \dot{l}_i\,{}^{A}\hat{\boldsymbol{s}}_i + l_i\,{}^{A}\dot{\hat{\boldsymbol{s}}}_i + \underbrace{{}^{A}\dot{\boldsymbol{a}}_i}_{=0} \tag{2.69} $$

Moreover, we have:

[1] Such equation is called the *velocity loop closure*.

- ${}^A\dot{\boldsymbol{R}}_B\,{}^B\boldsymbol{b}_i = {}^A\boldsymbol{\omega} \times {}^A\boldsymbol{R}_B\,{}^B\boldsymbol{b}_i = {}^A\boldsymbol{\omega} \times {}^A\boldsymbol{b}_i$ in which ${}^A\boldsymbol{\omega}$ denotes the angular velocity of the moving platform expressed in the fixed frame $\{\boldsymbol{A}\}$.
- $l_i\,{}^A\dot{\hat{\boldsymbol{s}}}_i = l_i\big({}^A\boldsymbol{\omega}_i \times \hat{\boldsymbol{s}}_i\big)$ in which ${}^A\boldsymbol{\omega}_i$ is the angular velocity of strut i express in fixed frame $\{\boldsymbol{A}\}$.

By multiplying both sides by ${}^A\hat{\boldsymbol{s}}_i$, (2.70) is obtained.

$$ {}^A\hat{\boldsymbol{s}}_i\,{}^A\boldsymbol{v}_p + \underbrace{{}^A\hat{\boldsymbol{s}}_i\big({}^A\boldsymbol{\omega} \times {}^A\boldsymbol{b}_i\big)}_{=({}^A\boldsymbol{b}_i \times {}^A\hat{\boldsymbol{s}}_i)\,{}^A\boldsymbol{\omega}} = \dot{l}_i + \underbrace{{}^A\hat{s}_i l_i\big({}^A\boldsymbol{\omega}_i \times {}^A\hat{\boldsymbol{s}}_i\big)}_{=0} \tag{2.70} $$

Equation (2.70) can be rearranged in matrix form to obtain (2.71), with $\dot{\boldsymbol{\mathcal{L}}} = [\dot{l}_1 \ \dots \ \dot{l}_6]^\intercal$ the vector of strut velocities, and $\dot{\boldsymbol{\mathcal{X}}} = [{}^A\boldsymbol{v}_p,\ {}^A\boldsymbol{\omega}]^\intercal$ the vector of platform velocity and angular velocity.

$$ \boxed{\dot{\boldsymbol{\mathcal{L}}} = \boldsymbol{J}\dot{\boldsymbol{\mathcal{X}}}} \tag{2.71} $$

The matrix $\boldsymbol{J}$ is called the Jacobian matrix and is defined by (2.72), with ${}^A\hat{\boldsymbol{s}}_i$ the orientation of the struts expressed in $\{A\}$ and ${}^A\boldsymbol{b}_i$ the position of the joints with respect to O_B and express in $\{A\}$.

$$ \boldsymbol{J} = \begin{bmatrix} {}^A\hat{\boldsymbol{s}}_1{}^\intercal & ({}^A\boldsymbol{b}_1 \times {}^A\hat{\boldsymbol{s}}_1)^\intercal \\ {}^A\hat{\boldsymbol{s}}_2{}^\intercal & ({}^A\boldsymbol{b}_2 \times {}^A\hat{\boldsymbol{s}}_2)^\intercal \\ {}^A\hat{\boldsymbol{s}}_3{}^\intercal & ({}^A\boldsymbol{b}_3 \times {}^A\hat{\boldsymbol{s}}_3)^\intercal \\ {}^A\hat{\boldsymbol{s}}_4{}^\intercal & ({}^A\boldsymbol{b}_4 \times {}^A\hat{\boldsymbol{s}}_4)^\intercal \\ {}^A\hat{\boldsymbol{s}}_5{}^\intercal & ({}^A\boldsymbol{b}_5 \times {}^A\hat{\boldsymbol{s}}_5)^\intercal \\ {}^A\hat{\boldsymbol{s}}_6{}^\intercal & ({}^A\boldsymbol{b}_6 \times {}^A\hat{\boldsymbol{s}}_6)^\intercal \end{bmatrix} \tag{2.72} $$

Therefore, the Jacobian matrix $\boldsymbol{J}$ links the rate of change of the strut length to the velocity and angular velocity of the top platform with respect to the fixed base through a set of linear equations. However, $\boldsymbol{J}$ needs to be recomputed for every Stewart platform pose because it depends on the actual pose of the manipulator.

Approximate Solution to the Forward and Inverse Kinematic Problems For small displacements $\delta\boldsymbol{\mathcal{X}} = [\delta x, \delta y, \delta z, \delta\theta_x, \delta\theta_y, \delta\theta_z]^\intercal$ around an operating point $\boldsymbol{\mathcal{X}}_0$ (for which the Jacobian was computed), the associated joint displacement $\delta\boldsymbol{\mathcal{L}} = [\delta l_1,\ \delta l_2,\ \delta l_3,\ \delta l_4,\ \delta l_5,\ \delta l_6]^\intercal$ can be computed using the Jacobian (2.73).

$$ \boxed{\delta\boldsymbol{\mathcal{L}} = \boldsymbol{J}\delta\boldsymbol{\mathcal{X}}} \tag{2.73} $$

Similarly, for small joint displacements $\delta\boldsymbol{\mathcal{L}}$, it is possible to find the induced small displacement of the mobile platform (2.74).

$$ \boxed{\delta\boldsymbol{\mathcal{X}} = \boldsymbol{J}^{-1}\delta\boldsymbol{\mathcal{L}}} \tag{2.74} $$

These two relations solve the forward and inverse kinematic problems for small displacement in a *approximate* way. While this approximation offers limited value for inverse kinematics, which can be solved analytically, it proves particularly useful for the forward kinematic problem where exact analytical solutions are difficult to obtain.

Range Validity of the Approximate Inverse Kinematics The accuracy of the Jacobian-based forward kinematics solution was estimated by a simple analysis. For a series of platform positions, the exact strut lengths are computed using the analytical inverse kinematics equation (2.68). These strut lengths are then used with the Jacobian to estimate the platform pose (2.74), from which the error between the estimated and true poses can be calculated, both in terms of position ϵ_D and orientation ϵ_R.

For motion strokes from 1 µm to 10 mm, the errors are estimated for all direction of motion, and the worst case errors are shown in Figure 2.107. The results demonstrate that for displacements up to approximately 0.1 % of the hexapod's size (which corresponds to 100 µm as the size of the Stewart platform is here $\approx$ 100 mm), the Jacobian approximation provides excellent accuracy.

Since the maximum required stroke of the active platform ($\approx$ 100 µm) is three orders of magnitude smaller than its overall size ($\approx$ 100 mm), the Jacobian matrix can be considered constant throughout the workspace. It can be computed once at the rest position and used for both forward and inverse kinematics with high accuracy.

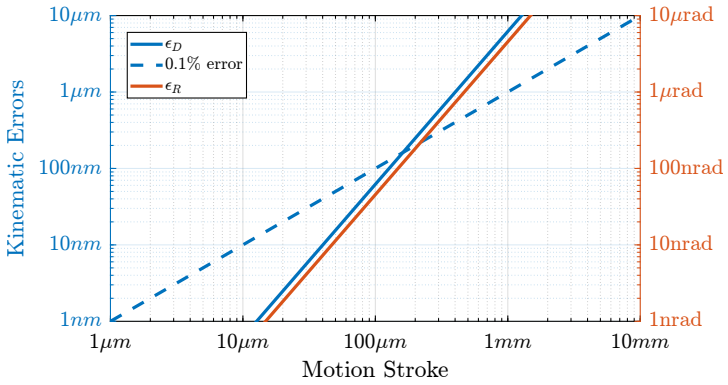

Figure 2.107: Errors associated with the use of the Jacobian matrix to solve the forward kinematic problem. A Stewart platform with a height of 100 mm was used to perform this analysis. ϵ_D corresponds to the distance between the true position and the estimated position. ϵ_R corresponds to the angular motion between the true orientation and the estimated orientation.

Static Forces The static force analysis of the Stewart platform can be performed using the principle of virtual work. This principle states that for a system in static equilibrium, the total virtual work of all forces acting on the system must be zero for any virtual displacement compatible with the system's constraints.

Let $\boldsymbol{f} = [f_1, f_2, \cdots, f_6]^\intercal$ represent the vector of actuator forces applied in each strut, and $\boldsymbol{\mathcal{F}} = [\boldsymbol{F}, \boldsymbol{n}]^\intercal$ denote the external wrench (combined force $\boldsymbol{F}$ and torque $\boldsymbol{n}$) acting on the mobile platform at point $\boldsymbol{O}_B$. The virtual work δW consists of two contributions:

- The work performed by the actuator forces through virtual strut displacements $\delta\boldsymbol{\mathcal{L}}$: $\boldsymbol{f}^\intercal \delta\boldsymbol{\mathcal{L}}$
- The work performed by the external wrench through virtual platform displacements $\delta\boldsymbol{\mathcal{X}}$: $-\boldsymbol{\mathcal{F}}^\intercal \delta\boldsymbol{\mathcal{X}}$

Thus, the principle of virtual work can be expressed as:

$$\delta W = \boldsymbol{f}^\intercal \delta\boldsymbol{\mathcal{L}} - \boldsymbol{\mathcal{F}}^\intercal \delta\boldsymbol{\mathcal{X}} = 0 \tag{2.75}$$

Using the Jacobian relationship that links virtual displacements (2.73), this equation becomes:

$$(\boldsymbol{f}^\intercal \boldsymbol{J} - \boldsymbol{\mathcal{F}}^\intercal)\delta\boldsymbol{\mathcal{X}} = 0 \tag{2.76}$$

Because this equation must hold for any virtual displacement $\delta\boldsymbol{\mathcal{X}}$, the force mapping relationships (2.77) can be derived.

$$\boldsymbol{f}^\intercal \boldsymbol{J} - \boldsymbol{\mathcal{F}}^\intercal = 0 \quad \Rightarrow \quad \boxed{\boldsymbol{\mathcal{F}} = \boldsymbol{J}^\intercal \boldsymbol{f}} \quad \text{and} \quad \boxed{\boldsymbol{f} = \boldsymbol{J}^{-\intercal} \boldsymbol{\mathcal{F}}} \tag{2.77}$$

These equations establish that the transpose of the Jacobian matrix maps actuator forces to platform forces and torques, while its inverse transpose maps platform forces and torques to required actuator forces.

2.5.2.4 Static Analysis

The static stiffness characteristics of the Stewart platform play a crucial role in its performance, particularly for precision positioning applications. These characteristics are fundamentally determined by both the actuator properties and the platform geometry.

Starting from the individual actuators, the relationship between applied force f_i and resulting displacement δl_i for each strut i is characterized by its stiffness k_i:

$$f_i = k_i \delta l_i, \quad i = 1, \ldots, 6 \tag{2.78}$$

These individual relationships can be combined into a matrix form using the diagonal stiffness matrix $\boldsymbol{\mathcal{K}}$:

$$\boldsymbol{f} = \boldsymbol{\mathcal{K}} \cdot \delta\boldsymbol{\mathcal{L}}, \quad \boldsymbol{\mathcal{K}} = \text{diag}[k_1, \ldots, k_6] \tag{2.79}$$

By applying the force mapping relationships (2.77) derived in the previous section and the Jacobian relationship for small displacements (2.74), the relationship between applied wrench $\boldsymbol{\mathcal{F}}$ and resulting platform displacement $\delta\boldsymbol{\mathcal{X}}$ is obtained (2.80).

$$\boldsymbol{\mathcal{F}} = \underbrace{\boldsymbol{J}^\intercal \boldsymbol{\mathcal{K}} \boldsymbol{J}}_{\boldsymbol{K}} \cdot \delta\boldsymbol{\mathcal{X}} \tag{2.80}$$

where $\boldsymbol{K} = \boldsymbol{J}^\intercal \boldsymbol{\mathcal{K}} \boldsymbol{J}$ is identified as the platform stiffness matrix.

The inverse relationship is given by the compliance matrix $\boldsymbol{C}$:

$$\delta\boldsymbol{\mathcal{X}} = \underbrace{(\boldsymbol{J}^\intercal \boldsymbol{\mathcal{K}} \boldsymbol{J})^{-1}}_{\boldsymbol{C}} \boldsymbol{\mathcal{F}} \tag{2.81}$$

These relationships reveal that the overall platform stiffness and compliance characteristics are determined by two factors:

- The individual actuator stiffnesses represented by $\boldsymbol{\mathcal{K}}$

- The geometric configuration embodied in the Jacobian matrix $\boldsymbol{J}$

This geometric dependency means that the platform's stiffness varies throughout its workspace, as the Jacobian matrix changes with the platform's position and orientation. For the NASS application, where the workspace is small compared to the platform dimensions, these variations can be considered negligible. However, the initial geometric configuration significantly affects the overall stiffness characteristics. The relationship between maximum stroke and stiffness presents another important design consideration. As both parameters are influenced by the geometric configuration, their optimization involves inherent trade-offs that must be carefully balanced based on the application requirements. The optimization of this configuration to achieve the desired stiffness while having sufficient stroke will be addressed during the detailed design phase.

2.5.2.5 Dynamical Analysis

For initial analysis, a simplified representation of the system has been developed. This model assumes perfectly rigid bodies for both the platform and base, connected by massless struts through ideal joints that exhibit neither friction nor compliance.

Under these assumptions, the system dynamics can be expressed in Cartesian space as:

$$\boldsymbol{M}s^2\boldsymbol{\mathcal{X}} = \Sigma\boldsymbol{\mathcal{F}} \tag{2.82}$$

where $\boldsymbol{M}$ represents the platform mass matrix, $\boldsymbol{\mathcal{X}}$ the platform pose, and $\Sigma\boldsymbol{\mathcal{F}}$ the sum of forces acting on the platform.

The primary forces acting on the system are actuator forces $\boldsymbol{f}$, elastic forces due to strut stiffness $-\boldsymbol{\mathcal{K}}\boldsymbol{\mathcal{L}}$ and damping forces in the struts $\boldsymbol{\mathcal{C}}\dot{\boldsymbol{\mathcal{L}}}$.

$$\Sigma\boldsymbol{\mathcal{F}} = \boldsymbol{J}^\intercal(\boldsymbol{f} - \boldsymbol{\mathcal{K}}\boldsymbol{\mathcal{L}} - s\boldsymbol{\mathcal{C}}\boldsymbol{\mathcal{L}}), \quad \boldsymbol{\mathcal{K}} = \text{diag}(k_1 \ \dots \ k_6),\ \boldsymbol{\mathcal{C}} = \text{diag}(c_1 \ \dots \ c_6) \tag{2.83}$$

Combining these forces and using (2.74) yields the complete dynamic equation (2.84).

$$\boldsymbol{M}s^2\boldsymbol{\mathcal{X}} = \boldsymbol{\mathcal{F}} - \boldsymbol{J}^\intercal\boldsymbol{\mathcal{K}}\boldsymbol{J}\boldsymbol{\mathcal{X}} - \boldsymbol{J}^\intercal\boldsymbol{\mathcal{C}}\boldsymbol{J}s\boldsymbol{\mathcal{X}} \tag{2.84}$$

The transfer function matrix in the Cartesian frame becomes (2.85).

$$\frac{\mathcal{X}}{\mathcal{F}}(s) = (\boldsymbol{M}s^2 + \boldsymbol{J}^\intercal\boldsymbol{\mathcal{C}}\boldsymbol{J}s + \boldsymbol{J}^\intercal\boldsymbol{\mathcal{K}}\boldsymbol{J})^{-1} \tag{2.85}$$

Through coordinate transformation using the Jacobian matrix, the dynamics in the actuator space is obtained (2.86).

$$\frac{\boldsymbol{\mathcal{L}}}{\boldsymbol{f}}(s) = (\boldsymbol{J}^{-\intercal}\boldsymbol{M}\boldsymbol{J}^{-1}s^2 + \boldsymbol{\mathcal{C}} + \boldsymbol{\mathcal{K}})^{-1} \tag{2.86}$$

Although this simplified model provides useful insights, real Stewart platforms exhibit more complex behaviors. Several factors can significantly increase the model complexity, such as:

- Strut dynamics, including mass distribution and internal resonances [22]
- Joint compliance and friction effects [97, 98]
- Supporting structure dynamics and payload dynamics, which are both very critical for NASS

These additional effects render analytical modeling impractical for complete system analysis.

2.5.2.6 Conclusion

The fundamental characteristics of the Stewart platform have been analyzed in this chapter. Essential kinematic relationships were developed through loop closure equations, from which both exact and approximate solutions for the inverse and forward kinematic problems were derived. The Jacobian matrix was established as a central mathematical tool through which crucial insights into velocity relationships, static force transmission, and dynamic behavior of the platform were obtained.

For the NASS application, where displacements are typically limited to the micrometer range, the accuracy of linearized models using a constant Jacobian matrix has been demonstrated, by which both analysis and control can be significantly simplified. However, additional complexities such as strut masses, joint compliance, and supporting structure dynamics must be considered in the full dynamic behavior. This will be performed in the next section using a multi-body model.

All these characteristics (maneuverability, stiffness, dynamics, etc.) are fundamentally determined by the platform's geometry. While a reasonable geometric configuration will be used to validate the NASS during the conceptual phase, the optimization of these geometric parameters will be explored during the detailed design phase.

2.5.3 Multi-Body Model of Stewart Platforms

The dynamic modeling of Stewart platforms has traditionally relied on analytical approaches. However, these analytical models become increasingly complex when the dynamical behaviors of struts and joints must be captured. To overcome these limitations, a flexible multi-body approach was developed that can be readily integrated into the broader NASS model. Through this multi-body modeling approach, each component model (including joints, actuators, and sensors) can be progressively refined.

The analysis is structured as follows. First, the multi-body model is developed, and the geometric parameters, inertial properties, and actuator characteristics are established (Section 2.5.3.1). The model is then validated through comparison with the analytical equations in a simplified configuration (Section 2.5.3.2). Finally, the validated model is employed to analyze the active platform dynamics, from which insights for the control system design are derived (Section 2.5.3.3).

2.5.3.1 Model Definition

Geometry The Stewart platform's geometry is defined by two principal coordinate frames (Figure 2.108): a fixed base frame $\{F\}$ and a moving platform frame $\{M\}$. The joints connecting the actuators to these frames are located at positions ${}^{F}\boldsymbol{a}_i$ and ${}^{M}\boldsymbol{b}_i$ respectively. The PoI, denoted by frame $\{A\}$, is situated 150 mm above the moving platform frame $\{M\}$.

The geometric parameters of the active platform are summarized in Table 2.13. These parameters define the positions of all connection points in their respective coordinate frames. From these parameters, key kinematic properties can be derived: the strut orientations $\hat{\boldsymbol{s}}_i$, strut lengths l_i, and the system's Jacobian matrix $\boldsymbol{J}$.

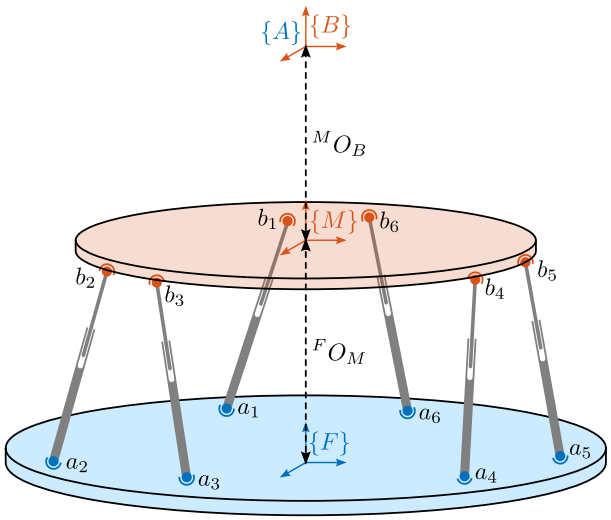

Figure 2.108: Geometrical parameters of the Stewart platform.

	x	y	z
$^M\boldsymbol{O}_B$	0	0	150
$^F\boldsymbol{O}_M$	0	0	95
$^F\boldsymbol{a}_1$	−92	−77	20
$^F\boldsymbol{a}_2$	92	−77	20
$^F\boldsymbol{a}_3$	113	−41	20
$^F\boldsymbol{a}_4$	21	118	20
$^F\boldsymbol{a}_5$	−21	118	20
$^F\boldsymbol{a}_6$	−113	−41	20
$^M\boldsymbol{b}_1$	−28	−106	−20
$^M\boldsymbol{b}_2$	28	−106	−20
$^M\boldsymbol{b}_3$	106	28	−20
$^M\boldsymbol{b}_4$	78	78	−20
$^M\boldsymbol{b}_5$	−78	78	−20
$^M\boldsymbol{b}_6$	−106	28	−20

Table 2.13: Parameter values in [mm]

Inertia of Plates The fixed base and moving platform were modelled as solid cylindrical bodies. The base platform was characterized by a radius of 120 mm and thickness of 15 mm, matching the dimensions of the positioning hexapod's top platform. The moving platform was similarly modelled with a radius of 110 mm and thickness of 15 mm. Both platforms were assigned a mass of 5 kg.

Joints The platform's joints play a crucial role in its dynamic behavior. At both the upper and lower connection points, various degrees of freedom can be modelled, including universal joints, spherical joints, and configurations with additional axial and lateral stiffness components. For each DoF, stiffness characteristics can be incorporated into the model.

In the conceptual design phase, a simplified joint configuration is employed: the bottom joints are modelled as two-degree-of-freedom universal joints, while the top joints are represented as three-degree-of-freedom spherical joints. These joints are considered massless and exhibit no stiffness along their degrees of freedom.

Actuators The actuator model comprises several key elements (Figure 2.109). At its core, each actuator is modelled as a prismatic joint with internal stiffness k_a and damping c_a, driven by a force source f. Similarly to what was found using the rotating 3-DoF model, a parallel stiffness k_p is added in parallel with the force sensor to ensure stability when considering spindle rotation effects.

Each actuator is equipped with two sensors: a force sensor providing measurements f_n and a relative motion sensor that measures the strut length l_i. The actuator parameters used in the conceptual phase are listed in Table 2.14.

This modular approach to actuator modeling allows for future refinements as the design evolves, enabling the incorporation of additional dynamic effects or sensor characteristics as needed.

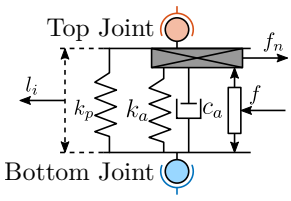

Figure 2.109: Model of the active platform actuators.

	Value
k_a	1 N/µm
c_a	50 Ns/m
k_p	0.05 N/µm

Table 2.14: Actuator parameters

2.5.3.2 Validation of the Multi-body Model

The developed multi-body model of the Stewart platform is represented schematically in Figure 2.110, highlighting the key inputs and outputs: actuator forces $\boldsymbol{f}$, force sensor measurements $\boldsymbol{f}_n$, and relative displacement measurements $\boldsymbol{\mathcal{L}}$. The frames $\{F\}$ and $\{M\}$ serve as interfaces for integration with other elements in the multi-body system. A three-dimensional visualization of the model is presented in Figure 2.111.

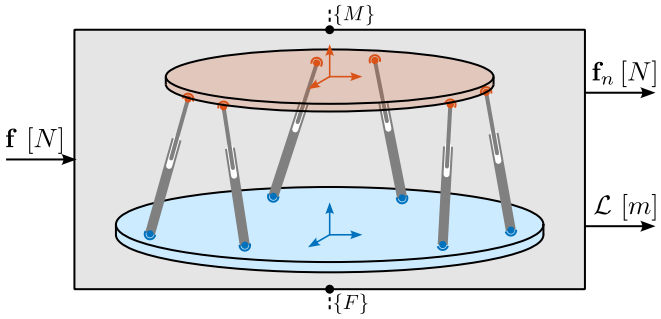

Figure 2.110: Active platform plant with inputs and outputs. Frames $\{F\}$ and $\{M\}$ can be connected to other elements in the model.

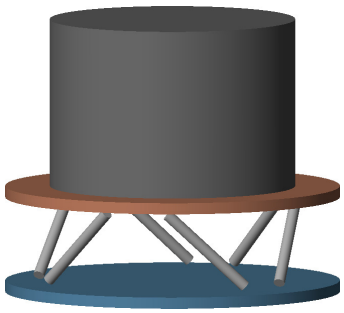

Figure 2.111: 3D representation of the multi-body model.

The validation of the multi-body model was performed using the simplest Stewart platform configuration, enabling direct comparison with the analytical transfer functions derived in Section 2.5.2.5. This configuration consists of massless universal joints at the base, massless spherical joints at the top platform, and massless struts with stiffness $k_a = 1\,\mathrm{N/\mu m}$ and damping $c_a = 10\,\mathrm{N/(m/s)}$. The geometric parameters remain as specified in Table 2.14.

While the moving platform itself is considered massless, a 10 kg cylindrical payload is mounted on top with a radius of $r = 110\,\mathrm{mm}$ and a height $h = 300\,\mathrm{mm}$.

For the analytical model, the stiffness, damping, and mass matrices are defined in (2.87).

$$\boldsymbol{\mathcal{K}} = \mathrm{diag}(k_a,\ k_a,\ k_a,\ k_a,\ k_a,\ k_a) \tag{2.87a}$$

$$\boldsymbol{\mathcal{C}} = \mathrm{diag}(c_a,\ c_a,\ c_a,\ c_a,\ c_a,\ c_a) \tag{2.87b}$$

$$\boldsymbol{M} = \mathrm{diag}\left(m,\ m,\ m,\ \frac{1}{12}m(3r^2+h^2),\ \frac{1}{12}m(3r^2+h^2),\ \frac{1}{2}mr^2\right) \tag{2.87c}$$

The transfer functions from the actuator forces to the strut displacements are computed using these matrices according to equation (2.86). These analytical transfer functions are then compared with those extracted from the multi-body model. The developed multi-body model yields a state-space representation with 12 states, corresponding to the 6-DoF of the moving platform.

Figure 2.112 presents a comparison between the analytical and multi-body transfer functions, specifically showing the response from the first actuator force to all six strut displacements. The close agreement between both approaches across the frequency spectrum validates the multi-body model's accuracy in capturing the system's dynamic behavior.

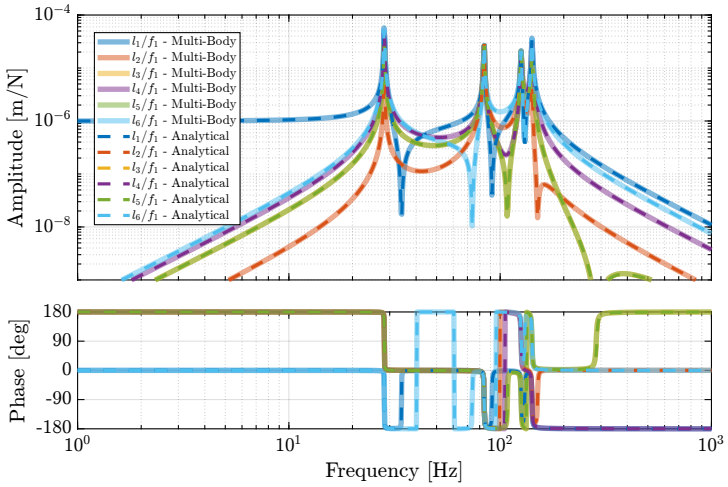

Figure 2.112: Comparison of the analytical transfer functions and the multi-body model.

2.5.3.3 Active Platform Dynamics

Following the validation of the multi-body model, a detailed analysis of the active platform dynamics was performed. The model parameters were set according to the specifications outlined in Section 2.5.3.1, with a payload mass of 10 kg. The transfer functions from actuator forces $\boldsymbol{f}$ to both strut displacements $\boldsymbol{\mathcal{L}}$ and force measurements $\boldsymbol{f}_n$ were derived from the multi-body model.

The transfer functions relating actuator forces to strut displacements are presented in Figure 2.113a. Due to the system's symmetrical design and identical strut configurations, all diagonal terms (transfer functions from force f_i to displacement l_i of the same strut) exhibit identical behavior. While the system has six degrees of freedom, only four distinct resonance frequencies were observed in the FRFs. This reduction from six to four observable modes is attributed to the system's symmetry, where two pairs of resonances occur at identical frequencies.

The system's behavior can be characterized in three frequency regions. At low frequencies, well below the first resonance, the plant demonstrates good decoupling between actuators, with the response dominated by the strut stiffness: $\boldsymbol{G}(j\omega) \xrightarrow[\omega \to 0]{} \boldsymbol{\mathcal{K}}^{-1}$. In the mid-frequency range, the system exhibits coupled dynamics through its resonant modes, reflecting the complex interactions between the platform's degrees of freedom. At high-frequencies, above the highest resonance, the response is governed by the payload's inertia mapped to the strut coordinates: $\boldsymbol{G}(j\omega) \xrightarrow[\omega \to \infty]{} \boldsymbol{J}\boldsymbol{M}^{-\intercal}\boldsymbol{J}^{\intercal}\frac{-1}{\omega^2}$

The force sensor transfer functions, shown in Figure 2.113b, display characteristics typical of collocated actuator-sensor pairs. Each actuator's transfer function to its associated force sensor exhibits alternating complex conjugate poles and zeros. The inclusion of parallel stiffness introduces an additional complex conjugate zero at low frequency, which was previously observed in the three-degree-of-freedom rotating model.

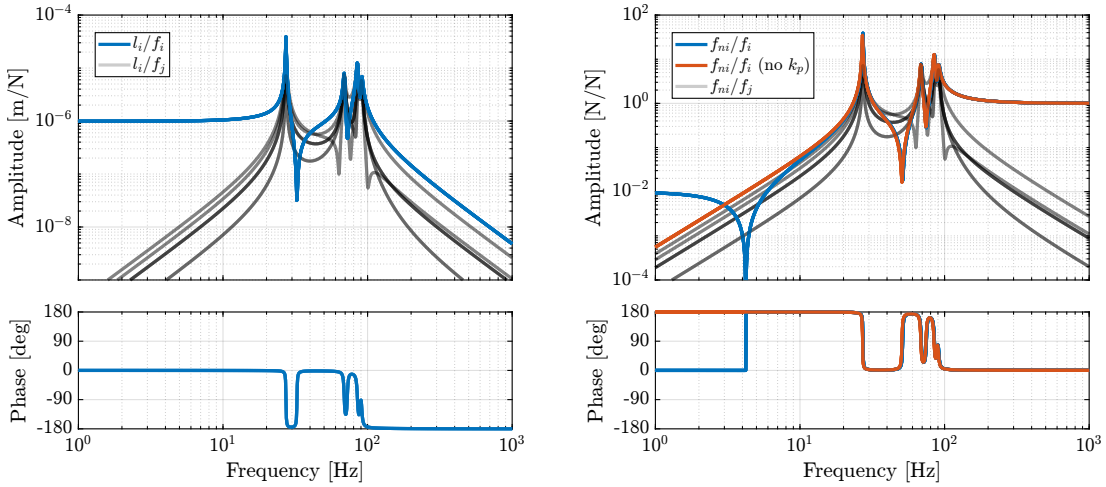

(a) $\boldsymbol{f}$ to $\boldsymbol{\mathcal{L}}$ **(b)** $\boldsymbol{f}$ to $\boldsymbol{f}_n$

Figure 2.113: Bode plot of the transfer functions computed using the multi-body model.

2.5.3.4 Conclusion

The multi-body modeling approach presented in this section provides a comprehensive framework for analyzing the dynamics of the active platform system. Through comparison with analytical solutions in a simplified configuration, the model's accuracy has been validated, demonstrating its ability to capture the essential dynamic behavior of the Stewart platform.

A key advantage of this modeling approach lies in its flexibility for future refinements. While the current implementation employs idealized joints for the conceptual design phase, the framework readily accommodates the incorporation of joint stiffness and other non-ideal effects. The joint stiffness, which is known to impact the performance of decentralized IFF control strategy [117], will be studied and optimized during the detailed design phase. The validated multi-body model will serve as a valuable tool for predicting system behavior and evaluating control performance throughout the design process.

2.5.4 Control of Stewart Platforms

The control of Stewart platforms presents distinct challenges compared to the uniaxial model due to their multi-input multi-output nature. Although the uniaxial model demonstrated the effectiveness of the HAC-LAC strategy, its extension to Stewart platforms requires careful considerations discussed in this section.

First, the distinction between centralized and decentralized control approaches is discussed in Section 2.5.4.1. The impact of the control space selection - either Cartesian or strut space - is then analyzed in Section 2.5.4.2, highlighting the trade-offs between direction-specific tuning and implementation simplicity.

Building on these analyses, a decentralized active damping strategy using Integral Force Feedback is developed in Section 2.5.4.3, followed by the implementation of a centralized High Authority Control for positioning in Section 2.5.4.4. This architecture, while simple, will be used to demonstrate the feasibility of the NASS concept and will provide a foundation for more sophisticated control strategies to be developed during the detailed design phase.

2.5.4.1 Centralized and Decentralized Control

In the control of MIMO systems, and more specifically of Stewart platforms, a fundamental architectural decision lies in the choice between centralized and decentralized control strategies.

In decentralized control, each actuator operates based on feedback from its associated sensor only, creating independent control loops, as illustrated in Figure 2.114. While mechanical coupling between the struts exists, control decisions are made locally, with each controller processing information from a single sensor-actuator pair. This approach offers simplicity in implementation and reduces computational requirements.

Conversely, centralized control uses information from all sensors to determine the control action of each actuator. This strategy potentially enables better performance by explicitly accounting for the mechanical coupling between the struts, though at the cost of increased complexity in both design and implementation.

The choice between these approaches depends significantly on the degree of interaction between the different control channels, and also on the available sensors and actuators. For instance, when using external metrology systems that measure the platform's global position, centralized control becomes necessary because each sensor measurement depends on all actuator inputs.

In the context of the active platform, two distinct control strategies were examined during the conceptual phase:

- Decentralized Integral Force Feedback (IFF), which uses collocated force sensors to implement independent control loops for each strut (Section 2.5.4.3)
- High Authority Control (HAC), which employs a centralized approach to achieve precise positioning based on external metrology measurements (Section 2.5.4.4)

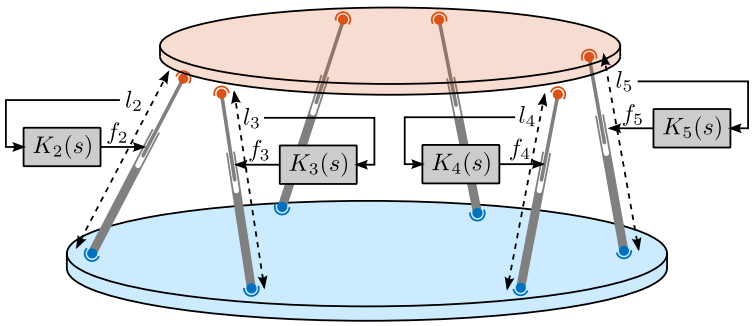

Figure 2.114: Decentralized control strategy using the encoders. The two controllers for the struts on the back are not shown.

2.5.4.2 Choice of the Control Space

When controlling a Stewart platform using external metrology that measures the pose of frame $\{B\}$ with respect to $\{A\}$, denoted as $\boldsymbol{\mathcal{X}}$, the control architecture can be implemented in either Cartesian or strut space. This choice affects both the control design and the obtained performance.

Control in the Strut space In this approach, as illustrated in Figure 2.115a, the control is performed in the space of the struts. The Jacobian matrix is used to solve the inverse kinematics in real-time by mapping position errors from Cartesian space $\boldsymbol{\epsilon}_{\mathcal{X}}$ to strut space $\boldsymbol{\epsilon}_{\mathcal{L}}$. A diagonal controller then processes these strut-space errors to generate force commands for each actuator.

The main advantage of this approach emerges from the plant characteristics in the strut space, as shown in Figure 2.116a. The diagonal terms of the plant (transfer functions from force to displacement of the same strut, as measured by the external metrology) are identical due to the system's symmetry. This simplifies the control design because only one controller needs to be tuned. Furthermore, at low frequencies, the plant exhibits good decoupling between the struts, allowing for effective independent control of each axis.

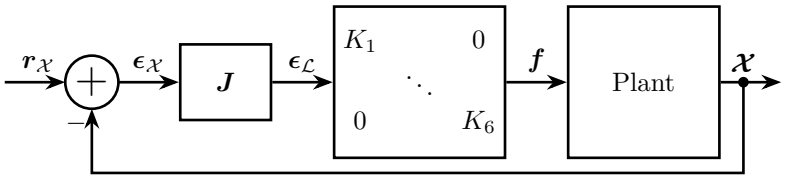

(a) Control in the frame of the struts. $\boldsymbol{J}$ is used to project errors in the frame of the struts

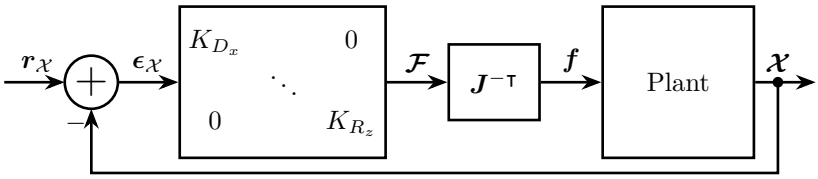

(b) Control in the Cartesian frame. $\boldsymbol{J}^{-\intercal}$ is used to project forces and torques on each strut

Figure 2.115: Two control strategies using the Jacobian matrix.

Control in Cartesian Space Alternatively, control can be implemented directly in Cartesian space, as illustrated in Figure 2.115b. Here, the controller processes Cartesian errors $\boldsymbol{\epsilon}_{\mathcal{X}}$ to generate forces and torques $\boldsymbol{\mathcal{F}}$, which are then mapped to actuator forces using the transpose of the inverse Jacobian matrix (2.77).

The plant behavior in Cartesian space, illustrated in Figure 2.116b, reveals interesting characteristics. Some degrees of freedom, particularly the vertical translation and rotation about the vertical axis, exhibit simpler second-order dynamics. A key advantage of this approach is that the control performance can be tuned individually for each direction. This is particularly valuable when performance requirements differ between directions - for instance, when higher positioning accuracy is required vertically than horizontally, or when certain rotational degrees of freedom can tolerate larger errors than others.

However, significant coupling exists between certain degrees of freedom, particularly between rotations and translations (e.g., $\epsilon_{R_x}/\mathcal{F}_y$ or $\epsilon_{D_y}/\mathcal{M}_x$).

For the conceptual validation of the NASS, control in the strut space was selected due to its simpler implementation and the beneficial decoupling properties observed at low frequencies. More sophisticated control strategies will be explored during the detailed design phase.

2.5.4.3 Active Damping with Decentralized IFF

The decentralized Integral Force Feedback (IFF) control strategy is implemented using independent control loops for each strut, similarly to what is shown in Figure 2.114, but using force sensors instead of relative motion sensors.

The corresponding block diagram of the control loop is shown in Figure 2.117, in which the controller $\boldsymbol{K}_{\text{IFF}}(s)$ is a diagonal matrix, where each diagonal element is a pure integrator (2.88).

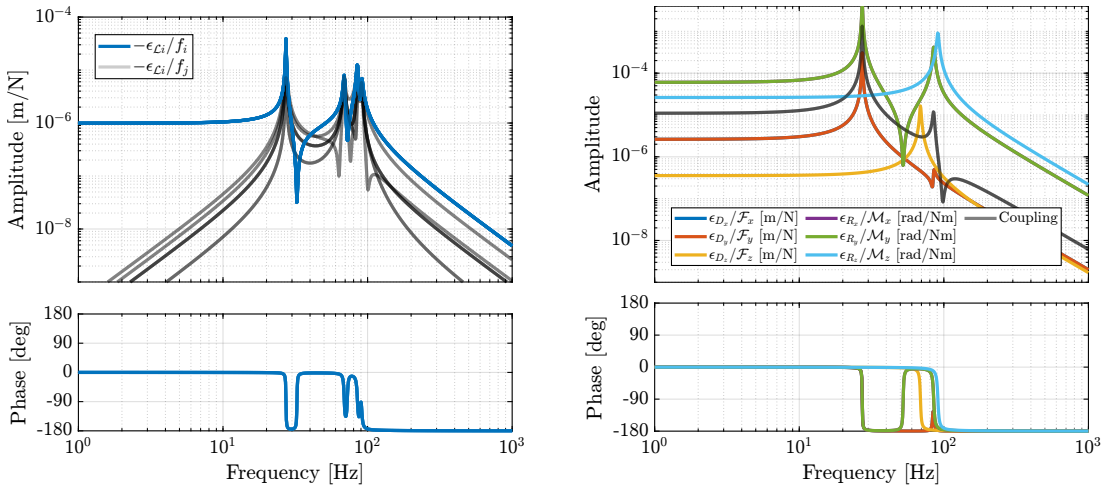

(a) Plant in the frame of the struts

(b) Plant in the Cartesian Frame

Figure 2.116: Bode plots of plants corresponding to the two control strategies shown in Figure 2.115.

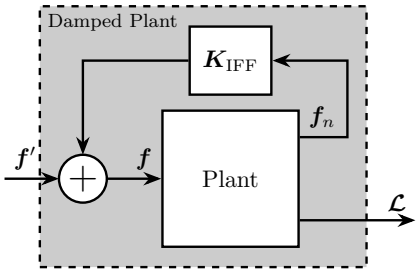

Figure 2.117: Schematic of the implemented decentralized IFF controller. The damped plant has input $\boldsymbol{f}'$.

$$\boldsymbol{K}_{\text{IFF}}(s) = g \cdot \begin{bmatrix} K_{\text{IFF}}(s) & & 0 \\ & \ddots & \\ 0 & & K_{\text{IFF}}(s) \end{bmatrix}, \quad K_{\text{IFF}}(s) = \frac{1}{s} \tag{2.88}$$

In this section, the stiffness in parallel with the force sensor was omitted since the Stewart platform is not subjected to rotation. The effect of this parallel stiffness is examined in the next section when the platform is integrated into the complete NASS.

Root locus analysis, shown in Figure 2.118b, reveals the evolution of the closed-loop poles as the controller gain g varies from 0 to ∞. A key characteristic of force feedback control with collocated sensor-actuator pairs is observed: all closed-loop poles are bounded to the left-half plane, indicating guaranteed stability [114]. This property is particularly valuable because the coupling is very large around resonance frequencies, enabling control of modes that would be difficult to include within the bandwidth using position feedback alone.

The bode plot of an individual loop gain (i.e. the loop gain of $K_{\text{IFF}}(s) \cdot \frac{f_{ni}}{f_i}(s)$), presented in Figure 2.118a, exhibits the typical characteristics of integral force feedback of having a phase bounded between $-90°$ and $90°$. The loop-gain is high around the resonance frequencies, indicating that the decentralized IFF provides significant control authority over these modes. This high gain, combined with the bounded phase, enables effective damping of the resonant modes while maintaining stability.

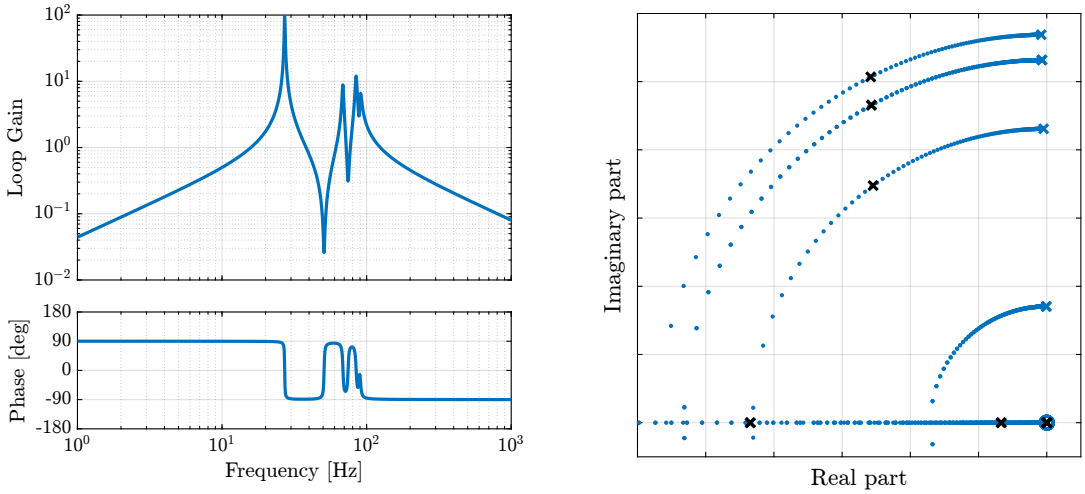

(a) Loop Gain: bode plot of $K_{\text{IFF}}(s)\frac{f_{n1}}{f_1}(s)$

(b) Root locus

Figure 2.118: Decentralized IFF. Loop Gain for an individual controller (a) and root locus (b). Black crosses are indicating the closed-loop poles for the chosen controller gain.

2.5.4.4 High Authority Control / Low Authority Control

The design of the High Authority Control positioning loop is now examined. The complete HAC-IFF control architecture is illustrated in Figure 2.119, where the reference signal $\boldsymbol{r}_{\mathcal{X}}$ represents the desired pose, and $\boldsymbol{\mathcal{X}}$ is the measured pose by the external metrology system.

Following the analysis from Section 2.5.4.2, the control is implemented in the strut space. The Jacobian matrix $\boldsymbol{J}^{-1}$ performs (approximate) real-time approximate inverse kinematics to map position errors from Cartesian space $\boldsymbol{\epsilon}_{\mathcal{X}}$ to strut space $\boldsymbol{\epsilon}_{\mathcal{L}}$. A diagonal High Authority Controller $\boldsymbol{K}_{\text{HAC}}$ then processes these errors in the frame of the struts.

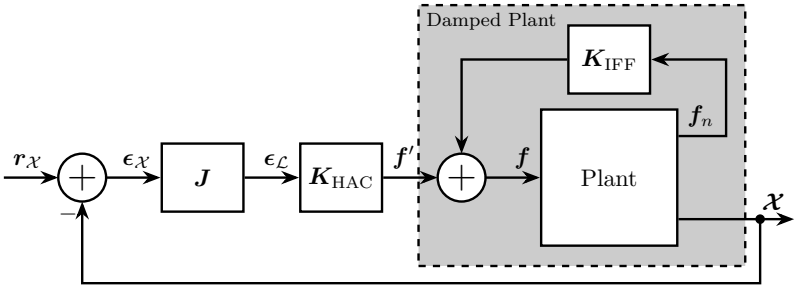

Figure 2.119: HAC-IFF control architecture with the High Authority Controller being implemented in the frame of the struts.

The effect of decentralized IFF on the plant dynamics can be observed by comparing two sets of transfer functions. Figure 2.120a shows the original transfer functions from actuator forces $\boldsymbol{f}$ to strut errors $\boldsymbol{\epsilon}_{\mathcal{L}}$, which are characterized by pronounced resonant peaks. When the decentralized IFF is implemented, the transfer functions from modified inputs $\boldsymbol{f}'$ to strut errors $\boldsymbol{\epsilon}_{\mathcal{L}}$ exhibit significantly attenuated resonances (Figure 2.120b). This damping of structural resonances serves two purposes: it reduces vibrations near resonances and simplifies the design of the high authority controller by providing simpler plant dynamics.

Based upon the damped plant dynamics shown in Figure 2.120b, a high authority controller was designed with the structure given in (2.89). The controller combines three elements: an integrator providing high gain at low frequencies,

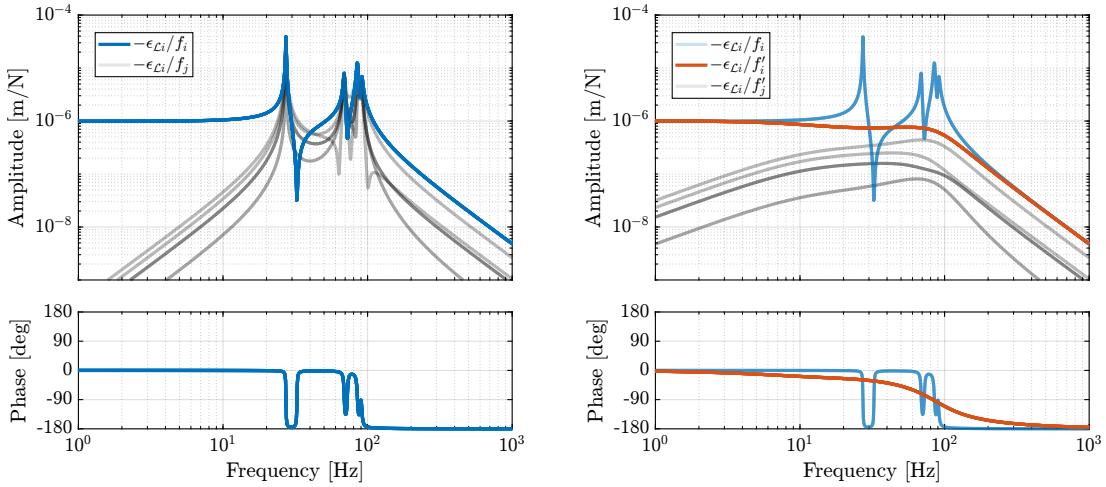

(a) Undamped plant in the frame of the struts

(b) Damped plant with Decentralized IFF

Figure 2.120: Plant in the frame of the strut for the High Authority Controller.

a lead compensator improving stability margins, and a low-pass filter for robustness against unmodelled high-frequency dynamics. The loop gain of an individual control channel is shown in Figure 2.121a.

$$\boldsymbol{K}_{\text{HAC}}(s) = \begin{bmatrix} K_{\text{HAC}}(s) & & 0 \\ & \ddots & \\ 0 & & K_{\text{HAC}}(s) \end{bmatrix}, \quad K_{\text{HAC}}(s) = g_0 \cdot \underbrace{\frac{\omega_c}{s}}_{\text{int}} \cdot \underbrace{\frac{1}{\sqrt{\alpha}} \frac{1 + \frac{s}{\omega_c/\sqrt{\alpha}}}{1 + \frac{s}{\omega_c\sqrt{\alpha}}}}_{\text{lead}} \cdot \underbrace{\frac{1}{1 + \frac{s}{\omega_0}}}_{\text{LPF}} \tag{2.89}$$

The stability of the MIMO feedback loop is analyzed through the *characteristic loci* method. Such characteristic loci represent the eigenvalues of the loop gain matrix $\boldsymbol{G}(j\omega)\boldsymbol{K}(j\omega)$ plotted in the complex plane as the frequency varies from 0 to ∞. For MIMO systems, this method generalizes the classical Nyquist stability criterion: with the open-loop system being stable, the closed-loop system is stable if none of the characteristic loci encircle the -1 point [134]. As shown in Figure 2.121b, all loci remain to the right of the -1 point, validating the stability of the closed-loop system. Additionally, the distance of the loci from the -1 point provides information about stability margins of the coupled system.

2.5.4.5 Conclusion

The control architecture developed for the uniaxial and the rotating models was adapted for the Stewart platform.

Two fundamental choices were first addressed: the selection between centralized and decentralized approaches and the choice of control space. While control in Cartesian space enables direction-specific performance tuning, implementation in strut space was selected for the conceptual design phase due to two key advantages: good decoupling at low frequencies and identical diagonal terms in the plant transfer functions, allowing a single controller design to be replicated across all struts.

The HAC-LAC strategy was then implemented. The inner loop implements decentralized Integral Force Feedback for active damping. The collocated nature of the force sensors ensures stability despite strong coupling between struts at

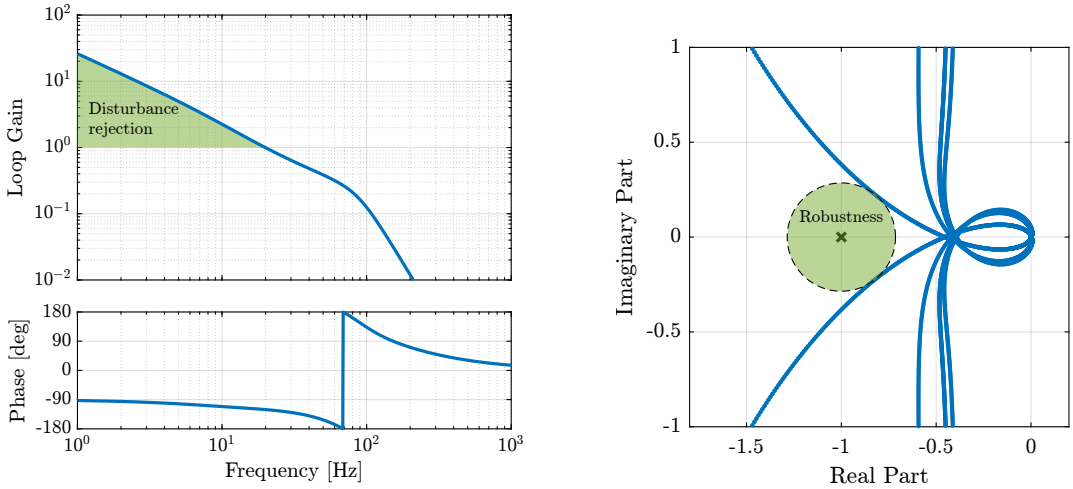

(a) Loop Gain

(b) Characteristic Loci

Figure 2.121: Decentralized HAC-IFF. Loop gain (a) is used for the design of the controller and to estimate the disturbance rejection level. Characteristic Loci (b) is used to verify the stability and robustness of the feedback loop.

resonance frequencies, enabling effective damping of structural modes. The outer loop implements High Authority Control, enabling precise positioning of the mobile platform.

Conclusion

After evaluating various architectures, the Stewart platform was selected for the active platform. The parallel kinematic structure offers superior dynamical characteristics, and its compact design satisfies the strict space constraints of the NASS. The extensive literature on Stewart platforms, including kinematic analysis, dynamic modeling and control, provides a robust theoretical foundation for this choice.

A configurable multi-body model of the Stewart platform was developed and validated against analytical equations. The modular nature of the model allows for progressive refinement of individual components (plates, joints and actuators) and geometry, making it a valuable tool throughout the development process. The validated model will be integrated into the broader multi-body representation of the micro-station, enabling comprehensive analysis of the complete NASS.

The use of this model extends beyond the current conceptual phase. It will serve as a crucial tool during the detailed design phase, where it will be used to optimize the design and guide the development of sophisticated control strategies. Furthermore, during the experimental phase, it will provide a theoretical framework for comparing and understanding measured dynamics.

The control aspects of the Stewart platform were addressed with particular attention to the challenges posed by its multi-input multi-output nature. Although the coupled dynamics of the system suggest the potential benefit of advanced control strategies, a simplified architecture was proposed for the validation of the NASS concept. This approach combines decentralized Integral Force Feedback for active damping with High Authority Control for positioning, which was implemented in the strut space to leverage the natural decoupling observed at low frequencies.

This study establishes the theoretical framework necessary for the subsequent development and validation of the NASS.

2.6 Validation of the NASS Concept

The previous chapters have established crucial foundational elements for the development of the Nano Active Stabilization System (NASS). The uniaxial model study demonstrated that very stiff active platform configurations should be avoided due to their high coupling with the micro-station dynamics. A rotating three-degree-of-freedom model revealed that soft active platform designs prove unsuitable due to gyroscopic effect induced by the spindle rotation. To further improve the model accuracy, a multi-body model of the micro-station was developed, which was carefully tuned using experimental modal analysis. Furthermore, a multi-body model of the active platform was created, that can then be seamlessly integrated with the micro-station model, as illustrated in Figure 2.122.

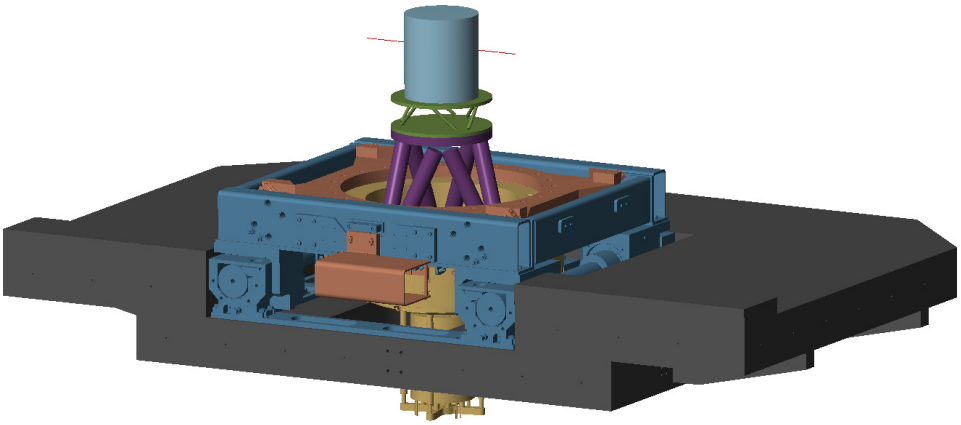

Figure 2.122: 3D view of the NASS multi-body model.

Building upon these foundations, this chapter presents the validation of the NASS concept. The investigation begins with the previously established active platform model with actuator stiffness $k_a = 1\,\mathrm{N}/\mu\mathrm{m}$. A thorough examination of the control kinematics is presented in Section 2.6.1, detailing how both external metrology and active platform internal sensors are used in the control architecture. The control strategy is then implemented in two steps: first, the decentralized IFF is used for active damping (Section 2.6.2), then a High Authority Control is develop to stabilize the sample's position in a large bandwidth (Section 2.6.3).

The robustness of the proposed control scheme was evaluated under various operational conditions. Particular attention was paid to system performance under changing payload masses and varying spindle rotational velocities.

This chapter concludes the conceptual design phase, with the simulation of tomography experiments providing strong evidence for the viability of the proposed NASS architecture.

2.6.1 Control Kinematics

Figure 2.123 presents a schematic overview of the NASS. This section focuses on the components of the "Instrumentation and Real-Time Control" block.

As established in the previous section on Stewart platforms, the proposed control strategy combines Decentralized Integral Force Feedback with a High Authority Controller performed in the frame of the struts.

For the Nano Active Stabilization System, computing the positioning errors in the frame of the struts involves three key steps. First, desired sample pose with respect to a fixed reference frame is computed using the micro-station kinematics as detailed in Section 2.6.1.1. This fixed frame is located at the X-ray beam focal point, as it is where the PoI needs to be

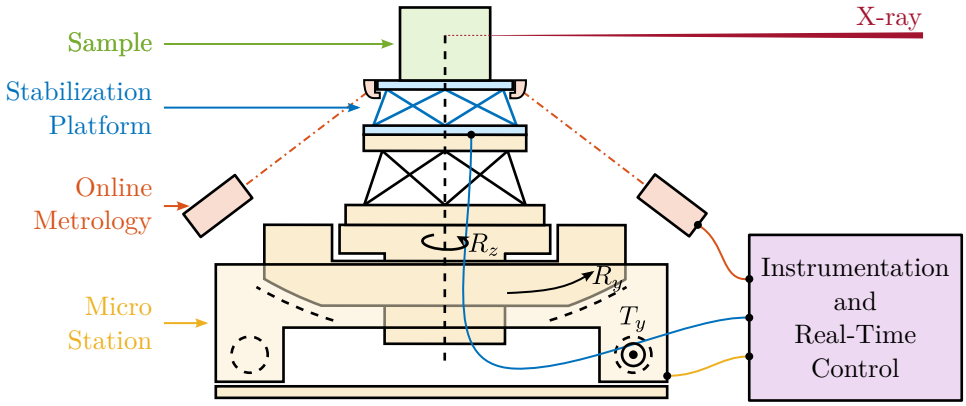

Figure 2.123: Schematic of the Nano Active Stabilization System.

positioned. Second, it measures the actual sample pose relative to the same fix frame, described in Section 2.6.1.2. Finally, it determines the sample pose error and maps these errors to the active platform struts, as explained in Section 2.6.1.3.

The complete control architecture is described in Section 2.6.1.4.

2.6.1.1 Micro Station Kinematics

The micro-station kinematics enables the computation of the desired sample pose from the reference signals of each micro-station stage. These reference signals consist of the desired lateral position r_{D_y}, tilt angle r_{R_y}, and spindle angle r_{R_z}. The hexapod pose is defined by six parameters: three translations ($r_{D_{\mu x}}$, $r_{D_{\mu y}}$, $r_{D_{\mu z}}$) and three rotations ($r_{\theta_{\mu x}}$, $r_{\theta_{\mu y}}$, $r_{\theta_{\mu z}}$).

Using these reference signals, the desired sample position relative to the fixed frame is expressed through the homogeneous transformation matrix $\boldsymbol{T}_{\mu\text{-station}}$, as defined in equation (2.90).

$$\boldsymbol{T}_{\mu\text{-station}} = \boldsymbol{T}_{D_y} \cdot \boldsymbol{T}_{R_y} \cdot \boldsymbol{T}_{R_z} \cdot \boldsymbol{T}_{\text{hexapod}} \tag{2.90}$$

$$\begin{aligned}
\boldsymbol{T}_{D_y} &= \begin{bmatrix} 1 & 0 & 0 & 0 \\ 0 & 1 & 0 & r_{D_y} \\ 0 & 0 & 1 & 0 \\ 0 & 0 & 0 & 1 \end{bmatrix} \quad \boldsymbol{T}_{\text{hexapod}} = \left[\begin{array}{ccc|c} & \boldsymbol{R}_x(r_{\theta_{\mu x}})\boldsymbol{R}_y(r_{\theta_{\mu y}})\boldsymbol{R}_z(r_{\theta_{\mu z}}) & & \begin{matrix} r_{D_{\mu x}} \\ r_{D_{\mu y}} \\ r_{D_{\mu z}} \end{matrix} \\ \hline 0 & 0 & 0 & 1 \end{array}\right] \\
\boldsymbol{T}_{R_z} &= \begin{bmatrix} \cos(r_{R_z}) & -\sin(r_{R_z}) & 0 & 0 \\ \sin(r_{R_z}) & \cos(r_{R_z}) & 0 & 0 \\ 0 & 0 & 1 & 0 \\ 0 & 0 & 0 & 1 \end{bmatrix} \quad \boldsymbol{T}_{R_y} = \begin{bmatrix} \cos(r_{R_y}) & 0 & \sin(r_{R_y}) & 0 \\ 0 & 1 & 0 & 0 \\ -\sin(r_{R_y}) & 0 & \cos(r_{R_y}) & 0 \\ 0 & 0 & 0 & 1 \end{bmatrix}
\end{aligned} \tag{2.91}$$

2.6.1.2 Computation of the Sample's Pose Error

The external metrology system measures the sample position relative to the fixed granite. Due to the system's symmetry, this metrology provides measurements for 5-DoF: three translations (D_x, D_y, D_z) and two rotations (R_x, R_y).

The sixth DoF (R_z) is still required to compute the errors in the frame of the active platform struts (i.e. to compute the active platform inverse kinematics). This R_z rotation is estimated by combining measurements from the spindle encoder and the active platform's internal metrology. The active platform's metrology consists of relative motion sensors in each strut, such that the R_z rotation of the active platform can be estimated by solving the forward kinematics (2.74). Note that the positioning hexapod is not used for R_z rotation, and is therefore ignored for R_z estimation.

The measured sample pose is represented by the homogeneous transformation matrix $\boldsymbol{T}_{\text{sample}}$, as shown in equation (2.92).

$$\boldsymbol{T}_{\text{sample}} = \left[\begin{array}{ccc|c} & \boldsymbol{R}_x(R_x)\boldsymbol{R}_y(R_y)\boldsymbol{R}_z(R_z) & & \begin{matrix}D_x\\D_y\\D_z\end{matrix} \\ \hline 0 & 0 & 0 & 1 \end{array}\right] \tag{2.92}$$

2.6.1.3 Position Error in the Frame of the Struts

The homogeneous transformation formalism enables straightforward computation of the sample position error. This computation involves the previously computed homogeneous 4×4 matrices: $\boldsymbol{T}_{\mu\text{-station}}$ representing the desired pose, and $\boldsymbol{T}_{\text{sample}}$ representing the measured pose. Their combination yields $\boldsymbol{T}_{\text{error}}$, which expresses the position error of the sample in the frame of the rotating active platform, as shown in equation (2.93).

$$\boldsymbol{T}_{\text{error}} = \boldsymbol{T}_{\mu\text{-station}}^{-1} \cdot \boldsymbol{T}_{\text{sample}} \tag{2.93}$$

The known structure of the homogeneous transformation matrix facilitates efficient real-time inverse computation. From $\boldsymbol{T}_{\text{error}}$, the position and orientation errors $\boldsymbol{\epsilon}_{\mathcal{X}} = [\epsilon_{D_x},\ \epsilon_{D_y},\ \epsilon_{D_z},\ \epsilon_{R_x},\ \epsilon_{R_y},\ \epsilon_{R_z}]$ of the sample are extracted using equation (2.94):

$$\begin{aligned}
\epsilon_{D_x} &= \boldsymbol{T}_{\text{error}}(1,4) \\
\epsilon_{D_y} &= \boldsymbol{T}_{\text{error}}(2,4) \\
\epsilon_{D_z} &= \boldsymbol{T}_{\text{error}}(3,4) \\
\epsilon_{R_y} &= \text{atan2}(\boldsymbol{T}_{\text{error}}(1,3), \sqrt{\boldsymbol{T}_{\text{error}}(1,1)^2 + \boldsymbol{T}_{\text{error}}(1,2)^2}) \\
\epsilon_{R_x} &= \text{atan2}(-\boldsymbol{T}_{\text{error}}(2,3)/\cos(\epsilon_{R_y}), \boldsymbol{T}_{\text{error}}(3,3)/\cos(\epsilon_{R_y})) \\
\epsilon_{R_z} &= \text{atan2}(-\boldsymbol{T}_{\text{error}}(1,2)/\cos(\epsilon_{R_y}), \boldsymbol{T}_{\text{error}}(1,1)/\cos(\epsilon_{R_y}))
\end{aligned} \tag{2.94}$$

Finally, these errors are mapped to the strut space using the active platform Jacobian matrix (2.95).

$$\boldsymbol{\epsilon}_{\mathcal{L}} = \boldsymbol{J} \cdot \boldsymbol{\epsilon}_{\mathcal{X}} \tag{2.95}$$

2.6.1.4 Control Architecture - Summary

The complete control architecture is summarized in Figure 2.124. The sample pose is measured using external metrology for 5-DoF, while the sixth DoF (R_z) is estimated by combining measurements from the active platform encoders and spindle encoder.

The sample reference pose is determined by the reference signals of the translation stage, tilt stage, spindle, and positioning hexapod. The position error computation follows a two-step process: first, homogeneous transformation matrices are used to determine the error in the active platform frame. Then, the Jacobian matrix $\boldsymbol{J}$ maps these errors to individual strut coordinates.

For control purposes, force sensors mounted on each strut are used in a decentralized manner for active damping, as detailed in Section 2.6.2. Then, the high authority controller uses the computed errors in the frame of the struts to provides real-time stabilization of the sample position (Section 2.6.3).

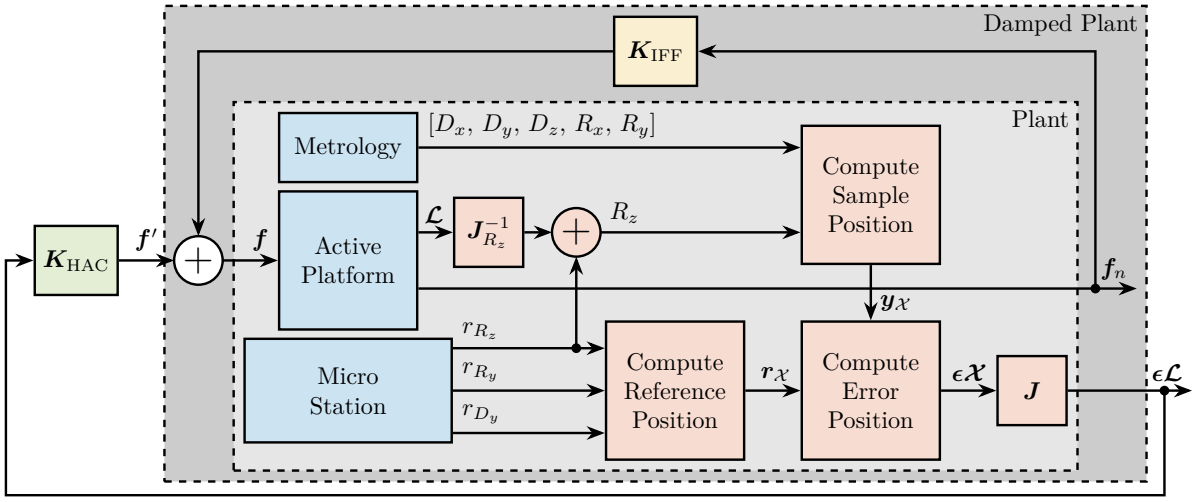

Figure 2.124: Control architecture for the NASS. Physical systems are shown in blue, control kinematics elements in red, decentralized Integral Force Feedback controller in yellow, and centralized high authority controller in green.

2.6.2 Decentralized Active Damping

Building on the uniaxial model study, this section implements decentralized Integral Force Feedback (IFF) as the first component of the HAC-LAC strategy. The springs in parallel to the force sensors were used to guarantee the control robustness, as observed with the 3-DoF rotating model. The objective here is to design a decentralized IFF controller that provides good damping of the active platform modes across payload masses ranging from 1 to 50 kg and rotational velocity up to 360 deg/s. The payloads used for validation have a cylindrical shape with 250 mm height and with masses of 1 kg, 25 kg, and 50 kg.

2.6.2.1 IFF Plant

Transfer functions from actuator forces f_i to force sensor measurements f_{mi} are computed using the multi-body model. Figure 2.125 examines how parallel stiffness affects plant dynamics, with identification performed at maximum spindle velocity $\Omega_z = 360$ deg/s and with a payload mass of 25 kg.

Without parallel stiffness (Figure 2.125a), the plant dynamics exhibits non-minimum phase zeros at low frequency, confirming predictions from the three-degree-of-freedom rotating model. Adding parallel stiffness (Figure 2.125b) transforms these into minimum phase complex conjugate zeros, enabling unconditionally stable decentralized IFF implementation.

Although both cases show significant coupling around the resonances, stability is guaranteed by the collocated arrangement of the actuators and sensors [114].

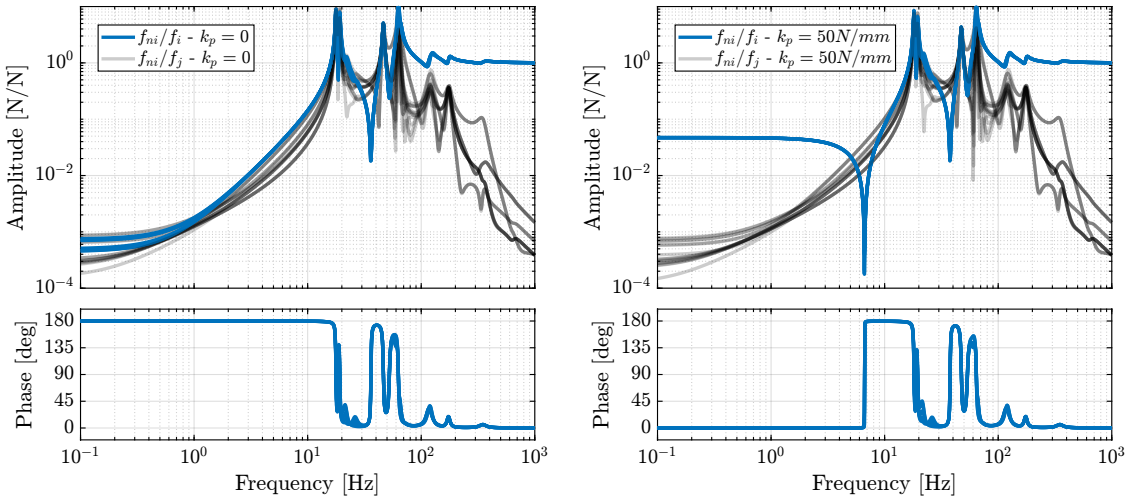

(a) without parallel stiffness

(b) with parallel stiffness

Figure 2.125: Effect of stiffness in parallel with the force sensor on the IFF plant with $\Omega_z = 360$ deg/s and a payload mass of 25 kg. The dynamics without parallel stiffness has non-minimum phase zeros at low frequency (a). The added parallel stiffness transforms the non-minimum phase zeros into complex conjugate zeros (b).

The effect of rotation, as shown in Figure 2.126a, is negligible as the actuator stiffness ($k_a = 1$ N/µm) is large compared to the negative stiffness induced by gyroscopic effects (estimated from the 3-DoF rotating model).

Figure 2.126b illustrate the effect of payload mass on the plant dynamics. The poles and zeros shift in frequency as the payload mass varies. However, their alternating pattern is preserved, which ensures the phase remains bounded between 0 and 180 degrees, thus maintaining good robustness.

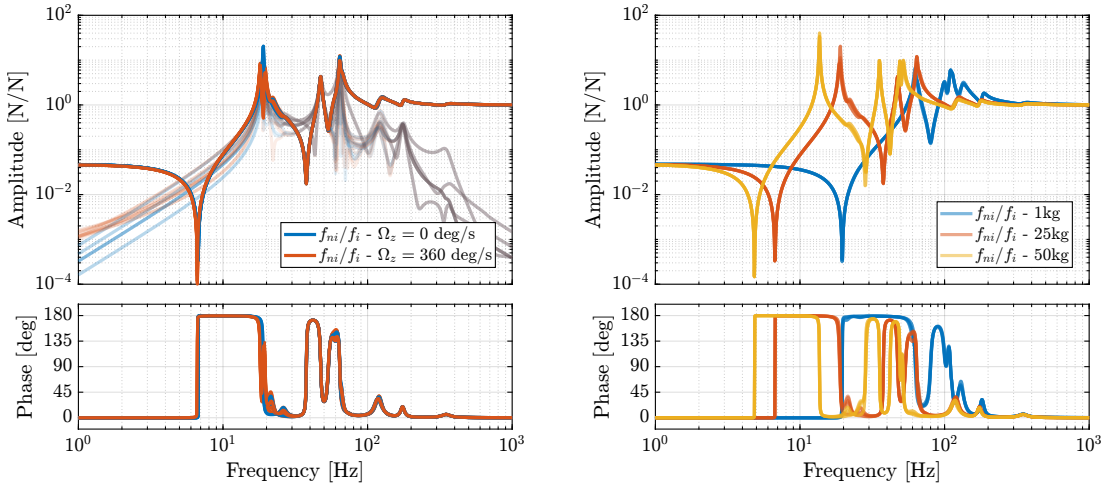

(a) Effect of Spindle rotation

(b) Effect of payload mass

Figure 2.126: Effect of the Spindle's rotational velocity on the IFF plant (a) and effect of the payload's mass on the IFF plant (b).

2.6.2.2 Controller Design

The previous analysis using the 3-DoF rotating model showed that decentralized Integral Force Feedback (IFF) with pure integrators is unstable due to the gyroscopic effects caused by spindle rotation. This finding was also confirmed with the multi-body model of the NASS: the system was unstable when using pure integrators and without parallel stiffness.

This instability can be mitigated by introducing sufficient stiffness in parallel with the force sensors. However, as illustrated in Figure 2.125b, adding parallel stiffness increases the low frequency gain. Using pure integrators would result in high loop gain at low frequencies, adversely affecting the damped plant dynamics, which is undesirable. To resolve this issue, a second-order high-pass filter is introduced to limit the low frequency gain, as shown in Equation (2.96).

$$\boldsymbol{K}_{\text{IFF}}(s) = g \cdot \begin{bmatrix} K_{\text{IFF}}(s) & & 0 \\ & \ddots & \\ 0 & & K_{\text{IFF}}(s) \end{bmatrix}, \quad K_{\text{IFF}}(s) = \frac{1}{s} \cdot \frac{\frac{s^2}{\omega_z^2}}{\frac{s^2}{\omega_z^2} + 2\xi_z \frac{s}{\omega_z} + 1} \tag{2.96}$$

The cut-off frequency of the second-order high-pass filter was tuned to be below the frequency of the complex conjugate zero for the highest mass, which is at 5 Hz. The overall gain was then increased to obtain a large loop gain around the resonances to be damped, as illustrated in Figure 2.127.

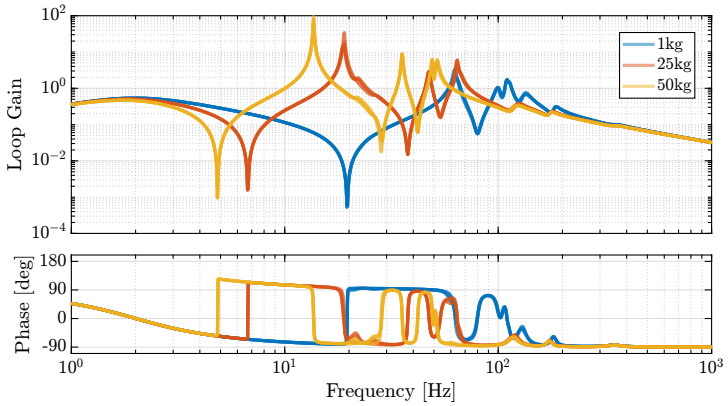

Figure 2.127: Loop gain for the decentralized IFF: $K_{\text{IFF}}(s) \cdot \frac{f_{mi}}{f_i}(s)$.

To verify stability, the root loci for the three payload configurations were computed, as shown in Figure 2.128. The results demonstrate that the closed-loop poles remain within the left-half plane, indicating the robustness of the applied decentralized IFF.

2.6.3 Centralized Active Vibration Control

The implementation of high-bandwidth position control for the active platform presents several technical challenges. The plant dynamics exhibits complex behavior influenced by multiple factors, including payload mass, rotational velocity, and the mechanical coupling between the active platform and the micro-station. This section presents the development and validation of a centralized control strategy designed to achieve precise sample positioning during high-speed tomography experiments.

First, a comprehensive analysis of the plant dynamics is presented in Section 2.6.3.1, examining the effects of spindle rotation, payload mass variation, and the implementation of Integral Force Feedback (IFF). Section 2.6.3.2 validates

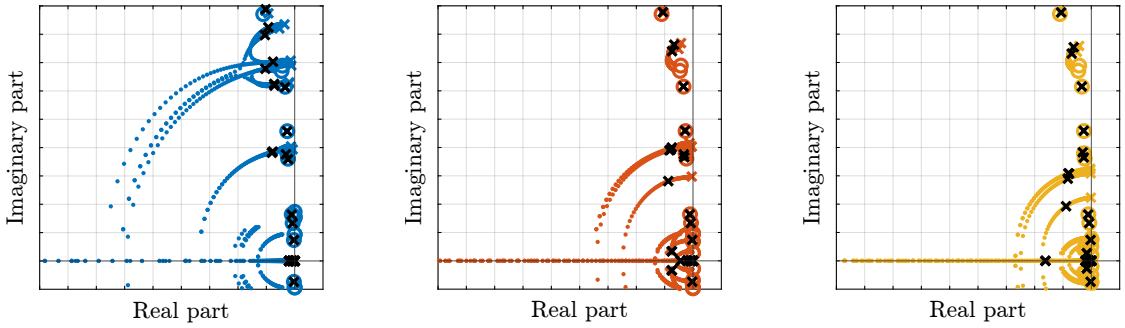

(a) 1 kg **(b)** 25 kg **(c)** 50 kg

Figure 2.128: Root loci for decentralized IFF for three payload masses. The closed-loop poles are shown by the black crosses.

previous modeling predictions that both overly stiff and compliant active platform configurations lead to degraded performance. Building upon these findings, Section 2.6.3.3 presents the design of a robust high-authority controller that maintains stability across varying payload masses while achieving the desired control bandwidth.

The performance of the developed control strategy was validated through simulations of tomography experiments in Section 2.6.3.4. These simulations included realistic disturbance sources and were used to evaluate the system performance against the stringent positioning requirements imposed by future beamline specifications. Particular attention was paid to the system's behavior under maximum rotational velocity conditions and its ability to accommodate varying payload masses, demonstrating the practical viability of the proposed control approach.

2.6.3.1 HAC Plant

The plant dynamics from force inputs $\boldsymbol{f}$ to the strut errors $\boldsymbol{\epsilon}_{\mathcal{L}}$ were first extracted from the multi-body model without the implementation of the decentralized IFF. The influence of spindle rotation on plant dynamics was investigated, and the results are presented in Figure 2.129a. While rotational motion introduces coupling effects at low frequencies, these effects remain minimal at operational velocities, owing to the high stiffness characteristics of the active platform assembly.

Payload mass emerged as a significant parameter affecting system behavior, as illustrated in Figure 2.129b. As expected, increasing the payload mass decreased the resonance frequencies while amplifying coupling at low frequency. These mass-dependent dynamic changes present considerable challenges for control system design, particularly for configurations with high payload masses.

Additional operational parameters were systematically evaluated, including the R_y tilt angle, R_z spindle position, and positioning hexapod position. These factors were found to exert negligible influence on the plant dynamics, which can be attributed to the effective mechanical decoupling achieved between the plant and micro-station dynamics. This decoupling characteristic ensures consistent performance across various operational configurations. This also validates the developed control strategy.

The Decentralized Integral Force Feedback was implemented in the multi-body model, and transfer functions from force inputs $\boldsymbol{f}'$ of the damped plant to the strut errors $\boldsymbol{\epsilon}_{\mathcal{L}}$ were extracted from this model.

The effectiveness of the IFF implementation was first evaluated with a 1 kg payload, as demonstrated in Figure 2.130a. The results indicate successful damping of the active platform resonance modes, although a minor increase in low-

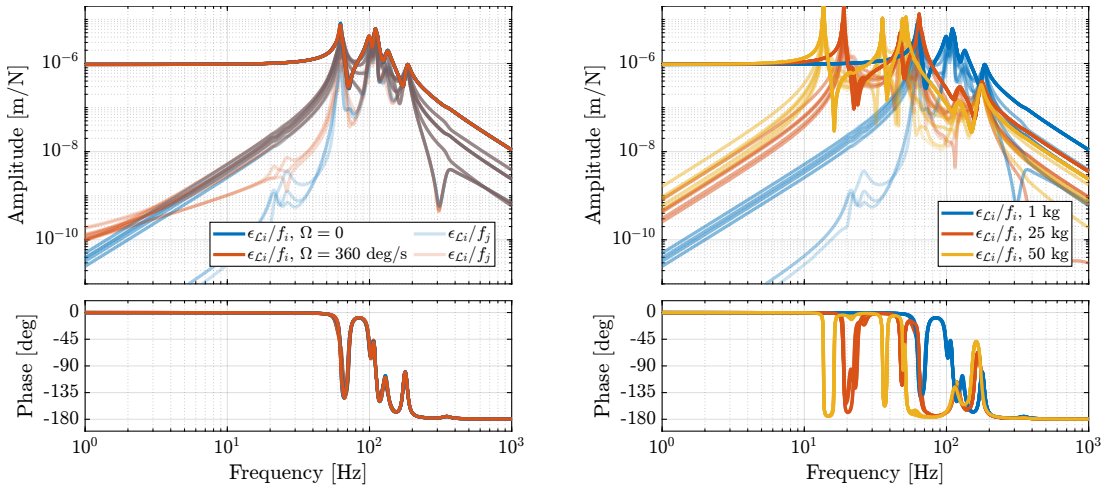

(a) Effect of rotational velocity Ω_z

(b) Effect of payload's mass

Figure 2.129: Effect of the Spindle's rotational velocity on the positioning plant (a) and effect of the payload's mass on the positioning plant (b).

frequency coupling was observed. This trade-off was considered acceptable, given the overall improvement in system behavior.

The benefits of IFF implementation were further assessed across the full range of payload configurations, and the results are presented in Figure 2.130b. For all tested payloads (1 kg, 25 kg and 50 kg), the decentralized IFF significantly damped the active platform modes and therefore simplified the system dynamics. More importantly, in the vicinity of the desired high authority control bandwidth (i.e. between 10 Hz and 50 Hz), the damped dynamics (shown in red) exhibited minimal gain and phase variations with frequency. For the undamped plants (shown in blue), achieving robust control with bandwidth above 10 Hz while maintaining stability across different payload masses would be practically impossible.

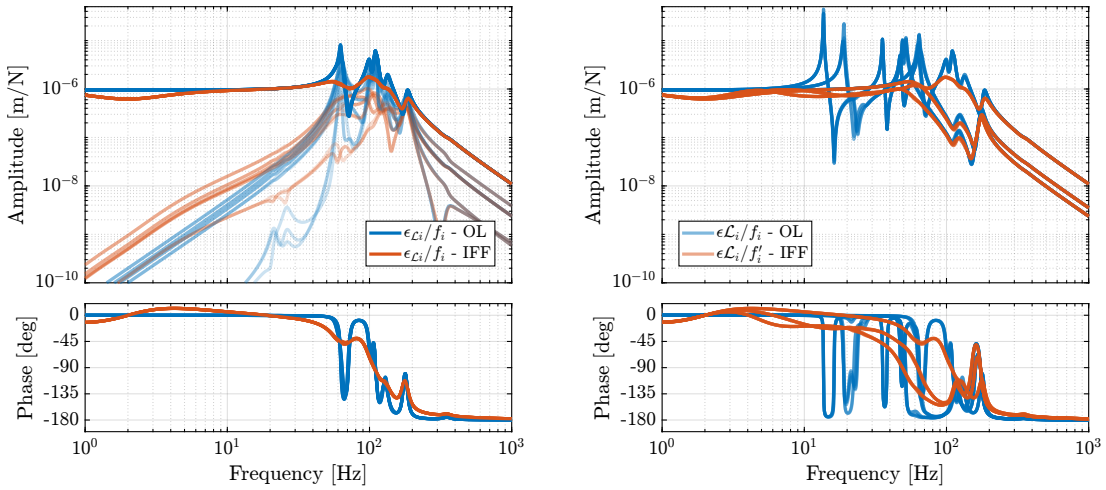

(a) Effect of IFF - $m = 1$ kg

(b) Effect of IFF on the set of plants to control

Figure 2.130: Effect of decentralized Integral Force Feedback on the positioning plant for a 1 kg sample mass (a). Direct terms are shown by solid lines while coupling terms are shown by shaded lines. The direct terms of the positioning plants for all considered payloads are shown in (b).

The coupling between the active platform and the micro-station was evaluated through a comparative analysis of plant dynamics under two mounting conditions. In the first configuration, the active platform was mounted on an ideally rigid support, while in the second configuration, it was installed on the micro-station with finite compliance.

As illustrated in Figure 2.131, the complex dynamics of the micro-station were found to have little impact on the plant dynamics. The only observable difference manifests as additional alternating poles and zeros above 100 Hz, a frequency range sufficiently beyond the control bandwidth to avoid interference with the system performance. This result confirms effective dynamic decoupling between the active platform and the supporting micro-station structure.

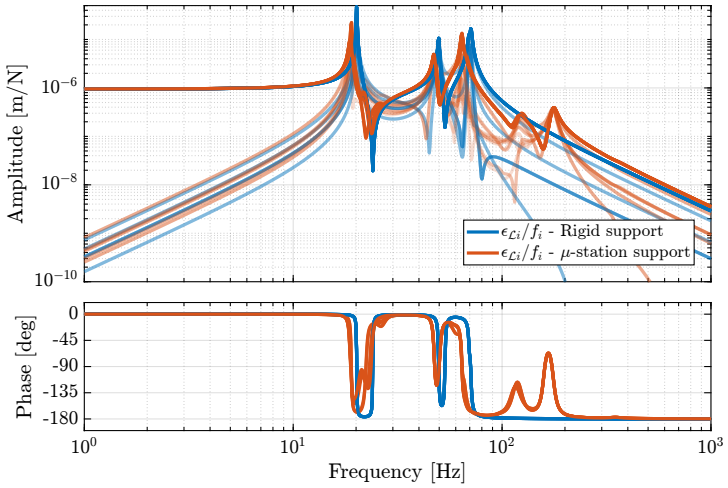

Figure 2.131: Effect of the micro-station limited compliance on the plant dynamics.

2.6.3.2 Effect of Active Platform Stiffness on System Dynamics

The influence of active platform stiffness was investigated to validate earlier findings from simplified uniaxial and three-degrees-of-freedom (3-DoF) models. These models suggest that a moderate stiffness of approximately 1 N/µm would provide better performance than either very stiff or very soft configurations.

For the stiff active platform analysis, a system with an actuator stiffness of 100 N/µm was simulated with a 25 kg payload. The transfer function from $\boldsymbol{f}$ to $\boldsymbol{\epsilon}_{\mathcal{L}}$ was evaluated under two conditions: mounting on an infinitely rigid base and mounting on the micro-station. As shown in Figure 2.132a, significant coupling was observed between the active platform and micro-station dynamics. This coupling introduces complex behavior that is difficult to model and predict accurately, thus corroborating the predictions of the simplified uniaxial model.

The soft active platform configuration was evaluated using a stiffness of 0.01 N/µm with a 25 kg payload. The dynamic response was characterized at three rotational velocities: 0, 36, and 360 deg/s. Figure 2.132b demonstrates that rotation substantially affects system dynamics, manifesting as instability at high rotational velocities, increased coupling due to gyroscopic effects, and rotation-dependent resonance frequencies. The current approach of controlling the position in the strut frame is inadequate for soft active platforms; but even shifting control to a frame matching the payload's Center of Mass would not overcome the substantial coupling and dynamic variations induced by gyroscopic effects.

2.6.3.3 Controller Design

A high authority controller was designed to meet two key requirements: stability for all payload masses (i.e. for all the damped plants of Figure 2.130b), and achievement of sufficient bandwidth (targeted at 10 Hz) for high performance op-

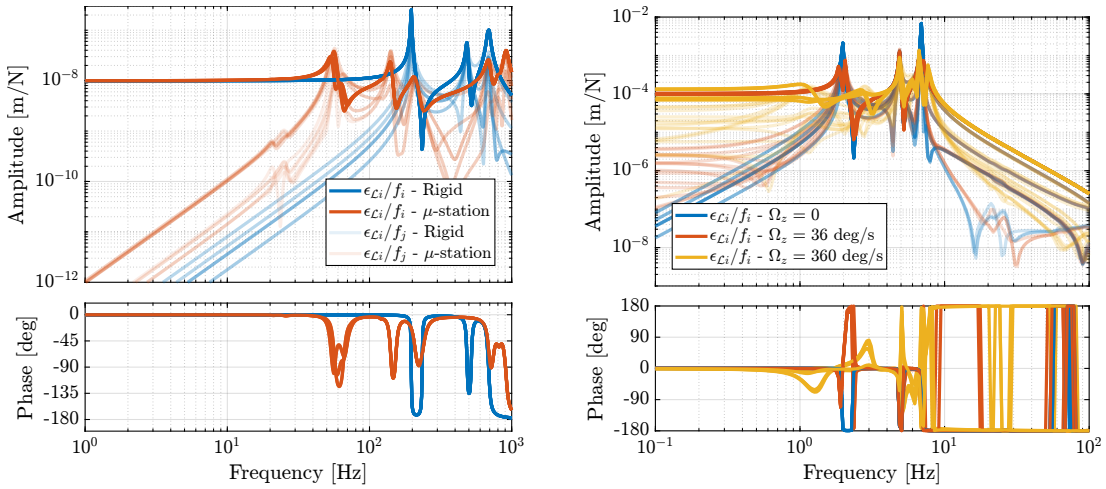

(a) $k_a = 100\,\mathrm{N/\mu m}$ - Coupling with the micro-station

(b) $k_a = 0.01\,\mathrm{N/\mu m}$ - Effect of Spindle rotation

Figure 2.132: Coupling between a stiff active platform ($k_a = 100\,\mathrm{N/\mu m}$) and the micro-station (a). Large effect of the spindle rotational velocity for a soft ($k_a = 0.01\,\mathrm{N/\mu m}$) active platform (b).

eration. The controller structure is defined in equation (2.97), incorporating an integrator term for low frequency performance, a lead compensator for phase margin improvement, and a low-pass filter for robustness against high-frequency modes.

$$K_{\text{HAC}}(s) = g_0 \cdot \underbrace{\frac{\omega_c}{s}}_{\text{int}} \cdot \underbrace{\frac{1}{\sqrt{\alpha}} \frac{1 + \frac{s}{\omega_c/\sqrt{\alpha}}}{1 + \frac{s}{\omega_c\sqrt{\alpha}}}}_{\text{lead}} \cdot \underbrace{\frac{1}{1 + \frac{s}{\omega_0}}}_{\text{LPF}}, \quad (\omega_c = 2\pi 10\,\text{rad/s},\ \alpha = 2,\ \omega_0 = 2\pi 80\,\text{rad/s}) \tag{2.97}$$

The controller performance was evaluated through two complementary analyses. First, the decentralized loop gain shown in Figure 2.133a, confirms the achievement of the desired 10 Hz bandwidth. Second, the characteristic loci analysis presented in Figure 2.133b demonstrates robustness for all payload masses, with adequate stability margins maintained throughout the operating envelope.

2.6.3.4 Tomography Experiment

The Nano Active Stabilization System concept was validated through time-domain simulations of scientific experiments, with a particular focus on tomography scanning because of its demanding performance requirements. Simulations were conducted at the maximum operational rotational velocity of $\Omega_z = 360$ deg/s to evaluate system performance under the most challenging conditions.

Performance metrics were established based on anticipated future beamline specifications, which specify a beam size of 200 nm (horizontal) by 100 nm (vertical). The primary requirement stipulates that the PoI must remain within beam dimensions throughout operation. The simulation included two principal disturbance sources: ground motion and spindle vibrations. Additional noise sources, including measurement noise and electrical noise from Digital to Analog Converter (DAC) and voltage amplifiers, were not included in this analysis, as these parameters will be optimized during the detailed design phase.

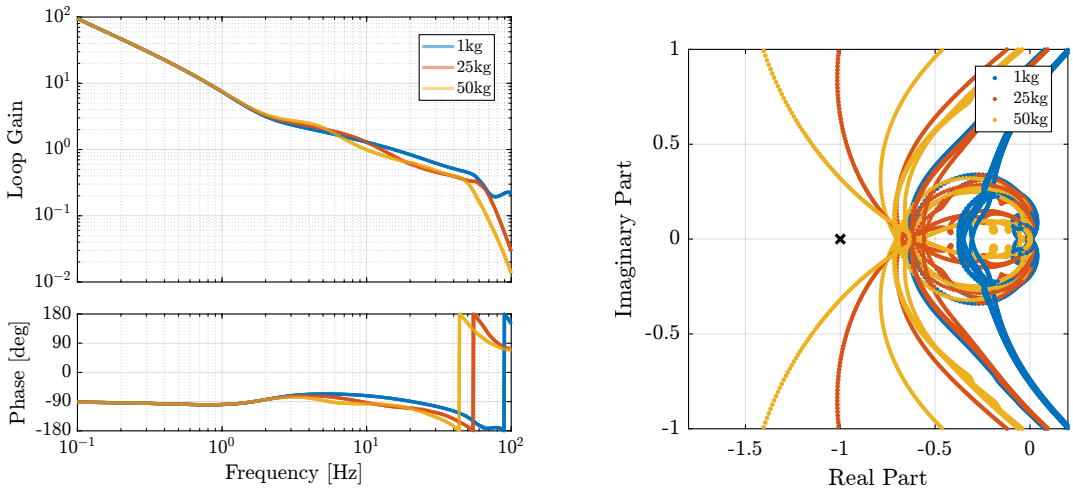

(a) Loop Gain **(b)** Characteristic Loci

Figure 2.133: High Authority Controller - "Diagonal Loop Gain" (a) and Characteristic Loci (b).

Figure 2.134 presents a comparative analysis of positioning errors under both open-loop and closed-loop conditions for a lightweight sample configuration (1 kg). The results demonstrate the system's capability to maintain the sample's position within the specified beam dimensions, thus validating the fundamental concept of the stabilization system.

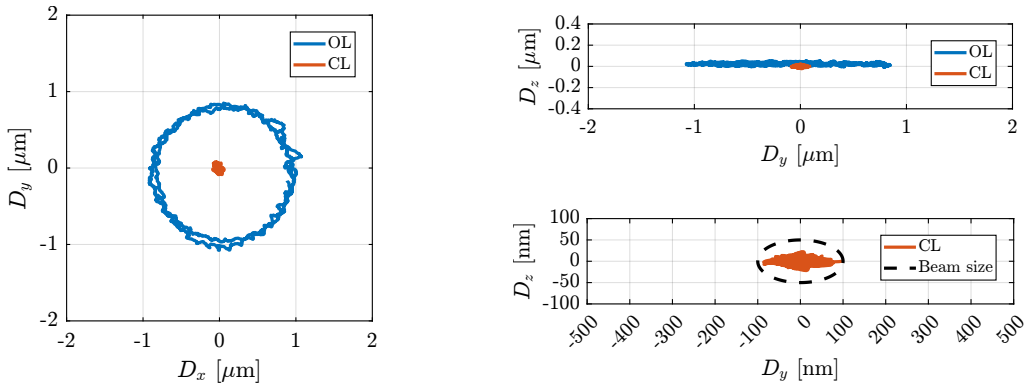

(a) XY plane **(b)** YZ plane

Figure 2.134: Position error of the sample in the XY (a) and YZ (b) planes during a simulation of a tomography experiment at 360 deg/s. 1 kg payload is placed on top of the active platform.

The robustness of the NASS to payload mass variation was evaluated through additional tomography scan simulations with 25 and 50 kg payloads, complementing the initial 1 kg test case. As illustrated in Figure 2.135, system performance exhibits some degradation with increasing payload mass, which is consistent with predictions from the control analysis. While the positioning accuracy for heavier payloads is outside the specified limits, it remains within acceptable bounds for typical operating conditions.

It should be noted that the maximum rotational velocity of 360 deg/s is primarily intended for lightweight payload applications. For higher mass configurations, rotational velocities are expected to be below 36 deg/s.

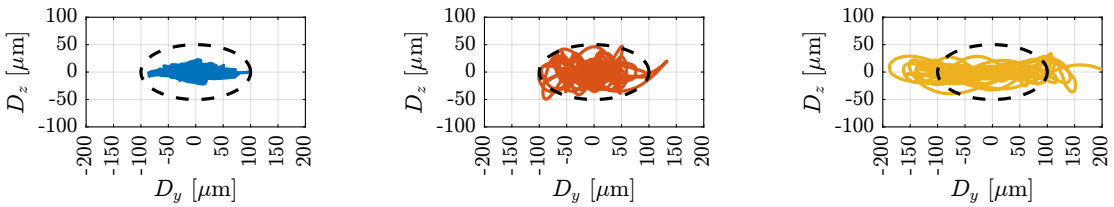

(a) $m = 1\,\text{kg}$ **(b)** $m = 25\,\text{kg}$ **(c)** $m = 50\,\text{kg}$

Figure 2.135: Simulation of tomography experiments at 360 deg/s. Beam size is indicated by the dashed black ellipse.

Conclusion

The development and analysis presented in this chapter have successfully validated the Nano Active Stabilization System concept, marking the completion of the conceptual design phase. A comprehensive control strategy has been established, effectively combining external metrology with active platform sensor measurements to achieve precise position control. The control strategy implements a High Authority Control - Low Authority Control architecture - a proven approach that has been specifically adapted to meet the unique requirements of the rotating NASS.

The decentralized Integral Force Feedback component has been demonstrated to provide robust active damping under various operating conditions. The addition of parallel springs to the force sensors has been shown to ensure stability during spindle rotation. The centralized High Authority Controller, operating in the frame of the struts for simplicity, has successfully achieved the desired performance objectives of maintaining a bandwidth of 10 Hz while maintaining robustness against payload mass variations. This investigation has confirmed that the moderate actuator stiffness of $1\,\text{N}/\mu\text{m}$ represents an adequate choice for the active platform, as both very stiff and very compliant configurations introduce significant performance limitations.

Simulations of tomography experiments have been performed, with positioning accuracy requirements defined by the expected minimum beam dimensions of 200 nm by 100 nm. The system has demonstrated excellent performance at maximum rotational velocity with lightweight samples. While some degradation in positioning accuracy has been observed with heavier payloads, as anticipated by the control analysis, the overall performance remains sufficient to validate the fundamental concept of the NASS.

Conceptual Design - Conclusion

The conceptual design phase of the Nano Active Stabilization System (NASS) has been successfully completed, establishing a robust foundation for the subsequent detailed design phase. Through a systematic progression from simplified to increasingly complex models, several critical findings have been established.

Using the simple uniaxial model revealed that a very stiff stabilization stage was unsuitable due to its strong coupling with the complex micro-station dynamics. Conversely, the three-degree-of-freedom rotating model demonstrated that very soft stabilization stage designs are equally problematic due to the gyroscopic effects induced by spindle rotation. A moderate stiffness of approximately $1\,\mathrm{N}/\mu\mathrm{m}$ was identified as the optimal configuration, providing an effective balance between decoupling from micro-station dynamics, insensitivity to spindle's rotation, and good disturbance rejection.

The multi-body modeling approach proved essential for capturing the complex dynamics of both the micro-station and the active platform. This model was tuned based on extensive modal analysis and vibration measurements. The Stewart platform architecture was selected for the active platform due to its good dynamical properties, compact design, and the ability to satisfy the strict space constraints of the NASS.

The HAC-LAC control strategy was successfully adapted to address the unique challenges presented by the rotating NASS. Decentralized Integral Force Feedback with parallel springs demonstrated robust active damping capabilities across different payload masses and rotational velocities. The centralized High Authority Controller, implemented in the frame of the struts, achieved the desired 10 Hz bandwidth with good robustness properties.

Simulations of tomography experiments validated the NASS concept, with positioning accuracy meeting the requirements defined by the expected minimum beam dimensions ($200\,\mathrm{nm} \times 100\,\mathrm{nm}$) for lightweight samples at maximum rotational velocity. As anticipated by the control analysis, some performance degradation was observed with heavier payloads, but the overall performance remained sufficient to validate the fundamental concept.

3 Detailed Design

Contents

Abstract

Following the validation of the Nano Active Stabilization System concept in the previous chapter through simulated tomography experiments, this chapter addresses the refinement of the preliminary conceptual model into an optimized implementation. The initial validation used an active platform with arbitrary geometry, where components such as flexible joints and actuators were modelled as ideal elements, employing simplified control strategies without consideration for instrumentation noise. This detailed design phase aims to optimize each component while ensuring none will limit the system's overall performance.

This chapter begins by determining the optimal geometric configuration for the active platform (Section 3.1). To this end, a review of existing Stewart platform designs is first presented, followed by an analysis of how geometric parameters influence the system's properties—mobility, stiffness, and dynamical response—with a particular emphasis on the cubic architecture. The chapter concludes by specifying the chosen active platform geometry and the associated actuator stroke and flexible joint angular travel requirements to achieve the desired mobility.

Section 3.2 introduces a hybrid modeling methodology that combines Finite Element Analysis (FEA) with multi-body dynamics to optimize critical active platform components. This approach is first experimentally validated using an Amplified Piezoelectric Actuator, establishing confidence in the modeling technique. The methodology is then applied to

two key elements: the actuators (Section 3.2.2) and the flexible joints (Section 3.2.3), enabling detailed optimization while maintaining computational efficiency for system-level simulations.

The control strategy is refined in Section 3.3, where three critical aspects are addressed. First, various approaches for optimally combining multiple sensors are examined, with particular emphasis on sensor fusion techniques. Second, different decoupling strategies for parallel manipulators are compared—an analysis notably lacking in the literature. Third, the optimization of controllers for decoupled plants is discussed, introducing a novel method for shaping closed-loop transfer functions using complementary filters.

Section 3.4 focuses on instrumentation selection using a dynamic error budgeting approach to establish maximum acceptable noise specifications for each component. The selected instrumentation is then experimentally characterized to verify compliance with these specifications, ensuring that the combined effect of all noise sources remains within acceptable limits.

The chapter concludes with a concise presentation of the obtained optimized active platform design, called the "nano-hexapod" (Section 3.5). With the detailed design completed and components procured, the project advances to the experimental validation phase, which will be addressed in the subsequent chapter.

3.1 Optimal Active Platform Geometry

The performance of a Stewart platform depends on its geometric configuration, especially the orientation of its struts and the positioning of its joints. During the conceptual design phase of the active platform, a preliminary geometry was selected based on general principles without detailed optimization. As the project advanced to the detailed design phase, a rigorous analysis of how geometry influences system performance became essential to ensure that the final design would meet the demanding requirements of the Nano Active Stabilization System (NASS).

In this chapter, the active platform geometry is optimized through careful analysis of how design parameters influence critical performance aspects: attainable workspace, mechanical stiffness, strut-to-strut coupling for decentralized control strategies, and dynamic response in Cartesian coordinates.

The chapter begins with a comprehensive review of existing Stewart platform designs in Section 3.1.1, surveying various approaches to geometry, actuation, sensing, and joint design from the literature. Section 3.1.2 develops the analytical framework that connects geometric parameters to performance characteristics, establishing quantitative relationships that guide the optimization process. Section 3.1.3 examines the cubic configuration, a specific architecture that has gathered significant attention, to evaluate its suitability for the NASS applications. Finally, Section 3.1.4 presents the optimized active platform geometry derived from these analyses and demonstrates how it addresses the specific requirements of the NASS.

3.1.1 Review of Stewart Platforms

The first parallel platform similar to the Stewart platform was built in 1954 by Gough [55], for a tyre test machine (shown in Figure 3.1a). Subsequently, Stewart proposed a similar design for a flight simulator (shown in Figure 3.1b) in a 1965 publication [139]. Since then, the Stewart platform (sometimes referred to as the Stewart-Gough platform) has been used across diverse applications [31], including large telescopes [78, 163], machine tools [124], and Synchrotron instrumentation [92, 152].

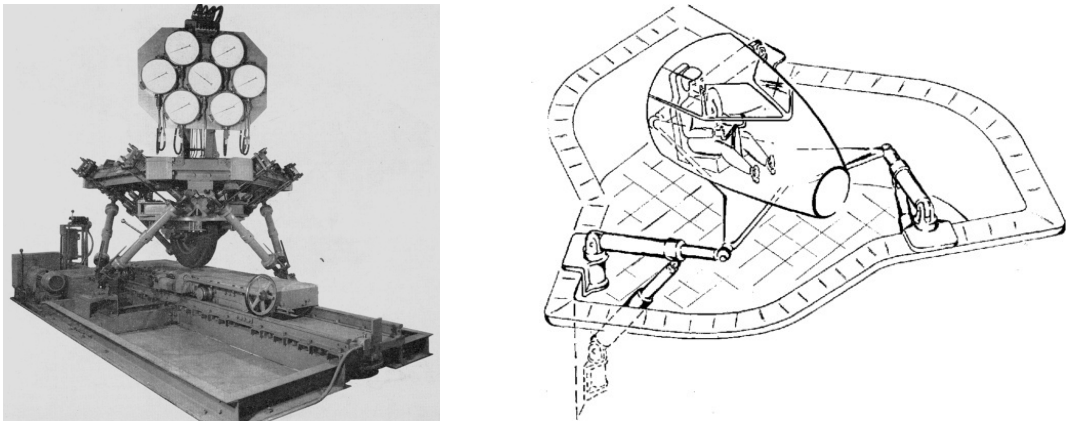

(a) Tyre test machine proposed by Gough [55]

(b) Flight simulator proposed by Stewart [139]

Figure 3.1: Two of the earliest developments of Stewart platforms.

As explained in Section 2.5.2, Stewart platforms comprise the following key elements: two plates connected by six struts, with each strut composed of a joint at each end, an actuator, and one or several sensors.

The specific geometry (i.e., position of joints and orientation of the struts) can be selected based on the application requirements, resulting in numerous designs throughout the literature. This discussion focuses primarily on Stewart platforms designed for nano-positioning and vibration control, which necessitates the use of flexible joints. The implementation of these flexible joints, will be discussed when designing the active platform flexible joints in Section 3.2.3. Long stroke Stewart platforms are not addressed here as their design presents different challenges, such as singularity-free workspace and complex kinematics [99].

In terms of actuation, mainly two types are used: voice coil actuators and piezoelectric actuators. Voice coil actuators, providing stroke ranges from 0.5 mm to 10 mm, are commonly implemented in cubic architectures (as illustrated in Figures 3.2a, 3.2b and 3.3a) and are mainly used for vibration isolation [96, 117, 119, 136, 145]. For applications requiring short stroke (typically smaller than 500 µm), piezoelectric actuators present an interesting alternative, as shown in [6, 51, 160]. Examples of piezoelectric-actuated Stewart platforms are presented in Figures 3.2c, 3.2d and 3.3c. Although less frequently encountered, magnetostrictive actuators have been successfully implemented in [164] (Figure 3.3b).

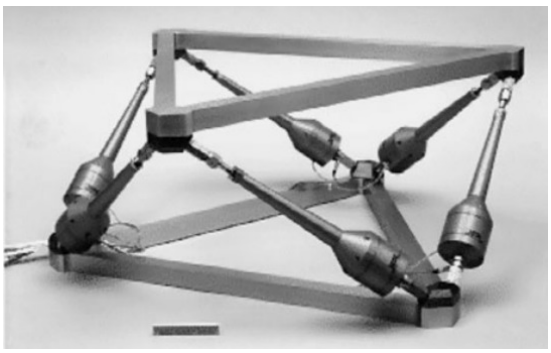

(a) California Institute of Technology - USA [136]

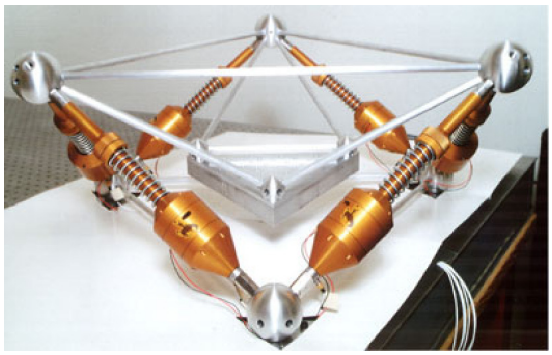

(b) University of Wyoming - USA [96]

(c) ULB - Belgium [5]

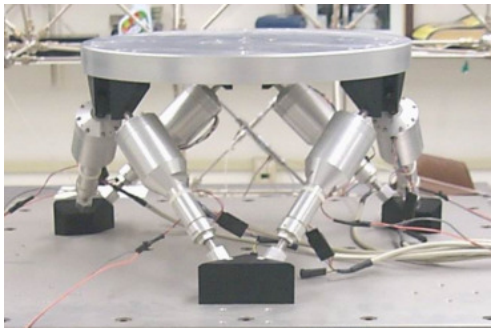

(d) Naval Postgraduate School - USA [6]

Figure 3.2: Some examples of developed Stewart platform with Cubic geometry.

The sensors integrated in these platforms are selected based on specific control requirements, as different sensors offer distinct advantages and limitations [59]. Force sensors are typically integrated within the struts in a collocated arrangement with actuators to enhance control robustness. Stewart platforms incorporating force sensors are frequently used for vibration isolation [119, 136] and active damping applications [5, 53], as exemplified in Figure 3.2c.

Inertial sensors (accelerometers and geophones) are commonly employed in vibration isolation applications [21, 24]. These sensors are predominantly aligned with the struts [59, 76, 87, 142, 144, 164], although they may also be fixed to the top platform [153].

For high-precision positioning applications, various displacement sensors are implemented, including Linear Variable Differential Transformers (LVDTs) [81, 87, 144, 145], capacitive sensors [146, 147], eddy current sensors [21, 51], and strain gauges [41]. Notably, some designs incorporate external sensing methodologies rather than integrating sensors within the struts [21, 87, 147]. A recent design [104], although not strictly speaking a Stewart platform, has demonstrated the use of 3-phase rotary motors with rotary encoders for achieving long-stroke and highly repeatable positioning, as illustrated in Figure 3.3d.

Two primary categories of Stewart platform geometry can be identified. The first is cubic architecture (examples presented in Figure 3.2), wherein struts are positioned along six sides of a cube (and therefore oriented orthogonally to each other). This architecture represents the most prevalent configuration for vibration isolation applications in the literature. Its distinctive properties will be examined in Section 3.1.3. The second category comprises non-cubic architectures (Figure 3.3), where strut orientation and joint positioning can be optimized according to defined performance criteria. The influence of strut orientation and joint positioning on Stewart platform properties is analyzed in Section 3.1.2.

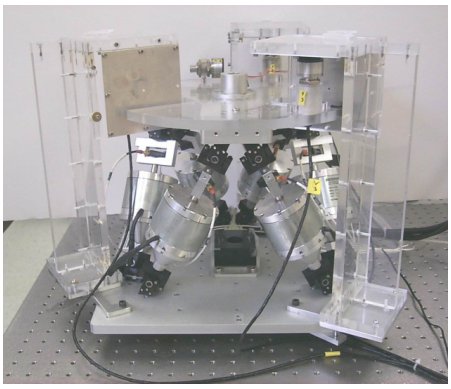

(a) Naval Postgraduate School - USA [21]

(b) Beihang University - China [164]

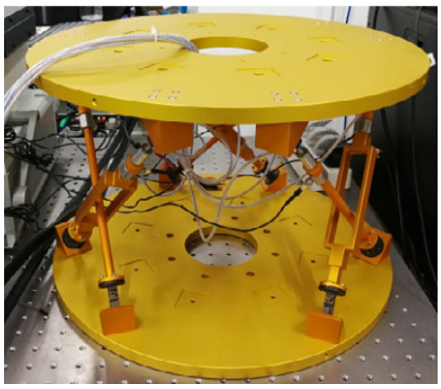

(c) Nanjing University - China [160]

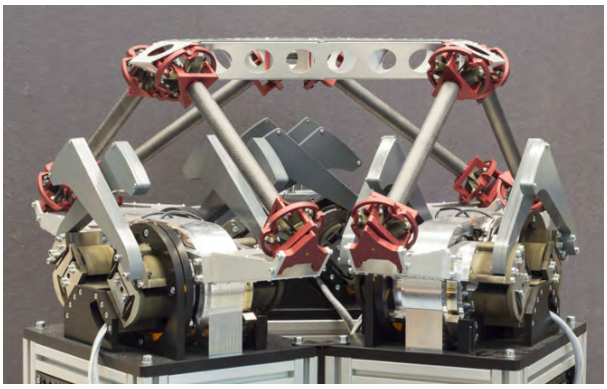

(d) University of Twente - Netherlands [104]

Figure 3.3: Some examples of developed Stewart platform with non-cubic geometry.

3.1.2 Kinematic Study of Stewart Platforms

As was demonstrated in Section 2.5.2, the geometry of the Stewart platform impacts the stiffness and compliance characteristics, the mobility (or workspace), the force authority, and the dynamics of the manipulator. It is therefore essential

to understand how the geometry impacts these properties, and to develop methodologies for optimizing the geometry for specific applications.

A useful analytical tool for this study is the Jacobian matrix, which depends on $\boldsymbol{b}_i$ (joints' position with respect to the top platform) and $\hat{\boldsymbol{s}}_i$ (struts' orientation). The choice of $\{A\}$ and $\{B\}$ frames, independently of the physical Stewart platform geometry, impacts the obtained kinematics and stiffness matrix, as these are defined for forces and motion evaluated at the chosen frame.

3.1.2.1 Platform Mobility / Workspace

The mobility of the Stewart platform (or any manipulator) is defined as the range of motion that it can perform. It corresponds to the set of possible poses (i.e., combined translation and rotation) of frame $\{B\}$ with respect to frame $\{A\}$. This represents a six-dimensional property which is difficult to represent. Depending on the applications, only the translation mobility (i.e., fixed orientation workspace) or the rotation mobility may be represented. This approach is equivalent to projecting the six-dimensional value into a three-dimensional space, which is easier to represent.

Mobility of parallel manipulators is inherently difficult to study as the translational and orientation workspace are coupled [100]. The analysis is significantly simplified when considering small motions, as the Jacobian matrix can be used to link the strut motion to the motion of frame $\{B\}$ with respect to $\{A\}$ through (3.1), which is a linear equation.

$$\begin{bmatrix} \delta l_1 \\ \delta l_2 \\ \delta l_3 \\ \delta l_4 \\ \delta l_5 \\ \delta l_6 \end{bmatrix} = \underbrace{\begin{bmatrix} {}^A\hat{\boldsymbol{s}}_1{}^\intercal & ({}^A\boldsymbol{b}_1 \times {}^A\hat{\boldsymbol{s}}_1)^\intercal \\ {}^A\hat{\boldsymbol{s}}_2{}^\intercal & ({}^A\boldsymbol{b}_2 \times {}^A\hat{\boldsymbol{s}}_2)^\intercal \\ {}^A\hat{\boldsymbol{s}}_3{}^\intercal & ({}^A\boldsymbol{b}_3 \times {}^A\hat{\boldsymbol{s}}_3)^\intercal \\ {}^A\hat{\boldsymbol{s}}_4{}^\intercal & ({}^A\boldsymbol{b}_4 \times {}^A\hat{\boldsymbol{s}}_4)^\intercal \\ {}^A\hat{\boldsymbol{s}}_5{}^\intercal & ({}^A\boldsymbol{b}_5 \times {}^A\hat{\boldsymbol{s}}_5)^\intercal \\ {}^A\hat{\boldsymbol{s}}_6{}^\intercal & ({}^A\boldsymbol{b}_6 \times {}^A\hat{\boldsymbol{s}}_6)^\intercal \end{bmatrix}}_{\boldsymbol{J}} \begin{bmatrix} \delta x \\ \delta y \\ \delta z \\ \delta\theta_x \\ \delta\theta_y \\ \delta\theta_z \end{bmatrix} \tag{3.1}$$

Therefore, the mobility of the Stewart platform (defined as the set of achievable $[\delta x\ \delta y\ \delta z\ \delta\theta_x\ \delta\theta_y\ \delta\theta_z]$) depends on two key factors: the stroke of each strut and the geometry of the Stewart platform (embodied in the Jacobian matrix). More specifically, the XYZ mobility only depends on the $\hat{\boldsymbol{s}}_i$ (orientation of struts), while the mobility in rotation also depends on $\boldsymbol{b}_i$ (position of top joints).

Mobility in Translation For simplicity, only translations are first considered (i.e., the Stewart platform is considered to have fixed orientation). In the general case, the translational mobility can be represented by a 3D shape having 12 faces, where each actuator limits the stroke along its axis in positive and negative directions. The faces are therefore perpendicular to the strut direction. The obtained mobility for the Stewart platform geometry shown in Figure 3.4a is computed and represented in Figure 3.4b.

With the previous interpretations of the 12 faces making the translational mobility 3D shape, it can be concluded that for a strut stroke of $\pm d$, a sphere with radius d is contained in the 3D shape and touches it in directions defined by the strut axes, as illustrated in Figure 3.4b. This means that the mobile platform can be translated in any direction with a stroke equal to the strut stroke.

To better understand how the geometry of the Stewart platform impacts the translational mobility, two configurations are compared with struts oriented vertically (Figure 3.5a) and struts oriented horizontally (Figure 3.5b). The vertically oriented struts configuration leads to greater stroke in the horizontal direction and reduced stroke in the vertical direction (Figure 3.5c). Conversely, horizontal oriented struts configuration provides more stroke in the vertical direction.

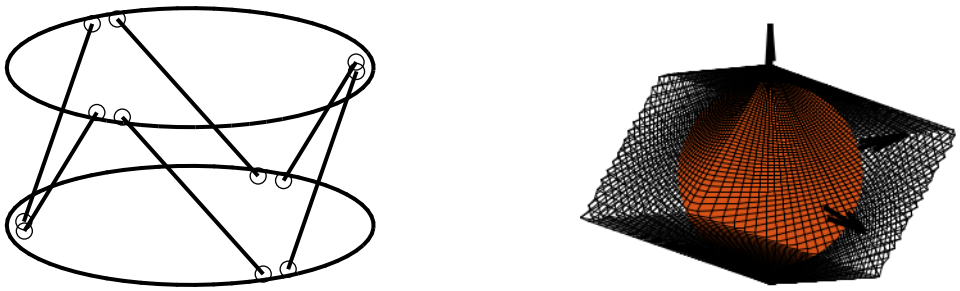

(a) Stewart platform geometry **(b)** Translational mobility

Figure 3.4: One Stewart platform geometry (a) and its associated translational mobility (b). A sphere with radius equal to the strut stroke is contained in the translational mobility shape.

It may seem counterintuitive that less stroke is available in the direction of the struts. This phenomenon occurs because the struts form a lever arm mechanism that amplifies the motion. The amplification factor increases when the struts have a high angle with the direction of motion and equals one (i.e. is minimal) when aligned with the direction of motion.

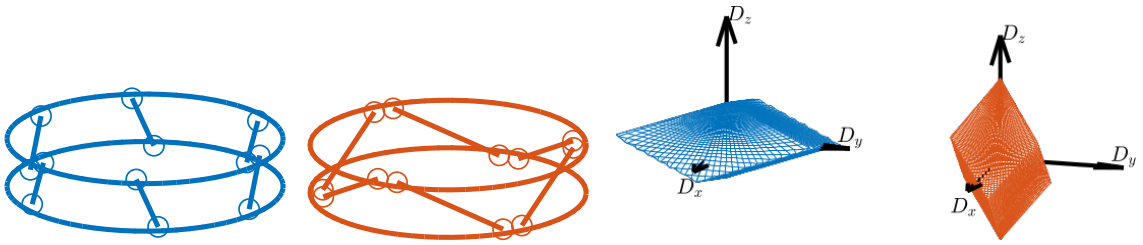

(a) Vertical struts **(b)** Horizontal struts **(c)** Translational mobility

Figure 3.5: Effect of strut orientation on the obtained mobility in translation. Two Stewart platform geometries are considered: struts oriented vertically (a) and struts oriented horizontally (b). Obtained mobility for both geometry are shown in (c).

Mobility in Rotation As shown by equation (3.1), the rotational mobility depends both on the orientation of the struts and on the location of the top joints. Similarly to the translational case, to increase the rotational mobility in one direction, it is advantageous to have the struts more perpendicular to the rotational direction.

For instance, having the struts more vertical (Figure 3.5a) provides less rotational stroke along the vertical direction than having the struts oriented more horizontally (Figure 3.5b).

Two cases are considered with the same strut orientation but with different top joint positions: struts positioned close to each other (Figure 3.6a) and struts positioned further apart (Figure 3.6b). The mobility for pure rotations is compared in Figure 3.6c. Having struts further apart decreases the "lever arm" and therefore reduces the rotational mobility.

Combined Translations and Rotations It is possible to consider combined translations and rotations, although displaying such mobility becomes more complex. For a fixed geometry and a desired mobility (combined translations and rotations), it is possible to estimate the required minimum actuator stroke. This analysis is conducted in Section 3.1.4 to estimate the required actuator stroke for the active platform geometry.

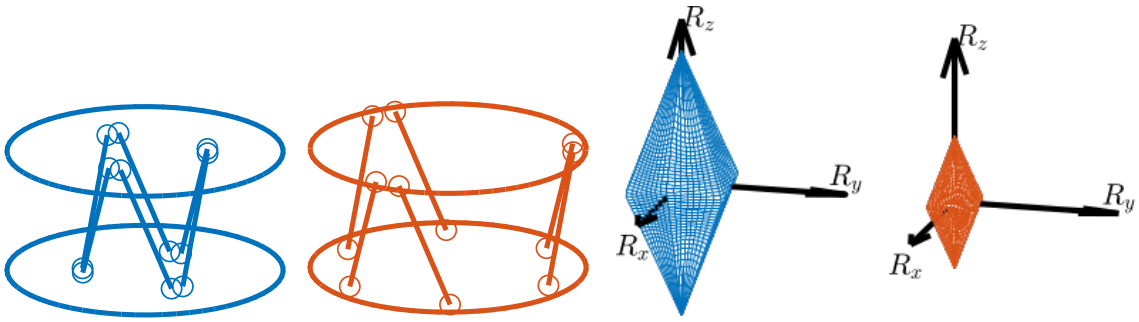

(a) Struts close together **(b)** Struts far apart **(c)** Rotational mobility

Figure 3.6: Effect of strut position on the obtained mobility in rotation. Two Stewart platform geometries are considered: struts close to each other (a) and struts further apart (b). Obtained mobility for both geometry are shown in (c).

3.1.2.2 Stiffness

The stiffness matrix defines how the top platform of the Stewart platform (i.e. frame $\{B\}$) deforms with respect to its fixed base (i.e. frame $\{A\}$) due to static forces/torques applied between frames $\{A\}$ and $\{B\}$. It depends on the Jacobian matrix (i.e., the geometry) and the strut axial stiffness as shown in equation (3.2). The contribution of joints stiffness is not considered here, as the joints were optimized after the geometry was fixed. However, theoretical frameworks for evaluating flexible joint contribution to the stiffness matrix have been established in the literature [97, 98].

$$\boldsymbol{K} = \boldsymbol{J}^{\intercal}\mathcal{K}\boldsymbol{J} \tag{3.2}$$

It is assumed that the stiffness of all struts is the same: $\mathcal{K} = k \cdot \boldsymbol{I}_6$. In that case, the obtained stiffness matrix linearly depends on the strut stiffness k, and is structured as shown in equation (3.3).

$$\boldsymbol{K} = k\boldsymbol{J}^{\intercal}\boldsymbol{J} = k\left[\begin{array}{c|c} \Sigma_{i=0}^{6}\hat{\boldsymbol{s}}_i \cdot \hat{\boldsymbol{s}}_i^{\intercal} & \Sigma_{i=0}^{6}\hat{\boldsymbol{s}}_i \cdot ({}^{A}\boldsymbol{b}_i \times {}^{A}\hat{\boldsymbol{s}}_i)^{\intercal} \\ \hline \Sigma_{i=0}^{6}({}^{A}\boldsymbol{b}_i \times {}^{A}\hat{\boldsymbol{s}}_i) \cdot \hat{\boldsymbol{s}}_i^{\intercal} & \Sigma_{i=0}^{6}({}^{A}\boldsymbol{b}_i \times {}^{A}\hat{\boldsymbol{s}}_i) \cdot ({}^{A}\boldsymbol{b}_i \times {}^{A}\hat{\boldsymbol{s}}_i)^{\intercal} \end{array}\right] \tag{3.3}$$

Translation Stiffness As shown by equation (3.3), the translation stiffnesses (the 3×3 top left terms of the stiffness matrix) only depend on the orientation of the struts and not their location: $\hat{\boldsymbol{s}}_i \cdot \hat{\boldsymbol{s}}_i^{\intercal}$. In the extreme case where all struts are vertical ($s_i = [0\,0\,1]$), a vertical stiffness of $6k$ is achieved, but with null stiffness in the horizontal directions. If two struts are oriented along the X axis, two struts along the Y axis, and two struts along the Z axis, then $\hat{\boldsymbol{s}}_i \cdot \hat{\boldsymbol{s}}_i^{\intercal} = 2\boldsymbol{I}_3$ and the stiffness is well distributed along all directions. This configuration corresponds to the cubic architecture, that is presented in Section 3.1.3.

When the struts are oriented more vertically, as shown in Figure 3.5a, the vertical stiffness increases while the horizontal stiffness decreases. Additionally, R_x and R_y stiffness increases while R_z stiffness decreases. The opposite conclusions apply if struts are oriented more horizontally, illustrated in Figure 3.5b.

Rotational Stiffness The rotational stiffnesses depend both on the orientation of the struts and on the location of the top joints with respect to the considered center of rotation (i.e., the location of frame $\{A\}$). With the same orientation but increased distances to the frame $\{A\}$ by a factor of 2, the rotational stiffness is increased by a factor of 4.

Therefore, the compact Stewart platform depicted in Figure 3.6a has less rotational stiffness than the Stewart platform shown in Figure 3.6b.

Diagonal Stiffness Matrix Having a diagonal stiffness matrix $\boldsymbol{K}$ can be beneficial for control purposes as it would make the plant in the Cartesian frame decoupled at low frequency. This property depends on both the geometry and the chosen $\{A\}$ frame. For specific geometry and choice of $\{A\}$ frame, it is possible to achieve a diagonal K matrix. This is discussed in Section 3.1.3.1.

3.1.2.3 Dynamical Properties

The dynamical equations (both in the Cartesian frame and in the frame of the struts) for the Stewart platform were derived during the conceptual phase with simplifying assumptions (massless struts and perfect joints). The dynamics depends both on the geometry (Jacobian matrix) and on the payload being placed on top of the platform. Under very specific conditions, the equations of motion in the Cartesian frame, given by equation (3.4), can be decoupled. These conditions are studied in Section 3.1.3.2.

$$\frac{\mathcal{X}}{\mathcal{F}}(s) = (\boldsymbol{M}s^2 + \boldsymbol{J}^\intercal\boldsymbol{C}\boldsymbol{J}s + \boldsymbol{J}^\intercal\boldsymbol{K}\boldsymbol{J})^{-1} \tag{3.4}$$

In the frame of the struts, the equations of motion (3.5) are well decoupled at low frequency. This is why most Stewart platforms are controlled in the frame of the struts: below the resonance frequency, the system is well decoupled and Single Input Single Output (SISO) control may be applied for each strut, independently of the payload being used.

$$\frac{\mathcal{L}}{\mathcal{f}}(s) = (\boldsymbol{J}^{-\intercal}\boldsymbol{M}\boldsymbol{J}^{-1}s^2 + \boldsymbol{C} + \boldsymbol{K})^{-1} \tag{3.5}$$

Coupling between sensors (force sensors, relative position sensors or inertial sensors) in different struts may also be important for decentralized control. In section 3.1.3.3, it will be studied whether the Stewart platform geometry can be optimized to have lower coupling between the struts.

3.1.2.4 Conclusion

The effects of two changes in the manipulator's geometry, namely the position and orientation of the struts, are summarized in Table 3.1. These results could have been easily deduced based on mechanical principles, but thanks to the kinematic analysis, they can be quantified. These trade-offs provide important guidelines when choosing the Stewart platform geometry.

3.1.3 The Cubic Architecture

The Cubic configuration for the Stewart platform was first proposed by Dr. Gough in a comment to the original paper by Dr. Stewart [139]. This configuration is characterized by active struts arranged in a mutually orthogonal configuration connecting the corners of a cube, as shown in Figure 3.7a.

Table 3.1: Effect of a change in geometry on the manipulator's stiffness and mobility.

Struts	Vertically Oriented	Increased separation
Vertical stiffness	↗	=
Horizontal stiffness	↘	=
Vertical rotation stiffness	↘	↗
Horizontal rotation stiffness	↗	↗
Vertical mobility	↘	=
Horizontal mobility	↗	=
Vertical rotation mobility	↗	↘
Horizontal rotation mobility	↘	↘

Typically, the struts have similar length to the cube's edges, as illustrated in Figure 3.7a. Practical implementations of such configurations can be observed in Figures 3.2a, 3.2b and 3.2d. It is also possible to implement designs with strut lengths smaller than the cube's edges (Figure 3.7b), as exemplified in Figure 3.2c.

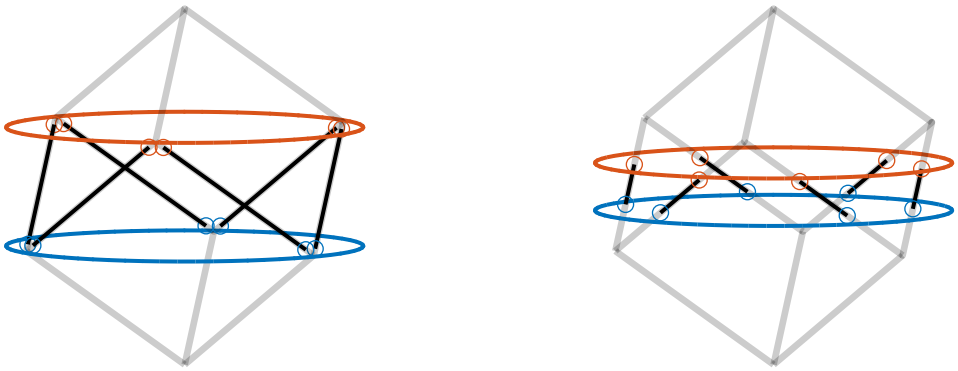

(a) Classical Cubic architecture **(b)** Alternative configuration

Figure 3.7: Typical Stewart platform cubic architectures in which struts' length is similar to the cube edges' length (a) or is taking just a portion of the edge (b).

Several advantageous properties attributed to the cubic configuration have contributed to its widespread adoption [52, 73, 117]: simplified kinematics relationships and dynamical analysis [52]; uniform stiffness in all directions [4]; uniform mobility [113, chapt.8.5.2]; and minimization of the cross coupling between actuators and sensors in different struts [117]. This minimization is attributed to the fact that the struts are orthogonal to each other, and is said to facilitate collocated sensor-actuator control system design, i.e., the implementation of decentralized control [52, 144].

These properties are examined in this section to assess their relevance for the active platform. The mobility and stiffness properties of the cubic configuration are analyzed in Section 3.1.3.1. Dynamical decoupling is investigated in Section 3.1.3.2, while decentralized control, crucial for the NASS, is examined in Section 3.1.3.3. Given that the cubic architecture imposes strict geometric constraints, alternative designs are proposed in Section 3.1.3.4. The ultimate objective is to determine the suitability of the cubic architecture for the active platform.

3.1.3.1 Static Properties

Stiffness Matrix for the Cubic Architecture Consider the cubic architecture shown in Figure 3.8a. The unit vectors corresponding to the edges of the cube are described by equation (3.6).

$$\hat{\boldsymbol{s}}_1 = \begin{bmatrix} \frac{\sqrt{2}}{\sqrt{3}} \\ 0 \\ \frac{1}{\sqrt{3}} \end{bmatrix} \quad \hat{\boldsymbol{s}}_2 = \begin{bmatrix} \frac{-1}{\sqrt{6}} \\ \frac{-1}{\sqrt{2}} \\ \frac{1}{\sqrt{3}} \end{bmatrix} \quad \hat{\boldsymbol{s}}_3 = \begin{bmatrix} \frac{-1}{\sqrt{6}} \\ \frac{1}{\sqrt{2}} \\ \frac{1}{\sqrt{3}} \end{bmatrix} \quad \hat{\boldsymbol{s}}_4 = \begin{bmatrix} \frac{\sqrt{2}}{\sqrt{3}} \\ 0 \\ \frac{1}{\sqrt{3}} \end{bmatrix} \quad \hat{\boldsymbol{s}}_5 = \begin{bmatrix} \frac{-1}{\sqrt{6}} \\ \frac{-1}{\sqrt{2}} \\ \frac{1}{\sqrt{3}} \end{bmatrix} \quad \hat{\boldsymbol{s}}_6 = \begin{bmatrix} \frac{-1}{\sqrt{6}} \\ \frac{1}{\sqrt{2}} \\ \frac{1}{\sqrt{3}} \end{bmatrix} \tag{3.6}$$

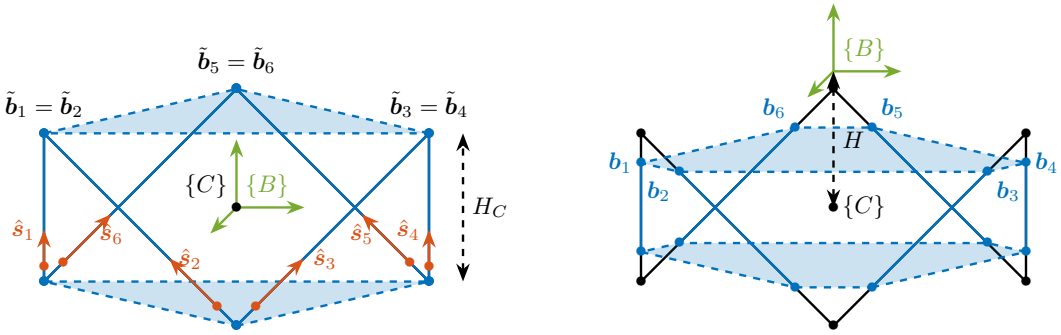

(a) Full cube **(b)** Cube's portion

Figure 3.8: Cubic architecture. Struts are represented in blue. The cube's center is indicated by a black dot. The Struts can match the cube's edges (a) or just take a portion of the edge (b).

Coordinates of the cube's vertices relevant for the top joints, expressed with respect to the cube's center, are shown in equation (3.7).

$$\tilde{\boldsymbol{b}}_1 = \tilde{\boldsymbol{b}}_2 = H_c \begin{bmatrix} \frac{1}{\sqrt{2}} \\ \frac{-\sqrt{3}}{\sqrt{2}} \\ \frac{1}{2} \end{bmatrix}, \quad \tilde{\boldsymbol{b}}_3 = \tilde{\boldsymbol{b}}_4 = H_c \begin{bmatrix} \frac{1}{\sqrt{2}} \\ \frac{\sqrt{3}}{\sqrt{2}} \\ \frac{1}{2} \end{bmatrix}, \quad \tilde{\boldsymbol{b}}_5 = \tilde{\boldsymbol{b}}_6 = H_c \begin{bmatrix} \frac{-2}{\sqrt{2}} \\ 0 \\ \frac{1}{2} \end{bmatrix} \tag{3.7}$$

In the case where top joints are positioned at the cube's vertices, a diagonal stiffness matrix is obtained as shown in equation (3.8). Translation stiffness is twice the stiffness of the struts, and rotational stiffness is proportional to the square of the cube's size H_c.

$$\boldsymbol{K}_{\{B\}=\{C\}} = k \begin{bmatrix} 2 & 0 & 0 & 0 & 0 & 0 \\ 0 & 2 & 0 & 0 & 0 & 0 \\ 0 & 0 & 2 & 0 & 0 & 0 \\ 0 & 0 & 0 & \frac{3}{2}H_c^2 & 0 & 0 \\ 0 & 0 & 0 & 0 & \frac{3}{2}H_c^2 & 0 \\ 0 & 0 & 0 & 0 & 0 & 6H_c^2 \end{bmatrix} \tag{3.8}$$

However, typically, the top joints are not placed at the cube's vertices but at positions along the cube's edges (Figure 3.8b). In that case, the location of the top joints can be expressed by equation (3.9), yet the computed stiffness matrix remains identical to Equation (3.8).

$$\boldsymbol{b}_i = \tilde{\boldsymbol{b}}_i + \alpha \hat{\boldsymbol{s}}_i \tag{3.9}$$

The stiffness matrix is therefore diagonal when the considered $\{B\}$ frame is located at the center of the cube (shown by frame $\{C\}$). This means that static forces (resp torques) applied at the cube's center will induce pure translations

(resp rotations around the cube's center). This specific location where the stiffness matrix is diagonal is referred to as the Center of Stiffness (CoK), analogous to the Center of Mass (CoM) where the mass matrix is diagonal.

Effect of Having Frame $\{B\}$ Off-centered When the reference frames $\{A\}$ and $\{B\}$ are shifted from the cube's center, off-diagonal elements emerge in the stiffness matrix.

Considering a vertical shift as shown in Figure 3.8b, the stiffness matrix transforms into that shown in Equation (3.10). Off-diagonal elements increase proportionally with the height difference between the cube's center and the considered $\{B\}$ frame.

$$\boldsymbol{K}_{\{B\}\neq\{C\}} = k \begin{bmatrix} 2 & 0 & 0 & 0 & -2H & 0 \\ 0 & 2 & 0 & 2H & 0 & 0 \\ 0 & 0 & 2 & 0 & 0 & 0 \\ 0 & 2H & 0 & \frac{3}{2}H_c^2 + 2H^2 & 0 & 0 \\ -2H & 0 & 0 & 0 & \frac{3}{2}H_c^2 + 2H^2 & 0 \\ 0 & 0 & 0 & 0 & 0 & 6H_c^2 \end{bmatrix} \tag{3.10}$$

This stiffness matrix structure is characteristic of Stewart platforms exhibiting symmetry, and is not an exclusive property of cubic architectures. Therefore, the stiffness characteristics of the cubic architecture are only distinctive when considering a reference frame located at the cube's center. This poses a practical limitation, as in most applications, the relevant frame (where motion is of interest and forces are applied) is located above the top platform.

It should be noted that for the stiffness matrix to be diagonal, the cube's center doesn't need to coincide with the geometric center of the Stewart platform. This observation leads to the interesting alternative architectures presented in Section 3.1.3.4.

Uniform Mobility The translational mobility of the Stewart platform with constant orientation was analyzed. Considering limited actuator stroke (elongation of each strut), the maximum achievable positions in XYZ space were estimated. The resulting mobility in X, Y, and Z directions for the cubic architecture is illustrated in Figure 3.9a.

The translational workspace analysis reveals that for the cubic architecture, the achievable positions form a cube whose axes align with the struts, with the cube's edge length corresponding to the strut axial stroke. These findings suggest that the mobility pattern is more subtle than sometimes described in the literature [98], exhibiting uniformity primarily along directions aligned with the cube's edges rather than uniform spherical distribution in all XYZ directions. This configuration still offers more consistent mobility characteristics compared to alternative architectures illustrated in Figure 3.4.

The rotational mobility, illustrated in Figure 3.9b, exhibits greater achievable angular stroke in the R_x and R_y directions compared to the R_z direction. Furthermore, an inverse relationship exists between the cube's dimension and rotational mobility, with larger cube sizes corresponding to more limited angular displacement capabilities.

3.1.3.2 Dynamical Decoupling

This section examines the dynamics of the cubic architecture in the Cartesian frame which corresponds to the transfer function from forces and torques $\boldsymbol{\mathcal{F}}$ to translations and rotations $\boldsymbol{\mathcal{X}}$ of the top platform. When relative motion sensors are integrated in each strut (measuring $\boldsymbol{\mathcal{L}}$), the pose $\boldsymbol{\mathcal{X}}$ is computed using the Jacobian matrix as shown in Figure 3.10.

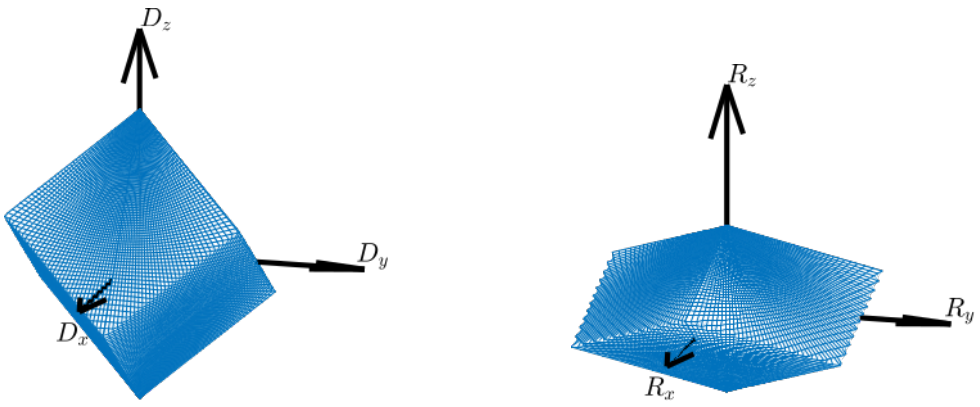

(a) Mobility in translation

(b) Mobility in rotation

Figure 3.9: Mobility of a Stewart platform with Cubic architecture. Both for translations (a) and rotations (b).

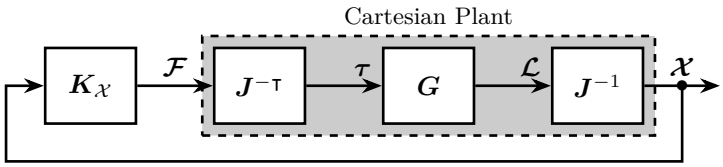

Figure 3.10: Typical control architecture in the cartesian frame.

Low Frequency and High-Frequency Coupling As derived during the conceptual design phase, the dynamics from $\mathcal{F}$ to $\mathcal{X}$ is described by Equation (3.4). At low frequency, the behavior of the platform depends on the stiffness matrix (3.11).

$$\frac{\mathcal{X}}{\mathcal{F}}(j\omega) \xrightarrow[\omega \to 0]{} \boldsymbol{K}^{-1} \tag{3.11}$$

In Section 3.1.3.1, it was demonstrated that for the cubic configuration, the stiffness matrix is diagonal if frame $\{B\}$ is positioned at the cube's center. In this case, the "Cartesian" plant is decoupled at low frequency. At high-frequency, the behavior is governed by the mass matrix (evaluated at frame $\{B\}$) (3.12).

$$\frac{\mathcal{X}}{\mathcal{F}}(j\omega) \xrightarrow[\omega \to \infty]{} -\omega^2 \boldsymbol{M}^{-1} \tag{3.12}$$

To achieve a diagonal mass matrix, the Center of Mass of the mobile components must coincide with the $\{B\}$ frame, and the principal axes of inertia must align with the axes of the $\{B\}$ frame.

To verify these properties, a cubic Stewart platform with a cylindrical payload was analyzed (Figure 3.11). Transfer functions from $\mathcal{F}$ to $\mathcal{X}$ were computed for two specific locations of the $\{B\}$ frames. When the $\{B\}$ frame was positioned at the Center of Mass, coupling at low frequency was observed due to the non-diagonal stiffness matrix (Figure 3.12a). Conversely, when positioned at the Center of Stiffness, coupling occurred at high-frequency due to the non-diagonal mass matrix (Figure 3.12b).

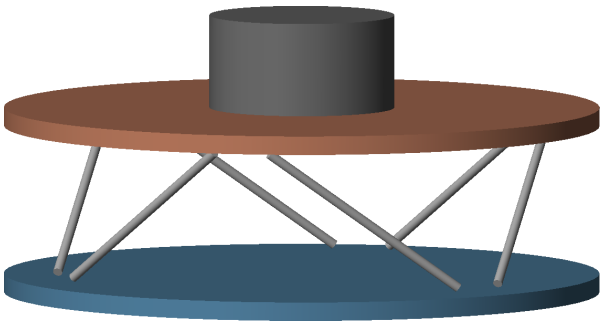

Figure 3.11: Cubic Stewart platform with cylindrical payload located on the top platform.

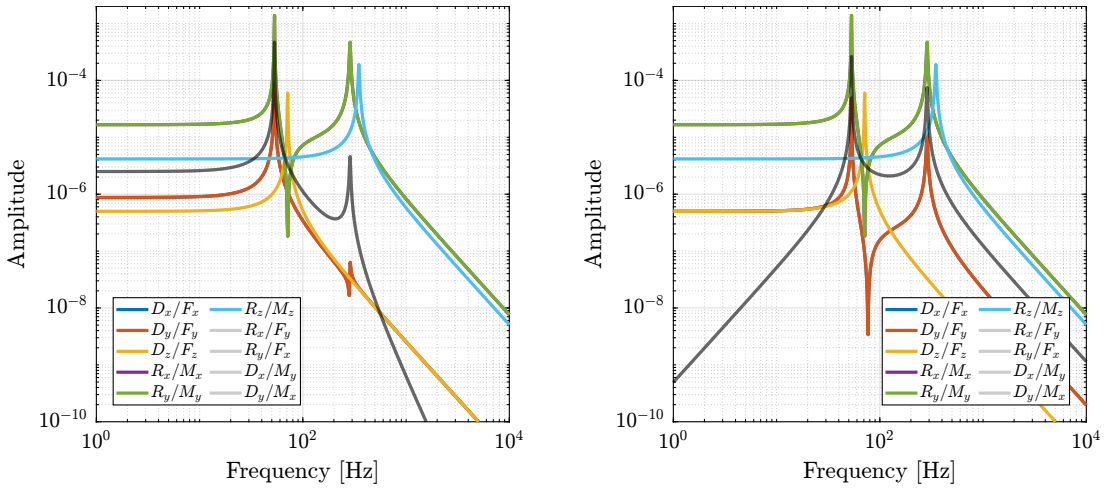

(a) $\{B\}$ at the center of mass

(b) $\{B\}$ at the cube's center

Figure 3.12: Transfer functions for a cubic Stewart platform expressed in the Cartesian frame. Two locations of the $\{B\}$ frame are considered: at the center of mass of the moving body (a) and at the cube's center (b).

Payload's CoM at the Cube's Center An effective strategy for improving dynamical performances involves aligning the cube's center (Center of Stiffness) with the Center of Mass of the moving components [87]. This can be achieved by positioning the payload below the top platform, such that the Center of Mass of the moving body coincides with the cube's center (Figure 3.13a). This approach was physically implemented in several studies [73, 96], as shown in Figure 3.2b. The resulting dynamics are indeed well-decoupled (Figure 3.13b), taking advantage from diagonal stiffness and mass matrices. The primary limitation of this approach is that, for many applications including the NASS, the payload must be positioned above the top platform. If a design similar to Figure 3.13a were employed for the active platform, the X-ray beam would intersect with the struts during spindle rotation.

Conclusion The analysis of dynamical properties of the cubic architecture yields several important conclusions. Static decoupling, characterized by a diagonal stiffness matrix, is achieved when reference frames $\{A\}$ and $\{B\}$ are positioned at the cube's center. Note that this property can also be obtained with non-cubic architectures that exhibit symmetrical strut arrangements. Dynamic decoupling requires both static decoupling and coincidence of the mobile platform's Center of Mass with reference frame $\{B\}$. While this configuration offers powerful control advantages, it requires positioning the payload at the cube's center, which is highly restrictive and often impractical.

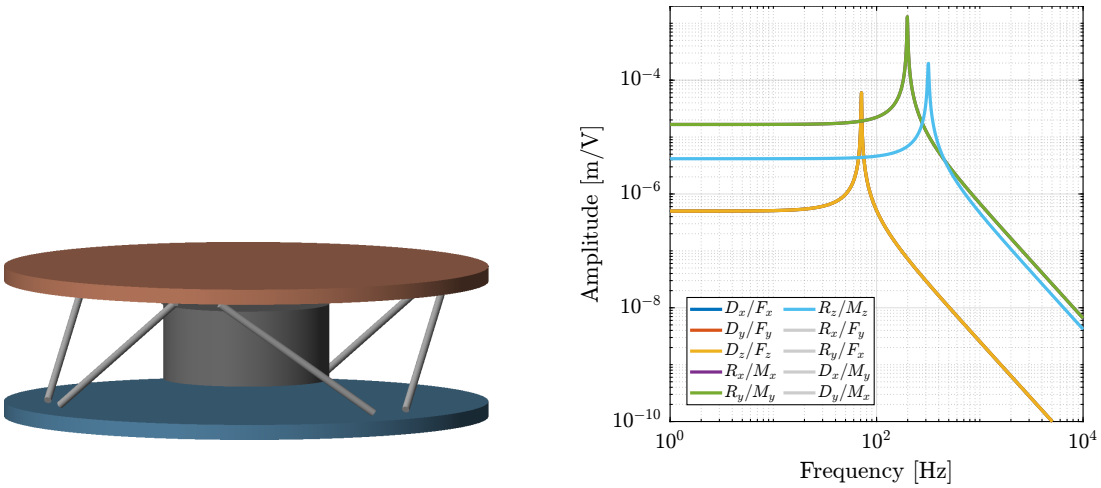

(a) Payload at the cube's center

(b) Fully decoupled cartesian plant

Figure 3.13: Cubic Stewart platform with payload at the cube's center (a). Obtained cartesian plant is fully decoupled (b).

3.1.3.3 Decentralized Control

The orthogonal arrangement of struts in the cubic architecture suggests a potential minimization of inter-strut coupling, which could theoretically create favorable conditions for decentralized control. Two sensor types integrated in the struts are considered: displacement sensors and force sensors. The control architecture is illustrated in Figure 3.14, where $\boldsymbol{K}_{\mathcal{L}}$ represents a diagonal transfer function matrix.

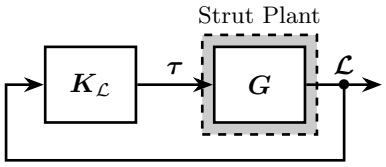

Figure 3.14: Decentralized control in the frame of the struts.

The obtained plant dynamics in the frame of the struts are compared for two Stewart platforms. The first employs a cubic architecture shown in Figure 3.11. The second uses a non-cubic Stewart platform shown in Figure 3.15, featuring identical payload and strut dynamics but with struts oriented more vertically to differentiate it from the cubic architecture.

Relative Displacement Sensors The transfer functions from actuator force in each strut to the relative motion of the struts are presented in Figure 3.16. As anticipated from the equations of motion from $\boldsymbol{f}$ to $\boldsymbol{\mathcal{L}}$ (3.5), the 6×6 plant is decoupled at low frequency. At high-frequency, coupling is observed as the mass matrix projected in the strut frame is not diagonal.

No significant advantage is evident for the cubic architecture (Figure 3.16b) compared to the non-cubic architecture (Figure 3.16a). The resonance frequencies differ between the two cases because the more vertical strut orientation in the non-cubic architecture alters the stiffness properties of the Stewart platform, consequently shifting the frequencies of various modes.

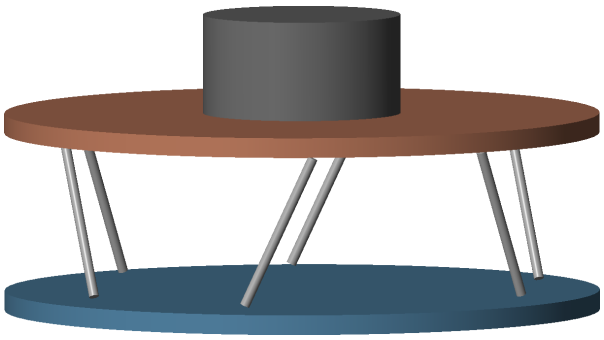

Figure 3.15: Stewart platform with non-cubic architecture.

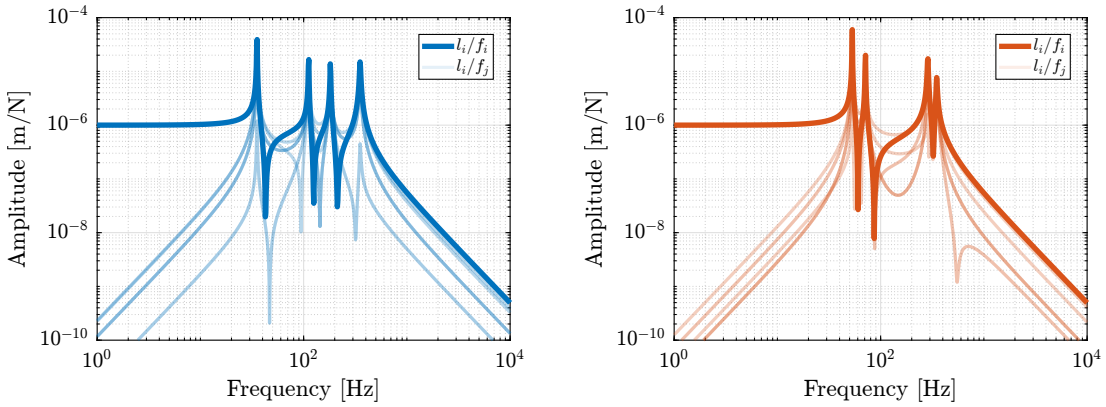

(a) Non cubic architecture

(b) Cubic architecture

Figure 3.16: Bode plot of the transfer functions from actuator force to relative displacement sensor in each strut. Both for a non-cubic architecture (a) and for a cubic architecture (b).

Force Sensors Similarly, the transfer functions from actuator force to force sensors in each strut were analyzed for both cubic and non-cubic Stewart platforms. The results are presented in Figure 3.17. The system demonstrates good decoupling at high-frequency in both cases, with no clear advantage for the cubic architecture.

Conclusion The presented results do not demonstrate the pronounced decoupling advantages often associated with cubic architectures in the literature. Both the cubic and non-cubic configurations exhibited similar coupling characteristics, suggesting that the benefits of orthogonal strut arrangement for decentralized control is less obvious than often reported in the literature.

3.1.3.4 Cubic architecture with Cube's center above the top platform

As demonstrated in Section 3.1.3.2, the cubic architecture can exhibit advantageous dynamical properties when the Center of Mass of the moving body coincides with the cube's center, resulting in diagonal mass and stiffness matrices. As shown in Section 3.1.3.1, the stiffness matrix is diagonal when the considered $\{B\}$ frame is located at the cube's center. However, the $\{B\}$ frame is typically positioned above the top platform where forces are applied and displacements are measured.

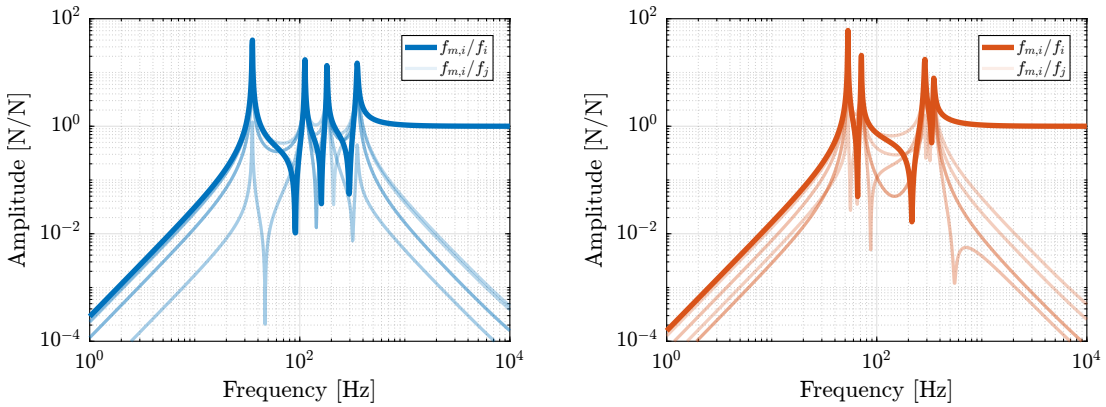

(a) Non cubic architecture

(b) Cubic architecture

Figure 3.17: Bode plot of the transfer functions from actuator force to force sensor in each strut. Both for a non-cubic architecture (a) and for a cubic architecture (b).

This section proposes modifications to the cubic architecture to enable positioning the payload above the top platform while still leveraging the advantageous dynamical properties of the cubic configuration.

Three key parameters define the geometry of the cubic Stewart platform: H, the height of the Stewart platform (distance from fixed base to mobile platform); H_c, the height of the cube, as shown in Figure 3.8a; and H_{CoM}, the height of the Center of Mass relative to the mobile platform (coincident with the cube's center).

Depending on the cube's size H_c in relation to H and H_{CoM}, different designs emerge. In the following examples, $H = 100\,\text{mm}$ and $H_{CoM} = 20\,\text{mm}$.

Small Cube When the cube size H_c is smaller than twice the height of the CoM H_{CoM} (3.13), the resulting design is shown in Figure 3.18.

$$H_c < 2H_{CoM} \tag{3.13}$$

This configuration is similar to that described in [51] (Figure 2.103a, page 108), although they do not explicitly identify it as a cubic configuration. Adjacent struts are parallel to each other, differing from the typical architecture where parallel struts are positioned opposite to each other.

This approach yields a compact architecture, but the small cube size may result in insufficient rotational stiffness.

Medium Sized Cube Increasing the cube's size such that (3.14) is verified produces an architecture with intersecting struts (Figure 3.19).

$$2H_{CoM} < H_c < 2(H_{CoM} + H) \tag{3.14}$$

This configuration resembles the design proposed in [160] (Figure 3.3c), although their design is not strictly cubic.

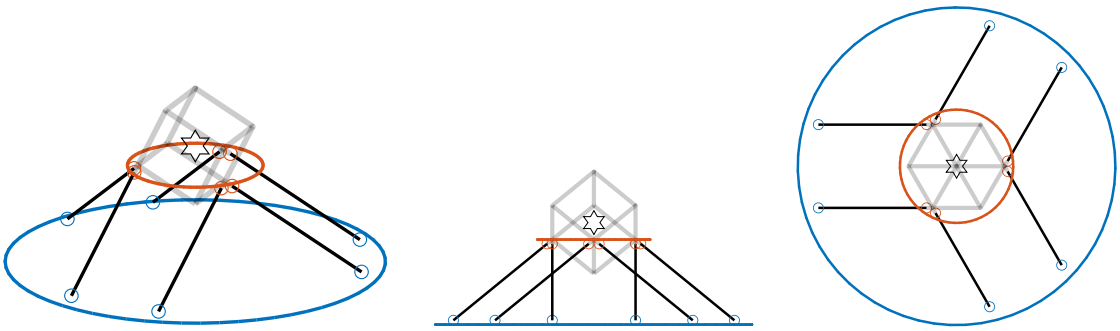

(a) Isometric view **(b)** Side view **(c)** Top view

Figure 3.18: Cubic architecture with cube's center above the top platform. A cube height of 40 mm is used.

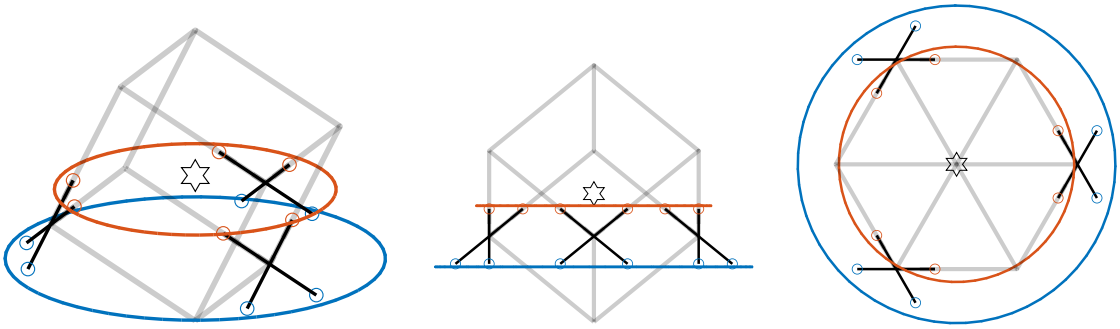

(a) Isometric view **(b)** Side view **(c)** Top view

Figure 3.19: Cubic architecture with cube's center above the top platform. A cube height of 140 mm is used.

Large Cube When the cube's height exceeds twice the sum of the platform height and CoM height (3.15), the architecture shown in Figure 3.20 is obtained.

$$2(H_{CoM} + H) < H_c \tag{3.15}$$

Platform Size For the proposed configuration, the top joints $\boldsymbol{b}_i$ (resp. the bottom joints $\boldsymbol{a}_i$) and are positioned on a circle with radius R_{b_i} (resp. R_{a_i}) described by Equation (3.16).

$$R_{b_i} = \sqrt{\frac{3}{2}H_c^2 + 2H_{CoM}^2} \tag{3.16a}$$

$$R_{a_i} = \sqrt{\frac{3}{2}H_c^2 + 2(H_{CoM} + H)^2} \tag{3.16b}$$

Since the rotational stiffness for the cubic architecture scales with the square of the cube's height (3.8), the cube's size can be determined based on rotational stiffness requirements. Subsequently, using Equation (3.16), the dimensions of the top and bottom platforms can be calculated.

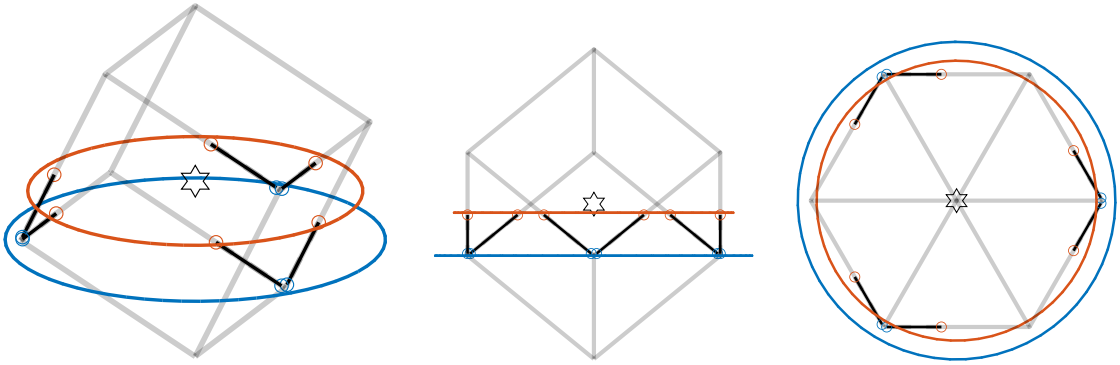

(a) Isometric view **(b)** Side view **(c)** Top view

Figure 3.20: Cubic architecture with cube's center above the top platform. A cube height of 240 mm is used.

3.1.3.5 Conclusion

The analysis of the cubic architecture for Stewart platforms yielded several important findings. While the cubic configuration provides uniform stiffness in the XYZ directions, it stiffness property becomes particularly advantageous when forces and torques are applied at the cube's center. Under these conditions, the stiffness matrix becomes diagonal, resulting in a decoupled Cartesian plant at low frequencies.

Regarding mobility, the translational capabilities of the cubic configuration exhibit uniformity along the directions of the orthogonal struts, rather than complete uniformity in the Cartesian space. This understanding refines the characterization of cubic architecture mobility commonly presented in literature.

The analysis of decentralized control in the frame of the struts revealed more nuanced results than expected. While cubic architectures are frequently associated with reduced coupling between actuators and sensors, this study showed that these benefits may be more subtle or context-dependent than commonly described. Under the conditions analyzed, the coupling characteristics of cubic and non-cubic configurations, in the frame of the struts, appeared similar.

Fully decoupled dynamics in the Cartesian frame can be achieved when the Center of Mass of the moving body coincides with the cube's center. However, this arrangement presents practical challenges, as the cube's center is traditionally located between the top and bottom platforms, making payload placement problematic for many applications.

To address this limitation, modified cubic architectures have been proposed with the cube's center positioned above the top platform. Three distinct configurations have been identified, each with different geometric arrangements but sharing the common characteristic that the cube's center is positioned above the top platform. This structural modification enables the alignment of the moving body's Center of Mass with the Center of Stiffness, resulting in beneficial decoupling properties in the Cartesian frame.

3.1.4 Kinematics of the Active Platform

Based on previous analysis, this section aims to determine the active platform optimal geometry. For the NASS, the chosen reference frames $\{A\}$ and $\{B\}$ coincide with the sample's PoI, which is positioned 150 mm above the top platform. This is the location where precise control of the sample's position is required, as it is where the x-ray beam is focused.

3.1.4.1 Requirements

The design of the active platform must satisfy several constraints. The device should fit within a cylinder with radius of 120 mm and height of 95 mm. Based on the measured errors of all stages of the micro-stations, and incorporating safety margins, the required mobility should enable combined translations in any direction of ± 50 µm. At any position, the system should be capable of performing R_x and R_y rotations of ± 50 µrad. Regarding stiffness, the resonance frequencies should be well above the maximum rotational velocity of 2π rad/s to minimize gyroscopic effects, while remaining below the problematic modes of the micro-station to ensure decoupling from its complex dynamics. In terms of dynamics, the design should facilitate implementation of Integral Force Feedback (IFF) in a decentralized manner, and provide good decoupling for the high authority controller in the frame of the struts.

3.1.4.2 Obtained Geometry

Based on the previous analysis of Stewart platform configurations, while the geometry can be optimized to achieve the desired trade-off between stiffness and mobility in different directions, the wide range of potential payloads, with masses ranging from 1 kg to 50 kg, makes it impossible to develop a single geometry that provides optimal dynamical properties for all possible configurations.

For the active platform design, the struts were oriented more vertically compared to a cubic architecture due to several considerations. First, the performance requirements in the vertical direction are more stringent than in the horizontal direction. This vertical strut orientation decreases the amplification factor in the vertical direction, providing greater resolution and reducing the effects of actuator noise. Second, the micro-station's vertical modes exhibit higher frequencies than its lateral modes. Therefore, higher resonance frequencies of the active platform in the vertical direction compared to the horizontal direction enhance the decoupling properties between the micro-station and the active platform.

Regarding dynamical properties, particularly for control in the frame of the struts, no specific optimization was implemented since the analysis revealed that strut orientation has minimal impact on the resulting coupling characteristics.

Consequently, the geometry was selected according to practical constraints. The height between the two plates is maximized and set at 95 mm. Both platforms take the maximum available size, with joints offset by 15 mm from the plate surfaces and positioned along circles with radii of 120 mm for the fixed joints and 110 mm for the mobile joints. The positioning angles, as shown in Figure 3.21b, are [255, 285, 15, 45, 135, 165] degrees for the top joints and [220, 320, 340, 80, 100, 200] degrees for the bottom joints.

The resulting geometry is illustrated in Figure 3.21. While minor refinements may occur during detailed mechanical design to address manufacturing and assembly considerations, the fundamental geometry will remain consistent with this configuration. This geometry serves as the foundation for estimating the required actuator stroke (Section 3.1.4.3), flexible joint stroke (Section 3.1.4.4) and to perform noise budgeting for instrumentation selection (Section 3.4).

Implementing a cubic architecture as proposed in Section 3.1.3.4 was considered. However, positioning the cube's center 150 mm above the top platform would have resulted in platform dimensions exceeding the maximum available size. Additionally, to benefit from the cubic configuration's dynamical properties, each payload would require careful calibration of inertia before placement on the active platform, ensuring that its Center of Mass coincides with the cube's center. Given the impracticality of consistently aligning the Center of Mass with the cube's center, the cubic architecture was deemed unsuitable for the NASS.

3.1.4.3 Required Actuator Stroke

With the geometry established, the actuator stroke necessary to achieve the desired mobility can be determined.

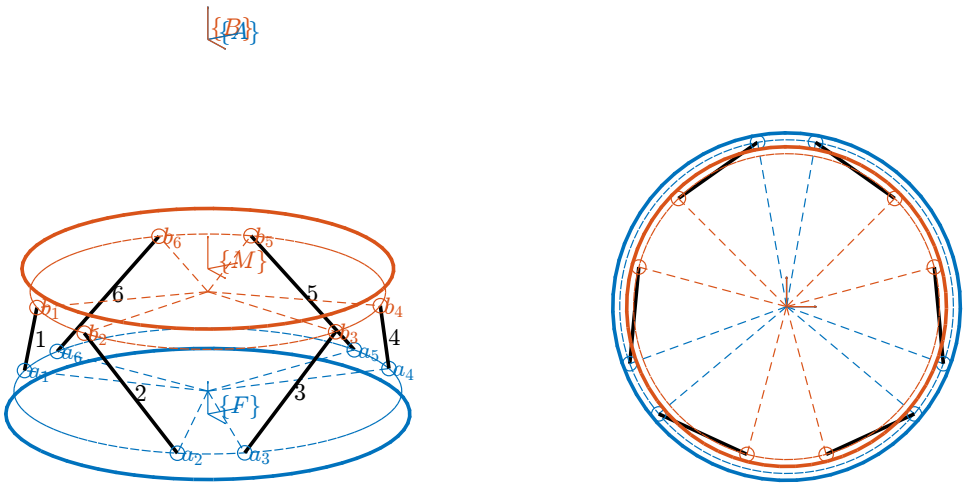

(a) Isometric view **(b)** Top view

Figure 3.21: Obtained architecture for the active platform.

The required mobility parameters include combined translations in the XYZ directions of ± 50 µm (essentially a cubic workspace). Additionally, at any point within this workspace, combined R_x and R_y rotations of ± 50 µrad, with R_z maintained at 0, should be possible.

Calculations based on the selected geometry indicate that an actuator stroke of ± 94 µm is required to achieve the desired mobility. This specification will be used during the actuator selection process in Section 3.2.2.

Figure 3.22 illustrates both the desired mobility (represented as a cube) and the calculated mobility envelope of the active platform with an actuator stroke of ± 94 µm. The diagram confirms that the required workspace fits within the system's capabilities.

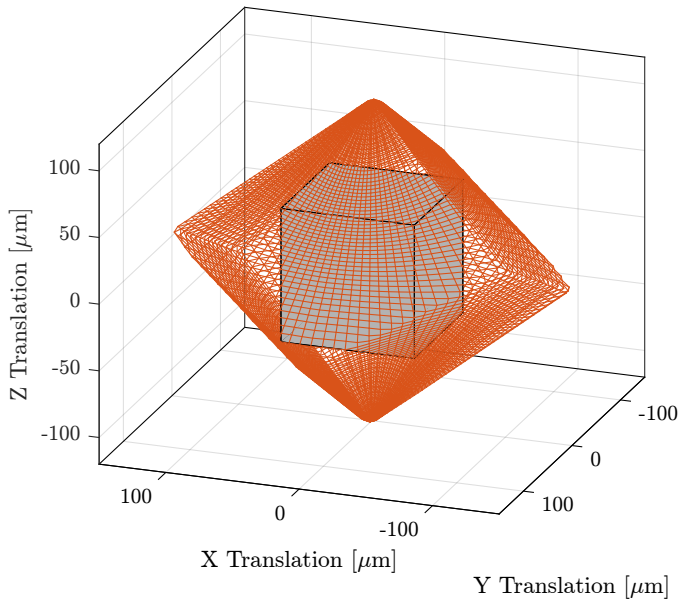

Figure 3.22: Specified translation mobility of the active platform (grey cube) and computed Mobility (red volume).

3.1.4.4 Required Joint Angular Stroke

With the active platform geometry and mobility requirements established, the flexible joint angular stroke necessary to avoid limiting the achievable workspace can be determined.

This analysis focuses solely on bending stroke, as the torsional stroke of the flexible joints is expected to be minimal given the absence of vertical rotation requirements. The required angular stroke for both fixed and mobile joints is estimated to be equal to 1 mrad. This specification will guide the design of the flexible joints in Section 3.2.3.

Conclusion

This chapter has explored the optimization of the active platform geometry for the Nano Active Stabilization System (NASS).

First, a review of existing Stewart platforms revealed two main geometric categories: cubic architectures, characterized by mutually orthogonal struts arranged along the edges of a cube, and non-cubic architectures with varied strut orientations. While cubic architectures are prevalent in the literature and attributed with beneficial properties such as simplified kinematics, uniform stiffness, and reduced cross-coupling, the performed analysis revealed that some of these advantages should be more nuanced or context-dependent than commonly described.

The analytical relationships between Stewart platform geometry and its mechanical properties were established, enabling a better understanding of the trade-offs between competing requirements such as mobility and stiffness along different axes. These insights were useful during the active platform geometry optimization.

For the cubic configuration, complete dynamical decoupling in the Cartesian frame can be achieved when the Center of Mass of the moving body coincides with the cube's center, but this arrangement is often impractical for real-world applications. Modified cubic architectures with the cube's center positioned above the top platform were proposed as a potential solution, but proved unsuitable for the active platform due to size constraints and the impracticality of ensuring that different payloads' centers of mass would consistently align with the cube's center.

For the active platform design, a key challenge was addressing the wide range of potential payloads (1 to 50 kg), which made it impossible to optimize the geometry for consistent dynamic performance across all usage scenarios. This led to a practical design approach where struts were oriented more vertically than in cubic configurations to address several application-specific needs: achieving higher resolution in the vertical direction (compared to the horizontal direction) by reducing amplification factors and better matching the micro-station's modal characteristics with higher vertical resonance frequencies.

3.2 Hybrid Modelling for Component Optimization

Addressing the need for both detailed component optimization and efficient system-level simulation—especially considering the limitations of full FEM for real-time control—a hybrid modeling approach was used. This combines Finite Element Analysis (FEA) with multi-body dynamics, employing reduced-order flexible bodies.

The theoretical foundations and implementation are presented in Section 3.2.1, where experimental validation was performed using an Amplified Piezoelectric Actuator. The framework was then applied to optimize two critical active platform elements: the actuators (Section 3.2.2) and the flexible joints (Section 3.2.3). Through this approach, system-level dynamic behavior under closed-loop control conditions could be successfully predicted while detailed component-level optimization was facilitated.

3.2.1 Reduced Order Flexible Bodies

Components exhibiting complex dynamical behavior are frequently found to be unsuitable for direct implementation within multi-body models. These components are traditionally analyzed using FEA software. However, a methodological bridge between these two analytical approaches has been established, whereby components whose dynamical properties have been determined through FEA can be integrated into multi-body models [20, 32, 57]. This combined multibody-FEA modeling approach presents significant advantages, as it enables the accurate FE modeling to specific elements while maintaining the computational efficiency of multi-body analysis for the broader system [121].

The investigation of this hybrid modeling approach is structured in three sections. First, the fundamental principles and methodological approaches of this modeling framework are introduced (Section 3.2.1.1). It is then illustrated through its practical application to the modelling of an Amplified Piezoelectric Actuator (APA) (Section 3.2.1.2). Finally, the validity of this modeling approach is demonstrated through experimental validation, wherein the obtained dynamics from the hybrid modelling approach is compared with measurements (Section 3.2.1.3).

3.2.1.1 Procedure

In this modeling approach, some components within the multi-body framework are represented as *reduced-order flexible bodies*, wherein their modal behavior is characterized through reduced mass and stiffness matrices derived from FEA models. These matrices are generated via modal reduction techniques, specifically through the application of component mode synthesis, thus establishing this design approach as a combined multibody-FEA methodology [91].

Standard FEA implementations typically involve thousands or even hundreds of thousands of degrees of freedom, rendering direct integration into multi-body simulations computationally prohibitive. The objective of modal reduction is therefore to substantially decrease the number of degrees of freedom while preserving the essential dynamic characteristics of the component.

The procedure for implementing this reduction involves several distinct stages. Initially, the component is modelled in a finite element software with appropriate material properties and boundary conditions. Subsequently, interface frames are defined at locations where the multi-body model will establish connections with the component. These frames serve multiple functions, including connecting to other parts, applying forces and torques, and measuring relative motion between defined frames.

Following the establishment of these interface parameters, modal reduction is performed using the Craig-Bampton method [30] (also known as the “fixed-interface method”), a technique that significantly reduces the number of degrees of freedom while still presenting the main dynamical characteristics. This transformation typically reduces the

model complexity from hundreds of thousands to fewer than hundred degrees of freedom. The number of degrees of freedom in the reduced model is determined by (3.17) where n represents the number of defined frames and p denotes the number of additional modes to be modelled. The outcome of this procedure is an $m \times m$ set of reduced mass and stiffness matrices, m being the total retained number of degrees of freedom, which can subsequently be incorporated into the multi-body model to represent the component's dynamic behavior.

$$m = 6 \times n + p \tag{3.17}$$

3.2.1.2 Example with an Amplified Piezoelectric Actuator

The presented modeling framework was first applied to an Amplified Piezoelectric Actuator (APA) for several reasons. Primarily, this actuator represents an excellent candidate for implementation within the active platform, as will be elaborated in Section 3.2.2. Additionally, an Amplified Piezoelectric Actuator (the APA95ML shown in Figure 3.23) was available in the laboratory for experimental testing.

The APA consists of multiple piezoelectric stacks arranged horizontally (depicted in blue in Figure 3.23) and of an amplifying shell structure (shown in red) that serves two purposes: the application of pre-stress to the piezoelectric elements and the amplification of their displacement in the vertical direction [25]. The selection of the APA for validation purposes was further justified by its capacity to simultaneously demonstrate multiple aspects of the modeling framework. The specific design of the APA allows for the simultaneous modeling of a mechanical structure analogous to a flexible joint, piezoelectric actuation, and piezoelectric sensing, thereby encompassing the principal elements requiring validation.

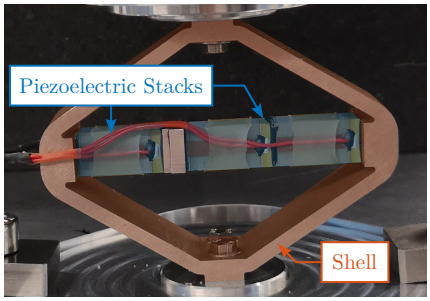

Figure 3.23: Picture of the APA95ML.

Parameter	Value
Nominal Stroke	100 µm
Blocked force	2100 N
Stiffness	21 N/µm

Table 3.2: APA95ML specifications

Finite Element Model The development of the Finite Element Model (FEM) for the APA95ML required the knowledge of the material properties, as summarized in Table 3.3. The finite element mesh, shown in Figure 3.24a, was then generated.

Table 3.3: Material properties used for FEA. E is the Young's modulus, ν the Poisson ratio and ρ the material density.

	E	ν	ρ
Stainless Steel	190 GPa	0.31	7800 kg/m^3
Piezoelectric Ceramics (PZT)	49.5 GPa	0.31	7800 kg/m^3

The definition of interface frames constitutes a critical aspect of the model preparation. Seven frames were established: one frame at the two ends of each piezoelectric stack to facilitate strain measurement and force application, and additional frames at the top and bottom of the structure to enable connection with external elements in the multi-body simulation.

Six additional modes were considered, resulting in total model order of 48. The modal reduction procedure was then executed, yielding the reduced mass and stiffness matrices that form the foundation of the component's representation in the multi-body simulation environment.

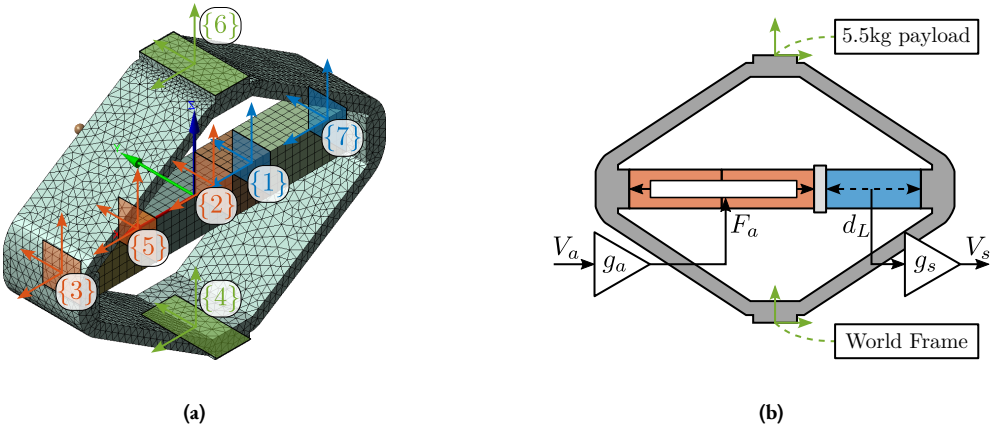

(a) (b)

Figure 3.24: Obtained mesh and defined interface frames (or "remote points") in the finite element model of the APA95ML (a). Interfaces with the multi-body model are shown in (b).

Super Element in the Multi-Body Model Previously computed reduced order mass and stiffness matrices were imported in a multi-body model block called "Reduced Order Flexible Solid". This block has several interface frames corresponding to the ones defined in the FEA software. Frame $\{4\}$ was connected to the "world" frame, while frame $\{6\}$ was coupled to a vertically guided payload. In this example, two piezoelectric stacks were used for actuation while one piezoelectric stack was used as a force sensor. Therefore, a force source F_a operating between frames $\{3\}$ and $\{2\}$ was used, while a displacement sensor d_L between frames $\{1\}$ and $\{7\}$ was used for the sensor stack. This is illustrated in Figure 3.24b.

However, to have access to the physical voltage input of the actuators stacks V_a and to the generated voltage by the force sensor V_s, conversion between the electrical and mechanical domains need to be determined.

Sensor and Actuator "constants" To link the electrical domain to the mechanical domain, an "actuator constant" g_a and a "sensor constant" g_s were introduced as shown in Figure 3.24b.

From [48, p. 123], the relation between relative displacement d_L of the sensor stack and generated voltage V_s is given by (3.18).

$$V_s = g_s \cdot d_L, \quad g_s = \frac{d_{33}}{\epsilon^T s^D n} \tag{3.18}$$

From [49] the relation between the force F_a and the applied voltage V_a is given by (3.19).

$$F_a = g_a \cdot V_a, \quad g_a = d_{33} n k_a, \quad k_a = \frac{c^E A}{L} \tag{3.19}$$

Unfortunately, it is difficult to know exactly which material is used for the piezoelectric stacks[1]. Yet, based on the available properties of the stacks in the data-sheet (summarized in Table 3.4), the soft Lead Zirconate Titanate "THP5H" from Thorlabs seemed to match quite well the observed properties.

Table 3.4: Stack Parameters.

Parameter	Value
Nominal Stroke	$20\,\mu m$
Blocked force	$4700\,N$
Stiffness	$235\,N/\mu m$
Voltage Range	$-20/150\,V$
Capacitance	$4.4\,\mu F$
Length	$20\,mm$
Stack Area	$10 \times 10\,mm^2$

The properties of this "THP5H" material used to compute g_a and g_s are listed in Table 3.5. From these parameters, $g_s = 5.1\,V/\mu m$ and $g_a = 26\,N/V$ were obtained.

Table 3.5: Piezoelectric properties used for the estimation of the sensor and actuator sensitivities.

Parameter	Value	Description
d_{33}	$680 \cdot 10^{-12}\,m/V$	Piezoelectric constant
ϵ^T	$4.0 \cdot 10^{-8}\,F/m$	Permittivity under constant stress
s^D	$21 \cdot 10^{-12}\,m^2/N$	Elastic compliance understand constant electric displacement
c^E	$48 \cdot 10^9\,N/m^2$	Young's modulus of elasticity
L	$20\,mm$ per stack	Length of the stack
A	$10^{-4}\,m^2$	Area of the piezoelectric stack
n	160 per stack	Number of layers in the piezoelectric stack

Identification of the APA Characteristics Initial validation of the Finite Element Model and its integration as a reduced-order flexible model within the multi-body model was accomplished through comparative analysis of key actuator characteristics against manufacturer specifications.

The stiffness of the APA95ML was estimated from the multi-body model by computing the axial compliance of the APA95ML (Figure 3.25), which corresponds to the transfer function from a vertical force applied between the two interface frames to the relative vertical displacement between these two frames. The inverse of the DC gain this transfer function corresponds to the axial stiffness of the APA95ML. A value of $23\,N/\mu m$ was found which is close to the specified stiffness in the datasheet of $k = 21\,N/\mu m$.

The multi-body model predicted a resonant frequency under block-free conditions of $\approx 2\,kHz$ (Figure 3.25), which is in agreement with the nominal specification.

In order to estimate the stroke of the APA95ML, the mechanical amplification factor, defined as the ratio between vertical displacement and horizontal stack displacement, was first determined. This characteristic was quantified through analysis of the transfer function relating horizontal stack motion to vertical actuator displacement, from which an amplification factor of 1.5 was derived.

The piezoelectric stacks, exhibiting a typical strain response of 0.1 % relative to their length (here equal to 20 mm), produce an individual nominal stroke of 20 µm (see data-sheet of the piezoelectric stacks on Table 3.4, page 165). As three stacks are used, the horizontal displacement is 60 µm. Through the established amplification factor of 1.5, this translates to a predicted vertical stroke of 90 µm which falls within the manufacturer-specified range of 80 µm and 120 µm.

[1] The manufacturer of the APA95ML was not willing to share the piezoelectric material properties of the stack.

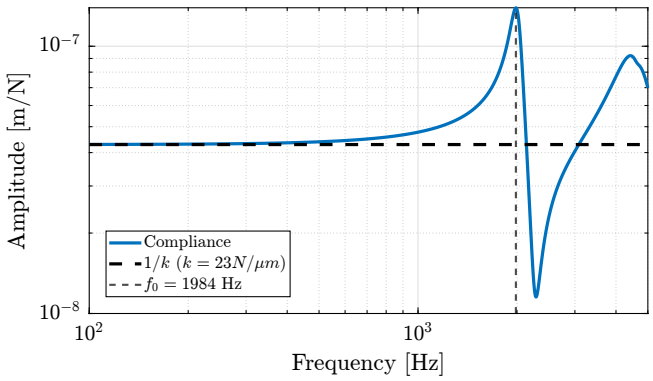

Figure 3.25: Estimated axial compliance of the APA95ML.

The high degree of concordance observed across multiple performance metrics provides a first validation of the ability to include FEM into multi-body model.

3.2.1.3 Experimental Validation

Further validation of the reduced-order flexible body methodology was undertaken through experimental investigation. The goal was to measure the dynamics of the APA95ML and to compare it with predictions derived from the multi-body model incorporating the actuator as a flexible element.

The test bench illustrated in Figure 3.26 was used, which consists of a 5.7 kg granite suspended on top of the APA95ML. The granite's motion was vertically guided with an air bearing system, and a fibered interferometer was used to measure its vertical displacement y. A Digital to Analog Converter (DAC) was used to generate the control signal u, which was subsequently conditioned through a voltage amplifier with a gain of 20, ultimately yielding the effective voltage V_a across the two piezoelectric stacks. Measurement of the sensor stack voltage V_s was performed using an ADC.

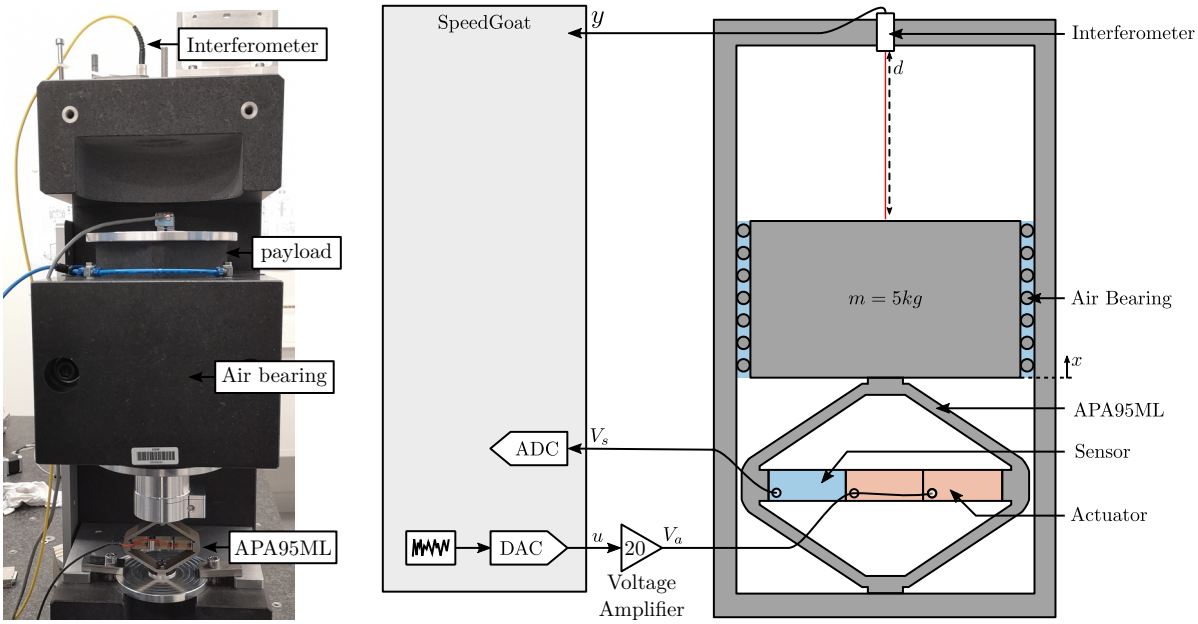

Figure 3.26: Test bench used to validate the presented modeling strategy.

Comparison of the Dynamics Frequency domain system identification techniques were used to characterize the dynamic behavior of the APA95ML. The identification procedure required careful choice of the excitation signal [110, chap. 5]. During all this experimental work, random noise excitation was predominantly employed.

The designed excitation signal is then generated and both input and output signals are synchronously acquired. From the obtained input and output data, the FRFs were derived. To improve the quality of the obtained frequency domain data, averaging and windowing were used [110, chap. 13].

The obtained FRFs from V_a to V_s and to y are compared with the theoretical predictions derived from the multi-body model in Figure 3.27.

The difference in phase between the model and the measurements can be attributed to the sampling time of 0.1 ms and to additional delays induced by electronic instrumentation related to the interferometer. The presence of a non-minimum phase zero in the measured system response (Figure 3.27b), shall be addressed during the experimental phase.

Regarding the amplitude characteristics, the constants g_a and g_s could be further refined through calibration against the experimental data.

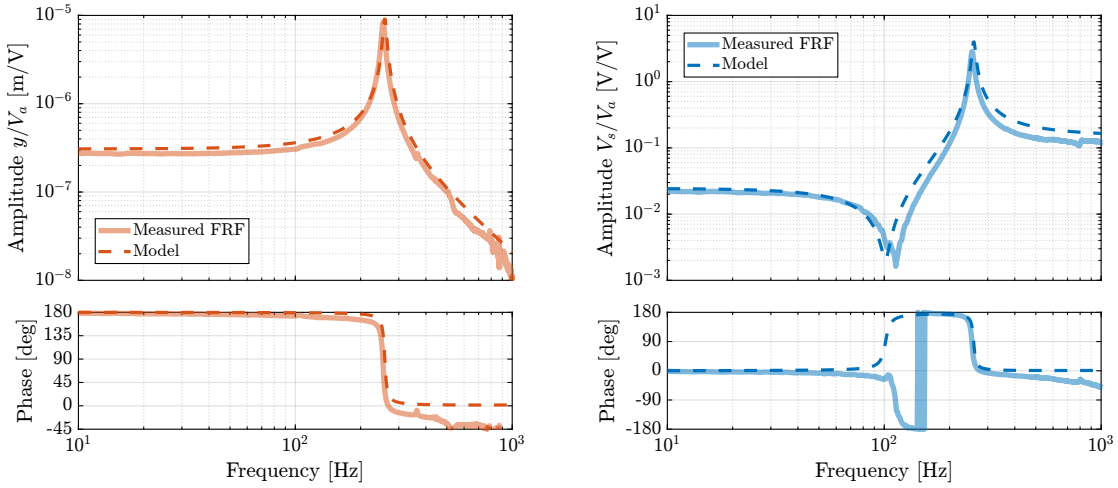

(a) from V_a to y **(b)** from V_a to V_s

Figure 3.27: Comparison of the measured frequency response functions and the finite element model of the APA95ML. Both for the dynamics from V_a to y (a) and from V_a to V_s (b).

Integral Force Feedback with APA To further validate this modeling methodology, its ability to predict closed-loop behavior was verified experimentally. Integral Force Feedback (IFF) was implemented using the force sensor stack, and the measured dynamics of the damped system were compared with model predictions across multiple feedback gains.

The IFF controller implementation, defined in equation 3.20, incorporated a tunable gain parameter g and was designed to provide integral action near the system resonances and to limit the low frequency gain using an high pass filter.

$$K_{\text{IFF}}(s) = \frac{g}{s + 2 \cdot 2\pi} \cdot \frac{s}{s + 0.5 \cdot 2\pi} \tag{3.20}$$

The theoretical damped dynamics of the closed-loop system was estimated using the model by computed the root locus plot shown in Figure 3.28a. For experimental validation, six gain values were tested: $g = [0,\ 10,\ 50,\ 100,\ 500,\ 1000]$. The measured FRFs for each gain configuration were compared with model predictions, as presented in Figure 3.28b.

The close agreement between experimental measurements and theoretical predictions across all gain configurations demonstrates the model's capability to accurately predict both open-loop and closed-loop system dynamics.

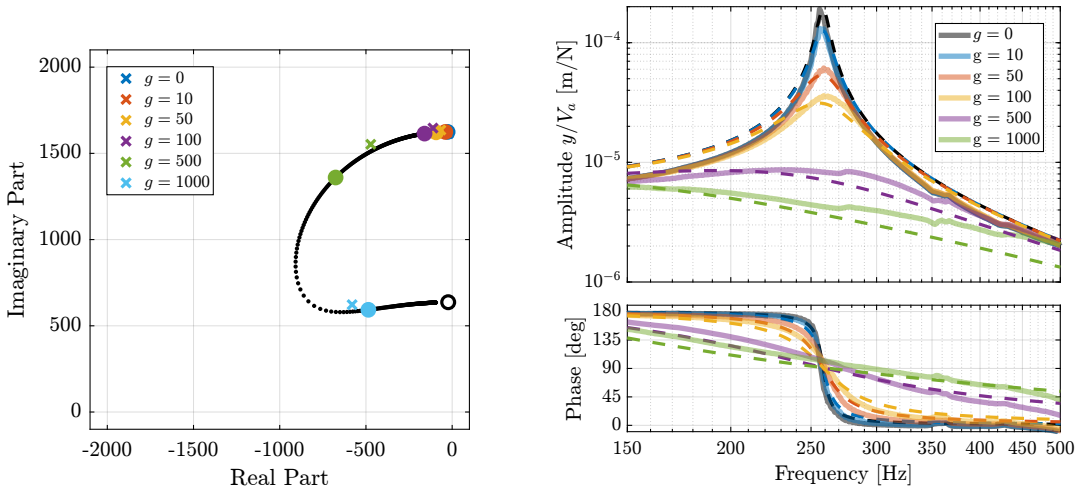

(a) Root locus plot

(b) Damped plants

Figure 3.28: Results using Integral Force Feedback with the APA95ML. Closed-loop poles as a function of the controller gain g are predicted by the root locus plot (a). Circles are predictions from the model while crosses are poles estimated from the experimental data. Damped plants estimated from the model (dashed curves) and measured ones (solid curves) are compared in (b) for all tested controller gains.

3.2.1.4 Conclusion

The experimental validation with an Amplified Piezoelectric Actuator confirms that this methodology accurately predicts both open-loop and closed-loop dynamic behaviors. This verification establishes its effectiveness for component design and system analysis applications.

The approach will be especially beneficial for optimizing actuators (Section 3.2.2) and flexible joints (Section 3.2.3) for the active platform.

3.2.2 Actuator Selection

3.2.2.1 Choice of the Actuator based on Specifications

The actuator selection process was driven by several critical requirements derived from previous dynamic analyses. A primary consideration is the actuator stiffness, which significantly impacts system dynamics through multiple mechanisms. The spindle rotation induces gyroscopic effects that modify plant dynamics and increase coupling, necessitating sufficient stiffness. Conversely, the actuator stiffness must be carefully limited to ensure the active platform's suspension modes remain below the problematic modes of the micro-station to limit the coupling between the two structures. These competing requirements suggest an optimal stiffness of approximately 1 N/µm.

Additional specifications arise from the control strategy and physical constraints. The implementation of the decentralized Integral Force Feedback (IFF) architecture necessitates force sensors to be collocated with each actuator. The system's geometric constraints limit the actuator height to 50 mm, given the active platform's maximum height of 95 mm and the presence of flexible joints at each strut extremity. Furthermore, the actuator stroke must exceed the micro-station positioning errors while providing additional margin for mounting adjustments and operational flexibility. An actuator stroke of $\approx 200\,\mu m$ is therefore required.

Three actuator technologies were evaluated (examples of such actuators are shown in Figure 3.29): voice coil actuators, piezoelectric stack actuators, and amplified piezoelectric actuators. Variable reluctance actuators were not considered despite their superior efficiency compared to voice coil actuators, as their inherent nonlinearity would introduce control complexity.

(a) Voice Coil **(b)** Piezoelectric stack **(c)** Amplified Piezoelectric Actuator

Figure 3.29: Example of actuators considered for the active platform. Voice coil from Sensata Technologies (a). Piezoelectric stack actuator from Physik Instrumente (b). Amplified Piezoelectric Actuator from DSM (c).

Voice coil actuators (shown in Figure 3.29a), when combined with flexure guides of wanted stiffness ($\approx 1\,N/\mu m$), would require forces in the order of 200 N to achieve the specified 200 µm displacement. While these actuators offer excellent linearity and long strokes capabilities, the constant force requirement would result in significant steady-state current, leading to thermal loads that could compromise system stability. Their advantages (linearity and long stroke) were not considered adapted for this application, diminishing their benefits relative to piezoelectric solutions.

Conventional piezoelectric stack actuators (shown in Figure 3.29b) present two significant limitations for the current application. Their stroke is inherently limited to approximately 0.1 % of their length, meaning that even with the maximum allowable height of 50 mm, the achievable stroke would only be 50 µm, insufficient for the application. Additionally, their extremely high stiffness, typically around $100\,N/\mu m$, exceeds the desired specifications by two orders of magnitude.

Amplified Piezoelectric Actuators emerged as the optimal solution by addressing these limitations through a specific mechanical design. The incorporation of a shell structure serves multiple purposes: it provides mechanical amplification of the piezoelectric displacement, reduces the effective axial stiffness to more suitable levels for the application, and creates a compact vertical profile. Furthermore, the multi-stack configuration enables one stack to be dedicated to force sensing, ensuring excellent collocation with the actuator stacks, a critical feature for implementing robust decentralized IFF [135, 151]. Moreover, using APA for active damping has been successfully demonstrated in similar applications [4].

Several specific APA models were evaluated against the established specifications (Table 3.6). The APA300ML emerged as the optimal choice. This selection was further reinforced by previous experience with APAs from the same manufacturer[1], and particularly by the successful validation of the modeling methodology with a similar actuator (Section 3.2.1.2). The demonstrated accuracy of the modeling approach for the APA95ML provides confidence in the

[1] Cedrat technologies.

reliable prediction of the APA300ML's dynamic characteristics, thereby supporting both the selection decision and subsequent dynamical analyses.

Table 3.6: List of some amplified piezoelectric actuators that could be used for the active platform.

Specification	APA150M	**APA300ML**	APA400MML	FPA-0500E-P	FPA-0300E-S
Stroke $> 200\,\mu m$	187	304	368	432	240
Stiffness $\approx 1\,N/\mu m$	0.7	1.8	0.55	0.87	0.58
Resolution $< 2\,nm$	2	3	4	n/a	n/a
Blocked Force $> 100\,N$	127	546	201	376	139
Height $< 50\,mm$	22	30	24	27	16

3.2.2.2 APA300ML - Reduced Order Flexible Body

The validation of the APA300ML started by incorporating a "reduced order flexible body" into the multi-body model as explained in Section 3.2.1. The FEA model was developed with particular attention to the placement of reference frames, as illustrated in Figure 3.30b. Seven distinct frames were defined, with blue frames designating the force sensor stack interfaces for strain measurement, red frames denoting the actuator stack interfaces for force application and green frames for connecting to other elements. 120 additional modes were added during the modal reduction for a total order of 162. While this high order provides excellent accuracy for validation purposes, it proves computationally intensive for simulations.

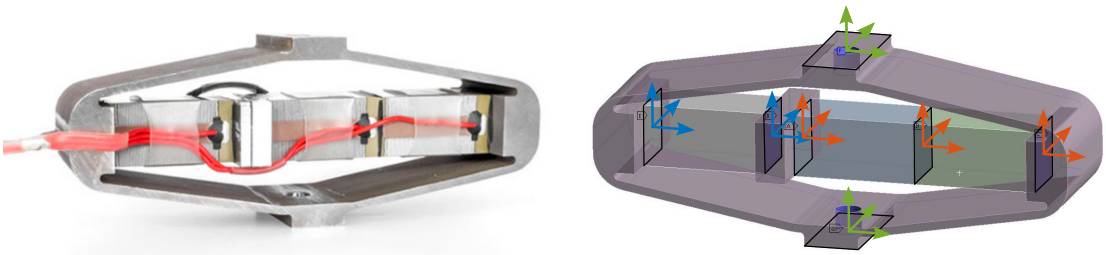

(a) Picture of the APA300ML **(b)** FEM of the APA300ML

Figure 3.30: Amplified Piezoelectric Actuator APA300ML. Picture shown in (a). Frames (or "remote points") used for the modal reduction are shown in (b).

The sensor and actuator "constants" (g_s and g_a) derived in Section 3.2.1.2 for the APA95ML were used for the APA300ML model, as both actuators employ identical piezoelectric stacks.

3.2.2.3 Simpler 2-DoF Model of the APA300ML

To facilitate efficient time-domain simulations while maintaining essential dynamic characteristics, a simplified two-degree-of-freedom model, adapted from [135], was developed.

This model, illustrated in Figure 3.31, comprises three components. The mechanical shell is characterized by its axial stiffness k_1 and damping c_1. The actuator is modelled with stiffness k_a and damping c_a, incorporating a force source f. This force is related to the applied voltage V_a through the actuator constant g_a. The sensor stack is modelled with stiffness k_e and damping c_e, with its deformation d_L being converted to the output voltage V_s through the sensor sensitivity g_s.

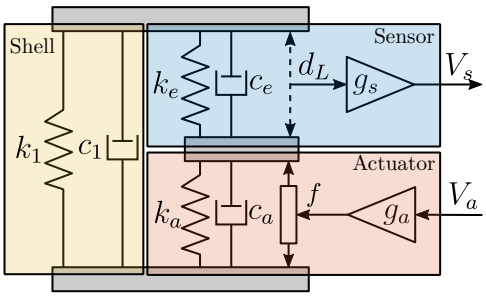

Figure 3.31: Schematic of the 2-DoF model of the Amplified Piezoelectric Actuator.

While providing computational efficiency, this simplified model has inherent limitations. It considers only axial behavior, treating the actuator as infinitely rigid in other directions. Several physical characteristics are not explicitly represented, including the mechanical amplification factor and the actual stress the piezoelectric stacks. Nevertheless, the model's primary advantage lies in its simplicity, adding only four states to the system model.

The model requires tuning of 8 parameters (k_1, c_1, k_e, c_e, k_a, c_a, g_s, and g_a) to match the dynamics extracted from the FEA.

The shell parameters k_1 and c_1 were determined first through analysis of the zero in the V_a to V_s transfer function. The physical interpretation of this zero can be understood through root locus analysis: as controller gain increases, the poles of a closed-loop system converge to the open-loop zeros. The open-loop zero therefore corresponds to the poles of the system with a theoretical infinite-gain controller that ensures zero force in the sensor stack. This condition effectively represents the dynamics of an APA without the force sensor stack (i.e. an APA with only the shell). This physical interpretation enables straightforward parameter tuning: k_1 determines the frequency of the zero, while c_1 defines its damping characteristic.

The stack parameters (k_a, c_a, k_e, c_e) were then derived from the first pole of the V_a to y response. Given that identical piezoelectric stacks are used for both sensing and actuation, the relationships $k_e = 2k_a$ and $c_e = 2c_a$ were enforced, reflecting the series configuration of the dual actuator stacks. Finally, the sensitivities g_s and g_a were adjusted to match the DC gains of the respective transfer functions.

The resulting parameters, listed in Table 3.7, yield dynamic behavior that closely matches the high-order FEM, as demonstrated in Figure 3.32. While higher-order modes and non-axial flexibility are not captured, the model accurately represents the fundamental dynamics within the operational frequency range.

Table 3.7: Summary of the obtained parameters for the 2-DoF APA300ML model.

Parameter	Value
k_1	0.30 N/µm
k_e	4.3 N/µm
k_a	2.15 N/µm
c_1	18 Ns/m
c_e	0.7 Ns/m
c_a	0.35 Ns/m
g_a	2.7 N/V
g_s	0.53 V/µm

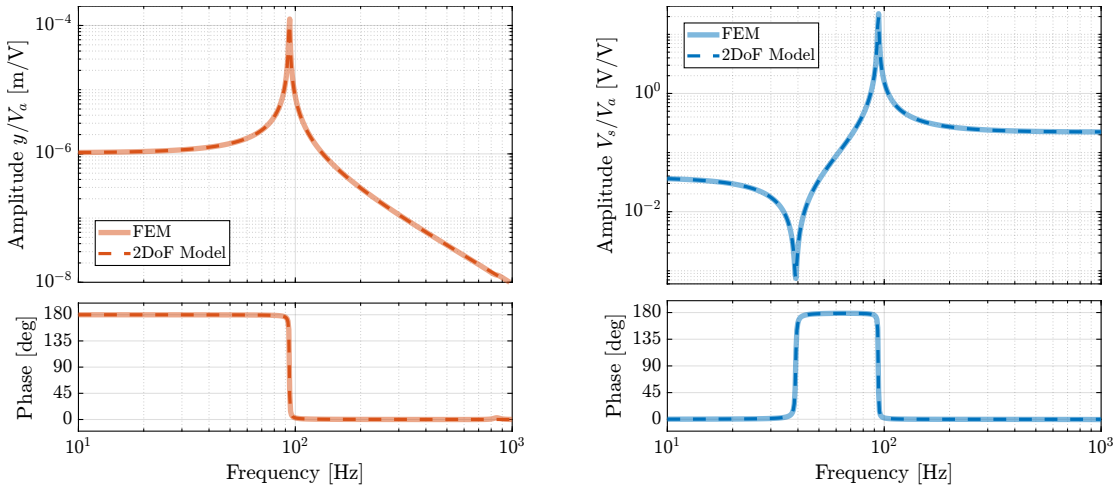

(a) from V_a to d_i

(b) from V_a to V_s

Figure 3.32: Comparison of the transfer functions extracted from the finite element model of the APA300ML and of the 2-DoF model. Both for the dynamics from V_a to d_i (a) and from V_a to V_s (b).

3.2.2.4 Electrical characteristics of the APA

The behavior of piezoelectric actuators is characterized by coupled constitutive equations that establish relationships between electrical properties (charges, voltages) and mechanical properties (stress, strain) [127, chapter 5.5].

To evaluate the impact of electrical boundary conditions on the system dynamics, experimental measurements were conducted using the APA95ML, comparing the transfer function from V_a to y under two distinct configurations. With the force sensor stack in open-circuit condition (analogous to voltage measurement with high input impedance) and in short-circuit condition (similar to charge measurement with low output impedance). As demonstrated in Figure 3.33, short-circuiting the force sensor stack results in a minor decrease in resonance frequency. The developed models of the APA do not represent such behavior, but as this effect is quite small, this validates the simplifying assumption made in the models.

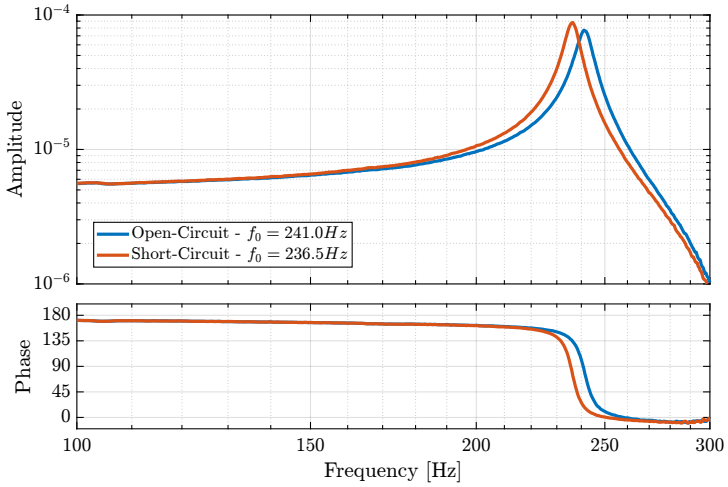

Figure 3.33: Effect of the electrical boundaries of the force sensor stack on the APA95ML resonance frequency.

However, the electrical characteristics of the APA remain crucial for instrumentation design. Proper consideration must be given to voltage amplifier specifications and force sensor signal conditioning requirements. These aspects will be addressed in the instrumentation chapter.

3.2.2.5 Validation with the Active Platform

The integration of the APA300ML model within the active platform simulation framework served two validation objectives: to validate the APA300ML choice through analysis of system dynamics with APA modelled as flexible bodies, and to validate the simplified 2-DoF model through comparative analysis with the full FEM implementation.

The dynamics predicted using the flexible body model align well with the design requirements established during the conceptual phase. The dynamics from $\boldsymbol{u}$ to $\boldsymbol{V}_s$ exhibits the desired alternating pole-zero pattern (Figure 3.34a), a critical characteristic for implementing robust decentralized Integral Force Feedback. Additionally, the model predicts no problematic high-frequency modes in the dynamics from $\boldsymbol{u}$ to $\boldsymbol{\epsilon}_{\mathcal{L}}$ (Figure 3.34b), maintaining consistency with earlier conceptual simulations. These findings suggest that the control performance targets established during the conceptual phase remain achievable with the selected actuator.

Comparative analysis between the high-order FEM implementation and the simplified 2-DoF model (Figure 3.34) demonstrates remarkable agreement in the frequency range of interest. This validates the use of the simplified model for time-domain simulations. The reduction in model order is substantial: while the FEM implementation results in approximately 300 states (36 states per actuator plus 12 additional states), the 2-DoF model requires only 24 states for the complete active platform.

These results validate both the selection of the APA300ML and the effectiveness of the simplified modeling approach for the active platform.

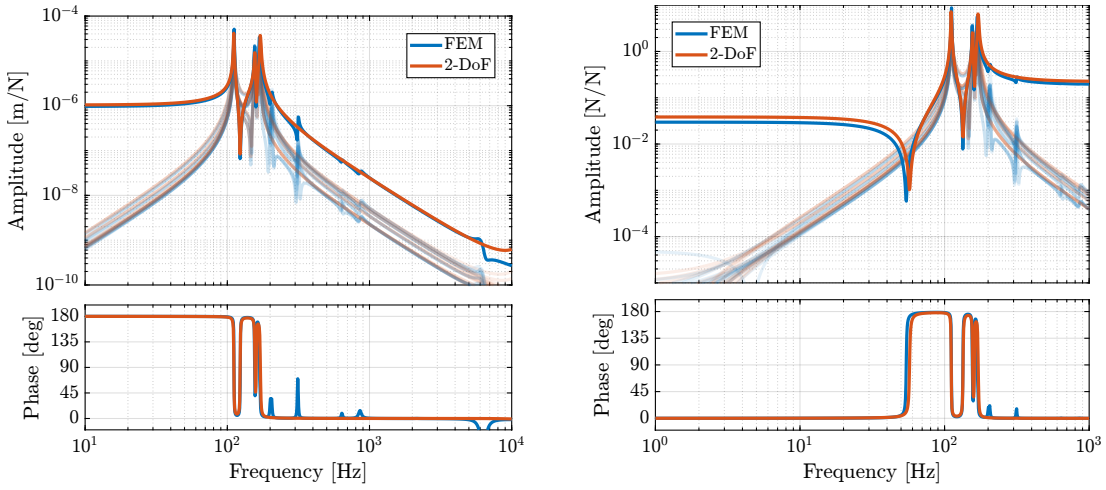

(a) $\boldsymbol{f}$ to $\boldsymbol{\epsilon}_{\mathcal{L}}$ **(b)** $\boldsymbol{f}$ to $\boldsymbol{f}_m$

Figure 3.34: Comparison of the dynamics obtained between an active platform having the actuators modelled with FEM and an active platform having actuators modelled as 2-DoF system. Both from actuator force $\boldsymbol{f}$ to strut motion measured by external metrology $\boldsymbol{\epsilon}_{\mathcal{L}}$ (b) and to the force sensors $\boldsymbol{f}_m$ (a).

3.2.3 Flexible Joint Design

High-precision position control at the nanometer scale requires systems to be free from friction and backlash, as these nonlinear phenomena severely limit achievable positioning accuracy. This fundamental requirement prevents the use of conventional joints, necessitating instead the implementation of flexible joints that achieve motion through elastic deformation. For Stewart platforms requiring nanometric precision, numerous flexible joint designs have been developed and successfully implemented, as illustrated in Figure 3.35. For design simplicity and component standardization, identical joints are employed at both ends of the active platform struts.

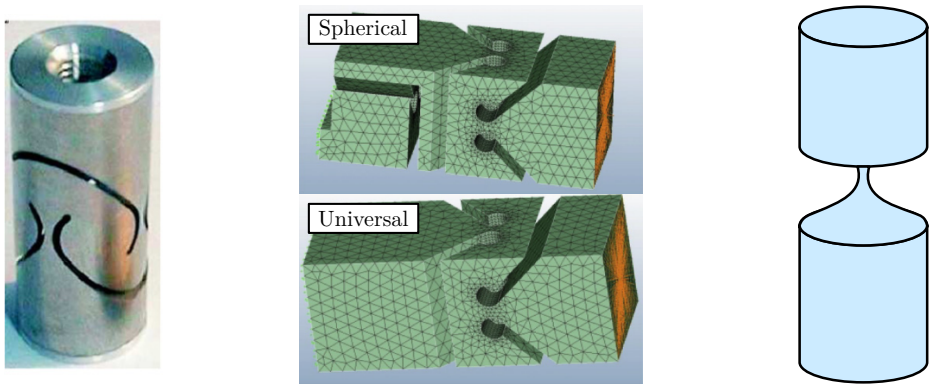

Figure 3.35: Example of different flexible joints geometry used for Stewart platforms. (a) Typical "universal" flexible joint used in [117]. (b) Torsional stiffness can be explicitly specified as done in [160]. (c) "Thin" flexible joints having "notch curves" [41].

While ideally these joints would permit free rotation about defined axes while maintaining infinite rigidity in other degrees of freedom, practical implementations exhibit parasitic stiffness that can impact control performance [97]. This section examines how these non-ideal characteristics affect system behavior, focusing particularly on bending/torsional stiffness (Section 3.2.3.1) and axial compliance (Section 3.2.3.2).

The analysis of bending and axial stiffness effects enables the establishment of comprehensive specifications for the flexible joints. These specifications guide the development and optimization of a flexible joint design through FEA (Section 3.2.3.3). The validation process, detailed in Section 3.2.3.4, begins with the integration of the joints as "reduced order flexible bodies" in the active platform model, followed by the development of computationally efficient lower-order models that preserve the essential dynamic characteristics of the flexible joints.

3.2.3.1 Bending and Torsional Stiffness

The presence of bending stiffness in flexible joints causes the forces applied by the struts to deviate from the strut direction [97] and can affect system dynamics.

To quantify these effects, simulations were conducted with the micro-station considered rigid and using simplified 1-DoF actuators (stiffness of $1\,\mathrm{N}/\mu\mathrm{m}$) without parallel stiffness to the force sensors. Flexible joint bending stiffness was varied from 0 (ideal case) to $500\,\mathrm{Nm}/\mathrm{rad}$.

Analysis of the plant dynamics reveals two significant effects. For the transfer function from $\boldsymbol{f}$ to $\boldsymbol{\epsilon}_{\mathcal{L}}$, bending stiffness increases low-frequency coupling, though this remains small for realistic stiffness values (Figure 3.36a). In [97], it is established that forces remain effectively aligned with the struts when the flexible joint bending stiffness is much small

than the actuator stiffness multiplied by the square of the strut length. For the active platform, this corresponds to having the bending stiffness much lower than 9000 Nm/rad. This condition is more readily satisfied with the relatively stiff actuators selected, and could be problematic for softer Stewart platforms.

For the force sensor plant, bending stiffness introduces complex conjugate zeros at low frequency (Figure 3.36b). This behavior resembles having parallel stiffness to the force sensor as was the case with the APA300ML (see Figure 3.34b). However, this time the parallel stiffness does not come from the considered strut, but from the bending stiffness of the flexible joints of the other five struts. This characteristic impacts the achievable damping using decentralized Integral Force Feedback [117]. This is confirmed by the root locus plot in Figure 3.37a. This effect becomes less significant when using the selected APA300ML actuators (Figure 3.37b), which already incorporate parallel stiffness by design which is higher than the one induced by flexible joint stiffness.

A parallel analysis of torsional stiffness revealed similar effects, though these proved less critical for system performance.

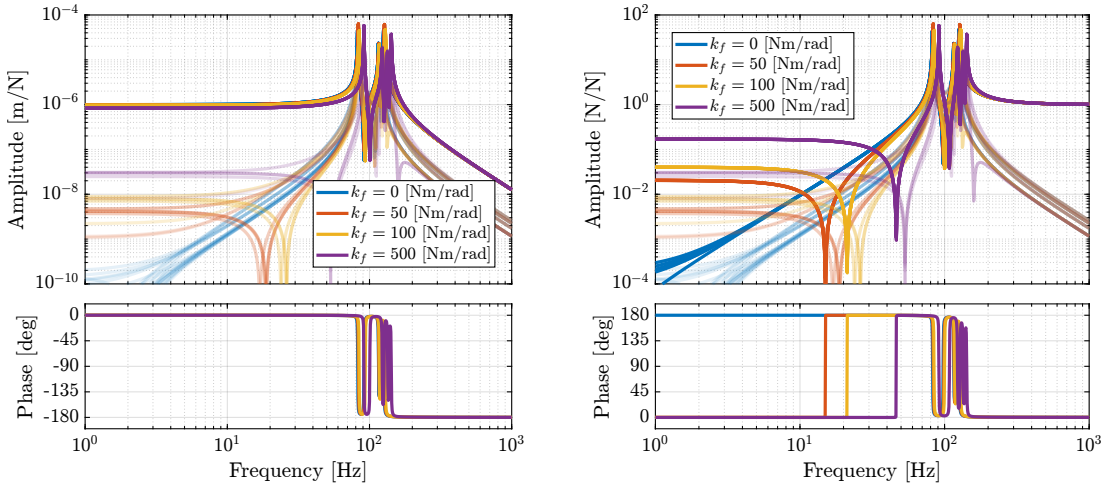

(a) $\boldsymbol{f}$ to $\boldsymbol{\epsilon}_{\mathcal{L}}$ **(b)** $\boldsymbol{f}$ to $\boldsymbol{f}_m$

Figure 3.36: Effect of bending stiffness of the flexible joints on the plant dynamics. Both from actuator force $\boldsymbol{f}$ to strut motion measured by external metrology $\boldsymbol{\epsilon}_{\mathcal{L}}$ (a) and to the force sensors $\boldsymbol{f}_m$ (b).

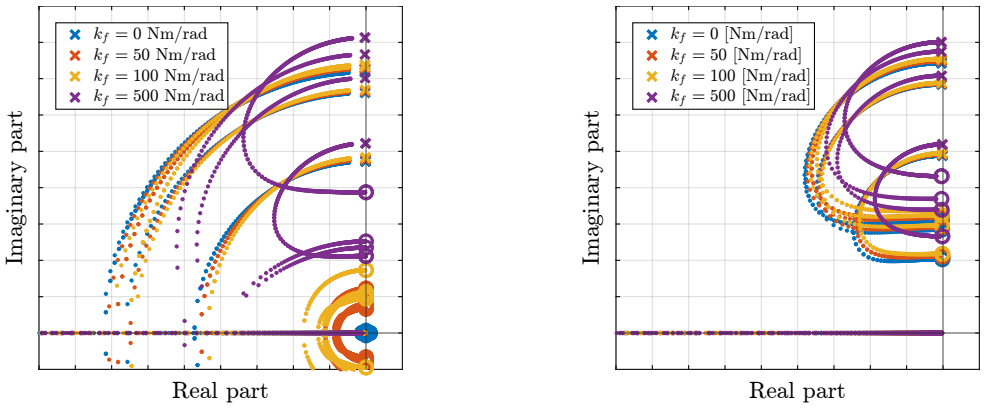

(a) 1-DoF actuators **(b)** APA300ML actuators

Figure 3.37: Effect of bending stiffness of the flexible joints on the attainable damping with decentralized IFF. For 1-DoF actuators (a), and with the 2-DoF model of the APA300ML (b).

3.2.3.2 Axial Stiffness

The limited axial stiffness (k_a) of flexible joints introduces an additional compliance between the actuation point and the measurement point. As explained in [113, chapter 6] and in [121] (effect called "actuator flexibility"), such intermediate flexibility invariably degrades control performance. Therefore, determining the minimum acceptable axial stiffness that maintains active platform performance becomes crucial.

The analysis incorporates the strut mass (112g per APA300ML) to accurately model internal resonance effects. A parametric study was conducted by varying the axial stiffness from 1 N/µm (matching actuator stiffness) to 1000 N/µm (approximating rigid behavior). The resulting dynamics (Figure 3.38) reveal distinct effects on system dynamics.

The force-sensor (IFF) plant exhibits minimal sensitivity to axial compliance, as evidenced by both FRFs (Figure 3.38b) and root locus analysis (Figure 3.39a).

However, the transfer function from $\boldsymbol{f}$ to $\boldsymbol{\epsilon}_{\mathcal{L}}$ demonstrates significant effects: internal strut modes appear at high-frequencies, introducing substantial cross-coupling between axes. This coupling is quantified through Relative Gain Array (RGA) analysis of the damped system (Figure 3.39b), which confirms increasing interaction between control channels at frequencies above the joint-induced resonance.

Above this resonance frequency, two critical limitations emerge. First, the system exhibits strong coupling between control channels, making decentralized control strategies ineffective. Second, control authority diminishes significantly near the resonant frequencies. These effects fundamentally limit achievable control bandwidth, making high axial stiffness essential for system performance.

Based on this analysis, an axial stiffness specification of 100 N/µm was established for the active platform joints.

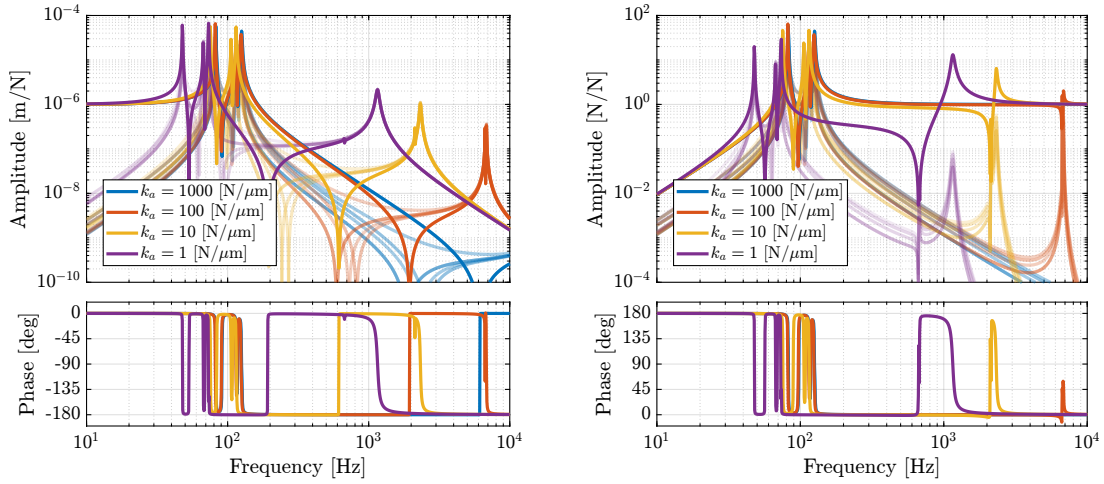

(a) $\boldsymbol{f}$ to $\boldsymbol{\epsilon}_{\mathcal{L}}$ **(b)** $\boldsymbol{f}$ to $\boldsymbol{f}_m$

Figure 3.38: Effect of axial stiffness of the flexible joints on the plant dynamics. Both from actuator force $\boldsymbol{f}$ to strut motion measured by external metrology $\boldsymbol{\epsilon}_{\mathcal{L}}$ (a) and to the force sensors $\boldsymbol{f}_m$ (b).

3.2.3.3 Specifications and Design of Flexible Joints

The design of flexible joints for precision applications requires careful consideration of multiple mechanical characteristics. Critical specifications include sufficient bending stroke to ensure long-term operation below yield stress, high

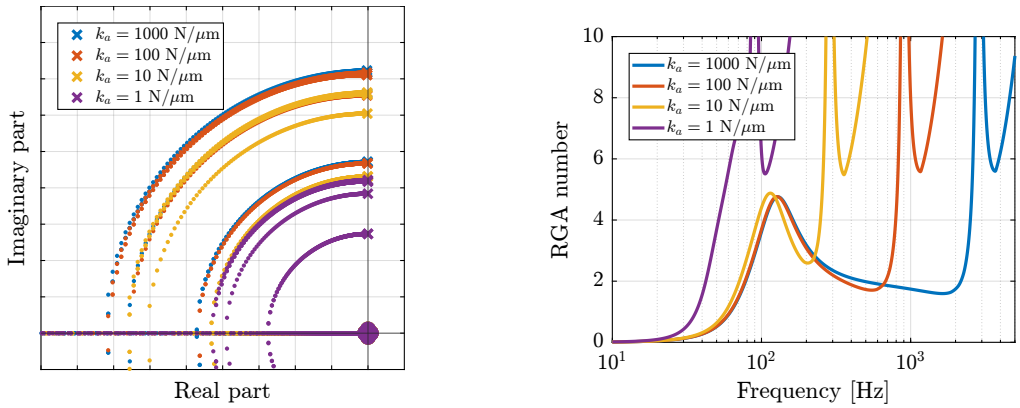

(a) Root locus

(b) RGA number

Figure 3.39: Effect of axial stiffness of the flexible joints on the attainable damping with decentralized IFF (a). Estimation of the coupling of the damped plants using the RGA-number (b).

axial stiffness for precise positioning, low bending and torsional stiffnesses to minimize parasitic forces, adequate load capacity, and well-defined rotational axes. Based on the dynamic analysis presented in previous sections, quantitative specifications were established and are summarized in Table 3.8.

Table 3.8: Specifications for the flexible joints and estimated characteristics from the Finite Element Model.

	Specification	FEM
Axial Stiffness k_a	$> 100\,\mathrm{N/\mu m}$	94
Shear Stiffness k_s	$> 1\,\mathrm{N/\mu m}$	13
Bending Stiffness k_f	$< 100\,\mathrm{Nm/rad}$	5
Torsion Stiffness k_t	$< 500\,\mathrm{Nm/rad}$	260
Bending Stroke	$> 1\,\mathrm{mrad}$	24.5

Among various possible flexible joint architectures, the design shown in Figure 3.40 was selected for three key advantages. First, the geometry creates coincident x and y rotation axes, ensuring well-defined kinematic behavior, important for the precise definition of the active platform Jacobian matrix. Second, the design allows easy tuning of different directional stiffnesses through a limited number of geometric parameters. Third, the architecture inherently provides high axial stiffness while maintaining the required compliance in rotational degrees of freedom.

The joint geometry was optimized through parametric FEA. The optimization process revealed an inherent trade-off between maximizing axial stiffness and achieving sufficiently low bending/torsional stiffness, while maintaining material stresses within acceptable limits. The final design, featuring a neck dimension of 0.25 mm, achieves mechanical properties closely matching the target specifications, as verified through FEA and summarized in Table 3.8.

3.2.3.4 Validation with the Active Platform

The designed flexible joint was first validated through integration into the active platform model using reduced-order flexible bodies derived from FEA. This high-fidelity representation was created by defining two interface frames (Figure 3.41) and extracting six additional modes, resulting in reduced-order mass and stiffness matrices of dimension 18×18. The computed transfer functions from actuator forces to both force sensor measurements ($\boldsymbol{f}$ to $\boldsymbol{f}_m$) and external metrology ($\boldsymbol{f}$ to $\boldsymbol{\epsilon}_{\mathcal{L}}$) demonstrate dynamics consistent with predictions from earlier analyses (Figure 3.42), thereby validating the joint design.

(a) 3D view **(b)** Key dimensions

Figure 3.40: Designed flexible joints.

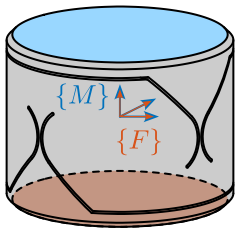

Figure 3.41: Defined frames for the reduced order flexible body. The two flat interfaces are considered rigid, and are linked to the two frames $\{F\}$ and $\{M\}$ both located at the center of rotation.

While this detailed modeling approach provides high accuracy, it results in a significant increase in system model order. The complete active platform model incorporates 240 states: 12 for the payload (6-DoF), 12 for the 2-DoF struts, and 216 for the flexible joints (18 states for each of the 12 joints). To improve computational efficiency, a low order representation was developed using simplified joint elements with compliance only along the wanted degrees of freedom.

After evaluating various configurations, a compromise was achieved by modeling bottom joints with bending and axial stiffness (k_f and k_a), and top joints with bending, torsional, and axial stiffness (k_f, k_t and k_a). This simplification reduces the total model order to 48 states: 12 for the payload, 12 for the struts, and 24 for the joints (12 each for bottom and top joints). While additional degrees of freedom could potentially capture more dynamic features, the selected configuration preserves essential system characteristics while minimizing computational complexity.

Conclusion

In this chapter, the methodology of combining Finite Element Analysis with multi-body modeling has been demonstrated and validated, proving particularly valuable for the detailed design of active platform components. The approach was first validated using an amplified piezoelectric actuator, where predicted dynamics showed excellent agreement with experimental measurements for both open and closed-loop behavior. This validation established confidence in the method's ability to accurately predict component behavior within a larger system.

The methodology was then successfully applied to optimize two critical components. For the actuators, it enabled validation of the APA300ML selection while providing both high-fidelity and computationally efficient models for system simulation. Similarly, for the flexible joints, the analysis of bending and axial stiffness effects led to clear specifications and an optimized design that balances competing mechanical requirements. In both cases, the ability to seamlessly integrate finite element models into the multi-body framework proved essential for understanding component interactions and their impact on system-level dynamics.

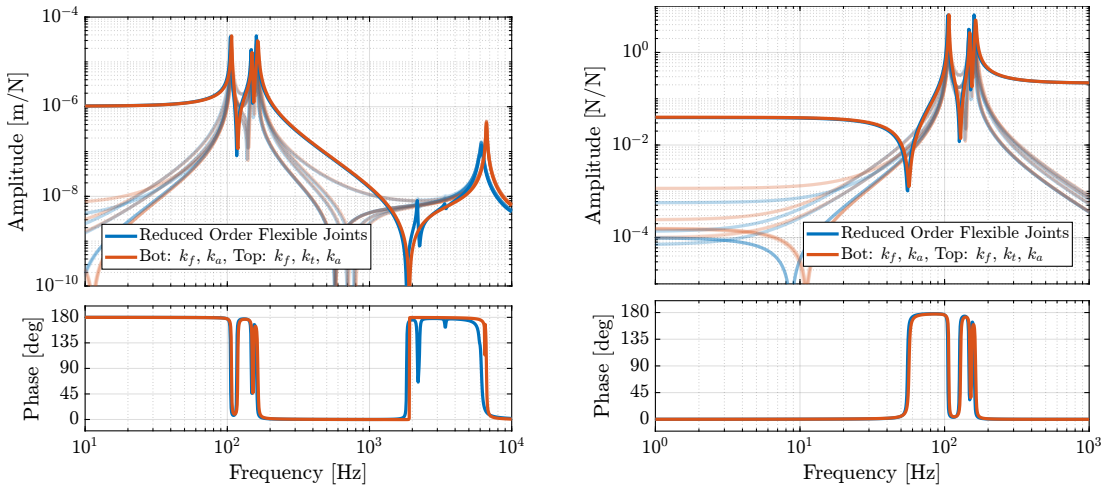

(a) $\boldsymbol{f}$ to $\boldsymbol{\epsilon}_{\mathcal{L}}$ **(b)** $\boldsymbol{f}$ to $\boldsymbol{f}_m$

Figure 3.42: Comparison of the dynamics obtained between an active platform including joints modelled with FEM and an active platform having 2-DoF bottom joints and 3-DoF top joints. Both from actuator force $\boldsymbol{f}$ to strut motion measured by external metrology $\boldsymbol{\epsilon}_{\mathcal{L}}$ (a) and to the force sensors $\boldsymbol{f}_m$ (b).

A key outcome of this work is the development of reduced-order models that maintain prediction accuracy while enabling efficient time-domain simulation. Such model reduction, guided by detailed understanding of component behavior, provides the foundation for subsequent control system design and optimization.

3.3 Control Optimization

Three critical elements for the control of parallel manipulators such as the active platform were identified: effective use and combination of multiple sensors, appropriate plant decoupling strategies, and robust controller design for the decoupled system.

During the conceptual design phase of the NASS, pragmatic approaches were implemented for each of these elements. The High Authority Control / Low Authority Control architecture was selected for combining sensors. Control was implemented in the frame of the struts, leveraging the inherent low-frequency decoupling of the plant where all decoupled elements exhibited similar dynamics, thereby simplifying the Single Input Single Output (SISO) controller design process. For these decoupled plants, open-loop shaping techniques were employed to tune the individual controllers.

While these initial strategies proved effective in validating the NASS concept, this work explores alternative approaches with the potential to further enhance the performance. Section 3.3.1 examines different methods for combining multiple sensors, with particular emphasis on sensor fusion techniques that are based on complementary filters. A novel approach for designing these filters is proposed, which allows optimization of the sensor fusion effectiveness.

Section 3.3.2 presents a comparative analysis of various decoupling strategies, including Jacobian decoupling, modal decoupling, and Singular Value Decomposition (SVD) decoupling. Each method is evaluated in terms of its theoretical foundations, implementation requirements, and performance characteristics, providing insights into their respective advantages for different applications.

Finally, Section 3.3.3 addresses the challenge of controller design for decoupled plants. A method for directly shaping closed-loop transfer functions using complementary filters is proposed, offering an intuitive approach to achieving desired performance specifications while ensuring robustness to plant uncertainty.

3.3.1 Multiple Sensor Control

The literature review of Stewart platforms revealed a wide diversity of designs with various sensor and actuator configurations. Control objectives (such as active damping, vibration isolation, or precise positioning) directly dictate sensor selection, whether inertial, force, or relative position sensors.

In cases where multiple control objectives must be achieved simultaneously, as is the case for the NASS where the Stewart platform must both position the sample and provide isolation from micro-station vibrations, combining multiple sensors within the control architecture has been demonstrated to yield significant performance benefits [59]. From the literature, three principal approaches for combining sensors have been identified: High Authority Control / Low Authority Control, sensor fusion, and two-sensor control architectures.

The HAC-LAC approach employs a dual-loop control strategy in which two control loops are using different sensors for distinct purposes (Figure 3.43a). In [88], vibration isolation is provided by accelerometers collocated with the voice coil actuators, while external rotational sensors are used to achieve pointing control. In [53], force sensors collocated with the magnetostrictive actuators are used for active damping using decentralized IFF, and subsequently accelerometers are employed for adaptive vibration isolation. Similarly, in [153], piezoelectric actuators with collocated force sensors are used in a decentralized manner to provide active damping while accelerometers are implemented in an adaptive feedback loop to suppress periodic vibrations. In [158], force sensors are integrated in the struts for decentralized force feedback while accelerometers fixed to the top platform are employed for centralized control.

The second approach, sensor fusion (illustrated in Figure 3.43c), involves filtering signals from two sensors using complementary filters[1] and summing them to create an improved sensor signal. In [59], geophones (used at low frequency)

[1] A set of two complementary filters are two transfer functions that sum to one.

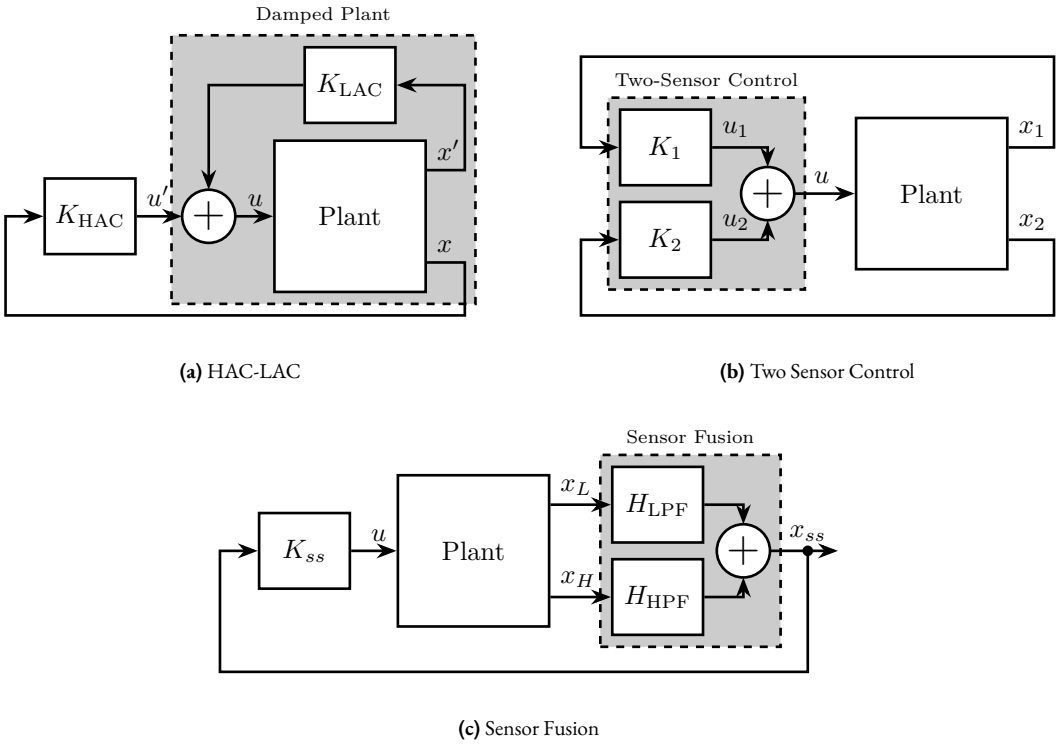

(a) HAC-LAC

(b) Two Sensor Control

(c) Sensor Fusion

Figure 3.43: Different control architectures combining multiple sensors. High Authority Control / Low Authority Control (a), Two-Sensor Control (b) and Sensor Fusion (c).

are merged with force sensors (used at high-frequency). It is demonstrated that combining both sensors using sensor fusion can improve performance compared to using only one of the two sensors. In [148], sensor fusion architecture is implemented with an accelerometer and a force sensor. This implementation is shown to simultaneously achieve high damping of structural modes (through the force sensors) while maintaining very low vibration transmissibility (through the accelerometers).

In [12], the performance of sensor fusion is compared with the more general case of "two-sensor control" (illustrated in Figure 3.43b). It is highlighted that "two-sensor control" provides greater control freedom, potentially enhancing performance. In [144], the use of force sensors and geophones is compared for vibration isolation purposes. Geophones are shown to provide better isolation performance than load cells but suffer from poor robustness. Conversely, the controller based on force sensors exhibited inferior performance (due to the presence of a pair of low frequency zeros), but demonstrated better robustness properties. A "two-sensor control" approach was proven to perform better than controllers based on individual sensors while maintaining better robustness. A Linear Quadratic Gaussian (LQG) was employed to optimize the two-input/one-output controller.

Beyond these three main approaches, other control architectures have been proposed for different purposes. For instance, in [160], a first control loop based on force sensors and relative motion sensors is implemented to compensate for parasitic stiffness of the flexible joints. Subsequently, the system is decoupled in the modal space (facilitated by the removal of parasitic stiffness) and accelerometers are employed for vibration isolation.

The HAC-LAC architecture was previously investigated during the conceptual phase and successfully implemented to validate the NASS concept, demonstrating excellent performance. At the other end of the spectrum, the two-sensor approach yields greater control design freedom but introduces increased complexity in tuning, and thus was not pursued in this study. This work instead focuses on sensor fusion, which represents a promising middle ground between the proven HAC-LAC approach and the more complex two-sensor control strategy.

A review of sensor fusion is first presented in Section 3.3.1.1. Then, in Section 3.3.1.2, both the robustness of the fusion and the noise characteristics of the resulting "fused sensor" are derived and expressed as functions of the complementary filters' norms. A synthesis method for shaping complementary filters is proposed in Section 3.3.1.3. The investigation is then extended beyond the conventional two-sensor scenario, demonstrating how the proposed complementary filter synthesis can be generalized for applications requiring the fusion of three or more sensors (Section 3.3.1.4).

3.3.1.1 Review of Sensor Fusion

Measuring a physical quantity using sensors is always subject to several limitations. First, the accuracy of the measurement is affected by various noise sources, such as electrical noise from the conditioning electronics. Second, the frequency range in which the measurement is relevant is bounded by the bandwidth of the sensor. One way to overcome these limitations is to combine several sensors using a technique called "sensor fusion" [13]. Fortunately, a wide variety of sensors exists, each with different characteristics. By carefully selecting the sensors to be fused, a "super sensor" is obtained that combines the benefits of the individual sensors.

In some applications, sensor fusion is employed to increase measurement bandwidth [132, 166]. For instance, in [132], the bandwidth of a position sensor is extended by fusing it with an accelerometer that provides high-frequency motion information. In other applications, sensor fusion is used to obtain an estimate of the measured quantity with reduced noise [16, 69, 70, 111]. More recently, the fusion of sensors measuring different physical quantities has been proposed to enhance control properties [28, 162]. In [28], an inertial sensor used for active vibration isolation is fused with a sensor collocated with the actuator to improve the stability margins of the feedback controller.

Beyond Stewart platforms, practical applications of sensor fusion are numerous. It is widely implemented for attitude estimation in autonomous vehicles such as unmanned aerial vehicles [8, 29, 75] and underwater vehicles [11, 109]. Sensor fusion offers significant benefits for high-performance positioning control as demonstrated in [132, 162, 166]. It has also been identified as a key technology for improving the performance of active vibration isolation systems [148]. Emblematic examples include the isolation stages of gravitational wave detectors [28, 61] such as those employed at LIGO [69, 70] and Virgo [90].

Two principal methods are employed to perform sensor fusion: using complementary filters [7] or using Kalman filtering [15]. For sensor fusion applications, these methods share many relationships [15, 16, 50, 63]. However, Kalman filtering requires assumptions about the probabilistic characteristics of sensor noise [16], whereas complementary filters do not impose such requirements. Furthermore, complementary filters offer advantages over Kalman filtering for sensor fusion through their general applicability, low computational cost [63], and intuitive nature, as their effects can be readily interpreted in the frequency domain.

A set of filters is considered complementary if the sum of their transfer functions equals one at all frequencies. In early implementations of complementary filtering, analog circuits were used to physically realize the filters [7]. While analog complementary filters remain in use today [103, 162], digital implementation is now more common as it provides greater flexibility.

Various design methods have been developed to optimize complementary filters. The most straightforward approach is based on analytical formulas, which depending on the application may be first order [29, 161, 162], second order [8, 75, 140], or higher orders [28, 95, 132, 140, 166]. Since the characteristics of the super sensor depend on proper complementary filter design [39], several optimization techniques have emerged—ranging from optimizing parameters for analytical formulas [50, 75] to employing convex optimization tools [69, 70] such as linear matrix inequalities [109]. As demonstrated in [111], complementary filter design can be linked to the standard mixed-sensitivity control problem, allowing powerful classical control theory tools to be applied. For example, in [75], two gains of a Proportional Integral (PI) controller are optimized to minimize super sensor noise.

All these complementary filter design methods share the common objective of creating a super sensor with desired characteristics, typically in terms of noise and dynamics. As reported in [111, 166], phase shifts and magnitude bumps in the super sensor dynamics may occur if complementary filters are poorly designed or if sensors are improperly calibrated. Therefore, the robustness of the fusion must be considered when designing complementary filters. Despite the numerous design methods proposed in the literature, a simple approach that specifies desired super sensor characteristics while ensuring good fusion robustness has been lacking.

Fortunately, both fusion robustness and super sensor characteristics can be linked to complementary filter magnitude [39]. Based on this relationship, the present work introduces an approach to designing complementary filters using $\mathcal{H}_\infty$-synthesis, which enables intuitive shaping of complementary filter magnitude in a straightforward manner.

3.3.1.2 Sensor Fusion and Complementary Filters Requirements

A general sensor fusion architecture using complementary filters is shown in Figure 3.44, where multiple sensors (in this case two) measure the same physical quantity x. The sensor output signals $\hat{x}_1$ and $\hat{x}_2$ represent estimates of x. These estimates are filtered by complementary filters and combined to form a new estimate $\hat{x}$.

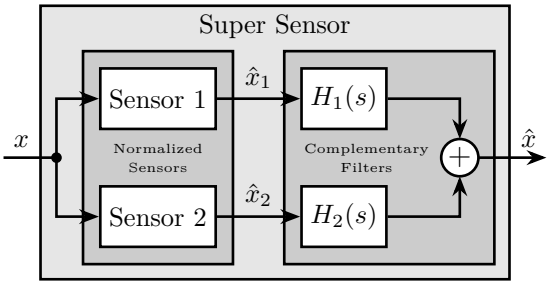

Figure 3.44: Schematic of a sensor fusion architecture using complementary filters.

The complementary property of filters $H_1(s)$ and $H_2(s)$ requires that the sum of their transfer functions equals one at all frequencies (3.21).

$$H_1(s) + H_2(s) = 1 \tag{3.21}$$

Sensor Models and Sensor Normalization To analyze sensor fusion architectures, appropriate sensor models are required. The model shown in Figure 3.45a consists of a Linear Time Invariant (LTI) system $G_i(s)$ representing the sensor dynamics and an input n_i representing sensor noise. The model input x is the measured physical quantity, and its output $\tilde{x}_i$ is the "raw" output of the sensor.

Prior to filtering the sensor outputs $\tilde{x}_i$ with complementary filters, the sensors are typically normalized to simplify the fusion process. This normalization involves using an estimate $\hat{G}_i(s)$ of the sensor dynamics $G_i(s)$, and filtering the sensor output by the inverse of this estimate $\hat{G}_i^{-1}(s)$, as shown in Figure 3.45b. It is assumed that the sensor inverse $\hat{G}_i^{-1}(s)$ is proper and stable. This approach ensures that the units of the estimates $\hat{x}_i$ match the units of the physical quantity x. The sensor dynamics estimate $\hat{G}_i(s)$ may be a simple gain or a more complex transfer function.

Two normalized sensors are then combined to form a super sensor as shown in Figure 3.46. The two sensors measure the same physical quantity x with dynamics $G_1(s)$ and $G_2(s)$, and with uncorrelated noises n_1 and n_2. The signals from both normalized sensors are fed into two complementary filters $H_1(s)$ and $H_2(s)$ and then combined to yield an estimate $\hat{x}$ of x. The super sensor output $\hat{x}$ is therefore described by (3.22).

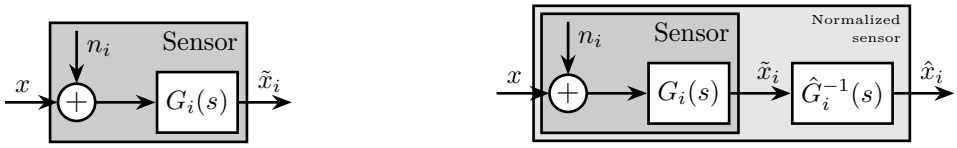

(a) Model with noise n_i and acrshort:lti transfer function $G_i(s)$ **(b)** Normalized sensor using the inverse of an estimate $\hat{G}$

Figure 3.45: Sensor models with and without normalization.

$$\hat{x} = \Big(H_1(s)\hat{G}_1^{-1}(s)G_1(s) + H_2(s)\hat{G}_2^{-1}(s)G_2(s)\Big)x + H_1(s)\hat{G}_1^{-1}(s)G_1(s)n_1 + H_2(s)\hat{G}_2^{-1}(s)G_2(s)n_2 \quad (3.22)$$

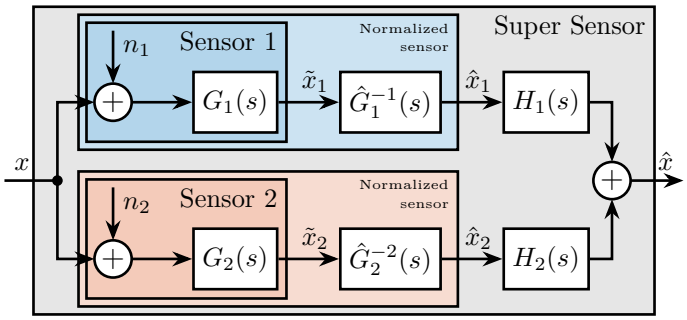

Figure 3.46: Sensor fusion architecture with two normalized sensors.

Noise Sensor Filtering First, consider the case where all sensors are perfectly normalized (3.23). The effects of imperfect normalization will be addressed subsequently.

$$\frac{\hat{x}_i}{x} = \hat{G}_i(s)G_i(s) = 1 \quad (3.23)$$

In that case, the super sensor output $\hat{x}$ equals x plus the filtered noise from both sensors (3.24). From this equation, it is evident that the complementary filters $H_1(s)$ and $H_2(s)$ operate solely on the sensor noise. Thus, this sensor fusion architecture allows filtering of sensor noise without introducing distortion in the measured physical quantity. This fundamental property necessitates that the two filters are complementary.

$$\hat{x} = x + H_1(s)n_1 + H_2(s)n_2 \quad (3.24)$$

The estimation error ϵ_x, defined as the difference between the sensor output $\hat{x}$ and the measured quantity x, is computed for the super sensor (3.25).

$$\epsilon_x \triangleq \hat{x} - x = H_1(s)n_1 + H_2(s)n_2 \quad (3.25)$$

As shown in (3.26), the Power Spectral Density (PSD) of the estimation error Φ_{ϵ_x} depends both on the norm of the two complementary filters and on the PSD of the noise sources Φ_{n_1} and Φ_{n_2}.

$$\Phi_{\epsilon_x}(\omega) = |H_1(j\omega)|^2 \Phi_{n_1}(\omega) + |H_2(j\omega)|^2 \Phi_{n_2}(\omega) \tag{3.26}$$

If the two sensors have identical noise characteristics ($\Phi_{n_1}(\omega) = \Phi_{n_2}(\omega)$), simple averaging ($H_1(s) = H_2(s) = 0.5$) would minimize the super sensor noise. This represents the simplest form of sensor fusion using complementary filters.

However, sensors typically exhibit high noise levels in different frequency regions. In such cases, to reduce the noise of the super sensor, $|H_1(j\omega)|$ should be minimized when $\Phi_{n_1}(\omega)$ exceeds $\Phi_{n_2}(\omega)$, and $|H_2(j\omega)|$ should be minimized when $\Phi_{n_2}(\omega)$ exceeds $\Phi_{n_1}(\omega)$. Therefore, by appropriately shaping the norm of the complementary filters, the noise of the super sensor can be minimized.

Sensor Fusion Robustness In practical systems, sensor normalization is rarely perfect, and condition (3.23) is not fully satisfied. To analyze such imperfections, a multiplicative input uncertainty is included into the sensor dynamics (Figure 3.47a). The nominal model is the estimated model used for normalization $\hat{G}_i(s)$, $\Delta_i(s)$ is any stable transfer function satisfying $|\Delta_i(j\omega)| \leq 1, \ \forall\omega$, and $w_i(s)$ is a weighting transfer function representing the magnitude of uncertainty.

Since the nominal sensor dynamics is taken as the normalized filter, the normalized sensor model can be further simplified as shown in Figure 3.47b.

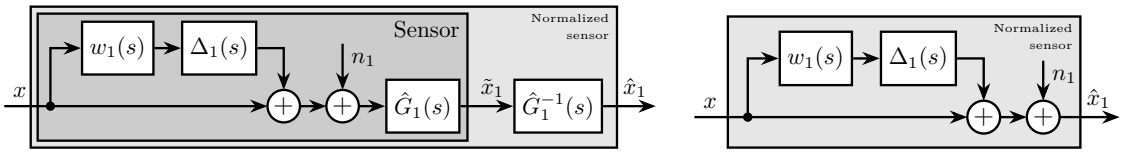

(a) Sensor with multiplicative input uncertainty

(b) Simplified normalized sensor model

Figure 3.47: Sensor models with dynamical uncertainty.

The sensor fusion architecture including sensor models with dynamical uncertainty is illustrated in Figure 3.48a. The super sensor dynamics (3.27) is no longer unity but depends on the sensor dynamical uncertainty weights $w_i(s)$ and the complementary filters $H_i(s)$. The dynamical uncertainty of the super sensor can be graphically represented in the complex plane by a circle centered on 1 with a radius equal to $|w_1(j\omega)H_1(j\omega)| + |w_2(j\omega)H_2(j\omega)|$ (Figure 3.48b).

$$\frac{\hat{x}}{x} = 1 + w_1(s)H_1(s)\Delta_1(s) + w_2(s)H_2(s)\Delta_2(s) \tag{3.27}$$

The super sensor dynamical uncertainty, and consequently the robustness of the fusion clearly depends on the complementary filters' norm. As it is generally desired to limit the dynamical uncertainty of the super sensor, the norm of the complementary filter $|H_i(j\omega)|$ should be made small when $|w_i(j\omega)|$ is large, i.e., at frequencies where the sensor dynamics is uncertain.

3.3.1.3 Complementary Filters Shaping

As established in Section 3.3.1.2, the super sensor's noise characteristics and robustness are directly dependent on the complementary filters' norm. A synthesis method enabling precise shaping of these norms would therefore offer substantial practical benefits. This section develops such an approach by formulating the design objective as a standard $\mathcal{H}_\infty$

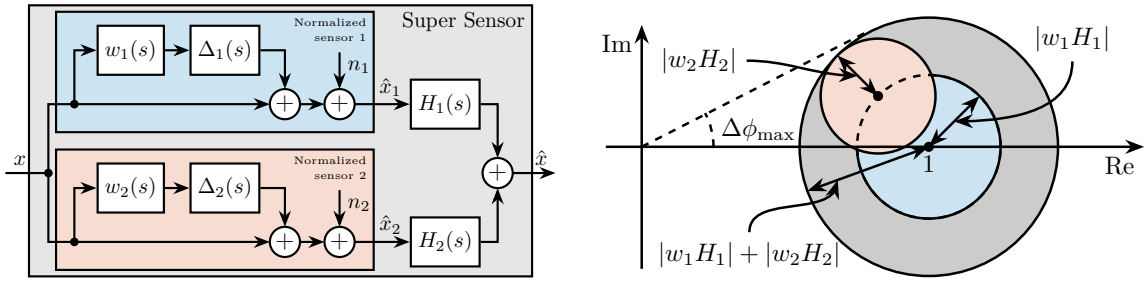

(a) Sensor Fusion Architecture

(b) Uncertainty region

Figure 3.48: Sensor fusion architecture with sensor dynamics uncertainty (a). Uncertainty region (b) of the super sensor dynamics in the complex plane (grey circle). The contribution of both sensors 1 and 2 to the total uncertainty are represented respectively by a blue circle and a red circle. The uncertainty region is function of frequency, which is omitted.

optimization problem. The methodology for designing appropriate weighting functions (which specify desired complementary filter shape during synthesis) is examined in detail, and the efficiency of the proposed method is validated with a simple example.

Synthesis Objective The primary objective is to shape the norms of two filters $H_1(s)$ and $H_2(s)$ while ensuring they maintain their complementary property as defined in (3.21). This is equivalent to finding proper and stable transfer functions $H_1(s)$ and $H_2(s)$ that satisfy conditions (3.28a), (3.28b), and (3.28c). Weighting transfer functions $W_1(s)$ and $W_2(s)$ are strategically selected to define the maximum desired norm of the complementary filters during the synthesis process.

$$H_1(s) + H_2(s) = 1 \tag{3.28a}$$

$$|H_1(j\omega)| \leq \frac{1}{|W_1(j\omega)|} \quad \forall\omega \tag{3.28b}$$

$$|H_2(j\omega)| \leq \frac{1}{|W_2(j\omega)|} \quad \forall\omega \tag{3.28c}$$

Shaping of Complementary Filters using $\mathcal{H}_\infty$ synthesis The synthesis objective can be expressed as a standard $\mathcal{H}_\infty$ optimization problem by considering the generalized plant $P(s)$ illustrated in Figure 3.49a and mathematically described by (3.29).

$$\begin{bmatrix} z_1 \\ z_2 \\ v \end{bmatrix} = P(s) \begin{bmatrix} w \\ u \end{bmatrix}; \quad P(s) = \begin{bmatrix} W_1(s) & -W_1(s) \\ 0 & W_2(s) \\ 1 & 0 \end{bmatrix} \tag{3.29}$$

Applying standard $\mathcal{H}_\infty$-synthesis to the generalized plant $P(s)$ is equivalent to finding a stable filter $H_2(s)$ that, based on input v, generates an output signal u such that the $\mathcal{H}_\infty$ norm of the system shown in Figure 3.49b from w to $[z_1,\ z_2]$ does not exceed unity, as expressed in (3.30).

$$\left\| \begin{matrix} (1 - H_2(s))W_1(s) \\ H_2(s)W_2(s) \end{matrix} \right\|_\infty \leq 1 \tag{3.30}$$

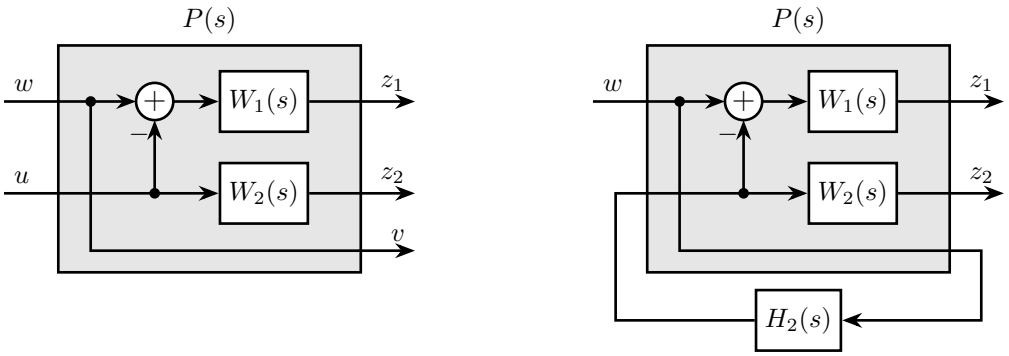

(a) Generalized plant

(b) Generalized plant with the synthesized filter

Figure 3.49: Architecture for the $\mathcal{H}_\infty$-synthesis of complementary filters.

By defining $H_1(s)$ as the complement of $H_2(s)$ (3.31), the $\mathcal{H}_\infty$-synthesis objective becomes equivalent to (3.32), ensuring that conditions (3.28b) and (3.28c) are satisfied.

$$H_1(s) \triangleq 1 - H_2(s) \tag{3.31}$$

$$\left\| \begin{matrix} H_1(s)W_1(s) \\ H_2(s)W_2(s) \end{matrix} \right\|_\infty \leq 1 \tag{3.32}$$

Therefore, applying $\mathcal{H}_\infty$-synthesis to the standard plant $P(s)$ generates two filters, $H_2(s)$ and $H_1(s) \triangleq 1 - H_2(s)$, that are complementary as required by (3.28), with norms bounded by the specified constraints in (3.28b) and (3.28c).

It should be noted that there exists only an implication (not an equivalence) between the $\mathcal{H}_\infty$ norm condition in (3.32) and the initial synthesis objectives in (3.28b) and (3.28c). Consequently, the optimization may be somewhat conservative with respect to the set of filters on which it operates [134, Chap. 2.8.3].

Weighting Functions Design Weighting functions play a crucial role during synthesis by specifying the maximum allowable norms for the complementary filters. The proper design of these weighting functions is essential for the successful implementation of the proposed $\mathcal{H}_\infty$-synthesis approach.

Three key considerations should guide the design of weighting functions. First, only proper and stable transfer functions should be employed. Second, the order of the weighting functions should remain reasonably small to minimize computational costs associated with solving the optimization problem and to facilitate practical implementation of the filters (as the order of the synthesized filters equals the sum of the weighting functions' orders). Third, the fundamental limitations imposed by the complementary property (3.21) must be respected, which implies that $|H_1(j\omega)|$ and $|H_2(j\omega)|$ cannot both be made small at the same frequency.

When designing complementary filters, it is typically desirable to specify their slopes, "blending" frequency, and maximum gains at low and high frequencies. To facilitate the expression of these specifications, formula (3.33) is proposed for the design of weighting functions. The parameters in this formula are $G_0 = \lim_{\omega \to 0} |W(j\omega)|$ (the low-frequency gain), $G_\infty = \lim_{\omega \to \infty} |W(j\omega)|$ (the high-frequency gain), $G_c = |W(j\omega_c)|$ (the gain at a specific frequency ω_c in rad/s), and n (the slope between high and low frequency, which also corresponds to the order of the weighting function). The typical magnitude response of a weighting function generated using (3.33) is illustrated in Figure 3.50.

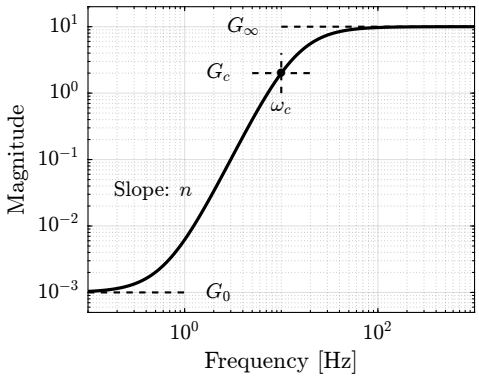

Figure 3.50: Magnitude of a weighting function generated using (3.33), $G_0 = 10^{-3}$, $G_\infty = 10$, $\omega_c = 10\,\text{Hz}$, $G_c = 2$, $n = 3$.

$$W(s) = \left(\frac{\frac{1}{\omega_c} \sqrt{\frac{1-\left(\frac{G_0}{G_c}\right)^{\frac{2}{n}}}{1-\left(\frac{G_c}{G_\infty}\right)^{\frac{2}{n}}}}\, s + \left(\frac{G_0}{G_c}\right)^{\frac{1}{n}}}{\frac{1}{G_\infty^{\frac{1}{n}}} \frac{1}{\omega_c} \sqrt{\frac{1-\left(\frac{G_0}{G_c}\right)^{\frac{2}{n}}}{1-\left(\frac{G_c}{G_\infty}\right)^{\frac{2}{n}}}}\, s + \frac{1}{G_c^{\frac{1}{n}}}} \right)^n \tag{3.33}$$

Validation of the Proposed Synthesis Method The proposed methodology for designing complementary filters is now applied to a simple example. Consider the design of two complementary filters $H_1(s)$ and $H_2(s)$ with the following requirements:

- The blending frequency should be approximately 10 Hz
- The slope of $|H_1(j\omega)|$ should be $+2$ below 10 Hz, with a low-frequency gain of 10^{-3}
- The slope of $|H_2(j\omega)|$ should be -3 above 10 Hz, with a high-frequency gain of 10^{-3}

The first step involves translating these requirements by appropriately designing the weighting functions. The formula proposed in (3.33) is employed for this purpose. The parameters used are summarized in Table 3.9. The inverse magnitudes of the designed weighting functions, which represent the maximum allowable norms of the complementary filters, are depicted by the dashed lines in Figure 3.51.

	$W_1(s)$	$W_2(s)$
G_0	0.1	1000
G_∞	1000	0.1
ω_c	$2\pi \cdot 10$	$2\pi \cdot 10$
G_c	0.45	0.45
n	2	3

Table 3.9: Parameters for $W_1(s)$ and $W_2(s)$

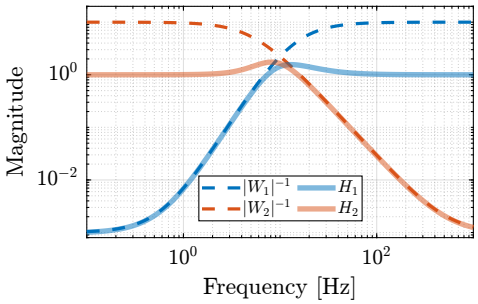

Figure 3.51: Weights and obtained filters.

Standard $\mathcal{H}_\infty$-synthesis is then applied to the generalized plant shown in Figure 3.49a. This yields the filter $H_2(s)$ that minimizes the $\mathcal{H}_\infty$ norm from input w to outputs $[z_1,\ z_2]^\intercal$. The resulting $\mathcal{H}_\infty$ norm is found to be close to unity, indicating successful synthesis: the norms of the complementary filters remain below the specified upper bounds. This is confirmed by the Bode plots of the obtained complementary filters in Figure 3.51. This straightforward example demonstrates that the proposed methodology for shaping complementary filters is both simple and effective.

3.3.1.4 Synthesis of a set of Three Complementary Filters

Some applications require the fusion of more than two sensors [50, 140]. At LIGO, for example, a super sensor is formed by merging three distinct sensors: a LVDT, a seismometer, and a geophone [95].

For merging $n > 2$ sensors with complementary filters, two architectural approaches are possible, as illustrated in Figure 3.52. Fusion can be implemented either "sequentially," using $n-1$ sets of two complementary filters (Figure 3.52a), or "in parallel," employing a single set of n complementary filters (Figure 3.52b).

While conventional sensor fusion synthesis techniques can be applied to the sequential approach, parallel architecture implementation requires a novel synthesis method for multiple complementary filters. Previous literature has offered only simple analytical formulas for this purpose [50, 140]. This section presents a generalization of the proposed complementary filter synthesis method to address this gap.

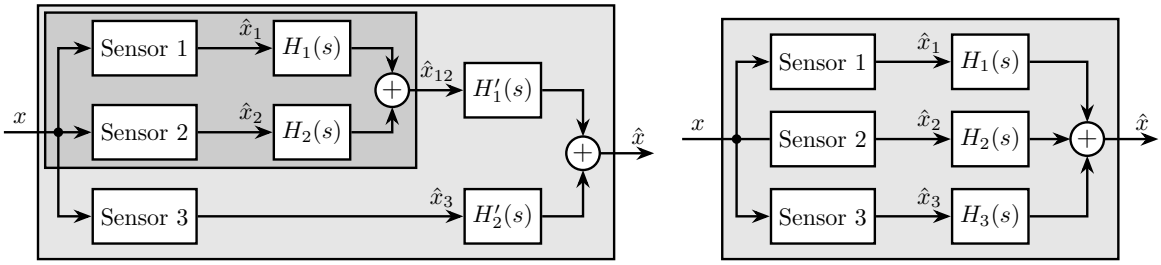

(a) Sequential fusion **(b)** Parallel fusion

Figure 3.52: Sensor fusion architectures when more than two sensors are to be merged.

The synthesis objective is to compute a set of n stable transfer functions $[H_1(s),\ H_2(s),\ \ldots,\ H_n(s)]$ that satisfy conditions (3.34a) and (3.34b).

$$\sum_{i=1}^{n} H_i(s) = 1 \tag{3.34a}$$

$$|H_i(j\omega)| < \frac{1}{|W_i(j\omega)|}, \quad \forall\omega,\ i = 1 \ldots n \tag{3.34b}$$

The transfer functions $[W_1(s),\ W_2(s),\ \ldots,\ W_n(s)]$ are weights selected to specify the maximum complementary filters' norm during synthesis.

This synthesis objective is closely related to the one described in Section 3.3.1.3, and the proposed synthesis method represents a generalization of the approach previously presented. A set of n complementary filters can be shaped by applying standard $\mathcal{H}_\infty$-synthesis to the generalized plant $P_n(s)$ described by (3.35).

$$\begin{bmatrix} z_1 \\ \vdots \\ z_n \\ v \end{bmatrix} = P_n(s) \begin{bmatrix} w \\ u_1 \\ \vdots \\ u_{n-1} \end{bmatrix}; \quad P_n(s) = \begin{bmatrix} W_1 & -W_1 & \dots & \dots & -W_1 \\ 0 & W_2 & 0 & \dots & 0 \\ \vdots & \ddots & \ddots & \ddots & \vdots \\ \vdots & & \ddots & \ddots & 0 \\ 0 & \dots & \dots & 0 & W_n \\ 1 & 0 & \dots & \dots & 0 \end{bmatrix} \tag{3.35}$$

If the synthesis is successful, a set of $n-1$ filters $[H_2(s),\ H_3(s),\ \dots,\ H_n(s)]$ is obtained such that (3.36) is satisfied.

$$\left\| \begin{matrix} (1 - [H_2(s) + H_3(s) + \cdots + H_n(s)])W_1(s) \\ H_2(s)W_2(s) \\ \vdots \\ H_n(s)W_n(s) \end{matrix} \right\|_\infty \leq 1 \tag{3.36}$$

$H_1(s)$ is then defined using (3.37), which ensures the complementary property for the set of n filters (3.34a). Condition (3.34b) is satisfied through (3.36).

$$H_1(s) \triangleq 1 - \left[H_2(s) + H_3(s) + \cdots + H_n(s)\right] \tag{3.37}$$

To validate the proposed method for synthesizing a set of three complementary filters, an example is provided. The sensors to be merged are a displacement sensor (effective from DC up to 1 Hz), a geophone (effective from 1 to 10 Hz), and an accelerometer (effective above 10 Hz). Three weighting functions are designed using formula (3.33), and their inverse magnitudes are shown in Figure 3.53b (dashed curves).

Consider the generalized plant $P_3(s)$ shown in Figure 3.53a, which is also described by (3.38).

$$\begin{bmatrix} z_1 \\ z_2 \\ z_3 \\ v \end{bmatrix} = P_3(s) \begin{bmatrix} w \\ u_1 \\ u_2 \end{bmatrix}; \quad P_3(s) = \begin{bmatrix} W_1(s) & -W_1(s) & -W_1(s) \\ 0 & W_2(s) & 0 \\ 0 & 0 & W_3(s) \\ 1 & 0 & 0 \end{bmatrix} \tag{3.38}$$

Standard $\mathcal{H}_\infty$-synthesis is performed on the generalized plant $P_3(s)$. Two filters, $H_2(s)$ and $H_3(s)$, are obtained such that the $\mathcal{H}_\infty$ norm of the closed-loop transfer from w to $[z_1,\ z_2,\ z_3]$ of the system in Figure 3.53a is less than one. Filter $H_1(s)$ is defined using (3.39), thus ensuring the complementary property of the obtained set of filters.

$$H_1(s) \triangleq 1 - \left[H_2(s) + H_3(s)\right] \tag{3.39}$$

Figure 3.53b displays the three synthesized complementary filters (solid lines), confirming the successful synthesis.

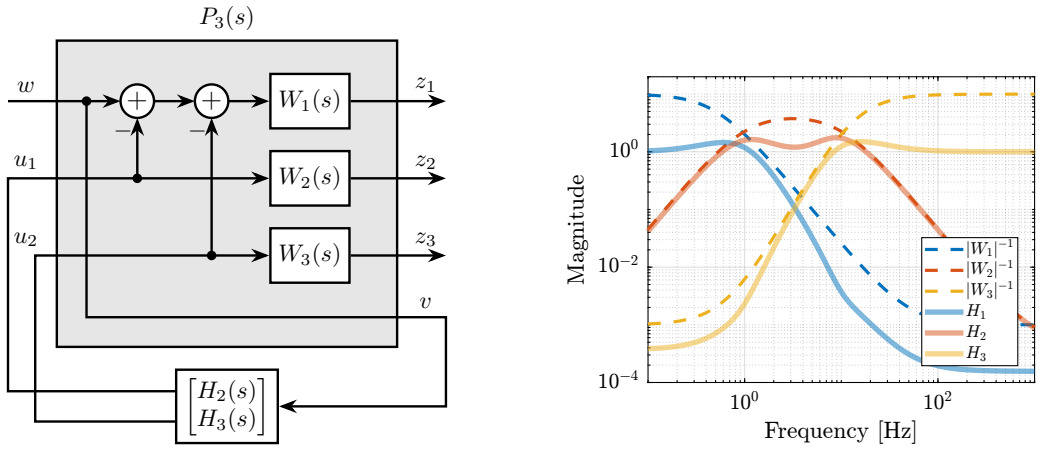

(a) Generalized plant with the synthesized filter

(b) Weights and obtained filters

Figure 3.53: Architecture for the $\mathcal{H}_\infty$-synthesis of three complementary filters (a). Bode plot of the inverse weighting functions and of the three obtained complementary filters (b).

3.3.1.5 Conclusion

A new method for designing complementary filters using the $\mathcal{H}_\infty$-synthesis has been proposed. This approach allows shaping of the filter magnitudes through the use of weighting functions during synthesis. This capability is particularly valuable in practice since the characteristics of the super sensor are directly linked to the complementary filters' magnitude. Consequently, typical sensor fusion objectives can be effectively translated into requirements on the magnitudes of the filters.

For the NASS, the HAC-LAC strategy was found to perform well and to offer the advantages of being both intuitive to understand and straightforward to tune. Looking forward, it would be interesting to investigate how sensor fusion (particularly between the force sensors and external metrology) compares to the HAC-IFF approach in terms of performance and robustness.

3.3.2 Decoupling Strategies for Parallel Manipulators

The control of parallel manipulators (and any MIMO system in general) typically involves a two-step approach: first decoupling the plant dynamics (using various strategies discussed in this section), followed by the application of SISO control for the decoupled plant (discussed in section 3.3.3).

When sensors are integrated within the struts, decentralized control may be applied, as the system is already well decoupled at low frequency. For instance, [51] implemented a system where each strut consists of piezoelectric stack actuators and eddy current displacement sensors, with separate PI controllers for each strut. A similar control architecture was proposed in [41] using strain gauge sensors integrated in each strut.

An alternative strategy involves decoupling the system in the Cartesian frame using Jacobian matrices. As demonstrated during the study of Stewart platform kinematics, Jacobian matrices can be used to map actuator forces to forces and torques applied on the top platform. This approach enables the implementation of controllers in a defined frame. It has been applied with various sensor types including force sensors [98], relative displacement sensors [81], and inertial sensors [1, 88]. The Cartesian frame in which the system is decoupled is typically chosen at the PoI (i.e., where the motion is of interest) or at the Center of Mass.

Modal decoupling represents another noteworthy decoupling strategy, wherein the "local" plant inputs and outputs are mapped to the modal space. In this approach, multiple SISO plants, each corresponding to a single mode, can be controlled independently. This decoupling strategy has been implemented for active damping applications [67], which is logical as it is often desirable to dampen specific modes. The strategy has also been employed in [118] for vibration isolation purposes using geophones, and in [160] using force sensors.

Another completely different strategy would be to implement a multivariable control directly on the coupled system. $\mathcal{H}_\infty$ and μ-synthesis were applied to a Stewart platform model in [86]. In [158], decentralized force feedback was first applied, followed by $\mathcal{H}_2$-synthesis for vibration isolation based on accelerometers. $\mathcal{H}_\infty$-synthesis was also employed in [76] for active damping based on accelerometers. A comparative study between $\mathcal{H}_\infty$-synthesis and decentralized control in the frame of the struts was performed in [144]. Their experimental closed-loop results indicated that the $\mathcal{H}_\infty$ controller did not outperform the decentralized controller in the frame of the struts. These limitations were attributed to the model's poor ability to predict off-diagonal dynamics, which is crucial for $\mathcal{H}_\infty$-synthesis.

The purpose of this section is to compare several methods for the decoupling of parallel manipulators, an analysis that appears to be lacking in the literature. A simplified parallel manipulator model is introduced in Section 3.3.2.1 as a test case for evaluating decoupling strategies. The decentralized plant (transfer functions from actuators to sensors integrated in the struts) is examined in Section 3.3.2.2. Three approaches are investigated across subsequent sections: Jacobian matrix decoupling (Section 3.3.2.3), modal decoupling (Section 3.3.2.4), and Singular Value Decomposition (SVD) decoupling (Section 3.3.2.5). Finally, a comparative analysis with concluding observations is provided in Section 3.3.2.6.

3.3.2.1 3-DoF Test Model

Instead of using the Stewart platform for comparing decoupling strategies, a simplified parallel manipulator is employed to facilitate the analysis. The system illustrated in Figure 3.54 is used for this purpose. It has three degrees of freedom and incorporates three parallel struts. Being a fully parallel manipulator, it is therefore quite similar to the Stewart platform.

Two reference frames are defined within this model: frame $\{M\}$ with origin O_M at the Center of Mass of the solid body, and frame $\{K\}$ with origin O_K at the Center of Stiffness of the parallel manipulator.

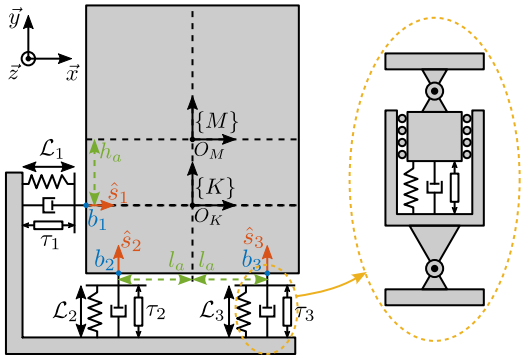

Figure 3.54: Model used to compare decoupling strategies.

	Description	Value
l_a		0.5 m
h_a		0.2 m
k	Actuator stiffness	10 N/µm
c	Actuator damping	200 Ns/m
m	Payload mass	40 kg
I	Payload R_z inertia	5 kgm^2

Table 3.10: Model parameters

The equations of motion are derived by applying Newton's second law to the suspended mass, expressed at its center of mass (3.40), where $\boldsymbol{\mathcal{X}}_{\{M\}}$ represents the two translations and one rotation with respect to the Center of Mass, and $\boldsymbol{\mathcal{F}}_{\{M\}}$ denotes the forces and torque applied at the Center of Mass.

$$\boldsymbol{M}_{\{M\}}\ddot{\boldsymbol{\mathcal{X}}}_{\{M\}}(t) = \sum \boldsymbol{\mathcal{F}}_{\{M\}}(t), \quad \boldsymbol{\mathcal{X}}_{\{M\}} = \begin{bmatrix} x \\ y \\ R_z \end{bmatrix}, \quad \boldsymbol{\mathcal{F}}_{\{M\}} = \begin{bmatrix} F_x \\ F_y \\ M_z \end{bmatrix} \tag{3.40}$$

The Jacobian matrix $\boldsymbol{J}_{\{M\}}$ is employed to map the spring, damping, and actuator forces to XY forces and Z torque expressed at the center of mass (3.41).

$$\boldsymbol{J}_{\{M\}} = \begin{bmatrix} 1 & 0 & h_a \\ 0 & 1 & -l_a \\ 0 & 1 & l_a \end{bmatrix} \tag{3.41}$$

Subsequently, the equation of motion relating the actuator forces τ to the motion of the mass $\boldsymbol{\mathcal{X}}_{\{M\}}$ is derived (3.42).

$$\boldsymbol{M}_{\{M\}}\ddot{\boldsymbol{\mathcal{X}}}_{\{M\}}(t) + \boldsymbol{J}_{\{M\}}^{\intercal}\boldsymbol{\mathcal{C}}\boldsymbol{J}_{\{M\}}\dot{\boldsymbol{\mathcal{X}}}_{\{M\}}(t) + \boldsymbol{J}_{\{M\}}^{\intercal}\boldsymbol{\mathcal{K}}\boldsymbol{J}_{\{M\}}\boldsymbol{\mathcal{X}}_{\{M\}}(t) = \boldsymbol{J}_{\{M\}}^{\intercal}\boldsymbol{\tau}(t) \tag{3.42}$$

The matrices representing the payload inertia, actuator stiffness, and damping are shown in (3.43).

$$\boldsymbol{M}_{\{M\}} = \begin{bmatrix} m & 0 & 0 \\ 0 & m & 0 \\ 0 & 0 & I \end{bmatrix}, \quad \boldsymbol{\mathcal{K}} = \begin{bmatrix} k & 0 & 0 \\ 0 & k & 0 \\ 0 & 0 & k \end{bmatrix}, \quad \boldsymbol{\mathcal{C}} = \begin{bmatrix} c & 0 & 0 \\ 0 & c & 0 \\ 0 & 0 & c \end{bmatrix} \tag{3.43}$$

The parameters employed for the subsequent analysis are summarized in Table 3.10, which includes values for geometric parameters (l_a, h_a), mechanical properties (actuator stiffness k and damping c), and inertial characteristics (payload mass m and rotational inertia I).

3.3.2.2 Control in the Frame of the Struts

The dynamics in the frame of the struts are first examined. The equation of motion relating actuator forces $\boldsymbol{\tau}$ to strut relative motion $\boldsymbol{\mathcal{L}}$ is derived from equation (3.42) by mapping the Cartesian motion of the mass to the relative motion of the struts using the Jacobian matrix $\boldsymbol{J}_{\{M\}}$ defined in (3.41). The obtained transfer function from $\boldsymbol{\tau}$ to $\boldsymbol{\mathcal{L}}$ is shown in (3.44).

$$\frac{\boldsymbol{\mathcal{L}}}{\boldsymbol{\tau}}(s) = \boldsymbol{G}_{\mathcal{L}}(s) = \left(\boldsymbol{J}_{\{M\}}^{-\intercal}\boldsymbol{M}_{\{M\}}\boldsymbol{J}_{\{M\}}^{-1}s^2 + \boldsymbol{\mathcal{C}}s + \boldsymbol{\mathcal{K}}\right)^{-1} \tag{3.44}$$

At low frequencies, the plant converges to a diagonal constant matrix whose diagonal elements are equal to the actuator stiffnesses (3.45). At high-frequency, the plant converges to the mass matrix mapped in the frame of the struts, which is generally highly non-diagonal.

$$\boldsymbol{G}_{\mathcal{L}}(j\omega) \xrightarrow[\omega \to 0]{} \boldsymbol{\mathcal{K}}^{-1} \tag{3.45}$$

The magnitude of the coupled plant $\boldsymbol{G}_{\mathcal{L}}$ is illustrated in Figure 3.55. This representation confirms that at low frequencies (below the first suspension mode), the plant is well decoupled. Depending on the symmetry present in the system, certain diagonal elements may exhibit identical values, as demonstrated for struts 2 and 3 in this example.

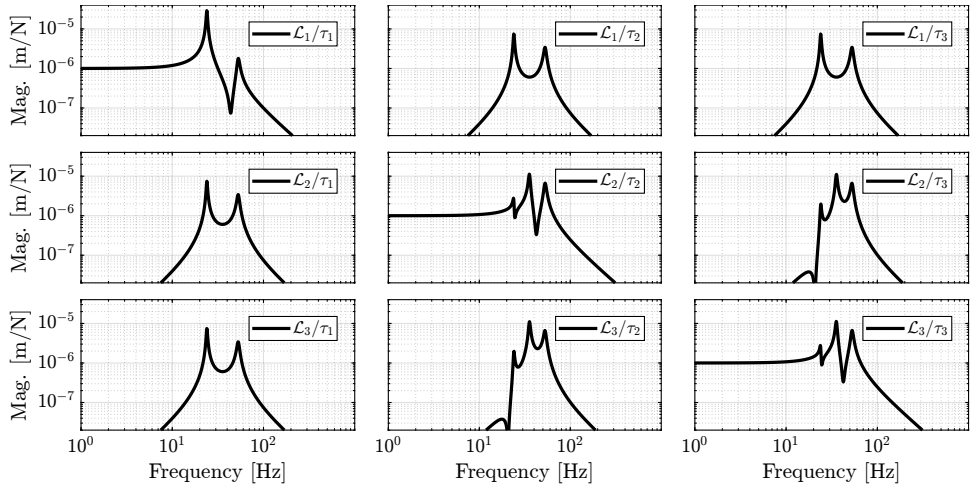

Figure 3.55: Model dynamics from actuator forces to relative displacement sensor of each strut.

3.3.2.3 Jacobian Decoupling

Jacobian Matrix The Jacobian matrix $\boldsymbol{J}_{\{O\}}$ serves a dual purpose in the decoupling process: it converts strut velocity $\dot{\mathcal{L}}$ to payload velocity and angular velocity $\dot{\boldsymbol{\mathcal{X}}}_{\{O\}}$, and it transforms actuator forces $\boldsymbol{\tau}$ to forces/torque applied on the payload $\boldsymbol{\mathcal{F}}_{\{O\}}$, as expressed in equation (3.46).

$$\dot{\boldsymbol{\mathcal{X}}}_{\{O\}} = \boldsymbol{J}_{\{O\}}\dot{\boldsymbol{\mathcal{L}}}, \quad \dot{\boldsymbol{\mathcal{L}}} = \boldsymbol{J}_{\{O\}}^{-1}\dot{\boldsymbol{\mathcal{X}}}_{\{O\}} \tag{3.46a}$$

$$\boldsymbol{\mathcal{F}}_{\{O\}} = \boldsymbol{J}_{\{O\}}^{\mathsf{T}}\boldsymbol{\tau}, \quad \boldsymbol{\tau} = \boldsymbol{J}_{\{O\}}^{-\mathsf{T}}\boldsymbol{\mathcal{F}}_{\{O\}} \tag{3.46b}$$

The resulting plant (Figure 3.56) have inputs and outputs with clear physical interpretations:

- $\boldsymbol{\mathcal{F}}_{\{O\}}$ represents forces/torques applied on the payload at the origin of frame $\{O\}$
- $\boldsymbol{\mathcal{X}}_{\{O\}}$ represents translations/rotation of the payload expressed in frame $\{O\}$

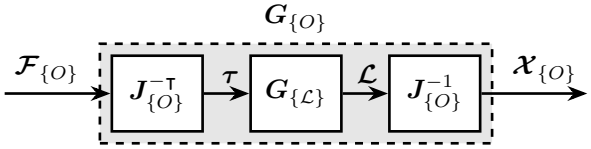

Figure 3.56: Block diagram of the decoupling the plant in a frame $\{O\}$ using Jacobian matrix $\boldsymbol{J}_{\{O\}}$

The transfer function from $\boldsymbol{\mathcal{F}}_{\{O\}}$ to $\boldsymbol{\mathcal{X}}_{\{O\}}$, denoted $\boldsymbol{G}_{\{O\}}(s)$ can be computed using (3.47).

$$\frac{\boldsymbol{\mathcal{X}}_{\{O\}}}{\boldsymbol{\mathcal{F}}_{\{O\}}}(s) = \boldsymbol{G}_{\{O\}}(s) = \left(\boldsymbol{J}_{\{O\}}^{\intercal}\boldsymbol{J}_{\{M\}}^{-\intercal}\boldsymbol{M}_{\{M\}}\boldsymbol{J}_{\{M\}}^{-1}\boldsymbol{J}_{\{O\}}s^2 + \boldsymbol{J}_{\{O\}}^{\intercal}\boldsymbol{\mathcal{C}}\boldsymbol{J}_{\{O\}}s + \boldsymbol{J}_{\{O\}}^{\intercal}\boldsymbol{\mathcal{K}}\boldsymbol{J}_{\{O\}}\right)^{-1} \tag{3.47}$$

The frame $\{O\}$ can be selected according to specific requirements, but the decoupling properties are significantly influenced by this choice. Two natural reference frames are particularly relevant: the Center of Mass and the Center of Stiffness.

Center of Mass When the decoupling frame is located at the Center of Mass (frame $\{M\}$ in Figure 3.54), the Jacobian matrix and its inverse are expressed as in (3.48).

$$\boldsymbol{J}_{\{M\}} = \begin{bmatrix} 1 & 0 & h_a \\ 0 & 1 & -l_a \\ 0 & 1 & l_a \end{bmatrix}, \quad \boldsymbol{J}_{\{M\}}^{-1} = \begin{bmatrix} 1 & \frac{h_a}{2l_a} & \frac{-h_a}{2l_a} \\ 0 & \frac{1}{2} & \frac{1}{2} \\ 0 & \frac{-1}{2l_a} & \frac{1}{2l_a} \end{bmatrix} \tag{3.48}$$

Analytical formula of the plant $\boldsymbol{G}_{\{M\}}(s)$ is derived (3.49).

$$\frac{\boldsymbol{\mathcal{X}}_{\{M\}}}{\boldsymbol{\mathcal{F}}_{\{M\}}}(s) = \boldsymbol{G}_{\{M\}}(s) = \left(\boldsymbol{M}_{\{M\}}s^2 + \boldsymbol{J}_{\{M\}}^{\intercal}\boldsymbol{\mathcal{C}}\boldsymbol{J}_{\{M\}}s + \boldsymbol{J}_{\{M\}}^{\intercal}\boldsymbol{\mathcal{K}}\boldsymbol{J}_{\{M\}}\right)^{-1} \tag{3.49}$$

At high-frequency, the plant converges to the inverse of the mass matrix, which is a diagonal matrix (3.50).

$$\boldsymbol{G}_{\{M\}}(j\omega) \xrightarrow[\omega\to\infty]{} -\omega^2\boldsymbol{M}_{\{M\}}^{-1} = -\omega^2\begin{bmatrix} 1/m & 0 & 0 \\ 0 & 1/m & 0 \\ 0 & 0 & 1/I \end{bmatrix} \tag{3.50}$$

Consequently, the plant exhibits effective decoupling at frequencies above the highest suspension mode as shown in Figure 3.57a. This strategy is typically employed in systems with low-frequency suspension modes [19], where the plant approximates decoupled mass lines.

The low-frequency coupling observed in this configuration has a clear physical interpretation. When a static force is applied at the Center of Mass, the suspended mass rotates around the Center of Stiffness. This rotation is due to torque induced by the stiffness of the first actuator (i.e. the one on the left side), which is not aligned with the force application point. This phenomenon is illustrated in Figure 3.57b.

Center of Stiffness When the decoupling frame is located at the Center of Stiffness, the Jacobian matrix and its inverse are expressed as in (3.51).

$$\boldsymbol{J}_{\{K\}} = \begin{bmatrix} 1 & 0 & 0 \\ 0 & 1 & -l_a \\ 0 & 1 & l_a \end{bmatrix}, \quad \boldsymbol{J}_{\{K\}}^{-1} = \begin{bmatrix} 1 & 0 & 0 \\ 0 & \frac{1}{2} & \frac{1}{2} \\ 0 & \frac{-1}{2l_a} & \frac{1}{2l_a} \end{bmatrix} \tag{3.51}$$

The frame $\{K\}$ was selected based on physical reasoning, positioned in line with the side strut and equidistant between the two vertical struts. However, it could alternatively be determined through analytical methods to ensure that $\boldsymbol{J}_{\{K\}}^{\intercal}\boldsymbol{\mathcal{K}}\boldsymbol{J}_{\{K\}}$ forms a diagonal matrix. It should be noted that the existence of such a Center of Stiffness (i.e. a frame

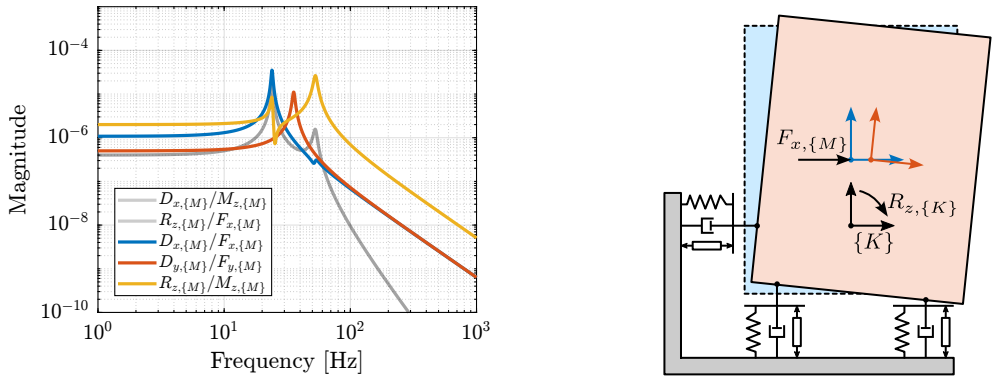

(a) Dynamics at the CoM

(b) Static force applied at the CoM

Figure 3.57: Plant decoupled using the Jacobian matrix expresssed at the center of mass (a). The physical reason for low frequency coupling is illustrated in (b).

$\{K\}$ for which $\boldsymbol{J}_{\{K\}}^{\intercal}\boldsymbol{\mathcal{K}}\boldsymbol{J}_{\{K\}}$ is diagonal) is not guaranteed for arbitrary systems. This property is typically achievable only in systems exhibiting specific symmetrical characteristics, as is the case in the present example.

The analytical expression for the plant in this configuration was then computed (3.52).

$$\frac{\boldsymbol{\mathcal{X}}_{\{K\}}}{\boldsymbol{\mathcal{F}}_{\{K\}}}(s) = \boldsymbol{G}_{\{K\}}(s) = \left(\boldsymbol{J}_{\{K\}}^{\intercal}\boldsymbol{J}_{\{M\}}^{-\intercal}\boldsymbol{M}_{\{M\}}\boldsymbol{J}_{\{M\}}^{-1}\boldsymbol{J}_{\{K\}}s^2 + \boldsymbol{J}_{\{K\}}^{\intercal}\boldsymbol{\mathcal{C}}\boldsymbol{J}_{\{K\}}s + \boldsymbol{J}_{\{K\}}^{\intercal}\boldsymbol{\mathcal{K}}\boldsymbol{J}_{\{K\}}\right)^{-1} \tag{3.52}$$

Figure 3.58 presents the dynamics of the plant when decoupled using the Jacobian matrix expressed at the Center of Stiffness. The plant is well decoupled below the suspension mode with the lowest frequency (3.53), making it particularly suitable for systems with high stiffness.

$$\boldsymbol{G}_{\{K\}}(j\omega) \xrightarrow[\omega\to 0]{} \boldsymbol{J}_{\{K\}}^{-1}\boldsymbol{\mathcal{K}}^{-1}\boldsymbol{J}_{\{K\}}^{-\intercal} \tag{3.53}$$

The physical reason for high-frequency coupling is illustrated in Figure 3.58b. When a high-frequency force is applied at a point not aligned with the Center of Mass, it induces rotation around the Center of Mass.

3.3.2.4 Modal Decoupling

Modal decoupling represents an approach based on the principle that a mechanical system's behavior can be understood as a combination of contributions from various modes [121]. To convert the dynamics in the modal space, the equations of motion are first written with respect to the center of mass (3.54).

$$\boldsymbol{M}_{\{M\}}\ddot{\boldsymbol{\mathcal{X}}}_{\{M\}}(t) + \boldsymbol{C}_{\{M\}}\dot{\boldsymbol{\mathcal{X}}}_{\{M\}}(t) + \boldsymbol{K}_{\{M\}}\boldsymbol{\mathcal{X}}_{\{M\}}(t) = \boldsymbol{J}_{\{M\}}^{\intercal}\boldsymbol{\tau}(t) \tag{3.54}$$

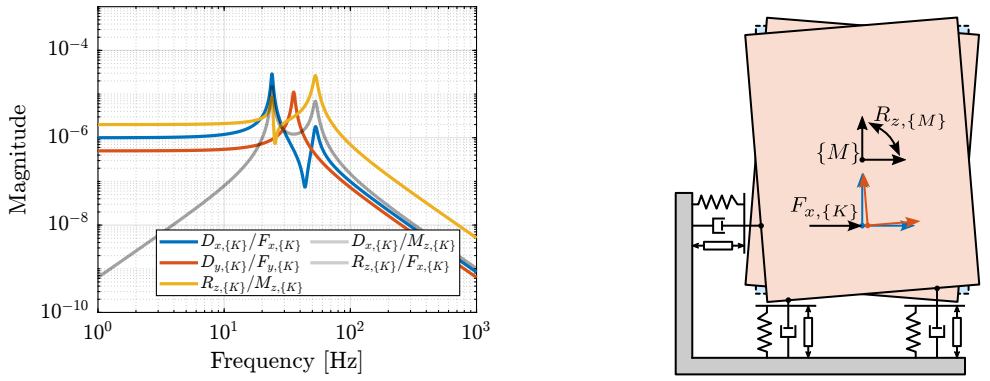

(a) Dynamics at the CoK

(b) High-frequency force applied at the CoK

Figure 3.58: Plant decoupled using the Jacobian matrix expresssed at the center of stiffness (a). The physical reason for high-frequency coupling is illustrated in (b).

For modal decoupling, a change of variables is introduced (3.55) where $\boldsymbol{\mathcal{X}}_m$ represents the modal amplitudes and $\boldsymbol{\Phi}$ is a $n \times n$[1] matrix whose columns correspond to the mode shapes of the system, computed from $\boldsymbol{M}_{\{M\}}$ and $\boldsymbol{K}_{\{M\}}$.

$$\boldsymbol{\mathcal{X}}_{\{M\}} = \boldsymbol{\Phi}\boldsymbol{\mathcal{X}}_m \tag{3.55}$$

By pre-multiplying equation (3.54) by $\boldsymbol{\Phi}^\intercal$ and applying the change of variable (3.55), a new set of equations of motion is obtained (3.56) where $\boldsymbol{\tau}_m$ represents the modal input, while $\boldsymbol{M}_m$, $\boldsymbol{C}_m$, and $\boldsymbol{K}_m$ denote the modal mass, damping, and stiffness matrices respectively.

$$\underbrace{\boldsymbol{\Phi}^\intercal \boldsymbol{M} \boldsymbol{\Phi}}_{\boldsymbol{M}_m} \ddot{\boldsymbol{\mathcal{X}}}_m(t) + \underbrace{\boldsymbol{\Phi}^\intercal \boldsymbol{C} \boldsymbol{\Phi}}_{\boldsymbol{C}_m} \dot{\boldsymbol{\mathcal{X}}}_m(t) + \underbrace{\boldsymbol{\Phi}^\intercal \boldsymbol{K} \boldsymbol{\Phi}}_{\boldsymbol{K}_m} \boldsymbol{\mathcal{X}}_m(t) = \underbrace{\boldsymbol{\Phi}^\intercal \boldsymbol{J}^\intercal \boldsymbol{\tau}(t)}_{\boldsymbol{\tau}_m(t)} \tag{3.56}$$

The inherent mathematical structure of the mass, damping, and stiffness matrices [84, chapt. 8] ensures that modal matrices are diagonal [113, chapt. 2.3]. This diagonalization transforms equation (3.56) into a set of n decoupled equations, enabling independent control of each mode without cross-interaction.

To implement this approach from a decentralized plant, the architecture shown in Figure 3.59 is employed. Inputs of the decoupling plant are the modal inputs $\boldsymbol{\tau}_m$ and the outputs are the modal amplitudes $\boldsymbol{\mathcal{X}}_m$. This implementation requires knowledge of the system's equations of motion, from which the mode shapes matrix $\boldsymbol{\Phi}$ is derived. The resulting decoupled system features diagonal elements each representing second-order resonant systems that are straightforward to control individually.

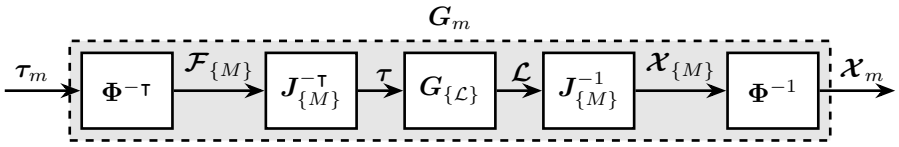

Figure 3.59: Modal Decoupling Architecture.

[1] n corresponds to the number of degrees of freedom, here $n = 3$.

Modal decoupling was then applied to the test model. First, the eigenvectors $\boldsymbol{\Phi}$ of $\boldsymbol{M}_{\{M\}}^{-1}\boldsymbol{K}_{\{M\}}$ were computed (3.57). While analytical derivation of eigenvectors could be obtained for such a simple system, they are typically computed numerically for practical applications.

$$\boldsymbol{\Phi} = \begin{bmatrix} \frac{I-h_a^2 m-2l_a^2 m-\alpha}{2h_a m} & 0 & \frac{I-h_a^2 m-2l_a^2 m+\alpha}{2h_a m} \\ 0 & 1 & 0 \\ 1 & 0 & 1 \end{bmatrix}, \quad \alpha = \sqrt{\left(I + m(h_a^2 - 2l_a^2)\right)^2 + 8m^2 h_a^2 l_a^2} \tag{3.57}$$

The numerical values for the eigenvector matrix and its inverse are shown in (3.58).

$$\boldsymbol{\Phi} = \begin{bmatrix} -0.905 & 0 & -0.058 \\ 0 & 1 & 0 \\ 0.424 & 0 & -0.998 \end{bmatrix}, \quad \boldsymbol{\Phi}^{-1} = \begin{bmatrix} -1.075 & 0 & 0.063 \\ 0 & 1 & 0 \\ -0.457 & 0 & -0.975 \end{bmatrix} \tag{3.58}$$

The two computed matrices were implemented in the control architecture of Figure 3.59, resulting in three distinct second order plants as depicted in Figure 3.60a. Each of these diagonal elements corresponds to a specific mode, as shown in Figure 3.60b, resulting in a perfectly decoupled system.

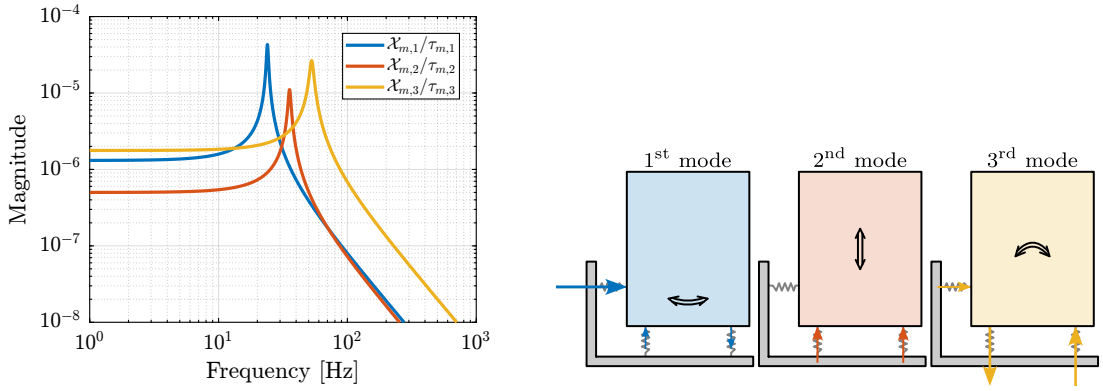

(a) Decoupled plant in modal space

(b) Individually controlled modes

Figure 3.60: Plant using modal decoupling consists of second order plants (a). Decoupled elements can be used to invidiually address the modes illustrated in (b).

3.3.2.5 SVD Decoupling

Singular Value Decomposition Singular Value Decomposition (SVD) represents a powerful mathematical tool with extensive applications in data analysis [18, chapt. 1] and multivariable control systems where it is particularly valuable for analyzing directional properties in multivariable systems [134].

The SVD constitutes a unique matrix decomposition applicable to any complex matrix $\boldsymbol{X} \in \mathbb{C}^{n\times m}$, expressed as:

$$\boldsymbol{X} = \boldsymbol{U}\boldsymbol{\Sigma}\boldsymbol{V}^H \tag{3.59}$$

where $\boldsymbol{U} \in \mathbb{C}^{n\times n}$ and $\boldsymbol{V} \in \mathbb{C}^{m\times m}$ are unitary matrices with orthonormal columns, and $\boldsymbol{\Sigma} \in \mathbb{R}^{n\times n}$ is a diagonal matrix with real, non-negative entries. For real matrices $\boldsymbol{X}$, the resulting $\boldsymbol{U}$ and $\boldsymbol{V}$ matrices are also real, making them suitable for decoupling applications.

Decoupling using the SVD The procedure for SVD-based decoupling begins with identifying the system dynamics from inputs to outputs, typically represented as a Frequency Response Function (FRF), which yields a complex matrix $\boldsymbol{G}(\omega_i)$ for multiple frequency points ω_i. A specific frequency is then selected for optimal decoupling, with the targeted crossover frequency ω_c often serving as an appropriate choice.

Since real matrices are required for the decoupling transformation, a real approximation of the complex measured response at the selected frequency must be computed. In this work, the method proposed in [82] was used as it preserves maximal orthogonality in the directional properties of the input complex matrix.

Following this approximation, a real matrix $\tilde{\boldsymbol{G}}(\omega_c)$ is obtained, and SVD is performed on this matrix. The resulting (real) unitary matrices $\boldsymbol{U}$ and $\boldsymbol{V}$ are structured such that $\boldsymbol{V}^{-\intercal}\tilde{\boldsymbol{G}}(\omega_c)\boldsymbol{U}^{-1}$ forms a diagonal matrix. These singular input and output matrices are then applied to decouple the system as illustrated in Figure 3.61, and the decoupled plant is described by (3.60).

$$\boldsymbol{G}_{\text{SVD}}(s) = \boldsymbol{U}^{-1}\boldsymbol{G}_{\{\mathcal{L}\}}(s)\boldsymbol{V}^{-\intercal} \tag{3.60}$$

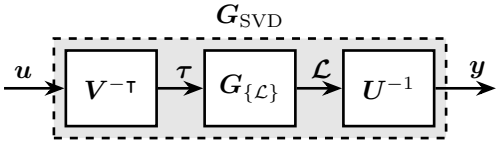

Figure 3.61: Decoupled plant $\boldsymbol{G}_{\text{SVD}}$ using the Singular Value Decomposition.

Implementation of SVD decoupling requires access to the system's FRF, at least in the vicinity of the desired decoupling frequency. This information can be obtained either experimentally or derived from a model. While this approach ensures effective decoupling near the chosen frequency, it provides no guarantees regarding decoupling performance away from this frequency. Furthermore, the quality of decoupling depends significantly on the accuracy of the real approximation, potentially limiting its effectiveness for plants with high damping.

Test on the 3-DoF model Plant decoupling using the Singular Value Decomposition was then applied on the test model. A decoupling frequency of 100 Hz was used. The plant response at that frequency, as well as its real approximation and the obtained $\boldsymbol{U}$ and $\boldsymbol{V}$ matrices are shown in (3.61).

$$\begin{aligned}
\boldsymbol{G}_{\{\mathcal{L}\}}(\omega_c = 2\pi\cdot 100) &= 10^{-9}\begin{bmatrix} -99-j2.6 & 74+j4.2 & -74-j4.2 \\ 74+j4.2 & -247-j9.7 & 102+j7.0 \\ -74-j4.2 & 102+j7.0 & -247-j9.7 \end{bmatrix} \\
\xrightarrow[\text{approximation}]{\text{real}} \tilde{\boldsymbol{G}}_{\{\mathcal{L}\}}(\omega_c) &= 10^{-9}\begin{bmatrix} -99 & 74 & -74 \\ 74 & -247 & 102 \\ -74 & 102 & -247 \end{bmatrix} \\
\xrightarrow[\text{SVD}]{} \boldsymbol{U} = \begin{bmatrix} 0.34 & 0 & 0.94 \\ -0.66 & 0.71 & 0.24 \\ 0.66 & 0.71 & -0.24 \end{bmatrix}&,\ \boldsymbol{V} = \begin{bmatrix} -0.34 & 0 & -0.94 \\ 0.66 & -0.71 & -0.24 \\ -0.66 & -0.71 & 0.24 \end{bmatrix}
\end{aligned} \tag{3.61}$$

Using these $\boldsymbol{U}$ and $\boldsymbol{V}$ matrices, the decoupled plant is computed according to equation (3.60). The resulting plant, depicted in Figure 3.62, exhibits remarkable decoupling across a broad frequency range, extending well beyond the vicinity of ω_c. Additionally, the diagonal terms manifest as second-order dynamic systems, facilitating straightforward controller design.

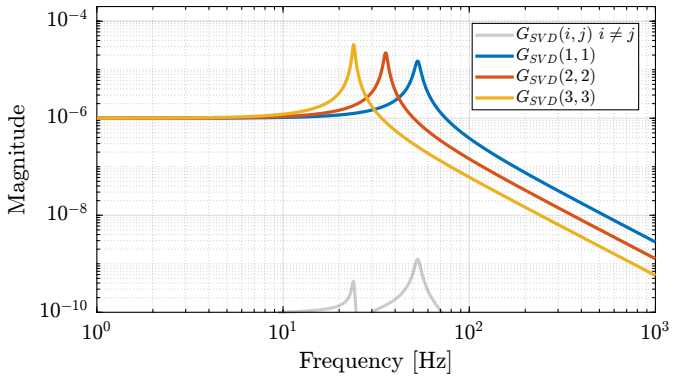

Figure 3.62: Plant dynamics $\boldsymbol{G}_{\text{SVD}}(s)$ obtained after decoupling using Singular Value Decomposition.

As it was surprising to obtain such a good decoupling at all frequencies, a variant system with identical dynamics but different sensor configurations was examined. Instead of using relative motion sensors collocated with the struts, three relative motion sensors were positioned as shown in Figure 3.63a. Although Jacobian matrices could theoretically be used to map these sensors to the frame of the struts, application of the same SVD decoupling procedure yielded the plant response shown in Figure 3.63b, which exhibits significantly greater coupling. Notably, the coupling demonstrates local minima near the decoupling frequency, consistent with the fact that the decoupling matrices were derived specifically for that frequency point.

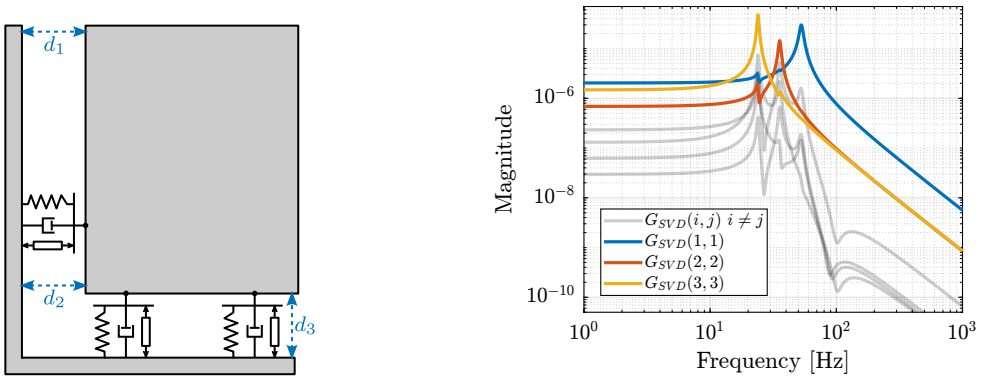

(a) Alternative location of sensors

(b) Obtained decoupled plant

Figure 3.63: SVD decoupling applied on the system schematically shown in (a). The obtained decoupled plant is shown in (b).

The exceptional performance of SVD decoupling on the plant with collocated sensors warrants further investigation. This effectiveness may be attributed to the symmetrical properties of the plant, as evidenced in the Bode plots of the decentralized plant shown in Figure 3.55. The phenomenon potentially relates to previous research on SVD controllers applied to systems with specific symmetrical characteristics [68].

3.3.2.6 Comparison of Decoupling Strategies

While the three proposed decoupling methods may appear similar in their mathematical implementation (each involving pre-multiplication and post-multiplication of the plant with constant matrices), they differ significantly in their underlying approaches and practical implications, as summarized in Table 3.11.

Each method employs a distinct conceptual framework: Jacobian decoupling is "topology-driven", relying on the geometric configuration of the system; modal decoupling is "physics-driven", based on the system's dynamical equations; and SVD decoupling is "data-driven", using measured FRFs.

The physical interpretation of decoupled plant inputs and outputs varies considerably among these methods. With Jacobian decoupling, inputs and outputs retain clear physical meaning, corresponding to forces/torques and translations/rotations in a specified reference frame. Modal decoupling arranges inputs to excite individual modes, with outputs combined to measure these modes separately. For SVD decoupling, inputs and outputs represent special directions ordered by decreasing controllability and observability at the chosen frequency, though physical interpretation becomes challenging for parallel manipulators.

This difference in interpretation relates directly to the "control space" in which the controllers operate. When these "control spaces" meaningfully relate to the control objectives, controllers can be tuned to directly match specific requirements. For Jacobian decoupling, the controller typically operates in a frame positioned at the point where motion needs to be controlled, for instance where the light is focused in the NASS application. Modal decoupling provides a natural framework when specific vibrational modes require targeted control. SVD decoupling generally results in a loss of physical meaning for the "control space", potentially complicating the process of relating controller design to practical system requirements.

The quality of decoupling achieved through these methods also exhibits distinct characteristics. Jacobian decoupling performance depends on the chosen reference frame, with optimal decoupling at low-frequency when aligned at the Center of Stiffness, or at high-frequency when aligned with the Center of Mass. Systems designed with coincident centers of mass and stiffness may achieve excellent decoupling using this approach. Modal decoupling offers good decoupling across all frequencies, though its effectiveness relies on the model accuracy, with discrepancies potentially resulting in significant off-diagonal elements. SVD decoupling can be implemented using measured data without requiring a model, with optimal performance near the chosen decoupling frequency, though its effectiveness may diminish at other frequencies and depends on the quality of the real approximation of the response at the selected frequency point.

Table 3.11: Comparison of decoupling strategies.

	Jacobian	**Modal**	**SVD**
Philosophy	Topology Driven	Physics Driven	Data Driven
Requirements	Known geometry	Known equations of motion	Identified FRF
Decoupling Matrices	Jacobian matrix $\boldsymbol{J}_{\{O\}}$	Eigenvectors $\boldsymbol{\Phi}$	SVD matrices $\boldsymbol{U}$ and $\boldsymbol{V}$
Decoupled Plant	$\boldsymbol{G}_{\{O\}}(s) = \boldsymbol{J}_{\{O\}}^{-1}\boldsymbol{G}_{\mathcal{L}}(s)\boldsymbol{J}_{\{O\}}^{-\intercal}$	$\boldsymbol{G}_{m}(s) = \boldsymbol{\Phi}^{-1}\boldsymbol{G}_{\mathcal{X}}(s)\boldsymbol{\Phi}^{-\intercal}$	$\boldsymbol{G}_{\text{SVD}}(s) = \boldsymbol{U}^{-1}\boldsymbol{G}(s)\boldsymbol{V}^{-\intercal}$
Controller	$\boldsymbol{K}_{\{O\}}(s) = \boldsymbol{J}_{\{O\}}^{-\intercal}\boldsymbol{K}_{d}(s)\boldsymbol{J}_{\{O\}}^{-1}$	$\boldsymbol{K}_{m}(s) = \boldsymbol{\Phi}^{-\intercal}\boldsymbol{K}_{d}(s)\boldsymbol{\Phi}^{-1}$	$\boldsymbol{K}_{\text{SVD}}(s) = \boldsymbol{V}^{-\intercal}\boldsymbol{K}_{d}(s)\boldsymbol{U}^{-1}$
Interpretation	Forces/Torques to Displacement/Rotation in chosen frame	Inputs (resp. outputs) to excite (resp. sense) individual modes	Directions of max to min controllability/observability
Effectiveness	Decoupling at low or high frequency depending on the chosen frame	Good decoupling at all frequencies	Good decoupling near the chosen frequency
Pros	Retain physical meaning of inputs / outputs. Controller acts on a meaningfully "frame"	Ability to target specific modes. Simple 2^{nd} order diagonal plants	Good Decoupling near the crossover. Very General and requires no model
Cons	Good decoupling at all frequency can only be obtained for specific mechanical architecture	Relies on the accuracy of equation of motions. Robustness to unmodelled dynamics may be poor	Loss of physical meaning of inputs /outputs. Decoupling away from the chosen frequency may be poor

3.3.3 Closed-Loop Shaping using Complementary Filters

Once the system is properly decoupled using one of the approaches described in Section 3.3.2, SISO controllers can be individually tuned for each decoupled "directions". Several ways to design a controller to obtain a given performance while ensuring good robustness properties can be implemented.

In some cases "fixed" controller structures are used, such as PI and PID controllers, whose parameters are manually tuned [41, 51, 160].

Another popular method is Open-Loop shaping, which was used during the conceptual phase. Open-loop shaping involves tuning the controller through a series of "standard" filters (leads, lags, notches, low-pass filters, ...) to shape the open-loop transfer function $G(s)K(s)$ according to desired specifications, including bandwidth, gain and phase margins [127, chapt. 4.4.7]. Open-Loop shaping is very popular because the open-loop transfer function is a linear function of the controller, making it relatively straightforward to tune the controller to achieve desired open-loop characteristics. Another key advantage is that controllers can be tuned directly from measured FRFs of the plant without requiring an explicit model.

However, the behavior (i.e. performance) of a feedback system is a function of closed-loop transfer functions. Specifications can therefore be expressed in terms of the magnitude of closed-loop transfer functions, such as the sensitivity, plant sensitivity, and complementary sensitivity transfer functions [134, chapt. 3]. With open-loop shaping, closed-loop transfer functions are changed only indirectly, which may make it difficult to directly address the specifications that are in terms of the closed-loop transfer functions.

In order to synthesize a controller that directly shapes the closed-loop transfer functions (and therefore the performance metric), $\mathcal{H}_\infty$-synthesis may be used [134]. This approach requires a good model of the plant and expertise in selecting weighting functions that will define the wanted shape of different closed-loop transfer functions [14]. $\mathcal{H}_\infty$-synthesis has been applied for the Stewart platform [76], yet when benchmarked against more basic decentralized controllers, the performance gains proved small [59, 144].

In this section, an alternative controller synthesis scheme is proposed in which complementary filters are used for directly shaping the closed-loop transfer functions (i.e., directly addressing the closed-loop performances). In Section 3.3.3.1, the proposed control architecture is presented. In Section 3.3.3.2, typical performance requirements are translated into the shape of the complementary filters. The design of the complementary filters is briefly discussed in Section 3.3.3.3, and analytical formulas are proposed such that it is possible to change the closed-loop behavior of the system in real-time. Finally, in Section 3.3.3.4, a numerical example is used to show how the proposed control architecture can be implemented in practice.

3.3.3.1 Control Architecture

Virtual Sensor Fusion The idea of using complementary filters in the control architecture originates from sensor fusion techniques [28], where two sensors are combined using complementary filters. Building upon this concept, "virtual sensor fusion" [150] replaces one physical sensor with a model G of the plant. The corresponding control architecture is illustrated in Figure 3.64a, where G' represents the physical plant to be controlled, G is a model of the plant, k is the controller, and H_L and H_H are complementary filters satisfying $H_L(s) + H_H(s) = 1$. In this arrangement, the physical plant is controlled at low frequencies, while the plant model is used at high-frequency to enhance robustness.

Although the control architecture shown in Figure 3.64a appears to be a multi-loop system, it should be noted that no non-linear saturation-type elements are present in the inner loop (containing k, G, and H_H, all numerically implemented). Consequently, this structure is mathematically equivalent to the single-loop architecture illustrated in Figure 3.64b.

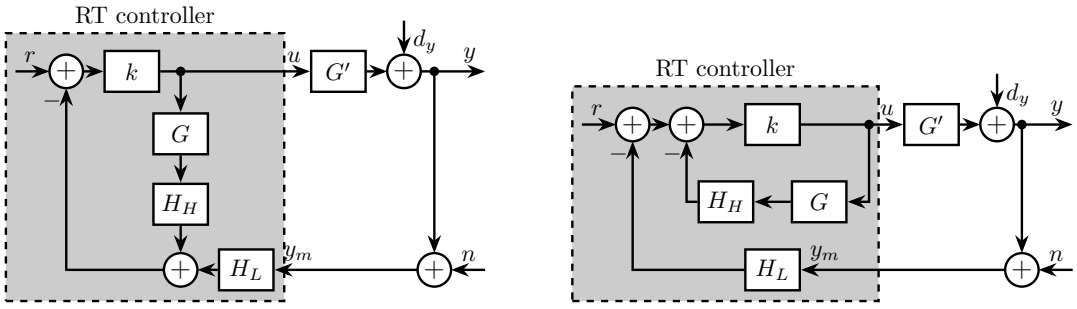

(a) Virtual Sensor Fusion **(b)** Equivalent Architecture

Figure 3.64: Control architecture for virtual sensor fusion (a) and equivalent architecture (b). Signals are the reference input r, the output perturbation d_y, the measurement noise n and the control input u.

Asymptotic Behavior When considering the extreme case of very high values for k, the effective controller $K(s)$ converges to the inverse of the plant model multiplied by the inverse of the high-pass filter, as expressed in (3.62).

$$\lim_{k\to\infty} K(s) = \lim_{k\to\infty} \frac{k}{1 + H_H(s)G(s)k} = \big(H_H(s)G(s)\big)^{-1} \tag{3.62}$$

If the resulting K is improper, a low-pass filter with sufficiently high corner frequency can be added to ensure its causal realization. Furthermore, for K to be stable, both G and H_H must be minimum phase transfer functions.

With these assumptions, the resulting control architecture is illustrated in Figure 3.65, where the complementary filters H_L and H_H remain the only tuning parameters. The dynamics of this closed-loop system are described by equations (3.63a) and (3.63a).

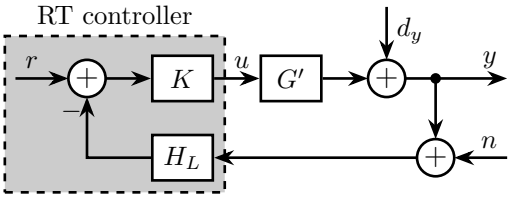

Figure 3.65: Equivalent classical feedback control architecture.

$$y = \frac{H_H dy + G'G^{-1}r - G'G^{-1}H_L n}{H_H + G'G^{-1}H_L} \tag{3.63a}$$

$$u = \frac{-G^{-1}H_L dy + G^{-1}r - G^{-1}H_L n}{H_H + G'G^{-1}H_L} \tag{3.63b}$$

At frequencies where the model accurately represents the physical plant ($G^{-1}G' \approx 1$), the denominator simplifies to $H_H + G'G^{-1}H_L \approx H_H + H_L = 1$, and the closed-loop transfer functions are then described by equations (3.64a) and (3.64b).

$$y = H_H dy \qquad + r \qquad - H_L n \tag{3.64a}$$
$$u = -G^{-1} H_L dy + G^{-1} r - G^{-1} H_L n \tag{3.64b}$$

The sensitivity transfer function equals the high-pass filter $S = \frac{y}{dy} = H_H$, and the complementary sensitivity transfer function equals the low-pass filter $T = \frac{y}{n} = H_L$. Hence, when the plant model closely approximates the actual dynamics, the closed-loop transfer functions converge to the designed complementary filters, allowing direct translation of performance requirements into the design of the complementary.

3.3.3.2 Translating the Performance Requirements into the Shape of the Complementary Filters

Performance specifications in a feedback system can usually be expressed as upper bounds on the magnitudes of closed-loop transfer functions such as the sensitivity and complementary sensitivity transfer functions [14]. The design of a controller $K(s)$ to obtain the desired shape of these closed-loop transfer functions is known as closed-loop shaping.

In the proposed control architecture, the closed-loop transfer functions (3.63) are expressed in terms of the complementary filters $H_L(s)$ and $H_H(s)$ rather than directly through the controller $K(s)$. Therefore, performance requirements must be translated into constraints on the shape of these complementary filters.

Nominal Stability (NS) A closed-loop system is stable when all its elements (here K, G', and H_L) are stable and the sensitivity function $S = \frac{1}{1+G'KH_L}$ is stable. For the nominal system ($G' = G$), the sensitivity transfer function equals the high-pass filter: $S(s) = H_H(s)$.

Nominal Stability (NS) is therefore guaranteed when H_L, H_H, and G are stable, and both G and H_H are minimum phase (ensuring K is stable). Consequently, stable and minimum phase complementary filters must be employed.

Nominal Performance (NP) Performance specifications can be formalized using weighting functions w_H and w_L, where performance is achieved when (3.65) is satisfied. The weighting functions define the maximum magnitude of the closed-loop transfer functions as a function of frequency, effectively determining their "shape".

$$|w_H(j\omega)S(j\omega)| \leq 1 \quad \forall\omega \tag{3.65a}$$
$$|w_L(j\omega)T(j\omega)| \leq 1 \quad \forall\omega \tag{3.65b}$$

For the nominal system, $S = H_H$ and $T = H_L$, hence the performance specifications can be converted on the shape of the complementary filters (3.66).

$$\boxed{\text{NP} \iff \begin{cases} |w_H(j\omega)H_H(j\omega)| \leq 1 & \forall\omega \\ |w_L(j\omega)H_L(j\omega)| \leq 1 & \forall\omega \end{cases}} \tag{3.66}$$

For disturbance rejection, the magnitude of the sensitivity function $|S(j\omega)| = |H_H(j\omega)|$ should be minimized, particularly at low frequencies where disturbances are usually most prominent. Similarly, for noise attenuation, the magnitude

of the complementary sensitivity function $|T(j\omega)| = |H_L(j\omega)|$ should be minimized, especially at high-frequency where measurement noise typically dominates. Classical stability margins (gain and phase margins) are also related to the maximum amplitude of the sensitivity transfer function. Typically, maintaining $|S|_\infty \leq 2$ ensures a gain margin of at least 2 and a phase margin of at least 29°.

Therefore, by carefully selecting the shape of the complementary filters, Nominal Performance (NP) specifications can be directly addressed in an intuitive manner.

Robust Stability (RS) Robust stability refers to a control system's ability to maintain stability despite discrepancies between the actual system G' and the model G used for controller design. These discrepancies may arise from unmodelled dynamics or nonlinearities.

To represent these model-plant differences, input multiplicative uncertainty as illustrated in Figure 3.66a is employed. The set of possible plants Π_i is described by (3.67), with the weighting function w_I selected such that all possible plants G' are contained within the set Π_i.

$$\Pi_i : \quad G'(s) = G(s)\big(1 + w_I(s)\Delta_I(s)\big); \quad |\Delta_I(j\omega)| \leq 1 \, \forall\omega \tag{3.67}$$

(a) Input multiplicative uncertainty

(b) Nyquist plot - Effect of multiplicative uncertainty

Figure 3.66: Input multiplicative uncertainty used to model the differences between the model and the physical plant (a). Effect of this uncertainty is illustrated on the Nyquist plot (b).

When considering input multiplicative uncertainty, Robust Stability (RS) can be derived graphically from the Nyquist plot (illustrated in Figure 3.66b), yielding to (3.68), as demonstrated in [134, chapt. 7.5.1].

$$\text{RS} \iff |w_I(j\omega)L(j\omega)| \leq |1 + L(j\omega)| \quad \forall\omega \tag{3.68}$$

After algebraic manipulation, robust stability is guaranteed when the low-pass complementary filter H_L satisfies (3.69).

$$\boxed{\text{RS} \iff |w_I(j\omega)H_L(j\omega)| \leq 1 \quad \forall\omega} \tag{3.69}$$

Robust Performance (RP) Robust performance ensures that performance specifications (3.65) are met even when the plant dynamics fluctuates within specified bounds (3.70).

$$\text{RP} \iff |w_H(j\omega)S(j\omega)| \leq 1 \quad \forall G' \in \Pi_I, \, \forall\omega \tag{3.70}$$

Transforming this condition into constraints on the complementary filters yields:

$$\boxed{\text{RP} \iff |w_H(j\omega)H_H(j\omega)| + |w_I(j\omega)H_L(j\omega)| \leq 1,\ \forall\omega} \tag{3.71}$$

The Robust Performance (RP) condition effectively combines both nominal performance (3.66) and robust stability conditions (3.69). If both NP and RS conditions are satisfied, robust performance will be achieved within a factor of 2 [134, chapt. 7.6]. Therefore, for SISO systems, ensuring robust stability and nominal performance is typically sufficient.

3.3.3.3 Complementary Filter Design

As proposed in Section 3.3.1, complementary filters can be shaped using standard $\mathcal{H}_\infty$-synthesis techniques. This approach is particularly well-suited since performance requirements were expressed as upper bounds on the magnitude of the complementary filters.

Alternatively, analytical formulas for complementary filters may be employed. For some applications, first-order complementary filters as shown in Equation (3.72) are sufficient.

$$H_L(s) = \frac{1}{1 + s/\omega_0} \tag{3.72a}$$

$$H_H(s) = \frac{s/\omega_0}{1 + s/\omega_0} \tag{3.72b}$$

A significant advantage of using analytical formulas for complementary filters is that key parameters such as ω_0 can be tuned in real-time, as illustrated in Figure 3.67. This real-time tunability allows rapid testing of different control bandwidths to evaluate performance and robustness characteristics.

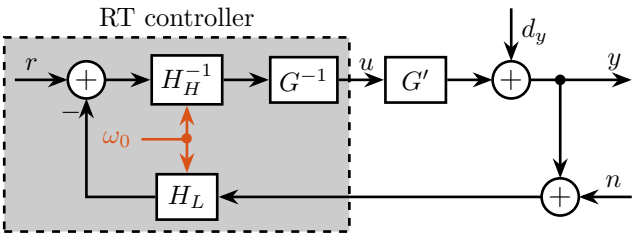

Figure 3.67: Implemented digital complementary filters with parameter ω_0 that can be changed in real-time.

For many practical applications, first order complementary filters are not sufficient. Specifically, a slope of $+2$ at low frequencies for the sensitivity transfer function (enabling accurate tracking of ramp inputs) and a slope of -2 for the complementary sensitivity transfer function are often desired. For these cases, the complementary filters analytical formula in Equation (3.73) is proposed.

$$H_L(s) = \frac{(1+\alpha)(\frac{s}{\omega_0}) + 1}{\left(\frac{s}{\omega_0} + 1\right)\left((\frac{s}{\omega_0})^2 + \alpha\frac{s}{\omega_0} + 1\right)} \tag{3.73a}$$

$$H_H(s) = \frac{(\frac{s}{\omega_0})^2\left(\frac{s}{\omega_0} + 1 + \alpha\right)}{\left(\frac{s}{\omega_0} + 1\right)\left((\frac{s}{\omega_0})^2 + \alpha\frac{s}{\omega_0} + 1\right)} \tag{3.73b}$$

The influence of parameters α and ω_0 on the magnitude response of these complementary filters is illustrated in Figure 3.68. The parameter α primarily affects the damping characteristics near the crossover frequency as well as high and low frequency magnitudes, while ω_0 determines the frequency at which the transition between high-pass and low-pass behavior occurs. These filters can also be implemented in the digital domain with analytical formulas, preserving the ability to adjust α and ω_0 in real-time.

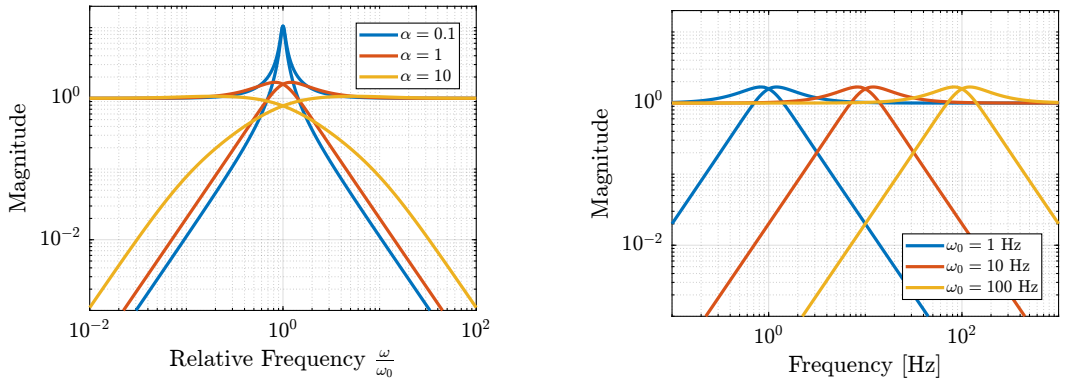

(a) Effect of α

(b) Effect of ω_0

Figure 3.68: Shape of proposed analytical complementary filters. Effect of α (a) and ω_0 (b) are shown.

3.3.3.4 Numerical Example

To implement the proposed control architecture in practice, the following procedure is proposed:

1. Identify the plant to be controlled to obtain the plant model G.
2. Design the weighting function w_I such that all possible plants G' are contained within the uncertainty set Π_i.
3. Translate performance requirements into upper bounds on the complementary filters as explained in Section 3.3.3.2.
4. Design the weighting functions w_H and w_L and generate the complementary filters using $\mathcal{H}_\infty$-synthesis as described in Section 3.3.1.3. If the synthesis fails to produce filters satisfying the defined upper bounds, either revise the requirements or develop a more accurate model G that will allow for a smaller w_I. For simpler cases, the analytical formulas for complementary filters presented in Section 3.3.3.3 can be employed.
5. If $K(s) = H_H^{-1}(s)G^{-1}(s)$ is not proper, add low-pass filters with sufficiently high corner frequencies to ensure realizability.

To evaluate this control architecture, a simple test model representative of many synchrotron positioning stages is used (Figure 3.69a). In this model, a payload with mass m is positioned on top of a stage. The objective is to accurately position the sample relative to the X-ray beam.

The relative position y between the payload and the X-ray is measured, which typically involves measuring the relative position between the focusing optics and the sample. Various disturbance forces affect positioning stability, including stage vibrations d_w and direct forces applied to the sample d_F (such as cable forces). The positioning stage itself is characterized by stiffness k, internal damping c, and a controllable force F.

The model of the plant $G(s)$ from actuator force F to displacement y is described by Equation (3.74).

$$G(s) = \frac{1}{ms^2 + cs + k}, \quad m = 20\,\text{kg},\ k = 1\,\text{N/µm},\ c = 100\,\text{N/(m/s)} \tag{3.74}$$

The plant dynamics include uncertainties related to limited support compliance, unmodelled flexible dynamics and payload dynamics. These uncertainties are represented using a multiplicative input uncertainty weight (3.75), which specifies the magnitude of uncertainty as a function of frequency.

$$w_I(s) = 10 \cdot \frac{(s+100)^2}{(s+1000)^2} \tag{3.75}$$

Figure 3.69b illustrates both the nominal plant dynamics and the complete set of possible plants Π_i encompassed by the uncertainty model.

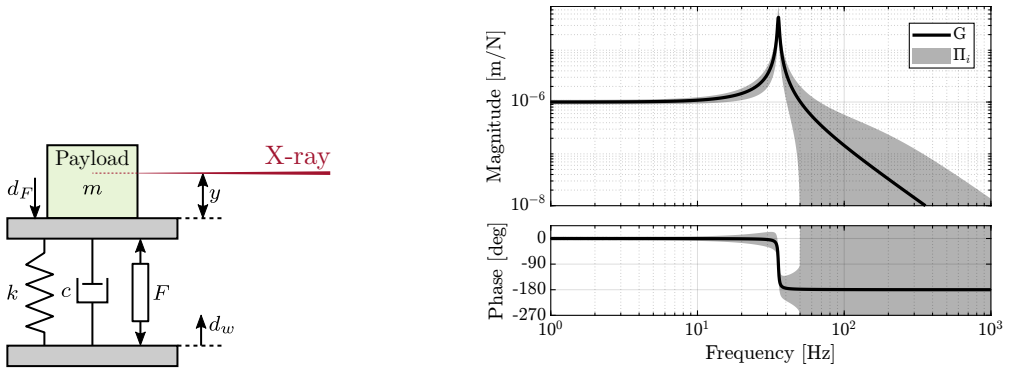

(a) Test model

(b) Bode plot of $G(s)$ and associated uncertainty set

Figure 3.69: Schematic of the test system (a). Bode plot of $G(s) = y/F$ and the associated uncertainty set (b).

Requirements and Choice of Complementary Filters As discussed in Section 3.3.3.2, nominal performance requirements can be expressed as upper bounds on the shape of the complementary filters. For this example, the requirements are:

- track ramp inputs (i.e. constant velocity scans) with zero steady-state error: a $+2$ slope at low frequencies for the magnitude of the sensitivity function $|S(j\omega)|$ is required
- filtering of measurement noise above 300 Hz, where sensor noise is significant (requiring a filtering factor of approximately 100 above this frequency)

- maximizing disturbance rejection

Additionally, robust stability must be ensured, requiring the closed-loop system to remain stable despite the dynamic uncertainties modelled by w_I. This condition is satisfied when the magnitude of the low-pass complementary filter $|H_L(j\omega)|$ remains below the inverse of the uncertainty weight magnitude $|w_I(j\omega)|$, as expressed in Equation (3.69).

Robust performance is achieved when both nominal performance and robust stability conditions are simultaneously satisfied.

All requirements imposed on H_L and H_H are visualized in Figure 3.70a. While $\mathcal{H}_\infty$-synthesis could be employed to design the complementary filters, analytical formulas were used for this relatively simple example. The second-order complementary filters from Equation (3.73) were selected with parameters $\alpha = 1$ and $\omega_0 = 2\pi \cdot 20\,\text{Hz}$. There magnitudes are displayed in Figure 3.70a, confirming that these complementary filters are fulfilling the specifications.

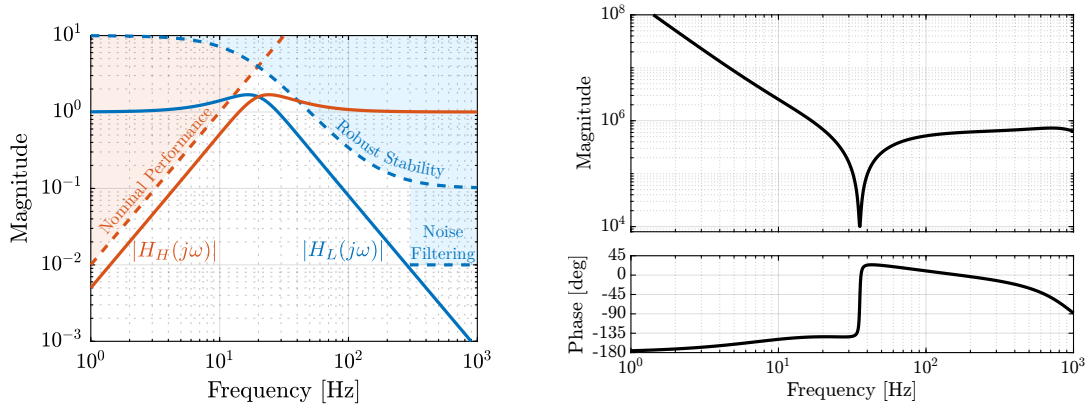

(a) Specifications and complementary filters

(b) Bode plot of $K(s) \cdot H_L(s)$

Figure 3.70: Performance requirements are compared with the complementary filters in (a). The bode plot of the obtained controller is shown in (b).

Controller Analysis The controller to be implemented takes the form $K(s) = \tilde{G}^{-1}(s)H_H^{-1}(s)$, where $\tilde{G}^{-1}(s)$ represents the plant inverse, which must be both stable and proper. To ensure properness, low-pass filters with high corner frequencies are added as shown in Equation (3.76).

$$\tilde{G}^{-1}(s) = \frac{ms^2 + cs + k}{1 + \frac{s}{2\pi \cdot 1000} + \left(\frac{s}{2\pi \cdot 1000}\right)^2} \tag{3.76}$$

The Bode plot of the controller multiplied by the complementary low-pass filter, $K(s) \cdot H_L(s)$, is presented in Figure 3.70b. The loop gain reveals several important characteristics:

- The presence of two integrators at low frequencies, enabling accurate tracking of ramp inputs
- A notch at the plant resonance frequency (arising from the plant inverse)
- A lead component near the control bandwidth of approximately 20 Hz, enhancing stability margins

Robustness and Performance Analysis Robust stability is assessed using the Nyquist plot shown in Figure 3.71a. Even when considering all possible plants within the uncertainty set, the Nyquist plot remains sufficiently distant from the critical point $(-1, 0)$, indicating robust stability with adequate margins.

Performance is evaluated by examining the closed-loop sensitivity and complementary sensitivity transfer functions, as illustrated in Figure 3.71b. It is shown that the sensitivity transfer function achieves the desired $+2$ slope at low frequencies and that the complementary sensitivity transfer function nominally provides the wanted noise filtering.

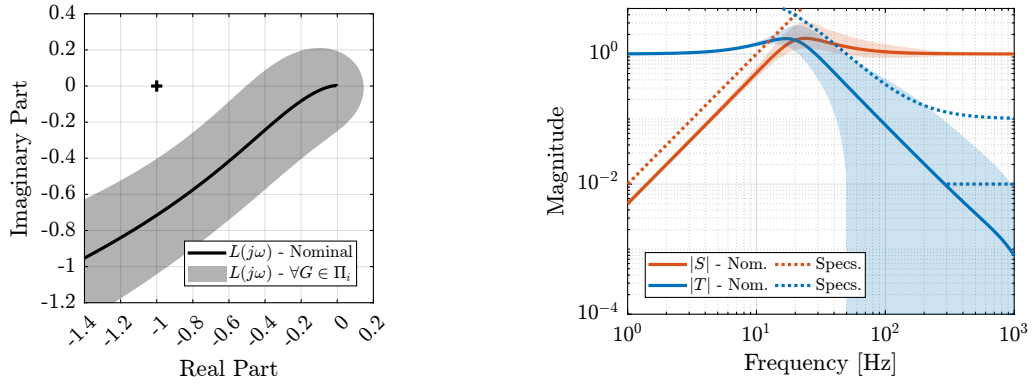

(a) Robust stability

(b) Nominal and robust performance

Figure 3.71: Validation of robust stability with the Nyquist plot (a) and validation of the nominal and robust performance with the magnitude of the closed-loop transfer functions (b).

3.3.3.5 Conclusion

In this section, a control architecture in which complementary filters are used for closed-loop shaping has been presented. This approach differs from traditional open-loop shaping in that no controller is manually designed; rather, appropriate complementary filters are selected to achieve the desired closed-loop behavior. The method shares conceptual similarities with mixed-sensitivity $\mathcal{H}_\infty$-synthesis, as both approaches aim to shape closed-loop transfer functions, but with notable distinctions in implementation and complexity.

While $\mathcal{H}_\infty$-synthesis offers greater flexibility and can be readily generalized to MIMO plants, the presented approach provides a simpler alternative that requires minimal design effort. Implementation only necessitates extracting a model of the plant and selecting appropriate analytical complementary filters, making it particularly interesting for applications where simplicity and intuitive parameter tuning are valued.

Due to time constraints, an extensive literature review comparing this approach with similar existing architectures, such as Internal Model Control [126], was not conducted. Consequently, it remains unclear whether the proposed architecture offers significant advantages over existing methods in the literature.

The control architecture has been presented for SISO systems, but can be applied to MIMO systems when sufficient decoupling is achieved. It will be experimentally validated with the NASS during the experimental phase.

Conclusion

In order to optimize the control of the Nano Active Stabilization System, several aspects of control theory were studied. Different approaches to combine sensors were compared in Section 3.3.1. While High Authority Control / Low

Authority Control (HAC-LAC) was successfully applied during the conceptual design phase, the focus of this work was extended to sensor fusion techniques where two or more sensors are combined using complementary filters. It was demonstrated that the performance of such fusion depends significantly on the magnitude of the complementary filters. To address this challenge, a synthesis method based on $\mathcal{H}_\infty$-synthesis was proposed, allowing for intuitive shaping of the complementary filters through weighting functions. For the NASS, while HAC-LAC remains a natural way to combine sensors, the potential benefits of sensor fusion merit further investigation.

Various decoupling strategies for parallel manipulators were examined in Section 3.3.2, including decentralized control, Jacobian decoupling, modal decoupling, and Singular Value Decomposition (SVD) decoupling. The main characteristics of each approach were highlighted, providing valuable insights into their respective strengths and limitations. Among the examined methods, Jacobian decoupling was determined to be most appropriate for the NASS, as it provides straightforward implementation while preserving the physical meaning of inputs and outputs.

With the system successfully decoupled, attention shifted to designing appropriate SISO controllers for each decoupled direction. A control architecture for directly shaping closed-loop transfer functions was proposed. It is based on complementary filters that can be designed using either the proposed $\mathcal{H}_\infty$-synthesis approach described earlier or through analytical formulas. Experimental validation of this method on the NASS will be conducted during the experimental tests on ID31.

3.4 Choice of Instrumentation

This chapter presents an approach to select and validate appropriate instrumentation for the Nano Active Stabilization System (NASS), ensuring each component meets specific performance requirements. Figure 3.72 illustrates the control diagram with all relevant noise sources whose effects on sample position will be evaluated throughout this analysis.

The selection process follows a three-stage methodology. First, dynamic error budgeting is performed in Section 3.4.1 to establish maximum acceptable noise specifications for each instrumentation component (ADC, DAC, and voltage amplifier). This analysis is based on the multi-body model with a 2-DoF APA model, focusing particularly on the vertical direction due to its more stringent requirements. From the calculated transfer functions, maximum acceptable amplitude spectral densities for each noise source are derived.

Section 3.4.2 then presents the selection of appropriate components based on these noise specifications and additional requirements.

Finally, Section 3.4.3 validates the selected components through experimental testing. Each instrument is characterized individually, measuring actual noise levels and performance characteristics. The measured noise characteristics are then incorporated into the multi-body model to confirm that the combined effect of all instrumentation noise sources remains within acceptable limits.

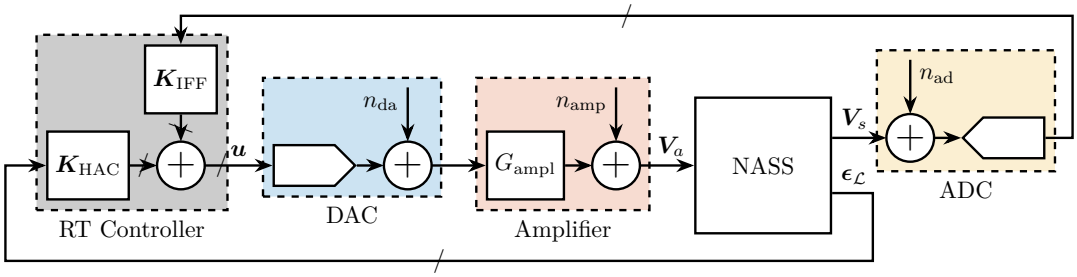

Figure 3.72: Block diagram of the NASS with considered instrumentation. The real-time controller is a Speedgoat machine.

3.4.1 Dynamic Error Budgeting

The primary goal of this analysis is to establish specifications for the maximum allowable noise levels of the instrumentation used for the NASS (ADC, DAC, and voltage amplifier) that would result in acceptable vibration levels in the system.

The procedure involves determining the closed-loop transfer functions from various noise sources to positioning error (Section 3.4.1.1). This analysis is conducted using the multi-body model with a 2-DoF Amplified Piezoelectric Actuator model that incorporates voltage inputs and outputs. Only the vertical direction is considered in this analysis as it presents the most stringent requirements; the horizontal directions are subject to less demanding constraints.

From these transfer functions, the maximum acceptable Amplitude Spectrum Density (ASD) of the noise sources is derived (Section 3.4.1.2). Since the voltage amplifier gain affects the amplification of DAC noise, an assumption of an amplifier gain of 20 was made.

3.4.1.1 Closed-Loop Sensitivity to Instrumentation Noise

Several key noise sources are considered in the analysis (Figure 3.72). These include the output voltage noise of the DAC (n_{da}), the output voltage noise of the voltage amplifier (n_{amp}), and the voltage noise of the ADC measuring the force sensor stacks (n_{ad}).

Encoder noise, which is only used to estimate R_z, has been found to have minimal impact on the vertical sample error and is therefore omitted from this analysis for clarity.

The transfer functions from these three noise sources (for one strut) to the vertical error of the sample are estimated from the multi-body model, which includes the APA300ML and the designed flexible joints (Figure 3.73).

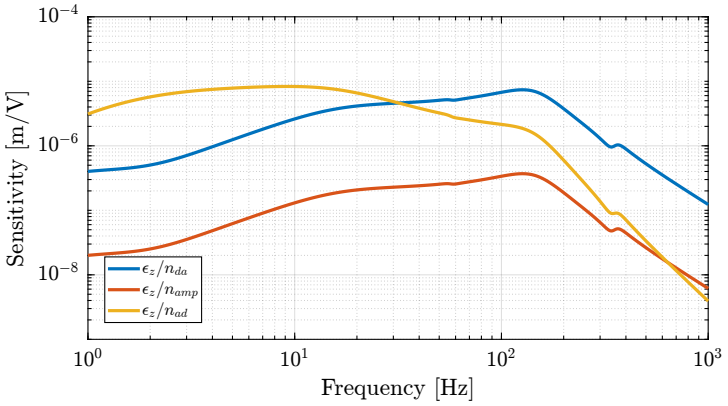

Figure 3.73: Transfer function from noise sources to vertical error, in closed-loop with the implemented HAC-LAC strategy.

3.4.1.2 Estimation of Maximum Acceptable Instrumentation Noise

The most stringent requirement for the system is maintaining vertical vibrations below the smallest expected beam size of 100 nm, which corresponds to a maximum allowed vibration of 15 nm RMS.

Several assumptions regarding the noise characteristics have been made. The DAC, ADC, and amplifier noise are considered uncorrelated, which is a reasonable assumption. Similarly, the noise sources corresponding to each strut are also assumed to be uncorrelated. This means that the Power Spectral Densitys (PSDs) of the different noise sources are summed.

Since the effect of each strut on the vertical error is identical due to symmetry, only one strut is considered for this analysis, and the total effect of the six struts is calculated as six times the effect of one strut in terms of power, which translates to a factor of $\sqrt{6} \approx 2.5$ for RMS values.

In order to derive specifications in terms of noise spectral density for each instrumentation component, a white noise profile is assumed, which is typical for these components.

The noise specification is computed such that if all components operate at their maximum allowable noise levels, the specification for vertical error will still be met. While this represents a pessimistic approach, it provides a reasonable estimate of the required specifications.

Based on this analysis, the obtained maximum noise levels are as follows: DAC maximum output noise ASD is established at 32 $\mu V/\sqrt{Hz}$, voltage amplifier maximum output voltage noise ASD at 650 $\mu V/\sqrt{Hz}$, and ADC maximum

measurement noise ASD at 35 $\mu V/\sqrt{Hz}$. In terms of RMS noise, these translate to 2.3 mV RMS for the DAC, less than 46 mV RMS for the voltage amplifier, and 2.5 mV RMS for the ADC.

If the Amplitude Spectral Density of the noise of the ADC, DAC, and voltage amplifiers all remain below these specified maximum levels, then the induced vertical error will be maintained below 15 nm RMS.

3.4.2 Selection of Instrumentation

3.4.2.1 Piezoelectric Voltage Amplifier

Several characteristics of piezoelectric voltage amplifiers must be considered for this application. To take advantage of the full stroke of the piezoelectric actuator, the voltage output should range between -20 and 150 V. The amplifier should accept an analog input voltage, preferably in the range of -10 to 10 V, as this is standard for most DACs.

Small signal Bandwidth and Output Impedance Small signal bandwidth is particularly important for feedback applications as it can limit the overall bandwidth of the complete feedback system.

A simplified electrical model of a voltage amplifier connected to a piezoelectric stack is shown in Figure 3.74. This model is valid for small signals and provides insight into the small signal bandwidth limitation [48, chap. 14]. In this model, R_o represents the output impedance of the amplifier. When combined with the piezoelectric load (represented as a capacitance C_p), it forms a first order low pass filter described by (3.77).

$$\frac{V_a}{V_i}(s) = \frac{1}{1 + \frac{s}{\omega_0}}, \quad \omega_0 = \frac{1}{R_o C_p} \tag{3.77}$$

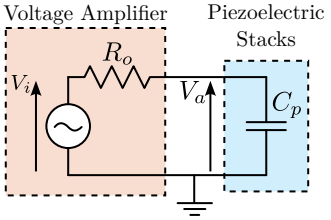

Figure 3.74: Electrical model of an amplifier with output impedance R_0 connected to a piezoelectric stack with capacitance C_p.

Consequently, the small signal bandwidth depends on the load capacitance and decreases as the load capacitance increases. For the APA300ML, the capacitive load of the two piezoelectric stacks corresponds to $C_p = 8.8\,\mu F$. If a small signal bandwidth of $f_0 = \frac{\omega_0}{2\pi} = 5\,kHz$ is desired, the voltage amplifier output impedance should be less than $R_0 = 3.6\,\Omega$.

Large signal Bandwidth Large signal bandwidth relates to the maximum output capabilities of the amplifier in terms of amplitude as a function of frequency.

Since the primary function of the NASS is position stabilization rather than scanning, this specification is less critical than the small signal bandwidth. However, considering potential scanning capabilities, a worst-case scenario of a constant velocity scan (triangular reference signal) with a repetition rate of $f_r = 100$ Hz using the full voltage range of the piezoelectric actuator ($V_{pp} = 170$ V) is considered.

There are two limiting factors for large signal bandwidth that should be evaluated:

1. Slew rate, which should exceed $2 \cdot V_{pp} \cdot f_r = 34\,\text{V/ms}$. This requirement is typically easily met by commercial voltage amplifiers.

2. Current output capabilities: as the capacitive impedance decreases inversely with frequency, it can reach very low values at high-frequency. To achieve high voltage at high-frequency, the amplifier must therefore provide substantial current. The maximum required current can be calculated as $I_{\text{max}} = 2 \cdot V_{pp} \cdot f \cdot C_p = 0.3\,\text{A}$.

Therefore, ideally, a voltage amplifier capable of providing 0.3 A of current would be interesting for scanning applications.

Output voltage noise As established in Section 3.4.1, the output noise of the voltage amplifier should be below 46 mV RMS.

It should be noted that the load capacitance of the piezoelectric stack filters the output noise of the amplifier, as illustrated by the low pass filter in Figure 3.74. Therefore, when comparing noise specifications from different voltage amplifier datasheets, it is essential to verify the capacitance of the load used during the measurement [137].

For this application, the output noise must remain below 46 mV RMS with a load of 8.8 µF and a bandwidth exceeding 5 kHz.

Choice of voltage amplifier The specifications are summarized in Table 3.12. The most critical characteristics are the small signal bandwidth (> 5 kHz) and the output voltage noise (< 46 mV RMS).

Several voltage amplifiers were considered, with their datasheet information presented in Table 3.12. One challenge encountered during the selection process was that manufacturers typically do not specify output noise as a function of frequency (i.e., the ASD of the noise), but instead provide only the RMS value, which represents the integrated value across all frequencies. This approach does not account for the frequency dependency of the noise, which is crucial for accurate error budgeting.

Additionally, the load conditions used to estimate bandwidth and noise specifications are often not explicitly stated. In many cases, bandwidth is reported with minimal load while noise is measured with substantial load, making direct comparisons between different models more complex. Note that for the WMA-200 amplifier, the manufacturer proposed to remove the 50 Ω output resistor to improve to small signal bandwidth above 10 kHz

The PD200 amplifier from PiezoDrive was ultimately selected because it meets all the requirements and is accompanied by clear documentation, particularly regarding noise characteristics and bandwidth specifications.

3.4.2.2 ADC and DAC

Analog-to-digital converters and digital-to-analog converters play key roles in the system, serving as the interface between the digital RT controller and the analog physical plant. The proper selection of these components is critical for system performance.

Synchronicity and Jitter For control systems, synchronous sampling of inputs and outputs of the real-time controller and minimal jitter are essential requirements [2, 3].

Table 3.12: Specifications for the voltage amplifier and considered commercial products.

Specifications	PD200 PiezoDrive	WMA-200 Falco	LA75B Cedrat	E-505 PI
Input Voltage Range: $\pm 10\,\mathrm{V}$	$\pm 10\,\mathrm{V}$	$\pm 8.75\,\mathrm{V}$	$-1/7.5\,\mathrm{V}$	$-2/12\,\mathrm{V}$
Output Voltage Range: $-20/150\,\mathrm{V}$	$-50/150\,\mathrm{V}$	$\pm 175\,\mathrm{V}$	$-20/150\,\mathrm{V}$	$-30/130\,\mathrm{V}$
Gain > 15	20	20	20	10
Output Current $> 300\,\mathrm{mA}$	$900\,\mathrm{mA}$	$150\,\mathrm{mA}$	$360\,\mathrm{mA}$	$215\,\mathrm{mA}$
Slew Rate $> 34\,\mathrm{V/ms}$	$150\,\mathrm{V/\mu s}$	$80\,\mathrm{V/\mu s}$	n/a	n/a
Output noise $< 46\,\mathrm{mV}$ RMS	$0.7\,\mathrm{mV}$	$0.05\,\mathrm{mV}$	$3.4\,\mathrm{mV}$	$0.6\,\mathrm{mV}$
(10uF load)	($10\,\mu\mathrm{F}$ load)	($10\,\mu\mathrm{F}$ load)	(n/a)	(n/a)
Small Signal Bandwidth $> 5\,\mathrm{kHz}$	$6.4\,\mathrm{kHz}$	$300\,\mathrm{Hz}$	$30\,\mathrm{kHz}$	n/a
($10\,\mu\mathrm{F}$ load)	($10\,\mu\mathrm{F}$ load)	($10\,\mu\mathrm{F}$ load)	(unloaded)	(n/a)
Output Impedance: $< 3.6\,\Omega$	n/a	$50\,\Omega$	n/a	n/a

Therefore, the ADC and DAC must be well interfaced with the Speedgoat real-time controller and triggered synchronously with the computation of the control signals. Based on this requirement, priority was given to ADC and DAC components specifically marketed by Speedgoat to ensure optimal integration.

Sampling Frequency, Bandwidth and delays Several requirements that may initially appear similar are actually distinct in nature.

First, the *sampling frequency* defines the interval between two sampled points and determines the Nyquist frequency. Then, the *bandwidth* specifies the maximum frequency of a measured signal (typically defined as the -3 dB point) and is often limited by implemented anti-aliasing filters. Finally, *delay* (or *latency*) refers to the time interval between the analog signal at the input of the ADC and the digital information transferred to the control system.

Sigma-Delta ADCs can provide excellent noise characteristics, high bandwidth, and high sampling frequency, but often at the cost of poor latency. Typically, the latency can reach 20 times the sampling period [127, chapt. 8.4]. Consequently, while Sigma-Delta ADCs are widely used for signal acquisition applications, they have limited utility in real-time control scenarios where latency is a critical factor.

For real-time control applications, successive-approximation ADC remain the predominant choice due to their single-sample latency characteristics.

ADC Noise Based on the dynamic error budget established in Section 3.4.1, the measurement noise ASD should not exceed $35\ \mu V/\sqrt{\mathrm{Hz}}$.

ADCs are subject to various noise sources. Quantization noise, which results from the discrete nature of digital representation, is one of these sources. To determine the minimum bit depth n required to meet the noise specifications, an ideal ADC where quantization error is the only noise source is considered.

The quantization step size, denoted as $q = \Delta V/2^n$, represents the voltage equivalent of the Least Significant Bit (LSB), with ΔV the full range of the ADC in volts, and F_s the sampling frequency in Hertz.

The quantization noise ranges between $\pm q/2$, and its probability density function is constant across this range (uniform distribution). Since the integral of this probability density function $p(e)$ equals one, its value is $1/q$ for $-q/2 < e < q/2$, as illustrated in Figure 3.75.

The variance (or time-average power) of the quantization noise is expressed by (3.78).

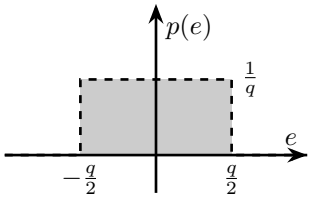

Figure 3.75: Probability density function $p(e)$ of the ADC quantization error e.

$$P_q = \int_{-q/2}^{q/2} e^2 p(e) de = \frac{q^2}{12} \tag{3.78}$$

To compute the power spectral density of the quantization noise, which is defined as the Fourier transform of the noise's autocorrelation function, it is assumed that noise samples are uncorrelated. Under this assumption, the autocorrelation function approximates a delta function in the time domain. Since the Fourier transform of a delta function equals one, the power spectral density becomes frequency-independent (white noise).

By Parseval's theorem, the power spectral density of the quantization noise Φ_q can be linked to the ADC sampling frequency and quantization step size (3.79).

$$\int_{-F_s/2}^{F_s/2} \Phi_q(f) df = \int_{-q/2}^{q/2} e^2 p(e) de \quad \Longrightarrow \quad \Phi_q = \frac{q^2}{12F_s} = \frac{\left(\frac{\Delta V}{2^n}\right)^2}{12F_s} \quad \text{in} \left[\frac{V^2}{\text{Hz}}\right] \tag{3.79}$$

From a specified noise amplitude spectral density Γ_{max}, the minimum number of bits required to keep quantization noise below Γ_{max} is calculated using (3.80).

$$n = \log_2\left(\frac{\Delta V}{\sqrt{12F_s} \cdot \Gamma_{\text{max}}}\right) \tag{3.80}$$

With a sampling frequency $F_s = 10\,\text{kHz}$, an input range $\Delta V = 20\,\text{V}$ and a maximum allowed ASD $\Gamma_{\text{max}} = 35\,\mu\text{V}/\sqrt{Hz}$, the minimum number of bits is $n_{\text{min}} = 10.7$, which is readily achievable with commercial ADCs.

DAC Output voltage noise Similar to the ADC requirements, the DAC output voltage noise ASD should not exceed $32\,\mu\text{V}/\sqrt{\text{Hz}}$. This specification corresponds to a $\pm 10\,\text{V}$ DAC with 11-bit resolution, which is easily attainable with current technology.

Choice of the ADC and DAC Board Based on the preceding analysis, the selection of suitable ADC and DAC components is straightforward.

For optimal synchronicity, a Speedgoat-integrated solution was chosen. The selected model is the IO131, which features 16 analog inputs based on the AD7609 with 16-bit resolution, $\pm 10\,\text{V}$ range, maximum sampling rate of 200kSPS (Samples per Second), simultaneous sampling, and differential inputs allowing the use of shielded twisted pairs for enhanced noise immunity. The board also includes 8 analog outputs based on the AD5754R with 16-bit resolution, $\pm 10\,\text{V}$ range, conversion time of $10\,\mu s$, and simultaneous update capability.

Although noise specifications are not explicitly provided in the datasheet, the 16-bit resolution should ensure performance well below the established requirements. This will be experimentally verified in Section 3.4.3.

3.4.2.3 Relative Displacement Sensors

The specifications for the relative displacement sensors include sufficient compactness for integration within each strut, noise levels below 6 nm RMS (derived from the 15 nm RMS vertical error requirement for the system divided by the contributions of six struts), and a measurement range exceeding 100 µm.

Several sensor technologies are capable of meeting these requirements [47]. These include optical encoders (Figure 3.76a), capacitive sensors (Figure 3.76c), and eddy current sensors (Figure 3.76b), each with their own advantages and implementation considerations.

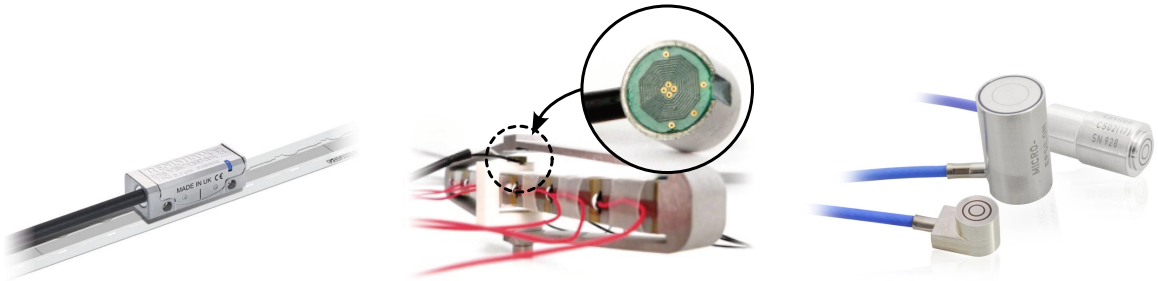

(a) Optical Linear Encoder **(b)** Eddy Current Sensor **(c)** Capacitive Sensor

Figure 3.76: Relative motion sensors considered for measuring the active platform strut motion.

From an implementation perspective, capacitive and eddy current sensors offer a slight advantage as they can be quite compact and can measure in line with the APA, as illustrated in Figure 3.77b. In contrast, optical encoders are bigger and they must be offset from the strut's action line, which introduces potential measurement errors (Abbe errors) due to potential relative rotations between the two ends of the APA, as shown in Figure 3.77a.

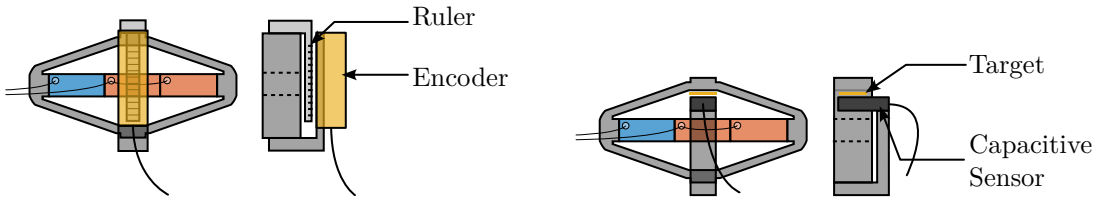

(a) Optical Encoder **(b)** Capacitive Sensor

Figure 3.77: Implementation of relative displacement sensors to measure the motion of the APA.

A practical consideration in the sensor selection process was the fact that sensor signals must pass through an electrical slip-ring due to the continuous spindle rotation. Measurements conducted on the slip-ring integrated in the microstation revealed substantial cross-talk between different slip-ring channels. To mitigate this issue, preference was given to sensors that transmit displacement measurements digitally, as these are inherently less susceptible to noise and cross-talk. Based on this criterion, an optical encoder with digital output was selected, where signal interpolation is performed directly in the sensor head.

The specifications of the considered relative motion sensor, the Renishaw Vionic, are summarized in Table 3.13, alongside alternative options that were considered.

Table 3.13: Specifications for the relative displacement sensors and considered commercial products.

Specifications	Renishaw Vionic	LION CPL190	Cedrat ECP500
Technology	Digital Encoder	Capacitive	Eddy Current
Bandwidth > 5 kHz	> 500 kHz	10 kHz	20 kHz
Noise < 6 nm RMS	1.6 nm RMS	4 nm RMS	15 nm RMS
Range > 100 µm	Ruler length	250 µm	500 µm
In line measurement		×	×
Digital Output	×		

3.4.3 Characterization of Instrumentation

3.4.3.1 Analog to Digital Converters

Measured Noise The measurement of ADC noise was performed by short-circuiting its input with a 50 Ω resistor and recording the digital values at a sampling rate of 10 kHz. The amplitude spectral density of the recorded values was computed and is presented in Figure 3.78. The ADC noise exhibits characteristics of white noise with an amplitude spectral density of $5.6\ \mu V/\sqrt{Hz}$ (equivalent to 0.4 mV RMS), which satisfies the established specifications. All ADC channels demonstrated similar performance, so only one channel's noise profile is shown.

If necessary, oversampling can be applied to further reduce the noise [83]. To gain w additional bits of resolution, the oversampling frequency f_{os} should be set to $f_{os} = 4^w \cdot F_s$. Given that the ADC can operate at 200 kSPS while the real-time controller runs at 10 kSPS, an oversampling factor of 16 can be employed to gain approximately two additional bits of resolution (reducing noise by a factor of 4). This approach is effective because the noise approximates white noise and its amplitude exceeds 1 LSB (0.3 mV) [60].

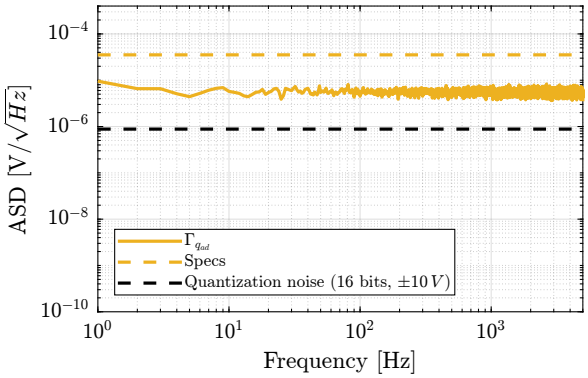

Figure 3.78: Measured ADC noise (IO318).

Reading of Piezoelectric Force Sensor To further validate the ADC's capability to effectively measure voltage generated by a piezoelectric stack, a test was conducted using the APA95ML. The setup is illustrated in Figure 3.79, where two stacks are used as actuators (connected in parallel) and one stack serves as a sensor. The voltage amplifier employed in this setup has a gain of 20.

Step signals with an amplitude of 1 V were generated using the DAC, and the ADC signal was recorded. The excitation signal (steps) and the measured voltage across the sensor stack are displayed in Figure 3.80b.

Two notable observations were made: an offset voltage of 2.26 V was present, and the measured voltage exhibited an exponential decay response to the step input. These phenomena can be explained by examining the electrical schematic shown in Figure 3.80a, where the ADC has an input impedance R_i and an input bias current i_n.

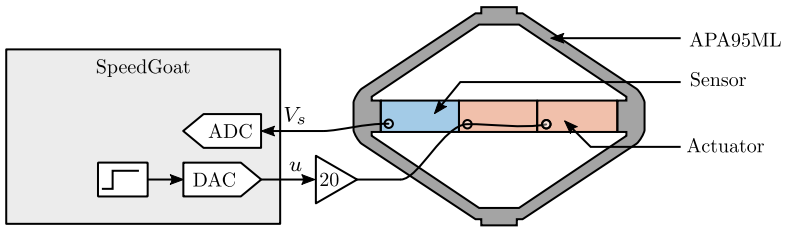

Figure 3.79: Schematic of the setup to validate the use of the ADC for reading the force sensor voltage.

The input impedance R_i of the ADC, in combination with the capacitance C_p of the piezoelectric stack sensor, forms an RC circuit with a time constant $\tau = R_i C_p$. The charge generated by the piezoelectric effect across the stack's capacitance gradually discharges into the input resistor of the ADC. Consequently, the transfer function from the generated voltage V_p to the measured voltage V_{ADC} is a first-order high-pass filter with the time constant τ.

An exponential curve was fitted to the experimental data, yielding a time constant $\tau = 6.5\,\text{s}$. With the capacitance of the piezoelectric sensor stack being $C_p = 4.4\,\mu\text{F}$, the internal impedance of the Speedgoat ADC was calculated as $R_i = \tau / C_p = 1.5\,M\Omega$, which closely aligns with the specified value of $1\,M\Omega$ found in the datasheet.

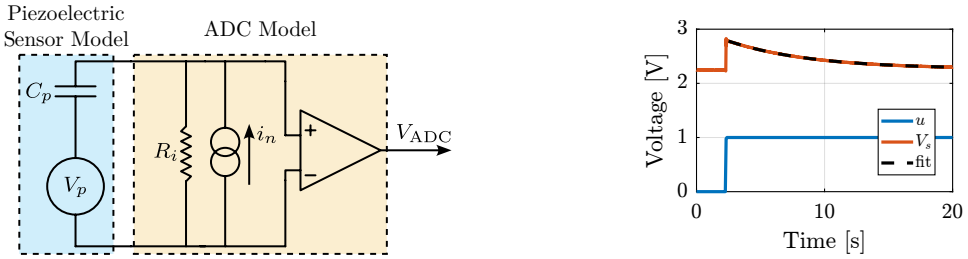

(a) Electrical Schematic

(b) Measured Signals

Figure 3.80: Electrical schematic of the ADC measuring the piezoelectric force sensor (a), adapted from [101]. Measured voltage V_s while step voltages are generated for the actuator stacks (b).

The constant voltage offset can be explained by the input bias current i_n of the ADC, represented in Figure 3.80a. At DC, the impedance of the piezoelectric stack is much larger than the input impedance of the ADC, and therefore the input bias current i_n passing through the internal resistance R_i produces a constant voltage offset $V_{\text{off}} = R_i \cdot i_n$. The input bias current i_n is estimated from $i_n = V_{\text{off}} / R_i = 1.5\,\mu\text{A}$.

In order to reduce the input voltage offset and to increase the corner frequency of the high pass filter, a resistor R_p can be added in parallel to the force sensor, as illustrated in Figure 3.81a. This modification produces two beneficial effects: a reduction of input voltage offset through the relationship $V_{\text{off}} = (R_p R_i)/(R_p + R_i) i_n$, and an increase in the high pass corner frequency f_c according to the equations $\tau = 1/(2\pi f_c) = (R_i R_p)/(R_i + R_p) C_p$.

To validate this approach, a resistor $R_p \approx 82\,k\Omega$ was added in parallel with the force sensor as shown in Figure 3.81a. After incorporating this resistor, the same step response tests were performed, with results displayed in Figure 3.81b. The measurements confirmed the expected improvements, with a substantially reduced offset voltage ($V_{\text{off}} = 0.15\,\text{V}$) and a much faster time constant ($\tau = 0.45\,\text{s}$). These results validate both the model of the ADC and the effectiveness of the added parallel resistor as a solution.

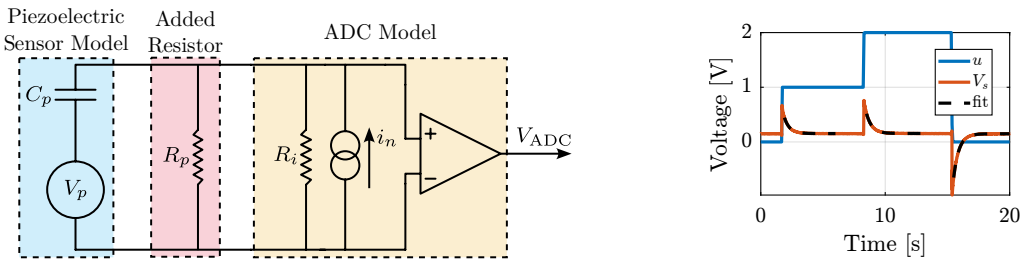

(a) Electrical Schematic **(b)** Measured Signals

Figure 3.81: Effect of an added resistor R_p in parallel to the force sensor. The electrical schematic is shown in (a) and the measured signals in (b).

3.4.3.2 Instrumentation Amplifier

Because the ADC noise may be too low to measure the noise of other instruments (anything below $5.6\,\mu V/\sqrt{Hz}$ cannot be distinguished from the noise of the ADC itself), a low noise instrumentation amplifier was employed. A Femto DLPVA-101-B-S amplifier with adjustable gains from 20 dB up to 80 dB was selected for this purpose.

The first step was to characterize the input[1] noise of the amplifier. This was accomplished by short-circuiting its input with a $50\,\Omega$ resistor and measuring the output voltage with the ADC (Figure 3.82). The maximum amplifier gain of $80\,textdB$ (equivalent to 10000) was used for this measurement.

The measured voltage n was then divided by 10000 to determine the equivalent noise at the input of the voltage amplifier n_a. In this configuration, the noise contribution from the ADC q_{ad} is rendered negligible due to the high gain employed. The resulting amplifier noise amplitude spectral density Γ_{n_a} and the (negligible) contribution of the ADC noise are presented in Figure 3.83.

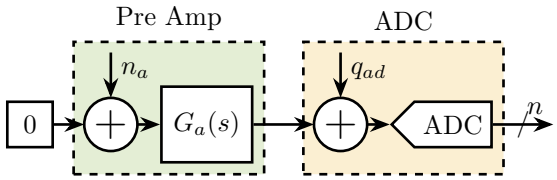

Figure 3.82: Measurement of the instrumentation amplifier input voltage noise.

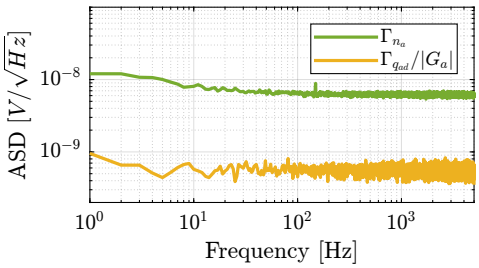

Figure 3.83: Obtained ASD of the instrumentation amplifier input voltage noise.

3.4.3.3 Digital to Analog Converters

Output Voltage Noise To measure the output noise of the DAC, the setup schematically represented in Figure 3.84 was used. The DAC was configured to output a constant voltage (zero in this case), and the gain of the pre-amplifier was adjusted such that the measured amplified noise was significantly larger than the noise of the ADC.

[1] For variable gain amplifiers, it is usual to refer to the input noise rather than the output noise, as the input referred noise is almost independent on the chosen gain.

The Amplitude Spectral Density $\Gamma_{n_{da}}(\omega)$ of the measured signal was computed, and verification was performed to confirm that the contributions of ADC noise and amplifier noise were negligible in the measurement.

The resulting Amplitude Spectral Density of the DAC's output voltage is displayed in Figure 3.85a. The noise profile is predominantly white with an ASD of $0.6\ \mu V/\sqrt{Hz}$. Minor 50 Hz noise is present, along with some low frequency $1/f$ noise, but these are not expected to pose issues as they are well within specifications. It should be noted that all DAC channels demonstrated similar performance, so only one channel measurement is presented.

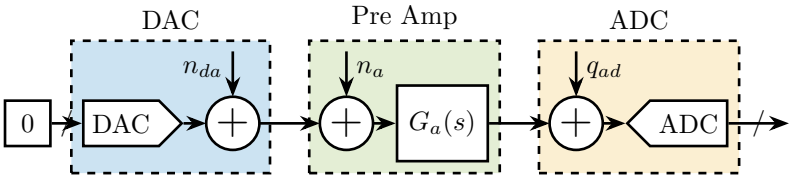

Figure 3.84: Measurement of the DAC output voltage noise. A pre-amplifier with a gain of 1000 is used before measuring the signal with the ADC.

Delay from ADC to DAC To measure the transfer function from DAC to ADC and verify that the bandwidth and latency of both instruments is sufficient, a direct connection was established between the DAC output and the ADC input. A white noise signal was generated by the DAC, and the ADC response was recorded.

The resulting FRF from the digital DAC signal to the digital ADC signal is presented in Figure 3.85b. The observed FRF corresponds to exactly one sample delay, which aligns with the specifications provided by the manufacturer.

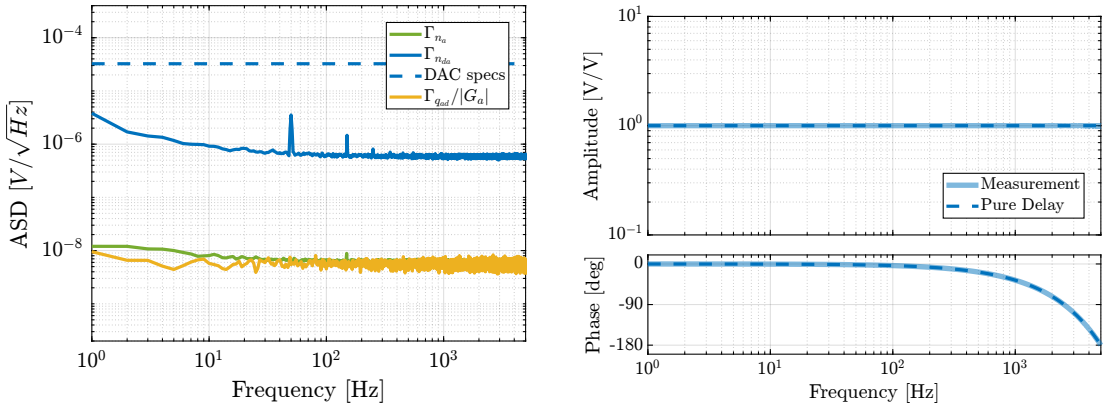

(a) Output noise of the DAC

(b) Transfer function from DAC to ADC

Figure 3.85: Measurement of the output voltage noise of the DAC (a) and measured transfer function from DAC to ADC (b) which corresponds to a "1-sample" delay.

3.4.3.4 Piezoelectric Voltage Amplifier

Output Voltage Noise The measurement setup for evaluating the PD200 amplifier noise is illustrated in Figure 3.86. The input of the PD200 amplifier was shunted with a 50 resistor to ensure that only the inherent noise of the amplifier itself was measured. The pre-amplifier gain was increased to produce a signal substantially larger than the noise floor of the ADC. Two piezoelectric stacks from the APA95ML were connected to the PD200 output to provide an appropriate load for the amplifier.

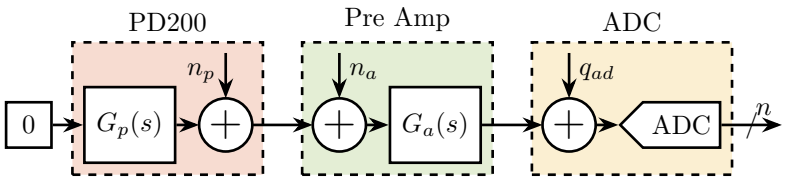

Figure 3.86: Setup used to measure the output voltage noise of the PD200 voltage amplifier. A gain $G_a = 1000$ was used for the instrumentation amplifier.

The Amplitude Spectral Density $\Gamma_n(\omega)$ of the signal measured by the ADC was computed. From this, the Amplitude Spectral Density of the output voltage noise of the PD200 amplifier n_p was derived, accounting for the gain of the pre-amplifier according to (3.81).

$$\Gamma_{n_p}(\omega) = \frac{\Gamma_n(\omega)}{|G_p(j\omega)G_a(j\omega)|} \tag{3.81}$$

The computed Amplitude Spectral Density of the PD200 output noise is presented in Figure 3.87. Verification was performed to confirm that the measured noise was predominantly from the PD200, with negligible contributions from the pre-amplifier noise or ADC noise. The measurements from all six amplifiers are displayed in this figure.

The noise spectrum of the PD200 amplifiers exhibits several sharp peaks. While the exact cause of these peaks is not fully understood, their amplitudes remain below the specified limits and should not adversely affect system performance.

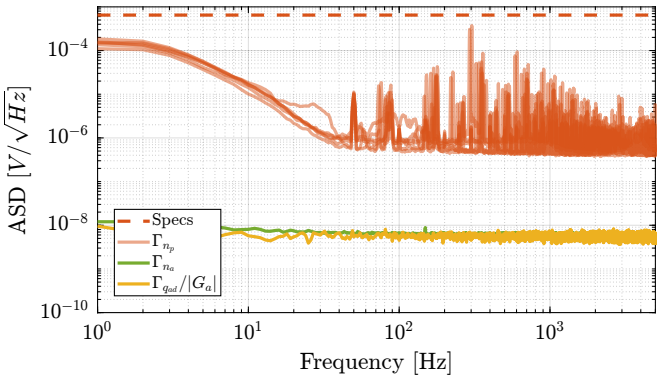

Figure 3.87: Measured output voltage noise of the PD200 amplifiers.

Small Signal Bandwidth The small signal dynamics of all six PD200 amplifiers were characterized through FRF measurements.

A logarithmic sweep sine excitation voltage was generated using the Speedgoat DAC with an amplitude of 0.1 V, spanning frequencies from 1 Hz to 5 kHz. The output voltage of the PD200 amplifier was measured via the monitor voltage output of the amplifier, while the input voltage (generated by the DAC) was measured with a separate ADC channel of the Speedgoat system. This measurement approach eliminates the influence of ADC-DAC-related time delays in the results.

All six amplifiers demonstrated consistent transfer function characteristics. The amplitude response remains constant across a wide frequency range, and the phase shift is limited to less than 1 degree up to 500 Hz, well within the specified requirements.

The identified dynamics shown in Figure 3.88 can be accurately modelled as either a first-order low-pass filter or as a simple constant gain.

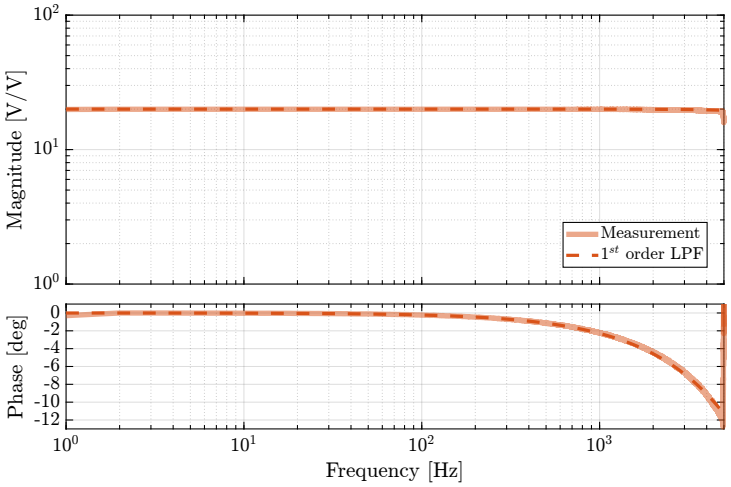

Figure 3.88: Identified dynamics from input voltage to output voltage of the PD200 voltage amplifier.

3.4.3.5 Linear Encoders

To measure the noise of the encoder, the head and ruler were rigidly fixed together to ensure that no relative motion would be detected. Under these conditions, any measured signal would correspond solely to the encoder noise.

The measurement setup is shown in Figure 3.89. To minimize environmental disturbances, the entire bench was covered with a plastic bubble sheet during measurements.

The amplitude spectral density of the measured displacement (which represents the measurement noise) is presented in Figure 3.90. The noise profile exhibits characteristics of white noise with an amplitude of approximately 1 nm RMS, which complies with the system requirements.

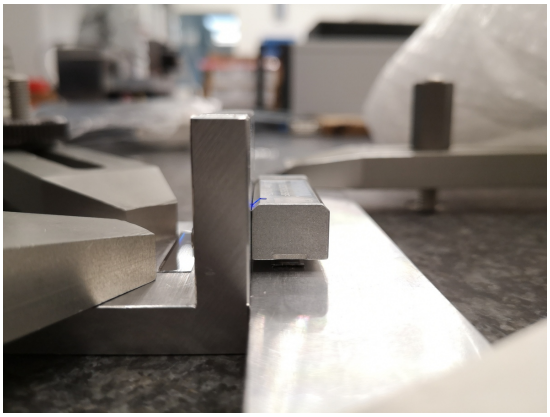

Figure 3.89: Test bench used to measure the encoder noise.

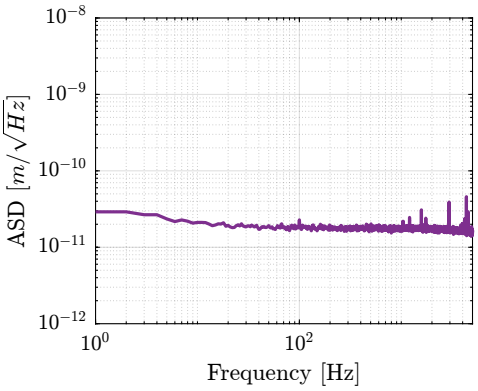

Figure 3.90: Measured encoder noise ASD.

3.4.3.6 Error Budgeting from Measured Instrumentation Noise

After characterizing all instrumentation components individually, their combined effect on the sample's vibration was assessed using the multi-body model. The vertical motion induced by the noise sources, specifically the ADC noise, DAC noise, and voltage amplifier noise, is presented in Figure 3.91. The total motion induced by all noise sources combined is approximately 0.7 nm RMS, which remains well within the specified limit of 15 nm RMS. This confirms that the selected instrumentation, with its measured noise characteristics, is suitable for the intended application.

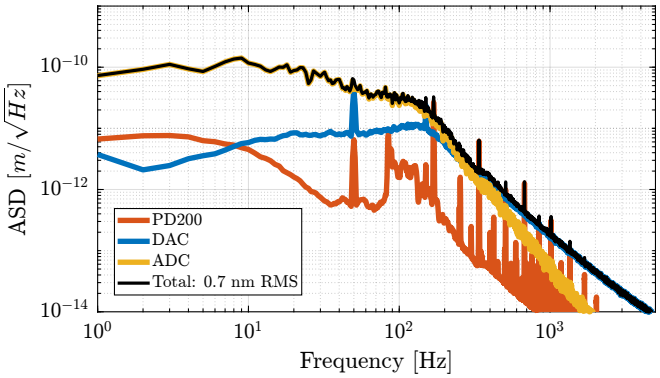

Figure 3.91: Closed-loop error budgeting using measured noise of instrumentation.

Conclusion

This section has presented a comprehensive approach to the selection and characterization of instrumentation for the nano active stabilization system. The multi-body model created earlier served as a key tool for embedding instrumentation components and their associated noise sources within the system analysis. From the most stringent requirement (i.e. the specification on vertical sample motion limited to 15 nm RMS), detailed specifications for each noise source were methodically derived through dynamic error budgeting.

Based on these specifications, appropriate instrumentation components were selected for the system. The selection process revealed certain challenges, particularly with voltage amplifiers, where manufacturer datasheets often lacked crucial information needed for accurate error budgeting, such as amplitude spectral densities under specific load conditions. Despite these challenges, suitable components were identified that theoretically met all requirements.

The selected instrumentation was procured and thoroughly characterized. Initial measurements of the ADC system revealed an issue with force sensor readout related to input bias current, which was successfully addressed by adding a parallel resistor to optimize the measurement circuit.

All components were found to meet or exceed their respective specifications. The ADC demonstrated noise levels of $5.6\,\mu V/\sqrt{Hz}$ (versus the $35\,\mu V/\sqrt{Hz}$ specification), the DAC showed $0.6\,\mu V/\sqrt{Hz}$ (versus $32\,\mu V/\sqrt{Hz}$ required), the voltage amplifiers exhibited noise well below the $650\,\mu V/\sqrt{Hz}$ limit, and the encoders achieved 1 nm RMS noise (versus the 6 nm RMS specification).

Finally, the measured noise characteristics of all instrumentation components were included into the multi-body model to predict the actual system performance. The combined effect of all noise sources was estimated to induce vertical sample vibrations of only 0.7 nm RMS, which is substantially below the 15 nm RMS requirement. This rigorous methodology spanning requirement formulation, component selection, and experimental characterization validates the instrumentation's ability to fulfill the nano active stabilization system's demanding performance specifications.

3.5 Obtained Design: the "Nano-Hexapod"

The detailed mechanical design of the active platform (also referred to as the "nano-hexapod"), depicted in Figure 3.92, is presented in this section. Several primary objectives guided the mechanical design. First, to ensure a well-defined Jacobian matrix used in the control architecture, accurate positioning of the top flexible joint rotation points and correct orientation of the struts were required. Secondly, space constraints necessitated that the entire platform fit within a cylinder with a radius of 120 mm and a height of 95 mm. Thirdly, because performance predicted by the multi-body model was fulfilling the requirements, the final design was intended to approximate the behavior of this "idealized" active platform as closely as possible. This objective implies that the frequencies of (un-modelled) flexible modes potentially detrimental to control performance needed to be maximized. Finally, considerations for ease of mounting, alignment, and maintenance were incorporated, specifically ensuring that struts could be easily replaced in the event of failure.

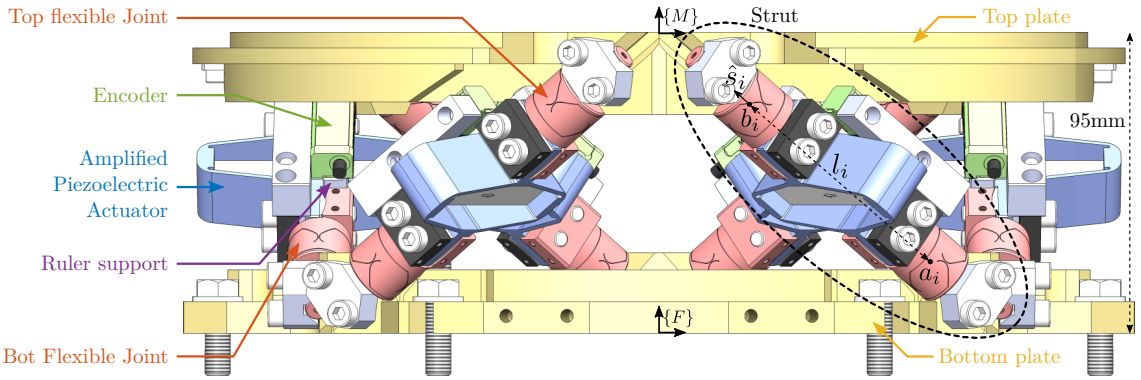

Figure 3.92: Obtained mechanical design of the active platform, called the "nano-hexapod".

3.5.1 Mechanical Design

Struts The strut design, illustrated in Figure 3.93, was driven by several factors. Stiff interfaces were required between the amplified piezoelectric actuator and the two flexible joints, as well as between the flexible joints and their respective mounting plates. Due to the limited angular stroke of the flexible joints, it was critical that the struts could be assembled such that the two cylindrical interfaces were coaxial while the flexible joints remained in their unstressed, nominal rest position. To facilitate this alignment, cylindrical washers (Figure 3.93a) were integrated into the design to compensate for potential deviations from perfect flatness between the two APA interface planes (Figure 3.94b). Furthermore, a dedicated mounting bench was developed to enable precise alignment of each strut, even when accounting for typical machining inaccuracies. The mounting procedure is described in Section 4.3.1. Lastly, the design needed to permit the mounting of an encoder parallel to the strut axis, as shown in Figure 3.93b.

The flexible joints, shown in Figure 3.94a, were manufactured using wire-cut Electrical Discharge Machining (EDM). First, the part being quite fragile, stemming from its 0.25 mm neck dimension, is easier to machine using wire-cut EDM thanks to the very small cutting forces compared to classical machining. Furthermore, wire-cut EDM allows for tight machining tolerances of complex shapes. The material chosen for the flexible joints is a stainless steel designated *X5CrNiCuNb16-4* (alternatively known as F16Ph). This selection was based on its high specified yield strength (exceeding 1 GPa after appropriate heat treatment) and its high fatigue resistance.

As shown in Figure 3.94a, the interface designed to connect with the APA possesses a cylindrical shape, facilitating the use of the aforementioned cylindrical washers for alignment. A slotted hole was incorporated to permit alignment of the flexible joint with the APA via a dowel pin. Additionally, two threaded holes were included on the sides for mounting the encoder components. The interface connecting the flexible joint to the platform plates will be described subsequently.

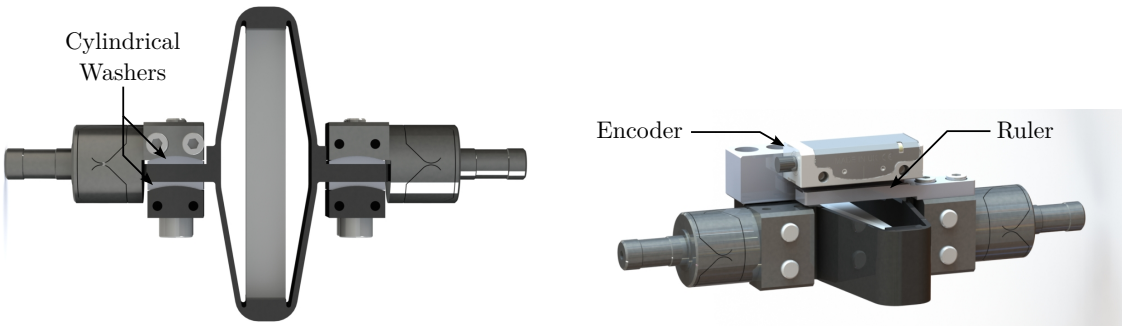

(a) Before encoder integration **(b)** With the mounted encoder

Figure 3.93: Design of the nano-hexapod struts. Before (a) and after (b) encoder integration.

Modifications to the standard mechanical interfaces of the APA300ML were requested from the manufacturer. The modified design features two planar surfaces and a dowel hole for precise location and orientation, as illustrated in Figure 3.94b.

(a) Flexible joint **(b)** Amplified Piezoelectric Actuator

Figure 3.94: Two main components of the struts: the flexible joint (a) and the amplified piezoelectric actuator (b).

Accurate measurement of the relative displacement within each strut requires the encoders to sense the motion between the rotational centers of the two associated flexible joints. To achieve this, two interface parts, fabricated from aluminum, were designed. These parts serve to fix the encoder head and the associated scale (ruler) to the two flexible joints, as depicted in Figure 3.93b.

PLATES The design of the top and bottom plates of the nano-hexapod was governed by two main requirements: maximizing the frequency of flexible modes and ensuring accurate positioning of the top flexible joints and well-defined orientation of the struts. To maximize the natural frequencies associated with plate flexibility, a network of reinforcing ribs was incorporated into the design, as shown for the top plate in Figure 3.95. Although topology optimization methods were considered, the implemented ribbed design was found to provide sufficiently high natural frequencies for the flexible modes.

The interfaces for the joints on the plates incorporate V-grooves (red planes in Figure 3.95). The cylindrical portion of each flexible joint is constrained within its corresponding V-groove through two distinct line contacts, illustrated in Figure 3.96a. These grooves consequently serve to define the nominal orientation of the struts. High machining

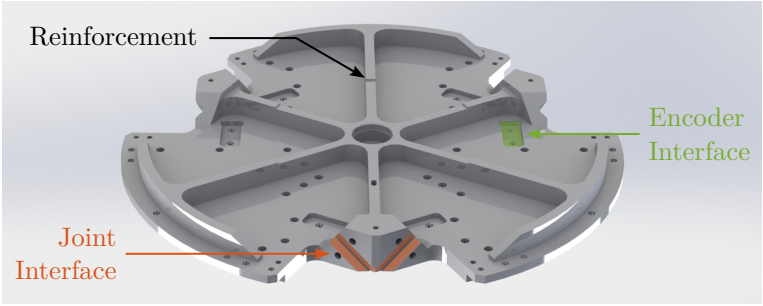

Figure 3.95: The mechanical design for the top platform incorporates precisely positioned V-grooves for the joint interfaces (displayed in red). The purpose of the encoder interface (shown in green) is later detailed.

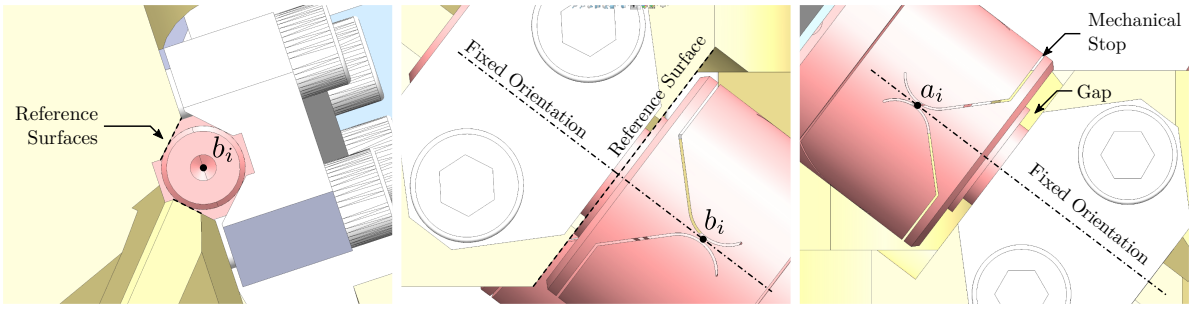

(a) Flexible Joint Clamping **(b)** Top positioning **(c)** Bottom Positioning

Figure 3.96: Clamping of the flexible points on the nano-hexapod plates. Both top and bottom flexible joints are clamped to the plates as shown in (a). While the top flexible joints are in contact with the top plate for precise positioning of its center of rotation (b), the bottom joints are just oriented (c).

accuracy for these features is essential to ensure that the flexible joints are in their neutral, unstressed state when the nano-hexapod is assembled.

Furthermore, the flat interface surface of each top flexible joint is designed to be in direct contact with the top platform surface, as shown in Figure 3.96b. This contact ensures that the centers of rotation of the top flexible joints, are precisely located relative to the top platform coordinate system. The bottom flexible joints, however, are primarily oriented by the V-grooves without the same precise positional constraint against the bottom plate, as shown in Figure 3.96c.

Both plates were specified to be manufactured from a martensitic stainless steel, X30Cr13. This material was selected primarily for its high hardness, which minimizes the risk of deformation of the reference surfaces during the clamping of the flexible joints. This characteristic is expected to permit repeated assembly and disassembly of the struts, should maintenance or reconfiguration be necessary.

Finite Element Analysis A Finite Element Analysis (FEA) of the complete nano-hexapod assembly was performed to identify modes that could potentially affect performance. The analysis revealed that the first six modes correspond to "suspension" modes, where the top plate effectively moves as a rigid body, and motion primarily involves axial displacement of the six struts (an example is shown in Figure 3.97a). Following these suspension modes, numerous "local" modes associated with the struts themselves were observed in the frequency range between 205 Hz and 420 Hz. One such mode is represented in Figure 3.97b. Although these modes do not appear to induce significant motion of the top platform, they do cause relative displacement between the encoder components (head and scale) mounted on the strut. Consequently, such modes could potentially degrade control performance if the nano-hexapod's position is regulated using these encoder measurements. The extent to which these modes might be detrimental is difficult to es-

tablish at this stage, as it depends on whether they are significantly excited by the APA actuation and their sensitivity to strut alignment. Finally, the FEA indicated that flexible modes of the top plate itself begin to appear at frequencies above 650 Hz, with the first such mode shown in Figure 3.97c.

(a) Suspension mode **(b)** Strut - Local mode **(c)** Top plate mode

Figure 3.97: Finite Element Model of the nano-hexapod. The first six modes are "suspension" modes in which the top plate behaves as a rigid body (a). Then modes of the struts have natural frequencies from 205 Hz to 420 Hz (b). Finally, the first flexible mode of the top plate is at 650 Hz (c).

Alternative Encoder Placement In anticipation of potential issues arising from the local modes of the struts affecting encoder measurements, an alternative mounting strategy for the encoders was designed. In this configuration, the encoders are fixed directly to the top and bottom plates instead of the struts, as illustrated in Figure 3.98.

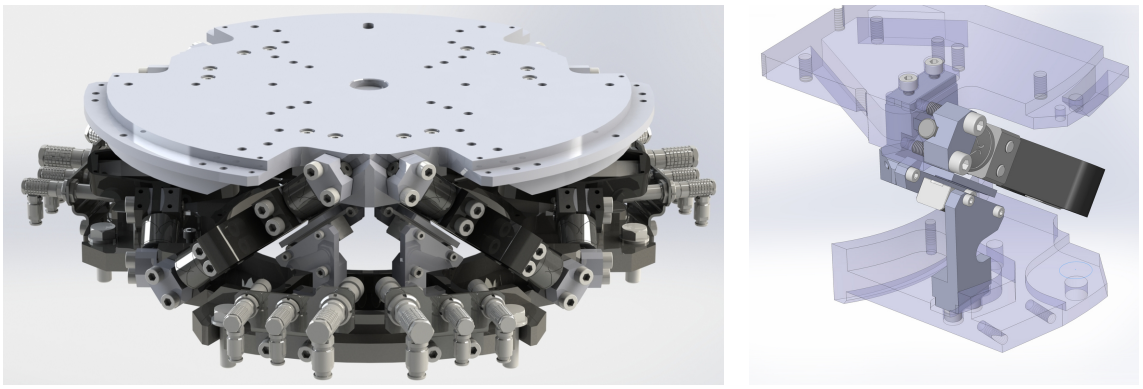

(a) Nano-Hexapod with encoders fixed to the plates **(b)** Zoom on encoder mounting

Figure 3.98: Alternative location of the encoders: fixed to the plates.

Dedicated supports, machined from aluminum, were designed for this purpose. It was verified through FEA that the natural modes of these supports occur at frequencies sufficiently high (first mode estimated at 1120 Hz) to not be problematic for control. Precise positioning of these encoder supports is achieved through machined pockets in both the top and bottom plates, visible in Figure 3.95 (indicated in green). Although the encoders in this arrangement are aligned parallel to the nominal strut axes, they no longer measure the exact relative displacement along the strut between the flexible joint centers. This geometric discrepancy implies that if the relative motion control of the nano-hexapod is based directly on these encoder readings, the kinematic calculations may be slightly inaccurate, potentially affecting the overall positioning accuracy of the platform.

3.5.2 Multi-Body Model

Prior to the procurement of mechanical components, the multi-body simulation model of the active platform was refined to incorporate the finalized design geometries. Two distinct configurations, corresponding to the two encoder

mounting strategies discussed previously, were considered in the model, as displayed in Figure 3.99: one with encoders fixed to the struts, and another with encoders fixed to the plates. In these models, the top and bottom plates were represented as rigid bodies, with their inertial properties calculated directly from the 3D geometry.

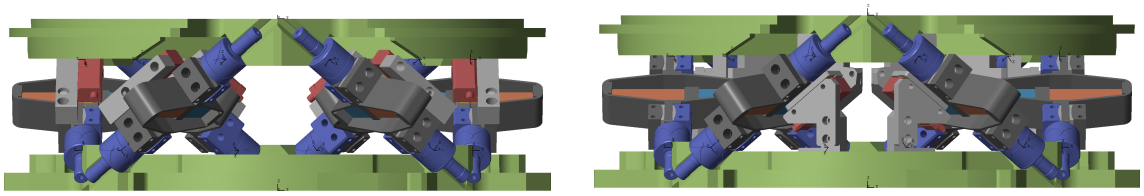

(a) Encoders fixed to the struts **(b)** Encoders fixed to the plates

Figure 3.99: 3D representation of the multi-body model. There are two configurations: encoders fixed to the struts (a) and encoders fixed to the plates (b).

Flexible Joints Several levels of detail were considered for modeling the flexible joints within the multi-body model: 2-DoF models incorporating only bending stiffness, 3-DoF models including additional torsional stiffness, and 4-DoF models further incorporating axial stiffness were evaluated. The multi-body representation corresponding to the 4-DoF configuration is shown in Figure 3.100. This model is composed of three distinct solid bodies interconnected by joints, whose stiffness properties were derived from FEA of the joint component.

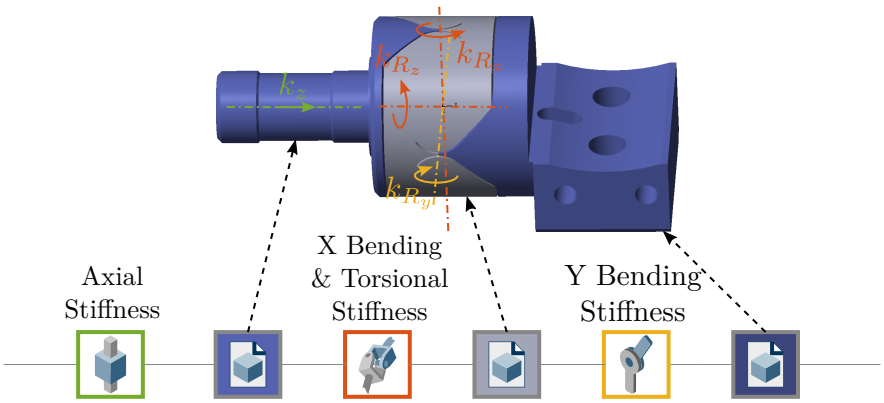

Figure 3.100: 4-DoF multi-body model of the flexible joints. Axial, bending and torsional stiffnesses are modelled.

Amplified Piezoelectric Actuators The Amplified Piezoelectric Actuators were incorporated into the multi-body model following the methodology detailed in Section 3.2.2. Two distinct representations of the APA can be used within the simulation: a simplified 2-DoF model capturing the axial behavior, or a more complex "Reduced Order Flexible Body" model derived from a FEM.

Encoders In earlier modeling stages, the relative displacement sensors (encoders) were implemented as a direct measurement of the relative distance between the joint connection points $\boldsymbol{a}_i$ and $\boldsymbol{b}_i$. However, as indicated by the FEA results discussed previously, the flexible modes inherent to the struts could potentially affect the encoder measurement. Therefore, a more sophisticated model of the optical encoder was necessary.

The optical encoders operate based on the interaction between an encoder head and a graduated scale or ruler. The optical encoder head contains a light source that illuminates the ruler. A reference frame $\{E\}$ fixed to the scale, represents the light position on the scale, as illustrated in Figure 3.101. The ruler features a precise grating pattern (in this case, with

a 20 µm pitch), and its position is associated with the reference frame $\{R\}$. The displacement measured by the encoder corresponds to the relative position of the encoder frame $\{E\}$ (specifically, the point where the light interacts with the scale) with respect to the ruler frame $\{R\}$, projected along the measurement direction defined by the scale.

An important consequence of this measurement principle is that a relative rotation between the encoder head and the ruler, as depicted conceptually in Figure 3.101b, can induce a measured displacement.

(a) Aligned encoder and ruler

(b) Rotation of the encoder head

Figure 3.101: Representation of the encoder multi-body model. Measurement d_i corresponds to the x position of the encoder frame $\{E\}$ expresssed in the ruller frame $\{R\}$ (a). A rotation of the encoder therefore induces a measured displacement (b).

Validation of the Designed Active Platform The refined multi-body model of the nano-hexapod was integrated into the multi-body micro-station model. Dynamical analysis was performed, confirming that the platform's behavior closely approximates the dynamics of the "idealized" model used during the conceptual design phase. Consequently, closed-loop performance simulations replicating tomography experiments yielded metrics highly comparable to those previously predicted (as presented in Section 2.6.3.4). Given this similarity and because analogous simulations are conducted and detailed during the experimental validation phase (Section 4.5.4), these specific results are not reiterated here.

Detailed Design - Conclusion

In this chapter, a comprehensive approach to the detailed design of the nano-hexapod for the Nano Active Stabilization System has been presented. The design process was structured around four key aspects: geometry optimization, component design, control strategy refinement, and instrumentation selection.

The geometry optimization began with a review of existing Stewart platform designs, followed by analytical modeling of the relationship between geometric parameters and performance characteristics. While cubic architectures are prevalent in the literature due to their purported advantages in decoupling and uniform stiffness, the analysis revealed that these benefits are more nuanced than commonly described. For the nano-hexapod application, struts were oriented more vertically than in a cubic configuration to address the stringent vertical performance requirements and to better match the micro-station's modal characteristics.

For component optimization, a hybrid modeling methodology was used that combined FEA with multi-body dynamics. This approach, validated experimentally using an Amplified Piezoelectric Actuator, enabled both detailed component-level optimization and efficient system-level simulation. Through this methodology, the APA300ML was selected as the optimal actuator, offering the necessary combination of stroke, stiffness, and force sensing capabilities required for the application. Similarly, the flexible joints were designed with careful consideration of bending and axial stiffness requirements, resulting in a design that balances competing mechanical demands.

For control optimization, three critical challenges were addressed. First, the problem of optimally combining multiple sensors was investigated and was focused on the design of complementary filters for sensor fusion. A $\mathcal{H}_\infty$-synthesis technique was formulated for designing complementary filters with precisely shaped magnitude responses. Second, various decoupling strategies for parallel manipulators were compared, filling a notable gap in current literature. Among the evaluated techniques (decentralized control, Jacobian decoupling, modal decoupling, and SVD decoupling), Jacobian decoupling was identified as the most suitable for the NASS due to its simplicity and ability to maintain physical interpretation of the decoupled plant's inputs and outputs. Third, a novel control architecture was developed that leverages complementary filters for direct shaping of closed-loop transfer functions. This framework, which will be validated during the experimental phase, offers an intuitive alternative to traditional methods by allowing designers to directly specify desired closed-loop characteristics in a simple and intuitive way.

The instrumentation selection was guided by dynamic error budgeting, which established maximum acceptable noise specifications for each component. The selected components—including the IO131 ADC/DAC board, PD200 voltage amplifiers, and Vionic linear encoders—were then experimentally characterized to verify their performance. All components were found to meet or exceed their specifications, with the combined effect of all noise sources estimated to induce vertical sample vibrations of only 1.5 nm RMS, well below the 15 nm RMS requirement.

The outcome of this detailed design process is a nano-hexapod and associated instrumentation specifically tailored to the NASS applications. Following the completion of this design phase and the subsequent procurement of all specified components, the project progressed to the experimental validation stage, which forms the focus of the next chapter.

4 Experimental Validation

Contents

Abstract

The experimental validation follows a systematic approach, beginning with the characterization of individual components before advancing to evaluate the assembled system's performance (illustrated in Figure 4.1). Section 4.1 focuses on the Amplified Piezoelectric Actuator (APA300ML), examining its electrical properties, and dynamical behavior. Two models are developed and validated: a simplified two-degree-of-freedom model and a more complex super-element extracted from FEA. The implementation of Integral Force Feedback is also experimentally evaluated to assess its effectiveness in adding damping to the system.

In Section 4.2, the flexible joints are characterized to ensure they meet the required specifications for stiffness and stroke. A dedicated test bench is developed to measure the bending stiffness, with error analysis performed to validate the measurement accuracy.

Section 4.3 examines the assembly and testing of the struts, which integrate the APAs and flexible joints. The mounting procedure is detailed, with particular attention to ensure consistent performance across multiple struts. Dynamical measurements are performed to verify whether the dynamics of the struts are corresponding to the multi-body model.

The assembly and testing of the complete nano-hexapod is presented in Section 4.4. A suspended table is developed to isolate the hexapod's dynamics from support dynamics, enabling accurate identification of its dynamical properties. The experimental FRFs are compared with the multi-body model predictions to validate the modeling approach. The effects of various payload masses are also investigated.

Finally, Section 4.5 presents the validation of the NASS on the ID31 beamline. A short-stroke metrology system is developed to measure the sample position relative to the granite base. The HAC-LAC control architecture is implemented and tested under various experimental conditions, including payload masses up to 39 kg and for typical experiments, including tomography scans, reflectivity measurements, and diffraction tomography.

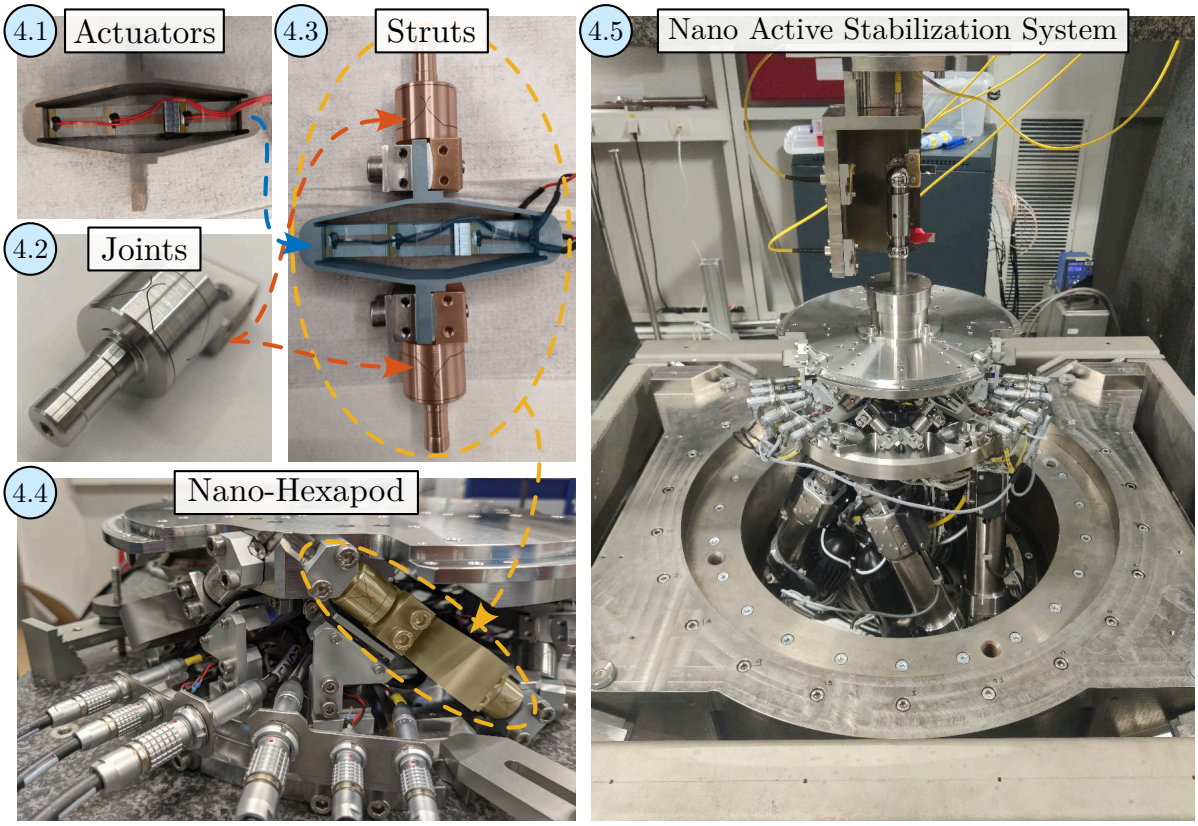

Figure 4.1: Overview of the experimental validation phase. The actuators and flexible joints and individual tested and then integrated into the struts. The Nano-hexapod is then mounted and the complete system is validated on the ID31 beamline.

4.1 Amplified Piezoelectric Actuators

In this chapter, the goal is to ensure that the received APA300ML (shown in Figure 4.2) are complying with the requirements and that the dynamical models of the actuator accurately represent its dynamics.

In section 4.1.1, the mechanical tolerances of the APA300ML interfaces are checked together with the electrical properties of the piezoelectric stacks and the achievable stroke. The flexible modes of the APA300ML, which were estimated using a FEM, are compared with measurements.

Using a dedicated test bench, dynamical measurements are performed (Section 4.1.2). The dynamics from the generated DAC voltage (going through the voltage amplifier and then to two actuator stacks) to the induced axial displacement and to the measured voltage across the force sensor stack are estimated. Integral Force Feedback is experimentally applied, and the damped plants are estimated for several feedback gains.

Two different models of the APA300ML are presented. First, in Section 4.1.3, a two-degree-of-freedom model is presented, tuned, and compared with the measured dynamics. This model is proven to accurately represent the APA300ML's axial dynamics while having low complexity.

Then, in Section 4.1.4, a *super element* of the APA300ML is extracted using a FEM and imported into the multi-body model. This more complex model also captures well capture the axial dynamics of the APA300ML.

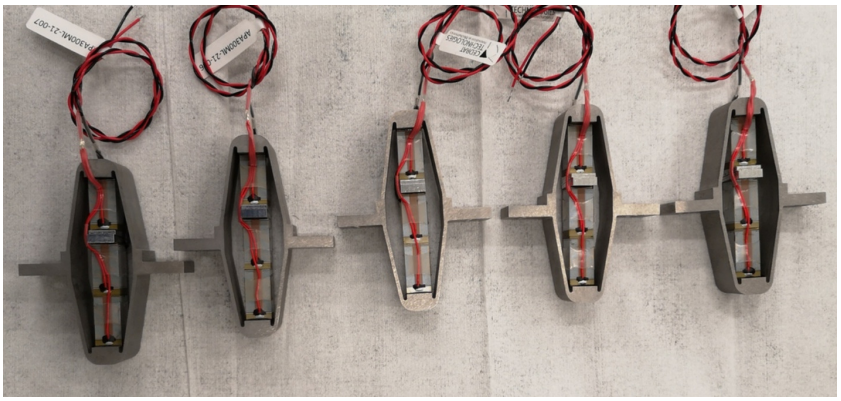

Figure 4.2: 5 of the 7 received APA300ML.

4.1.1 Static Measurements

Before measuring the dynamical characteristics of the APA300ML, simple measurements are performed. First, the tolerances (especially flatness) of the mechanical interfaces are checked in Section 4.1.1.1. Then, the capacitances of the piezoelectric stacks are measured in Section 4.1.1.2. The achievable strokes of the APA300ML are measured using a displacement probe in Section 4.1.1.3. Finally, in Section 4.1.1.4, the flexible modes of the APA are measured and compared with a FEM.

4.1.1.1 Geometrical Measurements

To measure the flatness of the two mechanical interfaces of the APA300ML, a small measurement bench is installed on top of a metrology granite with excellent flatness. As shown in Figure 4.3, the APA is fixed to a clamp while a measuring

probe[1] is used to measure the height of four points on each of the APA300ML interfaces. From the XYZ coordinates of the measured eight points, the flatness is estimated by best fitting[2] a plane through all the points. The measured flatness values, summarized in Table 4.1, are within the specifications.

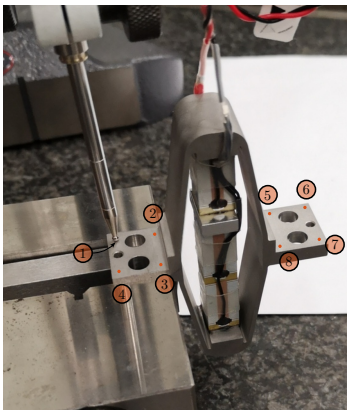

Figure 4.3: Measurement setup for flatness estimation.

	Flatness [µm]
APA 1	8.9
APA 2	3.1
APA 3	9.1
APA 4	3.0
APA 5	1.9
APA 6	7.1
APA 7	18.7

Table 4.1: Estimated flatness of the APA300ML interfaces

4.1.1.2 Electrical Measurements

From the documentation of the APA300ML, the total capacitance of the three stacks should be between 18 µF and 26 µF with a nominal capacitance of 20 µF.

The capacitance of the APA300ML piezoelectric stacks was measured with the LCR meter[3] shown in Figure 4.4. The two stacks used as the actuator and the stack used as the force sensor were measured separately. The measured capacitance values are summarized in Table 4.2 and the average capacitance of one stack is $\approx$ 5µF. However, the measured capacitance of the stacks of "APA 3" is only half of the expected capacitance. This may indicate a manufacturing defect.

The measured capacitance is found to be lower than the specified value. This may be because the manufacturer measures the capacitance with large signals (−20 V to 150 V), whereas it was here measured with small signals [156].

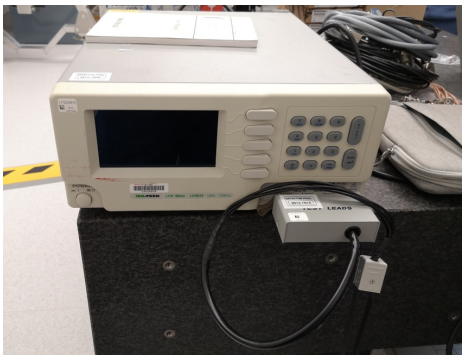

Figure 4.4: Used LCR meter.

	Sensor Stack	**Actuator Stacks**
APA 1	5.10	10.03
APA 2	4.99	9.85
APA 3	1.72	5.18
APA 4	4.94	9.82
APA 5	4.90	9.66
APA 6	4.99	9.91
APA 7	4.85	9.85

Table 4.2: Measured capacitance in µF

[1] Heidenhain MT25, specified accuracy of ±0.5 µm.
[2] The Matlab `fminsearch` command is used to fit the plane.
[3] LCR-819 from Gwinstek, with a specified accuracy of 0.05%. The measured frequency is set at 1 kHz.

4.1.1.3 Stroke and Hysteresis Measurement

To compare the stroke of the APA300ML with the datasheet specifications, one side of the APA is fixed to the granite, and a displacement probe[1] is located on the other side as shown in Figure 4.5.

The voltage across the two actuator stacks is varied from -20 V to 150 V using a DAC[2] and a voltage amplifier[3]. Note that the voltage is slowly varied as the displacement probe has a very low measurement bandwidth (see Figure 4.6a).

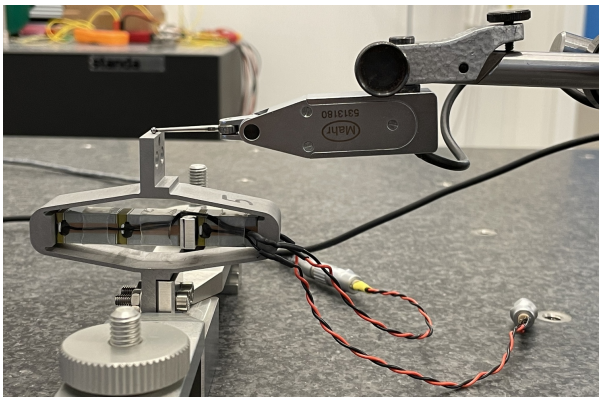

Figure 4.5: Test bench to measure the APA stroke.

The measured APA displacement is shown as a function of the applied voltage in Figure 4.6b. Typical hysteresis curves for piezoelectric stack actuators can be observed. The measured stroke is approximately 250 µm when using only two of the three stacks. This is even above what is specified as the nominal stroke in the data-sheet (304 µm, therefore $\approx$ 200 µm if only two stacks are used). For the NASS, this stroke is sufficient because the positioning errors to be corrected using the nano-hexapod are expected to be in the order of 10 µm.

It is clear from Figure 4.6b that "APA 3" has an issue compared with the other units. This confirms the abnormal electrical measurements made in Section 4.1.1.2. This unit was sent back to Cedrat, and a new one was shipped back. From now on, only the six remaining amplified piezoelectric actuators that behave as expected will be used.

4.1.1.4 Flexible Mode Measurement

In this section, the flexible modes of the APA300ML are investigated both experimentally and through finite element modeling. To experimentally estimate these modes, the APA is fixed at one end (see Figure 4.8). A Laser Doppler Vibrometer[4] is used to measure the difference of motion between two "red" points and an instrumented hammer[5] is used to excite the flexible modes. Using this setup, the transfer function from the injected force to the measured rotation can be computed under different conditions, and the frequency and mode shapes of the flexible modes can be estimated.

The flexible modes for the same condition (i.e. one mechanical interface of the APA300ML fixed) are estimated using a finite element software, and the results are shown in Figure 4.7.

The measured FRFs computed from the experimental setups of figures 4.8a and 4.8b are shown in Figure 4.9. The y bending mode is observed at 280 Hz and the x bending mode is at 412 Hz. These modes are measured at higher

[1] Millimar 1318 probe, specified linearity better than 1 µm.
[2] The DAC used is the one included in the IO131 card sold by Speedgoat. It has an output range of ± 10 V and 16-bits resolution.
[3] PD200 from PiezoDrive. The gain is 20 V/V.
[4] Polytec controller 3001 with sensor heads OFV512.
[5] Kistler 9722A.

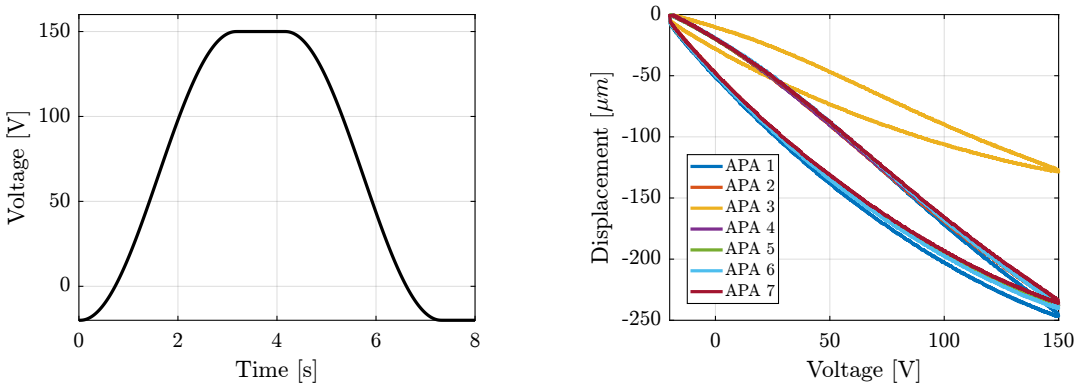

(a) Applied voltage for stroke estimation

(b) Hysteresis curves of the APA

Figure 4.6: Generated voltage across the two piezoelectric stack actuators to estimate the stroke of the APA300ML (a). Measured displacement as a function of applied voltage (b).

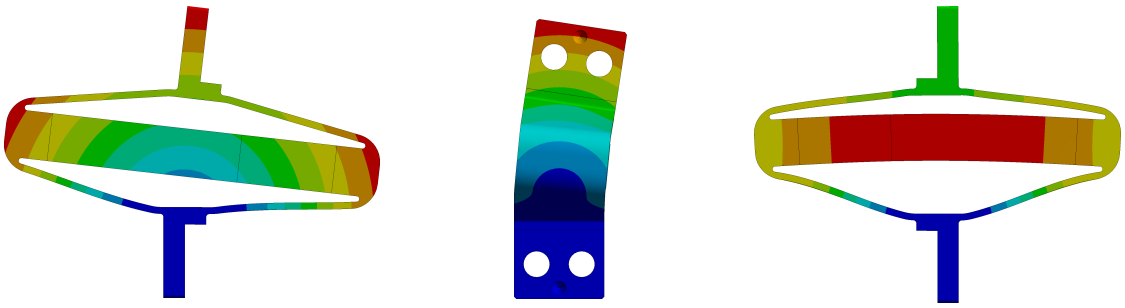

(a) Y-bending mode (268 Hz)

(b) X-bending mode (399 Hz)

(c) Z-axial mode (706 Hz)

Figure 4.7: First three modes of the APA300ML in a fix-free condition estimated from a Finite Element Model.

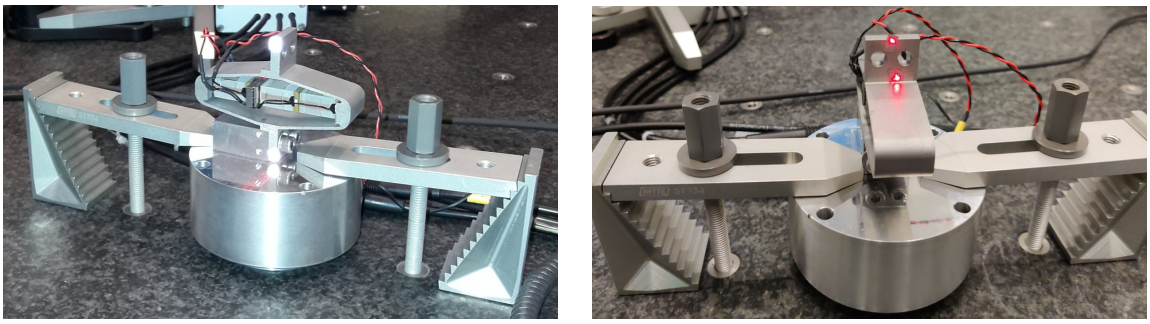

(a) X bending

(b) Y Bending

Figure 4.8: Experimental setup to measure the flexible modes of the APA300ML. For the bending in the X direction (a), the hammer impact point is at the back of the top measurement point. For the bending in the Y direction (b), the hammer impact point is located at the back of the top measurement point.

frequencies than the frequencies estimated from the FEM (see frequencies in Figure 4.7). This is the opposite of what is usually observed (i.e. having lower resonance frequencies in practice than the estimation from a FEM). This could be explained by underestimation of the Young's modulus of the steel used for the shell (190 GPa was used for the model, but steel with Young's modulus of 210 GPa could have been used). Another explanation is the shape difference between the manufactured APA300ML and the 3D model, for instance thicker blades.

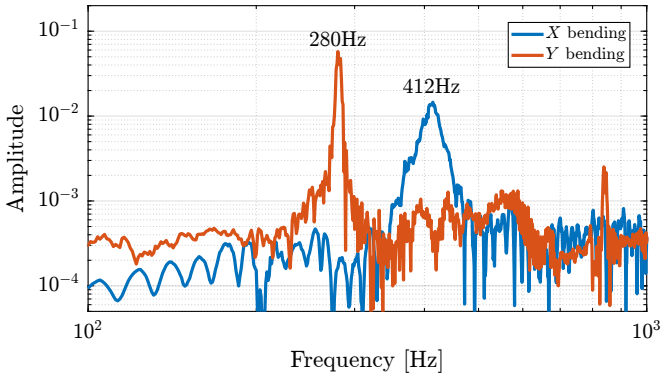

Figure 4.9: Frequency response functions for the two tests using the instrumented hammer and the laser vibrometer. The Y-bending mode is measured at 280 Hz and the X-bending mode at 412 Hz.

4.1.2 Dynamical Measurements

After the measurements on the APA were performed in Section 4.1.1, a new test bench was used to better characterize the dynamics of the APA300ML. This test bench, depicted in Figure 4.10, comprises the APA300ML fixed at one end to a stationary granite block and at the other end to a 5 kg granite block that is vertically guided by an air bearing. Thus, there is no friction when actuating the APA300ML, and it will be easier to characterize its behavior independently of other factors. An encoder[1] is used to measure the relative movement between the two granite blocks, thereby measuring the axial displacement of the APA.

Axial stiffness To estimate the stiffness of the APA, a weight with known mass $m_a = 6.4\,\text{kg}$ is added on top of the suspended granite and the deflection Δd_e is measured using the encoder. The APA stiffness can then be estimated from equation (4.1), with $g \approx 9.8\,\text{m/s}^2$ the acceleration of gravity.

$$k_{\text{apa}} = \frac{m_a g}{\Delta d_e} \tag{4.1}$$

The measured displacement d_e as a function of time is shown in Figure 4.11. It can be seen that there are some drifts in the measured displacement (probably due to piezoelectric creep), and that the displacement does not return to the initial position after the mass is removed (probably due to piezoelectric hysteresis). These two effects induce some uncertainties in the measured stiffness.

The stiffnesses are computed for all APAs from the two displacements d_1 and d_2 (see Figure 4.11) leading to two stiffness estimations k_1 and k_2. These estimated stiffnesses are summarized in Table 4.3 and are found to be close to the specified nominal stiffness of the APA300ML $k = 1.8\,\text{N}/\mu\text{m}$.

[1] Renishaw Vionic, resolution of 2.5 nm.

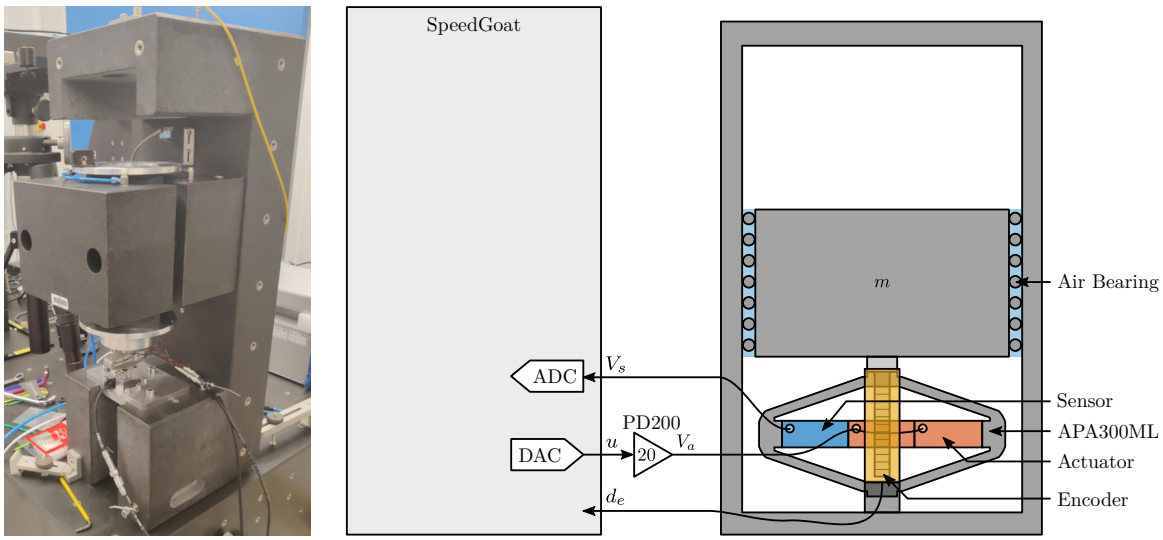

(a) Picture of the test bench

(b) Schematic of the test bench

Figure 4.10: Test bench used to measure the dynamics of the APA300ML. u is the output DAC voltage, V_a the output amplifier voltage (i.e. voltage applied across the actuator stacks), d_e the measured displacement by the encoder and V_s the measured voltage across the sensor stack.

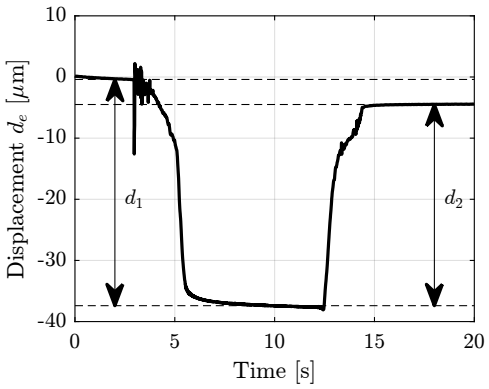

Figure 4.11: Displacement when adding and removing the payload.

APA	k_1	k_2
1	1.68	1.9
2	1.69	1.9
4	1.7	1.91
5	1.7	1.93
6	1.7	1.92
8	1.73	1.98

Table 4.3: Measured axial stiffnesses in N/µm

The stiffness can also be computed using equation (4.2) by knowing the main vertical resonance frequency $\omega_z \approx 95$ Hz (estimated from the dynamical measurements shown in Figure 4.12) and the suspended mass $m_{\text{sus}} = 5.7$ kg.

$$\omega_z = \sqrt{\frac{k}{m_{\text{sus}}}} \tag{4.2}$$

The obtained stiffness is $k \approx 2\,\text{N}/\mu\text{m}$ which is close to the values found in the documentation and using the "static deflection" method.

It is important to note that changes to the electrical impedance connected to the piezoelectric stacks affect the mechanical compliance (or stiffness) of the piezoelectric stack [101, chap. 2].

To estimate this effect for the APA300ML, its stiffness is estimated using the "static deflection" method in two cases:

- k_{os}: piezoelectric stacks left unconnected (or connect to the high impedance ADC)
- k_{sc}: piezoelectric stacks short-circuited (or connected to the voltage amplifier with small output impedance)

The open-circuit stiffness is estimated at $k_{oc} \approx 2.3\,\mathrm{N/\mu m}$ while the closed-circuit stiffness $k_{sc} \approx 1.7\,\mathrm{N/\mu m}$.

Dynamics In this section, the dynamics from the excitation voltage u to the encoder measured displacement d_e and to the force sensor voltage V_s is identified.

First, the dynamics from u to d_e for the six APA300ML are compared in Figure 4.12a. The obtained FRFs are similar to those of a (second order) mass-spring-damper system with:

- A "stiffness line" indicating a static gain equal to $\approx -17\,\mu\mathrm{m/V}$. The negative sign comes from the fact that an increase in voltage stretches the piezoelectric stack which reduces the height of the APA
- A lightly damped resonance at 95 Hz
- A "mass line" up to $\approx$ 800 Hz, above which additional resonances appear. These additional resonances might be due to the limited stiffness of the encoder support or from the limited compliance of the APA support. The flexible modes studied in section 4.1.1.4 seem not to impact the measured axial motion of the actuator.

The dynamics from u to the measured voltage across the sensor stack V_s for the six APA300ML are compared in Figure 4.12b.

A lightly damped resonance (pole) is observed at 95 Hz and a lightly damped anti-resonance (zero) at 41 Hz. No additional resonances are present up to at least 2 kHz indicating that Integral Force Feedback can be applied without stability issues from high-frequency flexible modes. The zero at 41 Hz seems to be non-minimum phase (the phase *decreases* by 180 degrees whereas it should have *increased* by 180 degrees for a minimum phase zero). This is further investigated.

As illustrated by the root locus plot, the poles of the *closed-loop* system converges to the zeros of the *open-loop* plant as the feedback gain increases. The significance of this behavior varies with the type of sensor used, as explained in [113, chap. 7.6]. Considering the transfer function from u to V_s, if a controller with a very high gain is applied such that the sensor stack voltage V_s is kept at zero, the sensor (and by extension, the actuator stacks since they are in series) experiences negligible stress and strain. Consequently, the closed-loop system virtually corresponds to one in which the piezoelectric stacks are absent, leaving only the mechanical shell. From this analysis, it can be inferred that the axial stiffness of the shell is $k_{shell} = m\omega_0^2 = 5.7 \cdot (2\pi \cdot 41)^2 = 0.38\,\mathrm{N/\mu m}$ (which is close to what is found using a FEM).

All the identified dynamics of the six APA300ML (both when looking at the encoder in Figure 4.12a and at the force sensor in Figure 4.12b) are almost identical, indicating good manufacturing repeatability for the piezoelectric stacks and the mechanical shell.

Non Minimum Phase Zero? It was surprising to observe a non-minimum phase zero on the transfer function from u to V_s (Figure 4.12b). It was initially thought that this non-minimum phase behavior was an artifact arising from the measurement. A longer measurement was performed using different excitation signals (noise, slow sine sweep, etc.) to determine if the phase behavior of the zero changes (Figure 4.13). The coherence (Figure 4.13a) is good even in the vicinity of the lightly damped zero, and the phase (Figure 4.13b) clearly indicates non-minimum phase behavior.

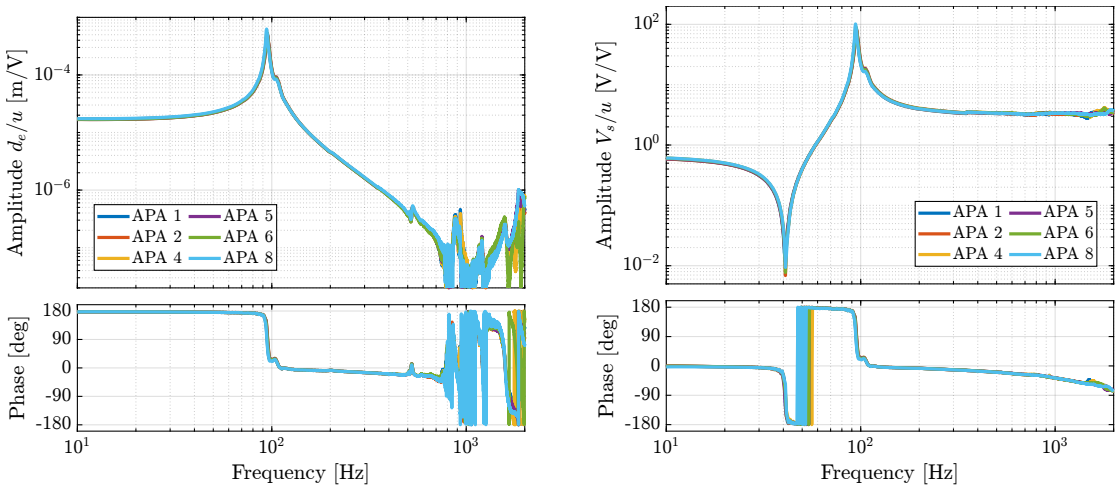

(a) FRF from u to d_e

(b) FRF from u to V_s

Figure 4.12: Measured frequency response function from generated voltage u to the encoder displacement d_e (a) and to the force sensor voltage V_s (b) for the six APA300ML.

Such non-minimum phase zero when using load cells has also been observed on other mechanical systems [59, 136, 144]. It could be due to small non-linearity in the system, but the reason for this non-minimum phase for the APA300ML is not yet clear.

However, this is not so important here because the zero is lightly damped (i.e. very close to the imaginary axis), and the closed loop poles (see the root locus plot in Figure 4.17b) should not be unstable, except for very large controller gains that will never be applied in practice.

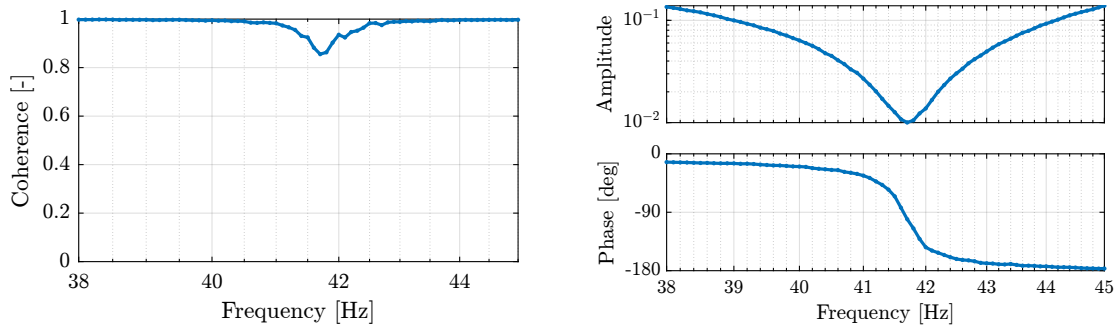

(a) Coherence

(b) Zoom on the non-minimum phase zero

Figure 4.13: Measurement of the anti-resonance found in the transfer function from u to V_s. The coherence (a) is quite good around the anti-resonance frequency. The phase (b) shows a non-minimum phase behavior.

Effect of the resistor on the IFF Plant A resistor $R \approx 80.6\,k\Omega$ is added in parallel with the sensor stack, which forms a high-pass filter with the capacitance of the piezoelectric stack (capacitance estimated at ≈ 5 µF).

As explained before, this is done to limit the voltage offset due to the input bias current of the ADC as well as to limit the low frequency gain.

The (low frequency) transfer function from u to V_s with and without this resistor were measured and compared in Figure 4.14. It is confirmed that the added resistor has the effect of adding a high-pass filter with a cut-off frequency of ≈ 0.39 Hz.

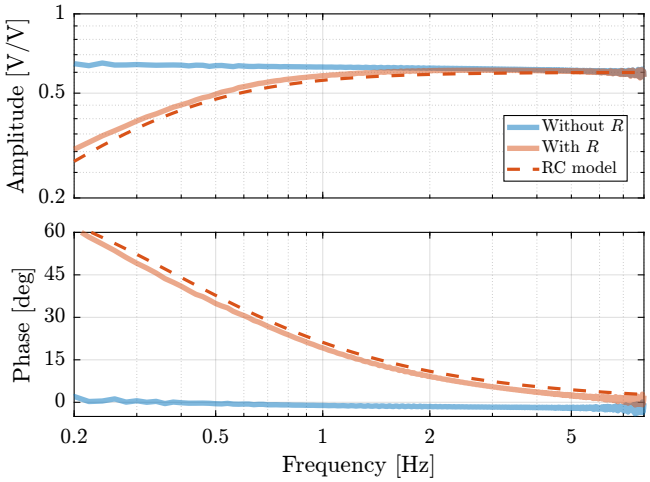

Figure 4.14: Transfer function from u to V_s with and without the resistor R in parallel with the piezoelectric stack used as the force sensor.

Integral Force Feedback To implement the Integral Force Feedback strategy, the measured FRF from u to V_s (Figure 4.12b) is fitted using the transfer function shown in equation (4.3). The parameters were manually tuned, and the obtained values are $\omega_{\text{HPF}} = 0.4$ Hz, $\omega_z = 42.7$ Hz, $\xi_z = 0.4\,\%$, $\omega_p = 95.2$ Hz, $\xi_p = 2\,\%$ and $g_0 = 0.64$.

$$G_{\text{IFF},m}(s) = g_0 \cdot \frac{1 + 2\xi_z \frac{s}{\omega_z} + \frac{s^2}{\omega_z^2}}{1 + 2\xi_p \frac{s}{\omega_p} + \frac{s^2}{\omega_p^2}} \cdot \frac{s}{\omega_{\text{HPF}} + s} \tag{4.3}$$

A comparison between the identified plant and the manually tuned transfer function is shown in Figure 4.15.

The implemented Integral Force Feedback Controller transfer function is shown in equation (4.4). It contains a high-pass filter (cut-off frequency of 2 Hz) to limit the low-frequency gain, a low-pass filter to add integral action above 20 Hz, a second low-pass filter to add robustness to high-frequency resonances, and a tunable gain g.

$$K_{\text{IFF}}(s) = -10 \cdot g \cdot \frac{s}{s + 2\pi \cdot 2} \cdot \frac{1}{s + 2\pi \cdot 20} \cdot \frac{1}{s + 2\pi \cdot 2000} \tag{4.4}$$

To estimate how the dynamics of the APA changes when the Integral Force Feedback controller is implemented, the test bench shown in Figure 4.16 is used. The transfer function from the "damped" plant input $u\prime$ to the encoder displacement d_e is identified for several IFF controller gains g.

The identified dynamics were then fitted by second order transfer functions[1]. A comparison between the identified damped dynamics and the fitted second-order transfer functions is shown in Figure 4.17a for different gains g. It is clear that a large amount of damping is added when the gain is increased and that the frequency of the pole is shifted to lower frequencies.

[1] The transfer function fitting was computed using the `vectfit3` routine, see [56].

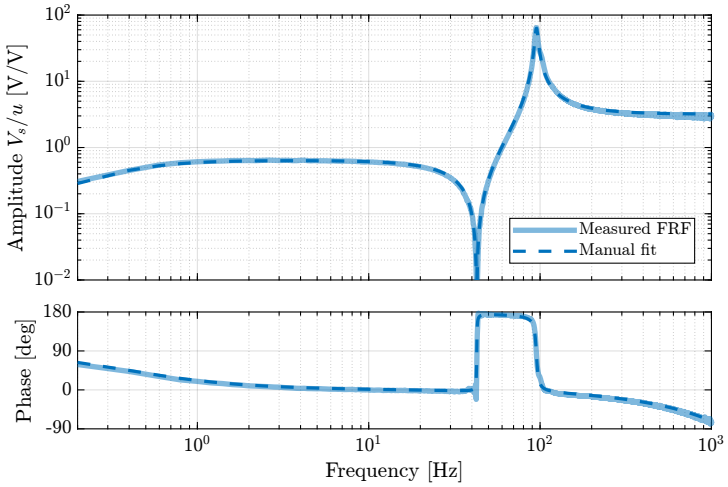

Figure 4.15: Identified IFF plant and manually tuned model of the plant (a time delay of 200 µs is added to the model of the plant to better match the identified phase). Note that a minimum-phase zero is identified here even though the coherence is not good around the frequency of the zero.

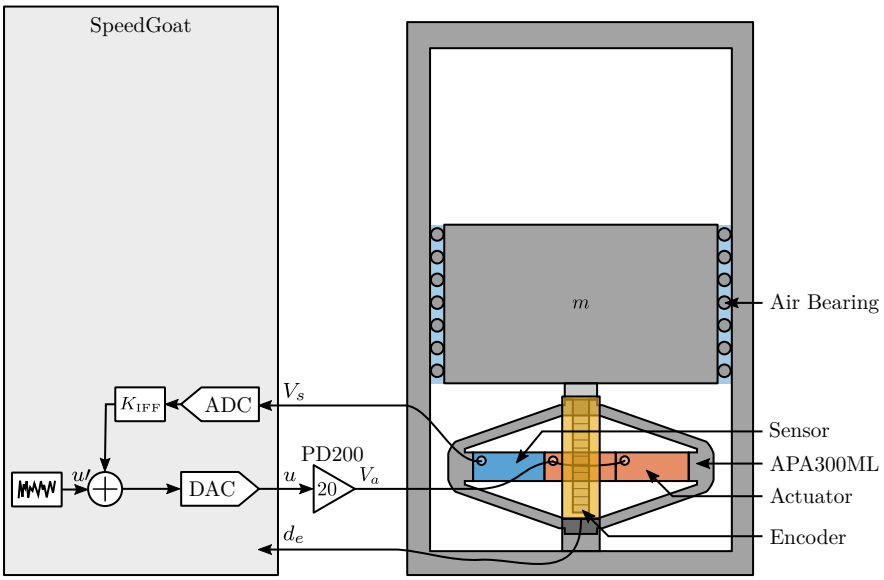

Figure 4.16: Implementation of Integral Force Feedback in the Speedgoat. The damped plant has a new input u'.

The evolution of the pole in the complex plane as a function of the controller gain g (i.e. the "root locus") is computed in two cases. First using the IFF plant model (4.3) and the implemented controller (4.4). Second using the fitted transfer functions of the damped plants experimentally identified for several controller gains. The two obtained root loci are compared in Figure 4.17b and are in good agreement considering that the damped plants were fitted using only a second-order transfer function.

4.1.3 Two-degree-of-freedom Model

In this section, a multi-body model (Figure 4.18) of the measurement bench is used to tune the two-degree-of-freedom model of the APA using the measured FRFs.

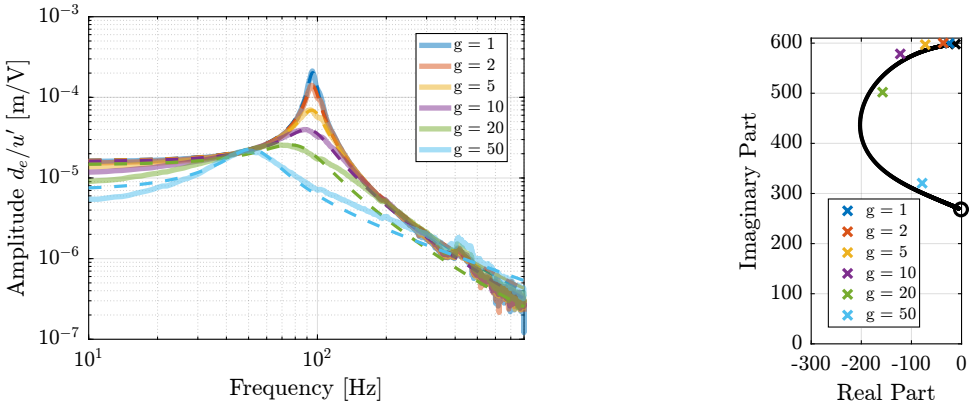

(a) Measured frequency response functions of damped plants for several IFF gains (solid lines). Identified 2nd order plants that match the experimental data (dashed lines)

(b) Root locus plot using the plant model (black) and poles of the identified damped plants (color crosses)

Figure 4.17: Experimental results of applying Integral Force Feedback to the APA300ML. Obtained damped plant (a) and root locus (b) corresponding to the implemented IFF controller (4.4).

This two-degree-of-freedom model is developed to accurately represent the APA300ML dynamics while having low complexity and a low number of associated states. After the model is presented, the procedure for tuning the model is described, and the obtained model dynamics is compared with the measurements.

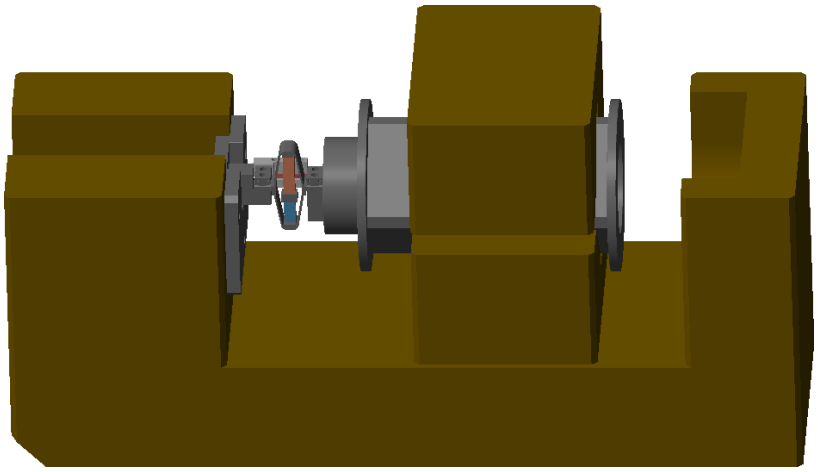

Figure 4.18: Screenshot of the multi-body model.

Two-degree-of-freedom APA Model The model of the amplified piezoelectric actuator is shown in Figure 4.19. It can be decomposed into three components:

- the shell whose axial properties are represented by k_1 and c_1
- the actuator stacks whose contribution to the axial stiffness is represented by k_a and c_a. The force source f represents the axial force induced by the force sensor stacks. The sensitivity g_a (in N/m) is used to convert the applied voltage V_a to the axial force f

- the sensor stack whose contribution to the axial stiffness is represented by k_e and c_e. A sensor measures the stack strain d_e which is then converted to a voltage V_s using a sensitivity g_s (in V/m)

Such a simple model has some limitations:

- it only represents the axial characteristics of the APA as it is modelled as infinitely rigid in the other directions
- some physical insights are lost, such as the amplification factor and the real stress and strain in the piezoelectric stacks
- the creep and hysteresis of the piezoelectric stacks are not modelled as the model is linear

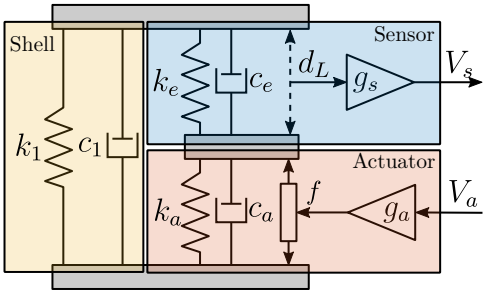

Figure 4.19: Schematic of the two-degree-of-freedom model of the APA300ML, adapted from [135].

9 parameters (m, k_1, c_1, k_e, c_e, k_a, c_a, g_s and g_a) have to be tuned such that the dynamics of the model (Figure 4.20) well represents the identified dynamics in Section 4.1.2.

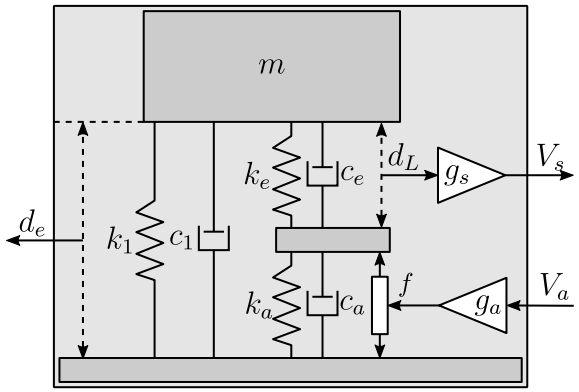

Figure 4.20: Schematic of the two-degree-of-freedom model of the APA300ML with input V_a and outputs d_e and V_s.

First, the mass m supported by the APA300ML can be estimated from the geometry and density of the different parts or by directly measuring it using a precise weighing scale. Both methods lead to an estimated mass of $m = 5.7\,\text{kg}$.

Then, the axial stiffness of the shell was estimated at $k_1 = 0.38\,\text{N}/\mu\text{m}$ in Section 4.1.2 from the frequency of the anti-resonance seen on Figure 4.12b. Similarly, c_1 can be estimated from the damping ratio of the same anti-resonance and is found to be close to 5 Ns/m.

Then, it is reasonable to assume that the sensor stacks and the two actuator stacks have identical mechanical characteristics[1]. Therefore, we have $k_e = 2k_a$ and $c_e = 2c_a$ as the actuator stack is composed of two stacks in series. In this case, the total stiffness of the APA model is described by (4.5).

[1]Note that this is not completely correct as electrical boundaries of the piezoelectric stack impacts its stiffness and that the sensor stack is almost open-circuited while the actuator stacks are almost short-circuited.

$$k_{\text{tot}} = k_1 + \frac{k_e k_a}{k_e + k_a} = k_1 + \frac{2}{3} k_a \tag{4.5}$$

Knowing from (4.6) that the total stiffness is $k_{\text{tot}} = 2\,\text{N}/\mu\text{m}$, we get from (4.5) that $k_a = 2.5\,\text{N}/\mu\text{m}$ and $k_e = 5\,\text{N}/\mu\text{m}$.

$$\omega_0 = \frac{k_{\text{tot}}}{m} \Longrightarrow k_{\text{tot}} = m\omega_0^2 = 2\,\text{N}/\mu\text{m} \quad \text{with } m = 5.7\,\text{kg and } \omega_0 = 2\pi \cdot 95\,\text{rad}/s \tag{4.6}$$

Then, c_a (and therefore $c_e = 2c_a$) can be tuned to match the damping ratio of the identified resonance. $c_a = 50\,\text{Ns/m}$ and $c_e = 100\,\text{Ns/m}$ are obtained.

In the last step, g_s and g_a can be tuned to match the gain of the identified transfer functions.

The obtained parameters of the model shown in Figure 4.20 are summarized in Table 4.4.

Table 4.4: Summary of the obtained parameters for the 2-DoF APA300ML model.

Parameter	Value
m	5.7 kg
k_1	0.38 N/µm
k_e	5.0 N/µm
k_a	2.5 N/µm
c_1	5 Ns/m
c_e	100 Ns/m
c_a	50 Ns/m
g_a	−2.58 N/V
g_s	0.46 V/µm

The dynamics of the two-degree-of-freedom model of the APA300ML are extracted using optimized parameters (listed in Table 4.4) from the multi-body model. This is compared with the experimental data in Figure 4.21. A good match can be observed between the model and the experimental data, both for the encoder (Figure 4.21a) and for the force sensor (Figure 4.21b). This indicates that this model represents well the axial dynamics of the APA300ML.

4.1.4 Reduced Order Flexible Model

In this section, a *super element* of the APA300ML is computed using a finite element software[1]. It is then imported into multi-body (in the form of a stiffness matrix and a mass matrix) and included in the same model that was used in 4.1.3. This procedure is illustrated in Figure 4.22. Several *remote points* are defined in the FEM (here illustrated by colorful planes and numbers from `1` to `5`) and are then made accessible in the multi-body software as shown at the right by the "frames" `F1` to `F5`.

For the APA300ML *super element*, 5 *remote points* are defined. Two *remote points* (`1` and `2`) are fixed to the top and bottom mechanical interfaces of the APA300ML and will be used to connect the APA300ML with other mechanical elements. Two *remote points* (`3` and `4`) are located across two piezoelectric stacks and are used to apply internal forces representing the actuator stacks. Finally, two *remote points* (`4` and `5`) are located across the third piezoelectric stack, and will be used to measure the strain of the sensor stack.

[1] Ansys® was used.

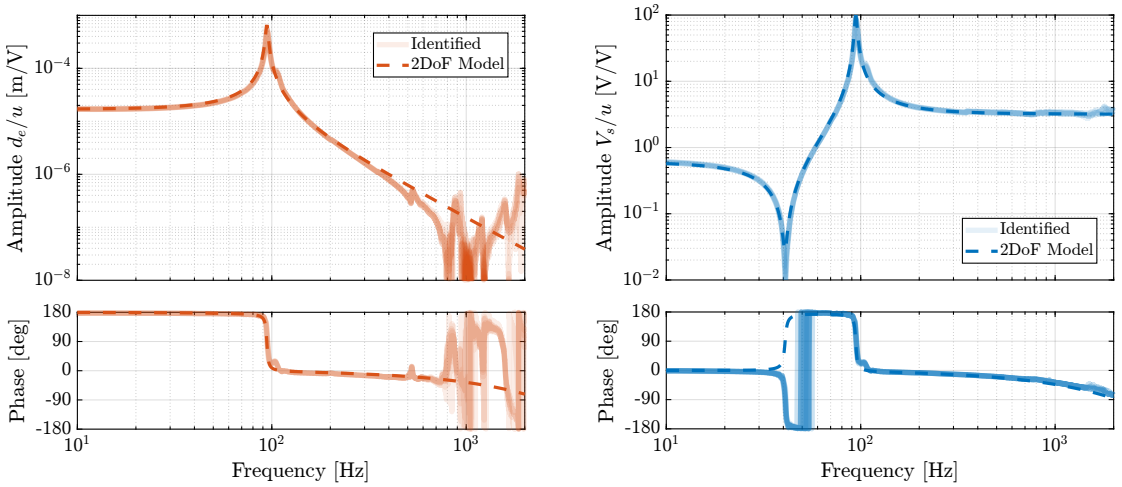

(a) from u to d_e **(b)** from u to V_s

Figure 4.21: Comparison of the measured frequency response functions and the identified dynamics from the 2-DoF model of the APA300ML. Both for the dynamics from u to d_e (a) and from u to V_s (b).

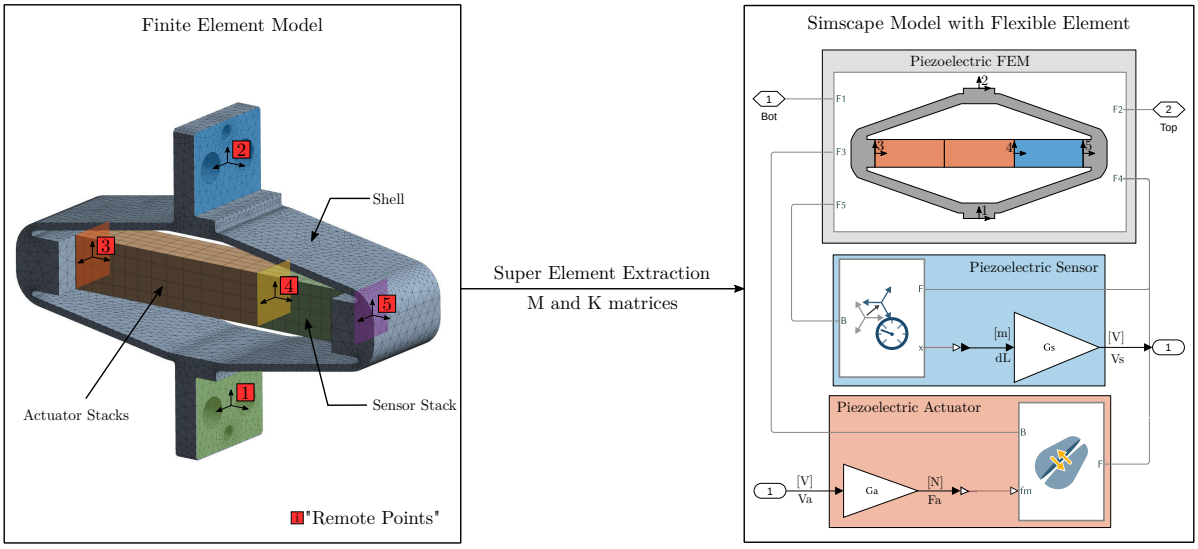

Figure 4.22: Finite Element Model of the APA300ML with "remotes points" on the left. Multi-Body model with included "Reduced Order Flexible Solid" on the right (here in Simulink-Simscape software).

Identification of the Actuator and Sensor "Constants" Once the APA300ML *super element* is included in the multi-body model, the transfer function from F_a to d_L and d_e can be extracted. The gains g_a and g_s are then tuned such that the gains of the transfer functions match the identified ones. By doing so, $g_s = 4.9\,\mathrm{V/\mu m}$ and $g_a = 23.2\,\mathrm{N/V}$ are obtained.

To ensure that the sensitivities g_a and g_s are physically valid, it is possible to estimate them from the physical properties of the piezoelectric stack material.

From [48, p. 123], the relation between relative displacement d_L of the sensor stack and generated voltage V_s is given by (4.7a) and from [49] the relation between the force F_a and the applied voltage V_a is given by (4.7b).

$$V_s = \underbrace{\frac{d_{33}}{\epsilon^T s^D n}}_{g_s} d_L \tag{4.7a}$$

$$F_a = \underbrace{d_{33} n k_a}_{g_a} \cdot V_a, \quad k_a = \frac{c^E A}{L} \tag{4.7b}$$

Unfortunately, the manufacturer of the stack was not willing to share the piezoelectric material properties of the stack used in the APA300ML. However, based on the available properties of the APA300ML stacks in the data-sheet, the soft Lead Zirconate Titanate "THP5H" from Thorlabs seemed to match quite well the observed properties. The properties of this "THP5H" material used to compute g_a and g_s are listed in Table 4.5.

From these parameters, $g_s = 5.1\,\mathrm{V/\mu m}$ and $g_a = 26\,\mathrm{N/V}$ were obtained, which are close to the constants identified using the experimentally identified transfer functions.

Table 4.5: Piezoelectric properties used for the estimation of the sensor and actuator sensitivities.

Parameter	Value	Description
d_{33}	$680 \cdot 10^{-12}$ m/V	Piezoelectric constant
ϵ^T	$4.0 \cdot 10^{-8}$ F/m	Permittivity under constant stress
s^D	$21 \cdot 10^{-12}$ m^2/N	Elastic compliance understand constant electric displacement
c^E	$48 \cdot 10^{9}$ N/m^2	Young's modulus of elasticity
L	20 mm per stack	Length of the stack
A	10^{-4} m^2	Area of the piezoelectric stack
n	160 per stack	Number of layers in the piezoelectric stack

Comparison of the Obtained Dynamics The obtained dynamics using the *super element* with the tuned "sensor sensitivity" and "actuator sensitivity" are compared with the experimentally identified FRFs in Figure 4.23. A good match between the model and the experimental results was observed. It is however surprising that the model is "softer" than the measured system, as FEMs usually overestimate the stiffness (see Section 4.1.1.4 for possible explanations).

Using this simple test bench, it can be concluded that the *super element* model of the APA300ML captures the axial dynamics of the actuator (the actuator stacks, the force sensor stack as well as the shell used as a mechanical lever).

Conclusion

In this study, the amplified piezoelectric actuators "APA300ML" have been characterized to ensure that they fulfill all the requirements determined during the detailed design phase. Geometrical features such as the flatness of its interfaces, electrical capacitance, and achievable strokes were measured in Section 4.1.1. These simple measurements allowed for the early detection of a manufacturing defect in one of the APA300ML.

Then in Section 4.1.2, using a dedicated test bench, the dynamics of all the APA300ML were measured and were found to all match very well (Figure 4.12). This consistency indicates good manufacturing tolerances, facilitating the modeling and control of the nano-hexapod. Although a non-minimum zero was identified in the transfer function from u to V_s (Figure 4.13), it was found not to be problematic because a large amount of damping could be added using the integral force feedback strategy (Figure 4.17).

Then, two different models were used to represent the APA300ML dynamics. In Section 4.1.3, a simple two-degree-of-freedom mass-spring-damper model was presented and tuned based on the measured dynamics. After following a

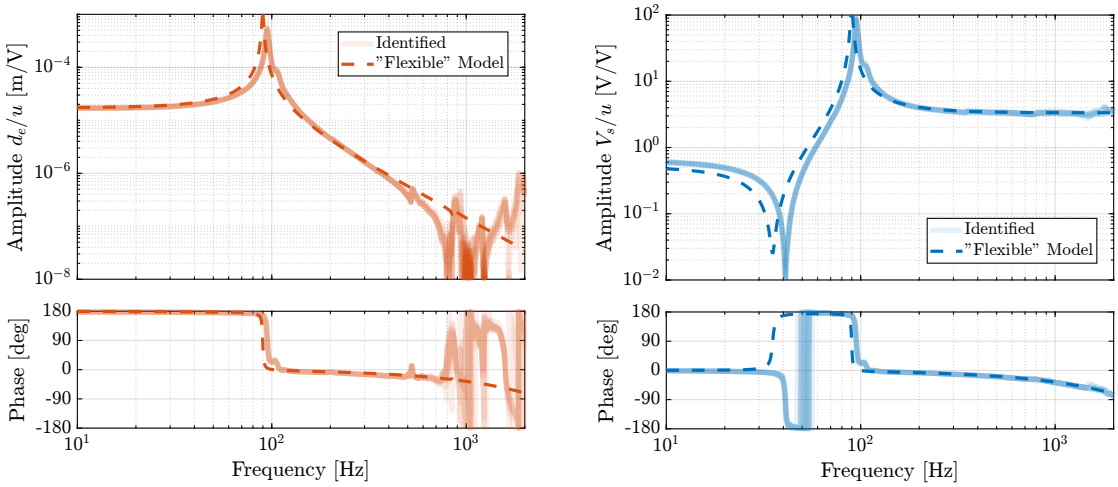

(a) from u to d_e

(b) from u to V_s

Figure 4.23: Comparison of the measured frequency response functions and the identified dynamics from the finite element model of the APA300ML. Both for the dynamics from u to d_e (a) and from u to V_s (b).

tuning procedure, the model dynamics was shown to match very well with the experiment. However, this model only represents the axial dynamics of the actuators, assuming infinite stiffness in other directions.

In Section 4.1.4, a *super element* extracted from a FEM was used to model the APA300ML. Here, the *super element* represents the dynamics of the APA300ML in all directions. However, only the axial dynamics could be compared with the experimental results, yielding a good match. The benefit of employing this model over the two-degree-of-freedom model is not immediately apparent due to its increased complexity and the larger number of model states involved. Nonetheless, the *super element* model's value will become clear in subsequent sections, when its capacity to accurately model the APA300ML's flexibility across various directions will be important.

4.2 Flexible Joints

At both ends of the nano-hexapod struts, a flexible joint is used. Ideally, these flexible joints would behave as perfect spherical joints, that is to say no bending and torsional stiffness, infinite shear and axial stiffness, unlimited bending and torsional stroke, no friction, and no backlash.

Deviations from these ideal properties will impact the dynamics of the Nano-Hexapod and could limit the attainable performance. During the detailed design phase, specifications in terms of stiffness and stroke were determined and are summarized in Table 4.6.

Table 4.6: Specifications for the flexible joints and estimated characteristics from the Finite Element Model.

	Specification	FEM
Axial Stiffness	$> 100\,\text{N}/\mu\text{m}$	94
Shear Stiffness	$> 1\,\text{N}/\mu\text{m}$	13
Bending Stiffness	$< 100\,\text{Nm}/\text{rad}$	5
Torsion Stiffness	$< 500\,\text{Nm}/\text{rad}$	260
Bending Stroke	$> 1\,\text{mrad}$	24.5

After optimization using a FEM, the geometry shown in Figure 4.24 has been obtained and the corresponding flexible joint characteristics are summarized in Table 4.6. This flexible joint is a monolithic piece of stainless steel[1] manufactured using wire electrical discharge machining. It serves several functions, as shown in Figure 4.24a, such as:

- Rigid interfacing with the nano-hexapod plates (yellow surfaces)
- Rigid interfacing with the amplified piezoelectric actuator (blue surface)
- Allow two rotations between the "yellow" and the "blue" interfaces. The rotation axes are represented by the dashed lines that intersect

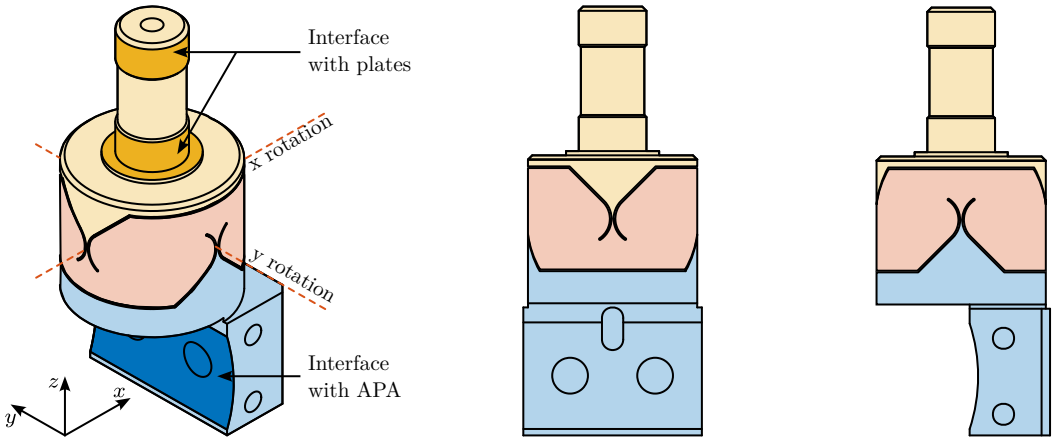

(a) Isometric view **(b)** YZ plane **(c)** XZ plane

Figure 4.24: Geometry of the optimized flexible joints.

Sixteen flexible joints have been ordered (shown in Figure 4.25a) such that some selection can be made for the twelve that will be used on the nano-hexapod.

[1] The alloy used is called *F16PH*, also refereed as "1.4542"

(a) 15 of the 16 received flexible joints

(b) Zoom on one flexible joint

Figure 4.25: Pictures of the received 16 flexible joints.

In this document, the received flexible joints are characterized to ensure that they fulfill the requirements and such that they can well be modelled.

First, the flexible joints are visually inspected, and the minimum gaps (responsible for most of the joint compliance) are measured (Section 4.2.1). Then, a test bench was developed to measure the bending stiffness of the flexible joints. The development of this test bench is presented in Section 4.2.2, including a noise budget and some requirements in terms of instrumentation. The test bench is then used to measure the bending stiffnesses of all the flexible joints. Results are shown in Section 4.2.3

4.2.1 Dimensional Measurements

4.2.1.1 Measurement Bench

Two dimensions are critical for the bending stiffness of the flexible joints. These dimensions can be measured using a profilometer. The dimensions of the flexible joint in the YZ plane will contribute to the X-bending stiffness, whereas the dimensions in the X-Z plane will contribute to the Y-bending stiffness.

The setup used to measure the dimensions of the "X" flexible beam is shown in Figure 4.26a. What is typically observed is shown in Figure 4.26b. It is then possible to estimate the dimension of the flexible beam with an accuracy of ≈ 5 µm,

4.2.1.2 Measurement Results

The specified flexible beam thickness (gap) is 250 µm. Four gaps are measured for each flexible joint (2 in the x direction and 2 in the y direction). The "beam thickness" is then estimated as the mean between the gaps measured on opposite sides.

A histogram of the measured beam thicknesses is shown in Figure 4.27. The measured thickness is less than the specified value of 250 µm, but this optical method may not be very accurate because the estimated gap can depend on the lighting of the part and of its proper alignment. However, what is more important than the true value of the thickness is the consistency between all flexible joints.

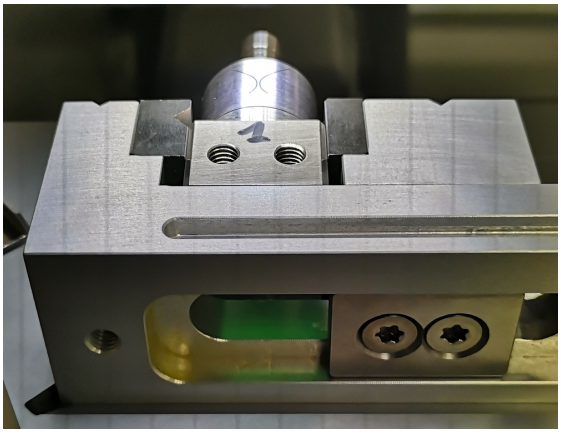

(a) Flexible joint fixed on the profilometer

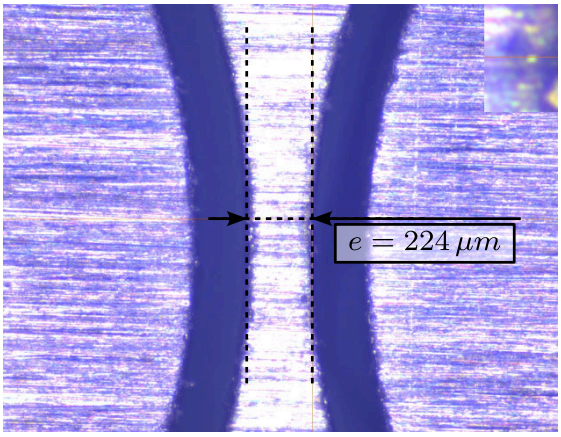

(b) Picture of the gap

Figure 4.26: Setup to measure the dimensions of the flexible "neck" corresponding to the X-bending stiffness. The flexible joint is fixed to the profilometer (a) and an image is obtained with which the "neck" size can be estimated (b).

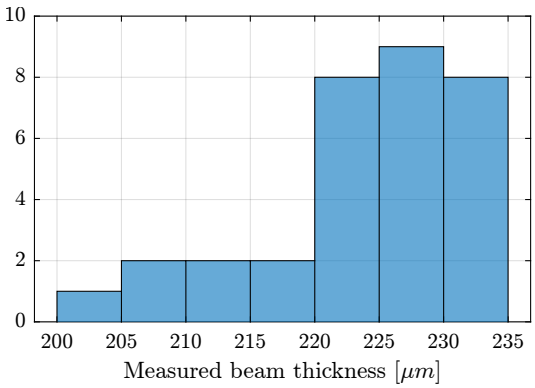

Figure 4.27: Histogram for the measured beams' thicknesses.

4.2.1.3 Defects in Flexible Joints

Using this profilometer allowed to detect flexible joints with manufacturing defects such as non-symmetrical shapes (see Figure 4.28a) or flexible joints with machining chips stuck in the gap (see Figure 4.28b).

4.2.2 Characterization Test Bench

The most important characteristic of the flexible joint to be measured is its bending stiffness $k_{R_x} \approx k_{R_y}$.

To estimate the bending stiffness, the basic idea is to apply a torque T_x to the flexible joints and to measure its angular deflection θ_x. The bending stiffness can then be computed from equation (4.8).

$$\boxed{k_{R_x} = \frac{T_x}{\theta_x}, \quad k_{R_y} = \frac{T_y}{\theta_y}} \tag{4.8}$$

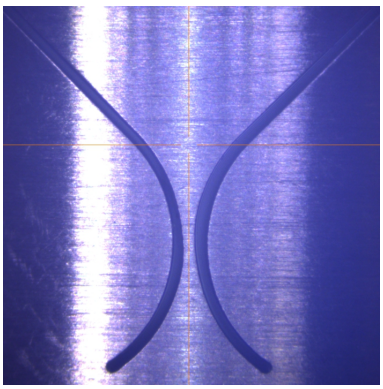

(a) Non-Symmetrical shape

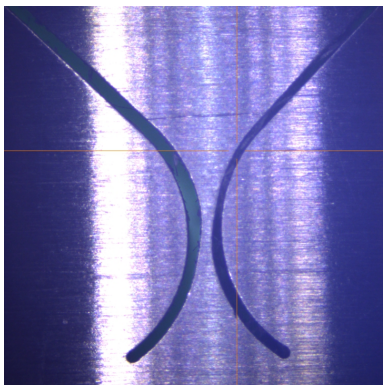

(b) "Chips" stuck in the air gap

Figure 4.28: Example of two flexible joints that were considered unsatisfactory after visual inspection.

4.2.2.1 Measurement Principle

Torque and Rotation Measurement To apply torque T_y between the two mobile parts of the flexible joint, a known "linear" force F_x can be applied instead at a certain distance h with respect to the rotation point. In this case, the equivalent applied torque can be estimated from equation (4.9). Note that the application point of the force should be sufficiently far from the rotation axis such that the resulting bending motion is much larger than the displacement due to shear. Such effects are studied in Section 4.2.2.2.

$$T_y = hF_x, \quad T_x = hF_y \tag{4.9}$$

Similarly, instead of directly measuring the bending motion θ_y of the flexible joint, its linear motion d_x at a certain distance h from the rotation points is measured. The equivalent rotation is estimated from (4.10).

$$\theta_y = \tan^{-1}\left(\frac{d_x}{h}\right) \approx \frac{d_x}{h}, \quad \theta_x = \tan^{-1}\left(\frac{d_y}{h}\right) \approx \frac{d_y}{h} \tag{4.10}$$

Then, the bending stiffness can be estimated from (4.11).

$$k_{R_x} = \frac{T_x}{\theta_x} = \frac{hF_y}{\tan^{-1}\left(\frac{d_y}{h}\right)} \approx h^2\frac{F_y}{d_y} \tag{4.11a}$$

$$k_{R_y} = \frac{T_y}{\theta_y} = \frac{hF_x}{\tan^{-1}\left(\frac{d_x}{h}\right)} \approx h^2\frac{F_x}{d_x} \tag{4.11b}$$

The working principle of the measurement bench is schematically shown in Figure 4.29. One part of the flexible joint is fixed to a rigid frame while a (known) force F_x is applied to the other side of the flexible joint. The deflection of the joint d_x is measured using a displacement sensor.

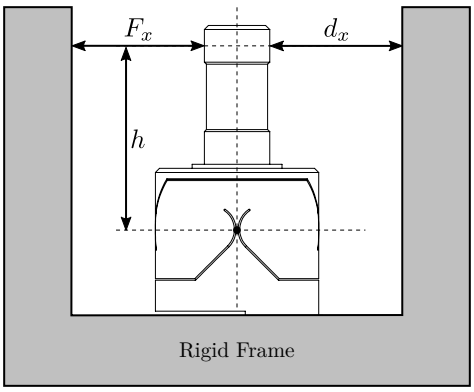

Figure 4.29: Test bench used to estimate the bending stiffness k_{R_y} of the flexible joints by measuring F_x, d_x and h.

Required External Applied Force The bending stiffness is foreseen to be $k_{R_y} \approx k_{R_x} \approx 5\,\frac{Nm}{rad}$ and its stroke $\theta_{y,\text{max}} \approx \theta_{x,\text{max}} \approx 25\,\text{mrad}$. The height between the flexible point (center of the joint) and the point where external forces are applied is $h = 22.5\,\text{mm}$ (see Figure 4.29).

The bending θ_y of the flexible joint due to the force F_x is given by equation (4.12).

$$\theta_y = \frac{T_y}{k_{R_y}} = \frac{F_x h}{k_{R_y}} \tag{4.12}$$

Therefore, the force that must be applied to test the full range of the flexible joints is given by equation (4.13). The measurement range of the force sensor should then be higher than $5.5\,\text{N}$.

$$F_{x,\text{max}} = \frac{k_{R_y}\theta_{y,\text{max}}}{h} \approx 5.5\,\text{N} \tag{4.13}$$

Required Actuator Stroke and Sensors Range The flexible joint is designed to allow a bending motion of $\pm 25\,\text{mrad}$. The corresponding stroke at the location of the force sensor is given by (4.14). To test the full range of the flexible joint, the means of applying a force (explained in the next section) should allow a motion of at least $0.5\,\text{mm}$. Similarly, the measurement range of the displacement sensor should also be higher than $0.5\,\text{mm}$.

$$d_{x,\text{max}} = h\tan(R_{x,\text{max}}) \approx 0.5\,\text{mm} \tag{4.14}$$

Force and Displacement Measurements To determine the applied force, a load cell will be used in series with the mechanism that applied the force. The measured deflection of the flexible joint will be indirectly estimated from the displacement of the force sensor itself (see Section 4.2.2.3). Indirectly measuring the deflection of the flexible joint induces some errors because of the limited stiffness between the force sensor and the displacement sensor. Such an effect will be estimated in the error budget (Section 4.2.2.2)

4.2.2.2 Error Budget

To estimate the accuracy of the measured bending stiffness that can be obtained using this measurement principle, an error budget is performed.

Based on equation (4.11), several errors can affect the accuracy of the measured bending stiffness:

- Errors in the measured torque M_x, M_y: this is mainly due to inaccuracies in the load cell and of the height estimation h
- Errors in the measured bending motion of the flexible joints θ_x, θ_y: errors from limited shear stiffness, from the deflection of the load cell itself, and inaccuracy of the height estimation h

If only the bending stiffness is considered, the induced displacement is described by (4.15).

$$d_{x,b} = h \tan(\theta_y) = h \tan\left(\frac{F_x \cdot h}{k_{R_y}}\right) \tag{4.15}$$

Effect of Shear The applied force F_x will induce some shear $d_{x,s}$ which is described by (4.16) with k_s the shear stiffness of the flexible joint.

$$d_{x,s} = \frac{F_x}{k_s} \tag{4.16}$$

The measured displacement d_x is affected shear, as shown in equation (4.17).

$$d_x = d_{x,b} + d_{x,s} = h \tan\left(\frac{F_x \cdot h}{k_{R_y}}\right) + \frac{F_x}{k_s} \approx F_x \left(\frac{h^2}{k_{R_y}} + \frac{1}{k_s}\right) \tag{4.17}$$

The estimated bending stiffness k_{est} then depends on the shear stiffness (4.18).

$$k_{R_y,\text{est}} = h^2 \frac{F_x}{d_x} \approx k_{R_y} \frac{1}{1 + \frac{k_{R_y}}{k_s h^2}} \approx k_{R_y} \left(1 - \underbrace{\frac{k_{R_y}}{k_s h^2}}_{\epsilon_s}\right) \tag{4.18}$$

With an estimated shear stiffness $k_s = 13\,\text{N}/\mu\text{m}$ from the FEM and an height $h = 25\,\text{mm}$, the estimation errors of the bending stiffness due to shear is $\epsilon_s < 0.1\,\%$

Effect of Load Cell Limited Stiffness As explained in the previous section, because the measurement of the flexible joint deflection is indirectly performed with the encoder, errors will be made if the load cell experiences some compression.

Suppose the load cell has an internal stiffness k_f, the same reasoning that was made for the effect of shear can be applied here. The estimation error of the bending stiffness due to the limited stiffness of the load cell is then described by (4.19).

$$k_{R_y,\text{est}} = h^2 \frac{F_x}{d_x} \approx k_{R_y} \frac{1}{1 + \frac{k_{R_y}}{k_F h^2}} \approx k_{R_y} \Big(1 - \underbrace{\frac{k_{R_y}}{k_F h^2}}_{\epsilon_f}\Big) \tag{4.19}$$

With an estimated load cell stiffness of $k_f \approx 1\,\text{N}/\mu\text{m}$ (from the documentation), the errors due to the load cell limited stiffness is around $\epsilon_f = 1\,\%$.

Height Estimation Error Now consider an error δh in the estimation of the height h as described by (4.20).

$$h_{\text{est}} = h + \delta h \tag{4.20}$$

The computed bending stiffness will be (4.21).

$$k_{R_y,\text{est}} \approx h_{\text{est}}^2 \frac{F_x}{d_x} \approx k_{R_y} \Big(1 + \underbrace{2\frac{\delta h}{h} + \frac{\delta h^2}{h^2}}_{\epsilon_h}\Big) \tag{4.21}$$

The height estimation is foreseen to be accurate to within $|\delta h| < 0.4\,\text{mm}$ which corresponds to a stiffness error $\epsilon_h < 3.5\,\%$.

Force and Displacement Sensors Accuracy An optical encoder is used to measure the displacement (see Section 4.2.2.3) whose maximum non-linearity is 40 nm. As the measured displacement is foreseen to be 0.5 mm, the error ϵ_d due to the encoder non-linearity is negligible $\epsilon_d < 0.01\,\%$.

The accuracy of the load cell is specified at 1 % and therefore, estimation errors of the bending stiffness due to the limited load cell accuracy should be $\epsilon_F < 1\,\%$

Conclusion The different sources of errors are summarized in Table 4.7. The most important source of error is the estimation error of the distance between the flexible joint rotation axis and its contact with the force sensor. An overall accuracy of $\approx 5\,\%$ can be expected with this measurement bench, which should be sufficient for an estimation of the bending stiffness of the flexible joints.

Table 4.7: Summary of the error budget for the estimation of the bending stiffness.

Effect	Error
Shear effect	$\epsilon_s < 0.1\,\%$
Load cell compliance	$\epsilon_f = 1\,\%$
Height error	$\epsilon_h < 3.5\,\%$
Displacement sensor	$\epsilon_d < 0.01\,\%$
Force sensor	$\epsilon_F < 1\,\%$

4.2.2.3 Mechanical Design

As explained in Section 4.2.2.1, the flexible joint's bending stiffness is estimated by applying a known force to the flexible joint's tip and by measuring its deflection at the same point.

The force is applied using a load cell[1] such that the applied force to the flexible joint's tip is directly measured. To control the height and direction of the applied force, a cylinder cut in half is fixed at the tip of the force sensor (pink element in Figure 4.30b) that initially had a flat surface. Doing so, the contact between the flexible joint cylindrical tip and the force sensor is a point (intersection of two cylinders) at a precise height, and the force is applied in a known direction. To translate the load cell at a constant height, it is fixed to a translation stage[2] which is moved by hand.

Instead of measuring the displacement directly at the tip of the flexible joint (with a probe or an interferometer for instance), the displacement of the load cell itself is measured. To do so, an encoder[3] is used, which measures the motion of a ruler. This ruler is fixed to the translation stage in line (i.e. at the same height) with the application point to reduce Abbe errors (see Figure 4.30a).

The flexible joint can be rotated by 90° in order to measure the bending stiffness in the two directions. The obtained design of the measurement bench is shown in Figure 4.30a while a zoom on the flexible joint with the associated important quantities is shown in Figure 4.30b.

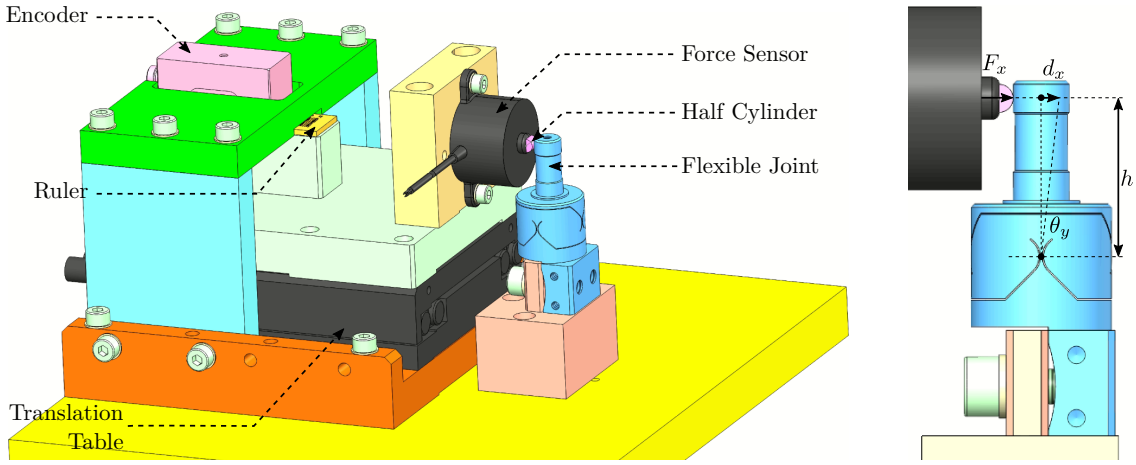

(a) Schematic of the test bench to measure the bending stiffness of the flexible joints **(b)** Zoom

Figure 4.30: 3D view of the test bench developed to measure the bending stiffness of the flexible joints. Different parts are shown in (a) while a zoom on the flexible joint is shown in (b).

4.2.3 Bending Stiffness Measurement

A picture of the bench used to measure the X-bending stiffness of the flexible joints is shown in Figure 4.31a. A closer view of the force sensor tip is shown in Figure 4.31b.

4.2.3.1 Load Cell Calibration

In order to estimate the measured errors of the load cell "FC2231", it is compared against another load cell[4]. The two load cells are measured simultaneously while they are pushed against each other (see Figure 4.32a). The contact between the two load cells is well defined as one has a spherical interface and the other has a flat surface.

[1] The load cell is FC22 from TE Connectivity. The measurement range is 50 N. The specified accuracy is 1 % of the full range.
[2] V-408 PIMag® linear stage is used. Crossed rollers are used to guide the motion.
[3] Resolute™ encoder with 1 nm resolution and ±40 nm maximum non-linearity.
[4] XFL212R-50N from TE Connectivity. The measurement range is 50 N. The specified accuracy is 1 % of the full range.

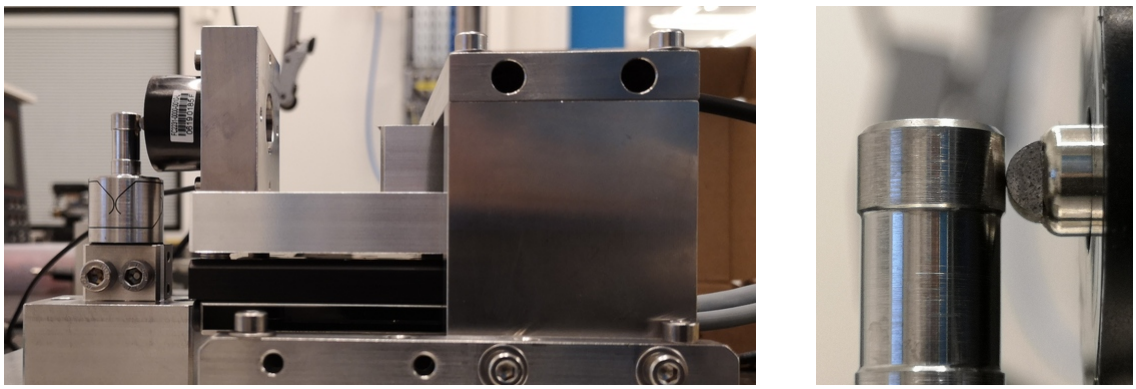

(a) Picture of the measurement bench

(b) Zoom on the tip

Figure 4.31: Manufactured test bench for compliance measurement of the flexible joints.

The measured forces are compared in Figure 4.32b. The gain mismatch between the two load cells is approximately 4 % which is higher than that specified in the data sheets. However, the estimated non-linearity is bellow 0.2 % for forces between 1 N and 5 N.

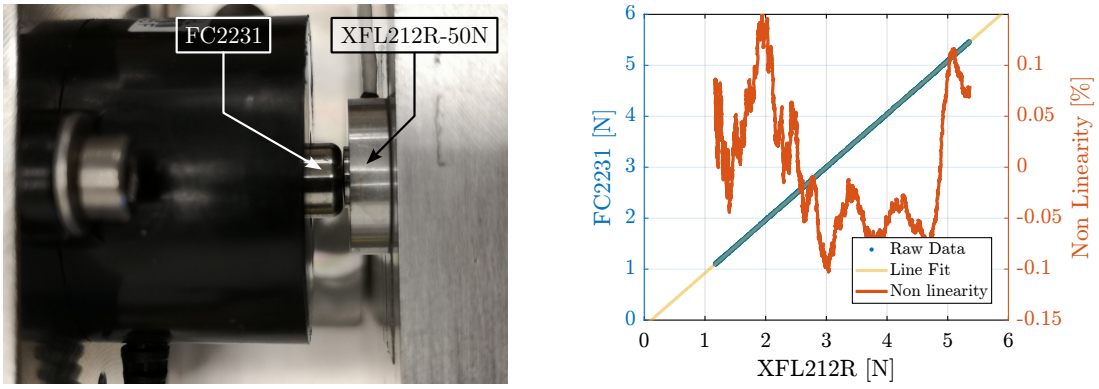

(a) Zoom on the two load cells in contact

(b) Measured two forces

Figure 4.32: Estimation of the load cell accuracy by comparing the measured force of two load cells. A picture of the measurement bench is shown in (a). Comparison of the two measured forces and estimated non-linearity are shown in (b).

4.2.3.2 Load Cell Stiffness

The objective of this measurement is to estimate the stiffness k_F of the force sensor. To do so, a stiff element (much stiffer than the estimated $k_F \approx 1\,\mathrm{N}/\mu\mathrm{m}$) is mounted in front of the force sensor, as shown in Figure 4.33a. Then, the force sensor is pushed against this stiff element while the force sensor and the encoder displacement are measured. The measured displacement as a function of the measured force is shown in Figure 4.33b. The load cell stiffness can then be estimated by computing a linear fit and is found to be $k_F \approx 0.68\,\mathrm{N}/\mu\mathrm{m}$.

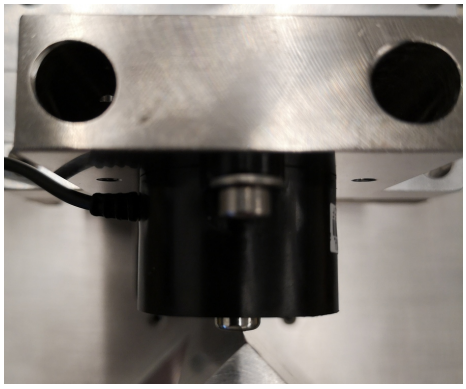

(a) Picture of the measurement bench

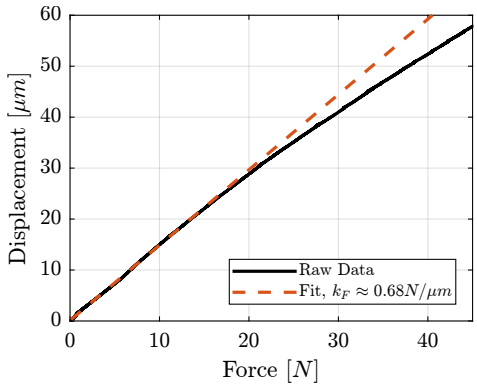

(b) Measured displacement as a function of the force

Figure 4.33: Estimation of the load cell stiffness. Measurement setup is shown in (a), and results are shown in (b).

4.2.3.3 Bending Stiffness Estimation

The actual stiffness is now estimated by manually moving the translation stage from a start position where the force sensor is not yet in contact with the flexible joint to a position where the flexible joint is on its mechanical stop.

The measured force and displacement as a function of time are shown in Figure 4.34a. Three regions can be observed: first, the force sensor tip is not in contact with the flexible joint and the measured force is zero; then, the flexible joint deforms linearly; and finally, the flexible joint comes in contact with the mechanical stop.

The angular motion θ_y computed from the displacement d_x is displayed as function of the measured torque T_y in Figure 4.34b. The bending stiffness of the flexible joint can be estimated by computing the slope of the curve in the linear regime (red dashed line) and is found to be $k_{R_y} = 4.4\,\text{Nm/rad}$. The bending stroke can also be estimated as shown in Figure 4.34b and is found to be $\theta_{y,\text{max}} = 20.9\,\text{mrad}$.

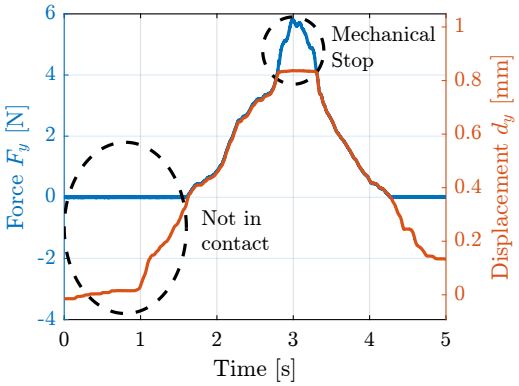

(a) Force and displacement measured as a function of time

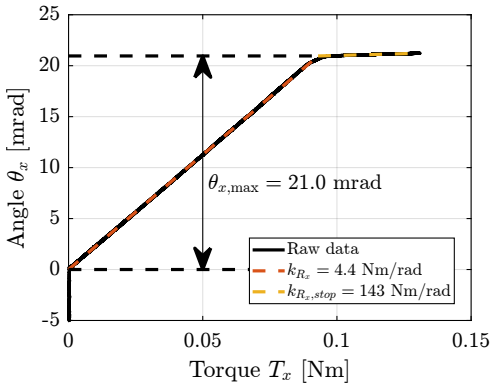

(b) Angular displacement measured as a function of the applied torque

Figure 4.34: Results obtained on the first flexible joint. The measured force and displacement are shown in (a). The estimated angular displacement θ_x as a function of the estimated applied torque T_x is shown in (b). The bending stiffness k_{R_x} of the flexible joint can be estimated by computing a best linear fit (red dashed line).

4.2.3.4 Measured Flexible Joints' Stiffnesses

The same measurement was performed for all the 16 flexible joints, both in the x and y directions. The measured angular motion as a function of the applied torque is shown in Figure 4.35a for the 16 flexible joints. This gives a first idea of the dispersion of the measured bending stiffnesses (i.e. slope of the linear region) and of the angular stroke.

A histogram of the measured bending stiffnesses is shown in Figure 4.35b. Most of the bending stiffnesses are between 4.6 Nm/rad and 5.0 Nm/rad.

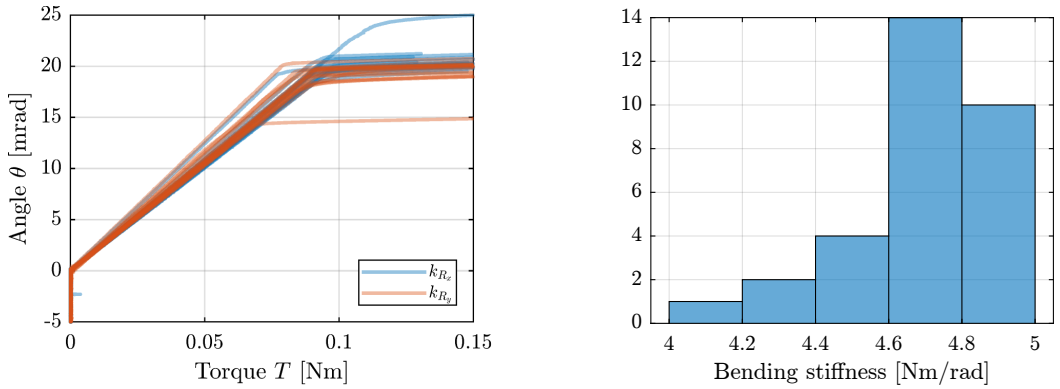

(a) Measured torque and angular motion for the flexible joints

(b) Histogram of the measured bending stiffness in the x and y directions

Figure 4.35: Measured k_{R_x} and k_{R_y} stiffnesses for the 16 flexible joints. Raw data are shown in (a). A histogram of the measured stiffnesses is shown in (b).

Conclusion

The flexible joints are a key element of the nano-hexapod. Careful dimensional measurements (Section 4.2.1) allowed for the early identification of faulty flexible joints. This was crucial in preventing potential complications that could have arisen from the installation of faulty joints on the nano-hexapod.

A dedicated test bench was developed to asses the bending stiffness of the flexible joints. Through meticulous error analysis and budgeting, a satisfactory level of measurement accuracy could be guaranteed. The measured bending stiffness values exhibited good agreement with the predictions from the FEM ($k_{R_x} = k_{R_y} = 5\,\text{Nm/rad}$). These measurements are helpful for refining the model of the flexible joints, thereby enhancing the overall accuracy of the nano-hexapod model. Furthermore, the data obtained from these measurements have provided the necessary information to select the most suitable flexible joints for the nano-hexapod, ensuring optimal performance.

4.3 Struts

The Nano-Hexapod struts (shown in Figure 4.36) are composed of two flexible joints that are fixed at the two ends of the strut, one Amplified Piezoelectric Actuator[1] and one optical encoder[2].

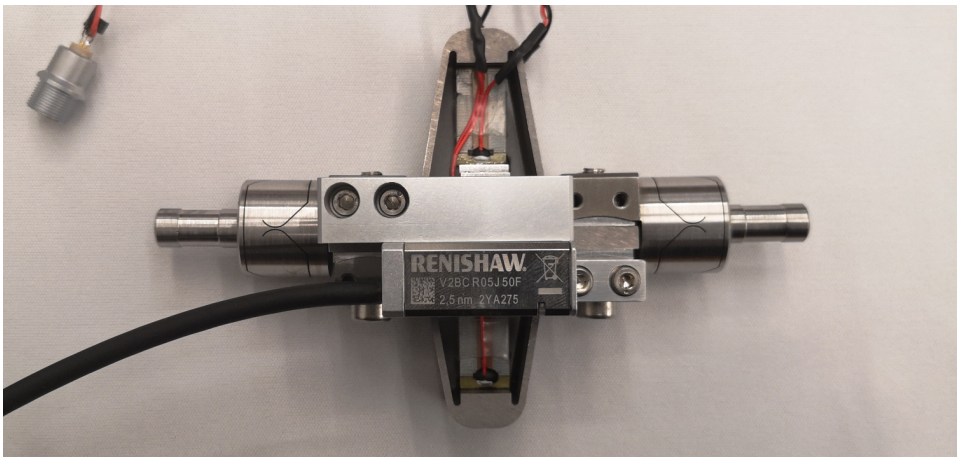

Figure 4.36: One strut including two flexible joints, an amplified piezoelectric actuator and an encoder.

After the strut elements have been individually characterized (see previous sections), the struts are assembled. The mounting procedure of the struts is explained in Section 4.3.1. A mounting bench was used to ensure coaxiality between the two ends of the struts. In this way, no angular stroke is lost when mounted to the nano-hexapod.

The flexible modes of the struts were then experimentally measured and compared with a FEM (Section 4.3.2).

Dynamic measurements of the strut are performed with the same test bench used to characterize the APA300ML dynamics (Section 4.3.3). It was found that the dynamics from the DAC voltage to the displacement measured by the encoder is complex due to the flexible modes of the struts (Section 4.3.2).

The strut models were then compared with the measured dynamics (Section 4.3.4). The model dynamics from the DAC voltage to the axial motion of the strut (measured by an interferometer) and to the force sensor voltage well match the experimental results. However, this is not the case for the dynamics from DAC voltage to the encoder displacement. It is found that the complex dynamics is due to a misalignment between the flexible joints and the APA.

4.3.1 Assembly Procedure

A mounting bench was developed to ensure:

- Good coaxial alignment between the interfaces (cylinders) of the flexible joints. This is important not to loose to much angular stroke during their mounting into the nano-hexapod
- Uniform length across all struts
- Precise alignment of the APA with the two flexible joints

[1] APA300ML from Cedrat Technologies.
[2] Vionic from Renishaw.

- Reproducible and consistent assembly between all struts

The mounting bench is shown in Figure 4.37a. It consists of a "main frame" (Figure 4.38a) precisely machined to ensure both correct strut length and strut coaxiality. The coaxiality is ensured by good flatness (specified at 20 µm) between surfaces A and B and between surfaces C and D. Such flatness was checked using a FARO arm[1] (see Figure 4.38b) and was found to comply with the requirements. The strut length (defined by the distance between the rotation points of the two flexible joints) was ensured by using precisely machined dowel holes.

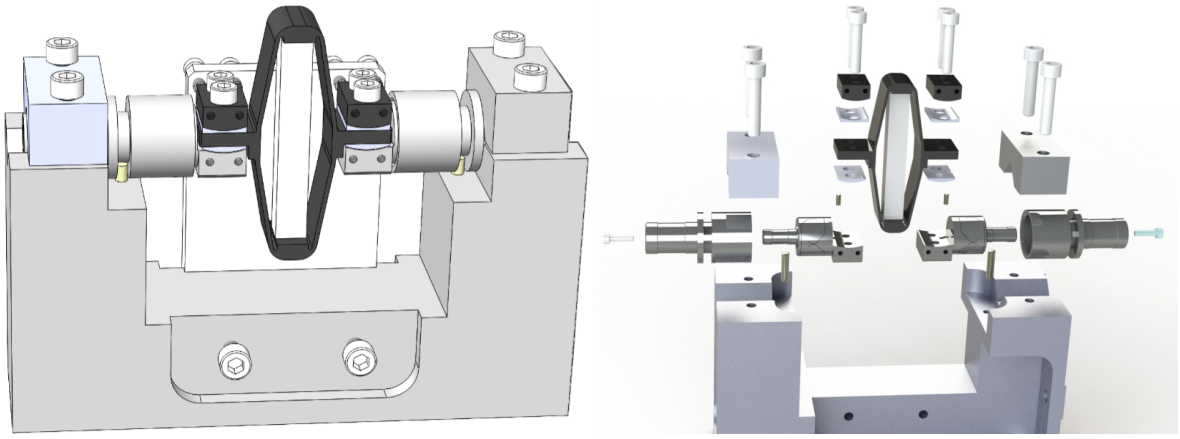

(a) 3D view of the mounting bench **(b)** Exploded view

Figure 4.37: Strut mounting bench.

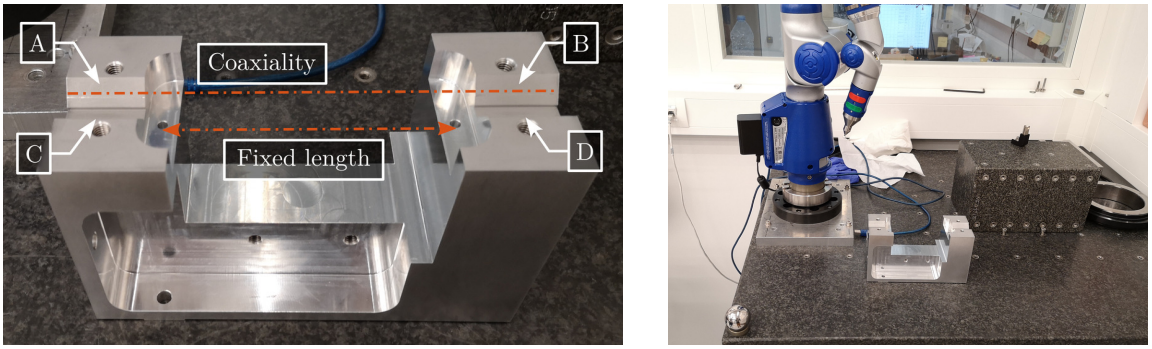

(a) Useful features of the main mounting element **(b)** Dimensional check

Figure 4.38: Part that ensures good coaxiality of the two flexible joints and correct struts length.

The flexible joints were not directly fixed to the mounting bench but were fixed to a cylindrical "sleeve" shown in Figures 4.39a and 4.39b. The goal of these "sleeves" is to avoid mechanical stress that could damage the flexible joints during the mounting process. These "sleeves" have one dowel groove (that are fitted to the dowel holes shown in Figure 4.38a) that will determine the length of the mounted strut.

The "sleeves" were mounted to the main element as shown in Figure 4.38a. The left sleeve has a thigh fit such that its orientation is fixed (it is roughly aligned horizontally), while the right sleeve has a loose fit such that it can rotate (it will get the same orientation as the fixed one when tightening the screws).

[1] FARO Arm Platinum 4ft, specified accuracy of $\pm 13\mu m$.

(a) Cylindrical Interface (Top) **(b)** Cylindrical Interface (Bottom) **(c)** Mounted flexible joints

Figure 4.39: Preparation of the flexible joints by fixing them in their cylindrical "sleeves".

The cylindrical washers and the APA300ML are stacked on top of the flexible joints, as shown in Figure 4.40b and screwed together using a torque screwdriver. A dowel pin is used to laterally align the APA300ML with the flexible joints (see the dowel slot on the flexible joints in Figure 4.39c). Two cylindrical washers are used to allow proper mounting even when the two APA interfaces are not parallel.

The encoder and ruler are then fixed to the strut and properly aligned, as shown in Figure 4.40c.

Finally, the strut can be disassembled from the mounting bench (Figure 4.40d). Thanks to this mounting procedure, the coaxiality and length between the two flexible joint's interfaces can be obtained within the desired tolerances.

4.3.2 Measurement of Flexible Modes

A Finite Element Model[1] of the struts is developed and is used to estimate the flexible modes. The inertia of the encoder (estimated at 15 g) is considered. The two cylindrical interfaces were fixed (boundary conditions), and the first three flexible modes were computed. The mode shapes are displayed in Figure 4.41: an "X-bending" mode at 189 Hz, a "Y-bending" mode at 285 Hz and a "Z-torsion" mode at 400 Hz.

To experimentally measure these mode shapes, a Laser vibrometer[2] was used. It measures the difference of motion between two beam path (red points in Figure 4.42). The strut is then excited by an instrumented hammer, and the transfer function from the hammer to the measured rotation is computed.

The setup used to measure the "X-bending" mode is shown in Figure 4.42a. The "Y-bending" mode is measured as shown in Figure 4.42b and the "Z-torsion" measurement setup is shown in Figure 4.42c. These tests were performed with and without the encoder being fixed to the strut.

The obtained FRFs for the three configurations (X-bending, Y-bending and Z-torsion) are shown in Figure 4.43a when the encoder is not fixed to the strut and in Figure 4.43b when the encoder is fixed to the strut.

Table 4.8 summarizes the measured resonance frequencies and the computed ones using the Finite Element Model (FEM). The resonance frequencies of the 3 modes are only slightly decreased when the encoder is fixed to the strut. In addition, the computed resonance frequencies from the FEM are very close to the measured frequencies when the encoder is fixed to the strut. This validates the quality of the FEM.

[1] Using Ansys®. Flexible Joints and APA Shell are made of a stainless steel allow called *17-4 PH*. Encoder and ruler support material is aluminium.
[2] OFV-3001 controller and OFV512 sensor head from Polytec.

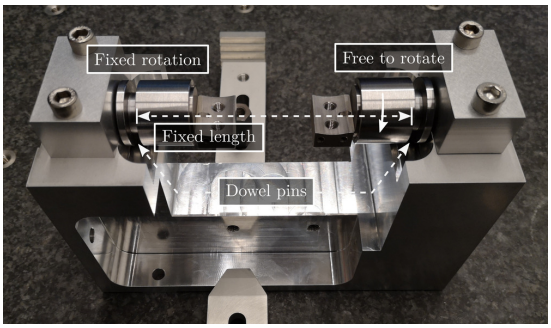

(a) Fix the flexible joints

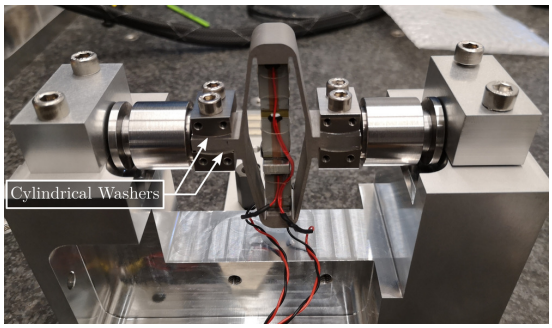

(b) Mount the APA with the cylindrical washers

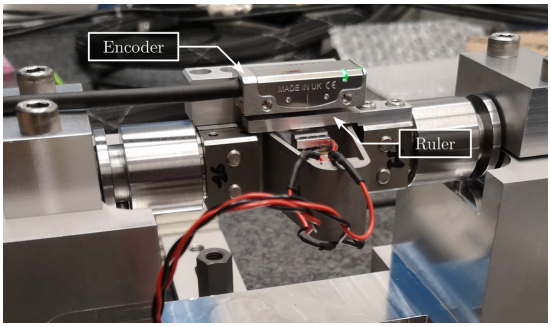

(c) Mount and align the encoder

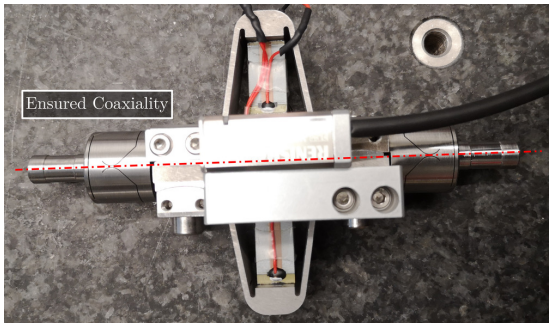

(d) Obtained mounted strut

Figure 4.40: Steps for mounting the struts.

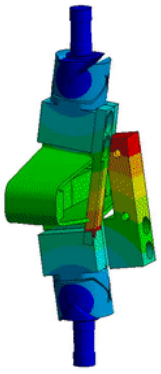

(a) X-bending mode (189 Hz)

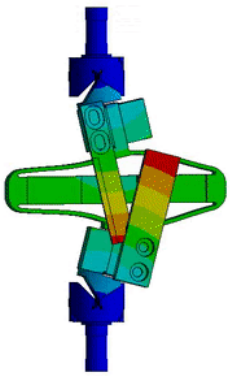

(b) Y-bending mode (285 Hz)

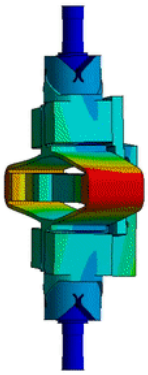

(c) Z-torsion mode (400 Hz)

Figure 4.41: Flexible modes of the struts estimated from a Finite Element Model.

Table 4.8: Estimated and measured frequencies of the flexible modes of the struts.

Mode	FEM with Encoder	Exp. with Encoder	Exp. without Encoder
X-Bending	189 Hz	198 Hz	226 Hz
Y-Bending	285 Hz	293 Hz	337 Hz
Z-Torsion	400 Hz	381 Hz	398 Hz

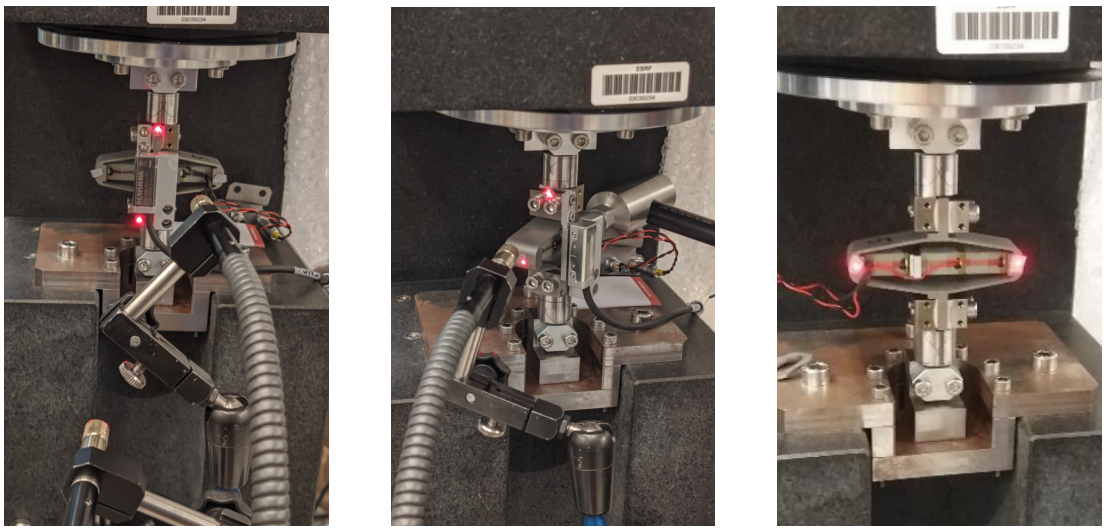

(a) X-bending mode **(b)** Y-bending mode **(c)** Z-torsion mode

Figure 4.42: Measurement of the flexible modes of the struts using a laser vibrometer.

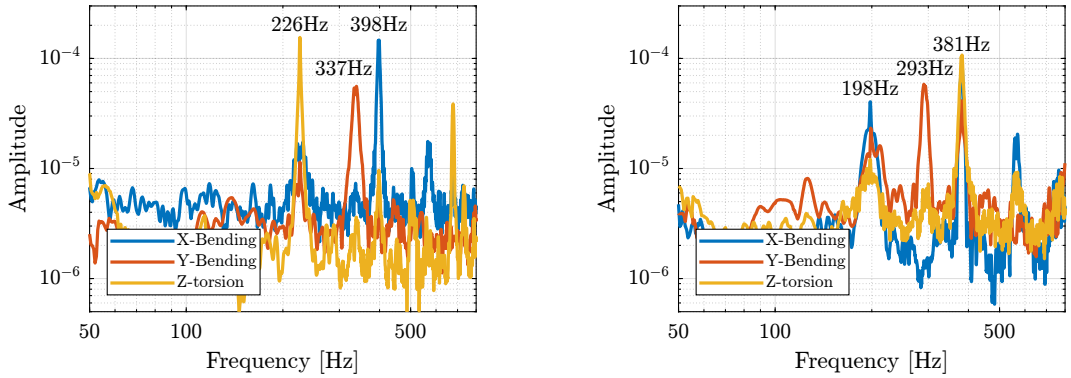

(a) without encoder **(b)** with the encoder

Figure 4.43: Measured frequency response functions without the encoder (a) and with the encoder (b).

4.3.3 Dynamical Measurements

In order to measure the dynamics of the strut, the test bench used to measure the APA300ML dynamics is being used again.

The strut mounted on the bench is shown in Figure 4.44a A schematic of the bench and the associated signals are shown in Figure 4.44b. A fiber interferometer[1] is used to measure the motion of the granite (i.e. the axial motion of the strut).

First, the effect of the encoder on the measured dynamics is investigated in Section 4.3.3.1. The dynamics observed by the encoder and interferometers are compared in Section 4.3.3.2. Finally, all measured struts are compared in terms of dynamics in Section 4.3.3.3.

[1] Two fiber intereferometers were used: an IDS3010 from Attocube and a quDIS from QuTools.

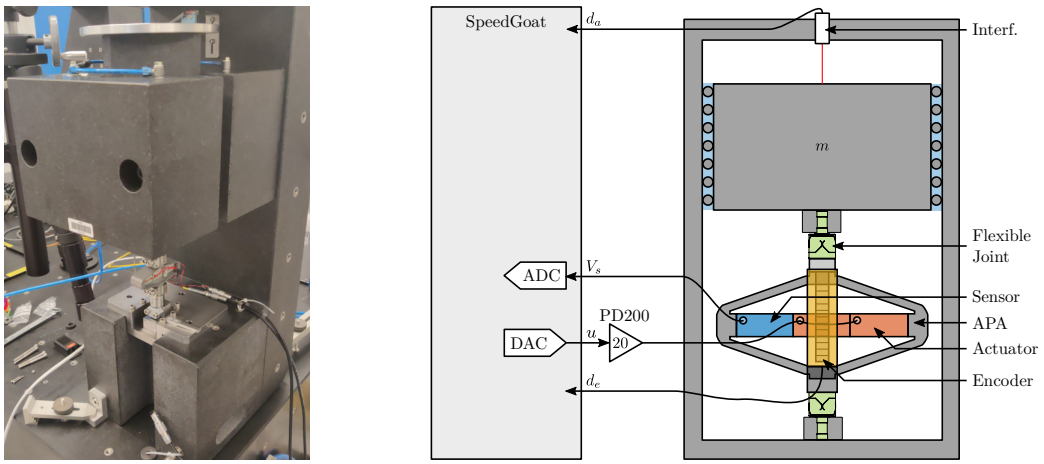

(a) Overview Picture

(b) Schematic

Figure 4.44: Experimental setup used to measure the dynamics of the struts.

4.3.3.1 Effect of the Encoder on the Measured Dynamics

System identification was performed without the encoder being fixed to the strut (Figure 4.45b) and with one encoder being fixed to the strut (Figure 4.45a).

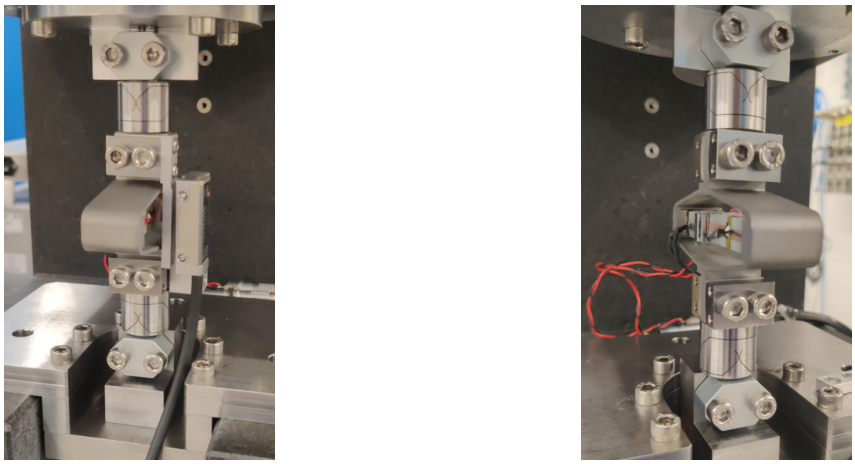

(a) Strut with encoder

(b) Strut without encoder

Figure 4.45: Strut fixed to the test bench with clamped flexible joints. The encoder can be fixed to the struts (a) or removed (b).

The obtained FRFs are compared in Figure 4.46. It was found that the encoder had very little effect on the transfer function from excitation voltage u to the axial motion of the strut d_a as measured by the interferometer (Figure 4.46a). This means that the axial motion of the strut is unaffected by the presence of the encoder. Similarly, it has little effect on the transfer function from u to the sensor stack voltage V_s (Figure 4.46b). This means that the encoder should have little effect on the effectiveness of the integral force feedback control strategy.

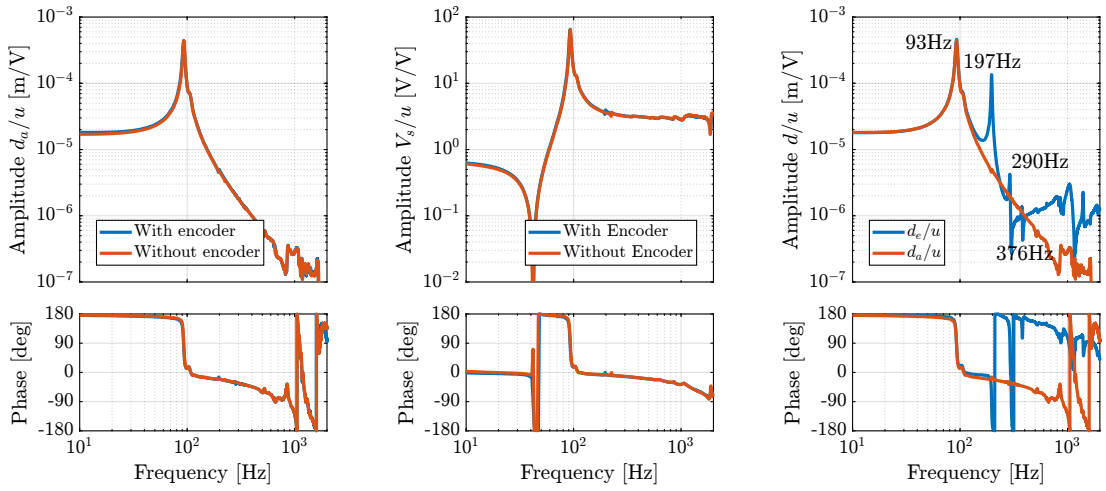

(a) u to d_a **(b)** u to V_s **(c)** u to d_e, d_a

Figure 4.46: Effect of having the encoder fixed to the struts on the measured dynamics from u to d_a (a) and from u to V_s (b). Comparison of the observed dynamics by the encoder and interferometers (c).

4.3.3.2 Comparison of the Encoder and Interferometer

The dynamics measured by the encoder (i.e. d_e/u) and interferometers (i.e. d_a/u) are compared in Figure 4.46c. The dynamics from the excitation voltage u to the displacement measured by the encoder d_e presents a behavior that is much more complex than the dynamics of the displacement measured by the interferometer (comparison made in Figure 4.46c). Three additional resonance frequencies can be observed at 197 Hz, 290 Hz and 376 Hz. These resonance frequencies match the frequencies of the flexible modes studied in Section 4.3.2.

The good news is that these resonances are not impacting the axial motion of the strut (which is what is important for the hexapod positioning). However, these resonances make the use of an encoder fixed to the strut difficult from a control perspective.

4.3.3.3 Comparison of all the Struts

The dynamics of all the mounted struts (only 5 at the time of the experiment) were then measured on the same test bench. The obtained dynamics from u to d_a are compared in Figure 4.47a while is dynamics from u to V_s are compared in Figure 4.47b. A very good match can be observed between the struts.

The same comparison is made for the transfer function from u to d_e (encoder output) in Figure 4.47c. In this study, large dynamics differences were observed between the 5 struts. Although the same resonance frequencies were seen for all of the struts (95 Hz, 200 Hz, 300 Hz and 400 Hz), the amplitude of the peaks were not the same. In addition, the location or even presence of complex conjugate zeros changes from one strut to another. The reason for this variability will be studied in the next section thanks to the strut model.

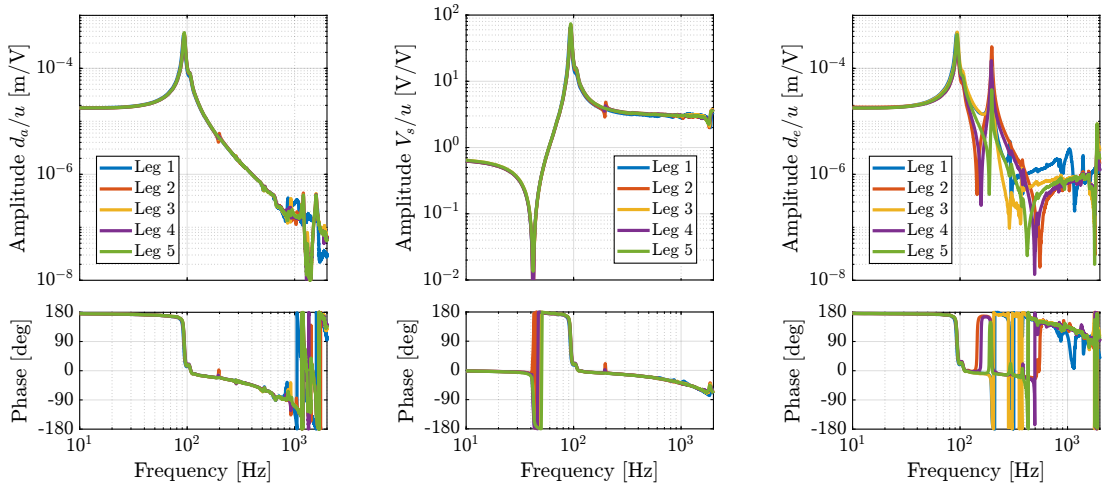

(a) u to d_a (interferometer) **(b)** u to V_s (force sensor) **(c)** u to d_e (encoder)

Figure 4.47: Comparison of the measured dynamics for five of the struts..

4.3.4 Strut Model

The multi-body model of the strut was included in the multi-body model of the test bench (see Figure 4.48). The obtained model was first used to compare the measured FRF with the existing model (Section 4.3.4.1).

Using a flexible APA model (extracted from a FEM), the effect of a misalignment of the APA with respect to flexible joints is studied (Section 4.3.4.2). It was found that misalignment has a large impact on the dynamics from u to d_e. This misalignment is estimated and measured in Section 4.3.4.3. The struts were then disassembled and reassemble a second time to optimize alignment (Section 4.3.4.4).

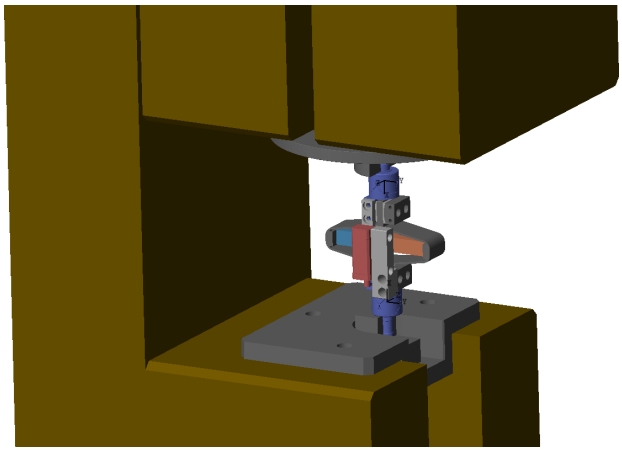

Figure 4.48: Multi-body model of the strut fixed to the bench.

4.3.4.1 Model Dynamics

Two models of the APA300ML are used here: a simple two-degree-of-freedom model and a model using a super-element extracted from a Finite Element Model. These two models of the APA300ML were tuned to best match the measured

FRFs of the APA alone. The flexible joints were modelled with the 4-DoF model (axial stiffness, two bending stiffnesses and one torsion stiffness). These two models are compared using the measured FRFs in Figure 4.49.

The model dynamics from DAC voltage u to the axial motion of the strut d_a (Figure 4.49a) and from DAC voltage u to the force sensor voltage V_s (Figure 4.49c) are well matching the experimental identification.

However, the transfer function from u to encoder displacement d_e are not well matching for both models. For the 2-DoF model, this is normal because the resonances affecting the dynamics are not modelled at all (the APA300ML is modelled as infinitely rigid in all directions except the translation along it's actuation axis). For the flexible model, it will be shown in the next section that by adding some misalignment between the flexible joints and the APA300ML, this model can better represent the observed dynamics.

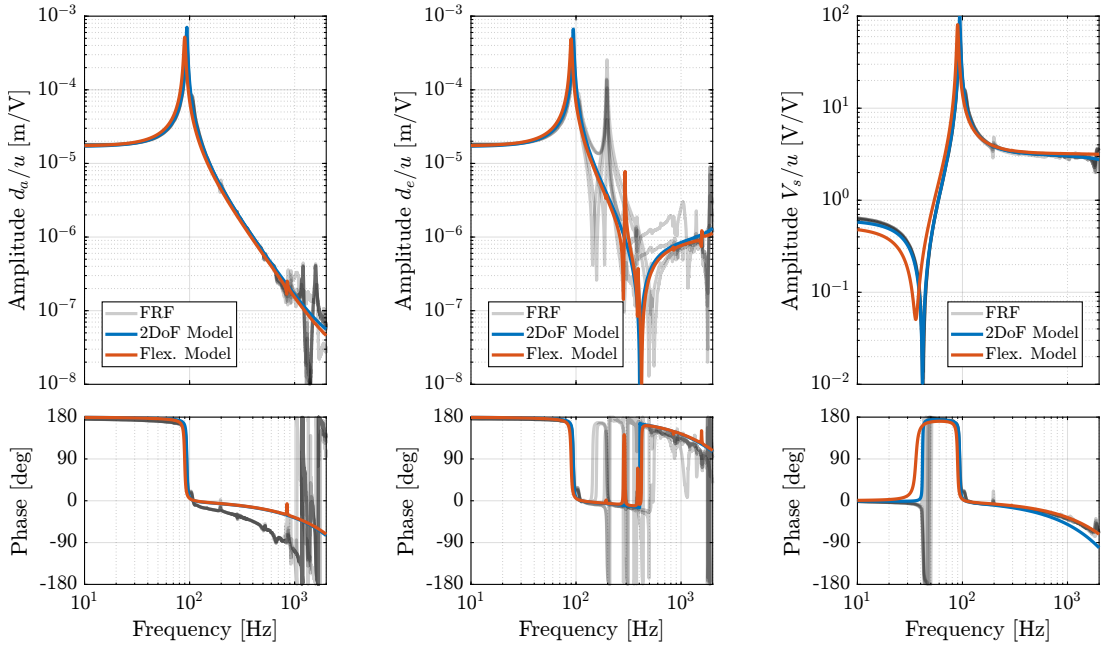

(a) u to d_a (interferometer) **(b)** u to d_e (encoder) **(c)** u to V_s (force sensor)

Figure 4.49: Comparison of the measured dynamics of the struts (black) with dynamics extracted from the multi-body model using the 2-DoF APA model (blue), and using the reduced order flexible model of the APA300ML model (red).

4.3.4.2 Effect of Strut Misalignment

As shown in Figure 4.47c, the identified dynamics from DAC voltage u to encoder measured displacement d_e are very different from one strut to the other. In this section, it is investigated whether poor alignment of the strut (flexible joints with respect to the APA) can explain such dynamics. For instance, consider Figure 4.50 where there is a misalignment in the y direction between the two flexible joints (well aligned thanks to the mounting procedure in Section 4.3.1) and the APA300ML. In this case, the "x-bending" mode at 200 Hz (see Figure 4.42a) can be expected to have greater impact on the dynamics from the actuator to the encoder.

To verify this assumption, the dynamics from the output DAC voltage u to the measured displacement by the encoder d_e is computed using the flexible APA model for several misalignments in the y direction. The obtained dynamics are shown in Figure 4.51a. The alignment of the APA with the flexible joints has a large influence on the dynamics from actuator voltage to the measured displacement by the encoder. The misalignment in the y direction mostly influences:

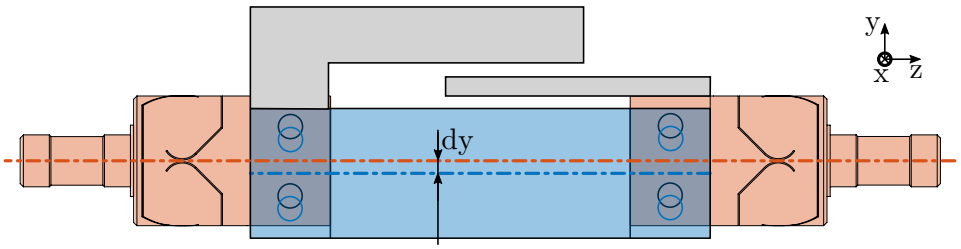

Figure 4.50: Misalignment between the joints and the APA.

- the presence of the flexible mode at 200 Hz (see mode shape in Figure 4.41a)
- the location of the complex conjugate zero between the first two resonances:
  - if $d_y < 0$: there is no zero between the two resonances and possibly not even between the second and third resonances
  - if $d_y > 0$: there is a complex conjugate zero between the first two resonances
- the location of the high-frequency complex conjugate zeros at 500 Hz (secondary effect, as the axial stiffness of the joint also has large effect on the position of this zero)

The same can be done for misalignments in the x direction. The obtained dynamics (Figure 4.51b) are showing that misalignment in the x direction mostly influences the presence of the flexible mode at 300 Hz (see mode shape in Figure 4.41b).

A comparison of the experimental FRFs in Figure 4.47c with the model dynamics for several y misalignments in Figure 4.51a indicates a clear similarity. This similarity suggests that the identified differences in dynamics are caused by misalignment.

4.3.4.3 Measured Strut Misalignment

During the initial mounting of the struts, as presented in Section 4.3.1, the positioning pins that were used to position the APA with respect to the flexible joints in the y directions were not used (not received at the time). Therefore, large y misalignments are expected.

To estimate the misalignments between the two flexible joints and the APA:

- the struts were fixed horizontally on the mounting bench, as shown in Figure 4.40c but without the encoder
- using a length gauge[1], the height difference between the flexible joints surface and the APA shell surface was measured for both the top and bottom joints and for both sides
- as the thickness of the flexible joint is 21 mm and the thickness of the APA shell is 20 mm, 0.5 mm of height difference should be measured if the two are perfectly aligned

Large variations in the y misalignment are found from one strut to the other (results are summarized in Table 4.9).

[1] Heidenhain MT25, specified accuracy of ± 0.5 µm.

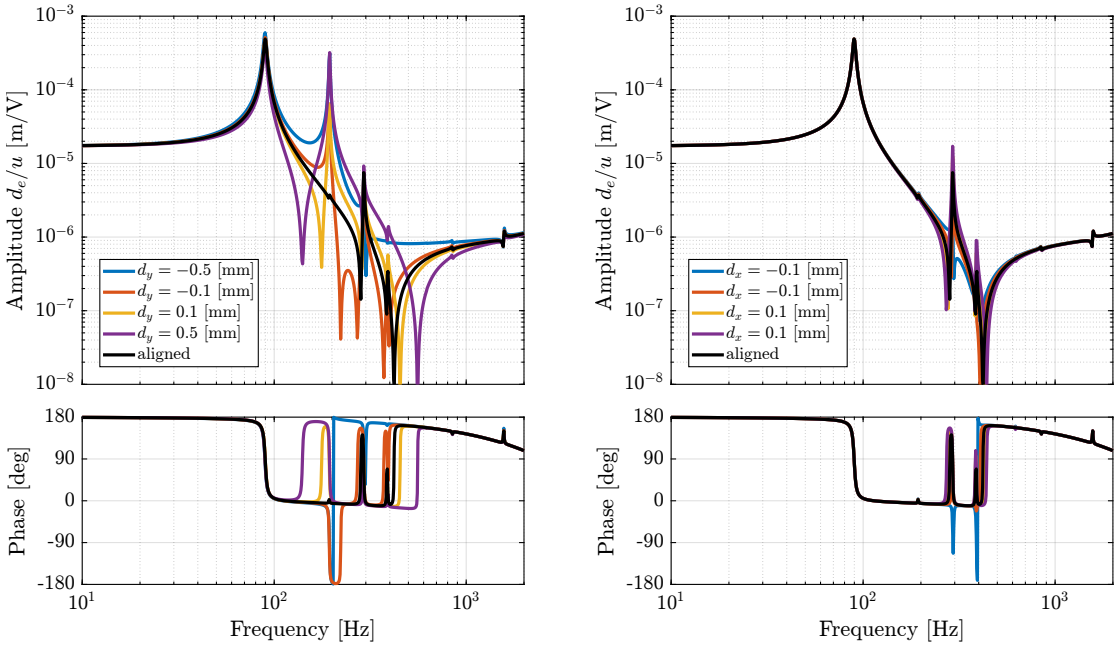

(a) Misalignment along y

(b) Misalignment along x

Figure 4.51: Effect of a misalignment between the flexible joints and the APA300ML in the y (a) and in the x direction (b).

To check the validity of the measurement, it can be verified that the sum of the measured thickness difference on each side is 1 mm (equal to the thickness difference between the flexible joint and the APA). Thickness differences for all the struts were found to be between 0.94 mm and 1.00 mm which indicate low errors compared to the misalignments found in Table 4.9.

Table 4.9: Measured y misalignment for each strut. Measurements are in mm.

Strut	Bot	Top
1	0.1	0.33
2	-0.19	0.14
3	0.41	0.32
4	-0.01	0.54
5	0.15	0.02

By using the measured y misalignment in the model with the flexible APA model, the model dynamics from u to d_e is closer to the measured dynamics, as shown in Figure 4.52. A better match in the dynamics can be obtained by fine-tuning both the x and y misalignments (yellow curves in Figure 4.52).

This confirms that misalignment between the APA and the strut axis (determined by the two flexible joints) is critical and inducing large variations in the dynamics from DAC voltage u to encoder measured displacement d_e. If encoders are fixed to the struts, the APA and flexible joints must be precisely aligned when mounting the struts.

In the next section, the struts are re-assembled with a "positioning pin" to better align the APA with the flexible joints. With a better alignment, the amplitude of the spurious resonances is expected to decrease, as shown in Figure 4.51a.

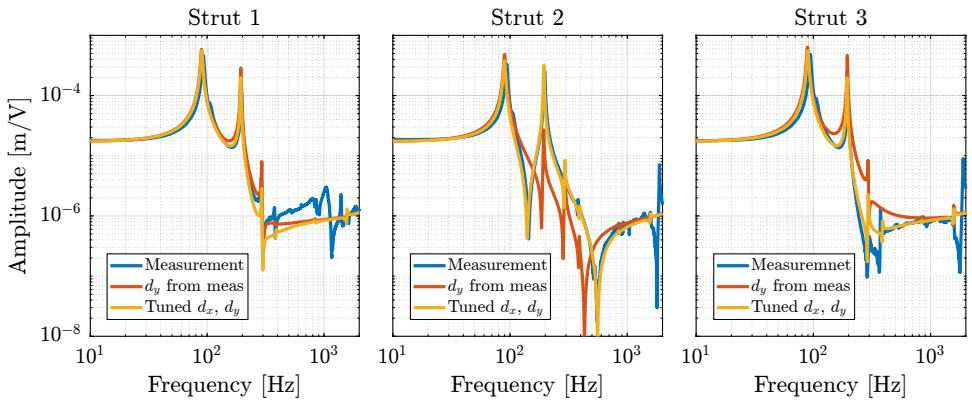

Figure 4.52: Comparison of the frequency response functions from DAC voltage u to measure displacement d_e by the encoders for three struts. The measured dynamics is shown in blue, the dynamics extracted from the model with the y misalignment estimated from measurements is shown in red, and the dynamics extracted from the model when both the x and y misalignments are tuned is shown in yellow.

4.3.4.4 Better Struts Alignment

After receiving the positioning pins, the struts were mounted again with the positioning pins. This should improve the alignment of the APA with the two flexible joints.

The alignment is then estimated using a length gauge, as described in the previous sections. Measured y alignments are summarized in Table 4.10 and are found to be bellow 55µm for all the struts, which is much better than before (see Table 4.9).

Table 4.10: Measured y misalignment after realigning the struts using dowel pins. Measurements are in mm.

Strut	Bot	Top
1	-0.02	0.01
2	0.055	0.0
3	0.01	-0.02
4	0.03	-0.03
5	0.0	0.0
6	-0.005	0.055

The dynamics of the re-aligned struts were then measured on the same test bench (Figure 4.44). A comparison of the initial strut dynamics and the dynamics of the re-aligned struts (i.e. with the positioning pin) is presented in Figure 4.53. Even though the struts are now much better aligned, not much improvement can be observed. The dynamics of the six aligned struts were also quite different from one another.

The fact that the encoders are fixed to the struts makes the control more challenging. Therefore, fixing the encoders to the nano-hexapod plates instead may be an interesting option.

Conclusion

The Hano-Hexapod struts are a key component of the developed Nano Active Stabilization System (NASS). A mounting bench was used to obtain struts with good interface coaxiality, equal lengths, and ideally the same dynamics. Using a test bench, it was found that while all the mounted struts had extremely similar dynamics when considering the axial

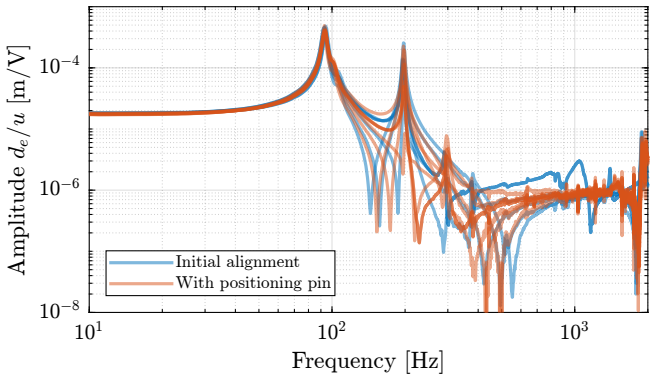

Figure 4.53: Comparison of the dynamics from u to d_e before and after proper alignment using the dowel pins.

motion and the integrated force sensor, the dynamics as seen by the encoder is much more complex and varied from one strut to the other.

Thanks to a FEM and experimental measurements, the modes inducing this complex dynamics was identified. The variability in the dynamics was attributed to the poor alignment of the APA with respect to the flexible joints. Even with better alignment using dowel pins, the observed dynamics by the encoder remained problematic. Therefore, the encoders will be fixed directly to the nano-hexapod plates rather than being fixed to the struts.

4.4 Nano-Hexapod

Prior to the nano-hexapod assembly, all the struts were mounted and individually characterized. In Section 4.4.1, the assembly procedure of the nano-hexapod is presented.

To identify the dynamics of the nano-hexapod, a special suspended table was developed, which consisted of a stiff "optical breadboard" suspended on top of four soft springs. The Nano-Hexapod was then mounted on top of the suspended table such that its dynamics is not affected by complex dynamics except from the suspension modes of the table that can be well characterized and modelled (Section 4.4.2).

The obtained nano-hexapod dynamics is analyzed in Section 4.4.3, and compared with the multi-body model in Section 4.4.4.

4.4.1 Assembly Procedure

The assembly of the nano-hexapod is critical for both avoiding additional stress in the flexible joints (that would result in a loss of stroke) and for precisely determining the Jacobian matrix. The goal was to fix the six struts to the two nano-hexapod plates (shown in Figure 4.54a) while the two plates were parallel and aligned vertically so that all the flexible joints did not experience any stress. To do so, a precisely machined mounting tool (Figure 4.54b) is used to position the two nano-hexapod plates during the assembly procedure.

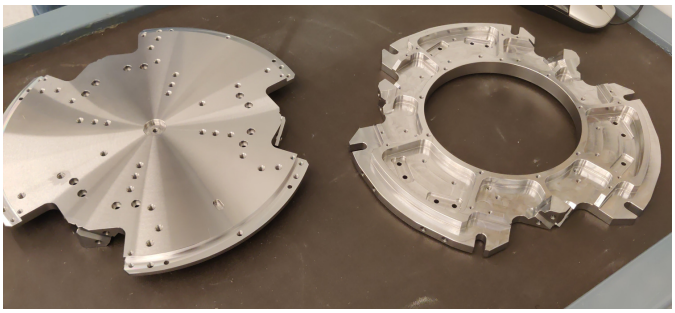

(a) Top and bottom plates

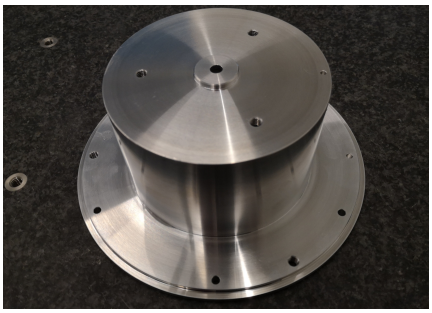

(b) Mounting tool

Figure 4.54: Nano-Hexapod plates (a) and mounting tool used to position the two plates during assembly (b).

The mechanical tolerances of the received plates were checked using a FARO arm[1] (Figure 4.55a) and were found to comply with the requirements[2]. The same was done for the mounting tool[3]. The two plates were then fixed to the mounting tool, as shown in Figure 4.55b. The main goal of this "mounting tool" is to position the flexible joint interfaces (the "V" shapes) of both plates so that a cylinder can rest on the 4 flat interfaces at the same time.

The quality of the positioning can be estimated by measuring the "straightness" of the top and bottom "V" interfaces. This corresponds to the diameter of the smallest cylinder which contains all points along the measured axis. This was again done using the FARO arm, and the results for all six struts are summarized in Table 4.11. The straightness was found to be better than 15 µm for all struts[4], which is sufficiently good to not induce significant stress of the flexible joint during assembly.

[1] FARO Arm Platinum 4ft, specified accuracy of $\pm 13\mu m$.

[2] Location of all the interface surfaces with the flexible joints were checked. The fittings (182H7 and 24H8) with the interface element were also checked.

[3] The height dimension is better than 40 µm. The diameter fitting of 182g6 and 24g6 with the two plates is verified.

[4] As the accuracy of the FARO arm is ± 13 µm, the true straightness is probably better than the values indicated. The limitation of the instrument is here reached.

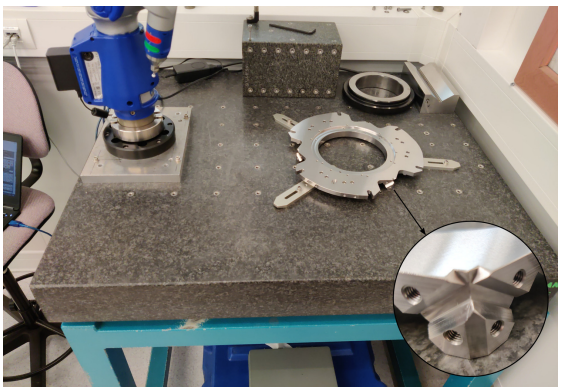

(a) Dimensional check of the bottom plate

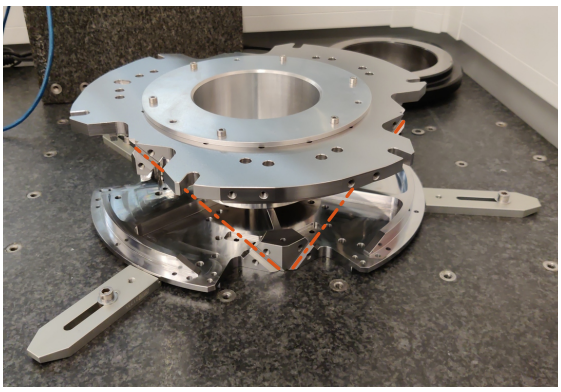

(b) Wanted coaxiality between strut interfaces

Figure 4.55: A FARO arm is used to dimensionally check the plates (a) and to verify coaxiality of the strut interfaces (b).

Table 4.11: Measured straightness between the V grooves for the six struts. Measurements were performed twice for each strut.

Strut	Meas 1	Meas 2
1	7 µm	3 µm
2	11 µm	11 µm
3	15 µm	14 µm
4	6 µm	6 µm
5	7 µm	5 µm
6	6 µm	7 µm

The encoder rulers and heads were then fixed to the top and bottom plates, respectively (Figure 4.56), and the encoder heads were aligned to maximize the received contrast.

(a) Encoder rulers

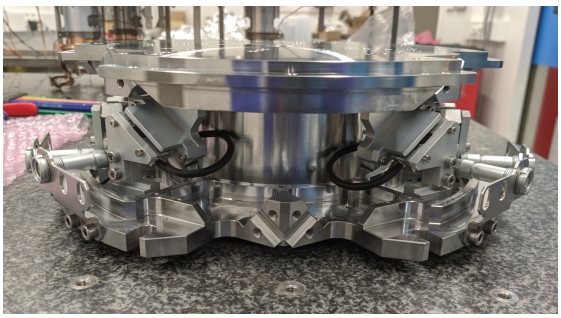

(b) Encoder heads

Figure 4.56: Mounting of the encoders to the Nano-hexapod. The rulers are fixed to the top plate (a) while encoders heads are fixed to the bottom plate (b).

The six struts were then fixed to the bottom and top plates one by one. First, the top flexible joint is fixed so that its flat reference surface is in contact with the top plate. This step precisely determines the position of the flexible joint with respect to the top plate. The bottom flexible joint is then fixed. After mounting all six struts, the mounting tool (Figure 4.54b) can be disassembled, and the nano-hexapod as shown in Figure 4.57 is fully assembled.

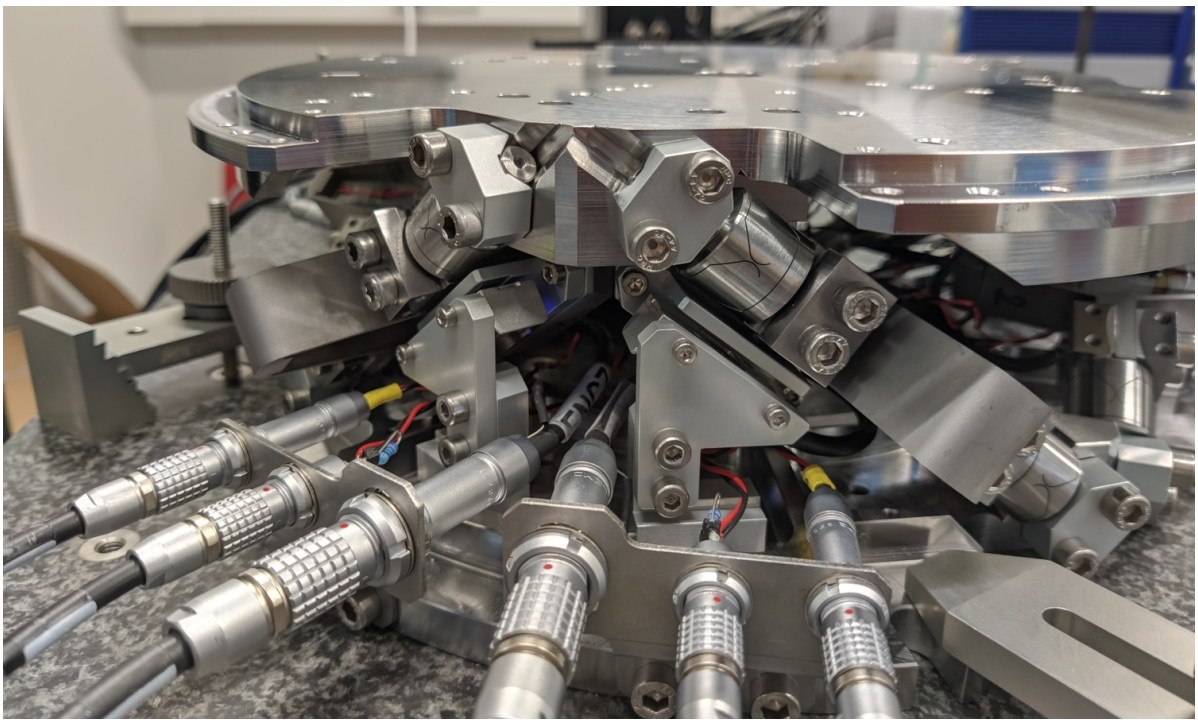

Figure 4.57: Mounted Nano-Hexapod.

4.4.2 Suspended Table

4.4.2.1 Introduction

When a dynamical system is fixed to a support (such as a granite or an optical table), its dynamics will couple to the support dynamics. This may results in additional modes appearing in the system dynamics, which are difficult to predict and model. To prevent this issue, the strategy adopted here is to mount the nano-hexapod on top a suspended table with low frequency suspension modes.

In this case, the modes of the suspended table were chosen to be at much lower frequency than those of the nano-hexapod such that good decoupling is obtained. Another key advantage is that the suspension modes of the table can be easily represented using a multi-body model. Therefore, the measured dynamics of the nano-hexapod on top of the suspended table can be compared to a multi-body model representing the same experimental conditions. The model of the Nano-Hexapod can thus be precisely tuned to match the measured dynamics.

The developed suspended table is described in Section 4.4.2.2. The modal analysis of the table is done in 4.4.2.3. Finally, the multi-body model representing the suspended table was tuned to match the measured modes (Section 4.4.2.4).

4.4.2.2 Experimental Setup

The design of the suspended table is quite straightforward. First, an optical table with high frequency flexible mode was selected[1]. Then, four springs[2] were selected with low spring rate such that the suspension modes are below 10 Hz. Finally, some interface elements were designed, and mechanical lateral mechanical stops were added (Figure 4.58).

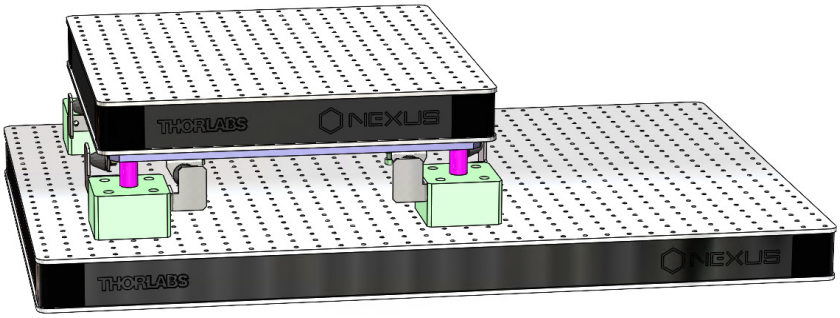

Figure 4.58: 3D View of the vibration table. The purple cylinders are representing the soft springs.

4.4.2.3 Modal Analysis of the Suspended Table

In order to perform a modal analysis of the suspended table, a total of 15 3-axis accelerometers[3] were fixed to the breadboard. Using an instrumented hammer, the first 9 modes could be identified and are summarized in Table 4.12. The first 6 modes are suspension modes (i.e. rigid body mode of the breadboard) and are located below 10 Hz. The next modes are the flexible modes of the breadboard as shown in Figure 4.60, and are located above 700 Hz.

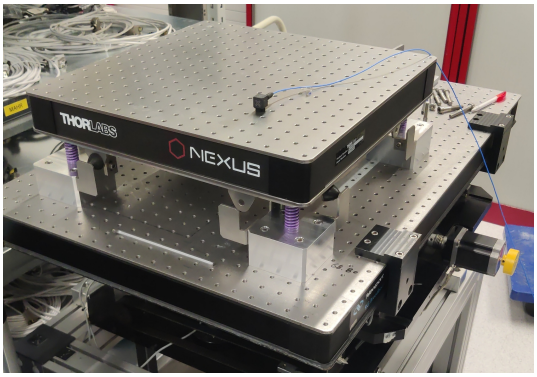

Figure 4.59: Mounted suspended table. Only 1 or the 15 accelerometer is mounted on top.

Modes	Frequency	Description
1,2	1.3 Hz	X-Y translations
3	2.0 Hz	Z rotation
4	6.9 Hz	Z translation
5,6	9.5 Hz	X-Y rotations
7	701 Hz	"Membrane" Mode
8	989 Hz	Complex mode
9	1025 Hz	Complex mode

Table 4.12: Obtained modes of the suspended table

4.4.2.4 Multi-body Model of the Suspended Table

The multi-body model of the suspended table consists simply of two solid bodies connected by 4 springs. The 4 springs are here modelled with "bushing joints" that have stiffness and damping properties in x, y, and z directions.

[1] The 450 mm × 450 mm × 60 mm Nexus B4545A from Thorlabs.
[2] "SZ8005 20 x 044" from Steinel. The spring rate is specified at 17.8 N/mm.
[3] PCB 356B18. Sensitivity is 1 V/g, measurement range is ±5 g and bandwidth is 0.5 to 5 kHz.

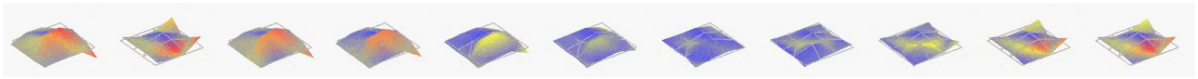

(a) Flexible mode at 701 Hz

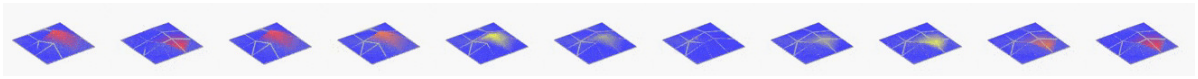

(b) Flexible mode at 989 Hz

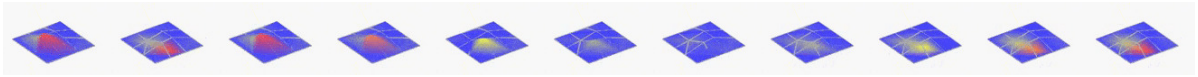

(c) Flexible mode at 1025 Hz

Figure 4.60: Three identified flexible modes of the suspended table.

The model order is 12, which corresponds to the 6 suspension modes. The inertia properties of the parts were determined from the geometry and material densities. The stiffness of the springs was initially set from the datasheet nominal value of 17.8 N/mm and then reduced down to 14 N/mm to better match the measured suspension modes. The stiffness of the springs in the horizontal plane is set at 0.5 N/mm. The obtained suspension modes of the multi-body model are compared with the measured modes in Table 4.13.

Table 4.13: Comparison of suspension modes of the multi-body model and the measured ones.

Directions	D_x, D_y	R_z	D_z	R_x, R_y
Multi-body	1.3 Hz	1.8 Hz	6.8 Hz	9.5 Hz
Experimental	1.3 Hz	2.0 Hz	6.9 Hz	9.5 Hz

4.4.3 Measured Active Platform Dynamics

The Nano-Hexapod was then mounted on top of the suspended table, as shown in Figure 4.61. All instrumentation (Speedgoat with ADC, DAC, piezoelectric voltage amplifiers and digital interfaces for the encoder) were configured and connected to the nano-hexapod using many cables.

A modal analysis of the nano-hexapod is first performed in Section 4.4.3.1. The results of the modal analysis will be useful to better understand the measured dynamics from actuators to sensors.

A block diagram of the (open-loop) system is shown in Figure 4.62. The FRFs from controlled signals $\boldsymbol{u}$ to the force sensors voltages $\boldsymbol{V}_s$ and to the encoders measured displacements $\boldsymbol{d}_e$ are experimentally identified in Section 4.4.3.2. The effect of the payload mass on the dynamics is discussed in Section 4.4.3.3.

4.4.3.1 Modal Analysis

To facilitate the future analysis of the measured plant dynamics, a basic modal analysis of the nano-hexapod is performed. Five 3-axis accelerometers were fixed on the top platform of the nano-hexapod (Figure 4.63) and the top platform was excited using an instrumented hammer.

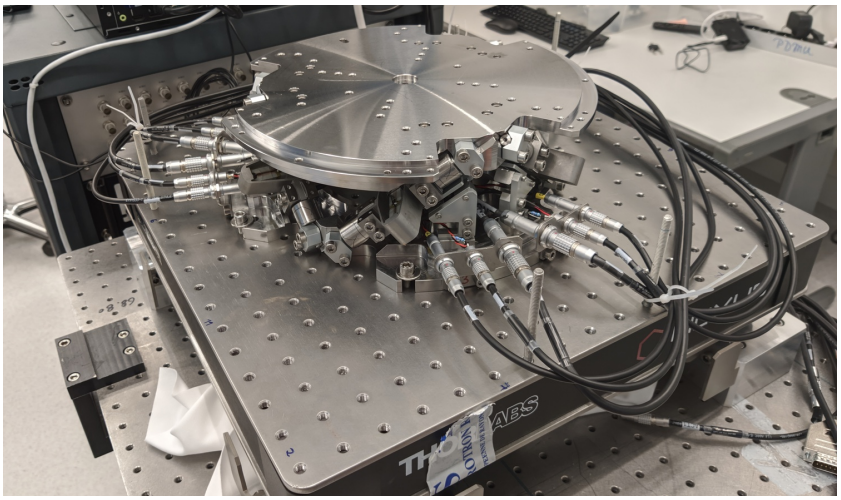

Figure 4.61: Mounted Nano-Hexapod on top of the suspended table.

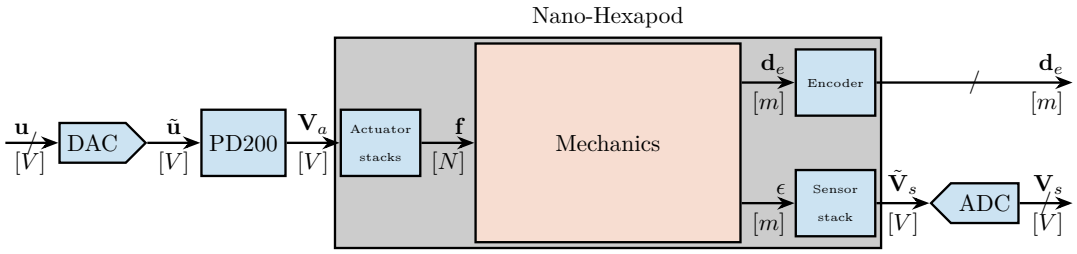

Figure 4.62: Block diagram of the studied system. The command signal is $\boldsymbol{u}$, and the measured signals are $\boldsymbol{d}_e$ and $\boldsymbol{V}_s$.

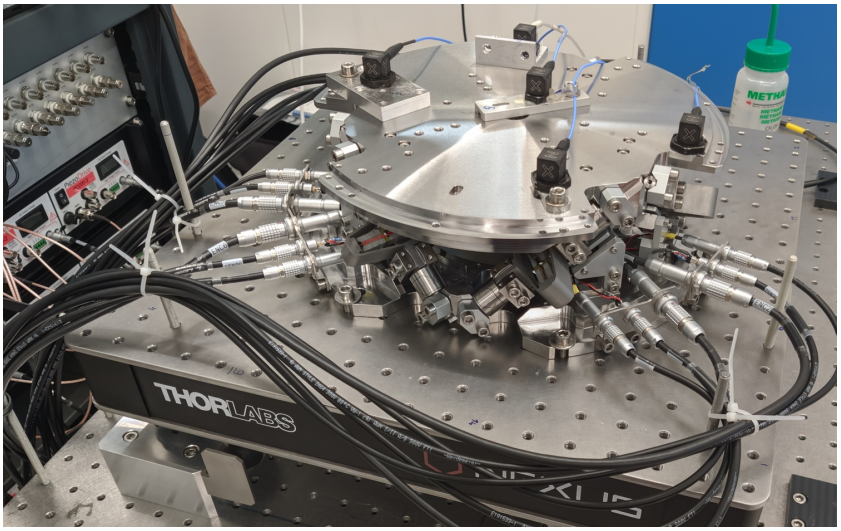

Figure 4.63: Five accelerometers fixed on top of the nano-hexapod to perform a modal analysis.

Between 100 Hz and 200 Hz, 6 suspension modes (i.e. rigid body modes of the top platform) were identified. At around 700 Hz, two flexible modes of the top plate were observed (see Figure 4.64). These modes are summarized in Table 4.14.

Table 4.14: Description of the identified modes of the Nano-Hexapod.

Mode	Frequency	Description
1	120 Hz	Suspension Mode: Y-translation
2	120 Hz	Suspension Mode: X-translation
3	145 Hz	Suspension Mode: Z-translation
4	165 Hz	Suspension Mode: Y-rotation
5	165 Hz	Suspension Mode: X-rotation
6	190 Hz	Suspension Mode: Z-rotation
7	692 Hz	(flexible) Membrane mode of the top platform
8	709 Hz	Second flexible mode of the top platform

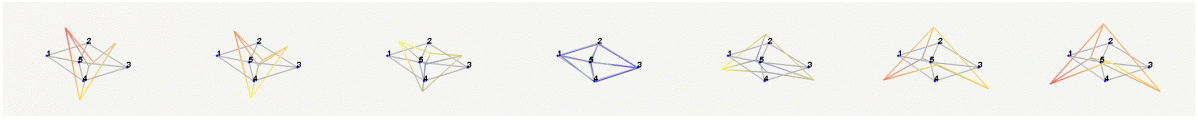

(a) Flexible mode at 692 Hz

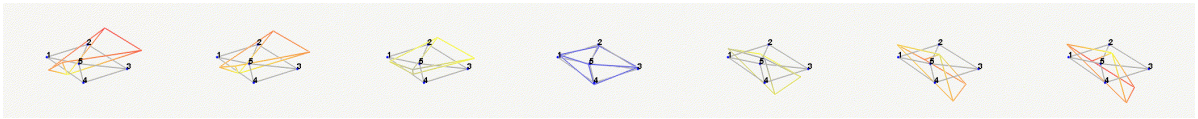

(b) Flexible mode at 709 Hz

Figure 4.64: Two identified flexible modes of the top plate of the Nano-Hexapod.

4.4.3.2 Identification of the Dynamics

The dynamics of the nano-hexapod from the six command signals (u_1 to u_6) to the six measured displacement by the encoders (d_{e1} to d_{e6}) and to the six force sensors (V_{s1} to V_{s6}) were identified by generating low-pass filtered white noise for each command signal, one by one.

The 6×6 FRF matrix from $\boldsymbol{u}$ ot $\boldsymbol{d}_e$ is shown in Figure 4.65. The diagonal terms are displayed using colored lines, and all the 30 off-diagonal terms are displayed by gray lines.

All six diagonal terms are well superimposed up to at least 1 kHz, indicating good manufacturing and mounting uniformity. Below the first suspension mode, good decoupling can be observed (the amplitude of all off-diagonal terms are $\approx$ 20 times smaller than the diagonal terms), indicating the correct assembly of all parts.

From 10 Hz up to 1 kHz, around 10 resonance frequencies can be observed. The first 4 are suspension modes (at 122 Hz, 143 Hz, 165 Hz and 191 Hz) which correlate the modes measured during the modal analysis in Section 4.4.3.1. Three modes at 237 Hz, 349 Hz and 395 Hz are attributed to the internal strut resonances (this will be checked in Section 4.4.4.2). Except for the mode at 237 Hz, their impact on the dynamics is small. The two modes at 665 Hz and 695 Hz are attributed to the flexible modes of the top platform. Other modes can be observed above 1 kHz, which can be attributed to flexible modes of the encoder supports or to flexible modes of the top platform.

Up to at least 1 kHz, an alternating pole/zero pattern is observed, which makes the control easier to tune. This would not have occurred if the encoders were fixed to the struts.

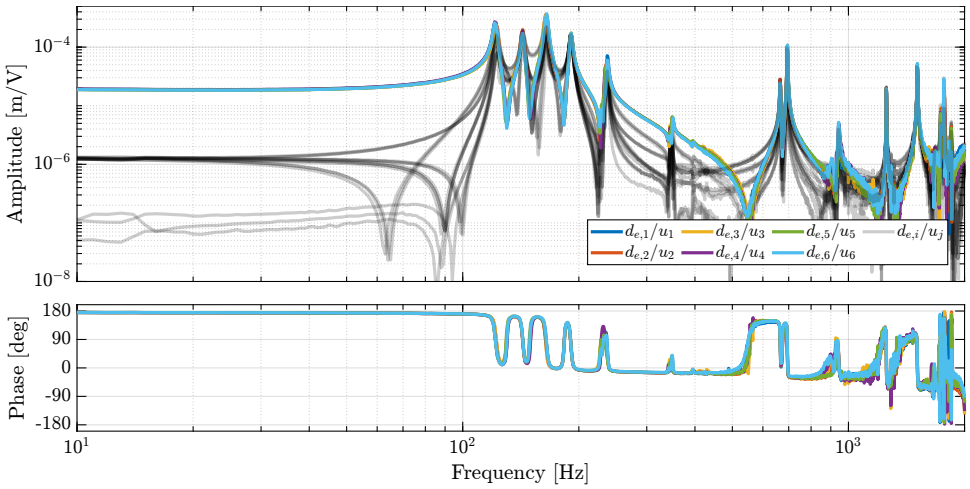

Figure 4.65: Measured FRFs from $\boldsymbol{u}$ to $\boldsymbol{d}_e$. The 6 direct terms are the colored lines, and the 30 coupling terms are the gray lines.

Similarly, the 6×6 FRF matrix from $\boldsymbol{u}$ to $\boldsymbol{V}_s$ is shown in Figure 4.66. Alternating poles and zeros can be observed up to at least 2 kHz, which is a necessary characteristics for applying decentralized IFF. Similar to what was observed for the encoder outputs, all the "diagonal" terms are well superimposed, indicating that the same controller can be applied to all the struts. The first flexible mode of the struts as 235 Hz has large amplitude, and therefore, it should be possible to add some damping to this mode using IFF.

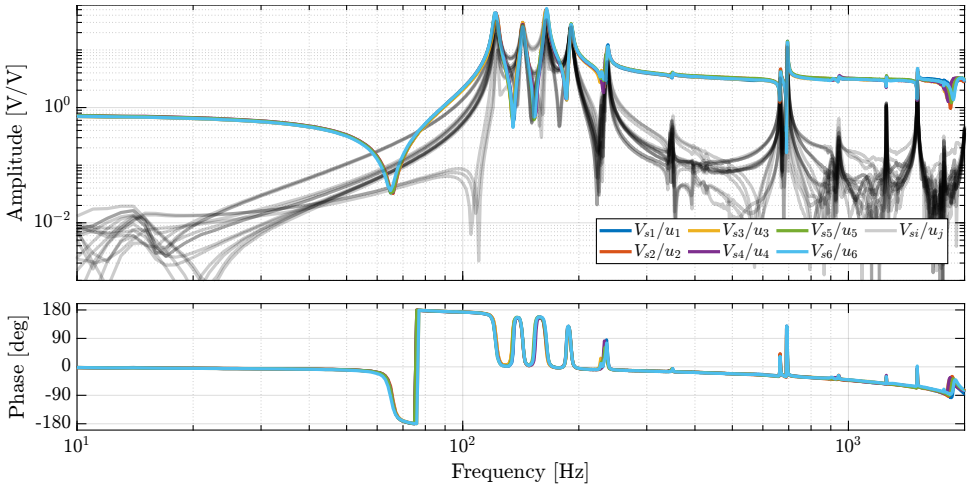

Figure 4.66: Measured FRF from $\boldsymbol{u}$ to $\boldsymbol{V}_s$. The 6 direct terms are the colored lines, and the 30 coupling terms are the gray lines.

4.4.3.3 Effect of Payload Mass on the Dynamics

One major challenge for controlling the NASS is the wanted robustness to a variation of payload mass; therefore, it is necessary to understand how the dynamics of the nano-hexapod changes with a change in payload mass.

To study how the dynamics changes with the payload mass, up to three "cylindrical masses" of 13 kg each can be added for a total of $\approx$ 40 kg. These three cylindrical masses on top of the nano-hexapod are shown in Figure 4.67.

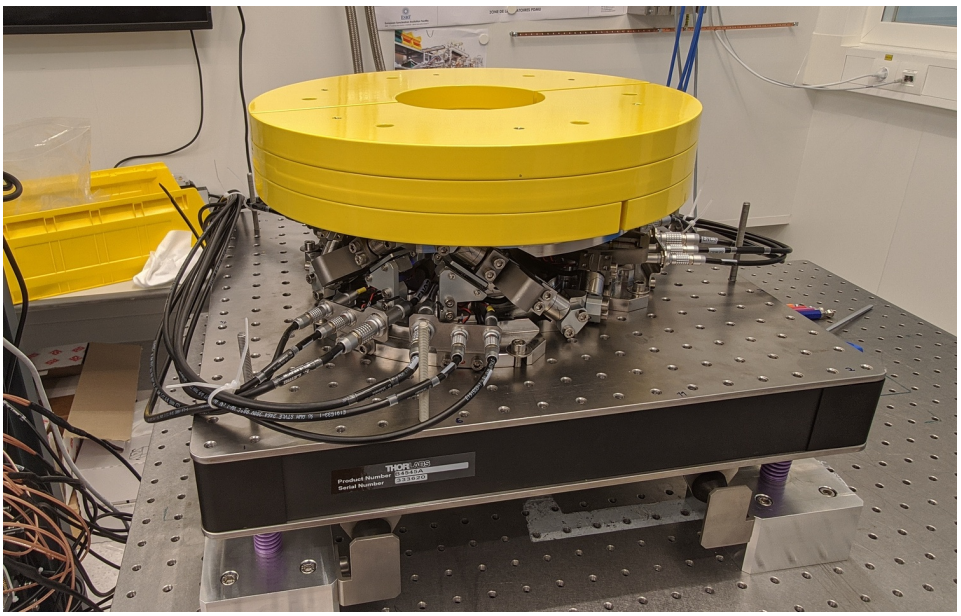

Figure 4.67: Picture of the nano-hexapod with the added three cylindrical masses for a total of $\approx$ 40 kg.

The obtained FRFs from actuator signal u_i to the associated encoder d_{ei} for the four payload conditions (no mass, 13 kg, 26 kg and 39 kg) are shown in Figure 4.68a. As expected, the frequency of the suspension modes decreased with increasing payload mass. The low frequency gain does not change because it is linked to the stiffness property of the nano-hexapod and not to its mass property.

The frequencies of the two flexible modes of the top plate first decreased significantly when the first mass was added (from $\approx$ 700 Hz to $\approx$ 400 Hz). This is because the added mass is composed of two half cylinders that are not fixed together. Therefore, it adds a lot of mass to the top plate without increasing stiffness in one direction. When more than one "mass layer" is added, the half cylinders are added at some angles such that rigidity is added in all directions (see how the three mass "layers" are positioned in Figure 4.67). In this case, the frequency of these flexible modes is increased. In practice, the payload should be one solid body, and no decrease in the frequency of this flexible mode should be observed. The apparent amplitude of the flexible mode of the strut at 237 Hz becomes smaller as the payload mass increased.

The measured FRFs from u_i to V_{si} are shown in Figure 4.68b. For all tested payloads, the measured FRF always have alternating poles and zeros, indicating that IFF can be applied in a robust manner.

4.4.4 Model Dynamics

In this section, the dynamics measured in Section 4.4.3 is compared with those estimated from the multi-body model. The nano-hexapod multi-body model was therefore added on top of the vibration table multi-body model, as shown in Figure 4.69.

The model should exhibit certain characteristics that are verified in this section. First, it should match the measured system dynamics from actuators to sensors presented in Section 4.4.3. Both the "direct" terms (Section 4.4.4.1) and "coupling" terms (Section 4.4.4.2) of the multi-body model are compared with the measured dynamics. Second, it should also represents how the system dynamics changes when a payload is fixed to the top platform. This is checked in Section 4.4.4.3.

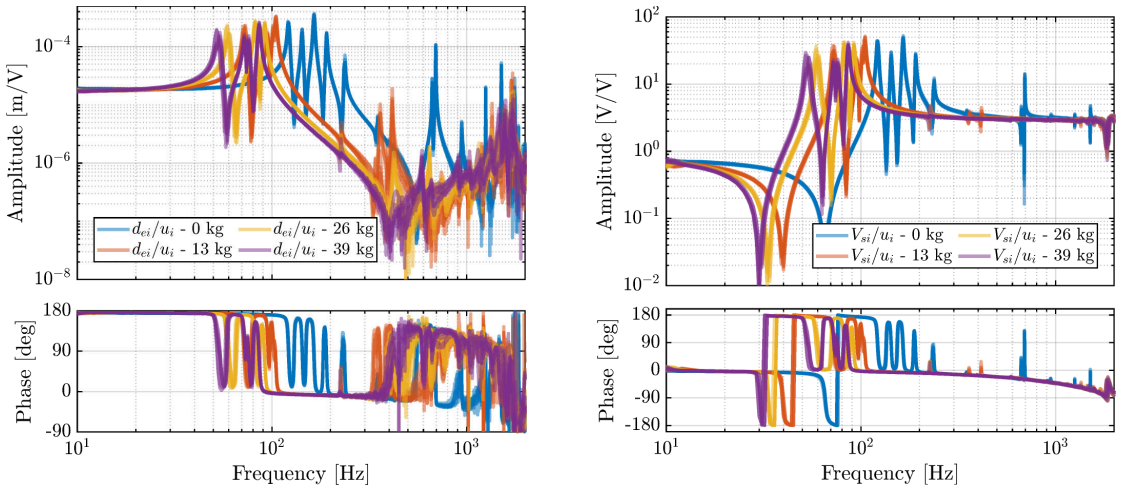

(a) u_i to d_{ei} (encoder)

(b) u_i to V_{si} (force sensor)

Figure 4.68: Measured Frequency Response Functions from u_i to d_{ei} (a) and from u_i to V_{si} (b) for all 4 payload conditions. Only diagonal terms are shown.

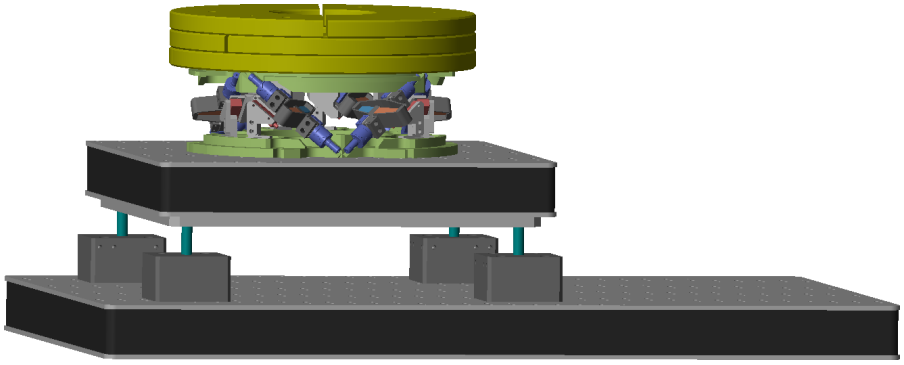

Figure 4.69: Multi-body model of the nano-hexapod on top of the suspended table. Three mass "layers" are here added.

4.4.4.1 Nano-Hexapod Model Dynamics

The multi-body model of the nano-hexapod was first configured with 4-DoF flexible joints, 2-DoF APA, and rigid top and bottom plates. The stiffness values of the flexible joints were chosen based on the values estimated using the test bench and on the FEM. The parameters of the APA model were determined from the test bench of the APA. The 6×6 transfer function matrices from $\boldsymbol{u}$ to $\boldsymbol{d}_e$ and from $\boldsymbol{u}$ to $\boldsymbol{V}_s$ are then extracted from the multi-body model.

First, is it evaluated how well the models matches the "direct" terms of the measured FRF matrix. To do so, the diagonal terms of the extracted transfer function matrices are compared with the measured FRF in Figure 4.70. It can be seen that the 4 suspension modes of the nano-hexapod (at 122 Hz, 143 Hz, 165 Hz and 191 Hz) are well modelled. The three resonances that were attributed to "internal" flexible modes of the struts (at 237 Hz, 349 Hz and 395 Hz) cannot be seen in the model, which is reasonable because the APAs are here modelled as a simple uniaxial 2-DoF system. At higher frequencies, no resonances can be observed in the model, as the top plate and the encoder supports are modelled as rigid bodies.

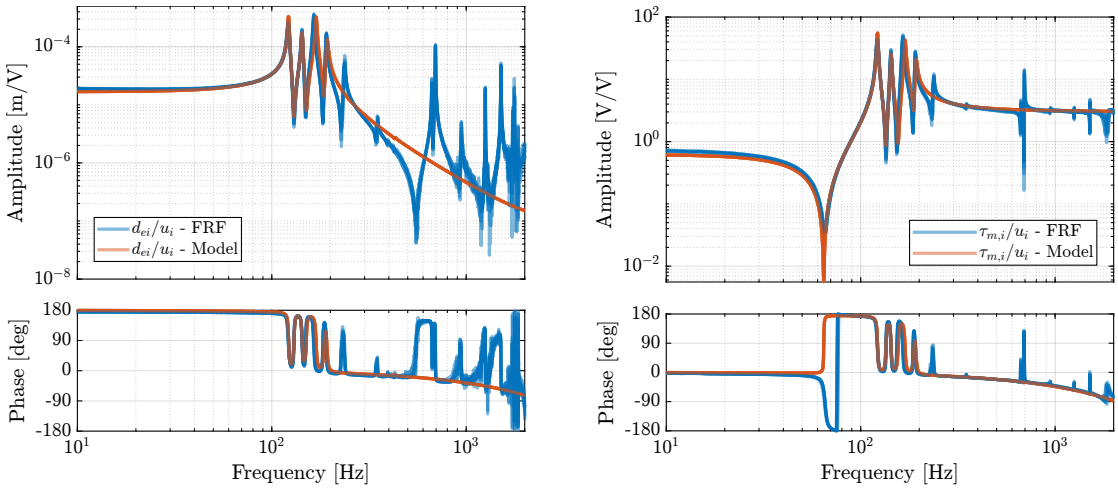

(a) from u to d_e (encoder)

(b) from u to V_s (force sensor)

Figure 4.70: Comparison of the diagonal elements (i.e. "direct" terms) of the measured FRF matrix and the dynamics identified from the multi-body model. Both for the dynamics from u to d_e (a) and from u to V_s (b).

4.4.4.2 Dynamical Coupling

Another desired feature of the model is that it effectively represents coupling in the system, as this is often the limiting factor for the control of MIMO systems. Instead of comparing the full 36 elements of the 6×6 FRF matrix from $\boldsymbol{u}$ to $\boldsymbol{d}_e$, only the first "column" is compared (Figure 4.71), which corresponds to the transfer function from the command u_1 to the six measured encoder displacements d_{e1} to d_{e6}. It can be seen that the coupling in the model matches the measurements well up to the first un-modelled flexible mode at 237 Hz. Similar results are observed for all other coupling terms and for the transfer function from $\boldsymbol{u}$ to $\boldsymbol{V}_s$.

The APA300ML was then modelled with a *super-element* extracted from a FE-software. The obtained transfer functions from u_1 to the six measured encoder displacements d_{e1} to d_{e6} are compared with the measured FRF in Figure 4.72. While the damping of the suspension modes for the *super-element* is underestimated (which could be solved by properly tuning the proportional damping coefficients), the flexible modes of the struts at 237 Hz and 349 Hz are well modelled. Even the mode 395 Hz can be observed in the model. Therefore, if the modes of the struts are to be modelled, the *super-element* of the APA300ML can be used at the cost of obtaining a much higher order model.

4.4.4.3 Effect of Payload Mass

Another important characteristic of the model is that it should represents the dynamics of the system well for all considered payloads. The model dynamics is therefore compared with the measured dynamics for 4 payloads (no payload, 13 kg, 26 kg and 39 kg) in Figure 4.73. The observed shift of the suspension modes to lower frequencies with increased payload mass is well represented by the multi-body model. The complex conjugate zeros also well match the experiments both for the encoder outputs (Figure 4.73a) and the force sensor outputs (Figure 4.73b).

Note that the model displays smaller damping than that observed experimentally for high values of the payload mass. One option could be to tune the damping as a function of the mass (similar to what is done with the Rayleigh damping). However, as decentralized IFF will be applied, the damping is actively brought, and the open-loop damping value should have very little impact on the obtained plant dynamics.

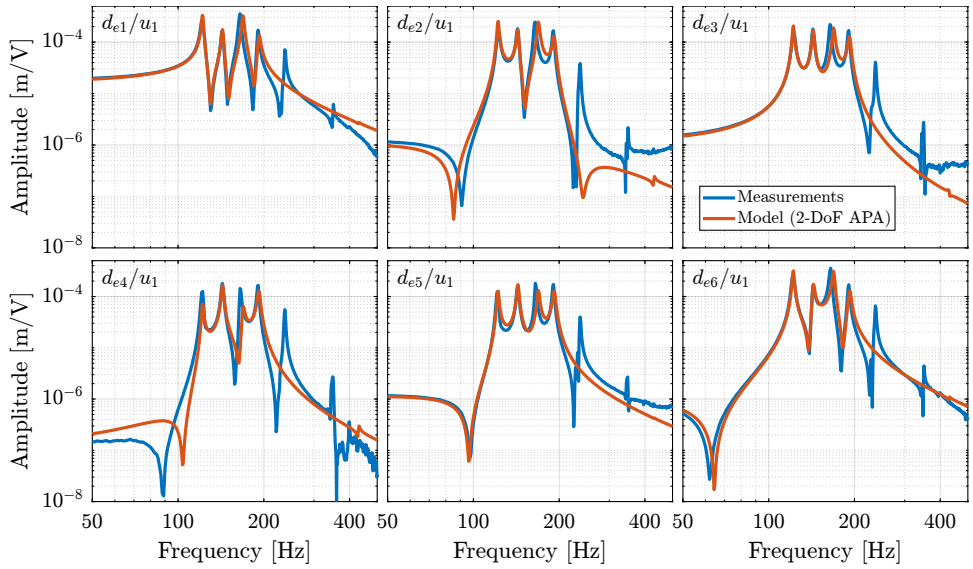

Figure 4.71: Comparison of the measured (in blue) and modelled (in red) FRFs from the first control signal u_1 to the six encoders d_{e1} to d_{e6}. The APA are here modelled with a 2-DoF mass-spring-damper system. No payload us used.

In order to also check if the model well represents the coupling when high payload masses are used, the transfer functions from u_1 to d_{e1} to d_{e6} are compared in the case of the 39 kg payload in Figure 4.74. Excellent match between experimental and model coupling is observed. Therefore, the model effectively represents the system coupling for different payloads.

Conclusion

The goal of this test bench was to obtain an accurate model of the nano-hexapod that could then be included on top of the micro-station model. The adopted strategy was to identify the nano-hexapod dynamics under conditions in which all factors that could have affected the nano-hexapod dynamics were considered. This was achieved by developing a suspended table with low frequency suspension modes that can be accurately modelled (Section 4.4.2). Although the dynamics of the nano-hexapod was indeed impacted by the dynamics of the suspended platform, this impact was also considered in the multi-body model.

The dynamics of the nano-hexapod was then identified in Section 4.4.3. Below the first suspension mode, good decoupling could be observed for the transfer function from $\boldsymbol{u}$ to $\boldsymbol{d}_e$, which enables the design of a decentralized positioning controller based on the encoders for relative positioning purposes. Many other modes were present above 700 Hz, which will inevitably limit the achievable bandwidth. The observed effect of the payload's mass on the dynamics was quite large, which also represents a complex control challenge.

The FRFs from the six DAC voltages $\boldsymbol{u}$ to the six force sensors voltages $\boldsymbol{V}_s$ all have alternating complex conjugate poles and complex conjugate zeros for all the tested payloads (Figure 4.73b). This indicates that it is possible to implement decentralized Integral Force Feedback in a robust manner.

The developed multi-body model of the nano-hexapod was found to accurately represents the suspension modes of the Nano-Hexapod (Section 4.4.4). Both FRF matrices from $\boldsymbol{u}$ to $\boldsymbol{V}_s$ and from $\boldsymbol{u}$ to $\boldsymbol{d}_e$ are well matching with the measurements, even when considering coupling (i.e. off-diagonal) terms, which are very important from a control perspective. At frequencies above the suspension modes, the Nano-Hexapod model became inaccurate because the flexible modes were not modelled. It was found that modeling the APA300ML using a *super-element* allows to model the internal res-

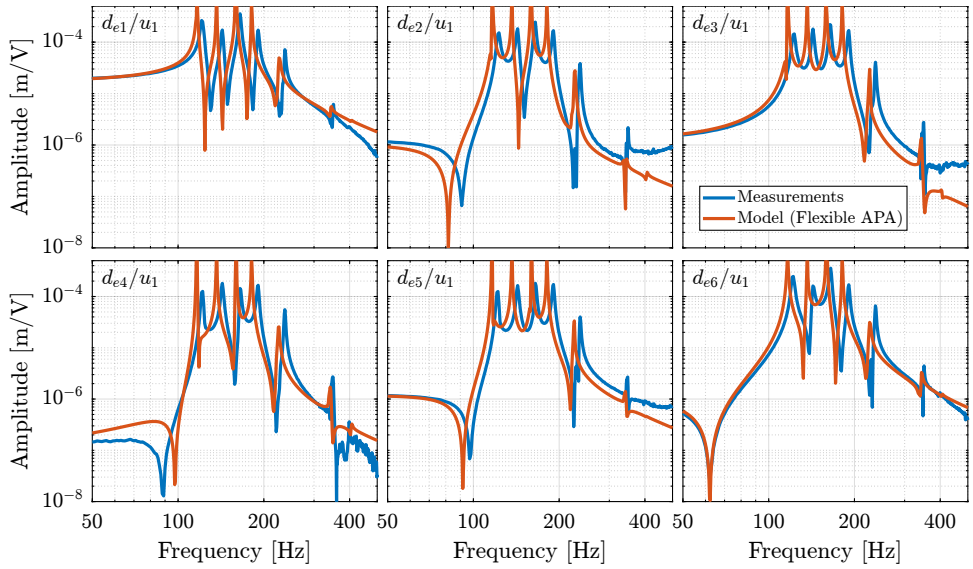

Figure 4.72: Comparison of the measured (in blue) and modelled (in red) FRFs from the first control signal u_1 to the six encoders d_{e1} to d_{e6}. The APA are here modelled with a "super-element". No payload us used.

onances of the struts. The same can be done with the top platform and the encoder supports; however, the model order would be higher and may become unpractical for simulation.

Obtaining a model that accurately represents the complex dynamics of the Nano-Hexapod was made possible by the modeling approach used in this study. This approach involved tuning and validating models of individual components (such as the APA and flexible joints) using dedicated test benches. The different models could then be combined to form the Nano-Hexapod dynamical model. If a model of the nano-hexapod was developed in one time, it would be difficult to tune all the model parameters to match the measured dynamics, or even to know if the model "structure" would be adequate to represent the system dynamics.

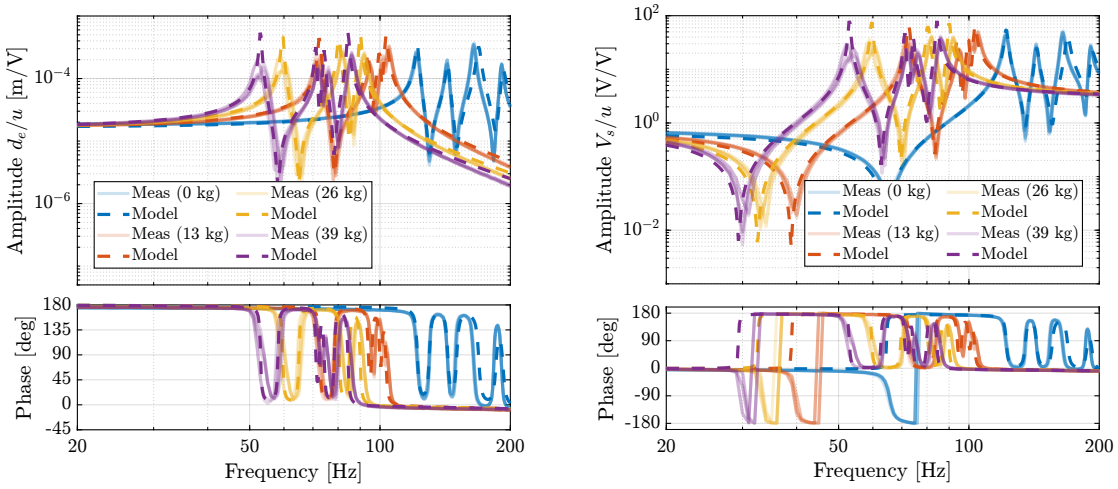

(a) from u to d_e (encoder)

(b) from u to V_s (force sensor)

Figure 4.73: Comparison of the diagonal elements (i.e. "direct" terms) of the measured FRF matrix and the dynamics identified from the multi-body model. Both for the dynamics from u to d_e (a) and from u to V_s (b).

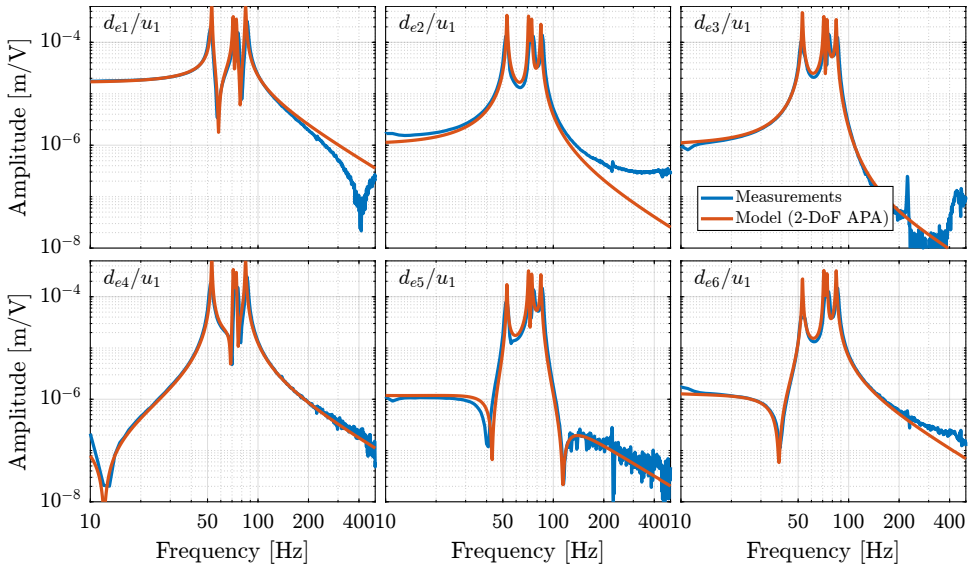

Figure 4.74: Comparison of the measured (in blue) and modelled (in red) FRF from the first control signal u_1 to the six encoders d_{e1} to d_{e6}. 39 kg payload is used.

4.5 Nano Active Stabilization System

To proceed with the full validation of the Nano Active Stabilization System (NASS), the nano-hexapod was mounted on top of the micro-station on ID31, as illustrated in figure 4.75. This section presents a comprehensive experimental evaluation of the complete system's performance on the ID31 beamline, focusing on its ability to maintain precise sample positioning under various experimental conditions.

Initially, the project planned to develop a long-stroke ($\approx$ 1 cm^3) 5-DoF metrology system to measure the sample position relative to the granite base. However, the complexity of this development prevented its completion before the experimental testing phase on ID31. To validate the nano-hexapod and its associated control architecture, an alternative short-stroke ($\approx$ 100 µm^3) metrology system was developed instead, which is presented in Section 4.5.1.

Then, several key aspects of the system validation are examined. Section 4.5.2 analyzes the identified dynamics of the nano-hexapod mounted on the micro-station under various experimental conditions, including different payload masses and rotational velocities. These measurements were compared with predictions from the multi-body model to verify its accuracy and applicability to control design.

Sections 4.5.3 and 4.5.4 focus on the implementation and validation of the HAC-LAC control architecture. First, Section 4.5.3 demonstrates the application of decentralized Integral Force Feedback for robust active damping of the nano-hexapod suspension modes. This is followed in Section 4.5.4 by the implementation of the high authority controller, which addresses low-frequency disturbances and completes the control system design.

Finally, Section 4.5.5 evaluates the NASS's positioning performances through a comprehensive series of experiments that mirror typical scientific applications. These include tomography scans at various speeds and with different payload masses, reflectivity measurements, and combined motion sequences that test the system's full capabilities.

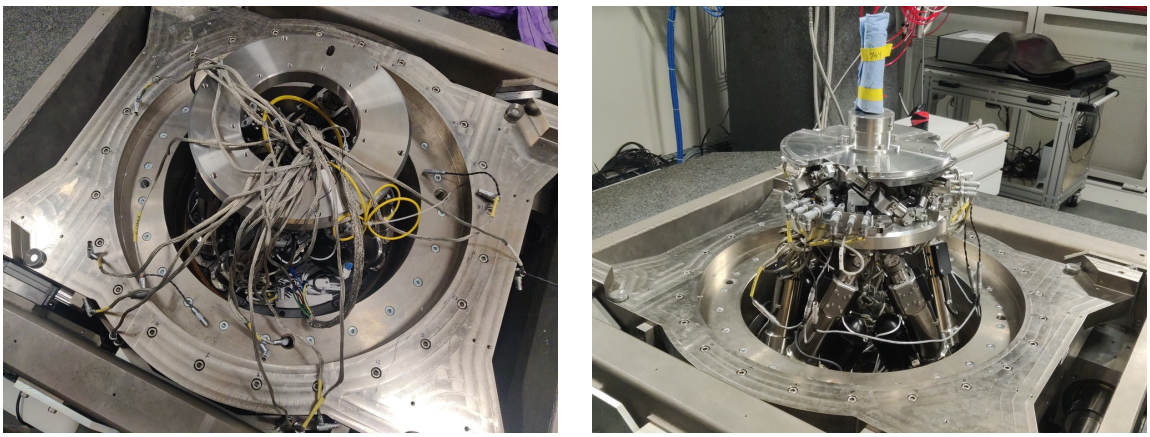

(a) Micro-station and nano-hexapod cables

(b) Nano-hexapod fixed on top of the micro-station

Figure 4.75: Picture of the micro-station without the nano-hexapod (a) and with the nano-hexapod (b).

4.5.1 Short Stroke Metrology System

The control of the nano-hexapod requires an external metrology system that measures the relative position of the nano-hexapod top platform with respect to the granite. As a long-stroke ($\approx$ 1 cm^3) metrology system was not yet developed, a short stroke ($\approx$ 100 µm^3) was used instead to validate the nano-hexapod control.

The first considered option was to use the "Spindle error analyzer" shown in Figure 4.76a. This system comprises 5 capacitive sensors facing two reference spheres. However, as the gap between the capacitive sensors and the spheres is very small[1], the risk of damaging the spheres and the capacitive sensors is too high.

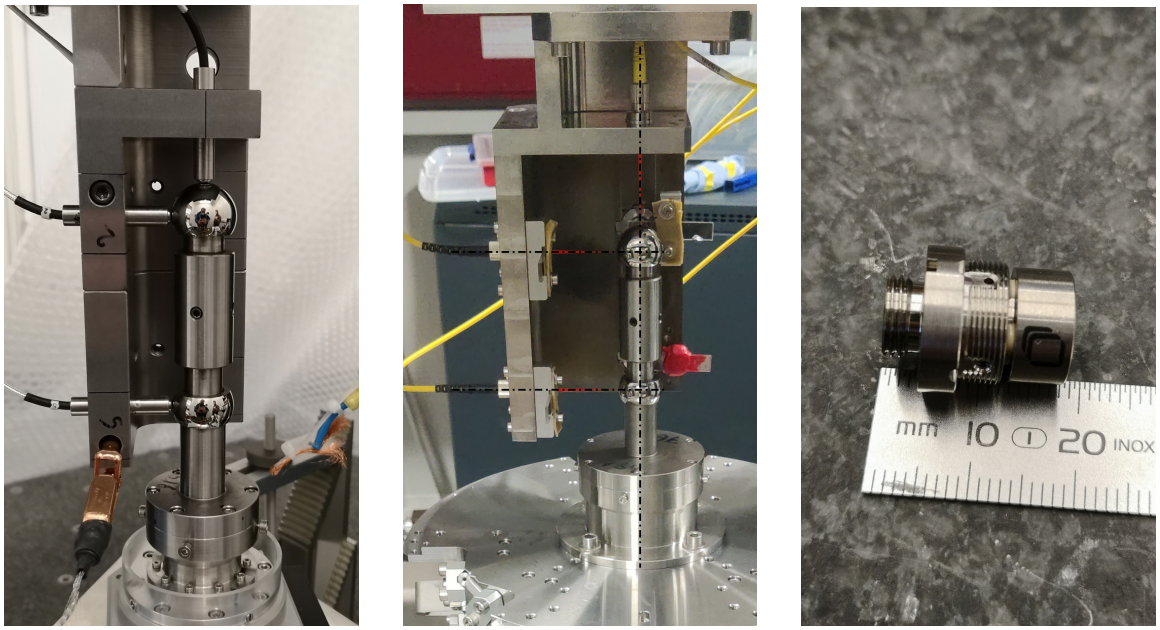

(a) Capacitive Sensors **(b)** Short-Stroke metrology **(c)** Interferometer head

Figure 4.76: Short stroke metrology system used to measure the sample position with respect to the granite in 5-DoF. The system is based on a "Spindle error analyzer" (a), but the capacitive sensors are replaced with fibered interferometers (b). One interferometer head is shown in (c).

Instead of using capacitive sensors, 5 fibered interferometers were used in a similar manner (Figure 4.76b). At the end of each fiber, a sensor head[2] (Figure 4.76c) is used, which consists of a lens precisely positioned with respect to the fiber's end. The lens focuses the light on the surface of the sphere, such that the reflected light comes back into the fiber and produces an interference. In this way, the gap between the head and the reference sphere is much larger (here around 40 mm), thereby removing the risk of collision.

Nevertheless, the metrology system still has a limited measurement range because of the limited angular acceptance of the fibered interferometers. Indeed, when the spheres are moving perpendicularly to the beam axis, the reflected light does not coincide with the incident light, and above some perpendicular displacement, the reflected light does not come back into the fiber, and no interference is produced.

4.5.1.1 Metrology Kinematics

The proposed short-stroke metrology system is schematized in Figure 4.77. The PoI is indicated by the blue frame $\{B\}$, which is located $H = 150\,\text{mm}$ above the nano-hexapod's top platform. The spheres have a diameter $d = 25.4\,\text{mm}$, and the indicated dimensions are $l_1 = 60\,\text{mm}$ and $l_2 = 16.2\,\text{mm}$. To compute the pose of $\{B\}$ with respect to the granite (i.e. with respect to the fixed interferometer heads), the measured (small) displacements $[d_1,\ d_2,\ d_3,\ d_4,\ d_5]$ by the interferometers are first written as a function of the (small) linear and angular motion of the $\{B\}$ frame $[D_x,\ D_y,\ D_z,\ R_x,\ R_y]$ (4.22).

[1] Depending on the measuring range, gap can range from $\approx 1\,\mu\text{m}$ to $\approx 100\,\mu\text{m}$.
[2] M12/F40 model from Attocube.

$$d_1 = D_y - l_2 R_x, \quad d_2 = D_y + l_1 R_x, \quad d_3 = -D_x - l_2 R_y, \quad d_4 = -D_x + l_1 R_y, \quad d_5 = -D_z \tag{4.22}$$

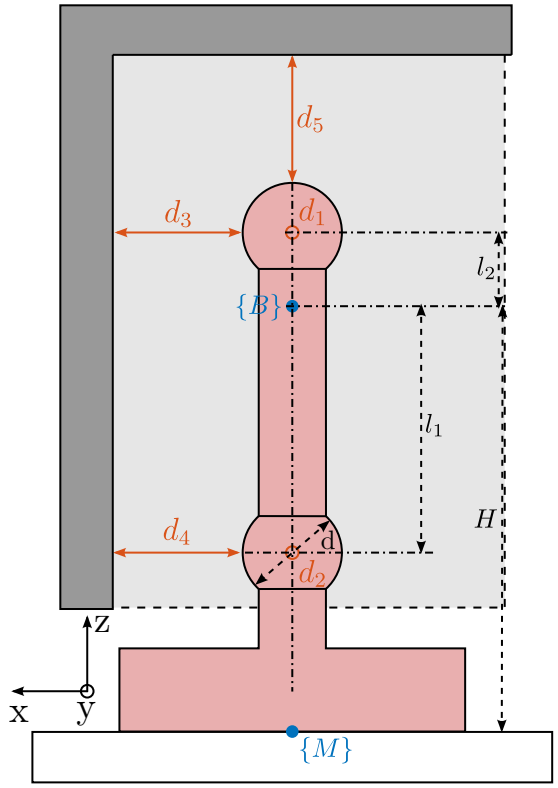

Figure 4.77: Schematic of the measurement system. The measured distances are indicated by red arrows.

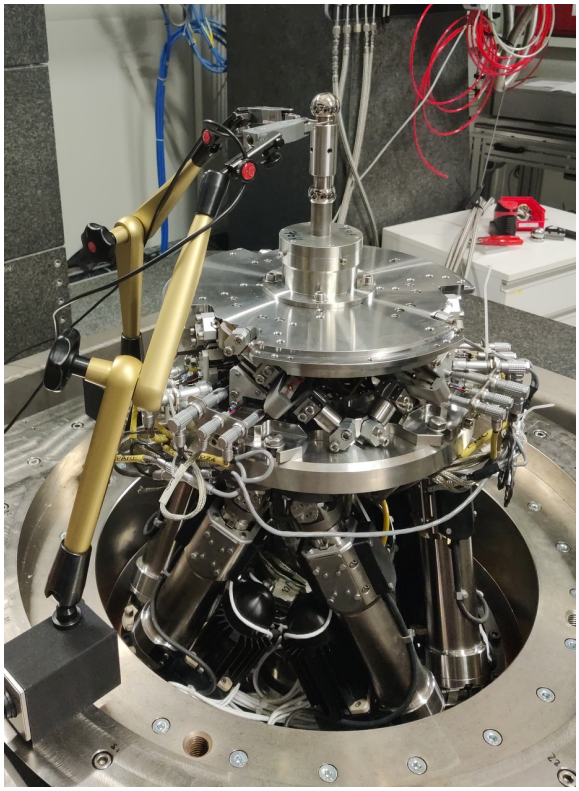

Figure 4.78: The top sphere is aligned with the rotation axis of the spindle using two probes.

The five equations (4.22) can be written in matrix form, and then inverted to have the pose of the $\{B\}$ frame as a linear combination of the measured five distances by the interferometers (4.23).

$$\begin{bmatrix} D_x \\ D_y \\ D_z \\ R_x \\ R_y \end{bmatrix} = \underbrace{\begin{bmatrix} 0 & 1 & 0 & -l_2 & 0 \\ 0 & 1 & 0 & l_1 & 0 \\ -1 & 0 & 0 & 0 & -l_2 \\ -1 & 0 & 0 & 0 & l_1 \\ 0 & 0 & -1 & 0 & 0 \end{bmatrix}^{-1}}_{\boldsymbol{J_d}} \cdot \begin{bmatrix} d_1 \\ d_2 \\ d_3 \\ d_4 \\ d_5 \end{bmatrix} \tag{4.23}$$

4.5.1.2 Rough Alignment of the Reference Spheres

The two reference spheres must be well aligned with the rotation axis of the spindle. To achieve this, two measuring probes were used as shown in Figure 4.78.

To not damage the sensitive sphere surface, the probes are instead positioned on the cylinder on which the sphere is mounted. The probes are first fixed to the bottom (fixed) cylinder to align the first sphere with the spindle axis. The probes are then fixed to the top (adjustable) cylinder, and the same alignment is performed.

With this setup, the alignment accuracy of both spheres with the spindle axis was expected to around 10 µm. The accuracy was probably limited by the poor coaxiality between the cylinders and the spheres. However, this first alignment should be sufficient to position the two sphere within the acceptance range of the interferometers.

4.5.1.3 Tip-Tilt Adjustment of the Interferometers

The short-stroke metrology system was placed on top of the main granite using granite blocs (Figure 4.79). Granite is used for its good mechanical and thermal stability.

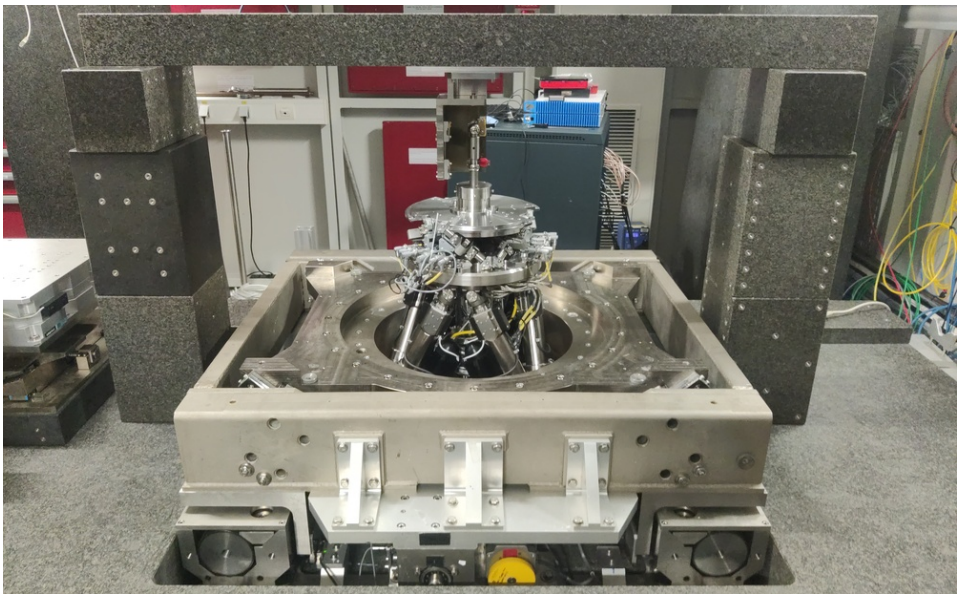

Figure 4.79: Granite gantry used to fix the short-stroke metrology system.

The interferometer beams must be placed with respect to the two reference spheres as close as possible to the ideal case shown in Figure 4.77. Therefore, their positions and angles must be well adjusted with respect to the two spheres. First, the vertical positions of the spheres is adjusted using the positioning hexapod to match the heights of the interferometers. Then, the horizontal position of the gantry is adjusted such that the intensity of the light reflected back in the fiber of the top interferometer is maximized. This is equivalent as to optimize the perpendicularity between the interferometer beam and the sphere surface (i.e. the concentricity between the top beam and the sphere center).

The lateral sensor heads (i.e. all except the top one) were each fixed to a custom tip-tilt adjustment mechanism. This allows them to be individually oriented so that they all point to the spheres' center (i.e. perpendicular to the sphere surface). This is achieved by maximizing the intensity of the reflected light of each interferometer.

After the alignment procedure, the top interferometer should coincide with the spindle axis, and the lateral interferometers should all be in the horizontal plane and intersect the centers of the spheres.

4.5.1.4 Fine Alignment of Reference Spheres using Interferometers

Thanks to the first alignment of the two reference spheres with the spindle axis (Section 4.5.1.2) and to the fine adjustment of the interferometer orientations (Section 4.5.1.3), the spindle can perform complete rotations while still having interference for all five interferometers. Therefore, this metrology can be used to better align the axis defined by the centers of the two spheres with the spindle axis.

The alignment process requires few iterations. First, the spindle is scanned, and alignment errors are recorded. From the errors, the motion of the positioning hexapod to better align the spheres with the spindle axis is computed and the positioning hexapod is positioned accordingly. Then, the spindle is scanned again, and new alignment errors are recorded.

This iterative process is first performed for angular errors (Figure 4.80a) and then for lateral errors (Figure 4.80b). The remaining errors after alignment are in the order of ± 5 µrad in R_x and R_y orientations, ± 1 µm in D_x and D_y directions, and less than 0.1 µm vertically.

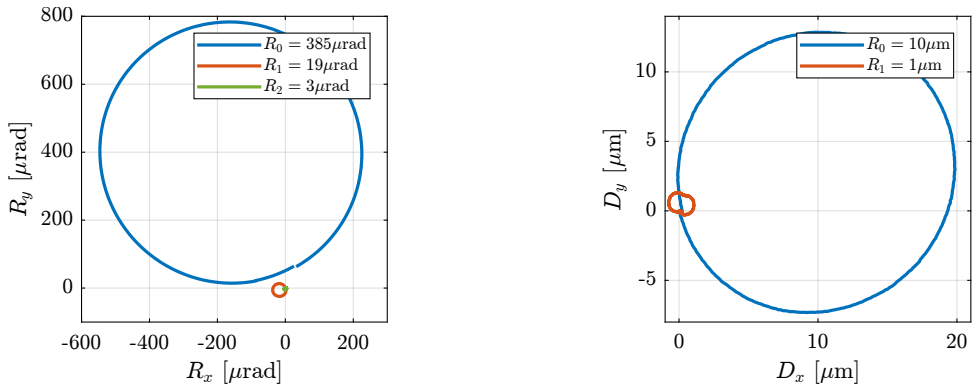

(a) Angular alignment

(b) Lateral alignment

Figure 4.80: Measured angular (a) and lateral (b) errors during full spindle rotation. Between two rotations, the positioning hexapod is adjusted to better align the two spheres with the rotation axis.

4.5.1.5 Estimated Measurement Volume

Because the interferometers point to spheres and not flat surfaces, the lateral acceptance is limited. To estimate the metrology acceptance, the positioning hexapod was used to perform three accurate scans of ± 1 mm, respectively along the x, y and z axes. During these scans, the 5 interferometers are recorded individually, and the ranges in which each interferometer had enough coupling efficiency to be able to measure the displacement were estimated. Results are summarized in Table 4.15. The obtained lateral acceptance for pure displacements in any direction is estimated to be around ± 0.5 mm, which is enough for the current application as it is well above the micro-station errors to be actively corrected by the NASS.

4.5.1.6 Estimated Measurement Errors

When using the NASS, the accuracy of the sample positioning is determined by the accuracy of the external metrology. However, the validation of the nano-hexapod, the associated instrumentation, and the control architecture is independent of the accuracy of the metrology system. Only the bandwidth and noise characteristics of the external metrology are important. However, some elements that affect the accuracy of the metrology system are discussed here.

Table 4.15: Estimated measurement range for each interferometer, and for three different directions.

	D_x	D_y	D_z
d_1 (y)	1.0 mm	> 2 mm	1.35 mm
d_2 (y)	0.8 mm	> 2 mm	1.01 mm
d_3 (x)	> 2 mm	1.06 mm	1.38 mm
d_4 (x)	> 2 mm	0.99 mm	0.94 mm
d_5 (z)	1.33 mm	1.06 mm	> 2 mm

First, the "metrology kinematics" (discussed in Section 4.5.1.1) is only approximate (i.e. valid for small displacements). This can be easily seen when performing lateral $[D_x,\ D_y]$ scans using the positioning hexapod while recording the vertical interferometer (Figure 4.81a). As the top interferometer points to a sphere and not to a plane, lateral motion of the sphere is seen as a vertical motion by the top interferometer.

Then, the reference spheres have some deviations relative to an ideal sphere [1]. These sphere are originally intended for use with capacitive sensors that integrate shape errors over large surfaces. When using interferometers, the size of the "light spot" on the sphere surface is a circle with a diameter approximately equal to 50 µm, and therefore the measurement is more sensitive to shape errors with small features.

As the light from the interferometer travels through air (as opposed to being in vacuum), the measured distance is sensitive to any variation in the refractive index of the air. Therefore, any variation in air temperature, pressure or humidity will induce measurement errors. For instance, for a measurement length of 40 mm, a temperature variation of $0.1°$ (which is typical for the ID31 experimental hutch) induces errors in the distance measurement of ≈ 4 nm.

Interferometers are also affected by noise [155]. The effect of noise on the translation and rotation measurements is estimated in Figure 4.81b.

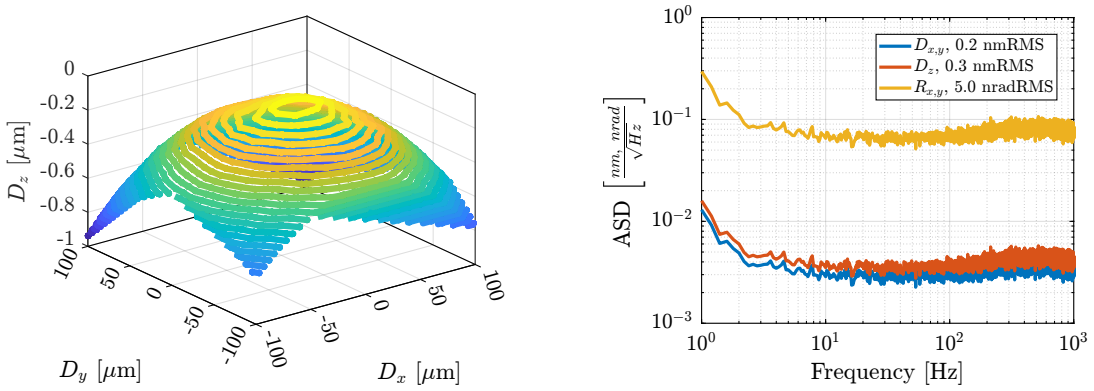

(a) Z measurement during an XY mapping

(b) Interferometer noise

Figure 4.81: Estimated measurement errors of the metrology. Cross-coupling between lateral motion and vertical measurement is shown in (a). The effect of interferometer noise on the measured translations and rotations is shown in (b).

4.5.2 Open Loop Plant

The NASS plant is schematically illustrated in Figure 4.82. The input $\boldsymbol{u} = [u_1,\ u_2,\ u_3,\ u_4,\ u_5,\ u_6]$ is the command signal, which corresponds to the voltages generated for each piezoelectric actuator. After amplification, the voltages across the piezoelectric stack actuators are $\boldsymbol{V}_a = [V_{a1},\ V_{a2},\ V_{a3},\ V_{a4},\ V_{a5},\ V_{a6}]$.

[1] The roundness of the spheres is specified at 50 nm.

From the setpoint of micro-station stages (r_{D_y} for the translation stage, r_{R_y} for the tilt stage and r_{R_z} for the spindle), the reference pose of the sample $\boldsymbol{r}_{\mathcal{X}}$ is computed using the micro-station's kinematics. The sample's position $\boldsymbol{y}_{\mathcal{X}} = [D_x,\ D_y,\ D_z,\ R_x,\ R_y,\ R_z]$ is measured using multiple sensors. First, the five interferometers $\boldsymbol{d} = [d_1,\ d_2,\ d_3,\ d_4,\ d_5]$ are used to measure five degrees of freedom $[D_x,\ D_y,\ D_z,\ R_x,\ R_y]$ of the sample. The sixth DoF of the sample (R_z) is computed from the spindle's setpoint r_{R_z} and from the 6 encoders $\boldsymbol{d}_e$ integrated in the nano-hexapod.

The sample's position $\boldsymbol{y}_{\mathcal{X}}$ is compared to the reference position $\boldsymbol{r}_{\mathcal{X}}$ to compute the position error in the frame of the (rotating) nano-hexapod $\boldsymbol{\epsilon}_{\boldsymbol{\mathcal{X}}} = [\epsilon_{D_x},\ \epsilon_{D_y},\ \epsilon_{D_z},\ \epsilon_{R_x},\ \epsilon_{R_y},\ \epsilon_{R_z}]$. Finally, the Jacobian matrix $\boldsymbol{J}$ of the nano-hexapod is used to map $\boldsymbol{\epsilon}_{\boldsymbol{\mathcal{X}}}$ in the frame of the nano-hexapod struts $\boldsymbol{\epsilon}_{\boldsymbol{\mathcal{L}}} = [\epsilon_{\mathcal{L}_1},\ \epsilon_{\mathcal{L}_2},\ \epsilon_{\mathcal{L}_3},\ \epsilon_{\mathcal{L}_4},\ \epsilon_{\mathcal{L}_5},\ \epsilon_{\mathcal{L}_6}]$.

Voltages generated by the force sensor piezoelectric stacks $\boldsymbol{V}_s = [V_{s1},\ V_{s2},\ V_{s3},\ V_{s4},\ V_{s5},\ V_{s6}]$ will be used for active damping.

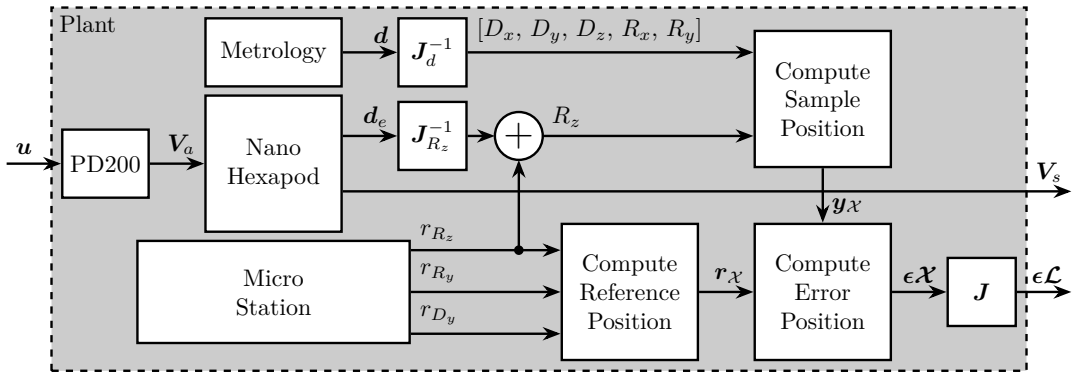

Figure 4.82: Schematic of the NASS plant.

4.5.2.1 Open-Loop Plant Identification

The dynamics of the plant is first identified for a fixed spindle angle (at 0 deg) and without any payload. The model dynamics is also identified under the same conditions.

A comparison between the model and the measured dynamics is presented in Figure 4.83. A good match can be observed for the diagonal dynamics (except the high-frequency modes which are not modelled). However, the coupling of the transfer function from command signals $\boldsymbol{u}$ to the estimated strut motion from the external metrology $\boldsymbol{\epsilon}_{\boldsymbol{\mathcal{L}}}$ is larger than expected (Figure 4.83a).

The experimental time delay estimated from the FRF (Figure 4.83a) is larger than expected. After investigation, it was found that the additional delay was due to a digital processing unit[1] that was used to get the interferometers' signals in the Speedgoat. This issue was later solved.

4.5.2.2 Better Angular Alignment

One possible explanation of the increased coupling observed in Figure 4.83a is the poor alignment between the external metrology axes (i.e. the interferometer supports) and the nano-hexapod axes. To estimate this alignment, a decentralized low-bandwidth feedback controller based on the nano-hexapod encoders was implemented. This allowed to perform two straight motions of the nano-hexapod along its x and y axes. During these two motions, external metrology measurements were recorded and the results are shown in Figure 4.84. It was found that there was a misalignment of 2.7

[1] The "PEPU" [64] was used for digital protocol conversion between the interferometers and the Speedgoat.

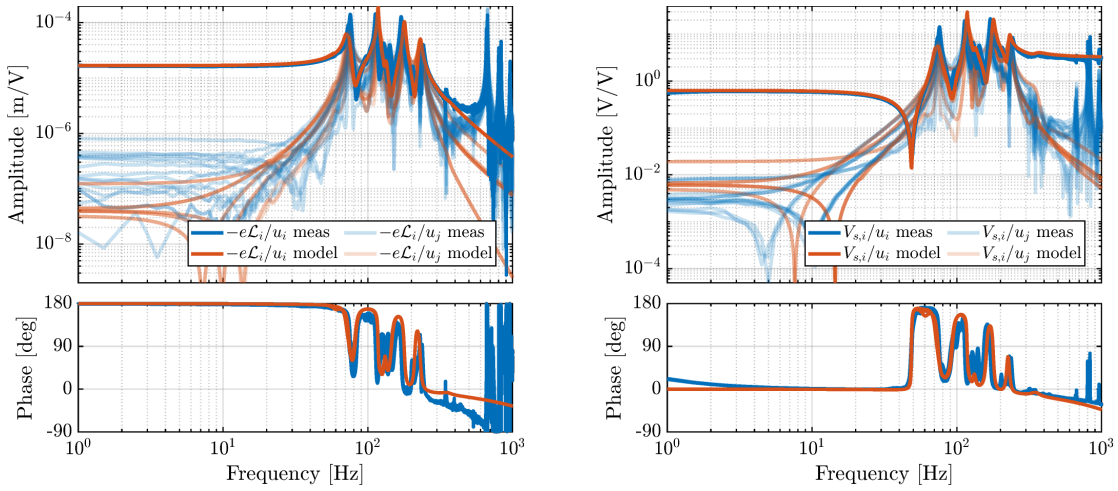

(a) External Metrology

(b) Force Sensors

Figure 4.83: Comparison between the measured dynamics and the multi-body model dynamics. Both for the external metrology (a) and for force sensors (b). Direct terms are displayed with solid lines while off-diagonal (i.e. coupling) terms are displayed with shaded lines.

degrees (rotation around the vertical axis) between the interferometer axes and nano-hexapod axes. This was corrected by adding an offset to the spindle angle. After alignment, the same motion was performed using the nano-hexapod while recording the signal of the external metrology. Results shown in Figure 4.84b are indeed indicating much better alignment.

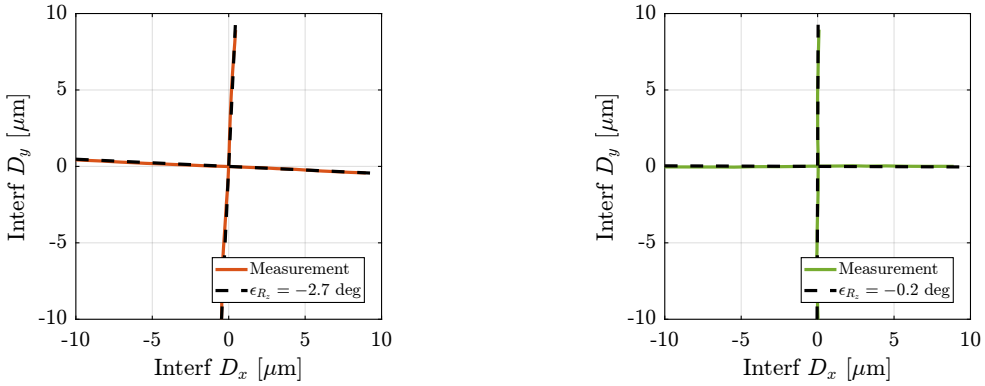

(a) Before alignment

(b) After alignment

Figure 4.84: Measurement of nano-hexapod's axes in the frame of the external metrology. Before (a) and after alignment (b).

The dynamics of the plant was identified again after fine alignment and compared with the model dynamics in Figure 4.85. Compared to the initial identification shown in Figure 4.83a, the obtained coupling was decreased and was close to the coupling obtained with the multi-body model. At low frequency (below 10 Hz), all off-diagonal elements have an amplitude $\approx$ 100 times lower than the diagonal elements, indicating that a low bandwidth feedback controller can be implemented in a decentralized manner (i.e. 6 SISO controllers). Between 650 Hz and 1000 Hz, several modes can be observed, which are due to flexible modes of the top platform and the modes of the two spheres adjustment mechanism. The flexible modes of the top platform can be passively damped, whereas the modes of the two reference spheres should not be present in the final application.

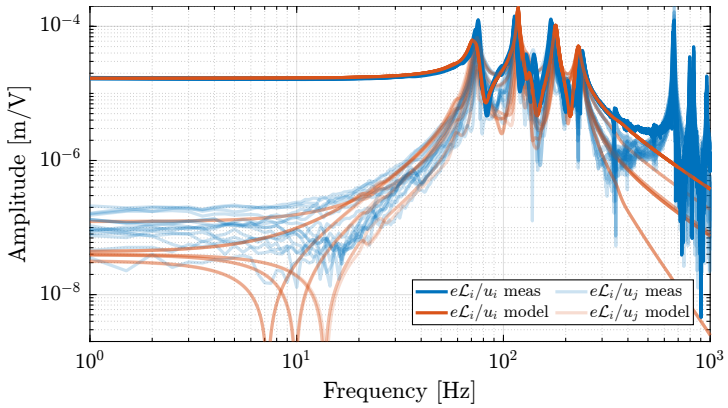

Figure 4.85: Decrease of the coupling after better R_z alignment.

4.5.2.3 Effect of Payload Mass

To determine how the system dynamics changes with the payload, open-loop identification was performed for four payload conditions shown in Figure 4.86. The obtained direct terms are compared with the model dynamics in Figure 4.87. It was found that the model well predicts the measured dynamics under all payload conditions. Therefore, the model can be used for model-based control if necessary.

It is interesting to note that the anti-resonances in the force sensor plant now appear as minimum-phase, as the model predicts (Figure 4.87b).

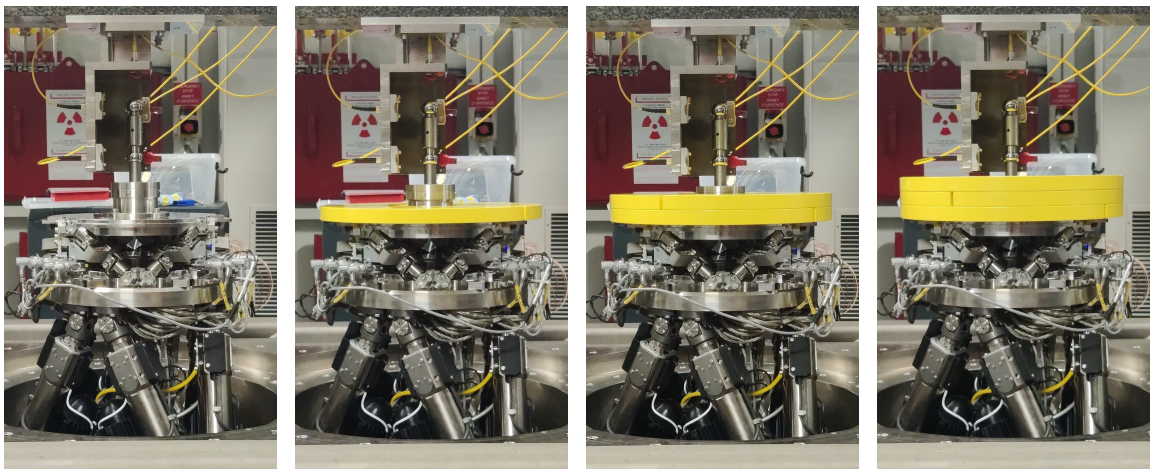

(a) $m = 0\,\text{kg}$ **(b)** $m = 13\,\text{kg}$ **(c)** $m = 26\,\text{kg}$ **(d)** $m = 39\,\text{kg}$

Figure 4.86: Four tested payload conditions: (a) no payload, (b) 13 kg payload, (c) 26 kg payload, (d) 39 kg payload.

4.5.2.4 Effect of Spindle Rotation

To verify that all the kinematics in Figure 4.82 are correct and to check whether the system dynamics is affected by Spindle rotation or not, three identification experiments were performed: no spindle rotation, spindle rotation at 36 deg/s and at 180 deg/s.

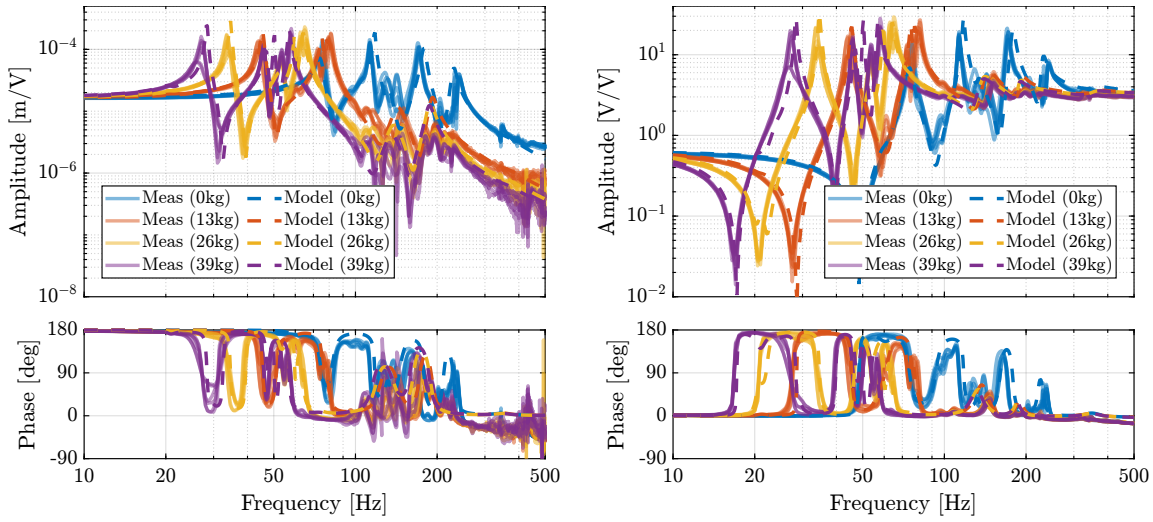

(a) from u to $\epsilon\mathcal{L}$ (strut error)

(b) from u to V_s (force sensor)

Figure 4.87: Comparison of the diagonal elements (i.e. "direct" terms) of the measured FRF matrix and the dynamics identified from the multi-body model. Both for the dynamics from u to $\epsilon\mathcal{L}$ (a) and from u to V_s (b).

The obtained dynamics from command signal u to estimated strut error $\epsilon\mathcal{L}$ are displayed in Figure 4.88. Both direct terms (Figure 4.88a) and coupling terms (Figure 4.88b) are unaffected by the rotation. The same can be observed for the dynamics from command signal to encoders and to force sensors. This confirms that spindle's rotation has no significant effect on plant dynamics. This also indicates that the metrology kinematics is correct and is working in real-time.

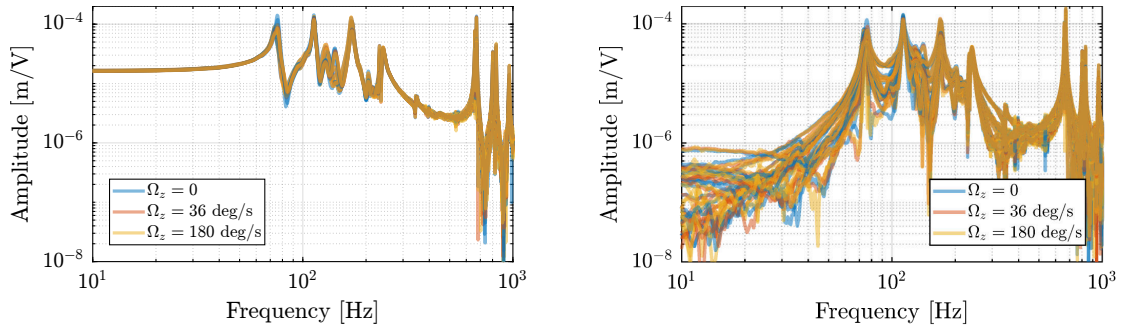

(a) Direct terms

(b) Coupling terms

Figure 4.88: Effect of the spindle rotation on the plant dynamics from u to $\epsilon\mathcal{L}$. Three rotational velocities are tested (0 deg/s, 36 deg/s and 180 deg/s). Both direct terms (a) and coupling terms (b) are displayed.

Conclusion

The identified FRFs from command signals $\boldsymbol{u}$ to the force sensors $\boldsymbol{V}_s$ and to the estimated strut errors $\boldsymbol{\epsilon\mathcal{L}}$ are well matching the dynamics of the developed multi-body model. The effect of payload mass is shown to be well predicted by the model, which can be useful if robust model based control is to be used. The spindle rotation has no visible effect on the measured dynamics, indicating that controllers should be robust against spindle rotation.

4.5.3 Decentralized Integral Force Feedback

In this section, the low authority control part is first validated. It consists of a decentralized Integral Force Feedback controller $\boldsymbol{K}_{\text{IFF}}$, with all the diagonal terms being equal (4.25).

$$\boldsymbol{K}_{\text{IFF}} = K_{\text{IFF}} \cdot \boldsymbol{I}_6 = \begin{bmatrix} K_{\text{IFF}} & & 0 \\ & \ddots & \\ 0 & & K_{\text{IFF}} \end{bmatrix} \tag{4.24}$$

The decentralized Integral Force Feedback is implemented as shown in the block diagram of Figure 4.89.

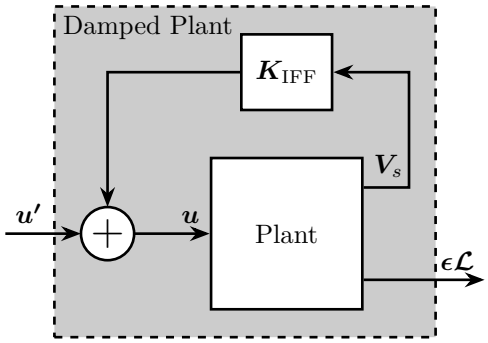

Figure 4.89: Block diagram of the implemented decentralized IFF controller. The controller $\boldsymbol{K}_{\text{IFF}}$ is a diagonal controller.

4.5.3.1 IFF Plant

As the multi-body model is used to evaluate the stability of the IFF controller and to optimize the achievable damping, it is first checked whether this model accurately represents the system dynamics.

In the previous section (Figure 4.87b), it was shown that the model well captures the dynamics from each actuator to its collocated force sensor, and that for all considered payloads. Nevertheless, it is also important to model accurately the coupling in the system. To verify that, instead of comparing the 36 elements of the 6×6 frequency response matrix from $\boldsymbol{u}$ to $\boldsymbol{V_s}$, only 6 elements are compared in Figure 4.90. Similar results were obtained for all other 30 elements and for the different payload conditions. This confirms that the multi-body model can be used to tune the IFF controller.

4.5.3.2 IFF Controller

A decentralized IFF controller was designed to add damping to the suspension modes of the nano-hexapod for all considered payloads. The frequency of the suspension modes are ranging from $\approx$ 30 Hz to $\approx$ 250 Hz (Figure 4.87b), and therefore, the IFF controller should provide integral action in this frequency range. A second-order high-pass filter (cut-off frequency of 10 Hz) was added to limit the low frequency gain (4.25).

$$K_{\text{IFF}} = g_0 \cdot \underbrace{\frac{1}{s}}_{\text{int}} \cdot \underbrace{\frac{s^2/\omega_z^2}{s^2/\omega_z^2 + 2\xi_z s/\omega_z + 1}}_{\text{2nd order LPF}}, \quad (g_0 = -100,\ \omega_z = 2\pi 10\,\text{rad/s},\ \xi_z = 0.7) \tag{4.25}$$

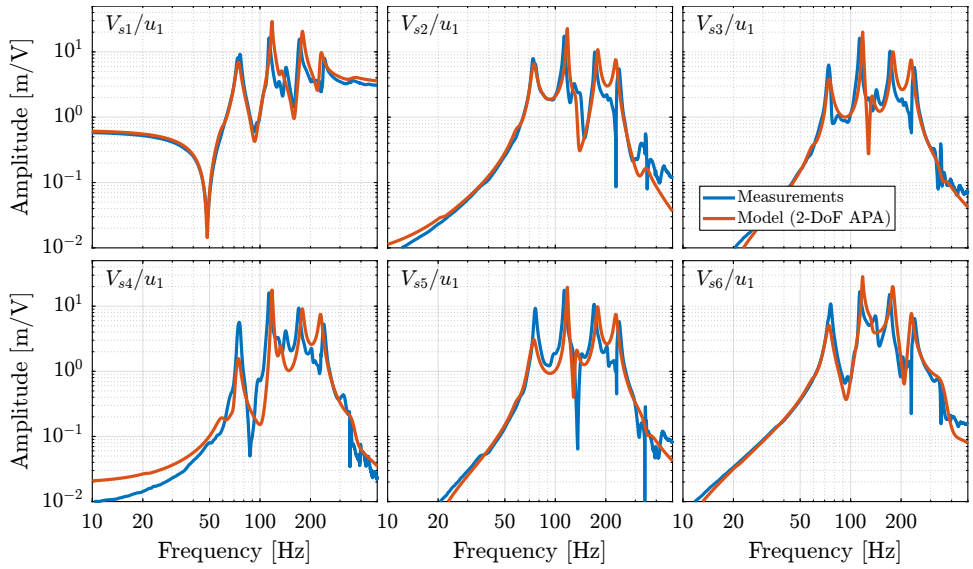

Figure 4.90: Comparison of the measured (in blue) and modelled (in red) FRFs from the first control signal u_1 to the six force sensor voltages V_{s1} to V_{s6}.

The bode plot of the decentralized IFF controller is shown in Figure 4.91a and the "decentralized loop-gains" for all considered payload masses are shown in Figure 4.91b. It can be seen that the loop-gain is larger than 1 around the suspension modes, which indicates that some damping should be added to the suspension modes.

To estimate the added damping, a root-locus plot was computed using the multi-body model (Figure 4.92). It can be seen that for all considered payloads, the poles are bounded to the "left-half plane" indicating that the decentralized IFF is robust. The closed-loop poles for the chosen gain value are represented by black crosses. It can be seen that while damping can be added for all payloads (as compared to the open-loop case), the optimal value of the gain is different for each payload. For low payload masses, a higher IFF controller gain can lead to better damping. However, in this study, it was chosen to implement a "fixed" (i.e. non-adaptive) decentralized IFF controller.

4.5.3.3 Damped Plant

As the model accurately represents the system dynamics, it can be used to estimate the damped plant, i.e. the transfer functions from $\boldsymbol{u}'$ to $\boldsymbol{\mathcal{L}}$. The obtained damped plants are compared to the open-loop plants in Figure 4.93a. The peak amplitudes corresponding to the suspension modes were approximately reduced by a factor 10 for all considered payloads, indicating the effectiveness of the decentralized IFF control strategy.

To experimentally validate the Decentralized IFF controller, it was implemented and the damped plants (i.e. the transfer function from $\boldsymbol{u}'$ to $\epsilon\boldsymbol{\mathcal{L}}$) were identified for all payload conditions. The obtained FRFs are compared with the model in Figure 4.93b verifying the good correlation between the predicted damped plant using the multi-body model and the experimental results.

Conclusion

The implementation of a decentralized Integral Force Feedback controller was successfully demonstrated. Using the multi-body model, the controller was designed and optimized to ensure stability across all payload conditions while providing significant damping of suspension modes. The experimental results validated the model predictions, showing

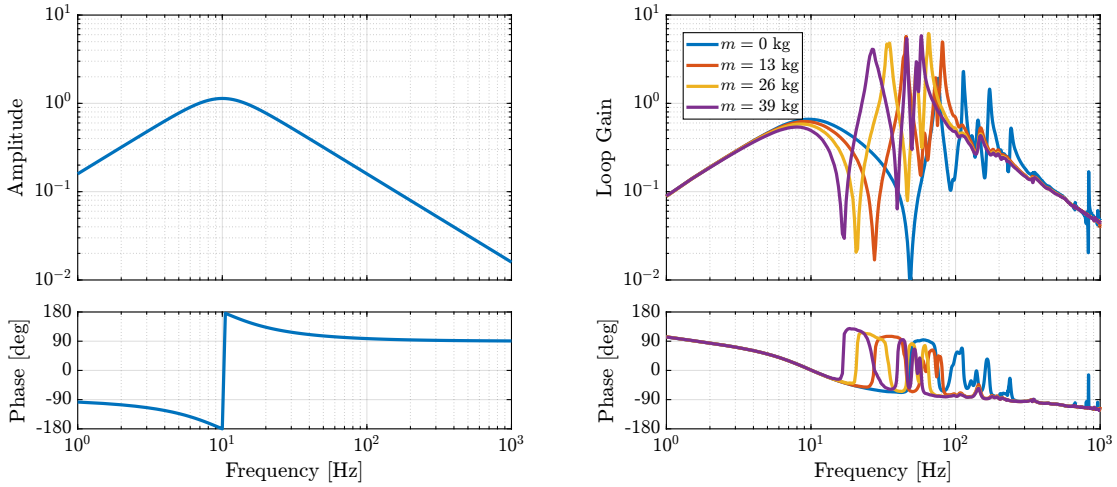

(a) Bode plot of K_{IFF}

(b) Decentralized loop gains

Figure 4.91: Bode plot of the decentralized IFF controller (a). The decentralized controller K_{IFF} multiplied by the identified dynamics from u_1 to V_{s1} for all payloads are shown in (b).

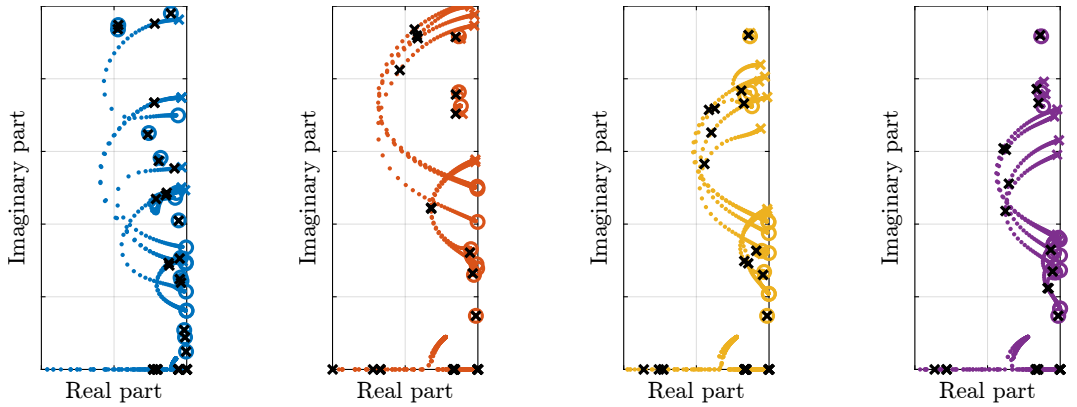

(a) $m = 0\,\text{kg}$ **(b)** $m = 13\,\text{kg}$ **(c)** $m = 26\,\text{kg}$ **(d)** $m = 39\,\text{kg}$

Figure 4.92: Root loci for the decentralized IFF controller, computed using the multi-body model. Black crosses indicate the closed-loop poles for the chosen value of the gain.

a reduction in peak amplitudes by approximately a factor of 10 across the full payload range (0 to 39 kg). Although higher gains could achieve better damping performance for lighter payloads, the chosen fixed-gain configuration represents a robust compromise that maintains stability and performance under all operating conditions. The good correlation between the modelled and measured damped plants confirms the effectiveness of using the multi-body model for both controller design and performance prediction.

4.5.4 High Authority Control in the Frame of the Struts

In this section, a High-Authority-Controller is developed to actively stabilize the sample position. The corresponding control architecture is shown in Figure 4.94.

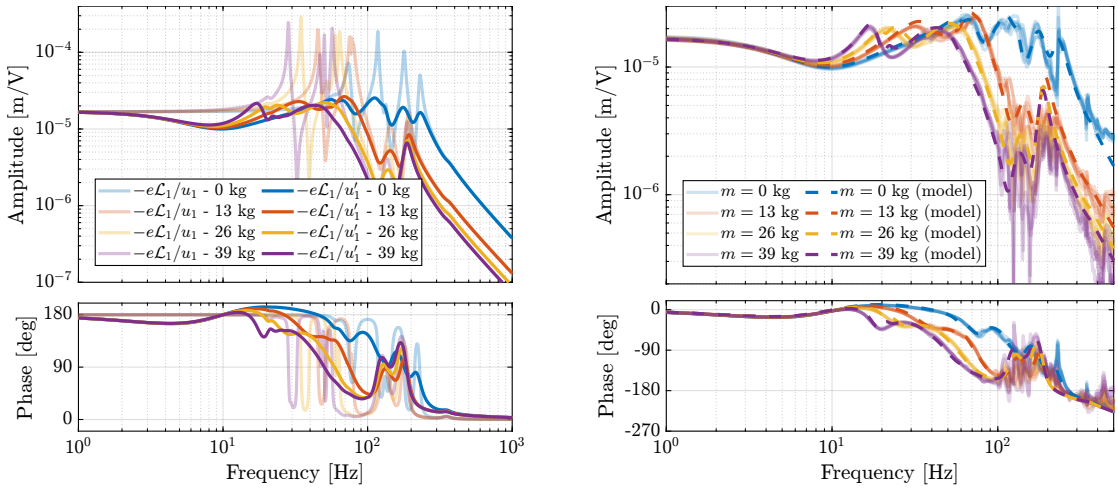

(a) Effect of IFF on the plant

(b) Comparison of model and experimental results

Figure 4.93: Comparison of the open-loop plant and the damped plant with decentralized IFF, estimated from the multi-body model (a). Comparison of measured damped and modelled plants for all considered payloads (b). Only "direct" terms ($\epsilon\mathcal{L}_i/u_i'$) are displayed for simplicity.

As the diagonal terms of the damped plants were found to be all equal (thanks to the system's symmetry and manufacturing and mounting uniformity, see Figure 4.93b), a diagonal high authority controller $\boldsymbol{K}_{\text{HAC}}$ is implemented with all diagonal terms being equal (4.26).

$$\boldsymbol{K}_{\text{HAC}} = K_{\text{HAC}} \cdot \boldsymbol{I}_6 = \begin{bmatrix} K_{\text{HAC}} & & 0 \\ & \ddots & \\ 0 & & K_{\text{HAC}} \end{bmatrix} \tag{4.26}$$

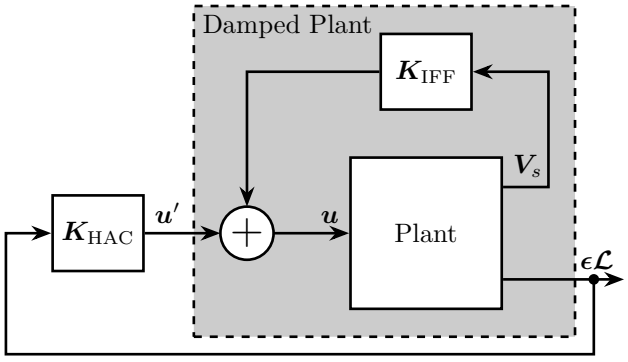

Figure 4.94: Block diagram of the implemented HAC-IFF controllers. The controller $\boldsymbol{K}_{\text{HAC}}$ is a diagonal controller.

4.5.4.1 Damped Plant

To verify whether the multi-body model accurately represents the measured damped dynamics, both the direct terms and coupling terms corresponding to the first actuator are compared in Figure 4.95. Considering the complexity of

the system's dynamics, the model can be considered to represent the system's dynamics with good accuracy, and can therefore be used to tune the feedback controller and evaluate its performance.

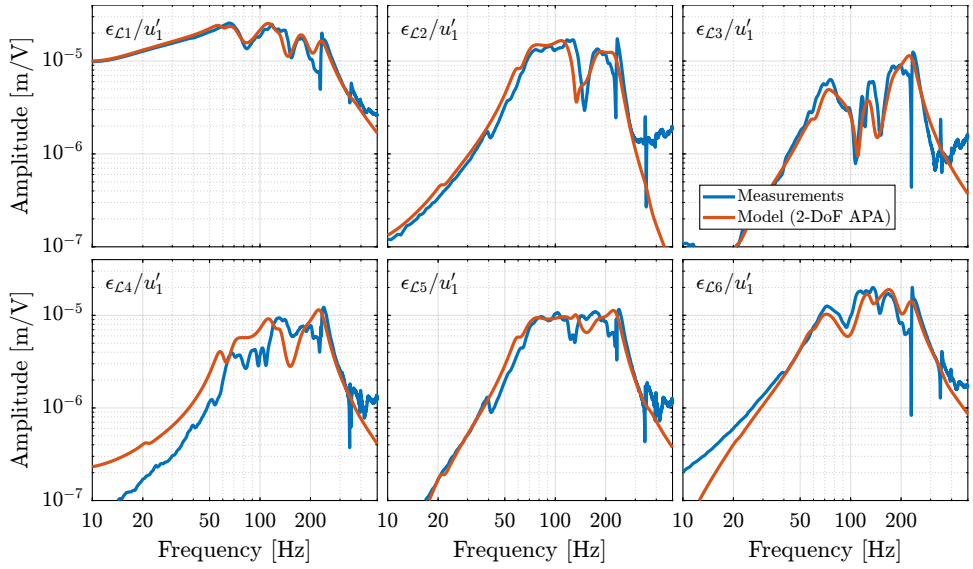

Figure 4.95: Comparison of the measured (in blue) and modelled (in red) FRFs from the first control signal (u'_1) of the damped plant to the estimated errors ($\epsilon_{\mathcal{L}_i}$) in the frame of the six struts by the external metrology.

The challenge here is to tune a high authority controller such that it is robust to the change in dynamics due to different payloads being used. Without using the HAC-LAC strategy, it would be necessary to design a controller that provides good performance for all undamped dynamics (blue curves in Figure 4.96), which is a very complex control problem. With the HAC-LAC strategy, the designed controller must be robust to all the damped dynamics (red curves in Figure 4.96), which is easier from a control perspective. This is one of the key benefits of using the HAC-LAC strategy.

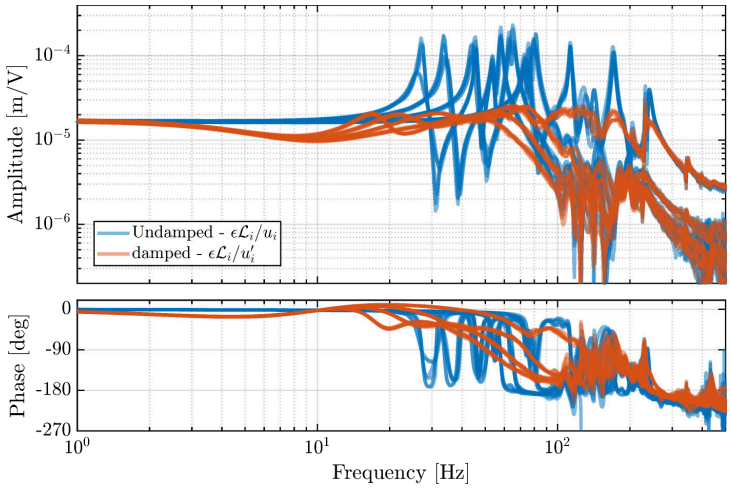

Figure 4.96: Comparison of the (six) direct terms for all (four) payload conditions in the undamped case (in blue) and the damped case (i.e. with the decentralized IFF being implemented, in red).

4.5.4.2 Interaction Analysis

The control strategy here is to apply a diagonal control in the frame of the struts; thus, it is important to determine the frequency at which the multivariable effects become significant, as this represents a critical limitation of the control approach. To conduct this interaction analysis, the Relative Gain Array (RGA) $\boldsymbol{\Lambda_G}$ is first computed using (4.27) for the plant dynamics identified with the multiple payload masses.

$$\boldsymbol{\Lambda_G}(\omega) = \boldsymbol{G}(j\omega) \star \left(\boldsymbol{G}(j\omega)^{-1}\right)^{\mathsf{T}}, \quad (\star \text{ means element wise multiplication}) \tag{4.27}$$

Then, RGA numbers are computed using (4.28) and are use as a metric for interaction [134, chapt. 3.4].

$$\text{RGA number}(\omega) = \|\boldsymbol{\Lambda_G}(\omega) - \boldsymbol{I}\|_{\text{sum}} \tag{4.28}$$

The obtained RGA numbers are compared in Figure 4.97. The results indicate that higher payload masses increase the coupling when implementing control in the strut reference frame (i.e., decentralized approach). This indicates that achieving high bandwidth feedback control is increasingly challenging as the payload mass increases. This behavior can be attributed to the fundamental approach of implementing control in the frame of the struts. Above the suspension modes of the nano-hexapod, the motion induced by the piezoelectric actuators is no longer dictated by kinematics but rather by the inertia of the different parts. This design choice, while beneficial for system simplicity, introduces inherent limitations in the system's ability to handle larger masses at high-frequency.

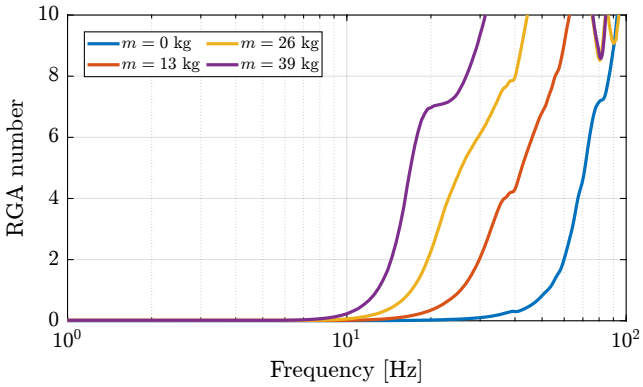

Figure 4.97: RGA-number for the damped plants - Comparison of all the payload conditions.

4.5.4.3 Robust Controller Design

A diagonal controller was designed to be robust against changes in payload mass, which means that every damped plant shown in Figure 4.96 must be considered during the controller design. For this controller design, a crossover frequency of 5 Hz was chosen to limit the multivariable effects, as explain in Section 4.5.4.2. One integrator is added to increase the low-frequency gain and a first-order low-pass filter with a cut-off frequency of 30 Hz is added to improve the robustness to dynamical uncertainty at high-frequency. The controller transfer function is shown in (4.29).

$$K_{\text{HAC}}(s) = g_0 \cdot \underbrace{\frac{\omega_c}{s}}_{\text{int}} \cdot \underbrace{\frac{1}{1 + \frac{s}{\omega_0}}}_{\text{LPF}}, \quad (\omega_c = 2\pi 5 \text{ rad/s},\ \omega_0 = 2\pi 30 \text{ rad/s}) \tag{4.29}$$

The obtained "decentralized" loop-gains (i.e. the diagonal element of the controller times the diagonal terms of the plant) are shown in Figure 4.98a. The closed-loop stability was verified by computing the characteristic Loci (Figure 4.98b). However, small stability margins were observed for the highest mass, indicating that some multivariable effects are at play.

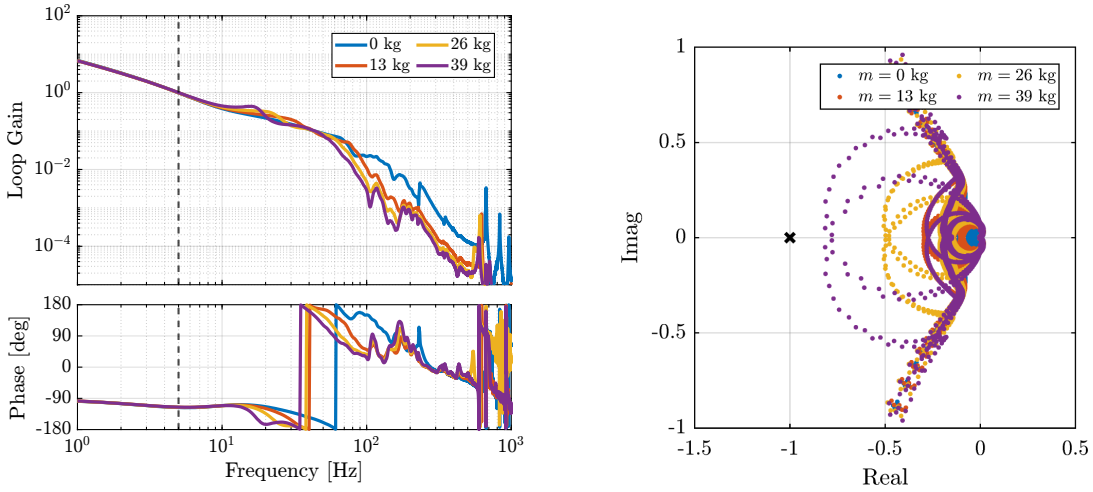

(a) Loop Gains

(b) Characteristic Loci

Figure 4.98: "Decentralized loop-gains" (a) and characteristic loci (b) for the robust high authority controller.

4.5.4.4 Performance - Tomography Scans

To estimate the performances that can be expected with this HAC-LAC architecture and the designed controller, simulations of tomography experiments were performed[1]. The rotational velocity was set to 180 deg/s, and no payload was added on top of the nano-hexapod. An open-loop simulation and a closed-loop simulation were performed and compared in Figure 4.99. The obtained closed-loop positioning accuracy was found to comply with the requirements as it succeeded to keep the PoI on the beam (Figure 4.99b).

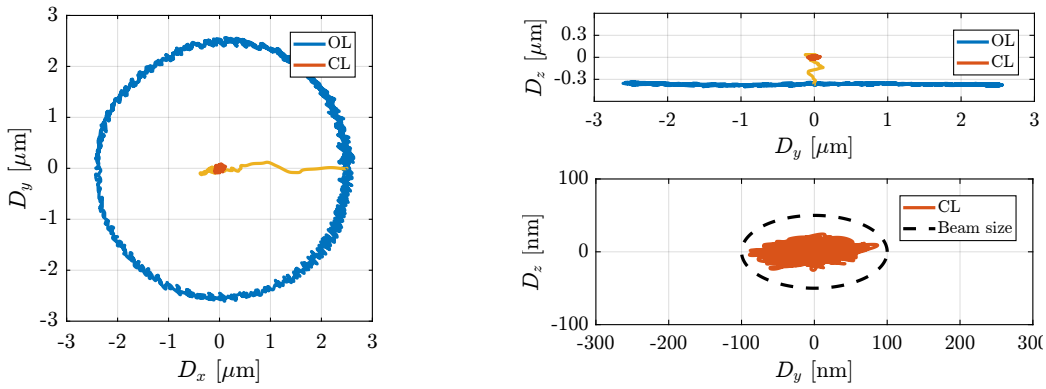

(a) XY plane

(b) YZ plane

Figure 4.99: Position error of the sample in the XY (a) and YZ (b) planes during a simulation of a tomography experiment at 180 deg/s. No payload is placed on top of the nano-hexapod.

[1]Note that the eccentricity of the PoI with respect to the Spindle rotation axis has been tuned based on measurements.

4.5.4.5 Robustness - Tomography Scans

To verify the robustness against payload mass variations, four simulations of tomography experiments were performed with payloads as shown Figure 4.86 (i.e. 0 kg, 13 kg, 26 kg and 39 kg). The rotational velocity was set at 6 deg/s, which is the typical rotational velocity for heavy samples.

The closed-loop systems were stable under all payload conditions, indicating good control robustness. However, the positioning errors worsen as the payload mass increases, especially in the lateral D_y direction, as shown in Figure 4.100. However, it was decided that this controller should be tested experimentally and improved only if necessary.

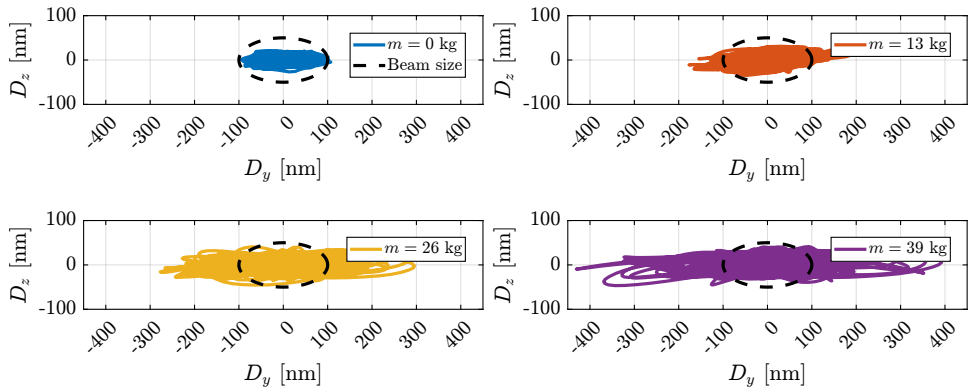

Figure 4.100: Positioning errors in the YZ plane during closed-loop simulations of tomography experiments.

Conclusion

In this section, a High-Authority-Controller was developed to actively stabilize the sample position. The multi-body model was first validated by comparing it with the measured frequency responses of the damped plant, which showed good agreement for both direct terms and coupling terms. This validation confirmed that the model can be reliably used to tune the feedback controller and evaluate its performance.

An interaction analysis using the RGA-number was then performed, which revealed that higher payload masses lead to increased coupling when implementing control in the strut reference frame. Based on this analysis, a diagonal controller with a crossover frequency of 5 Hz was designed, incorporating an integrator and a first-order low-pass filter.

Finally, tomography experiments were simulated to validate the HAC-LAC architecture. The closed-loop system remained stable under all tested payload conditions (0 to 39 kg). With no payload at 180 deg/s, the NASS successfully maintained the sample PoI in the beam, which fulfilled the specifications. At 6 deg/s, although the positioning errors increased with the payload mass (particularly in the lateral direction), the system remained stable. These results demonstrate both the effectiveness and limitations of implementing control in the frame of the struts.

4.5.5 Validation with Scientific Experiments

In this section, the goal is to evaluate the performance of the NASS and validate its use to perform typical scientific experiments. However, the online metrology prototype (presented in Section 4.5.1) does not allow samples to be placed on top of the nano-hexapod while being illuminated by the x-ray beam. Nevertheless, to fully validate the NASS, typical motions performed during scientific experiments can be mimicked, and the positioning performances can be evaluated.

Several scientific experiments were replicated, such as:

- Tomography scans: continuous rotation of the Spindle along the vertical axis (Section 4.5.5.1)
- Reflectivity scans: R_y rotations using the tilt-stage (Section 4.5.5.2)
- Vertical layer scans: D_z step motion or ramp scans using the nano-hexapod (Section 4.5.5.3)
- Lateral scans: D_y scans using the T_y translation stage (Section 4.5.5.4)
- Diffraction Tomography:continuous R_z rotation using the Spindle and lateral D_y scans performed at the same time using the translation stage (Section 4.5.5.5)

Unless explicitly stated, all closed-loop experiments were performed using the robust (i.e. conservative) high authority controller designed in Section 4.5.4.3. Higher performance controllers using complementary filters are investigated in Section 4.5.5.6.

For each experiment, the obtained performances are compared to the specifications for the most demanding case in which nano-focusing optics are used to focus the beam down to 200 nm $\times$ 100 nm. In this case, the goal is to keep the sample's PoI in the beam, and therefore the D_y and D_z positioning errors should be less than 200 nm and 100 nm peak-to-peak, respectively. The R_y error should be less than 1.7 µrad peak-to-peak. In terms of RMS errors, this corresponds to 30 nm in D_y, 15 nm in D_z and 250 nrad in R_y (a summary of the specifications is given in Table 4.16).

Results obtained for all experiments are summarized and compared to the specifications in Section 4.5.5.6.

Table 4.16: Positioning specifications for the Nano-Active-Stabilization-System.

	D_y	D_z	R_y
peak 2 peak	200 nm	100 nm	1.7 µrad
RMS	30 nm	15 nm	250 nrad

4.5.5.1 Tomography Scans

Slow Tomography Scans First, tomography scans were performed with a rotational velocity of 6 deg/s for all considered payload masses (shown in Figure 4.86). Each experimental sequence consisted of two complete spindle rotations: an initial open-loop rotation followed by a closed-loop rotation. The experimental results for the 26 kg payload are presented in Figure 4.101a.

Due to the static deformation of the micro-station stages under payload loading, a significant eccentricity was observed between the PoI and the spindle rotation axis. To establish a theoretical lower bound for open-loop errors, an ideal scenario was assumed, where the PoI perfectly aligns with the spindle rotation axis. This idealized case was simulated by first calculating the eccentricity through circular fitting (represented by the dashed black circle in Figure 4.101a), and then subtracting it from the measured data, as shown in Figure 4.101b. While this approach likely underestimates actual open-loop errors, as perfect alignment is practically unattainable, it enables a more balanced comparison with closed-loop performance.

The residual motion (i.e. after compensating for eccentricity) in the YZ is compared against the minimum beam size, as illustrated in Figure 4.102. Results are indicating the NASS succeeds in keeping the sample's PoI on the beam, except for the highest mass of 39 kg for which the lateral motion is a bit too high. These experimental findings are consistent with the predictions from the tomography simulations presented in Section 4.5.4.5.

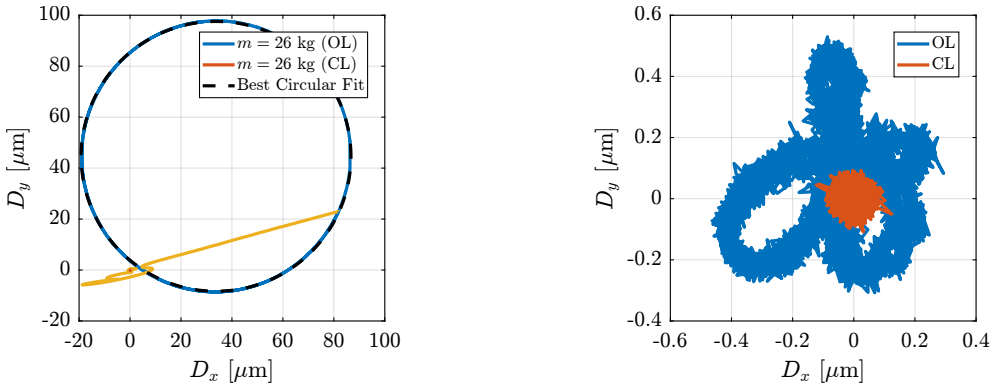

(a) Errors in XY plane

(b) Removed eccentricity

Figure 4.101: Tomography experiment with a rotation velocity of 6 deg/s, and payload mass of 26 kg. Errors in the XY plane are shown in (a). The estimated eccentricity is represented by the black dashed circle. The errors with subtracted eccentricity are shown in (b).

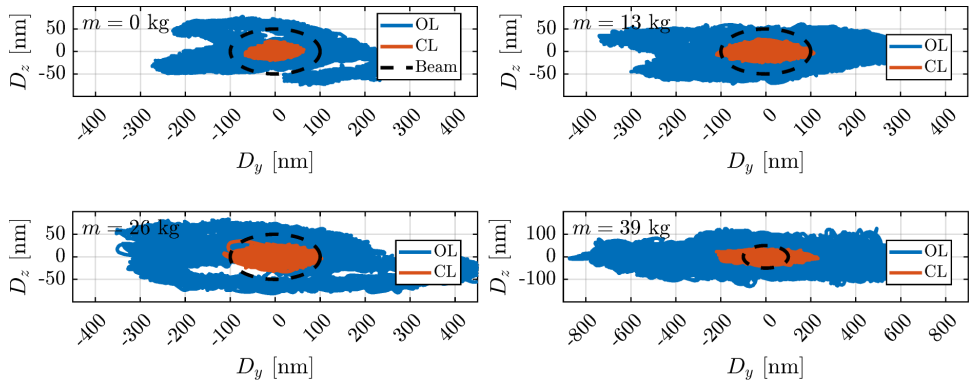

Figure 4.102: Measured errors in the YZ plane during tomography experiments at 6 deg/s for all considered payloads. In the open-loop case, the effect of eccentricity is removed from the data.

Fast Tomography Scans A tomography experiment was then performed with the highest rotational velocity of the Spindle: 180 deg/s[1]. The trajectory of the PoI during the fast tomography scan is shown in Figure 4.103. Although the experimental results closely match the simulation results (Figure 4.99), the actual performance was slightly lower than predicted. Nevertheless, even with this robust (i.e. conservative) HAC implementation, the system performance was already close to the specified requirements.

Cumulative Amplitude Spectra A comparative analysis was conducted using three tomography scans at 180 deg/s to evaluate the effectiveness of the HAC-LAC strategy in reducing positioning errors. The scans were performed under three conditions: open-loop, with decentralized IFF control, and with the complete HAC-LAC strategy. For this specific measurement, an enhanced high authority controller (discussed in Section 4.5.5.6) was optimized for low payload masses to meet the performance requirements.

Figure 4.104 presents the cumulative amplitude spectra of the position errors for all three cases. The results reveal two distinct control contributions: the decentralized IFF effectively attenuates vibrations near the nano-hexapod suspension modes (an achievement not possible with HAC alone), while the high authority controller suppresses low-frequency

[1] The highest rotational velocity of 360 deg/s could not be tested due to an issue in the Spindle's controller.

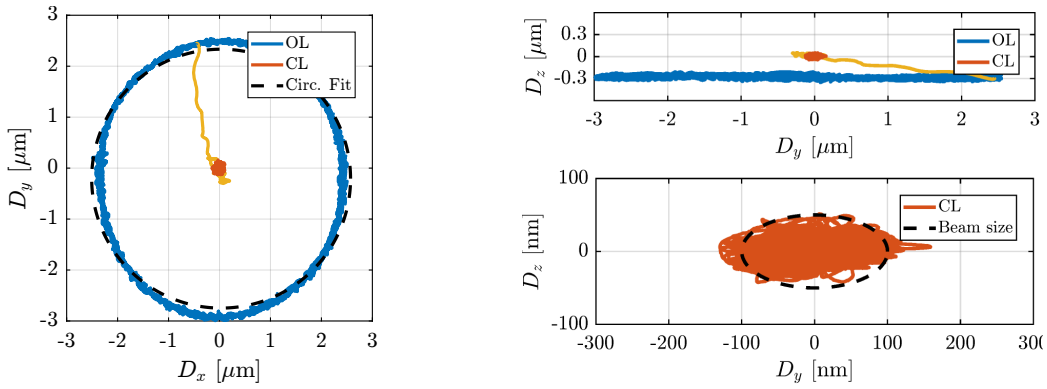

(a) XY plane **(b)** YZ plane

Figure 4.103: Experimental results of tomography experiment at 180 deg/s without payload. The position error of the sample is shown in the XY (a) and YZ (b) planes.

vibrations primarily arising from Spindle guiding errors. Notably, the spectral patterns in Figure 4.104 closely resemble the cumulative amplitude spectra computed in the project's early stages (Figure 2.27b in page45).

This experiment also illustrates that when needed, performance can be enhanced by designing controllers for specific experimental conditions rather than relying solely on robust controllers able to accommodate all payloads.

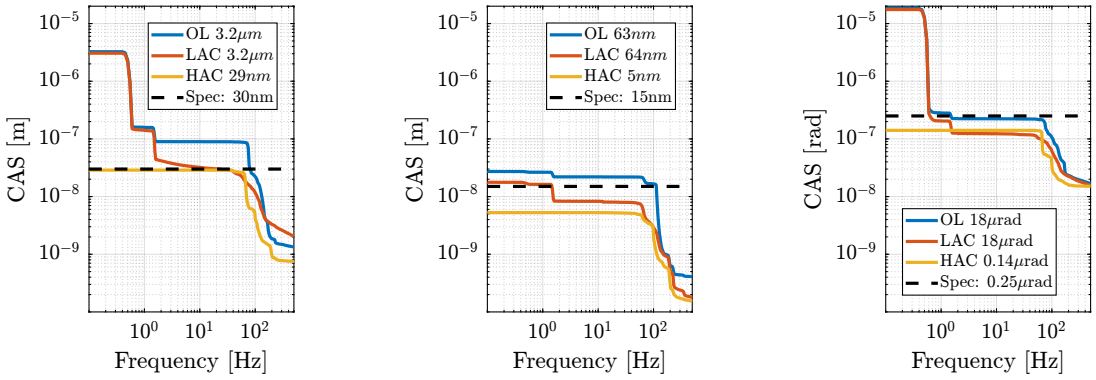

(a) Lateral (D_y) **(b)** Vertical (D_z) **(c)** Tilt (R_y)

Figure 4.104: Cumulative Amplitude Spectrum for tomography experiments at 180 deg/s. Open-Loop case, IFF, and HAC-LAC are compared. Specifications are indicated by black dashed lines. The RMS values are indicated in the legend.

4.5.5.2 Reflectivity Scans

X-ray reflectivity measurements involve scanning thin structures, particularly solid/liquid interfaces, through the beam by varying the R_y angle. In this experiment, a R_y scan was executed at a rotational velocity of 100 µrad/s, and the closed-loop positioning errors were monitored (Figure 4.105). The results confirmed that the NASS successfully maintained the PoI within the specified beam parameters throughout the scanning process.

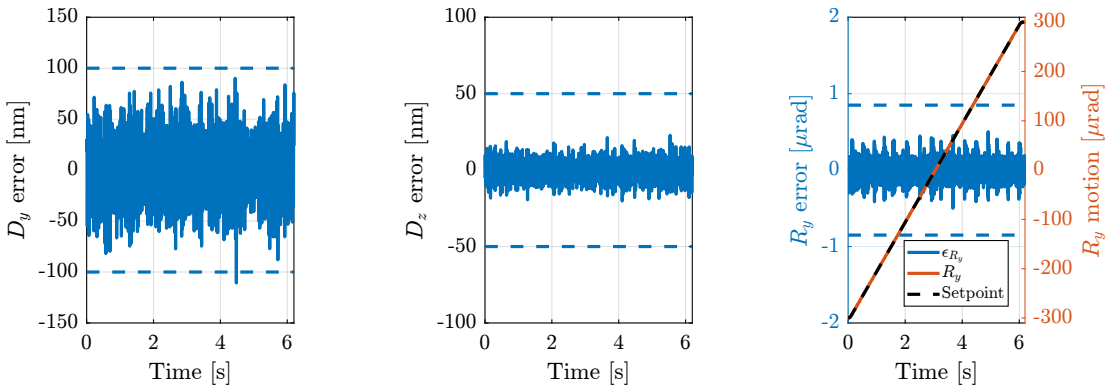

(a) Lateral (D_y) **(b)** Vertical (D_z) **(c)** Tilt (R_y)

Figure 4.105: Reflectivity scan (R_y) with a rotational velocity of 100 µrad/s.

4.5.5.3 Dirty Layer Scans

In some cases, samples are composed of several atomic "layers" that are first aligned in the horizontal plane through R_x and R_y positioning, followed by vertical scanning with precise D_z motion. These vertical scans can be executed either continuously or in a step-by-step manner.

Step by Step D_z Motion The vertical step motion was performed exclusively with the nano-hexapod. Testing was conducted across step sizes ranging from 10 nm to 1 µm. Results are presented in Figure 4.106. The system successfully resolved 10 nm steps (red curve in Figure 4.106a) if a 50ms integration time is considered for the detectors, which is compatible with many experimental requirements.

In step-by-step scanning procedures, the settling time is a critical parameter as it significantly affects the total experiment duration. The system achieved a response time of approximately 70 ms to reach the target position (within ±20 nm), as demonstrated by the 1 µm step response in Figure 4.106c. The settling duration typically decreases for smaller step sizes.

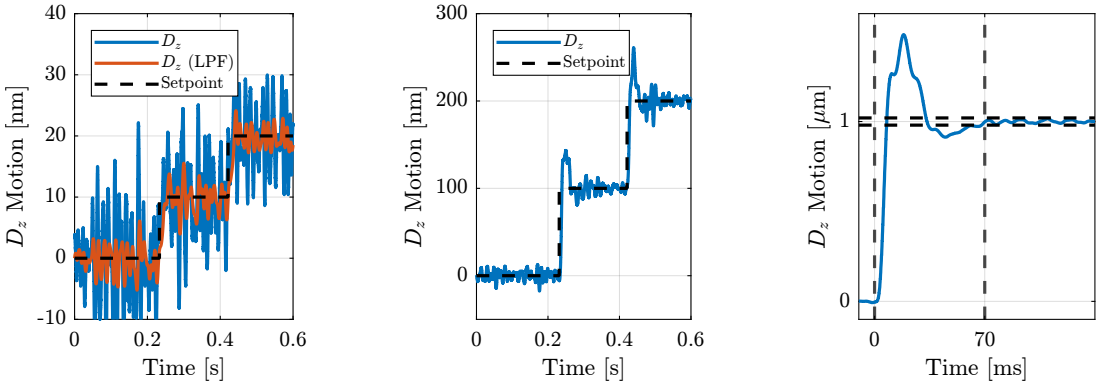

(a) 10 nm steps **(b)** 100 nm steps **(c)** 1 µm step

Figure 4.106: Vertical steps performed with the nano-hexapod. 10 nm steps are shown in (a) with the low-pass filtered data corresponding to an integration time of 50 ms. 100 nm steps are shown in (b). The response time to reach a peak-to-peak error of ±20 nm is ≈ 70 ms as shown in (c) for a 1 µm step.

CONTINUOUS D_z MOTION: DIRTY LAYER SCANS For these and subsequent experiments, the NASS performs "ramp scans" (constant velocity scans). To eliminate tracking errors, the feedback controller incorporates two integrators, compensating for the plant's lack of integral action at low frequencies.

Initial testing at 10 µm/s demonstrated positioning errors well within specifications (indicated by dashed lines in Figure 4.107).

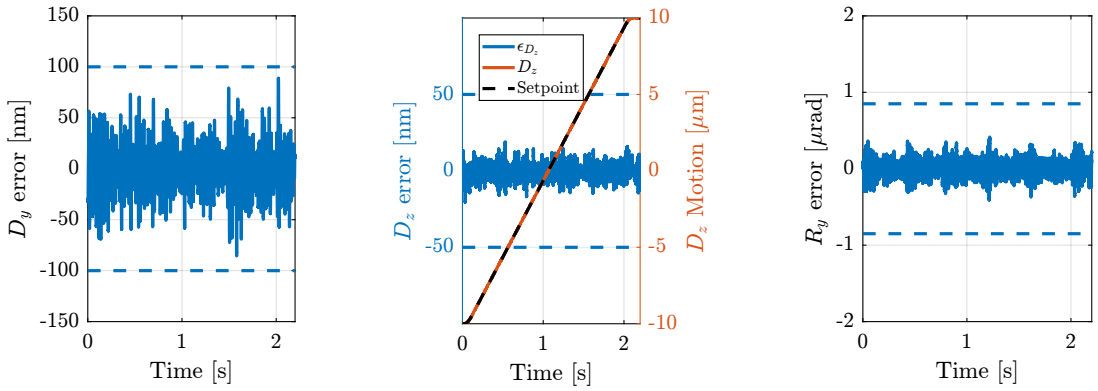

(a) Vertical (D_y) **(b)** Horizontal (D_z) **(c)** Tilt (R_y)

Figure 4.107: D_z scan at a velocity of 10 µm/s. D_z setpoint, measured position and error are shown in (b). Errors in D_y and R_y are respectively shown in (a) and (c).

A subsequent scan at 100 µm/s - the maximum velocity for high-precision D_z scans[1] - maintains positioning errors within specifications during the constant velocity phase, with deviations occurring only during acceleration and deceleration phases (Figure 4.108). Since detectors typically operate only during the constant velocity phase, these transient deviations do not compromise the measurement quality. However, performance during acceleration phases could be enhanced through the implementation of feedforward control.

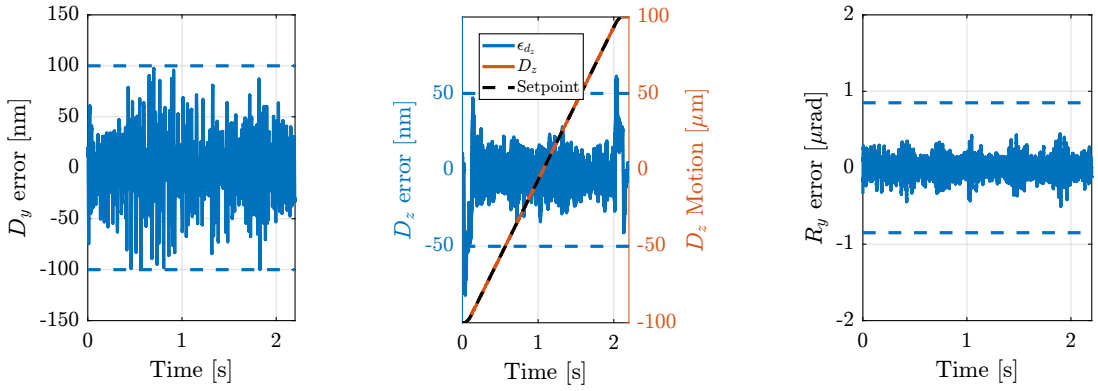

(a) Lateral (D_y) **(b)** Vertical (D_z) **(c)** Tilt (R_y)

Figure 4.108: D_z scan at a velocity of 100 µm/s. D_z setpoint, measured position and error are shown in (b). Errors in D_y and R_y are respectively shown in (a) and (c).

[1] Such scan could corresponding to a 1ms integration time (which is typically the smallest integration time) and 100 nm "resolution" (equal to the vertical beam size).

4.5.5.4 Lateral Scans

Lateral scans are executed using the T_y stage. The stepper motor controller[1] generates a setpoint that is transmitted to the Speedgoat. Within the Speedgoat, the system computes the positioning error by comparing the measured D_y sample position against the received setpoint, and the Nano-Hexapod compensates for positioning errors introduced during T_y stage scanning. The scanning range is constrained ± 100 µm due to the limited acceptance of the metrology system.

Slow Scan Initial testing were made with a scanning velocity of 10 µm/s, which is typical for these experiments. Figure 4.109 compares the positioning errors between open-loop (without NASS) and closed-loop operation. In the scanning direction, open-loop measurements reveal periodic errors (Figure 4.109a) attributable to the T_y stage's stepper motor. These micro-stepping errors, which are inherent to stepper motor operation, occur 200 times per motor rotation with approximately 1 mrad angular error amplitude. Given the T_y stage's lead screw pitch of 2 mm, these errors manifest as 10 µm periodic oscillations with $\approx$ 300 nm amplitude, which can indeed be seen in the open-loop measurements (Figure 4.109a).

In the vertical direction (Figure 4.109b), open-loop errors likely stem from metrology measurement error because the top interferometer points at a spherical target surface (see Figure 4.81a). Under closed-loop control, positioning errors remain within specifications in all directions.

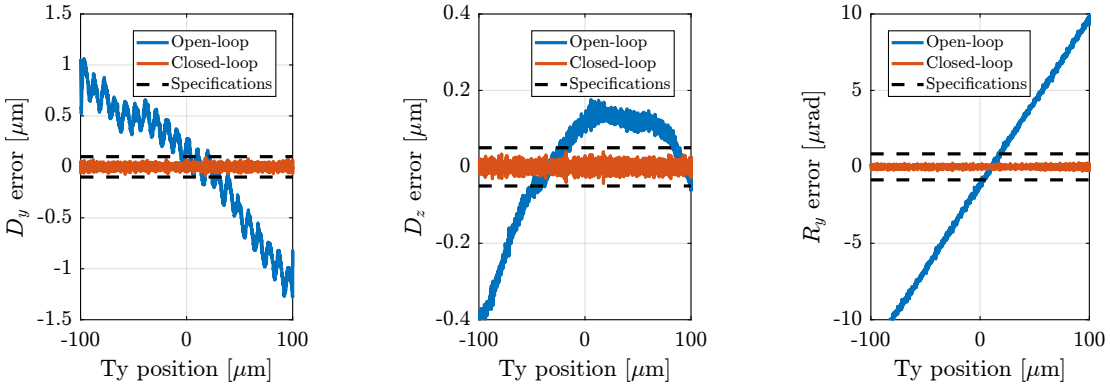

(a) Lateral (D_y) **(b)** Vertical (D_z) **(c)** Tilt (R_y)

Figure 4.109: Open-loop (in blue) and closed-loop (i.e. using the NASS, in red) during a 10 µm/s scan with the T_y stage.

Fast Scan The system performance was evaluated at an increased scanning velocity of 100 µm/s, and the results are presented in Figure 4.110. At this velocity, the micro-stepping errors generate 10 Hz vibrations, which are further amplified by micro-station resonances. These vibrations exceeded the NASS feedback controller bandwidth, resulting in limited attenuation under closed-loop control. This limitation exemplifies why stepper motors are suboptimal for "long-stroke/short-stroke" systems requiring precise scanning performance [37].

Two potential solutions exist for improving high-velocity scanning performance. First, the T_y stage's stepper motor could be replaced by a three-phase torque motor. Alternatively, since closed-loop errors in D_z and R_y directions remain within specifications (Figures 4.110b and 4.110c), detector triggering could be based on measured D_y position rather than time or T_y setpoint, reducing sensitivity to D_y vibrations. For applications requiring small D_y scans, the nano-hexapod can be used exclusively, although with limited stroke capability.

[1] The "IcePAP" [74] which is developed at the ESRF.

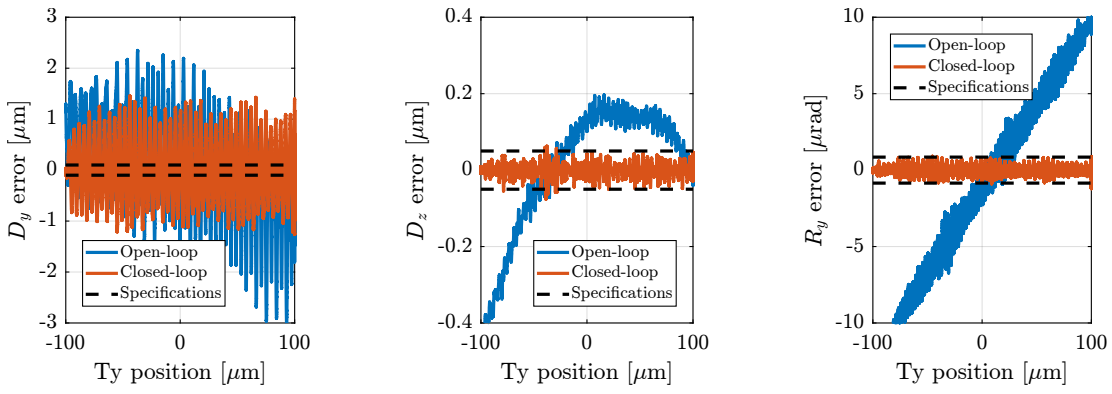

(a) Lateral (D_y) **(b)** Vertical (D_z) **(c)** Tilt (R_y)

Figure 4.110: Open-Loop (in blue) and Closed-loop (i.e. using the NASS, in red) during a 100 µm/s scan with the T_y stage.

4.5.5.5 Diffraction Tomography

In diffraction tomography experiments, the micro-station performs combined motions: continuous rotation around the R_z axis while performing lateral scans along D_y. For this validation, the spindle maintained a constant rotational velocity of 6 deg/s while the nano-hexapod performs the lateral scanning motion. To avoid high-frequency vibrations typically induced by the stepper motor, the T_y stage was not used, which constrained the scanning range to approximately ± 100 µm/s. The system performance was evaluated at three lateral scanning velocities: 0.1 mm/s, 0.5 mm/s, and 1 mm/s. Figure 4.111 presents both the D_y position setpoints and the corresponding measured D_y positions for all tested velocities.

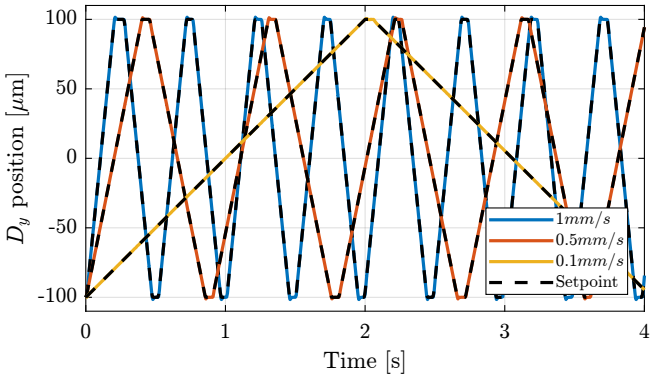

Figure 4.111: Lateral (D_y) motion for several configured velocities.

The positioning errors measured along D_y, D_z, and R_y directions are displayed in Figure 4.112. The system maintained positioning errors within specifications for both D_z and R_y (Figures 4.112b and 4.112c). However, the lateral positioning errors exceeded specifications during the acceleration and deceleration phases (Figure 4.112a). These large errors occurred only during $\approx$ 20 ms intervals; thus, a delay of 20 ms could be implemented in the detector the avoid integrating the beam when these large errors are occurring. Alternatively, a feedforward controller could improve the lateral positioning accuracy during these transient phases.

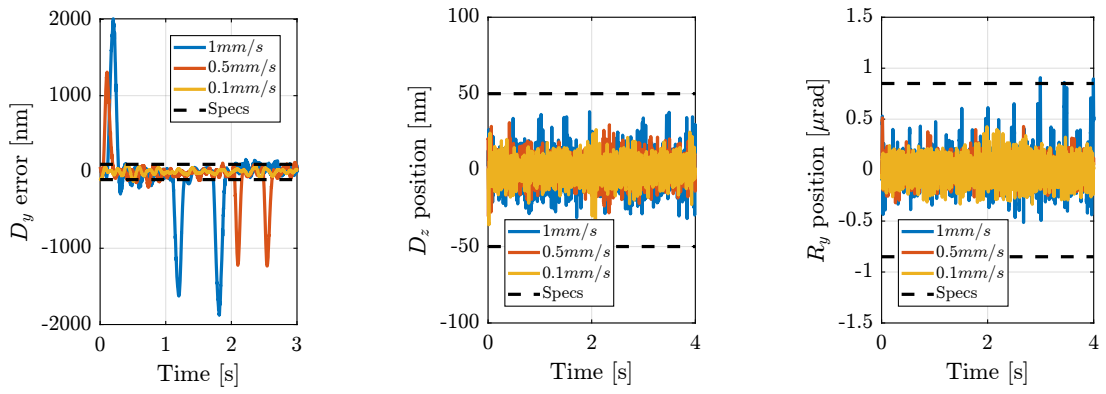

(a) D_y **(b)** D_z **(c)** R_y

Figure 4.112: Diffraction tomography scans (combined R_z and D_y motions) at several D_y velocities, $\Omega_z = 6$ deg/s.

4.5.5.6 Feedback Control using Complementary Filters

A control architecture based on complementary filters to shape the closed-loop transfer functions was proposed during the detail design phase (Section 3.3.3). Experimental validation of this architecture using the NASS is presented herein.

Given that performance requirements are specified in the Cartesian frame, decoupling of the plant within this frame was achieved using Jacobian matrices. Consequently, the control space comprises the directions D_x, D_y, D_z, R_x, and R_y. Control performance in each of these directions can be tuned independently. A schematic of the proposed control architecture is illustrated in Figure 4.113.

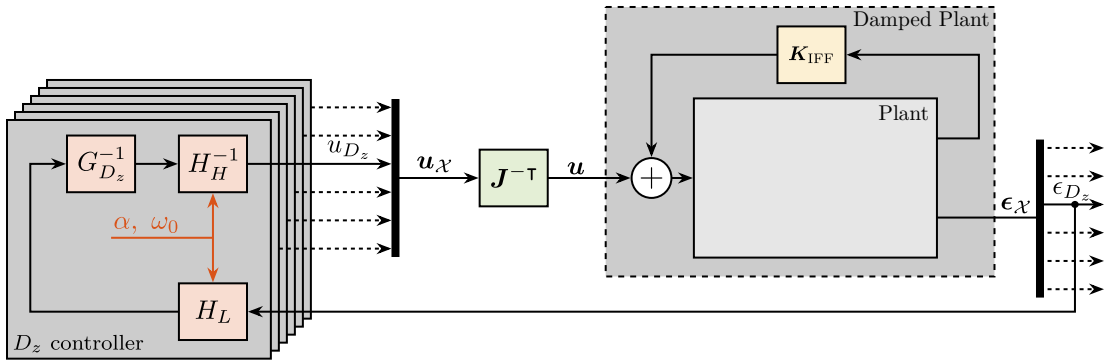

Figure 4.113: Control architecture using complementary filters proposed in Section 3.3.3, here adapted for the NASS. Jacobian matrices are used to have the control in the Cartesian frame. Only the D_z controller is shown. H_L and H_H are complementary filters.

Implementation of this control architecture necessitates a plant model, which must subsequently be inverted. This plant model was derived from the multi-body model incorporating the previously detailed 2-DoF APA (Section 4.1.3) model and 4-DoF flexible joints, such that the model order stays relatively low. Analytical formulas for complementary filters having 40 dB/dec slopes, proposed in Section 3.3.3.3, were used during this experimental validation.

An initial experimental validation was conducted under no-payload conditions, with control applied solely to the D_y, D_z, and R_y directions. Increased control bandwidth was achieved for the D_z and R_y directions through appropriate

tuning of the parameter ω_0. The experimentally measured closed-loop sensitivity transfer functions corresponding to these three controlled directions are presented in Figure 4.114a.

Another test was conducted with a 26 kg payload. For this configuration, complementary filters were implemented with $\omega_0 = 2\pi \cdot 10$ rad/s, and parameter α was varied. The resulting experimentally obtained closed-loop transfer functions are compared against the theoretical complementary filter responses in Figure 4.114b. As illustrated in the figure, a close correspondence between the measured closed-loop responses and the target complementary filter magnitude was observed. It also shows that the parameter α provides a mechanism for managing the trade-off between low-frequency disturbance rejection performance and the potential amplification of disturbances within the crossover frequency region.

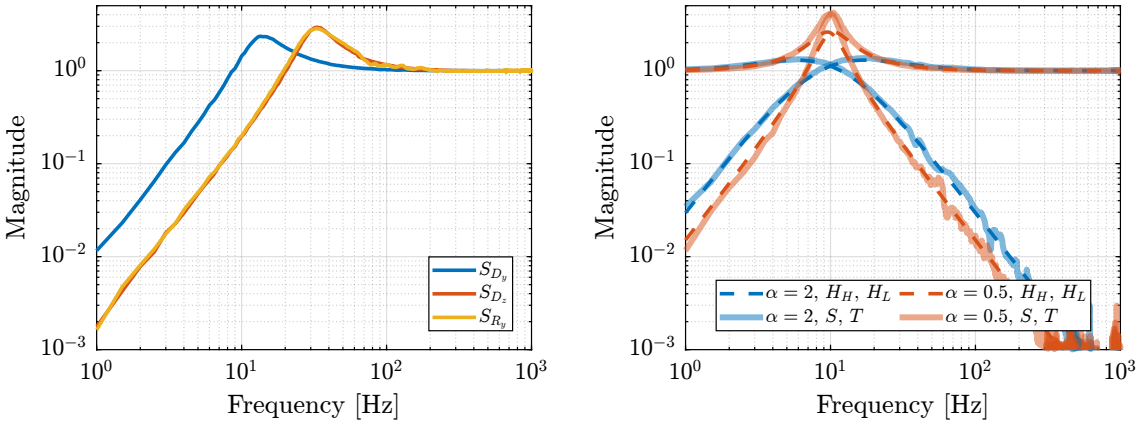

(a) Choice of bandwidth using ω_0, $m = 0$ kg

(b) Effect of a change of α, $m = 26$ kg

Figure 4.114: Measured closed-loop transfer functions. Different bandwidth can be specified for different directions using ω_0 (a). The shape can be adjusted using parameter α (b).

Finally, ω_0 was gradually increased to estimate the maximum bandwidth (i.e. the best low frequency disturbance rejection) that can be achieved with this architecture. No payload was used for this test, and the parameter ω_0 was increased for the controllers in the D_y and D_z directions. A value $\omega_0 = 2\pi \cdot 60$ rad/s could be achieved. Measured closed-loop transfer functions are shown in Figure 4.115, indicating a reduction of disturbances in the considered direction of 1000 at 1 Hz. For higher values of ω_0, the system became unstable in the vertical direction, probably because of the resonance at 250 Hz that is not well captured with the multi-body model (Figure 4.93b).

Conclusion

A comprehensive series of experimental validations was conducted to evaluate the NASS performance over a wide range of typical scientific experiments. The system demonstrated robust performance in most scenarios, with positioning errors generally remaining within specified tolerances (30 nm RMS in D_y, 15 nm RMS in D_z, and 250 nrad RMS in R_y).

For tomography experiments, the NASS successfully maintained good positioning accuracy at rotational velocities up to 180 deg/s with light payloads, though performance degraded somewhat with heavier masses. The HAC-LAC control architecture proved particularly effective, with the decentralized IFF providing damping of nano-hexapod suspension modes, while the high authority controller addressed low-frequency disturbances.

The vertical scanning capabilities were validated in both step-by-step and continuous motion modes. The system successfully resolved 10 nm steps with 50 ms detector integration time, while maintaining positioning accuracy during continuous scans at speeds up to 100 µm/s.

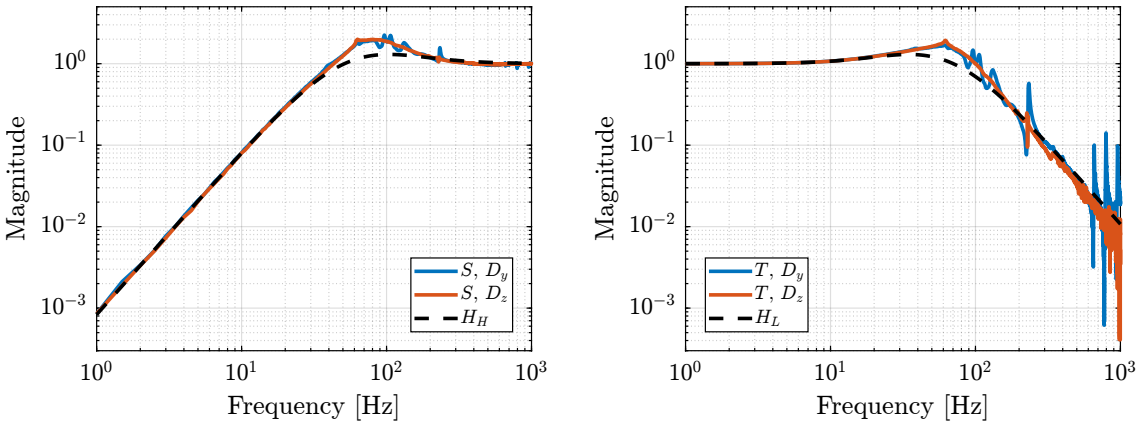

(a) Sensitivity

(b) Complementary Sensitivity

Figure 4.115: Measured Closed-Loop Sensitivity (a) and Complementary Sensitivity (b) transfer functions for the highest tested parameter $\omega_0 = 2\pi \cdot 60$ rad/s.

For lateral scanning, the system performed well at moderate speeds (10 µm/s) but showed limitations at higher velocities (100 µm/s) due to stepper motor-induced vibrations in the T_y stage.

The most challenging test case - diffraction tomography combining rotation and lateral scanning - demonstrated the system's ability to maintain vertical and angular stability while highlighting some limitations in lateral positioning during rapid accelerations. These limitations could be addressed through feedforward control or alternative detector triggering strategies.

Overall, the experimental results validate the effectiveness of the developed control architecture and demonstrate that the NASS meets most design specifications across a wide range of operating conditions (summarized in Table 4.17). The identified limitations, primarily related to high-speed lateral scanning and heavy payload handling, provide clear directions for future improvements.

Table 4.17: Summary of the experimental results performed using the NASS on ID31. Open-loop errors are indicated on the left of the arrows. Closed-loop errors that are outside the specifications are indicated in bold.

Experiments	D_y **[nmRMS]**	D_z **[nmRMS]**	R_y **[nradRMS]**
Tomography (6 deg/s)	142 ⇒ 15	32 ⇒ 5	464 ⇒ 56
Tomography (6 deg/s, 13 kg)	149 ⇒ 25	26 ⇒ 6	471 ⇒ 55
Tomography (6 deg/s, 26 kg)	202 ⇒ 25	36 ⇒ 7	1737 ⇒ 104
Tomography (6 deg/s, 39 kg)	297 ⇒ **53**	38 ⇒ 9	1737 ⇒ 170
Tomography (180 deg/s)	143 ⇒ **38**	24 ⇒ 11	252 ⇒ 130
Tomography (180 deg/s, custom HAC)	143 ⇒ 29	24 ⇒ 5	252 ⇒ 142
Reflectivity (100 µrad/s)	28	6	118
D_z scan (10 µm/s)	25	5	108
D_z scan (100 µm/s)	**35**	9	132
Lateral Scan (10 µm/s)	585 ⇒ 21	155 ⇒ 10	6300 ⇒ 60
Lateral Scan (100 µm/s)	1063 ⇒ **732**	167 ⇒ **20**	6445 ⇒ **356**
Diffraction tomography (6 deg/s, 0.1 mm/s)	**36**	7	113
Diffraction tomography (6 deg/s, 0.5 mm/s)	29	8	81
Diffraction tomography (6 deg/s, 1 mm/s)	**53**	10	135
Specifications	30	15	250

Conclusion

This chapter presented a comprehensive experimental validation of the Nano Active Stabilization System (NASS) on the ID31 beamline, demonstrating its capability to maintain precise sample positioning during various experimental scenarios. The implementation and testing followed a systematic approach, beginning with the development of a short-stroke metrology system to measure the sample position, followed by the successful implementation of a HAC-LAC control architecture, and concluding in extensive performance validation across diverse experimental conditions.

The short-stroke metrology system, while designed as a temporary solution, proved effective in providing high-bandwidth and low-noise 5-DoF position measurements. The careful alignment of the fibered interferometers targeting the two reference spheres ensured reliable measurements throughout the testing campaign.

The implementation of the control architecture validated the theoretical framework developed earlier in this project. The decentralized Integral Force Feedback (IFF) controller successfully provided robust damping of suspension modes across all payload conditions (0 to 39 kg), reducing peak amplitudes by approximately a factor of 10. The High Authority Controller (HAC) effectively rejects low-frequency disturbances, although its performance showed some dependency on payload mass, particularly for lateral motion control.

The experimental validation covered a wide range of scientific scenarios. The system demonstrated remarkable performance under most conditions, meeting the stringent positioning requirements (30 nm RMS in D_y, 15 nm RMS in D_z, and 250 nrad RMS in R_y) for the majority of test cases. Some limitations were identified, particularly in handling heavy payloads during rapid motions and in managing high-speed lateral scanning with the existing stepper motor T_y stage.

The successful validation of the NASS demonstrates that once an accurate online metrology system is developed, it will be ready for integration into actual beamline operations. The system's ability to maintain precise sample positioning across a wide range of experimental conditions, combined with its robust performance and adaptive capabilities, suggests that it will significantly enhance the quality and efficiency of X-ray experiments at ID31. Moreover, the systematic approach to system development and validation, along with a detailed understanding of performance limitations, provides valuable insights for future improvements and potential applications in similar high-precision positioning systems.

Experimental Validation - Conclusion

The experimental validation detailed in this chapter confirms that the Nano Active Stabilization System successfully augments the positioning capabilities of the micro-station, thereby enabling full use of the ESRF's new light source potential. A methodical approach was employed—first characterizing individual components and subsequently testing the integrated system—to comprehensively evaluate the NASS performance.

Initially, the Amplified Piezoelectric Actuators (APA300ML) were characterized, revealing consistent mechanical and electrical properties across multiple units. The implementation of Integral Force Feedback was shown to add significant damping to the system. Two models of the APA300ML were developed and validated: a simplified two-degree-of-freedom model and a more complex super-element extracted from FEA. Both models accurately represented the axial dynamics of the actuators, with the super-element model additionally capturing flexible modes.

The flexible joints were examined for geometric accuracy and bending stiffness, with measurements confirming compliance with design specifications. The experimental values demonstrated good agreement with finite element predictions, validating the joint design and enabling accurate modeling of their behavior within the system.

The strut assembly process was optimized to ensure consistent performance across the six struts. Dynamic testing revealed complex behavior in the transfer function from piezoelectric voltage to encoder displacement, attributed to misalignment between flexible joints and actuators. This finding led to the strategic decision to mount encoders on the nano-hexapod plates rather than on the struts.

The nano-hexapod was then assembled and mounted on a suspended table to characterize its dynamic behavior. The measurement setup enabled isolation of the hexapod's dynamics from potential influence of complex support dynamics. The experimental FRFs exhibited good correlation with the multi-body model, confirming that the model can be used for control system design.

Finally, the complete NASS was validated on the ID31 beamline using a short-stroke metrology system. The HAC-LAC control architecture successfully provided robust active damping of suspension modes and rejection of low-frequency disturbances across various payload conditions. Comprehensive testing under typical experimental scenarios—including tomography scans, reflectivity scans, and diffraction tomography—demonstrated the NASS ability to maintain the positioning errors within specifications (30 nm RMS in lateral direction, 15 nm RMS in vertical direction, and 250 nrad RMS in tilt direction). The system performed exceptionally well during vertical scans, though some limitations were identified during rapid lateral scanning and with heavier payloads.

With the implementation of an accurate online metrology system, the NASS will be ready for integration into the beamline environment, significantly enhancing the capabilities of high-precision X-ray experimentation on the ID31 beamline.

5 Conclusion and Future Work

5.1 Summary of Findings

The primary objective of this research was to enhance the positioning accuracy of the ID31 micro-station by approximately two orders of magnitude, to enable full exploitation of the new 4^{th} generation light source, without compromising the system's mobility or its capacity to handle payloads up to 50 kg.

To meet this demanding objective, the concept of a Nano Active Stabilization System (NASS) was proposed and developed. This system comprises an active stabilization platform positioned between the existing micro-station and the sample. Integrated with an external online metrology system and a custom control architecture, the NASS was designed to actively measure and compensate for positioning errors originating from various sources, including micro-station imperfections, thermal drift, and vibrations.

A rigorous and comprehensive mechatronic design methodology was consistently applied throughout the NASS development lifecycle. While the mechatronic approach itself is established, its thorough application in this thesis, from initial concept evaluation using simplified models to detailed design optimization and experimental validation informed by increasingly sophisticated models, offers useful insights into the existing literature. This documented process illustrates how models of varying complexity can be effectively used at different project phases, and how design decisions were systematically based on quantitative model predictions and analyses.

The conceptual design phase rigorously evaluated the feasibility of the NASS concept. A key original contribution of this work lies in the extension of active vibration control from traditional one or two degrees of freedom to a six degrees of freedom for a continuously rotating platform. Through progressive modeling, from simplified uniaxial representations to complex multi-body dynamic simulations, key design insights were obtained. It was determined that an active platform with moderate stiffness offered an optimal compromise, with good decoupling from the micro-station dynamics while mitigating gyroscopic effects induced by the spindle rotation. The multi-body modeling approach, informed by experimental modal analysis of the micro-station, was essential for capturing the system's complex dynamics. The Stewart platform architecture was selected for the active stage, and its viability was confirmed through closed-loop simulations employing a High Authority Control / Low Authority Control (HAC-LAC) strategy, demonstrating the NASS concept could meet the nanometer-level stability requirements under realistic operating conditions.

An original contribution was made in the area of active damping for rotating mechanical systems using Integral Force Feedback (IFF). It was found that the guaranteed stability property of the established IFF technique is compromised when applied to rotating platforms like the NASS. To address this, two specific modifications to the classical IFF control scheme were proposed and analyzed: one involving a minor adjustment to the control law itself, and the second incorporating physical springs in parallel with the force sensors. Stability conditions and optimal parameter tuning guidelines were derived for both modified schemes.

Following the conceptual validation, the detailed design phase focused on translating the NASS concept into an optimized, physically realizable system. Geometric optimization studies refined the Stewart platform configuration. Furthermore, a hybrid modeling technique combining Finite Element Analysis (FEA) with multi-body dynamics simulation was applied and experimentally validated. This approach enabled detailed optimization of components, such as the Amplified Piezoelectric Actuator (APA) and the flexible joint, while efficiently simulating the complete system dynamics.

Robustness was embedded directly into the active platform's design, rather than solely relying on complex post-design control synthesis techniques. This involved model-based evaluation of active stage designs to identify architectures inherently easier to control and the incorporation of collocated actuator/sensor pairs to leverage passivity-based guaranteed stability. Additionally, decoupling strategies for parallel manipulators were compared, addressing a topic identified as having limited treatment in the literature. This design approach facilitated the use of robust, readily tunable, and easily maintained controllers that met the specified performance targets.

For implementing sensor fusion, a novel method for designing complementary filters using $\mathcal{H}_\infty$-synthesis techniques was developed. This method allows explicit shaping of the filter norms, providing guarantees on the performance of the sensor fusion process.

Instrumentation selection (sensors, actuators, control hardware) was guided by dynamic error budgeting to ensure component noise levels met the overall nanometer-level performance target.

The final phase of the project was dedicated to the experimental validation of the developed NASS. Component tests confirmed the performance of the selected actuators and flexible joints, and allowed for the refinement of their respective models. Dynamic testing of the assembled nano-hexapod on an isolated test bench provided essential experimental data that correlated well with the predictions of the multi-body model.

The work culminated in the experimental validation of the complete NASS on the ID31 beamline. Experimental results demonstrated that the NASS, operating with the implemented HAC-LAC control architecture, successfully achieved the target positioning stability – maintaining residual errors below 30 nm RMS laterally, 15 nm RMS vertically, and 250 nrad RMS in tilt – during various experiments, including tomography scans with significant payloads. Crucially, the system's robustness to variations in sample mass and diverse experimental conditions was verified.

To the author's knowledge, this represents the first demonstration of such a 5-DoF active stabilization platform being used to enhance the accuracy of a complex positioning system to this level, uniquely combining high mobility, high payload capacity with nanometer-level accuracy.

The NASS enables the optimal use of the advanced capabilities of the ESRF-EBS beam, thereby opening new scientific opportunities on the ID31 beamline.

5.2 Perspectives

Although this research successfully validated the NASS concept, it concurrently highlighted specific areas where the system could be enhanced, alongside related topics that merit further investigation.

Automatic tuning of a multi-body model from an experimental modal analysis The manual tuning process employed to match the multi-body model dynamics with experimental measurements was found to be laborious. Systems like the micro-station can be conceptually modelled as interconnected solid bodies, springs, and dampers, with component inertia readily obtainable from 3D models. An interesting perspective is the development of methods for the automatic tuning of the multi-body model's stiffness matrix (representing the interconnecting spring stiffnesses) directly from experimental modal analysis data. Such a capability would enable the rapid generation of accurate dynamic models for existing end-stations, which could subsequently be used for detailed system analysis and simulation studies.

Better addressing plant uncertainty from a change of payload For most high-performance mechatronic systems like lithography machines or atomic force microscopes, payloads inertia are often known and fixed, allowing controllers to be precisely optimized. However, synchrotron end-stations frequently handle samples with widely varying masses and inertias – ID31 being an extreme example, but many require nanometer positioning for samples from very light masses up to 5 kg.

The conventional strategy involves implementing controllers with relatively small bandwidth to accommodate various payloads. When controllers are optimized for a specific payload, changing payloads may destabilize the feedback loops that needs to be re-tuned.

In this thesis, the HAC-IFF robust control approach was employed to maintain stability despite payload variations, though this resulted in relatively modest bandwidth. Therefore, a key objective for future work is to enhance the management of payload-induced plant uncertainty, aiming for improved performance without sacrificing robustness. Potential strategies to be explored include adaptive control (involving automatic plant identification and controller tuning after a change of payload) and robust control techniques such as μ-synthesis (allowing the controller to be synthesized while explicitly considering a specified range of payload masses).

Control based on Complementary Filters The control architecture based on complementary filters (detailed in Section 3.3.3) has been successfully implemented in several instruments at the European Synchrotron Radiation Facility. This approach has proven to be straightforward to implement and offers the valuable capability of modifying closed-loop behavior in real-time, which proves advantageous for many applications. For instance, the controller can be optimized according to the scan type: constant velocity scans benefit from a $+2$ slope for the sensitivity transfer function, while ptychography may be better served by a $+1$ slope with slightly higher bandwidth to minimize point-to-point transition times.

Nevertheless, a more rigorous analysis of this control architecture and its comparison with similar approaches documented in the literature is necessary to fully understand its capabilities and limitations.

Sensor Fusion While the HAC-LAC approach demonstrated a simple and comprehensive methodology for controlling the NASS, sensor fusion represents an interesting alternative that is worth investigating. While the synthesis method developed for complementary filters facilitates their design (Section 3.3.1), their application specifically for sensor fusion within the NASS context was not examined in detail.

One potential approach involves fusing external metrology (used at low frequencies) with force sensors (employed at high frequencies). This configuration could enhance robustness through the collocation of force sensors with actuators. The integration of encoder feedback into the control architecture could also be explored.

Development of multi-DoF metrology systems Although experimental validation using the short-stroke metrology prototype was achieved, the NASS remains unsuitable for beamline applications due to the lack of a long stroke metrology system. Efforts were initiated during this project to develop such a metrology system, though these were not presented herein as the focus was directed toward the active platform, instrumentation, and controllers. The development process revealed that the metrology system constitutes a complex mechatronic system, which could benefit significantly from the design approach employed throughout this thesis. This challenge is particularly complex when continuous rotation is combined with long stroke movements. Yet, the development of such metrology systems is considered critical for future end-stations, especially for future tomography end stations where nano-meter accuracy is desired across larger strokes.

Promising approaches have been presented in the literature. A ball lens retroreflector is used in [130], providing a $\approx$ 1 mm^3 measuring volume, but does not fully accommodate complete rotation. In [54], an interesting metrology approach is presented, using interferometers for long stroke/non-rotated movements and capacitive sensors for short stroke/rotated positioning.

Alternative Architecture for the NASS The original micro-station design was driven by optimizing positioning accuracy, using dedicated actuators for different degrees of freedom (leading to simple kinematics and a stacked configuration), and maximizing stiffness. This design philosophy ensured that the micro-station would remain functional for micro-focusing applications even if the NASS project did not meet expectations.

Analyzing the NASS as an complete system reveals that the positioning accuracy is primarily determined by the metrology system and the feedback control. Consequently, the underlying micro-station's own positioning accuracy has minimal influence on the final performances (it does however impact the required mobility of the active platform). Nevertheless, it remains crucial that the micro-station itself does not generate detrimental high-frequency vibrations, particularly during movements, as evidenced by issues previously encountered with stepper motors.

Designing a future end-station with the understanding that a functional NASS will ensure final positioning accuracy could allow for a significantly simplified long-stroke stage architecture, perhaps chosen primarily to facilitate the integration of the online metrology. One possible configuration, illustrated in Figure 5.1, would comprise a long-stroke Stewart platform providing the required mobility without generating high-frequency vibrations; a spindle that needs not deliver exceptional performance but should be stiff and avoid inducing high-frequency vibrations (an air-bearing spindle might not be essential); and a short-stroke Stewart platform for correcting errors from the long-stroke stage and spindle.

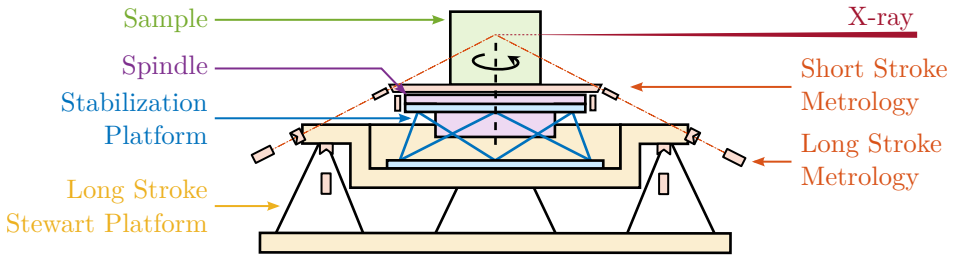

Figure 5.1: Proposed alternative configuration for an end-station including the Nano Active Stabilization System.

With this architecture, the online metrology could be divided into two systems, as proposed by [54]: a long-stroke metrology system potentially using interferometers, and a short-stroke metrology system using capacitive sensors, as successfully demonstrated by [152].

Development of long stroke high performance stage As an alternative to the short-stroke/long-stroke architecture, the development of a high-performance long-stroke stage seems worth investigating. Stages based on voice coils, offering nano-positioning capabilities with 3 mm stroke, have recently been reported in the literature [79, 130].

Magnetic levitation also emerges as a particularly interesting technology to be explored, especially for microscopy [45, 62] and tomography [42, 45] end-stations. Two notable designs illustrating these capabilities are shown in Figure 5.2. Specifically, a compact 6-DoF stage known as LevCube, providing a mobility of approximately 1 cm^3, is depicted in Figure 5.2a, while a 6-DoF stage featuring infinite rotation, is shown in Figure 5.2b. However, implementations of such magnetic levitation stages on synchrotron beamlines have yet to be documented in the literature.

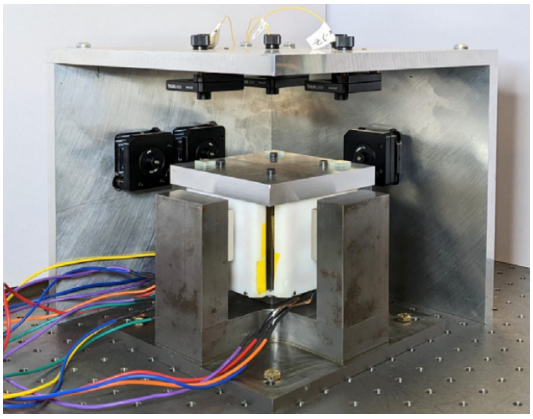

(a) LevCube with $\approx$ 1 cm^3 mobility [62]

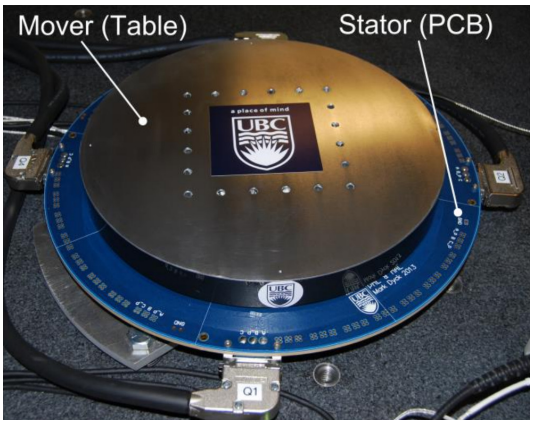

(b) Stage with infinite R_z rotation [42]

Figure 5.2: Example of magnetic levitation stages. LevCube allowing for 6-DoF control of the position with $\approx$ 1 cm^3 mobility (a). Magnetic levitation stage with infinite R_z rotation mobility (b).

Extending the design methodology to complete beamlines The application of dynamic error budgeting and the mechatronic design approach to an entire beamline represents an interesting direction for future work. During the early design phases of a beamline, performance metrics are typically expressed as integrated values (usually RMS values) rather than as functions of frequency. However, the frequency content of these performance metrics (such as beam stability, energy stability, and sample stability) is crucial, as factors like detector integration time can filter out high-frequency components. Therefore, adopting a design approach using dynamic error budgets, cascading from overall beamline requirements down to individual component specifications, is considered a potentially valuable direction for future investigation.

Bibliography

[1] H. Abbas and H. Hai. "Vibration isolation concepts for non-cubic Stewart Platform using modal control". In: *Proceedings of 11th International Bhurban Conference on Applied Sciences & Technology (IBCAST) Islamabad, Pakistan*. Jan. 2014. DOI: 10.1109/ibcast.2014.6778139 (cit. on p. 191).

[2] D. Y. Abramovitch. *Practical Methods for Real World Control Systems*. self-publishing, 2022 (cit. on p. 215).

[3] D. Y. Abramovitch, S. Andersson, K. K. Leang, W. Nagel, and S. Ruben. "A Tutorial on Real-Time Computing Issues for Control Systems". In: *2023 American Control Conference (ACC)*. May 2023, pp. 3751–3768. DOI: 10.23919/acc55779.2023.10156102 (cit. on p. 215).

[4] A. Abu Hanieh. "Active isolation and damping of vibrations via Stewart platform". PhD thesis. Université Libre de Bruxelles, Brussels, Belgium, 2003 (cit. on pp. 108, 149, 169).

[5] A. Abu Hanieh, M. Horodinca, and A. Preumont. "Stiff and Soft Stewart Platforms for Active Damping and Active Isolation of Vibrations". In: *Actuator 2002, 8th International Conference on New Actuators*. 2002 (cit. on pp. 108, 143).

[6] B. N. Agrawal and H.-J. Chen. "Algorithms for Active Vibration Isolation on Spacecraft Using a Stewart Platform". In: *Smart Materials and Structures* 13.4 (2004), pp. 873–880. DOI: 10.1088/0964-1726/13/4/025 (cit. on p. 143).

[7] W. G. Anderson and E. H. Fritze. "Instrument Approach System Steering Computer". In: *Proceedings of the IRE* 41.2 (1953), pp. 219–228. DOI: 10.1109/JRPROC.1953.274209 (cit. on p. 182).

[8] A.-J. Baerveldt and R. Klang. "A Low-Cost and Low-Weight Attitude Estimation System for an Autonomous Helicopter". In: *Proceedings of IEEE International Conference on Intelligent Engineering Systems*. 1997. DOI: 10.1109/ines.1997.632450 (cit. on p. 182).

[9] R. Barrett. *X-ray Optics at Accelerator-Based Light Sources*. Presentation. 2024 (cit. on p. 14).

[10] R. Barrett, R. Baker, P. Cloetens, et al. "Reflective Optics for Hard X-Ray Nanofocusing Applications At the Esrf". In: *Synchrotron Radiation News* 29.4 (2016), pp. 10–15. DOI: 10.1080/08940886.2016.1198668 (cit. on p. 13).

[11] P. Batista, C. Silvestre, and P. Oliveira. "Optimal Position and Velocity Navigation Filters for Autonomous Vehicles". In: *Automatica* 46.4 (2010), pp. 767–774 (cit. on p. 182).

[12] M. A. Beijen, D. Tjepkema, and J. van Dijk. "Two-Sensor Control in Active Vibration Isolation Using Hard Mounts". In: *Control Engineering Practice* 26 (2014), pp. 82–90. DOI: 10.1016/j.conengprac.2013.12.015 (cit. on p. 181).

[13] J. Bendat. "Optimum Filters for Independent Measurements of Two Related Perturbed Messages". In: *IRE Transactions on Circuit Theory* (1957). DOI: 10.1109/tct.1957.1086345 (cit. on p. 182).

[14] J. E. Bibel and D. S. Malyevac. *Guidelines for the selection of weighting functions for H-infinity control*. Tech. rep. Naval Surface Warfare Center Dahlgren div va, 1992 (cit. on pp. 202, 204).

[15] R. G. Brown. "Integrated Navigation Systems and Kalman Filtering: a Perspective". In: *Navigation* 19.4 (1972), pp. 355–362. DOI: 10.1002/j.2161-4296.1972.tb01706.x (cit. on p. 182).

[16] R. G. Brown and P. Y. C. Hwang. *Introduction to Random Signals and Applied Kalman Filtering with Matlab Exercises*. 4th ed. Wiley, 2012. ISBN: 0470609699 (cit. on p. 182).

[17] P. Brumund and T. Dehaeze. "Multibody Simulations with Reduced Order Flexible Bodies Obtained by FEA". In: *Proc. MEDSI'20* (Chicago, USA, Jul. 2021). 11. JACoW Publishing, Geneva, Switzerland, 2021, p. 286. DOI: 10.18429/JACoW-MEDSI2020-WEPB08 (cit. on p. 21).

[18] S. L. Brunton and J. N. Kutz. *Data-driven science and engineering: Machine learning, dynamical systems, and control*. Cambridge University Press, 2022 (cit. on p. 198).

[19] H. Butler. "Position Control in Lithographic Equipment". In: *IEEE Control Systems* 31.5 (2011), pp. 28–47. DOI: 10.1109/mcs.2011.941882 (cit. on p. 195).

[20] A. Cardona and M. Géradin. "A Superelement Formulation for Mechanism Analysis". In: *Computer Methods in Applied Mechanics and Engineering* 100.1 (1992), pp. 1–29. DOI: 10.1016/0045-7825(92)90112-W.

[21] H.-J. Chen, R. Bishop, and B. Agrawal. "Payload Pointing and Active Vibration Isolation Using Hexapod Platforms". In: *44th Structural Dynamics, and Materials Conference*. Apr. 2003. DOI: 10.2514/6.2003-1643 (cit. on pp. 143, 144).

[22] Y. Chen and J. E. McInroy. "Decoupled Control of Flexure-Jointed Hexapods Using Estimated Joint-Space Mass-Inertia Matrix". In: *IEEE Transactions on Control Systems Technology* 12.3 (2004), pp. 413–421. DOI: 10.1109/tcst.2004.824339 (cit. on p. 116).

[23] S. Chesné, A. Milhomem, and C. Collette. "Enhanced Damping of Flexible Structures Using Force Feedback". In: *Journal of Guidance, Control, and Dynamics* 39.7 (2016), pp. 1654–1658. DOI: 10.2514/1.g001620 (cit. on p. 56).

[24] W. Chi, D. Cao, D. Wang, et al. "Design and Experimental Study of a Vcm-Based Stewart Parallel Mechanism Used for Active Vibration Isolation". In: *Energies* 8.8 (2015), pp. 8001–8019. DOI: 10.3390/en8088001 (cit. on p. 143).

[25] F. Claeyssen, R. Le Letty, F. Barillot, and O. Sosnicki. "Amplified Piezoelectric Actuators: Static & Dynamic Applications". In: *Ferroelectrics* 351.1 (2007), pp. 3–14. DOI: 10.1080/00150190701351865 (cit. on p. 163).

[26] C. Collette, S. Janssens, and K. Artoos. "Review of Active Vibration Isolation Strategies". In: *Recent Patents on Mechanical Engineeringe* 4.3 (2011), pp. 212–219. DOI: 10.2174/2212797611104030212 (cit. on p. 55).

[27] C. Collette, S. Janssens, P. Fernandez-Carmona, et al. "Review: Inertial Sensors for Low-Frequency Seismic Vibration Measurement". In: *Bulletin of the Seismological Society of America* 102.4 (2012), pp. 1289–1300. DOI: 10.1785/0120110223 (cit. on p. 30).

[28] C. Collette and F. Matichard. "Sensor Fusion Methods for High Performance Active Vibration Isolation Systems". In: *Journal of Sound and Vibration* 342 (2015), pp. 1–21. DOI: 10.1016/j.jsv.2015.01.006 (cit. on pp. 40, 182, 202).

[29] P. Corke. "An Inertial and Visual Sensing System for a Small Autonomous Helicopter". In: *Journal of Robotic Systems* 21.2 (2004), pp. 43–51. DOI: 10.1002/rob.10127 (cit. on p. 182).

[30] R. R. Craig and M. C. C. Bampton. "Coupling of Substructures for Dynamic Analyses." In: *AIAA Journal* 6.7 (1968), pp. 1313–1319. DOI: 10.2514/3.4741 (cit. on p. 162).

[31] B. Dasgupta and T. S. Mruthyunjaya. "The Stewart Platform Manipulator: a Review". In: *Mechanism and Machine Theory* 35.1 (2000), pp. 15–40. DOI: 10.1016/s0094-114x(99)00006-3 (cit. on p. 142).

[32] B Fraeijs De Veubeke. "The Dynamics of Flexible Bodies". In: *International Journal of Engineering Science* 14.10 (1976), pp. 895–913. DOI: 10.1016/0020-7225(76)90102-6.

[33] T. Dehaeze. *Nano Active Stabilization of samples for tomography experiments: A mechatronic design approach (data, scripts and models)*. May 2025. DOI: 10.5281/zenodo.15254389 (cit. on p. 6).

[34] T. Dehaeze, J. Bonnefoy, and G. R. L. Collette. "Mechatronics Approach for the Development of a Nano-Active-Stabilization-System". In: *Proc. MEDSI'20* (Chicago, USA, Jul. 2021). 11. JACoW Publishing, Geneva, Switzerland, 2021, p. 93. DOI: 10.18429/JACoW-MEDSI2020-TUIO02 (cit. on pp. 21, 107).

[35] T. Dehaeze and C. Collette. "Active Damping of Rotating Platforms Using Integral Force Feedback". In: *Engineering Research Express* (Feb. 2021). DOI: 10.1088/2631-8695/abe803 (cit. on pp. 22, 52).

[36] T. Dehaeze and C. Collette. "Active Damping of Rotating Platforms using Integral Force Feedback". In: *Proceedings of the International Conference on Modal Analysis Noise and Vibration Engineering (ISMA)*. 2020 (cit. on p. 52).

[37] T. Dehaeze and L. Ducotté. "The Fastjack - A robust, UHV compatible and high performance linear actuator". In: EUSPEN. 2022 (cit. on p. 312).

[38] T. Dehaeze, M. Magnin Mattenet, and C. Collette. "Sample Stabilization For Tomography Experiments In Presence Of Large Plant Uncertainty". In: *MEDSI'18* (Paris, France). Mechanical Engineering Design of Synchrotron Radiation Equipment and Instrumentation 10. Geneva, Switzerland: JACoW Publishing, Dec. 2018, pp. 153–157. DOI: 10.18429/JACoW-MEDSI2018-WEOAMA02 (cit. on pp. 21, 107).

[39] T. Dehaeze, M. Verma, and C. Collette. "Complementary Filters Shaping Using $\mathcal{H}_\infty$ Synthesis". In: *7th International Conference on Control, Mechatronics and Automation (ICCMA)*. 2019, pp. 459–464. DOI: 10.1109/ICCMA46720.2019.8988642 (cit. on pp. 22, 182, 183).

[40] W. Dong, L. N. Sun, and Z. J. Du. "Design of a Precision Compliant Parallel Positioner Driven By Dual Piezoelectric Actuators". In: *Sensors and Actuators A: Physical* 135.1 (2007), pp. 250–256. DOI: 10.1016/j.sna.2006.07.011 (cit. on p. 107).

[41] Z. Du, R. Shi, and W. Dong. "A Piezo-Actuated High-Precision Flexible Parallel Pointing Mechanism: Conceptual Design, Development, and Experiments". In: *IEEE Transactions on Robotics* 30.1 (2014), pp. 131–137. DOI: 10.1109/tro.2013.2288800 (cit. on pp. 20, 144, 174, 191, 202).

[42] M. Dyck, X. Lu, and Y. Altintas. "Magnetically Levitated Six Degree of Freedom Rotary Table". In: *CIRP Annals* 64.1 (2015), pp. 353–356. DOI: 10.1016/j.cirp.2015.04.107 (cit. on p. 323).

[43] C. Engblom. "Nanoprobe Results: Metrology & Control in Stacked Closed-Loop Systems". In: *Proc. of International Conference on Accelerator and Large Experimental Control Systems (ICALEPCS'17)*. JACoW, Jan. 2018. DOI: 10.18429/JACoW-ICALEPCS2017-WEAPL04 (cit. on pp. 16, 17, 107).

[44] D. J. Ewins. *Modal Testing: Theory, Practice and Application, Second Edition*. Baldock, Hertfordshire, England Philadelphia, PA: Wiley-Blackwell, 2000, p. 562. ISBN: 0863802184 (cit. on pp. 75, 76, 79).

[45] A. Fahmy. "Magnetically levitated XY-THETA motion stage for X-ray microscopy applications". PhD thesis. The University of Texas at Austin, 2022 (cit. on p. 323).

[46] J. L. Fanson and T. K. V. Caughey. "Positive Position Feedback Control for Large Space Structures". In: *AIAA journal* 28.4 (1990), pp. 717–724 (cit. on p. 55).

[47] A. J. Fleming. "A Review of Nanometer Resolution Position Sensors: Operation and Performance". In: *Sensors and Actuators A: Physical* 190 (2013), pp. 106–126. DOI: 10.1016/j.sna.2012.10.016 (cit. on p. 218).

[48] A. J. Fleming and K. K. Leang. *Design, Modeling and Control of Nanopositioning Systems*. Advances in Industrial Control. Springer International Publishing, 2014. DOI: 10.1007/978-3-319-06617-2 (cit. on pp. 164, 214, 248).

[49] A. J. Fleming and K. K. Leang. "Integrated Strain and Force Feedback for High-Performance Control of Piezoelectric Actuators". In: *Sensors and Actuators A: Physical* 161.1-2 (2010), pp. 256–265 (cit. on pp. 164, 248).

[50] F. P. N. da Fonseca Cardoso Carreira, J. M. F. Calado, C. B. Cardeira, P. J. C. R. Oliveira, et al. "Complementary Filter Design with Three Frequency Bands: Robot Attitude Estimation". In: *2015 IEEE International Conference on Autonomous Robot Systems and Competitions*. 2015, pp. 168–173. DOI: 10.1109/ICARSC.2015.33 (cit. on pp. 182, 189).

[51] K. Furutani, M. Suzuki, and R. Kudoh. "Nanometre-Cutting Machine Using a Stewart-Platform Parallel Mechanism". In: *Measurement Science and Technology* 15.2 (2004), pp. 467–474. DOI: 10.1088/0957-0233/15/2/022 (cit. on pp. 108, 143, 144, 156, 191, 202).

[52] Z. J. Geng and L. S. Haynes. "Six Degree-Of-Freedom Active Vibration Control Using the Stewart Platforms". In: *IEEE Transactions on Control Systems Technology* 2.1 (1994), pp. 45–53. DOI: 10.1109/87.273110 (cit. on p. 149).

[53] Z. J. Geng, G. G. Pan, L. S. Haynes, B. K. Wada, and J. A. Garba. "An Intelligent Control System for Multiple Degree-Of-Freedom Vibration Isolation". In: *Journal of Intelligent Material Systems and Structures* 6.6 (1995), pp. 787–800. DOI: 10.1177/1045389x9500600607 (cit. on pp. 143, 180).

[54] R. R. Geraldes, G. B. Z. L. Moreno, F. R. Lena, et al. "The high-dynamic cryogenic sample stage for SAPOTI/CARNAÚBA at Sirius/LNLS". In: *Proceedings of XRM2022*. Jan. 2023. DOI: 10.1063/5.0168438 (cit. on pp. 16, 17, 105, 107, 322).

[55] V. E. Gough. "Universal Tyre Test Machine". In: *Proc. FISITA 9th Int. Technical Congr., London, 1962*. 1962, pp. 117–137 (cit. on p. 142).

[56] B. Gustavsen and A. Semlyen. "Rational Approximation of Frequency Domain Responses By Vector Fitting". In: *IEEE Transactions on Power Delivery* 14 (3 July 1999). DOI: 10.1109/61.772353 (cit. on p. 243).

[57] M. R. Hatch. *Vibration simulation using MATLAB and ANSYS*. CRC Press, 2000. ISBN: 978-1-58488-205-3 (cit. on p. 162).

[58] T. Hatsui and H. Graafsma. "X-Ray Imaging Detectors for Synchrotron and XFEL Sources". In: *IUCrJ* 2.3 (2015), pp. 371–383. DOI: 10.1107/s205225251500010x (cit. on p. 13).

[59] G. S. Hauge and M. E. Campbell. "Sensors and Control of a Space-Based Six-Axis Vibration Isolation System". In: *Journal of Sound and Vibration* 269.3-5 (2004), pp. 913–931. DOI: 10.1016/s0022-460x(03)00206-2 (cit. on pp. 20, 143, 180, 202, 242).

[60] M. W. Hauser. "Principles of Oversampling A/D Conversion". In: *Journal of Audio Engineering Society* (1991) (cit. on p. 219).

[61] J. V. van Heijningen. "Low-frequency performance improvement of seismic attenuation systems and vibration sensors for next generation gravitational wave detectors". PhD thesis. Vrije Universiteit, 2018 (cit. on p. 182).

[62] I. L. Heyman, J. Wu, and L. Zhou. "Levcube: a Six-Degree-Of-Freedom Magnetically Levitated Nanopositioning Stage With Centimeter-Range Xyz Motion". In: *Precision Engineering* 83 (2023), pp. 102–111. DOI: 10.1016/j.precisioneng.2023.04.008 (cit. on p. 323).

[63] W. T. Higgins. "A Comparison of Complementary and Kalman Filtering". In: *IEEE Transactions on Aerospace and Electronic Systems* 3 (1975), pp. 321–325 (cit. on p. 182).

[64] R. Hino, P. Fajardo, N. Janvier, T. Le Caër, and F. Le Mentec. "A Position Encoder Processing Unit". In: *Proceedings of the 16th Int. Conf. on Accelerator and Large Experimental Control Systems* ICALEPCS2017 (2018). DOI: 10.18429/JACOW-ICALEPCS2017-THPHA072 (cit. on p. 295).

[65] M. Holler, J. Raabe, A. Diaz, et al. "Omny-A Tomography Nano Cryo Stage". In: *Review of Scientific Instruments* 89.4 (2018), p. 043706. DOI: 10.1063/1.5020247 (cit. on pp. 16, 17, 107).

[66] M. Holler, J. Raabe, R. Wepf, et al. "Omny Pin-A Versatile Sample Holder for Tomographic Measurements At Room and Cryogenic Temperatures". In: *Review of Scientific Instruments* 88.11 (2017), p. 113701. DOI: 10.1063/1.4996092 (cit. on pp. 16, 17, 107).

[67] J. Holterman and T. J. A. de Vries. "Active Damping Based on Decoupled Collocated Control". In: *IEEE/ASME Transactions on Mechatronics* 10.2 (2005), pp. 135–145. DOI: 10.1109/tmech.2005.844702 (cit. on p. 192).

[68] M. Hovd, R. D. Braatz, and S. Skogestad. "SVD Controllers for $\mathcal{H}_2-$, $\mathcal{H}_\infty-$ and μ-optimal Control". In: *Automatica* 33.3 (1997), pp. 433–439 (cit. on p. 200).

[69] W. Hua, D. B. Debra, C. T. Hardham, B. T. Lantz, and J. A. Giaime. "Polyphase FIR Complementary Filters for Control Systems". In: *Proceedings of ASPE Spring Topical Meeting on Control of Precision Systems*. 2004, pp. 109–114 (cit. on p. 182).

[70] Wensheng Hua, R Adhikari, Daniel B DeBra, et al. "Low frequency vibration isolation and alignment system for advanced LIGO". PhD thesis. stanford university, 2005 (cit. on p. 182).

[71] X. Huang, K. Lauer, J. N. Clark, et al. "Fly-Scan Ptychography". In: *Scientific Reports* 5.1 (2015), p. 9074. DOI: 10.1038/srep09074 (cit. on p. 13).

[72] The MathWorks Inc. *MATLAB R2022a*. Natick, Massachusetts, United States, 2022.

[73] F. Jafari and J. E. McInroy. "Orthogonal Gough-Stewart Platforms for Micromanipulation". In: *IEEE Transactions on Robotics and Automation* 19.4 (Aug. 2003), pp. 595–603. ISSN: 1042-296X. DOI: 10.1109/tra.2003.814506 (cit. on pp. 149, 153).

[74] N. Janvier, J. M. Clement, P. Fajardo, and G. Cuní. "Icepap: an Advanced Motor Controller for Scientific Applications in Large User Facilities". In: *ICALEPCS2013, San Francisco*. 2013 (cit. on p. 312).

[75] A. Jensen, C. Coopmans, and Y. Chen. "Basics and guidelines of complementary filters for small UAS navigation". In: *2013 International Conference on Unmanned Aircraft Systems (ICUAS)*. May 2013. DOI: 10.1109/icuas.2013.6564726 (cit. on p. 182).

[76] J. Jiao, Y. Wu, K. Yu, and R. Zhao. "Dynamic Modeling and Experimental Analyses of Stewart Platform With Flexible Hinges". In: *Journal of Vibration and Control* 25.1 (2018), pp. 151–171. DOI: 10.1177/1077546318772474 (cit. on pp. 143, 192, 202).

[77] D. Karnopp, M. J. Crosby, and R. A. Harwood. "Vibration Control Using Semi-Active Force Generators". In: *Journal of Engineering for Industry* 96 (1974), pp. 619–626. DOI: 10.1115/1.3438373 (cit. on pp. 35, 55).

[78] G. Kazezkhan, B. Xiang, N. Wang, and A. Yusup. "Dynamic Modeling of the Stewart Platform for the Nanshan Radio Telescope". In: *Advances in Mechanical Engineering* 12.7 (2014). DOI: 10.1177/1687814020940072 (cit. on p. 142).

[79] J. Kelly, A. Male, N. Rubies, et al. "The Delta Robot-A Long Travel Nano-Positioning Stage for Scanning X-Ray Microscopy". In: *Review of Scientific Instruments* 93.4 (2022). DOI: 10.1063/5.0084806 (cit. on pp. 16, 17, 107, 323).

[80] B. J. Kenton and K. K. Leang. "Design and Control of a Three-Axis Serial-Kinematic High-Bandwidth Nanopositioner". In: *IEEE/ASME Transactions on Mechatronics* 17.2 (2012), pp. 356–369. DOI: 10.1109/tmech.2011.2105499 (cit. on p. 108).

[81] D. H. Kim, J.-Y. Kang, and K.-I. Lee. "Robust Tracking Control Design for a 6 Dof Parallel Manipulator". In: *Journal of Robotic Systems* 17.10 (2000), pp. 527–547. DOI: 10.1002/1097-4563(200010)17:10$<$527::AID-ROB2>3.0.CO;2-A (cit. on pp. 144, 191).

[82] B. A. Kouvaritakis. "Theory and Practice of the Characteristic Locus Design Method". In: *Proceedings of the Institution of Electrical Engineers* 126.6 (1979), p. 542. DOI: 10.1049/piee.1979.0131 (cit. on p. 199).

[83] Silicon Lab. *Improving the ADC resolution by oversampling and averaging*. Tech. rep. Silicon Laboratories, 2013 (cit. on p. 219).

[84] G. F. Lang. "Understanding modal vectors". In: *Topics in Modal Analysis & Testing, Volume 10*. Springer, 2017. Chap. 8, pp. 55–68 (cit. on p. 197).

[85] S. Leake, G. Chahine, H. Djazouli, et al. "The Nanodiffraction Beamline ID01/ESRF: a Microscope for Imaging Strain and Structure". In: *Journal of Synchrotron Radiation* 26.2 (2019), pp. 571–584. DOI: 10.1107/s160057751900078x (cit. on p. 15).

[86] L. Lei and W. Benli. "Multi Objective Robust Active Vibration Control for Flexure Jointed Struts of Stewart Platforms Via H_∞ and μ Synthesis". In: *Chinese Journal of Aeronautics* 21.2 (2008), pp. 125–133. DOI: 10.1016/s1000-9361(08)60016-3 (cit. on p. 192).

[87] X. Li. "Simultaneous, Fault-tolerant Vibration Isolation and Pointing Control of Flexure Jointed Hexapods". PhD thesis. University of Wyoming, 2001 (cit. on pp. 143, 144, 153).

[88] Xiaochun Li, Jerry C. Hamann, and John E. McInroy. "Simultaneous Vibration Isolation and Pointing Control of Flexure Jointed Hexapods". In: *Smart Structures and Materials 2001: Smart Structures and Integrated Systems*. Aug. 2001. DOI: 10.1117/12.436521 (cit. on pp. 180, 191).

[89] H. Lin and J. E. McInroy. "Disturbance Attenuation in Precise Hexapod Pointing Using Positive Force Feedback". In: *Control Engineering Practice* 14.11 (2006), pp. 1377–1386. DOI: 10.1016/j.conengprac.2005.10.002 (cit. on p. 55).

[90] T. Lucia. "Low Frequency Optimization and Performance of Advanced Virgo Seismic Isolation System". PhD thesis. University of Siena, 2018 (cit. on p. 182).

[91] Richard H MacNeal. "A Hybrid Method of Component Mode Synthesis". In: *Computers & Structures* 1.4 (1971), pp. 581–601. DOI: 10.1016/0045-7949(71)90031-9.

[92] P. Marion, F. Comin, G. Rostaining, et al. "Hexapods at the ESRF: mechanical aspects results obtained". In: *MEDSI 2004 proceedings*. 2004, pp. 1–9 (cit. on p. 142).

[93] B. de Marneffe. "Active and Passive Vibration Isolation and Damping via Shunted Transducers". PhD thesis. Université Libre de Bruxelles, Brussels, Belgium, 2007 (cit. on p. 58).

[94] G. Martínez-Criado, J. Villanova, R. Tucoulou, et al. "Id16b: a Hard X-Ray Nanoprobe Beamline At the Esrf for Nano-Analysis". In: *Journal of Synchrotron Radiation* 23.1 (2016), pp. 344–352. DOI: 10.1107/s1600577515019839 (cit. on pp. 15, 16).

[95] F Matichard, B Lantz, R Mittleman, et al. "Seismic Isolation of Advanced Ligo: Review of Strategy, Instrumentation and Performance". In: *Classical and Quantum Gravity* 32.18 (2015), p. 185003 (cit. on pp. 182, 189).

[96] J. E. McInroy. "Dynamic modeling of flexure jointed hexapods for control purposes". In: *Proceedings of the 1999 IEEE International Conference on Control Applications (Cat. No.99CH36328)*. 1999. DOI: 10.1109/cca.1999.806694 (cit. on pp. 143, 153).

[97] J. E. McInroy. "Modeling and Design of Flexure Jointed Stewart Platforms for Control Purposes". In: *IEEE/ASME Transactions on Mechatronics* 7.1 (2002), pp. 95–99. DOI: 10.1109/3516.990892 (cit. on pp. 116, 147, 174).

[98] J. E. McInroy and J. C. Hamann. "Design and Control of Flexure Jointed Hexapods". In: *IEEE Transactions on Robotics and Automation* 16.4 (2000), pp. 372–381. DOI: 10.1109/70.864229 (cit. on pp. 116, 147, 151, 191).

[99] J. P. Merlet. *Parallel Robots*. 2nd. Springer Publishing Company, Incorporated, 2006. ISBN: 9048170532 (cit. on p. 143).

[100] J.-P. Merlet. "Still a long way to go on the road for parallel mechanisms". In: *Proc. ASME 2002 DETC Conf., Montreal*. 2002 (cit. on p. 145).

[101] S. O. R. Moheimani and A. J. Fleming. *Piezoelectric Transducers for Vibration Control and Damping*. London: Springer, 2006. ISBN: 9781846283314 (cit. on pp. 220, 240).

[102] W. Monkhorst. "Dynamic Error Budgeting, a design approach". PhD thesis. Delft University, 2004 (cit. on p. 23).

[103] S. I. Moore, A. J. Fleming, and Y. K. Yong. "Capacitive Instrumentation and Sensor Fusion for High-Bandwidth Nanopositioning". In: *IEEE Sensors Letters* 3.8 (2019), pp. 1–3. DOI: 10.1109/lsens.2019.2933065 (cit. on p. 182).

[104] M. Naves. "Design and Optimization of Large Stroke Flexure Mechanisms". PhD thesis. Univeristy of Twente, May 2021. DOI: 10.3990/1.9789036549943 (cit. on p. 144).

[105] E. Nazaretski, D. S. Coburn, W. Xu, et al. "A New Kirkpatrick-Baez-Based Scanning Microscope for the Submicron Resolution X-Ray Spectroscopy (SRX) Beamline At Nsls-Ii". In: *Journal of Synchrotron Radiation* 29.5 (2022), pp. 1284–1291. DOI: 10.1107/s1600577522007056 (cit. on pp. 16, 17, 107).

[106] E. Nazaretski, K. Lauer, H. Yan, et al. "Pushing the Limits: an Instrument for Hard X-Ray Imaging Below 20 Nm". In: *Journal of Synchrotron Radiation* 22.2 (2015), pp. 336–341. DOI: 10.1107/s1600577514025715 (cit. on pp. 16, 17, 105, 107).

[107] E. Nazaretski, H. Yan, K. Lauer, et al. "Design and Performance of an X-Ray Scanning Microscope At the Hard X-Ray Nanoprobe Beamline of Nsls-Ii". In: *Journal of Synchrotron Radiation* 24.6 (2017), pp. 1113–1119. DOI: 10.1107/s1600577517011183 (cit. on p. 17).

[108] A. Okyay. "Mechatronic Design, Dynamics, Controls, and Metrology of a Long-Stroke Linear Nano-Positioner". PhD thesis. University of Waterloo, 2016 (cit. on p. 23).

[109] A. Pascoal, I. Kaminer, and P. Oliveira. "Navigation System Design Using Time-Varying Complementary Filters". In: *Guidance, Navigation, and Control Conference and Exhibit*. 1999. DOI: 10.2514/6.1999-4290 (cit. on p. 182).

[110] R. Pintelon and J. Schoukens. *System Identification : a Frequency Domain Approach*. Hoboken, N.J. Piscataway, NJ: Wiley IEEE Press, 2012. DOI: 10.1002/9781118287422 (cit. on p. 167).

[111] A. R. Plummer. "Optimal Complementary Filters and Their Application in Motion Measurement". In: *Proceedings of the Institution of Mechanical Engineers, Part I: Journal of Systems and Control Engineering* 220.6 (2006), pp. 489–507. DOI: 10.1243/09596518JSCE229 (cit. on pp. 182, 183).

[112] A. Preumont. *Random Vibration and Spectral Analysis*. Solid Mechanics and Its Applications. Springer Netherlands, 1994. DOI: 10.1007/978-94-017-2840-9 (cit. on p. 100).

[113] A. Preumont. *Vibration Control of Active Structures - Fourth Edition*. Solid Mechanics and Its Applications. Springer International Publishing, 2018. DOI: 10.1007/978-3-319-72296-2 (cit. on pp. 35, 37, 41, 63, 68, 108, 149, 176, 197, 241).

[114] A. Preumont, B. De Marneffe, and S. Krenk. "Transmission Zeros in Structural Control With Collocated Multi-Input/multi-Output Pairs". In: *Journal of guidance, control, and dynamics* 31.2 (2008), pp. 428–432 (cit. on pp. 56, 58, 123, 131).

[115] A. Preumont, J.-P. Dufour, and C. Malekian. "Active damping by a local force feedback with piezoelectric actuators". In: *32nd Structures, Structural Dynamics, and Materials Conference*. American Institute of Aeronautics and Astronautics, Apr. 1991. DOI: 10.2514/6.1991-989 (cit. on pp. 35, 55, 58).

[116] A. Preumont, A. François, F. Bossens, and A. Abu-Hanieh. "Force Feedback Versus Acceleration Feedback in Active Vibration Isolation". In: *Journal of Sound and Vibration* 257.4 (2002), pp. 605–613. DOI: 10.1006/jsvi.2002.5047 (cit. on pp. 35, 55, 56).

[117] A. Preumont, M. Horodinca, I. Romanescu, et al. "A Six-Axis Single-Stage Active Vibration Isolator Based on Stewart Platform". In: *Journal of Sound and Vibration* 300.3-5 (2007), pp. 644–661. DOI: 10.1016/j.jsv.2006.07.050 (cit. on pp. 108, 120, 143, 149, 174, 175).

[118] H. Pu, X. Chen, Z. Zhou, and X. Luo. "Six-Degree-Of-Freedom Active Vibration Isolation System With Decoupled Collocated Control". In: *Proceedings of the Institution of Mechanical Engineers, Part B: Journal of Engineering Manufacture* 226.2 (2011), pp. 313–325. DOI: 10.1177/0954405411414336 (cit. on p. 192).

[119] Z. H. Rahman, J. T. Spanos, and R. A. Laskin. "Multiaxis vibration isolation, suppression, and steering system for space observational applications". In: *Telescope Control Systems III*. May 1998. DOI: 10.1117/12.308821 (cit. on p. 143).

[120] P. Raimondi, N. Carmignani, L. R. Carver, et al. "Commissioning of the Hybrid Multibend Achromat Lattice At the European Synchrotron Radiation Facility". In: *Physical Review Accelerators and Beams* 24.11 (2021), p. 110701. DOI: 10.1103/physrevaccelbeams.24.110701 (cit. on p. 10).

[121] A. M. Rankers. "Machine dynamics in mechatronic systems: An engineering approach." PhD thesis. University of Twente, 1998. ISBN: 90-365-0957-2 (cit. on pp. 50, 162, 176, 196).

[122] C. Riekel. "Microfocus Workshop At the Esrf". In: *Synchrotron Radiation News* 2.1 (1989), pp. 8–9. DOI: 10.1080/08940888908261187 (cit. on p. 13).

[123] C. Riekel, M. Burghammer, and R. Davies. "Progress in Micro- and Nano-Diffraction At the Esrf Id13 Beamline". In: *IOP Conference Series: Materials Science and Engineering* 14 (2010), p. 012013. DOI: 10.1088/1757-899x/14/1/012013 (cit. on p. 15).

[124] M. Russo, D. Zhang, X.-J. Liu, and Z. Xie. "A Review of Parallel Kinematic Machine Tools: Design, Modeling, and Applications". In: *International Journal of Machine Tools and Manufacture* 196 (2024), p. 104118. DOI: 10.1016/j.ijmachtools.2024.104118 (cit. on p. 142).

[125] C. Sanchez-Cano, I. Romero-Canelón, Y. Yang, et al. "Synchrotron X-Ray Fluorescence Nanoprobe Reveals Target Sites for Organo-Osmium Complex in Human Ovarian Cancer Cells". In: *Chemistry - A European Journal* 23.11 (2017), pp. 2512–2516. DOI: 10.1002/chem.201605911 (cit. on pp. 12, 13).

[126] S. Saxena and Y. V. Hote. "Advances in Internal Model Control Technique: a Review and Future Prospects". In: *IETE Technical Review* 29.6 (2012), p. 461. DOI: 10.4103/0256-4602.105001 (cit. on p. 210).

[127] R. M. Schmidt, G. Schitter, and A. Rankers. *The Design of High Performance Mechatronics - Third Revised Edition*. Ios Press, 2020. ISBN: 978-1-64368-050-7 (cit. on pp. 17, 34, 172, 202, 216).

[128] V. Schoeppler, E. Reich, J. Vacelet, et al. "Shaping Highly Regular Glass Architectures: a Lesson From Nature". In: *Science Advances* 3.10 (2017), eaao2047. DOI: 10.1126/sciadv.aao2047 (cit. on p. 12).

[129] C. G. Schroer, M. Seyrich, M. Kahnt, et al. "PtyNAMi: Ptychographic Nano-Analytical Microscope at PETRA III: interferometrically tracking positions for 3D x-ray scanning microscopy using a ball-lens retroreflector". In: *X-Ray Nanoimaging: Instruments and Methods III*. Sept. 2017. DOI: 10.1117/12.2273710 (cit. on pp. 16, 17, 106, 107).

[130] A. Schropp, R. Döhrmann, S. Botta, et al. "Ptynami: Ptychographic Nano-Analytical Microscope". In: *Journal of Applied Crystallography* 53.4 (2020), pp. 957–971. DOI: 10.1107/s1600576720008420 (cit. on pp. 16, 17, 106, 107, 322, 323).

[131] M. Serrand and S. J. Elliott. "Multichannel Feedback Control for the Isolation of Base-Excited Vibration". In: *Journal of Sound and Vibration* 234.4 (2000), pp. 681–704. DOI: 10.1006/jsvi.2000.2891 (cit. on pp. 35, 55).

[132] F. R. Shaw and K. Srinivasan. "Bandwidth Enhancement of Position Measurements Using Measured Acceleration". In: *Mechanical Systems and Signal Processing* 4.1 (1990), pp. 23–38. DOI: 10.1016/0888-3270(90)90038-m (cit. on p. 182).

[133] Y. Shen, X. Luo, S. Wang, and X. Li. "Dynamic Analysis of a 5-dof Flexure-based Nanopositioning Stage". In: *Mathematical Problems in Engineering* 2019.1 (2019). DOI: 10.1155/2019/8501583 (cit. on pp. 107, 108).

[134] S. Skogestad and I. Postlethwaite. *Multivariable Feedback Control: Analysis and Design - Second Edition*. John Wiley, 2007. ISBN: 0470011688 (cit. on pp. 58, 125, 187, 198, 202, 205, 206, 304).

[135] A. Souleille, T. Lampert, V. Lafarga, et al. "A Concept of Active Mount for Space Applications". In: *CEAS Space Journal* 10.2 (2018), pp. 157–165 (cit. on pp. 169, 170, 246).

[136] J. Spanos, Z. Rahman, and G. Blackwood. "A Soft 6-axis Active Vibration Isolator". In: *Proceedings of 1995 American Control Conference - ACC'95*. 1995. DOI: 10.1109/acc.1995.529280 (cit. on pp. 143, 242).

[137] W. M. van Spengen. *High Voltage Amplifiers: So you think you have noise!* Tech. rep. Falco Systems, 2020 (cit. on p. 215).

[138] T. Stankevic, C. Engblom, F. Langlois, et al. "Interferometric Characterization of Rotation Stages for X-Ray Nanotomography". In: *Review of Scientific Instruments* 88.5 (2017), p. 053703. DOI: 10.1063/1.4983405 (cit. on pp. 16, 17, 107).

[139] D. Stewart. "A Platform With Six Degrees of Freedom". In: *Proceedings of the institution of mechanical engineers* 180.1 (1965), pp. 371–386 (cit. on pp. 108, 142, 148).

[140] D. P. Stoten. "Fusion of Kinetic Data Using Composite Filters". In: *Proceedings of the Institution of Mechanical Engineers, Part I: Journal of Systems and Control Engineering* 215.5 (2001), pp. 483–497 (cit. on pp. 182, 189).

[141] H. Taghirad. *Parallel robots : mechanics and control*. Boca Raton, FL: CRC Press, 2013. ISBN: 9781466555778 (cit. on pp. 88, 107).

[142] J. Tang, D. Cao, and T. Yu. "Decentralized Vibration Control of a Voice Coil Motor-Based Stewart Parallel Mechanism: Simulation and Experiments". In: *Proceedings of the Institution of Mechanical Engineers, Part C: Journal of Mechanical Engineering Science* 233.1 (2018), pp. 132–145. DOI: 10.1177/0954406218756941 (cit. on p. 143).

[143] Y. R. Teo and A. J. Fleming. "Optimal Integral Force Feedback for Active Vibration Control". In: *Journal of Sound and Vibration* 356 (Nov. 2015), pp. 20–33. DOI: 10.1016/j.jsv.2015.06.046 (cit. on p. 56).

[144] D. Thayer, M. Campbell, J. Vagners, and A. von Flotow. "Six-Axis Vibration Isolation System Using Soft Actuators and Multiple Sensors". In: *Journal of Spacecraft and Rockets* 39.2 (2002), pp. 206–212. DOI: 10.2514/2.3821 (cit. on pp. 143, 144, 149, 181, 192, 202, 242).

[145] D. Thayer and J. Vagners. "A look at the pole/zero structure of a Stewart platform using special coordinate basis". In: *Proceedings of the 1998 American Control Conference. ACC (IEEE Cat. No.98CH36207)*. 1998. DOI: 10.1109/acc.1998.703595 (cit. on pp. 143, 144).

[146] Y. Ting, H.-C. Jar, and C.-C. Li. "Measurement and Calibration for Stewart Micromanipulation System". In: *Precision Engineering* 31.3 (2007), pp. 226–233. DOI: 10.1016/j.precisioneng.2006.09.004 (cit. on p. 144).

[147] Y. Ting, C.-C. Li, and T. V. Nguyen. "Composite Controller Design for a 6dof Stewart Nanoscale Platform". In: *Precision Engineering* 37.3 (2013), pp. 671–683. DOI: 10.1016/j.precisioneng.2013.01.012 (cit. on p. 144).

[148] D. Tjepkema, J. van Dijk, and H. M. J. R. Soemers. "Sensor Fusion for Active Vibration Isolation in Precision Equipment". In: *Journal of Sound and Vibration* 331.4 (2012), pp. 735–749. DOI: 10.1016/j.jsv.2011.09.022 (cit. on pp. 181, 182).

[149] T. T. L. Tsang, T. G. F. Li, T. Dehaeze, and C. Collette. "Optimal Sensor Fusion Method for Active Vibration Isolation Systems in Ground-Based Gravitational-Wave Detectors". In: *Classical and Quantum Gravity* 39.18 (2022), p. 185007. DOI: 10.1088/1361-6382/ac8780 (cit. on p. 22).

[150] M. Verma, T. Dehaeze, G. Zhao, J. Watchi, and C. Collette. "Virtual Sensor Fusion for High Precision Control". In: *Mechanical Systems and Signal Processing* 150 (2020), p. 107241. DOI: 10.1016/j.ymssp.2020.107241 (cit. on pp. 22, 202).

[151] M. Verma, A. Pece, S. Hellegouarch, et al. "Dynamic Stabilization of Thin Aperture Light Collector Space Telescope Using Active Rods". In: *Journal of Astronomical Telescopes, Instruments, and Systems* 6.01 (2020), p. 1. DOI: 10.1117/1.jatis.6.1.014002 (cit. on p. 169).

[152] F. Villar, L. Andre, R. Baker, et al. "Nanopositioning for the Esrf Id16a Nano-Imaging Beamline". In: *Synchrotron Radiation News* 31.5 (2018), pp. 9–14. DOI: 10.1080/08940886.2018.1506234 (cit. on pp. 16, 17, 106, 107, 142, 322).

[153] C. Wang, X. Xie, Y. Chen, and Z. Zhang. "Investigation on Active Vibration Isolation of a Stewart Platform With Piezoelectric Actuators". In: *Journal of Sound and Vibration* 383 (Nov. 2016), pp. 1–19. ISSN: 0022-460X. DOI: 10.1016/j.jsv.2016.07.021 (cit. on pp. 143, 180).

[154] J. Wang, Y.-c. K. Chen, Q. Yuan, et al. "Automated Markerless Full Field Hard X-Ray Microscopic Tomography At Sub-50 Nm 3-dimension Spatial Resolution". In: *Applied Physics Letters* 100.14 (2012), p. 143107. DOI: 10.1063/1.3701579 (cit. on pp. 16, 17).

[155] J. Watchi, S. Cooper, B. Ding, C. M. Mow-Lowry, and C. Collette. "A Review of Compact Interferometers". In: *Review of Scientific Instruments* 89.12 (Dec. 2018), p. 121501. ISSN: 0034-6748. DOI: 10.1063/1.5052042 (cit. on p. 294).

[156] E. Wehrsdorfer, G. Borchhardt, W. Karthe, and G. Helke. "Large Signal Measurements on Piezoelectric Stacks". In: *Ferroelectrics* 174.1 (1995), pp. 259–275 (cit. on p. 236).

[157] J. Wright, C. Giacobbe, and M. Majkut. "New Opportunities At the Materials Science Beamline At Esrf To Exploit High Energy Nano-Focus X-Ray Beams". In: *Current Opinion in Solid State and Materials Science* 24.2 (2020), p. 100818. DOI: 10.1016/j.cossms.2020.100818 (cit. on pp. 15, 16).

[158] X. Xie, C. Wang, and Z. Zhang. "Modeling and Control of A Hybrid Passive/Active Stewart Vibration Isolation Platform". In: *INTER-NOISE and NOISE-CON Congress and Conference Proceedings*. Vol. 255. 6. Institute of Noise Control Engineering. 2017, pp. 1844–1853 (cit. on pp. 180, 192).

[159] W. Xu, H. Xu, D. Gavrilov, et al. "High-speed fly-scan capabilities for x-ray microscopy systems at NSLS-II". In: *X-Ray Nanoimaging: Instruments and Methods VI*. Oct. 2023. DOI: 10.1117/12.2675940 (cit. on pp. 13, 16, 17).

[160] X. Yang, H. Wu, B. Chen, S. Kang, and S. Cheng. "Dynamic Modeling and Decoupled Control of a Flexible Stewart Platform for Vibration Isolation". In: *Journal of Sound and Vibration* 439 (Jan. 2019), pp. 398–412. ISSN: 0022-460X. DOI: 10.1016/j.jsv.2018.10.007 (cit. on pp. 143, 144, 156, 174, 181, 192, 202).

[161] T.-J. Yeh, C.-Y. Su, and W.-J. Wang. "Modelling and Control of a Hydraulically Actuated Two-Degree-Of-Freedom Inertial Platform". In: *Proceedings of the Institution of Mechanical Engineers, Part I: Journal of Systems and Control Engineering* 219.6 (2005), pp. 405–417. DOI: 10.1243/095965105x33527 (cit. on p. 182).

[162] Y. K. Yong and A. J. Fleming. "High-Speed Vertical Positioning Stage With Integrated Dual-Sensor Arrangement". In: *Sensors and Actuators A: Physical* 248 (2016), pp. 184–192. ISSN: 0924-4247. DOI: 10.1016/j.sna.2016.06.042 (cit. on p. 182).

[163] H. Yun, L. Liu, Q. Li, W. Li, and L. Tang. "Development of an Isotropic Stewart Platform for Telescope Secondary Mirror". In: *Mechanical Systems and Signal Processing* 127 (2019), pp. 328–344. DOI: 10.1016/j.ymssp.2019.03.001 (cit. on p. 142).

[164] Z. Zhang, J. Liu, J. Mao, Y. Guo, and Y. Ma. "Six DOF active vibration control using stewart platform with non-cubic configuration". In: *2011 6th IEEE Conference on Industrial Electronics and Applications*. June 2011. DOI: 10.1109/iciea.2011.5975679 (cit. on pp. 143, 144).

[165] G. Zhao, A. Paknejad, A. Deraemaeker, and C. Collette. "$\mathcal{H}_\infty$ Optimization of an Integral Force Feedback Controller". In: *Journal of Vibration and Control* 25.17 (2019), pp. 2330–2339 (cit. on p. 56).

[166] M. Zimmermann and W. Sulzer. "High Bandwidth Orientation Measurement and Control Based on Complementary Filtering". In: *Robot Control 1991*. Robot Control 1991 (1992), pp. 525–530. DOI: 10.1016/b978-0-08-041276-4.50093-5 (cit. on pp. 182, 183).

List of Publications

Articles

M. Verma, T. Dehaeze, G. Zhao, J. Watchi, and C. Collette. "Virtual Sensor Fusion for High Precision Control". In: *Mechanical Systems and Signal Processing* 150 (2020), p. 107241. DOI: 10.1016/j.ymssp.2020.107241.

M. Verma, V. Lafarga, T. Dehaeze, and C. Collette. "Multi-Degree of Freedom Isolation System With High Frequency Roll-Off for Drone Camera Stabilization". In: *IEEE Access* (2020). DOI: 10.1109/ACCESS.2020.3027066.

T. Dehaeze and C. Collette. "Active Damping of Rotating Platforms Using Integral Force Feedback". In: *Engineering Research Express* (Feb. 2021). DOI: 10.1088/2631-8695/abe803.

T. T. L. Tsang, T. G. F. Li, T. Dehaeze, and C. Collette. "Optimal Sensor Fusion Method for Active Vibration Isolation Systems in Ground-Based Gravitational-Wave Detectors". In: *Classical and Quantum Gravity* 39.18 (2022), p. 185007. DOI: 10.1088/1361-6382/ac8780.

In Proceedings

T. Dehaeze, M. Magnin Mattenet, and C. Collette. "Sample Stabilization For Tomography Experiments In Presence Of Large Plant Uncertainty". In: *MEDSI'18* (Paris, France). Mechanical Engineering Design of Synchrotron Radiation Equipment and Instrumentation 10. Geneva, Switzerland: JACoW Publishing, Dec. 2018, pp. 153–157. DOI: 10.18429/JACoW-MEDSI2018-WEOAMA02.

T. Dehaeze, M. Verma, and C. Collette. "Complementary Filters Shaping Using $\mathcal{H}_\infty$ Synthesis". In: *7th International Conference on Control, Mechatronics and Automation (ICCMA)*. 2019, pp. 459–464. DOI: 10.1109/ICCMA46720.2019.8988642.

T. Dehaeze and C. Collette. "Active Damping of Rotating Platforms using Integral Force Feedback". In: *Proceedings of the International Conference on Modal Analysis Noise and Vibration Engineering (ISMA)*. 2020.

P. Brumund and T. Dehaeze. "Multibody Simulations with Reduced Order Flexible Bodies Obtained by FEA". In: *Proc. MEDSI'20* (Chicago, USA, Jul. 2021). 11. JACoW Publishing, Geneva, Switzerland, 2021, p. 286. DOI: 10.18429/JACoW-MEDSI2020-WEPB08.

T. Dehaeze, J. Bonnefoy, and G. R. L. Collette. "Mechatronics Approach for the Development of a Nano-Active-Stabilization-System". In: *Proc. MEDSI'20* (Chicago, USA, Jul. 2021). 11. JACoW Publishing, Geneva, Switzerland, 2021, p. 93. DOI: 10.18429/JACoW-MEDSI2020-TUIO02.

T. Dehaeze and L. Ducotté. "The Fastjack - A robust, UHV compatible and high performance linear actuator". In: EUSPEN. 2022.

Acronyms

Notation	Description
ADC	Analog to Digital Converter
APA	Amplified Piezoelectric Actuator
ASD	Amplitude Spectrum Density
CAS	Cumulative Amplitude Spectrum
CL	Closed Loop
CMIF	Complex Modal Indication Function
CoK	Center of Stiffness
CoM	Center of Mass
DAC	Digital to Analog Converter
DoF	Degrees of Freedom
EBS	Extremely Brilliant Source
EDM	Electrical Discharge Machining
ESRF	European Synchrotron Radiation Facility
FEA	Finite Element Analysis
FEM	Finite Element Model
FRF	Frequency Response Function
HAC	High Authority Control
HAC-LAC	High Authority Control / Low Authority Control
HPF	High Pass Filter
IFF	Integral Force Feedback
LPF	Low Pass Filter
LQG	Linear Quadratic Gaussian
LSB	Least Significant Bit
LTI	Linear Time Invariant
LVDT	Linear Variable Differential Transformer
MIF	Modal Indication Function
MIMO	Multi Inputs Multi Outputs
NASS	Nano Active Stabilization System
NP	Nominal Performance
NS	Nominal Stability
OL	Open Loop
PI	Proportional Integral
PID	Proportional Integral Derivative
PoI	Point of Interest
PSD	Power Spectral Density
RDC	Relative Damping Control
RGA	Relative Gain Array
RMS	Root Mean Square
RP	Robust Performance
RPM	Rotations Per Minute
RS	Robust Stability
SISO	Single Input Single Output
SPS	Samples per Second
SVD	Singular Value Decomposition
VC	Voice Coil